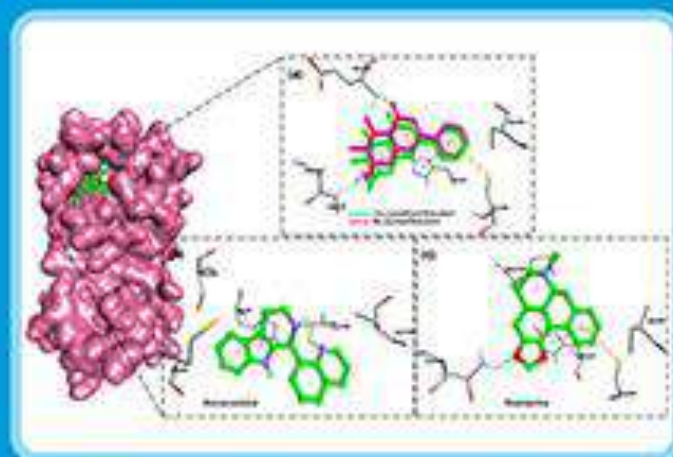


ISSN: 1411-9429 (print), 2460-1576 (online)

Indonesian Journal of Chemistry

Vol. 23, No. 3, June 2023



Approved by PRO PER-RIKES
No. 80/840/P/2022

Indonesian J. Chem

Vol. 23

No. 3

PP 583-608

Yogyakarta
June 2023

10.24127/ijc.v23i3.12345

Dye-Sensitized Solar Cell Photoelectrochemical Tandem System Performance Study: TiO₂ Nanotube/N719, BiVO₄/TiO₂ Nanotube, Ti³⁺/TiO₂ Nanotube for Nitrogen Reduction Reaction to Ammonia

Suharyadi Suharyadi*, Muhammad Iqbal Syauqi, Prita Amelia, Yunita Yunita, and Jarnuzi Gunlazard

Department of Chemistry, Faculty of Mathematics and Natural Sciences, Universitas Indonesia, Kampus UI, Depok 16424, Indonesia

* **Corresponding author:**

tel: +62-85719243866

email: suharyadi@ui.ac.id

Received: July 18, 2022

Accepted: February 17, 2023

DOI: 10.22146/ijc.76270

Abstract: Ammonia is commonly synthesized through the Haber-Bosch process, which produces large amounts of CO₂ emissions as it is carried out at extreme temperatures and pressures. An alternative technology is needed to synthesize ammonia which consumes less energy and is environmentally friendly. In this research, a Dye-Sensitized Solar Cell Photoelectrochemical tandem system (DSSC-PEC) was developed for the nitrogen reduction reaction (NRR) into ammonia. PEC cells utilized BiVO₄/TiO₂ Nanotube (BiVO₄/TiO₂NT) as a photoanode for water oxidation. BiVO₄/TiO₂NT was synthesized by the successive ionic layer adsorption and reaction (SILAR) with the cycles variation of 10, 15, and 20 cycles. The optimization method for 20 cycles (20s) gave the highest photocurrent of 0.352 mA/cm². As a cathode where the nitrogen reduction reaction to ammonia takes place, Ti³⁺/TiO₂NT was used. DSSC based on TiO₂NT/N719 with an efficiency of 1.13% was used as an energy booster in the reaction. Using this system with an electrodes area of 3 cm², under visible light irradiation on photoanode and DSSC while dark at the cathode, the rate of ammonia production, analyzed using the phenate method, was 0.022 μmol.h⁻¹.cm⁻² with solar to chemical conversion (SCC) efficiency of 0.003%.

Keywords: BiVO₄/TiO₂NT; DSSC-PEC; SILAR; NRR; ammonia

■ INTRODUCTION

Ammonia (NH₃) is an important chemical and is widely used in various chemical industrial applications and processes, especially in making fertilizers as a nutrient for plants [1]. Ammonia is produced through the Haber-Bosch process using H₂ and N₂ at high pressure (> 200 bar) and high temperature (> 673 K) [2]. However, the use of natural gas as a source of H₂ obtained by steam reforming of hydrocarbon sources consumes about 1–2% of the world's energy annually by releasing hundreds of millions of tons of CO₂ annually [3]. To minimize the negative environmental impact, it is necessary to find alternative technologies for making ammonia with low energy requirements, abundant raw materials, and not producing CO₂ gas. One way that has attracted the attention of many parties is to carry out nitrogen reduction reactions (NRR) through photoelectrochemistry [4].

Photoelectrochemistry (PEC) is a combination of photochemical and electrochemical processes. In the PEC setting, NRR occurs at the cathode site using a catalyst having an active site capable of activating the stable triple bond of N₂, while at the anode, a catalyst that can oxidize water well under visible light exposure is desired. Several studies have been conducted using the PEC method, Liu et al. [5] used a photoelectrochemical method for the reduction of N₂ to ammonia using black phosphorus-produced ammonia with a Faraday efficiency of 23.3%. Liu et al. [6] have developed a photocatalytic method using TiO₂ nanoparticles with oxygen vacancy for nitrogen fixation with the highest ammonia generation rate of 116 μmol.g⁻¹.h⁻¹.

TiO₂ is one of the semiconductors that is widely used as a photoelectrode in PEC cells with various advantages such as high efficiency, low cost, physical and

chemical stability, wide availability, non-corrosive, and environmentally friendly [7]. TiO_2 in the form of 1D nanostructures such as nanotubes (TiO_2NT) exhibits a very large surface-to-volume ratio and significantly increased light absorption [8-9]. It is well known that the population of Ti^{3+} in TiO_2 could serve as an active site to carry out the NRR reaction [2]. However, to be used as a photoanode, TiO_2 is still lacking. As it has a band gap of about 3.2 eV, the absorption only occurs in the UV region; TiO_2 is not an efficient photocatalyst under sunlight irradiation, which contains >95% infrared and visible light while only ~5% UV light. Therefore, it is very important to develop photocatalysts that can be used in both UV light (290–400 nm) and visible light (400–700 nm) to increase the efficiency of photocatalysis [10].

It is necessary to modify TiO_2 , one of which is the $\text{BiVO}_4/\text{TiO}_2\text{NT}$ heterojunction, to increase light absorption in the visible light region. BiVO_4 has a band gap of 2.4 eV. Zhu et al. [11] reported that the $\text{BiVO}_4/\text{TiO}_2$ heterojunction has 1.4 times higher photocatalytic activity compared to pure BiVO_4 . The incorporation of TiO_2 with another semiconductor not only affects the light absorption ability but can increase the specific surface area and pore diameter.

The use of the Dye-Sensitized Solar Cell Photoelectrochemical (DSSC-PEC) tandem system can increase light absorption in the visible light region compared to without DSSC. Several studies have been conducted on DSSC-PEC tandem cells, among others; Surahman [12] conducted the development of PEC cells using CdS nanoparticle sensitized TiO_2 nanotube arrays for hydrogen production with hydrogen gas formation rate of 13.44 L/min and energy efficiency cells through the process of breaking water by 4.78%. Samsudin et al. [13] developed a tandem DSSC-PEC system with thin films of $\text{BiVO}_4/\text{TiO}_2\text{NT}$ for hydrogen production to produce 692 mol of hydrogen in 120 min.

Research developments related to the performance of $\text{Ti}^{3+}/\text{TiO}_2\text{NT}$ for NRR applications, $\text{BiVO}_4/\text{TiO}_2\text{NT}$ as a photoanode, and DSSC N719 have been widely reported. However, the combined system of PEC-based $\text{BiVO}_4/\text{TiO}_2\text{NT}$ as photoanode, $\text{Ti}^{3+}/\text{TiO}_2\text{NT}$ as cathode,

and DSSC-based N719 as a whole tandem system to do NRR to ammonia, as far as the authors' knowledge, has not been reported. In this study, an evaluation of the performance of the DSSC-PEC tandem system for the NRR to ammonia was carried out using $\text{Ti}^{3+}/\text{TiO}_2\text{NT}$ as a cathode. As a photoanode, TiO_2NT -modified BiVO_4 was used using the SILAR method. As for the DSSC zone, $\text{TiO}_2\text{NT}/\text{N719}$ sandwich cells, I^-/I_3^- , and Pt/FTO electrolytes are used. This research is expected to contribute to the development of alternative methods for producing environmentally friendly ammonia with relatively low energy consumption.

■ EXPERIMENTAL SECTION

Materials

The materials used in this study were titanium plate (99.6% purity Baoji Jinsheng Metal Material Co. Ltd), acetone ($\text{C}_3\text{H}_6\text{O}$) ($\geq 99.5\%$ purity Sigma-Aldrich), bismuth nitrate pentahydrate ($\text{Bi}(\text{NO}_3)_3 \cdot 5\text{H}_2\text{O}$) (98% purity Sigma-Aldrich), ethanol ($\text{C}_2\text{H}_5\text{OH}$) (99.9% purity Sigma-Aldrich), ethylene glycol ($\text{C}_2\text{H}_6\text{O}$) (99.8% purity Sigma-Aldrich), ammonium vanadate (NH_4VO_3) ($\geq 99.0\%$ purity Sigma-Aldrich), FTO, sodium sulfate (Na_2SO_4) ($\geq 99\%$ purity Sigma-Aldrich), trisodium citrate ($\text{Na}_3\text{C}_6\text{H}_5\text{O}_7$) ($\geq 98\%$ purity Sigma-Aldrich), sodium hypochlorite (NaOCl) from Sigma-Aldrich, nitric acid (HNO_3) (65% purity Sigma-Aldrich), sodium hydroxide (NaOH) ($\geq 98\%$ purity Sigma-Aldrich), ammonium chloride (NH_4Cl) ($\geq 99.5\%$ purity Sigma-Aldrich), sodium nitroprusside (SNP) from Sigma-Aldrich, dye N719 (95% purity Sigma-Aldrich), Nafion membrane 117, and phenol (99% purity Sigma-Aldrich), and deionized water from OneMed.

Instrumentation

TiO_2NT and $\text{BiVO}_4/\text{TiO}_2\text{NT}$ were characterized using XRD (X'pert PRO merk PANalitical MPD PAW3040/60), FTIR (Shimadzu IR Prestige 21), UV-Vis DRS (Shimadzu UV-2450), SEM-EDX (Quanta 650 of Thermo Scientific), and Potentiostat (PAR-VersaStat II). While $\text{Ti}^{3+}/\text{TiO}_2\text{NT}$ was characterized using FTIR, UV Vis DRS, and Potentiostat.

Procedure

Synthesis of TiO_2 nanotubes (TiO_2NT) and $\text{Ti}^{3+}/\text{TiO}_2\text{NT}$

The titanium plate (0.3 mm thickness, 99.6%) was sanded with 1000 and 1500 cc abrasive paper, then sonicated in a solution of acetone, ethanol, and air deionized for 16 min, then dried in air. Anodization was conducted in an electrochemical cell consisting of two electrodes, a Ti plate ($4\text{ cm} \times 1.5\text{ cm} \times 0.02\text{ cm}$) as an anode, and stainless steel as a cathode. Ethylene glycol solution containing 0.3% NH_4F and 2% H_2O was used as an electrolyte. The distance between the two electrodes is set to about 1.5 cm. The anodizing potential was carried out at 40 V, and the anodization time of 45 min. After the anodization process, the samples were rinsed with deionized water and dried in the air, then calcined at a temperature of $450\text{ }^\circ\text{C}$ for 2 h with a temperature rise rate of $10\text{ }^\circ\text{C}/\text{min}^{-1}$ [12].

The synthesis of $\text{Ti}^{3+}/\text{TiO}_2\text{NT}$ used an electrochemical reduction method with a three-electrode system with TiO_2NT as the working electrode, Pt as the counter electrode, and Ag/AgCl as the reference electrode. Then put into 0.1 M Na_2SO_4 electrolyte solution and given a potential of -1.5 V for 20 min [14].

Synthesis of $\text{BiVO}_4/\text{TiO}_2\text{NT}$

A solution of 50 mL $\text{Bi}(\text{NO}_3)_3$ 0.02 M was prepared in beaker 1, and 50 mL NH_4VO_3 0.02 M was prepared in beaker 2. The solvent for NH_4VO_3 is deionized water,

while the solvent for $\text{Bi}(\text{NO}_3)_3$ is a mixture of nitric acid and water ($V_{\text{nitric acid}}:V_{\text{water}} = 1:19$). TiO_2 nanotube plate substrate was immersed in beaker 1 for 30 s and then immersed in beaker 2 for 30 s. This process is defined as one cycle. The process was done for 10, 15, and 20 cycles in ultrasonication, denoted as 10 s, 15 s, and 20 s, respectively. Each immersion of the TiO_2 nanotube plate was rinsed with deionized water and dried in the air after all cycles were completed. Then, the prepared samples were calcined at $500\text{ }^\circ\text{C}$ for 2 h at a heating rate of $10\text{ }^\circ\text{C}/\text{min}^{-1}$ [15].

DSSC fabrication, $\text{TiO}_2\text{NT}/\text{N719}$

TiO_2 nanotubes were immersed in a $300\text{ }\mu\text{M}$ N719 color solution (ethanol solvent) for 24 h. After 24 h of immersion, $\text{TiO}_2\text{NT}/\text{N719}$ was cleaned with ethanol and dried in the air [16]. $\text{TiO}_2\text{NT}/\text{N719}$ as an anode, electrolyte I^-/I_3^- , and Pt/FTO as a cathode. The arrangement of the DSSC cells follows a sandwich cell configuration, electrolyte I^-/I_3^- is dripped on the surface of the anode ($\text{TiO}_2\text{NT}/\text{N719}$), then parafilm as a separator between the anode and cathode to avoid short circuit current, and then closed with a cathode (Pt/FTO).

DSSC-PEC preparation and performance evaluation

PEC cells consist of $\text{BiVO}_4/\text{TiO}_2\text{NT}$ as a photoanode and $\text{Ti}^{3+}/\text{TiO}_2\text{NT}$ as a dark cathode. $\text{TiO}_2\text{NT}/\text{N719}$ as an anode in the DSSC zone is connected

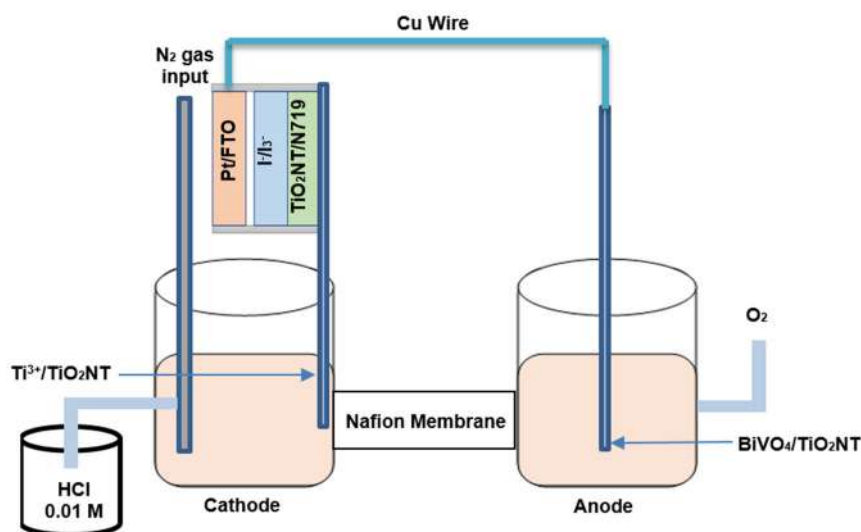


Fig 1. Schematic of DSSC-PEC Tandem System for A and B conditions (A: dark cathode, B: full irradiation)

to the PEC cathode ($\text{Ti}^{3+}/\text{TiO}_2\text{NT}$), while the PEC photoanode ($\text{BiVO}_4/\text{TiO}_2\text{NT}$) is connected to the DSSC cathode (Pt/FTO) with a copper wire. The evaluation of the system to produce NH_3 was conducted with two irradiation conditions. The A condition (dark cathode) was when the DSSC and anode were illuminated while the cathode was dark. The condition when all the systems (DSSC and PEC) were illuminated is denoted with B condition (full irradiation). The efficiency of ammonia conversion was calculated using the Solar to Chemical Conversion (SCC) equation as shown in Eq. (1) [2]:

$$\text{SCC Efficiency (\%)} = \frac{\Delta G \text{ for } \text{NH}_3 \text{ (J/mol)} \times \text{NH}_3 \text{ formed (mol)}}{\text{total input energy (W)} \times \text{reaction time (s)}} \times 100\% \quad (1)$$

■ RESULTS AND DISCUSSION

Characterization of Photoanode Materials

Fig. 2(a) shows the FTIR spectra of the synthesized materials. The results of FTIR characterization on TiO_2NT and $\text{BiVO}_4/\text{TiO}_2\text{NT}$ contained OH groups stretching at wavenumbers $3400\text{--}3000 \text{ cm}^{-1}$, OH bending at wavenumbers $1800\text{--}1400 \text{ cm}^{-1}$, Ti-O-Ti at wavenumbers $900\text{--}700 \text{ cm}^{-1}$. The wide peak at a wave number of around $400\text{--}700 \text{ cm}^{-1}$ is the asymmetric stretching of the vanadate due to the BiVO_4 monoclinic.

Fig. 2(b) shows the results of the XRD characterization of TiO_2NT and $\text{BiVO}_4/\text{TiO}_2\text{NT}$. In the TiO_2NT diffraction pattern, diffraction peaks were observed at positions 2θ : 25.31° , 35.05° , 38.26° , 40.11° , 48.09° , 53.05° , 53.88° , 55.06° , 63.06° , 70.60° , 76.19° , and 82.34° . Based on JCPDS data No. 00-02101272, the typical peaks of anatase crystals are at the 2θ positions: 25.281° , 37.801° , 38.576° , 48.050° , 53.801° , 55.062° , 70.311° , 75.032° , 76.020° , and 93.221° . Meanwhile, based on data from JCPDS No. 00-044-1294, the typical peaks of titanium metal are in the 2θ positions: 35.09° , 38.43° , 40.17° , 53.01° , 62.94° , 70.66° , 76.23° , 77.38° , and 82.30° . Based on the JCPDS data, it is known that the crystalline phase formed in the synthesized TiO_2NT is the anatase phase. In the $\text{BiVO}_4/\text{TiO}_2\text{NT}$ diffraction pattern, additional diffraction peaks were observed, which were then compared with JCPDS data No. 14-0688 for the monoclinic scheelite phase BiVO_4 [17]. It can be observed

at 10 cycles of SILAR deposition, and there was 1 additional peak at position 2θ 18.88° (110); at 15 cycles, there was 1 additional peak at position 2θ 28.91° (121), and at 20 cycles, there were 3 additional peaks at positions 2θ 18.88° (110), 28.91° (121), and 30.59° (040) indicating the presence of BiVO_4 . The intensity of the XRD peak should increase along with the increase of BiVO_4 thickness. However, our work observed an anomaly of difference peak observed at 10 and 15 cycles. This phenomenon may be caused by several factors: 1) The amount of BiVO_4 concentration on TiO_2NT was too small and not well dispersed for 10 and 15 cycles; 2) Different properties on the TiO_2NT substrate; 3) Physical damage of the sample, or; 4) The unstandardized SILAR deposition process, as the difference in each dipping time, pH solution, might lead to a different crystal growth orientation [18]. Of course, to prove these hypotheses, more elaborate work should be done. However, for this work, the samples were used as it is. Thus, based on the result of the three cycles, the best is SILAR with 20 cycles with 3 peaks of BiVO_4 ; this is because more BiVO_4 has been deposited on the TiO_2NT surface so that the dominant BiVO_4 facet is formed.

Fig. 2(c) shows UV-DRS spectra to determine the band gap value of the synthesized materials. Bandgap values can be calculated using the Tauc plot of the Kubelka-Munk function:

$$F(R)h\nu^2 = B(h\nu - E_g) \quad (2)$$

The equation is a direct band gap. Based on this equation, the bandgap value of TiO_2NT is 3.21 eV. Based on the literature, the band gap value of TiO_2NT is 3.20 eV [19]. This band gap value indicates that the synthesized TiO_2NT was in the anatase phase. Furthermore, the synthesized TiO_2NT was deposited with BiVO_4 through the SILAR process with 3 cycle variations, namely 10, 15, and 20 cycles. The resulting band gap value decreases as the number of cycles increases, where the band gap value is 2.83 eV, 2.81 eV, and 2.79 eV, respectively. Based on the literature, the band gap value of BiVO_4 is 2.4 eV [20], the bandgap value which is between the bandgap value of pure TiO_2NT anatase (3.20 eV) and BiVO_4 monoclinic (2.40 eV) indicates the

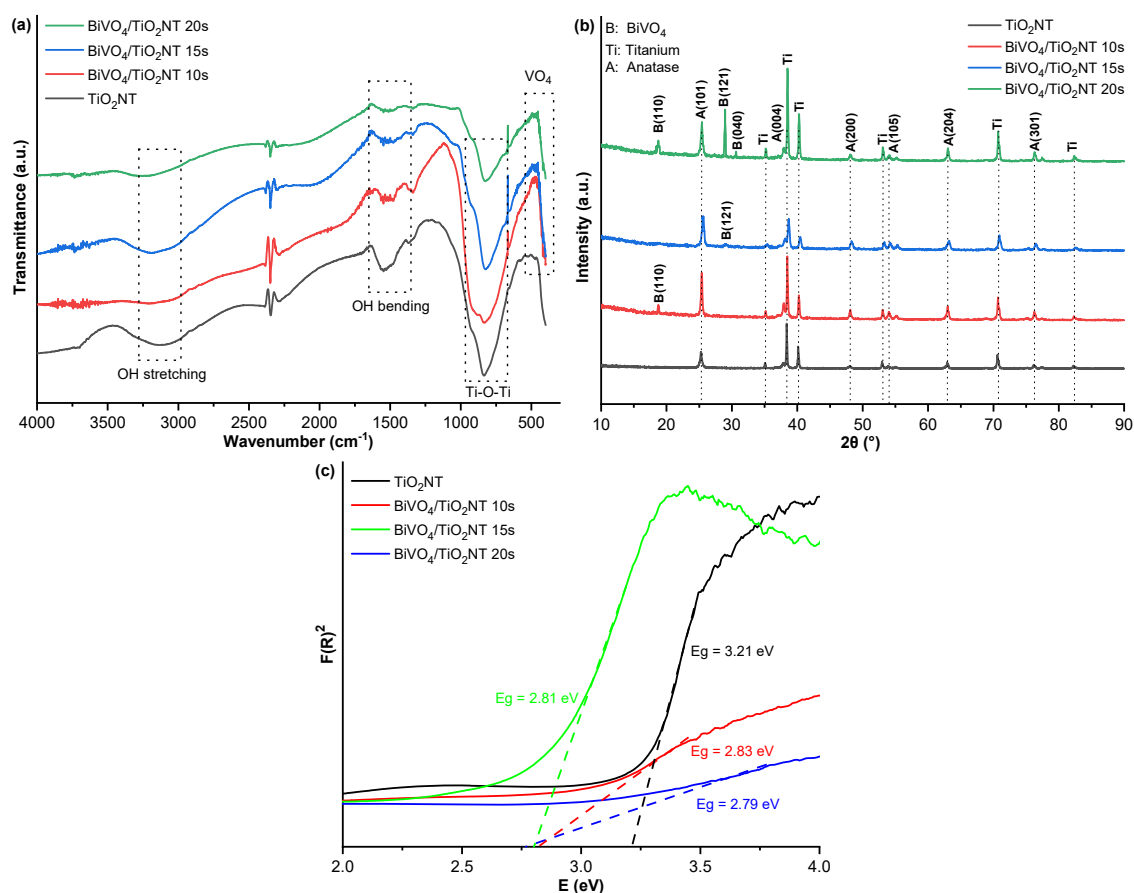


Fig 2. (a) FTIR spectrum; (b) XRD spectra; and (c) the Tauc plot of the Kubelka-Munk function of TiO_2NT and $\text{BiVO}_4/\text{TiO}_2\text{NT}$ with SILAR cycle variations

formation of a mixed phase of $\text{BiVO}_4/\text{TiO}_2\text{NT}$ heterojunction. The decrease in band gap value indicates that $\text{BiVO}_4/\text{TiO}_2\text{NT}$ synthesized by the SILAR method can be active against visible light [21].

The morphology of the synthesized TiO_2NT was then characterized using SEM-EDX. Fig. 3(a) and 3(b) show the morphology of TiO_2 at the surface and cross-section. Based on this figure, it can be observed that TiO_2 formed has nanotube morphology with an average pore diameter of about 56.44 nm and a tube height of 3.11 μm . Several factors affect the morphology of nanotubes, such as the time and anodization potential, the distance between the electrodes, and the composition of the electrolyte [22].

Fig. 3(c) and 3(d) show the SEM results of $\text{BiVO}_4/\text{TiO}_2\text{NT}$ 20 cycles (the 20s) surface and cross-section. It can be seen that the yellow BiVO_4 has stuck to the surface of the TiO_2NT and does not close the pores so

that it can increase the surface area. Fig. 4 shows the EDX spectra of TiO_2NT and $\text{BiVO}_4/\text{TiO}_2\text{NT}$ 20s synthesis results. Based on these results, it is known that the synthesized TiO_2NT is composed of Ti and O elements with a ratio of 1:2 atom percentage to form TiO_2 . While for the sample $\text{BiVO}_4/\text{TiO}_2\text{NT}$ 20s, the percentage atom of Bi:V:Ti:O is 2.1:2.2:26.6:69.1, which shows the amount mass of BiVO_4 deposited with 20 cycles is 23.97%.

Fig. 5(a) is the resulting curve for the photoelectrochemical activity of TiO_2NT and $\text{BiVO}_4/\text{TiO}_2\text{NT}$ using the Linear Sweep Voltammetry (LSV) method. The results obtained show a comparison of the current density response to the potential between TiO_2NT and $\text{BiVO}_4/\text{TiO}_2\text{NT}$ using visible light with a white LED lamp 13 W. The curve shows that $\text{BiVO}_4/\text{TiO}_2\text{NT}$ has a higher current density than TiO_2NT . As the number of SILAR cycles increases, the current density response also increases. This indicates

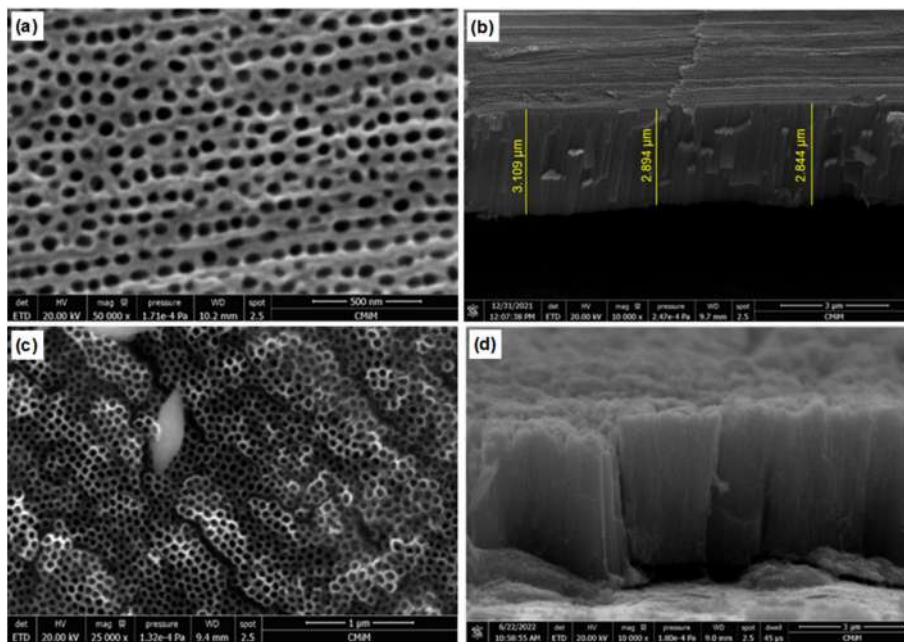


Fig 3. SEM results of (a) TiO₂NT surface 50,000×, (b) TiO₂NT cross-section 10,000×, (c) BiVO₄/TiO₂NT surface 25,000× and (d) BiVO₄/TiO₂NT cross-section 10,000× with 20 cycles SILAR

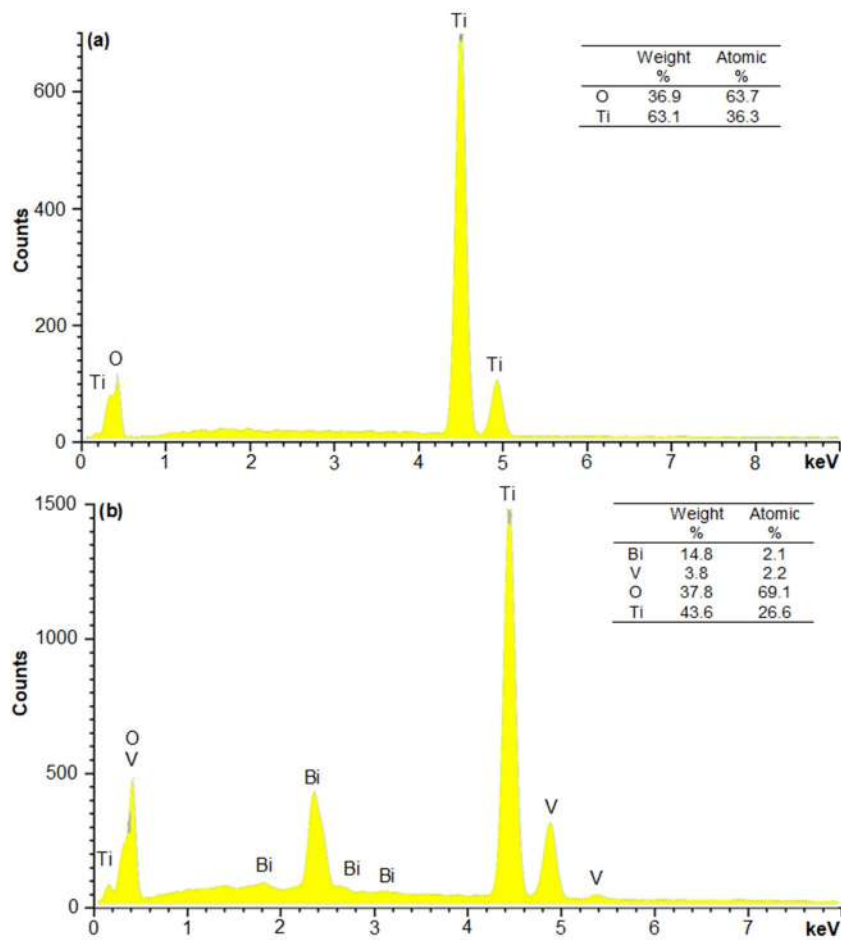


Fig 4. EDX results of (a) TiO₂NT and (b) BiVO₄/TiO₂NT with 20 cycles SILAR

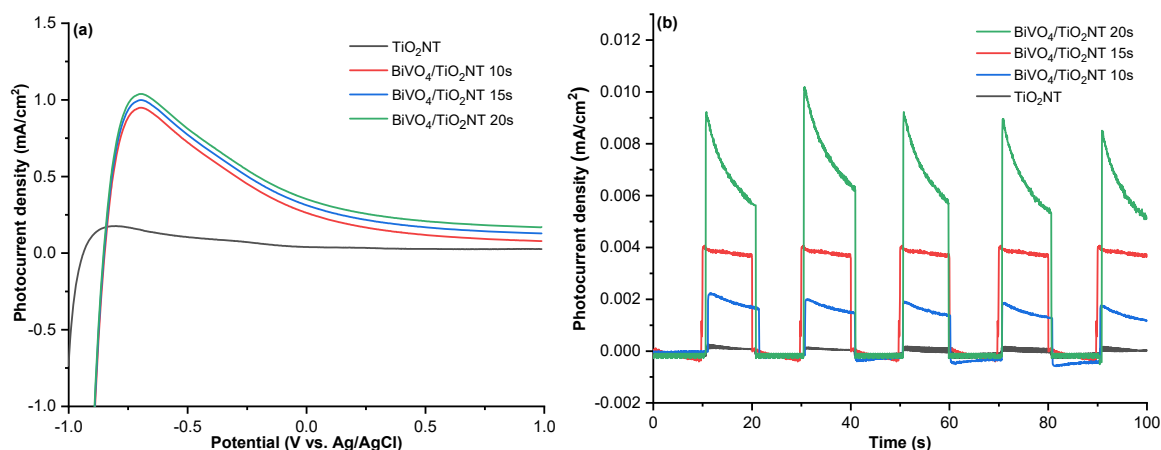


Fig 5. Photocurrent activity results using a potentiostat with 13 W white LED irradiation. Curves of (a) LSV scan rate 25 mV/s and (b) MPA at constant potential 0 V vs. Ag/AgCl

that the addition of BiVO_4 on the surface of TiO_2NT can increase the photocatalytic activity of TiO_2NT in the visible light region due to charge separation across the $\text{BiVO}_4/\text{TiO}_2\text{NT}$ interface. Fig. 5(b) is a Multiple Pulse Amperometry (MPA) curves that show the current density response of TiO_2NT and $\text{BiVO}_4/\text{TiO}_2\text{NT}$ on irradiation using visible light. Based on the obtained curve, it shows that $\text{BiVO}_4/\text{TiO}_2\text{NT}$ gives the highest current density response when exposed to visible light. The higher current density response was due to the distribution of BiVO_4 formed on the TiO_2NT surface.

In this case, 20 cycles of SILAR showed a higher current density response than 10 and 15 cycles, so the 20 cycles of $\text{BiVO}_4/\text{TiO}_2\text{NT}$ synthesis would be used as a photoanode for the nitrogen reduction reaction to ammonia.

Dark Cathode Characterization of $\text{Ti}^{3+}/\text{TiO}_2\text{NT}$

In this system, $\text{Ti}^{3+}/\text{TiO}_2\text{NT}$ functions as a dark cathode where the Nitrogen Reduction Reaction (NRR) occurs. The presence of Ti^{3+} species will be the active site as an electron donor for the reduction of nitrogen to ammonia, which causes an easy dissociation of $\text{N}\equiv\text{N}$ bonds. With some transformation of surface Ti from Ti^{3+} to Ti^{4+} , electrons will naturally be injected into N_2 [23].

Fig. 6(a) shows the FTIR spectra of TiO_2NT and $\text{Ti}^{3+}/\text{TiO}_2\text{NT}$ at a wavenumber of $4000\text{--}400\text{ cm}^{-1}$. It can be seen that the Ti-O-Ti absorption peak of $\text{Ti}^{3+}/\text{TiO}_2\text{NT}$ at a wave number of 900 cm^{-1} decreases compared to

TiO_2NT . This phenomenon is due to reduced Ti-O-Ti bonds at the surface due to the reduction process that can be associated with an increase in the Ti^{3+} population in TiO_2NT . At wave numbers $1700\text{--}1400\text{ cm}^{-1}$, the OH bending functional group indicates that there are water molecules adsorbed on the $\text{Ti}^{3+}/\text{TiO}_2\text{NT}$ surface [24].

Fig. 6(b) shows the UV-Vis spectrum of the $\text{Ti}^{3+}/\text{TiO}_2\text{NT}$ DRS. The band gap value of $\text{Ti}^{3+}/\text{TiO}_2\text{NT}$ can be determined by the Tauc plot of the Kubelka-Munk function, which is 3.13 eV. The band gap value obtained after presenting Ti^{3+} in TiO_2NT , there was a decrease in the band gap from 3.21 to 3.13 eV. The resulting band gap indicates that $\text{Ti}^{3+}/\text{TiO}_2\text{NT}$ is active in UV light.

Fig. 6(c) shows the results of LSV characterization on $\text{Ti}^{3+}/\text{TiO}_2\text{NT}$ irradiated with UV light, visible light, and dark conditions. The LSV test was conducted in the potential range of -1 to 1 V. These results indicate that $\text{Ti}^{3+}/\text{TiO}_2\text{NT}$ irradiated with UV lamps produces a higher current density than in visible light or dark conditions. This is directly proportional to the band gap value of $\text{Ti}^{3+}/\text{TiO}_2\text{NT}$, which is active against UV light. The high current density indicates that when $\text{Ti}^{3+}/\text{TiO}_2\text{NT}$ is irradiated with a UV lamp, there will be an excitation of electrons from the valence band to the conduction band.

Fig. 6(d) shows the results of the MPA characterization on $\text{Ti}^{3+}/\text{TiO}_2\text{NT}$ within 100 s. The results of this characterization indicate that $\text{Ti}^{3+}/\text{TiO}_2\text{NT}$

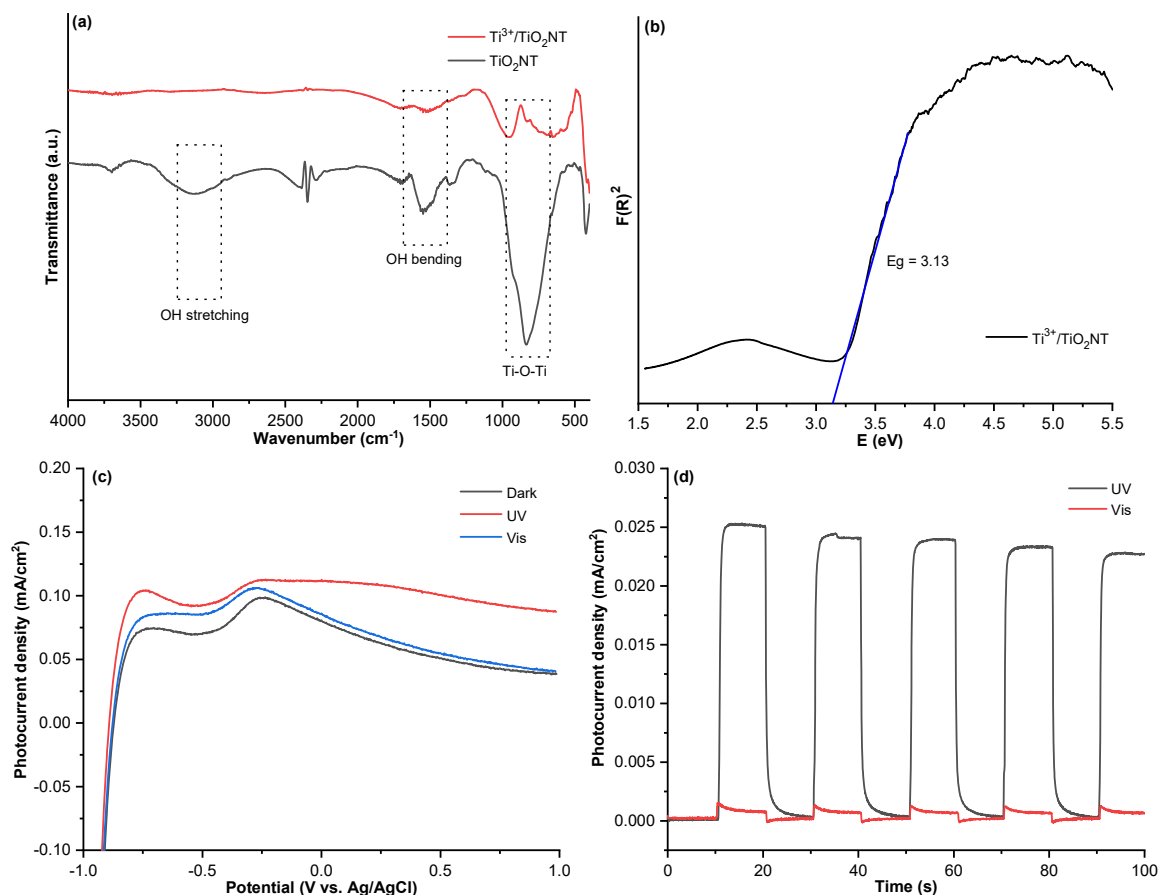


Fig 6. (a) FTIR spectrum, (b) The band gap value using the Tauc plot of the Kubelka-Munk function, (c) Linear Sweep Voltammetry, and (d) Multi Pulse Amperometry of $\text{Ti}^{3+}/\text{TiO}_2\text{NT}$

responds to UV light. When $\text{Ti}^{3+}/\text{TiO}_2\text{NT}$ is given a UV lamp, there will be an increase in current density, and when the UV lamp is turned off, there will be a significant decrease in current density. This increase in current density indicates that there is an excitation of electrons. At the same time, the decrease in current density indicates that there is a recombination of electrons from the conduction band to the valence band. However, when exposed to visible light, the current density is lower than given UV light. This indicates that the synthesized $\text{Ti}^{3+}/\text{TiO}_2\text{NT}$ has a strong response in the UV region [25].

DSSC Efficiency Characterization

DSSC efficiency test is measured by plotting the current versus potential curve in the range of 0 to 1 Volt. Fig. 7 shows the curve of the change in DSSC current to the given potential when irradiated using visible light from a white LED lamp. From the curve obtained, it can be

determined the value of J_{sc} , V_{oc} , P_{max} , P_{in} , fill factor, and efficiency of the DSSC according to the data listed in Table 1. By using a lamp power of 25.5 mW/cm^2 for irradiation, the DSSC cell efficiency is obtained at 1.13%

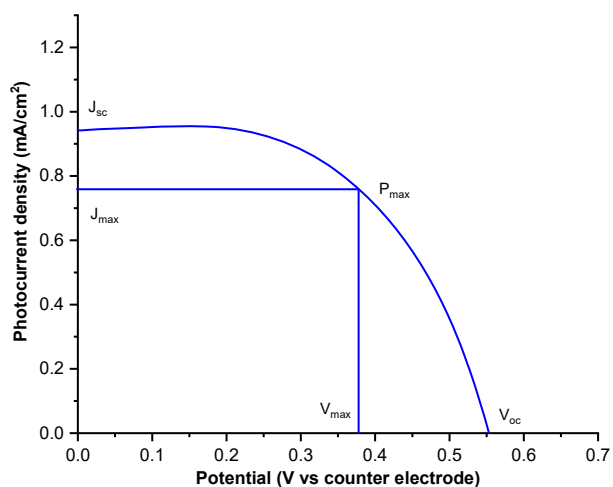


Fig 7. The Current versus Voltage curve of DSSC

Table 1. DSSC efficiency measurement data

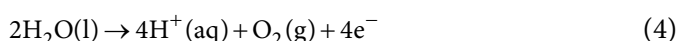
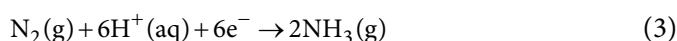
J_{\max} (mA/cm ²)	V_{\max} (V)	J_{sc} (mA/cm ²)	V_{oc} (V)	P_{\max} (mW/cm ²)	P_{in} (mW/cm ²)	FF	η (%)
0.75941	0.378	0.94188	0.552	0.28706	25.5	0.55212	1.13

with a fill factor value of 0.55212. This DSSC cell will then be used in a DSSC-PEC tandem cell for the reduction of nitrogen into ammonia to increase the electrons that enter the catalysis zone so that more ammonia will be produced.

Tandem System for N₂ Applications

The reaction process for reducing nitrogen to ammonia occurs in the DSSC-PEC tandem system. The nitrogen reduction reaction occurs in the Ti³⁺/TiO₂NT catalytic zone as the PEC cathode is connected to TiO₂NT/N719 as the DSSC anode. PEC anode, namely BiVO₄/TiO₂NT oxidation reaction, occurs in water to produce electrons (e⁻) and protons (H⁺). Then H⁺ will flow from the anode to the PEC cathode through the Nafion membrane while the electrons (e⁻) flow to the Pt/FTO as the DSSC cathode through the external circuit (cable). These electrons are used to reduce I₃⁻ to I⁻ ions in DSSC. At the PEC cathode, nitrogen is reduced to ammonia.

At the PEC, dark cathode, there is a nitrogen reduction reaction to ammonia, and at the photoanode, there is an oxidation reaction of water into protons and oxygen according to the following equation:



The resulting ammonia then flows into a reservoir containing a 0.01 M HCl solution to produce an ammonium chloride (NH₄Cl) solution.

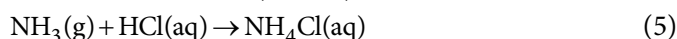


Fig. 8 shows experimental data on the amount of ammonia produced at two irradiation conditions (A: dark cathode, B: full irradiation). From the Fig. 8, it can be seen that the ammonia produced increased with increasing reaction time. The amount of ammonia produced in the DSSC+photoanode (A) irradiation region for 2, 4, and 6 h, respectively, was 0.180, 0.253, and 0.393 μmol . The amount of ammonia produced in the DSSC+PEC electrode (B) irradiation region for 2, 4, and 6 h,

respectively, was 0.173, 0.240, and 0.320 μmol . These results indicate that the cell system is well-operating under visible light [21]. In addition, the results under full irradiation (Condition B) are lower than the dark cathode (Condition A). It might be caused by when the PEC cathode (Ti³⁺/TiO₂NT) is irradiated, photon-generated active electrons in its conduction band, and these electrons find antagonistic behavior with electrons from the DSSC part due to the potential bias resulting in the system as a whole [26].

The percentage of energy efficiency in ammonia can be calculated using the Solar to Chemical Conversion (SCC) Eq. (1) [2]. SCC is the ratio between the amount of ammonia produced and the total energy given at a certain time. The free energy for the formation of ammonia from nitrogen gas and water is 399 kJ/mol. Total energy input (Watt) is the amount of light given from the irradiation source to the active area of the DSSC. The light intensity in this study was 3050 lux, which is equivalent to 4,466 W/m² with the irradiated DSSC area of 0.0003 m², so the total input power generated was 0.00134 W. Based on the calculation results

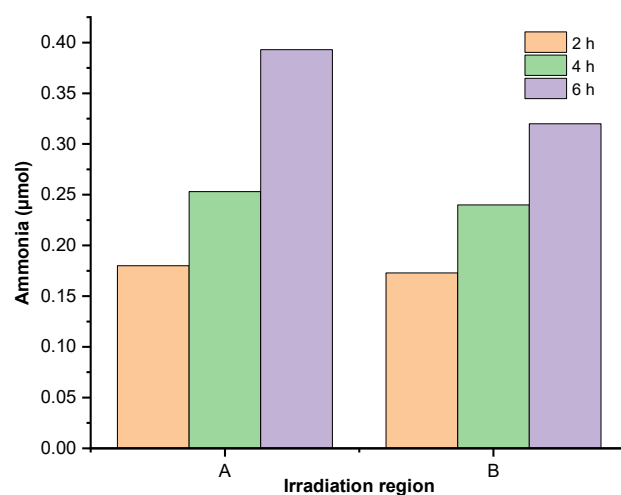


Fig 8. The amount of ammonia produced under various irradiation conditions during the reaction time of 2, 4, and 6 h (A: dark cathode, B: full irradiation)

results, the percentage of SCC for photoanode and dark cathode with a reaction time of 6 h is 0.003%.

■ CONCLUSION

In summary, the authors have successfully synthesized BiVO₄/TiO₂NT heterojunction, which is active in visible light by SILAR method with 3 cycles variations, namely 10, 15, and 20 cycles. Among the others, 20-cycle BiVO₄/TiO₂NT gave the best result as a photoanode, characterized by the smallest band gap energy and the highest photocurrent density for water oxidation (0.352 mA/cm²). In addition, for the NRR, the BiVO₄/TiO₂NT photoanode was used along with Ti³⁺/TiO₂NT cathode in the PEC system coupled with a DSSC based on TiO₂NT/N719 with an efficiency of 1.13% as an energy booster in the reaction. The DSSC-PEC tandem system under “A” condition (Dark cathode, irradiation on DSSC and photoanode) resulted in SCC efficiency of 0.003% and ammonia production of 0.022 mol.h⁻¹.cm⁻². Although still lacking, the result shows that the tandem DSSC-PEC system was able to reduce nitrogen (N₂) to ammonia (NH₃) with only visible light irradiation. There are many aspects that can be optimized for future development. First, the activity of the photoanode site could be enhanced more by further optimizing the amount of BiVO₄ deposited and directing the crystal growth on the active facets. Second, further optimization on DSSC efficiency and Ti³⁺ population as the active size at the cathode is predicted to be able to improve the performance of the whole system. Third, finding the best environment, such as electrolyte, temperature, also system design, especially at the cathode site, to enhance the selectivity of the system to NRR is still believed to be a major factor that should be addressed in future work. Thus, this work is expected to stimulate the development of the catalyst and system design for a better NRR visible active-photo(electro)catalytic system in the future.

■ ACKNOWLEDGMENTS

The authors gratefully acknowledge the support from DGHE, Directorate General of Higher Education, for funding the research (PDUPT research contract No. NKB-174/UN2.RST/HKP.05.00/2021).

■ REFERENCES

- [1] Chen, Q., Fan, G., Fu, H., Li, Z., and Zou, Z., 2018, Tandem photoelectrochemical cells for solar water splitting, *Adv. Phys.: X*, 3 (1), 1487267.
- [2] Hirakawa, H., Hashimoto, M., Shiraishi, Y., and Hirai, T., 2017, Photocatalytic conversion of nitrogen to ammonia with water on surface oxygen vacancies of titanium dioxide, *J. Am. Chem. Soc.*, 139 (31), 10929–10936.
- [3] Licht, S., Cui, B., Wang, B., Li, F.F., Lau, J., and Liu, S., 2014, Ammonia synthesis by N₂ and steam electrolysis in molten hydroxide suspensions of nanoscale Fe₂O₃, *Science*, 345 (6197), 637–640.
- [4] Li, C., Wang, T., and Gong, J., 2020, Alternative strategies toward sustainable ammonia synthesis, *Trans. Tianjin Univ.*, 26 (2), 67–91.
- [5] Liu D., Wang, J., Bian, S., Liu, Q., Gao, Y., Wang, X., Chu, P.K., and Yu, X.F., 2020, Photoelectrochemical synthesis of ammonia with black phosphorus, *Adv. Funct. Mater.*, 30 (24), 2002731.
- [6] Liu, Q.Y., Wang, H.D., Tang, R., Cheng, Q., and Yuan, Y.J., 2021, Rutile TiO₂ nanoparticles with oxygen vacancy for photocatalytic nitrogen fixation, *ACS Appl. Nano Mater.*, 4 (9), 8674–8679.
- [7] Dong, H., Zeng, G., Tang, L., Fan, C., Zhang, C., He, X., and He, Y., 2015, An overview on limitations of TiO₂-based particles for photocatalytic degradation of organic pollutants and the corresponding countermeasures, *Water Res.*, 79, 128–146.
- [8] Zhang, X., Yang, H., Zhang, B., Shen, Y., and Wang, M., 2016, BiOI-TiO₂ nanocomposites for photoelectrochemical water splitting, *Adv. Mater. Interfaces*, 3 (1), 1500273.
- [9] Syauqi, M.I., Prasetia, P., and Gunlazuardi, J., 2023, The influence of sodium alginate in water-based electrolyte on the morphology of TiO₂ nanotube prepared by anodization method, *Mater. Chem. Phys.*, 296, 127234.
- [10] Yunita, Y., Syauqi, M.I., and Gunlazuardi, J., 2022, Comparative study of bismuth ferrite deposition method on TiO₂ nanotube and performance of hydrogen evolution in a photoelectrochemical dye-

- sensitized solar cell tandem system, *Makara J. Sci.*, 26 (3), 190–199.
- [11] Zhu, X., Zhang, F., Wang, M., Gao, X., Luo, Y., Xue, J., Zhang, Y., Ding, J., Sun, S., Bao, J., and Gao, C., 2016, A shuriken-shaped $m\text{-BiVO}_4/\{001\}\text{-TiO}_2$ heterojunction: Synthesis, structure and enhanced visible light photocatalytic activity, *Appl. Catal., A*, 521, 42–49.
- [12] Surahman, H., 2017, Pengembangan Sel Fotoelektrokimia Menggunakan Elektroda TiO_2 Nanotube Arrays Tersensitisasi CdS Nanopartikel untuk Produksi Hidrogen, *Dissertation*, Universitas Indonesia.
- [13] Samsudin, M.F.R., Sufian, S., Mohamed, N.M., Bashiri, R., Wolfe, F., and Ramli, R.M., 2018, Enhancement of hydrogen production over screen-printed $\text{TiO}_2/\text{BiVO}_4$ thin film in the photoelectrochemical cells, *Mater. Lett.*, 211, 13–16.
- [14] Song, J., Zheng, M., Yuan, X., Li, Q., Wang, F., Ma, L., You, Y., Liu, S., Liu, P., Jiang, D., Ma, L., and Shen, W., 2017, Electrochemically induced Ti^{3+} self-doping of TiO_2 nanotube arrays for improved photoelectrochemical water splitting, *J. Mater. Sci.*, 52 (12), 6976–6986.
- [15] Shi, L., Xu, C., Sun, X., Zhang, H., Liu, Z., Qu, X., and Du, F., 2018, Facile fabrication of hierarchical $\text{BiVO}_4/\text{TiO}_2$ heterostructures for enhanced photocatalytic activities under visible-light irradiation, *J. Mater. Sci.*, 53 (16), 11329–11342.
- [16] Ramakrishnan, V.M., Pitchaiya, S., Muthukumarasamy, N., Kvamme, K., Rajesh, G., Agilan, S., Pugazhendhi, A., and Velauthapillai, D., 2020, Performance of TiO_2 nanoparticles synthesized by microwave and solvothermal methods as photoanode in dye-sensitized solar cells (DSSC), *Int. J. Hydrogen Energy*, 45 (51), 27036–27046.
- [17] Orimolade, B.O., and Arotiba, O.A., 2019, An exfoliated graphite-bismuth vanadate composite photoanode for the photoelectrochemical degradation of acid orange 7 dye, *Electrocatalysis*, 10 (4), 429–435.
- [18] Raidou, A., Benmalek, F., Sall, T., Aggour, M., Qachaou, A., Laanab, L., and Fahoume, M., 2014, Characterization of ZnO thin films grown by SILAR method, *Open Access Libr. J.*, 1 (3), 1–9.
- [19] Dette, C., Perez-Osorio, M.A., Kley, C.S., Punke, P., Patrick, C.E., Jacobson, P., Giustino, F., Jung, S.J., and Kern, K., 2014, TiO_2 anatase with a bandgap in the visible region, *Nano Lett.*, 14 (11), 6533–6538.
- [20] Wu, M., Jing, Q., Feng, X., and Chen, L., 2018, BiVO_4 microstructures with various morphologies: Synthesis and characterization, *Appl. Surf. Sci.*, 427, 525–532.
- [21] Drisya, K.T., Solís-López, M., Ríos-Ramírez, J.J., Durán-Álvarez, J.C., Rousseau, A., Velumani, S., Asomoza, R., Kassiba, A., Jantrania, A., and Castaneda, H., 2020, Electronic and optical competence of $\text{TiO}_2/\text{BiVO}_4$ nanocomposites in the photocatalytic processes, *Sci. Rep.*, 10 (1), 13507.
- [22] Macak, J.M., Hildebrand, H., Marten-Jahns, U., and Schmuki, P., 2008, Mechanistic aspects and growth of large diameter self-organized TiO_2 nanotubes, *J. Electroanal. Chem.*, 621 (2), 254–266.
- [23] Chen, X., Li, N., Kong, Z., Ong, W.J., and Zhao, X., 2018, Photocatalytic fixation of nitrogen to ammonia: State-of-the-art advancements and future prospects, *Mater. Horiz.*, 5 (1), 9–27.
- [24] Budiman, H., Wibowo, R., Zuas, O., and Gunlazuardi, J., 2021, Effect of annealing temperature on the characteristic of reduced highly ordered TiO_2 nanotube arrays and their CO gas-sensing performance, *Process. Appl. Ceram.*, 15 (4), 417–427.
- [25] Zhu, Y., Shah, M.W., and Wang, C., 2016, Insight into the role of Ti^{3+} in photocatalytic performance of shuriken-shaped $\text{BiVO}_4/\text{TiO}_{2-x}$ heterojunction, *Appl. Catal., B*, 203, 526–532.
- [26] An’Nur, F.K., Wihelmina, B.V., Gunlazuardi, J., and Wibowo, R., 2020, Tandem system of dyes sensitized solar cell-photo electro chemical (DSSC-PEC) employing TiO_2 nanotube/ BiOBr as dark cathode for nitrogen fixation, *AIP Conf. Proc.*, 2243, 020002.

Films from PVA and *Sansevieria trifasciata* Leaves Extracts as a Smartphone Protector with Radiation Reducing Property and Its LC-MS Analysis

Auliya Ilmiawati^{1,2*}, Melinia Falestin¹, Akhiruddin Maddu³, Luthfan Irfana¹,
Purwantiningsih Sugita¹, and Budi Arifin¹

¹Department of Chemistry, Faculty of Mathematics and Natural Sciences, IPB University,
Jl. Tanjung Kampus IPB Dramaga, Bogor 16680, Indonesia

²Tropical Biopharmaca Research Center-Institute of Research and Community Services, IPB University,
Jl. Taman Kencana No. 3, Kampus IPB Taman Kencana, Bogor 16128, Indonesia

³Department of Physics, Faculty of Mathematics and Natural Sciences, IPB University,
Jl. Meranti Kampus IPB Dramaga, Bogor 16680, Indonesia

* **Corresponding author:**

email: aulia_ilmiawati@apps.ipb.ac.id

Received: August 2, 2022

Accepted: April 17, 2023

DOI: 10.22146/ijc.76809

Abstract: *Sansevieria trifasciata* (mother-in-law's tongue), an ornamental plant widely found in Indonesia, can absorb electromagnetic radiation in various electronic devices. This study aims to find the best *S. trifasciata* extract as an electromagnetic and thermal radiation reducer emitted from a smartphone. *S. trifasciata* leaves were macerated using ethanol, acetone, and dichloromethane. The extract was mixed with PVA as a film and tested for electromagnetic radiation using a radiation measuring device type GM-3120. Thermal radiation was tested using a temperature sensor (PASCO CI-6505B) connected to a PASCO 550 Universal Interface. All smartphone protective films decreased radiation from the smartphone, and the acetone extract caused the most significant radiation decrease, with the best results at a concentration of 5%. An *S. trifasciata* extract contained alkaloids, saponins, steroids, phenolics, and tannins based on the phytochemical tests. Based on LC-MS data, the dominant compounds identified from the three extracts of *S. trifasciata* is a group of alkaloids, fatty acid, and steroid. The functional groups that are thought to play a role in reducing radiation are the C-O, C=O, and C-OH functional groups. A compound that is thought to contribute to the reduction in radiation is neuroscogenin, a steroid group.

Keywords: electromagnetic; radiation; smartphone; *S. trifasciata*; thermal

■ INTRODUCTION

Sansevieria trifasciata, with the local name mother-in-law's tongue or snake plant, is quite popular in Indonesia as an ornamental plant. The popularity of this plant has increased since NASA reported that this plant could absorb indoor pollutants such as formaldehyde, benzene, and trichloroethylene [1]. *S. trifasciata* shows potential for medicinal uses as an antioxidant [2], antibacterial [3], antidiabetic [4], hepatoprotective [5], antiallergic, anti-anaphylactic [6], cytotoxic [7], xanthine oxidase inhibitor [8], agents, as well as it has a therapeutic effect [9].

Besides that, *S. trifasciata* also shows activity as an absorber of pollutants and radiation, e.g., pollutant absorber [10], CO₂ emission reduction [11], removal of fishy odor [12], and adsorber of heavy metals [13-15]. Several reports show that the genus *Sansevieria* can absorb electromagnetic radiation from various electronic devices. The leaves of *S. trifasciata* var. *Laurentii* were reported to reduce exposure to electromagnetic radiation from television for one hour [16]. Another study reported that the extract could reduce indoor electromagnetic radiation by up to 16% [17]. Likewise, an anti-radiation bio screen made of this species can

reduce radiation from laptops by 24.45% [18]. There are also reports of differences in computer radiation before and after contact with *S. trifasciata* Laurentii and Golden Hahnii, with the most considerable radiation reduction of 53.86% [19].

Another device that has the potential to emit harmful radiation is the cell phone. Mobile phones have become a significant need in various circles of society, along with the development of models and features that are increasingly sophisticated so that they are dubbed smartphones. Without realizing it, its use poses dangers because of the radiation produced. Mobile phones' regular and long-term use can negatively impact biological systems, especially the brain. It also may cause neurodegenerative diseases [20]. The possible health hazard of cell phones can be classified into thermal and non-thermal effects. The thermal effect from the phone should not exceed the average body temperature, and if body core temperatures are $> 40\text{ }^{\circ}\text{C}$, it can lead to thermal stroke, which can be fatal [21]. The non-thermal effect comes from the electromagnetic radiation generated. Electromagnetic radiation from the phone significantly correlates with increasing thyroid-stimulating hormone [22] and can decrease sperm motility [23]. Therefore, a smartphone protector that could reduce smartphone radiation is needed.

One way to protect a smartphone is to use a casing or screen protector. Currently, no casing or screen protector can reduce radiation generated by smartphones. Therefore, we need a smartphone protector that can reduce radiation on smartphones. In a previous study, we tested an extract of *S. trifasciata* as a reducer of thermal radiation on smartphones. The film from a combination of polyvinyl alcohol (PVA) and 0.02% dichloromethane (DCM) fraction succeeded in reducing thermal radiation by $4.4\text{ }^{\circ}\text{C}$ in the first minute and was stable for up to 20 min. This composite film was more effective than commercial casing used as controls [24]. That research only tested heat radiation on smartphones, even though electromagnetic radiation from smartphones is also dangerous. Therefore, this study tested the activity of reducing heat and electromagnetic radiation from the film. Besides that, the previous research only used one solvent for extraction. Unlike this study, the film was

optimized using extracts from various solvents and found the best extract to be used as a casing or screen protector on a smartphone. It also analyses the components present in each extract to estimate which components play a role in reducing radiation.

For the first time, the activity of reducing thermal and electromagnetic radiation has been reported from various extracts of *S. trifasciata* with the comparison of LC-MS analysis of its various extracts.

■ EXPERIMENTAL SECTION

Materials

Samples of *S. trifasciata* were obtained from Tropical Biopharmaca Research Center (TropBRC), IPB University, Bogor, Indonesia. The plant is washed, dried, and mashed to 80 mesh. Ethanol 96%, acetone, and DCM were used as solvents for the isolation process and were obtained from Merck (Darmstadt, Germany). Film layers were formed from PVA with a molecular weight of 3,000 g/mol.

Instrumentation

LC-MS was utilized for structure analysis employing an LC system called Ultra Performance Liquid Chromatography (UPLC) and a mass spectrometer called the Vanquish Tandem Q Exactive Plus Orbitrap HRMS ThermoScientific. The following conditions were used in the column: C18 (1.5 μm , 100 \times 2.1 mm), temperature: $30\text{ }^{\circ}\text{C}$ (column), flow rate: 0.2 mL/min running 25 min, injection volume: 5 μL with MS system of ES (electrospray ionization) in positive ion mode, the capillary temperature of $320\text{ }^{\circ}\text{C}$ and detection at 50 eV, the solvent is methanol, and mobile phase: (a) $\text{H}_2\text{O} + 0.1\%$ formic acid and (b) acetonitrile + 0.1% formic acid. Electromagnetic radiation using a radiation measuring device BENETECH type GM-3120. Thermal radiation was tested using a temperature sensor (PASCO CI-6505B) connected to a PASCO 550 Universal Interface.

Procedure

Extraction and fractionation

Powdered *S. trifasciata* (750 g) leaves were divided and macerated with three solvents (ethanol 96%,

acetone, and DCM) for 3×24 h and were filtered. The filtrate was collected and concentrated with a rotary evaporator to obtain the blackish-brown concentrated extract. Then the extracts were prepared to be made into a film and tested for electromagnetic and thermal radiation on smartphones. The extract was tested for phytochemicals, including alkaloid, flavonoid, terpenoid, saponin, steroid, phenolic, and tannin compounds [25].

Preparation of blended film

The blended film uses a ratio of extract/fraction: PVA of 1:1 with a final volume of solution is 100 mL. The concentration of PVA used was 5%, while the extracts used were 0.5%, respectively. PVA solution with a concentration of 5% was prepared by dissolving 15 g of PVA in 300 mL of distilled water at 90 °C and adding 0.6 mL of glycerol as a plasticizer. Extract with a concentration of 0.5% was prepared by dissolving 0.25 g of extract in 50 mL of each solvent. Furthermore, the two solutions were allowed to stand until they reached a temperature of ± 25 °C. After reaching a temperature, the two solutions were homogenized for 10 min [26] (with modification). After degassing the solution in a vacuum desiccator, the homogeneous solution was poured onto an aluminium pane ($18 \times 10 \times 4$ cm). The solution was dried in an oven at 60 °C for 15 h per day to remove the residual solvents, followed by a drying process at ± 25 °C for 24 h. Then the films were peeled from the pane and kept until use [27].

Testing electromagnetic and thermal radiation on smartphones

The smartphone used in this test is the Vivo Y55 brand, which has been used for one year. Smartphones are made to do the same activity, making a call. Electromagnetic radiation from the rear and front of the smartphone was measured using a GM-3120 radiation meter for 10 s without and with a film protector. The protector tested were PVA + extract and PVA film only. The commercial casing (soft case) was also used as a comparison. The data is obtained by measuring the radiation from the smartphone before being covered by a protector (A) and after being covered by a protector (B), then calculating the percentage change with Eq. (1).

$$\% \text{ reduction of E - Field} = \frac{A - B}{A} \times 100\% \quad (1)$$

Thermal radiation was measured using a temperature sensor (PASCO CI-6505B) connected to the PASCO 550 Universal Interface. Each film formed is affixed to the smartphone's rear, making a video call, and placed in a closed box. Then, the temperature rise was recorded for 20 min by the sensor. The radiation was measured from a smartphone without a protector, with a commercial casing, a smartphone with PVA film, and a smartphone with film PVA + extract. All measurements were carried out 3 times, and the average value was taken.

RESULTS AND DISCUSSION

Radiation Absorption Activity

There are 2 types of electromagnetic radiation being measured, namely E-field and H-Field. The experimental results found that the E-field radiation gave a higher value (87–230 V/m) than the H-field radiation value (0–0.25 μ T). According to the International Commission on Non-Ionizing Radiation Protection (ICNIRP), the radiation limit level allowed for the unit of magnetic flux density is 0.3–0.4 T [28], along with the safety limit of the electric field is 90 and 127.27 V/m at 900 and 1800 MHz, respectively [29]. Corresponding on those data, we could notice that smartphone's magnetic field has the potential to cause danger.

Preliminary testing on the smartphone's rear shows a radiation range of 8.9 to 59 V/m, while the front of the smartphone shows a radiation range of 185 to 737 V/m. The front of the smartphone emits more radiation than the rear, so further testing focuses on the front. The measurement is carried out for 10 s to get the average value of the radiation because the radiation value is prone to change. The measurement results of electromagnetic and thermal radiation are presented in Fig. 1.

All treatments decreased the radiation compared to the initial conditions from the measurement results, and the percentage reduction of electromagnetic radiation on the front of the smartphone is presented in Fig. 1(a). It can be seen that the treatment that gave the most significant reduction in electromagnetic radiation was a film from a mixture of PVA + acetone extract, with a radiation reduction value of 47%, followed by a mixture

of PVA + DCM extract of 32%. The ethanol extract did not have a significant effect, as shown by the reduction in radiation was not too significant (11%). The decrease in radiation by the mixed PVA + acetone extract gave more excellent value than the commercial case used as a control and also more remarkable than the PVA film alone. It can be assumed that the effect of the decrease in electromagnetic radiation came from the acetone extract, not from PVA.

The measurement of thermal radiation was carried out for 30 min with 1200 data (1 data per second). However, the data used in the image represents the smartphone's temperature every 5 min (Fig. 1(b)). Smartphones without a protector (the films or casing) give higher thermal radiation than smartphones with a

protector. The results show that film from PVA + acetone extract and ethanol extract gave the best results (overlapping blue lines), followed by DCM extract. *S. trifasciata* plants have a significant effect in absorbing thermal radiation on smartphones compared to commercial casings; also, this effect comes not from PVA, which is used as a film mixture. As the measurement of electromagnetic radiation, the extract that gave the most extensive absorption in thermal radiation was acetone extract. It was seen that the film PVA + acetone extract was able to maintain the smartphone's temperature at around 32–33 °C. In contrast, the smartphone without the film had a temperature that increased to 37 °C.

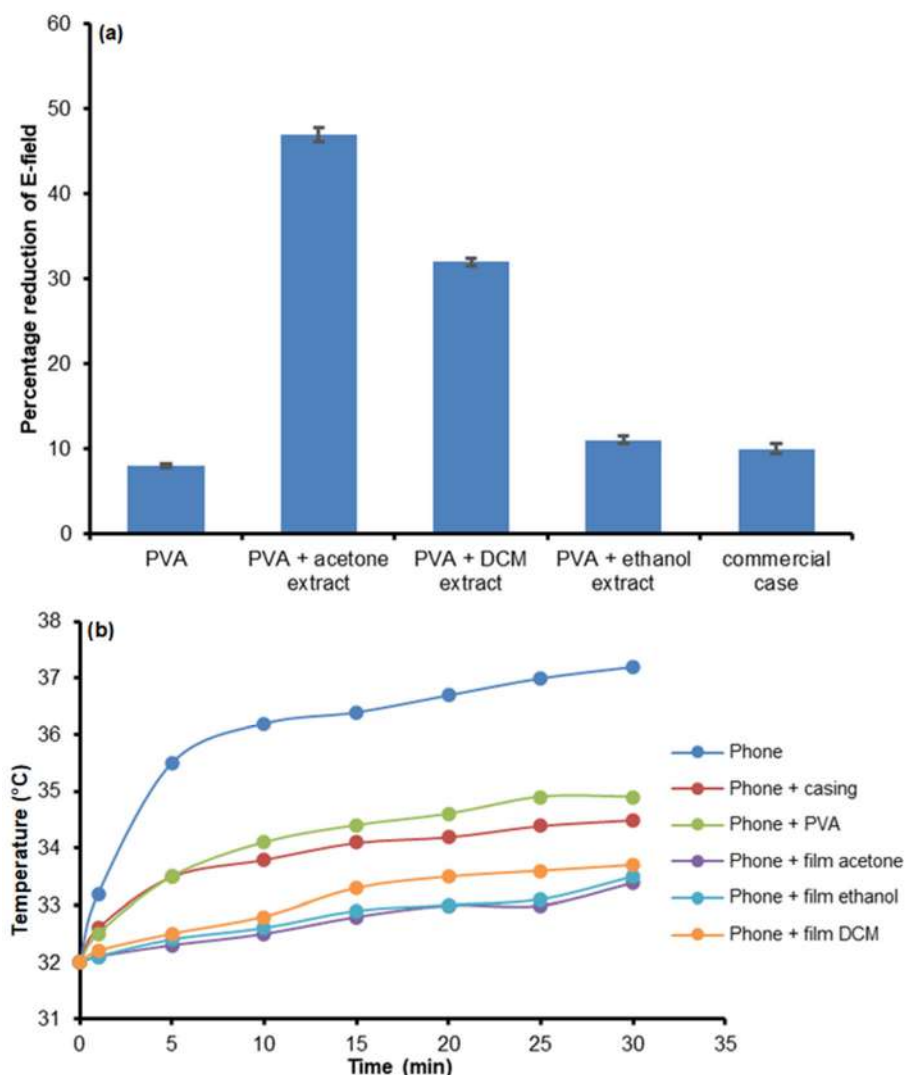


Fig 1. Percentage reduction of (a) E-field and (b) thermal radiation from the smartphone with various treatment

The radiation test was continued by varying the concentration ratio of the extract to PVA to ensure that the radiation reduction was due to the extract (not PVA). The results are presented in Fig. 2.

Based on the electromagnetic radiation test data in Fig. 2(a), it was seen that the film PVA + acetone extract gave the best results compared to other films, the same as before. However, the variation in the PVA:extract ratio did not seem to have any effect. Percentage reduction in radiation was not significantly different between the ratio of PVA:extract 1:2 and 2:1, as well as for other extracts. This means that the amount of extract to the amount of PVA does not affect the activity of the film, but it is clear that the mixture of PVA film with extract gives better results than PVA without extract. PVA has dielectric properties and thermal conductivity [30], so it can be used

as a base material to reduce electromagnetic radiation and accelerate heat transfer. However, the dielectric properties and thermal conductivity of PVA are still low, and the combination with the compounds present in *S. trifasciata* can improve the physical and mechanical properties of PVA. The number of compound components present in the extract or PVA did not affect the results, indicating that the compounds that play a role in *S. trifasciata* have the same active site as an absorber of electromagnetic radiation, which is thought to be a polar group.

The measurement results of thermal radiation (Fig. 2(b)) showed slightly different results with electromagnetic radiation. Overall the film derived from PVA:extract = 1:2 provides a better thermal radiation absorption effect than PVA:extract 2:1, even PVA:acetone

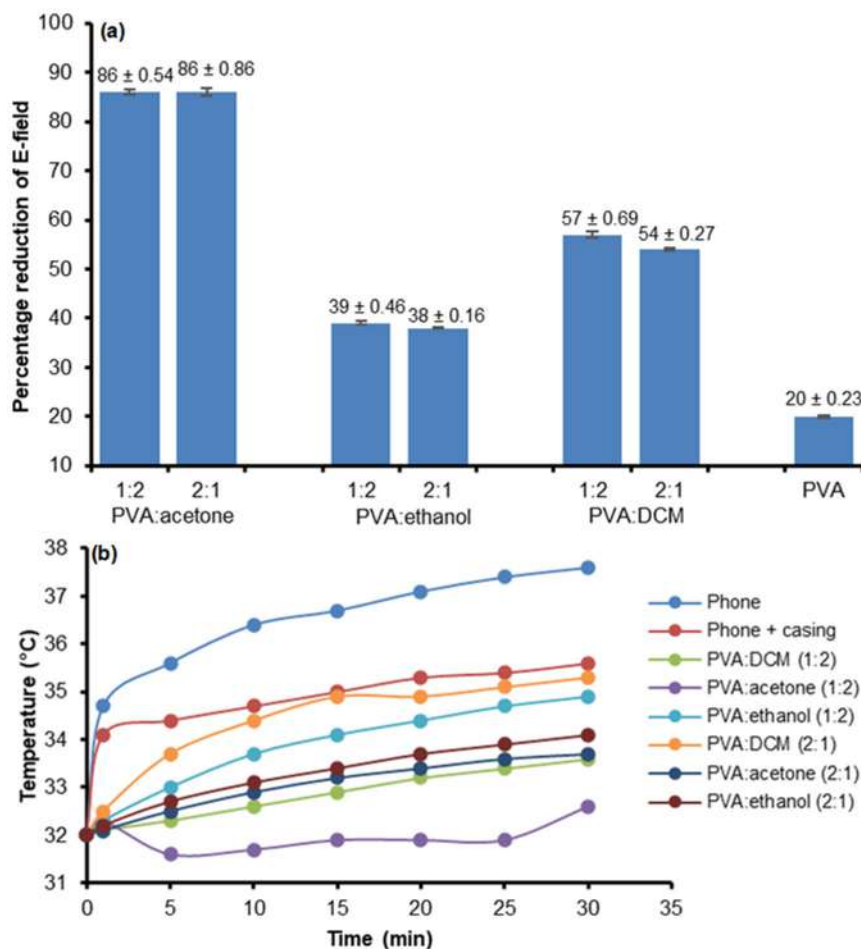


Fig 2. Percentage reduction of (a) E-field and (b) thermal radiation smartphone with films PVA:extract at various ratios

extract 1:2 (purple line) can reduce heat radiation to below the initial measurement temperature (32 °C). However, the film with a ratio of PVA:ethanol extract 2:1 had better activity than PVA:ethanol extract 1:2. Hence, variations in the concentration of PVA and extract on the absorption activity of electromagnetic and thermal radiation do not have a significant effect. However, the extract in the film makes the activity better than the control (commercial casing).

Furthermore, radiation testing was focused on the film PVA + acetone extract, and a comparison of the concentration of acetone extract was made to determine the best concentration of acetone extract. Variations of the concentration of acetone extract used are 0.01, 0.05, 0.1, 0.5, 1, and 5%. The data are presented in Fig. 3.

Based on the data in Fig. 3(a), it can be seen that the decrease in electromagnetic radiation was more significant with an increase in the concentration of acetone extract used. However, the results fluctuated at a concentration of 0.1 to 1%. The most considerable radiation reduction was obtained from film PVA + acetone extract 5% with a radiation reduction value of 62%. Therefore, the number of components in the acetone extract positively reduces electromagnetic radiation. Further research is needed at higher concentrations to obtain optimum concentrations.

The measurement of thermal radiation (Fig. 3(b)) shows slightly different results from the measurement of electromagnetic radiation. In the early minutes of the thermal radiation test, 0.1 and 0.5% acetone extracts could

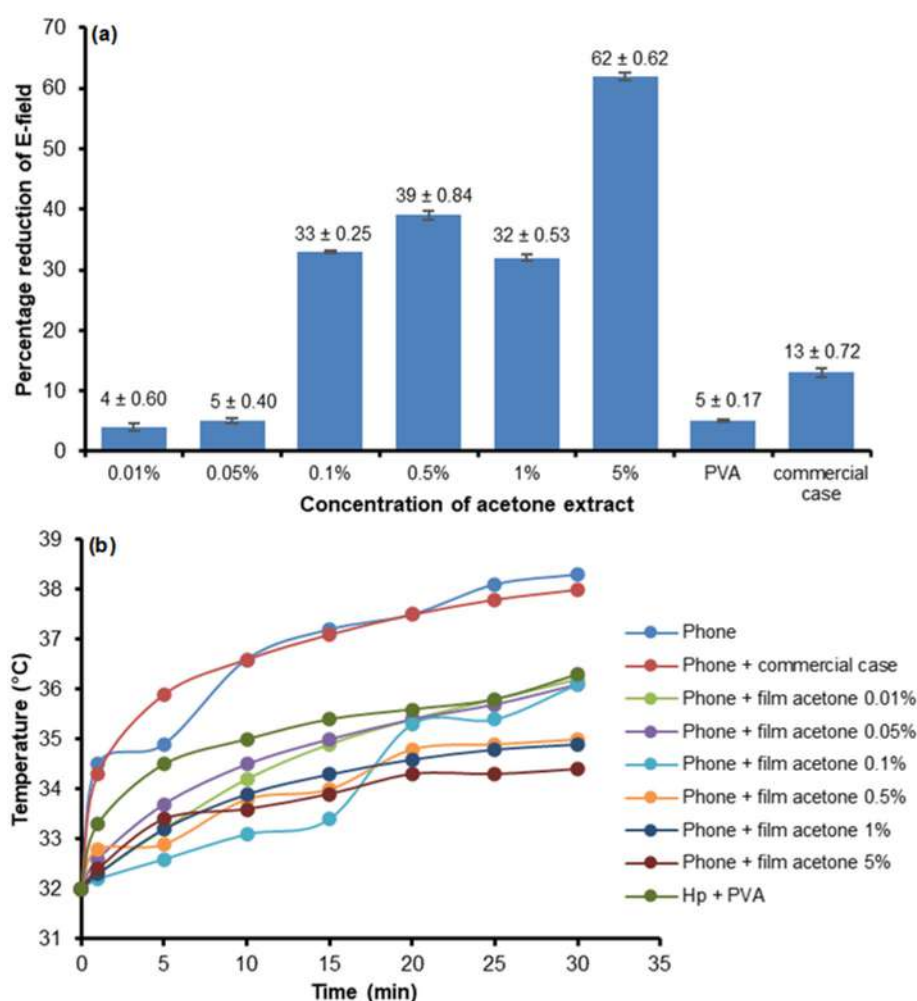


Fig 3. Percentage reduction of (a) E-field and (b) thermal radiation smartphone with film PVA + acetone extract at various ratios of extract

maintain smartphone temperatures better than 5% acetone extracts. However, starting at the 20th min, both extract concentrations showed a significant increase in temperature, in contrast to 5% acetone extract, which could stably maintain the smartphone's temperature up to the 30th min. Hence, higher acetone concentration will absorb thermal radiation stably. In contrast, the compounds present in the extract can absorb heat radiation at low concentrations. However, its ability will decrease because the number of components present is small or insufficient to withstand thermal radiation. Thus, it can be said that the best extract concentration for reducing electromagnetic and thermal radiation is 5%.

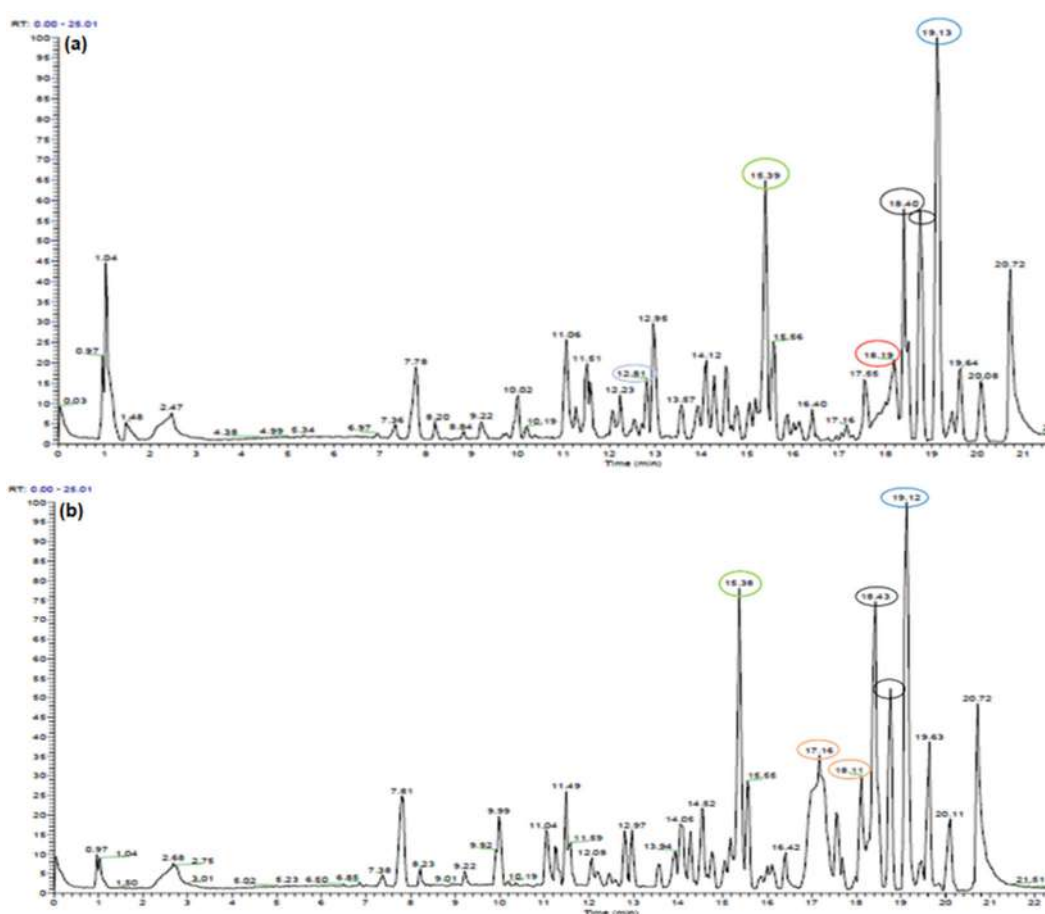
Identification of Compound

Maceration of *S. trifasciata* simplicia obtained 51.45 g of ethanol extract, 6.6 g of acetone extract, and 5.15 g of DCM extract, so the yield is 17.01, 2.95, and 2.3%, respectively. Ethanol solvent can extract more

compounds than the other two solvents. Furthermore, all extracts were tested for phytochemicals, and their mass was measured using LC-MS to identify the predicted compounds present in the three extracts. The results are presented in Table 1, as well as Fig. 4. Table 1 shows that the three extracts have similarities in the results of phytochemical tests, where all extracts are positive for alkaloid, saponin, phenolic, steroid, terpenoid, and tannin,

Table 1. Phytochemical test results extract of *S. trifasciata*

Functional group	Extract		
	Acetone	DCM	Ethanol
Alkaloid	+	+	+
Flavonoid	-	-	-
Saponin	+	+	+
Phenolic	+	+	+
Steroid	+	+	+
Terpenoid	+	+	+
Tannin	+	+	+



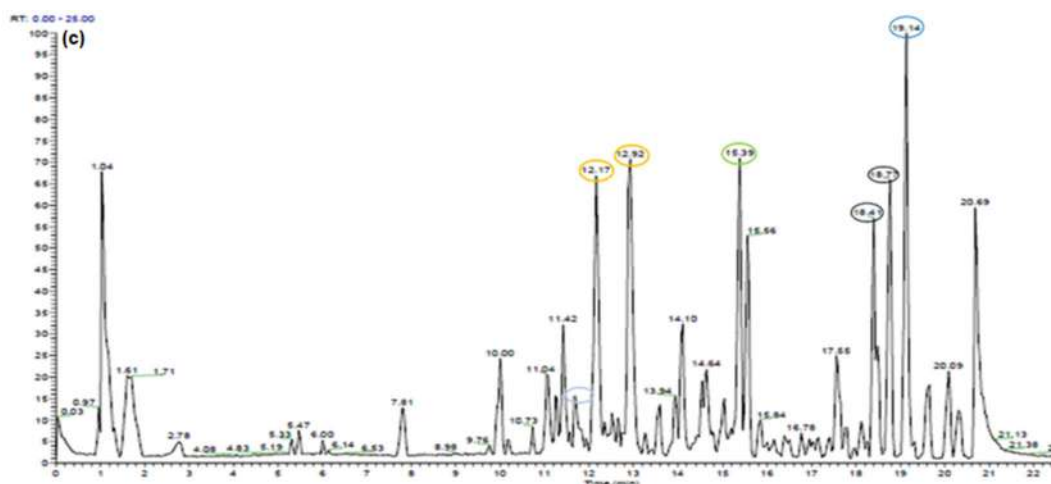


Fig 4. LC-MS chromatogram of *S. trifasciata* extract: (a) acetone, (b) DCM, and (c) ethanol extract

while negative for flavonoid. These results differ from previous studies using the same species but with different origins [24]. In a previous study, the phytochemical test of the ethanolic extract of *S. trifasciata* obtained positive results only for saponin and steroids. The place of growth will affect the secondary metabolites produced by a plant.

Based on the LC-MS chromatogram, it was seen that the three extracts had similar peaks, only different in intensity. The peak at the retention time of 20 min was indicated as the solvent peak. The LC-MS chromatograms of all extracts show four peaks at the retention time of 19.16, 18.79, 18.43, and 15.41 min with a high abundance. The mass spectrum peak with a 19.1 min retention time (blue circle in Fig. 4) makes it possible to have a $C_{35}H_{36}N_4O_5$ molecular formula with a 100% resemblance to a base peak of 593.28 identified as $[M+H]^+$. Based on search results with ChemSpider, Massbank, and Human

Metabolome Database (HMDB) software, some possible compounds are presented in Table 2.

All compounds estimated are alkaloids and the compounds that are predicted to be present in *S. trifasciata* extract is pheophorbide A (1) because it has a mass error of 2.39 ppm. This compound has also been identified in the 70% ethanol extract of *S. trifasciata* from Bogor [8]. Pheophorbide A is a chlorophyll derivative often present in green plants, such as *S. trifasciata*.

The peak mass spectrum with an 18.7 and 18.4 min retention time (the black circle in Fig. 4) can have a $C_{33}H_{40}N_2O_9$ molecular formula with a 100% resemblance to a base peak of 609.27 identified as $[M+H]^+$. Based on search results with ChemSpider, Massbank, and HMDB software, the possible compound is reserpine (7) and its derivative (isoreserpine) (8) (Fig. 5).

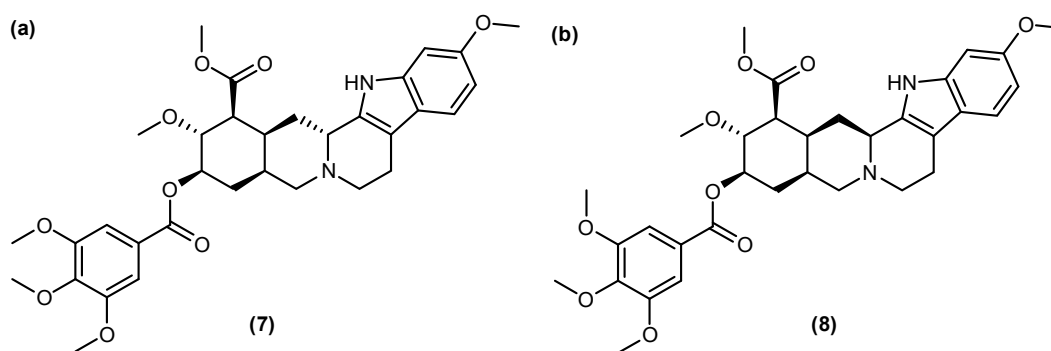


Fig 5. Structure (a) reserpine and (b) isoreserpine

Table 2. Several possible compounds at a retention time of minute 19.16

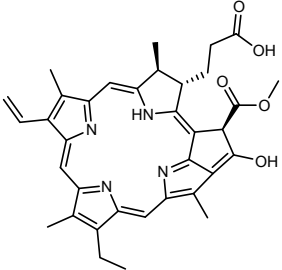
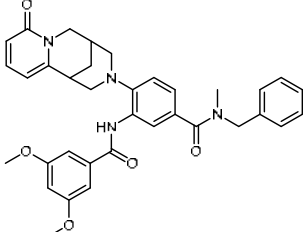
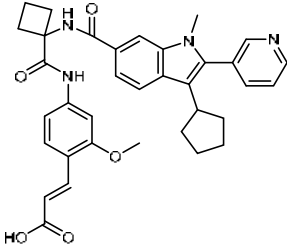
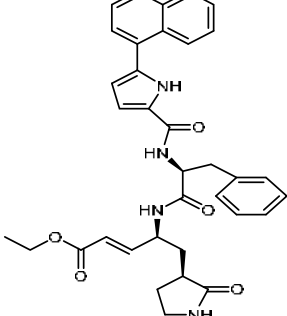
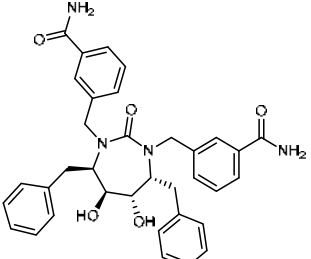
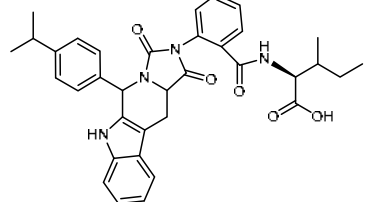
Compound	Functional group	Mass Error (ppm)	Structure
Pheophorbide A (1)	Alkaloid	2.93	
<i>N</i> -Benzyl-3-[(3,5-dimethoxybenzoyl)amino]- <i>N</i> -methyl-4-(6-oxo-7,11-diazatricyclo[7.3.1.0 _{2,7}]trideca-2,4-dien-11-yl)benzamide (2)	Alkaloid	2.99	
(2 <i>E</i>)-3-[4-({[1-({[3-Cyclopentyl-1-methyl-2-(2-pyridinyl)-1 <i>H</i> -indol-6-yl]carbonyl]amino)cyclobutyl]carbonyl]amino)-2-methoxyphenyl]acrylic acid (3)	Alkaloid	2.99	
Ethyl (2 <i>E</i> ,4 <i>S</i>)-4-[(<i>N</i> -{[5-(1-naphthyl)-1 <i>H</i> -pyrrol-2-yl]carbonyl}- <i>L</i> -phenylalanyl)amino]-5-[(3 <i>S</i>)-2-oxo-3-pyrrolidinyl]-2-pentenoate (4)	Alkaloid	2.99	
3,3'-{[(4 <i>R</i> ,5 <i>S</i> ,6 <i>S</i> ,7 <i>R</i>)-4,7-dibenzyl-5,6-dihydroxy-2-oxo-1,3-diazepane-1,3-diyl]dimethanediyl}dibenzamide (5)	Alkaloid	2.99	
<i>N</i> -{2-[(11 <i>aS</i>)-5-(4-Isopropylphenyl)-1,3-dioxo-5,6,11,11 <i>a</i> -tetrahydro-1 <i>H</i> -imidazo[1',5':1,6]pyrido[3,4- <i>b</i>]indol-2(3 <i>H</i>)-yl]benzoyl}- <i>L</i> -isoleucine (6)	Alkaloid	2.99	

Table 3. Several possible compounds at a retention time of minute 15.41

Compound	Functional group	Mass error (ppm)	Structure
(10 <i>E</i> ,12 <i>E</i>)-9-Oxo-10,12-octadecadienoic acid (9)	Fatty acid	2.37	
7-(3,4-dimethyl-5-pentylfuran-2-yl)heptanoic acid (10)	Fatty acid	2.38	
5-oxo-octadecenoic acid (11)	Fatty acid	2.38	
Colneleic acid (12)	Fatty acid	2.38	
13-Oxo-9 <i>E</i> ,11 <i>E</i> -octadecenoic acid (13)	Fatty acid	2.38	
8-(5-Hexyl-2-furyl)octanoic acid (14)	Fatty acid	2.38	

The peak mass spectrum at minute 15.4 (green circle in Fig. 4) may have a $C_{18}H_{30}O_3$ molecular formula with a 100% resemblance to a base peak of 295.23 identified as $[M+H]^+$. Based on search results with ChemSpider, Massbank, and HMDB software, some possible compounds are presented in Table 3.

All compounds estimated are fatty acids. Based on literature searches, there have been no reports regarding discovering these compounds from the *Sansevieria* plant. However, octadecanoic acid and its derivatives were identified in *S. trifasciata* and positively correlated with trimethylamine (TMA) adsorption [31].

Overall, the ethanol extract was seen to have more peaks with a higher peak intensity than the other extracts, as the yield of the ethanol extract was much larger than the other two extracts. The peaks that were different in intensity were at retention times of minute 12.92 and 12.17 (oranges circle in Fig. 4(c)), possibly having a $C_{17}H_{19}NO_5$ and $C_{17}H_{37}NO_3$ molecular formula,

respectively, with m/z 318.30 and 304.28 identified as $[M+H]^+$, which were estimated to be crinamidine (**15**) and 2-amino-1,3,4-heptadecanetriol (**16**). These two compounds appeared to have a reasonably large concentration in the ethanol extract but slightly in the acetone and DCM extracts. Crinamidine (**15**) was reported to have been isolated from *S. liberica* [32]. Meanwhile, the retention time of 12.8 min (light blue circle in Fig. 4(a) and 4(c)) was only found in acetone and ethanol extracts and not found in DCM extracts. It is possible to have a $C_{27}H_{38}O_3$ molecular formula, with m/z 411.29 identified as $[M+H]^+$, which was estimated to be norethisterone enanthate (**17**).

The compound present in the DCM extract but not in the acetone and ethanol extracts were estimated to be compound (1*S*,2*S*,3*aR*,4*S*,5*S*,9*R*,11*R*,13*aS*)-4,9,11-tris(acetyloxy)-3*a*-hydroxy-2,5,8,8,12-pentamethyl-1*H*,2*H*,3*H*,3*aH*,4*H*,5*H*,8*H*,9*H*,10*H*,11*H*,13*aH*-cyclopenta[12]annulene-1-yl benzoate (**18**) and

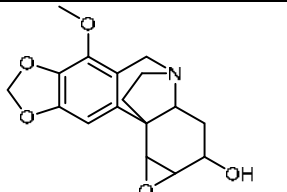
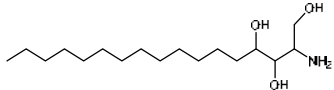
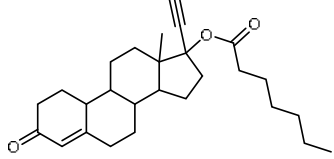
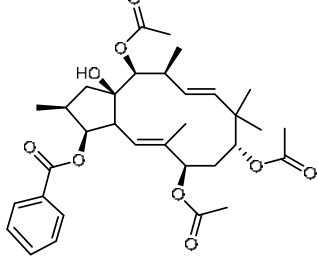
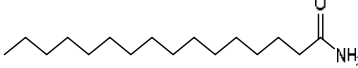
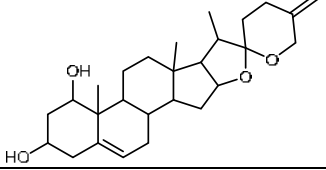
hexadecanamide (**19**) with molecular formula $C_{33}H_{44}O_9$ and $C_{16}H_{33}NO$, respectively, which were the base peaks at retention times of 17.16 and 18.11 min (purple circle in Fig. 4(b)) with m/z 585.29 and 256.26 identified as $[M+H]^+$. While the compounds contained in the acetone extract but not in the ethanol and DCM extracts are estimated to be a compound neoruscogenin (**20**) with the molecular formula $C_{29}H_{40}O_4$ which is the base peak at the retention time of 17.68 min (red circle in Fig. 4(a)) with m/z 429.37 identified as $[M+H]^+$. This compound was reported to have been isolated from *S. trifasciata* in Spain [33]. All critical data LC-MS are presented in Table 4.

Based on these data, it can be predicted that abundant components in the ethanol extract reduce radiation absorption activity; this may be due to the

antagonistic effect of the compounds present in the extract. In order to find out what functional groups are present in the best extracts, FTIR measurements were carried out on acetone extracts. The results are presented in Fig. 6.

Based on the FTIR spectrum, there is band 1, which is broad at wave number 3437 cm^{-1} , which is O-H stretching vibration, band 2 with sharp peak at 2944 cm^{-1} , which is methylene stretching vibration, band 3 with a sharp peak at 1733 cm^{-1} which is carbonyl stretching vibrations, band 4 with weak peak at 1669 cm^{-1} which is C=C stretching vibration. In addition, there are bands 5, 6, 7, and 8 with sharp peaks. Band 5 at 1435 cm^{-1} which is a shear bending vibration of methylene, band 6 at 1372 cm^{-1} which is an O-H bending

Table 4. Data LC-MS major in extract of *S. trifasciata*

Compound	RT (min)	Group Area			FG	MF	Mass error (ppm)	m/z	Structure
		Acetone	DCM	Ethanol					
Crinamidine (15)	12.92	1.58×10^9	7.24×10^8	3.53×10^9	Alkaloid	$C_{17}H_{19}NO_5$	2.90	317.13	
2-Amino-1,3,4-heptadecanetriol (16)	12.17	4.80×10^8	2.20×10^8	2.44×10^9	Alcohol	$C_{17}H_{37}NO_3$	3.23	303.27	
Norethisterone enanthate (17)	12.81	4.04×10^8	-	1.45×10^8	Steroid	$C_{27}H_{38}O_3$	3.22	410.28	
(1 <i>S</i> ,2 <i>S</i> ,3 <i>aR</i> ,4 <i>S</i> ,5 <i>S</i> ,9 <i>R</i> ,11 <i>R</i> ,13 <i>aS</i>)-4,9,11-tris(acetyloxy)-3a-hydroxy-2,5,8,8,12-pentamethyl-1 <i>H</i> ,2 <i>H</i> ,3 <i>H</i> ,3 <i>aH</i> ,4 <i>H</i> ,5 <i>H</i> ,8 <i>H</i> ,9 <i>H</i> ,10 <i>H</i> ,11 <i>H</i> ,13 <i>aH</i> -cyclopenta[12]annulen-1-yl benzoate (18)	17.16	-	6.41×10^9	-	Terpenoid	$C_{33}H_{44}O_9$	0.98	584.30	
Hexadecanamide (19)	18.11	-	1.33×10^9	-	Amide	$C_{16}H_{33}NO$	1.80	255.26	
Neoruscogenin (20)	17.69	5.84×10^8	-	-	Steroid	$C_{29}H_{40}O_4$	2.60	428.30	

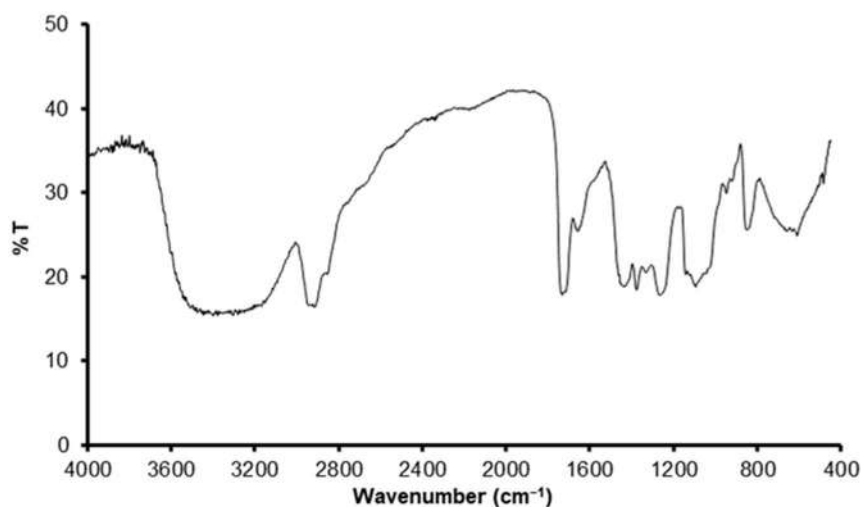


Fig 6. FTIR spectrum of PVA film + acetone extract

Table 5. FTIR absorption band of film PVA + acetone extract

Band	Wavenumber (cm ⁻¹)		Functional group
	Acetone extract	Literature [34]	
1	3437	3200–3650	O–H stretching (broad)
2	2944	~2926	–CH ₂ stretching
3	1733	1650–1850	C=O stretching
4	1669	1600–1660	C=C stretching
5	1435	~1465	–CH ₂ – bending
6	1372	1220–1440	O–H bending
7	1265	1000–1300	C–O stretching
8	1101	1000–1260	C–OH stretching

vibration in the plane, band 7 at 1265 cm⁻¹ which is a vibration C–O stretching, and band 8 at 1101 cm⁻¹ which is C–OH stretching vibration. Data for the 8 bands can be seen in Table 5.

According to a literature search by the authors, there have been no reports of compounds from natural materials that have activity as radiation absorbers. However, there are reports of Rubber magnets based on NBR and lithium ferrite that can absorb electromagnetic radiation [35]. However, based on our previous research, the fraction has the potential to be identified as steroid compound [24]. Moreover, the literature reports that the C–O, C=O, and C–OH functional groups are common functional groups contained in electromagnetic radiation-absorbing materials and work with a dipolar polarization mechanism [36]. In addition, the presence of a methyl group increases thermal conductivity more than halide because the methyl group

creates lattice vibrations or increases the phonon-free path [37]. In this study, the FTIR data showed the presence of the C–O, C=O, and C–OH functional groups, thus indicating that these functional groups contribute to reducing smartphone radiation. Neuroscogenin (20) was identified as a compound in acetone extract but not found in other extracts. This steroid compound has two C–OH groups, two C–O groups, and three methyl substituents. Based on this data, it could imply that neoruscogenin in the acetone extract contributes to the absorption of smartphone radiation.

CONCLUSION

In this study can be concluded that the acetone extract of *S. trifasciata* has the potential to be used as a screen protector on smartphones to reduce electromagnetic and thermal radiation emitted by

smartphones. However, it is suspected that the compound that has a role in increasing radiation absorption in smartphones is neoruscogenin, a steroid group.

■ ACKNOWLEDGMENTS

The authors gratefully acknowledged the IPB University through young lecturer research IPB University (No. 5508/IT3.L1/PT.01.03/P/B/2021).

■ AUTHOR CONTRIBUTIONS

Melinia Falestin conducted the experiment and calculation, Auliya Ilmiawati contribute to analyzing data and monitoring research, Akhiruddin Maddu contribute to providing tools and materials for heat radiation testing. Purwantiningsih Sugita, Budi Arifin, and Luthfan Irfana contribute to providing suggestions and input related to research. Auliya Ilmiawati wrote and revised the manuscript. All authors agreed to the final version of this manuscript.

■ REFERENCES

- [1] Wolverton, B.C., Johnson, A., and Bounds, K., 1989, *Interior Landscape Plants for Indoor Air Pollution Abatement: Final Report*, National Aeronautics and Space Administration, Washington, D.C., US, NASA-TM-101766.
- [2] Dohre, V., and Yadav, S., 2021, Impact of two different methods of extraction on total antioxidant activity and phenolic content in an uncommon plant (*Sansevieria trifasciata*) and commonly consumed fruits, *Flora and Fauna*, 27 (1), 35–41.
- [3] Febriani, Y., Mierza, V., Handayani, N.P., Surismayanti, S., and Ginting, I., 2019, Antibacterial activity of lidah mertua (*Sansevieria Trifasciata* Prain.) leaves extract on *Escherichia coli* and *Staphylococcus aureus*, *Open Access Maced. J. Med. Sci.*, 7 (22), 3882–3886.
- [4] Dey, B., Bhattacharjee, R., Mitra, A., Singla, R.K., and Pal, A., 2014, Mechanistic explorations of antidiabetic potentials of *Sansevieria trifasciata*, *Indo Global J. Pharm. Sci.*, 4 (2), 113–122.
- [5] Raslan, M.A., Abdel-Rahman, R.F., Fayed, H.M., Ogaly, H.A., and Taher, R.F., 2021, Metabolomic profiling of *Sansevieria trifasciata* hort ex. Prain leaves and roots by HPLC-PAD-ESI/MS and its hepatoprotective effect via activation of the NRF2/ARE signaling pathway in an experimentally induced liver fibrosis rat model, *Egypt. J. Chem.*, 64 (11), 6647–6671.
- [6] Andhare, R.N., Raut, M.K., and Naik, S.R., 2012, Evaluation of antiallergic and anti-anaphylactic activity of ethanolic extract of *Sansevieria trifasciata* leaves (EEST) in rodents, *J. Ethnopharmacol.*, 142 (3), 627–633.
- [7] Pinky, S.S., Monira, S., Hossein, M.A., and Hossein, A., 2020, Antioxidant, anti-inflammatory, cytotoxic, and analgesic activities of *Sansevieria trifasciata*, *Bangladesh Pharm. J.*, 23 (2), 195–200.
- [8] Abdullah, A., Angelina, A., Yumna, M., Arbianti, R., Utami, T.S., Hermansyah, H., and Ningsih, S., 2018, Flavonoid isolation and identification of mother-in-law's tongue leaves (*Sansevieria trifasciata*) and the inhibitory activities to xanthine oxidase enzyme, *E3S Web Conf.*, 67, 03011.
- [9] Afrasiabian, H., Hododi, R., Imanieh, M.H., and Salehi, A., 2017, Therapeutic effects of *Sansevieria Trifasciata* ointment in callosities of toes, *Global J. Health Sci.*, 9 (2), 264–268.
- [10] Ullah, H., Treesubstorn, C., and Thiravetyan, P., 2021, Enhancing mixed toluene and formaldehyde pollutant removal by *Zamioculcas zamiifolia* combined with *Sansevieria trifasciata* and its CO₂ emission, *Environ. Sci. Pollut. Res.*, 28 (1), 538–546.
- [11] Pamonpol, K., Areerob, T., and Prueksakorn, K., 2020, Indoor air quality improvement by simple ventilated practice and *Sansevieria trifasciata*, *Atmosphere*, 11 (3), 271.
- [12] Boraphech, P., and Thiravetyan, P., 2015, Removal of trimethylamine (fishy odor) by C₃ and CAM plants, *Environ. Sci. Pollut. Res.*, 22 (15), 11543–11557.
- [13] Yuningsih, L.M., Batubara, I., and Darusman, L.K., 2014, *Sansevieria trifasciata* properties as lead(II) ion biosorbent, *Makara J. Sci.*, 18 (2), 59–64.
- [14] Li, X., and Yang, Y., 2020, Preliminary study on Cd accumulation characteristics in *Sansevieria trifasciata* Prain, *Plant Divers.*, 42 (5), 351–355.

- [15] Winanti, S., Nurcahyo, A.D., Viona, E., Rosmalinda, R., and Mubarok, Y., 2012, Pengaruh lama adsorpsi ekstrak *Sansevieria* (lidah mertua) sebagai adsorben logam Ag dari limbah industri perak di Kotagede, *Pelita*, 8 (2), 55–64.
- [16] Mardlia, H.S., Cahyono, T., and Yulianto, Y., 2018, Pemakaian perasan lidah mertua (*Sansevieria trifasciata* Lorentii) terhadap pengurangan paparan radiasi elektromagnetik elektronik, *Jurnal Riset Kesehatan*, 7 (2), 72–79.
- [17] Mulyani, R.P., Abdullah, S., and Yulianto, Y., 2017, Pengaruh *Sansevieria* spp. terhadap penurunan tingkat radiasi elektromagnetik di laboratorium jurusan kesehatan lingkungan Purwokerto tahun 2016, *Buletin Keslingmas*, 36 (4), 463–469.
- [18] Maryana, N.A., Amri, C., and Muryani, S., 2018, Pengaruh bioscreen anti radiasi dari tanaman *Sansevieria trifasciata* Lorentii Mein Liebling terhadap penurunan radiasi laptop, *Sanitasi: Jurnal Kesehatan Lingkungan*, 9 (3), 111–115.
- [19] Panduwinata, R.A., Yamtana, Y., and Suyanto, A., 2021, Use of *Sansevieria trifasciata* to Reduce Computer Radiation in Internet Cafe Operators, *Joint International Conference of 8th Annual Conference on Industrial and System Engineering (ACISE) 2021 and 1st International Conference on Ergonomics, Safety, and Health (ICESH) 2021*, Semarang, Indonesia, July 13–14, 2021.
- [20] Kesari, K.K., Siddiqui, M.H., Meena, R., Verma, H.N., and Kumar, S., 2013, Cell phone radiation exposure on brain and associated biological systems, *Indian J. Exp. Biol.*, 51 (3), 187–200.
- [21] Cheshire, W.P., 2016, Thermoregulatory disorders and illness related to thermal and cool stress, *Auton. Neurosci.*, 196, 91–104.
- [22] Baby, N.M., Koshy, G., and Mathew, A., 2017, The Effect of electromagnetic radiation due to mobile phone use on thyroid function in medical students studying in a medical college in South India, *Indian J. Endocrinol. Metab.*, 21 (6), 797–802.
- [23] Gorpichenko, I., Nikitin, O., Banyra, O., and Shulyak, A., 2014, The influence of direct mobile phone radiation on sperm quality, *Cent. Eur. J. Urol.*, 67, 65–71.
- [24] Ilmiawati, A., Pujiyati, P., Hidayat, A., Sugita, P., Irfana, L., and Arifin, B., 2019, Blended film from PVA and *Sansevieria trifasciata* dichloromethane fraction for reducing thermal radiation from smartphones, *Makara J. Sci.*, 23 (2), 91–96.
- [25] Shaikh, J.R., and Patil, M.K., 2020, Qualitative tests for preliminary phytochemical screening: An overview, *Int. J. Chem. Stud.*, 8 (2), 603–608.
- [26] Nurly, H., Yan, Q., Song, B., and Shi, Y., 2019, Effect of carbon nanotubes reinforcement on the polyvinyl alcohol – polyethylene glycol double-network hydrogel composites: A general approach to shape memory and printability, *Eur. Polym. J.*, 110, 114–122.
- [27] Liu, Y., Wang, S., and Lan, W., 2018, Fabrication of antibacterial chitosan-PVA blended film using electrospray technique for food packaging applications, *Int. J. Biol. Macromol.*, 107, 848–854.
- [28] Alfarizi, P., Imansyah, F., Suryadi, D., Yacoub, R.R., and Marpaung, J., 2021, Identifikasi pengukuran intensitas radiasi medan elektromagnetik pada *smartphone* dan tingkat batas aman terhadap tubuh manusia, *Jurnal S1 Teknik Elektro Untan*, 2 (1), 1–8.
- [29] Sasongko, S.M., Muljono, A.B., Nrartha, I.M.A., Ginarsa, I.M., and Sultan, S., 2020, Sosialisasi radiasi telepon selular dan fenomena vampire energy di Desa Perampuan, Labuapi, Lombok Barat, *Jurnal Karya Pengabdian*, 2 (1), 45–52.
- [30] Rajeswari, N., Selvasekarapandian, S., Karthikeyan, S., Prabu, M., Hirankumar, G., Nithya, H., and Sanjeeviraja, C., 2011, Conductivity and dielectric properties of polyvinyl alcohol-polyvinylpyrrolidone poly blend film using non-aqueous medium, *J. Non-Cryst. Solids*, 357 (22-23), 3751–3756.
- [31] Boraphech, P., and Thiravetyan, P., 2015, Trimethylamine (fishy odor) adsorption by biomaterials: Effect of fatty acids, alkanes, and aromatic compounds in waxes, *J. Hazard. Mater.*, 284, 269–277.

- [32] Ikewuchi, C.C., Ayalogu, E.O., Onyeike, E.N., and Ikewuchi, J.C., 2011, Study on the alkaloid, allicin, glycoside and saponin composition of the leaves of *Sansevieria liberica* Gérôme and Labroy by gas chromatography, *Pac. J. Sci. Technol.*, 12 (1), 367–373.
- [33] González, A.G., Freire, R., García-Estrada, M.G., Salazar, J.A., and Suárez, E., 1972, New sources of steroid sapogenins—XIV: 25S-ruscogenin and sansevierigenin, two new spirostan sapogenins from *Sansevieria trifasciata*, *Tetrahedron*, 28 (5), 1289–1297.
- [34] Pavia, D.L., Lampman, G.M., Kriz, G.S., and Vyvyan, J.R., 2015, *Introduction to Spectroscopy*, 5th Ed., Cengage Learning, Stamford, US.
- [35] Kruželák, J., Kvasnicáková, A., Ušák, E., Ušáková, M., Dosoudil, R., and Hudec, I., 2020, Rubber magnets based on NBR and lithium ferrite with the ability to absorb electromagnetic radiation, *Polym. Adv. Technol.*, 31 (7), 1624–1633.
- [36] Qin, M., Zhang, L., and Wu, H., 2022, Dielectric loss mechanism in electromagnetic wave absorbing materials, *Adv. Sci.*, 9 (10), 2105553.
- [37] Ying, P., Zhang, J., Zhang, X., and Zhong, Z., 2020, Impacts of functional group substitution and pressure on the thermal conductivity of ZIF-8, *J. Phys. Chem. C*, 124 (11), 6274–6283.

Integral Membrane Properties of Polysulfone/Chitosan/Polyvinyl Alcohol Blend Incorporated with Rice Husk Ash Silica Gel

Nur Syazwanie Izzati Chik and Norin Zamiah Kassim Shaari*

School of Chemical Engineering, College of Engineering, Universiti Teknologi MARA, 40450 Selangor, Malaysia

* Corresponding author:

email: norinzamiah@uitm.edu.my

Received: August 11, 2022

Accepted: March 13, 2023

DOI: 10.22146/ijc.76999

Abstract: In this study, silica gel was extracted from rice husk ash using a modified acid-leaching process. The gel was then characterized using an X-ray Diffractometer (XRD) and an X-ray Fluorescence (XRF). At different loadings of 0, 0.05 and 0.10 wt.%, silica gel was used as a cross-linker in the membrane formulation. Fourier Transform Infrared Spectroscopy (FTIR) and Scanning Electron Microscopy (SEM) were used to characterize the membranes, while their performance was determined by pure water flux. XRD and XRF results revealed that the gel contained 76.85% silica. The presence of silica gel in membranes results in optimal water flux, indicating that the membranes have achieved good integral stability via the cross-linking process. Based on these positive findings, the applications of the membranes in the water-oil separation process will be evaluated in future work.

Keywords: cross-linking; integral membrane; rice husk ash; silica gel

■ INTRODUCTION

The world's rice consumption will continue to rise with the number of consumers. Because rice husk waste is abundant, some alternatives to add its value are being explored. The composition of rice husk (RH) comprises 70–80% cellulose and lignin, with 20–30% silica, alkali, and trace elements. RH has a high energy content of 16,720 kJ kg⁻¹, making it suitable for burning fuel or post-combustion [1]. When RH is burned between 350 and 750 °C, an amorphous shape of silica is formed, whereas a crystalline shape is formed when it is burned above 800 °C [2]. The yield of the ash is 25% when RH is burned.

The rice husk ash (RHA) is composed of 85–95% amorphous silica and a trace amount of alkali oxide [3]. The percentage of silica in rice varies according to its origin and the process of burning the husk. RHA is used in ceramics, construction, chemicals, and electronics because it increases the material's workability and mechanical properties [4-5]. Aside from that, it can be used as a filler for membranes, adsorbents, photoluminescent substances, and a filler for activated carbons [5]. RHA's popularity stems from the fact that it is both environmentally friendly and inexpensive.

On the other hand, silicate from rice husk ash can act as a cross-linker if incorporated into a membrane. This silica is introduced during the polymer-making process as a cross-linking reaction in which the polymer chain forms a network structure as a stabilization process during the reaction [6]. Inorganic silica gel is one of the inorganic materials that has been applied nowadays in wastewater treatment as a membrane for heavy metal removal and dyes. Having a structure with high porosity, hydrophilicity, and high activity makes the structure such a sponge for better adsorption. Silica gel is widely used because the pore structure inside the silica gel is easy to control, has strong selectivity, and high stability, and consists of silanol hydroxyl group. The silanol group is formed when the silicate tetrahedrons are condensed using oxygen as their binding site to generate the siloxane bond (Si–O–Si). Thus, the silanol group is originated from the siloxane bond when the synthetic silica is extracted from RHA. Moreover, this silica gel also increases the power of adsorption and selectivity to heavy metal ions [6].

There are two methods of extraction process: acid leaching and alkali leaching. Acid leaching is the most widely used method because it can produce silica at high

purity, where the silica has a large surface area for adsorption and with amorphous and mesoporous particles [7]. The amorphous structure is highly preferred for silica as the solubilities are enhanced as compared to the crystalline structure. This property is important in the membrane-making process as a homogeneous solution can be formed [8].

Acid leaching is the most common silica extraction method for RHA. This method is simple and does not require heating to a high temperature. RHA is cleaned of metal impurities with HCl before being treated with NaOH to produce sodium silicate. It was then followed by titration with HCl to form silica gel. This amorphous substance was derived from the dehydration process of silicate tetrahedrons to form a nanometer size of substance with siloxane bonds (Si–O–Si). In the membrane-making process, a study was reported on incorporating tetraethylorthosilicate as the silica nanoparticle into the blend polymer of polyvinyl alcohol/polyethylene glycol/glycerol [9]. It was found that the crosslinking process through the sol-gel method has improved the thermal and mechanical stabilities of the membranes. The sol-gel method involves the hydrolysis of silica, and the subsequent condensation process to form a covalent bond.

Aside from improving its properties, the incorporation of silica during the membrane formulation can combat the fouling and improve the hydrophilicity of the membrane [10]. By improving the interconnectivity of pores in the top layer and sub-layer of the membrane, these additives can avoid the formation of macro-voids, improve the flux, and increase the rejection of the respective pollutants [11-13]. According to Harun et al. [14], silica is chemically resistant and thermally stable. Furthermore, its high hydrophilicity manages to lessen fouling mechanisms by enhancing water permeation [14]. Previously, researchers investigated the use of tetraethylorthosilicate as a cross-linker in a composite hybrid membrane with polysulfone membrane as the support membrane. Results from antifouling evaluation revealed that the membranes exhibited good antifouling behavior with the use of humic acid as the foulant model with the additional advantage of high thermally stable and

high adsorption towards heavy metal [15].

The purpose of this study is to examine the outcome of the RHA silica extraction process using a modified acid-leaching method, as well as to evaluate the effect of the silica gel addition in the membrane formulation on the characteristics of the fabricated membranes.

■ EXPERIMENTAL SECTION

Materials

Polyvinyl alcohol (PVA, 87–89% hydrolyzed with a molecular weight average of 85,000–124,000) and polysulfone (PSF with a molecular weight of 22,000) were obtained from Sigma-Aldrich (M) Sdn Bhd, Malaysia. Aman Semesta Enterprise in Malaysia supplied the chitosan (CS). Merck Sdn. Bhd., Malaysia, supplied the 1-methyl-2-pyrrolidone (NMP) and polyethylene glycol 400 used in this study. R&M Chemicals, Malaysia, supplied the hydrochloric acid (HCl, 37% purity) and dimethyl sulfoxide. BT Science Sdn. Bhd. in Malaysia supplied the rice husk ash. Deionized water and distilled water were obtained from the UiTM Shah Alam Chemical Laboratory in Malaysia.

Instrumentation

Perkin Elmer Spectrum One Fourier Transform Infrared Spectroscopy (FTIR) instrument with Model Spectrum 400 was utilized to identify the emergence of functional groups in the silica gel as well as in the membrane. The analysis produces an infrared absorption spectrum, which identifies the presence of chemical bonds in the molecule. The wavelength was analyzed between 400 and 4000 cm^{-1} [16]. For the analysis of membrane surface morphology, a Field-Emission Scanning Electron Microscopy (FESEM) brand Joel: Model JSM-7600F was used. The pattern of the RHA silica gel was evaluated using a Rigaku X-ray Diffractometer: Model D/Max200V/PC with an accelerated voltage of 40 kV and a current of 30 mA. At a rate of 5°/min, the diffraction angle (2θ) was scanned from 10 to 80° [17]. X-ray Fluorescence Spectrometer (XRF) by Philip was utilized for the analysis of the extracted silica gel. The membrane filtration rig, which

uses nitrogen gas for purging, was used in the filtration process. The tools used for this study were a hot plate, magnetic stirrer, electrical balance, glassware, aluminium foil, filter paper, and pH paper.

Procedure

Silica extraction from RHA

The extraction method was adapted from de Lima et al. [17] with some modifications on the amount of raw RHA used and some parameters such as temperature and time. To 250 mL of distilled water, 25 g of raw RHA was added. To remove metal impurities, 8 g of HCl was added to the mixture. This is known as the pre-cleaning procedure. For 1 h, the solution was heated to 90 °C with continuous stirring at 650 rpm before it was left to cool overnight at room temperature. The filtration process was conducted through Smith 102 filter paper. The cleaned RHA was labeled on the permeated liquid. The permeated liquid was poured into a solution of 1 M NaOH with 250 mL volume. The mixture was heated at 80 °C and swirled at 600 rpm for 1 h in an alkaline leaching process. After it was left overnight, another filtration process was performed by using Smith 102 filter paper. The brownish liquid obtained from the filtration process was known as sodium silicate (Na_2SiO_3). The liquid has a pH of 14 after being tested with universal pH paper. For the gelling process, one normality of HCl was prepared. The titration using the HCl was conducted on the Na_2SiO_3 until it reached pH 7, at which point it solidified into a gel texture. The gel was left to mature for 24 h before it was then vigorously stirred with a magnetic stirrer at 1500 rpm to break it down into smaller sizes. It was then washed with

400 mL of distilled water. The washing procedure was repeated four times until the gel was clear (whitish). This step was taken to remove sodium chloride (NaCl) to obtain high-purity silica oxide (SiO_2) [17-19]. The reaction mechanism involved in the production of silica gel is depicted in Fig. 1. Fig. 2 depicts images of mature and washed silica gel, respectively. XRD, XRF, and FTIR were then used for the characterization of the silica gel.

PVA and CS solutions preparation

A 10 wt.% PVA solution was prepared by dissolving 10 g of PVA powder into 90 g of dimethyl sulfoxide for 4 h at 90 °C and 400 rpm stirring rate. After that, the solution was left to cool down. To make the CS solution, 0.02 g of CS was mixed with 99.98 g of 2 wt.% aqueous acetic acids, followed by heating at 90 °C for 4 h and at 400 rpm of stirring. The mixture was left to cool down before mixing [20].

Cross-linking process of PVA/CS solution

Both prepared PVA and CS solutions were mixed with 400 rpm stirring for 7 h while heated to 60 °C. Silica gel was poured into the mixture at a concentration of 0 to 0.10 wt.% of the total mixture [14]. As a catalyst, 1 mL of HCl 37% was added. The formulations of each membrane are shown in Table 1 [15,20]. Fig. 3 depicts the cross-linking reaction from the sol-gel method between the silicate from RHA gel and the hydroxyl group from PVA.

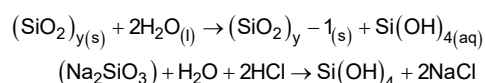


Fig 1. Reaction mechanism of silica gel [18]

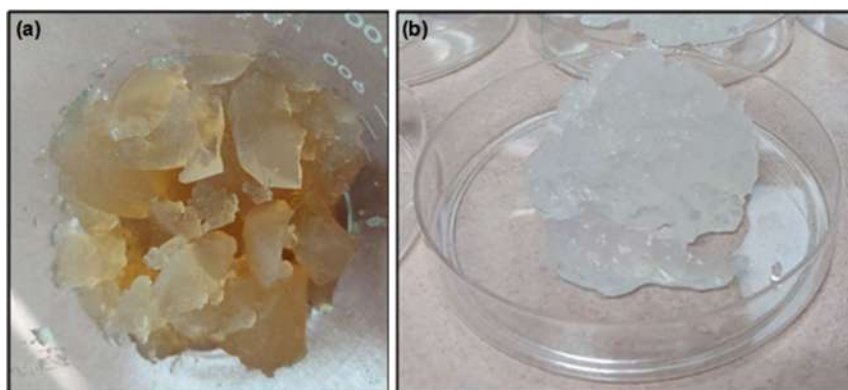
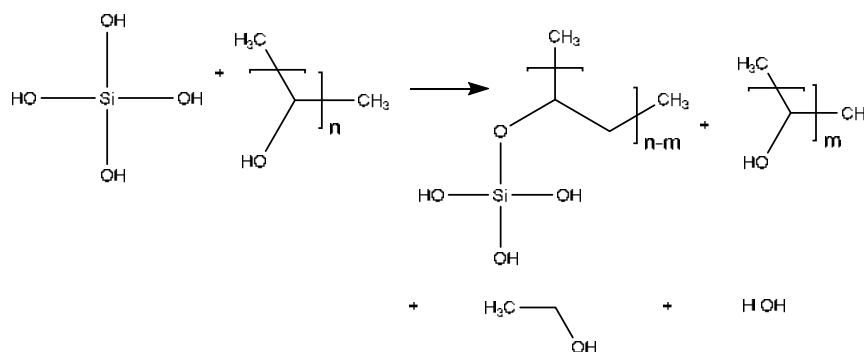


Fig 2. (a) Mature and (b) washed RHA silica gel

Table 1. The formulations of membranes

Membrane code	Hybrid solution			
	PVA solution (g)	CS solution (g)	Silica gel (wt.%)	HCl (mL)
MA	50.00	50.00	0.00	1.00
MB	50.00	50.00	0.05	1.00
MC	50.00	50.00	0.10	1.00

**Fig 3.** Reaction mechanism between RHA silica gel and a hydroxyl group from PVA [20]**Table 2.** Membrane formulations

Membrane	PSF solution (g)	Hybrid solution (g)
MA	50.00	1.00 (without silica)
MB	50.00	1.00 (0.05 wt.% silica)
MC	50.00	1.00 (0.10 wt.% silica)

Polysulfone (PSF) solution preparation

To make 13 wt.% PSF solution, 13 g of PSF beads were dissolved in 82 g of NMP, followed by adding 5 g of PEG 400. For approximately 6 h, the solution was heated at 60 °C and stirred at 400 rpm. The solution was left at room temperature before the membrane solution was prepared [15].

Membrane preparation

A 50 g PSF solution was mixed with one gram of each prepared hybrid membrane solution shown in Table 1. For 3 h, a stirring was set at 700 rpm while the mixture was being heated at 80 °C. The formulation for each membrane is shown in Table 2. For the membrane film-making process, the membrane solution was spread to a thickness of 100 μm with a Baker's Film Applicator on a glass plate. The plate was submerged in a water-containing coagulation bath for 24 h to solidify. This method was called the phase inversion method. Then, the film of the membrane was allowed to cure for 1 d at room temperature [20]. The films were characterized by functional groups using FTIR and surface morphology

using FESEM, and the performance was checked through pure water flux.

RHA silica gel yield calculation

Eq. 1 was used to determine the yield of RHA silica gel after the washing process;

$$Y_g = \frac{c}{m} \times 100\% \quad (1)$$

where *m* represents the weight of mature silica gel, *c* is the weight of washed silica gel, and *Y_g* is the yield of silica gel (%) after washing [21].

Analysis of water flux

A dead-end filtration rig was used for the water flux evaluation, which was conducted at room temperature. The apparatus was linked to a compressed nitrogen gas cylinder, which applied pressure to the feed solution. The filtration through the membrane was performed at 6 bars for 60 min, with sampling every 15 min. The flux was determined through the collected volume of the permeate solution. For each formulation, three membrane samples were tested before the average reading was recorded. The membrane was cut into a circular shape with an area of $0.196 \times 10^{-2} \text{ m}^2$. Eq. 2 was used to calculate the permeate flux;

$$J_p = \frac{Q_p}{A\Delta t} \quad (2)$$

where J_p is the permeate flux ($L\ m^{-2}h^{-1}$), Q_p is the volume of permeate (L), A the effective membrane area (m^2), and Δt is the sampling time (h) [22].

RESULTS AND DISCUSSION

RHA Silica Gel Analysis

Fig. 4 depicts the result from the XRD analysis. Based on the image, the silica gel shows an amorphous structure without the presence of NaCl because no crystalline peaks were observed in the range of 30 to 60° [19]. This result shows a similar pattern to the one obtained from the previous research by de Lima et al. [17], where the modified extraction process successfully extracted a high amount of SiO_2 [17]. It could be concluded that the washing method in this modified method has been carried out efficiently to remove all the NaCl. NaCl in the silica gel should be avoided because it may interfere with the cross-linking reaction in the membrane-making process [18].

A further investigation of the composition of the silica gel was performed through XRF analysis. Table 3 shows that the gel has 76.85% silica with 0.55% Na and 0.72% Cl. The remaining 21.88% of the total composition could be oxides and metal impurities. Although the washing process can remove all the NaCl, it fails to remove the metal impurities. Setyawan [19] discovered that RHA extraction yielded 86.17% SiO_2 , and the results

were relatively high in comparison to this finding. The reason could be due the RHA was obtained from different sources in local areas.

FTIR analysis of the RHA silica gel was performed in the 400–4000 cm^{-1} range. The spectra in Fig. 5 can identify a few major chemical groups. The strong and broad absorbance of the silanol O–H group stretching at peak 3296 cm^{-1} and symmetric stretching vibration band at peak 1635 cm^{-1} indicates another O–H group from water [6,23–24]. Si–O–Si absorption band was discovered at 1082 cm^{-1} [24–26].

Characteristics of Integral Membrane

The FTIR spectra of membranes MA, MB, and MC are shown in Fig. 6. The peaks of the three membranes are primarily composed of PSF/PVA/CS, with silica gel incorporated as a cross-linker in the formulations of MB and MC. Overall, the fingerprints of MB and MC differed only slightly due to the appearance of small peaks ranging from 400 to 4000 cm^{-1} . In the 2800–3600 cm^{-1} range, it

Table 3. The elements of silica gel

Element	Percentage (%)
Si	76.85
Na	0.55
Cl	0.72
Others	21.88

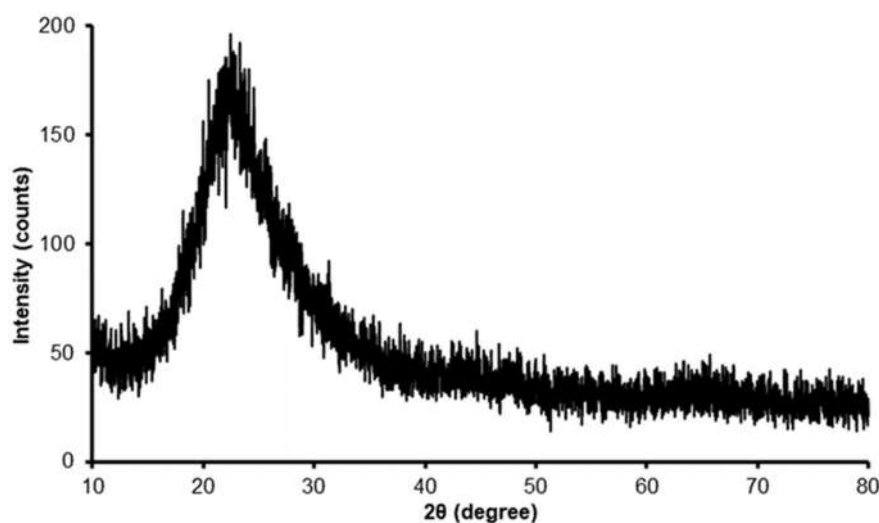


Fig 4. X-ray diffraction pattern of RHA silica gel

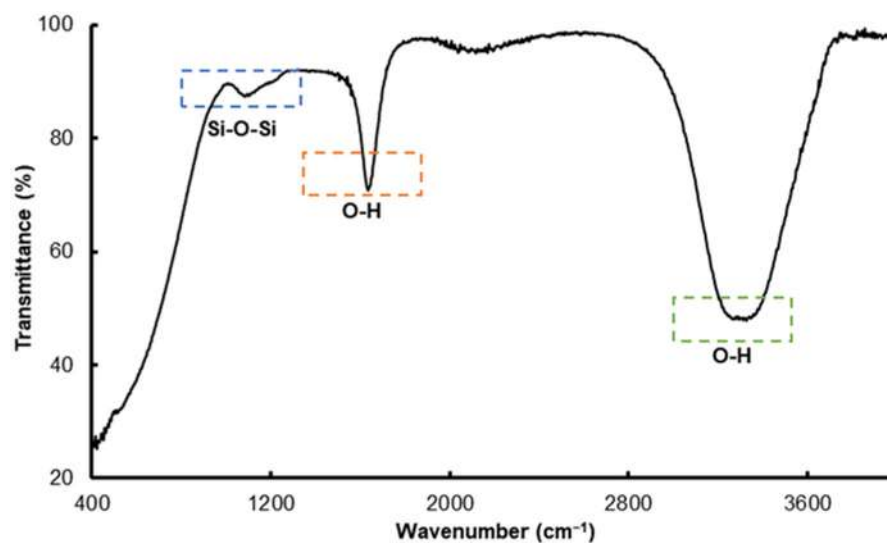


Fig 5. FTIR spectra of RHA silica gel

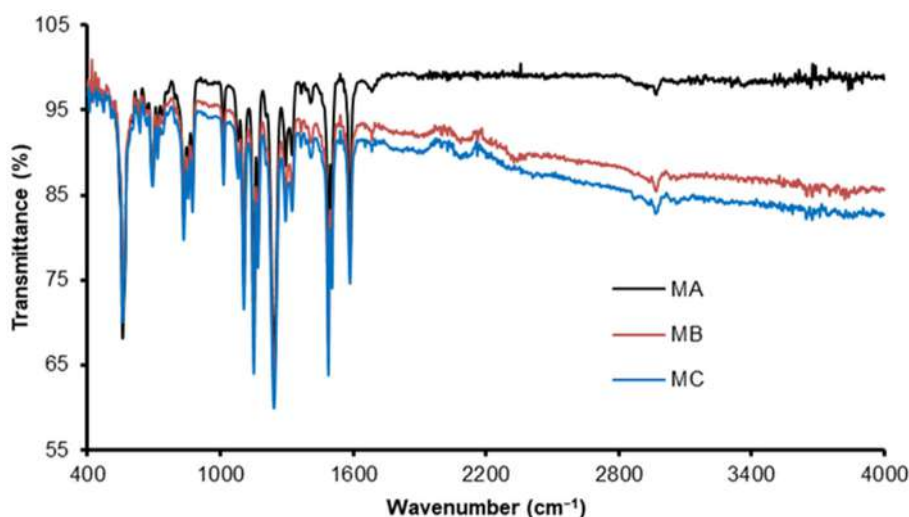


Fig 6. FTIR spectra of membranes

corresponded to the silanol O-H groups of silica gel that have overlapped with hydroxyl groups (O-H) of PVA for MB and MC. The spectra revealed that all membranes had C-H stretching that overlapped with amine bands at a peak around 2969 cm^{-1} , and the peak at 1600 cm^{-1} also corresponded to O-H groups [16,20]. The vibration modes of C=O and C-O bonds were coming from the unhydrolyzed vinyl acetate of PVA that was observed between 1100 and 1700 cm^{-1} [16]. The peaks of MB and MC at 2139 and 2156 cm^{-1} , respectively, represent the weak stretching band of C=C alkynes derived from conjugated silica gel [27-28]. The stretching mode of Si-O is usually assigned to the absorption band between 1000 and

1100 cm^{-1} for MB and MC [29], where the crosslinking process to form Si-O-C at 1107 cm^{-1} resulted in the overlapping to the original C-O bond. Despite being crosslinked by silica, the O-H groups stretching in membranes MB and MC at 2800 – 3600 cm^{-1} showed a membrane's hydrophilicity [26].

Fig. 7 depicts the surface morphology of membranes. Based on the images, it was observed that the pore structure of MA was uneven in size and had a larger pore size as compared to MB and MC. Membranes MB and MC had smaller pore sizes and denser surfaces that were caused by the reaction between the polymer blend's O-H group and the Si-O-H of the silica gel [16].

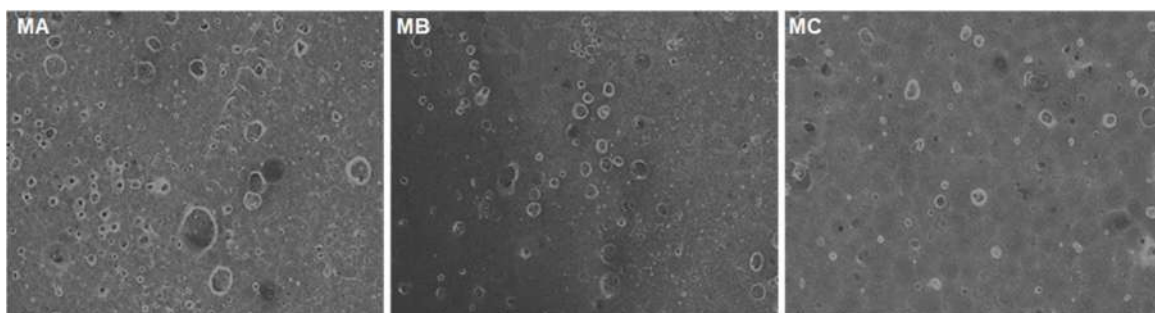


Fig 7. Surface morphology structure of membranes

Observing the surface structure of MB and MC, it was concluded that both membranes had a smooth surface, and no agglomeration was spotted, which proved that the crosslinking process with the silica gel was successful [18].

Water Flux Analysis

Fig. 8 depicts the pure water flux (PWF) results for MA, MB, and MC after 1 h of filtration. PWF is related to the surface structure of the membrane and its hydration properties, with a constant value of PWF indicating that the membrane porosity remained constant throughout the filtration time [22]. The increment in the water flux indicates changes in the permeable structure of the membrane [21].

According to Fig. 8, the flux for MA continues to increase until 1 h, indicating that there are changes in the pore sizes of the membrane [30]. The membrane must have ruptured, causing the pore size to increase. It was also observed through a visual that the membrane was swollen at the end of the filtration process. Realizing that PVA has an abundance of O–H groups, this situation was attributed to the membrane's lack of integral stability in the absence of a cross-linker such as RHA silica gel [31]. It could be related to Fig. 7 where the structure of the membrane MA was not compact without the cross-linking process, resulting in high water flux and swelling of the membrane.

Different flux patterns were observed in the MB and MC, where the flux began to decrease gradually after 15 min of filtration and continued to decrease until 1 h of filtration time. After 1 h, the fluxes for MB and MC were $40.7 \text{ L m}^{-2} \text{ h}^{-1}$ and $26.9 \text{ L m}^{-2} \text{ h}^{-1}$, respectively. It was

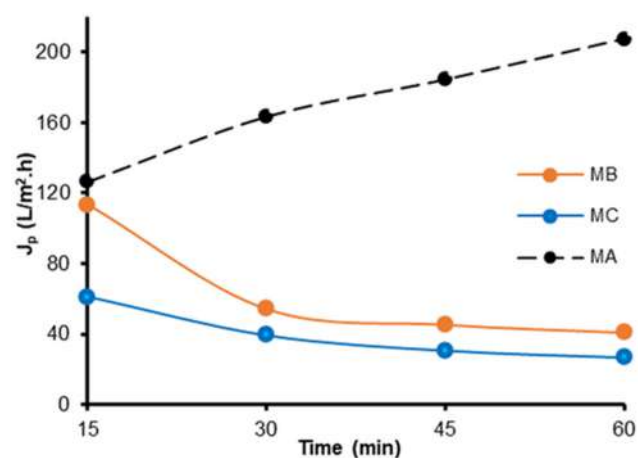


Fig 8. Pure water flux of membranes

observed that there was no pore enlargement on the surface of the membrane after the filtration process. This situation demonstrated that the crosslinking process improved the membrane's structure by providing higher membrane stability [31]. Although the crosslinking reaction utilized the O–H group from the polymer blend, the silica with good hydrophilicity compensated for the effect to ensure membranes MB and MC exhibited good water permeability [26,32]. MC has a lower flux than MB due to an increase in cross-linking degree due to a higher concentration of RHA silica gel added to the membrane formulation.

CONCLUSION

In conclusion, a modified acid leaching technique was found to successfully extract a significant amount of silica from the rice husk ash. The process also was successful in removing NaCl. Even though only 76.85% silica could be extracted, the incorporation of silica gel

in the membrane formulation had a significant effect in terms of improving the membrane polymer matrix through the cross-linking process, with the added benefit of homogeneous membrane solution being produced. Based on this promising result, additional research will be carried out to evaluate the performance of the membranes in the water-oil separation process.

■ ACKNOWLEDGMENTS

The study was supported by Universiti Teknologi MARA (UiTM) through a grant with a file number 600-RMC/GPK 5/3 (119/2020).

■ REFERENCES

- [1] Ilochonwu, C.E., Nwajagu, C.O., Onyenanu, I.U., and Nwonye, E.I., 2016, "Effect of Temperature in Extraction of High Purity Amorphous Silica from Rice Husk for Silicon Production" in *EPD Congress 2015*, Eds. Yurko, J.A., Allanore, A., Bartlett, L., Lee, J., Zhang, L., Tranell, G., Meteleva-Fischer, Y., Ikhmayies, S., Budiman, A.S., Tripathy, P., and Fredrickson, G., Springer, Cham, 219–227.
- [2] Rasoul, B.I., Günzel, F.K., and Rafiq, M.I., 2018, "Effect of Rice Husk Ash Properties on the Early Age and Long Term Strength of Mortar" in *High Tech Concrete: Where Technology and Engineering Meet*, Eds. Hordijk, D.A., and Luković, M., Springer International Publishing, Cham, 207–214.
- [3] Hossain, S.K.S., Mathur, L., Bhardwaj, A., and Roy, P.K., 2019, A facile route for the preparation of silica foams using rice husk ash, *Int. J. Appl. Ceram. Technol.*, 16 (3), 1069–1077.
- [4] Todkar, B.S., Deorukhkar, O.A., and Deshmukh, S.M., 2016, Extraction of silica from rice husk, *Int. J. Eng. Res. Dev.*, 12 (3), 69–74.
- [5] You, P.Y., Kamarudin, S.K., and Masdar, M.S., 2019, Improved performance of sulfonated polyimide composite membranes with rice husk ash as a bio-filler for application in direct methanol fuel cells, *Int. J. Hydrogen Energy*, 44 (3), 1857–1866.
- [6] Rohaeti, E., Primadiska, N.R., and Rafi, M., 2020, Silica modified L-lysine as Pb(II) adsorbent, *AIP Conf. Proc.*, 2243, 030020.
- [7] Steven, S., Restiawaty, E., Pasymi, P., and Bindar, Y., 2021, An appropriate acid leaching sequence in rice husk ash extraction to enhance the produced green silica quality for sustainable industrial silica gel purpose, *J. Taiwan Inst. Chem. Eng.*, 122, 51–57.
- [8] Ditzinger, F., Price, D.J., Ilie, A.R., Köhl, N.J., Jankovic, S., Tsakiridou, G., Aleandri, S., Kalantzi, L., Holm, R., Nair, A., Saal, C., Griffin, B., and Kuentz, M., 2019, Lipophilicity and hydrophobicity considerations in bio-enabling oral formulations approaches - A PEARRL review, *J. Pharm. Pharmacol.*, 71 (4), 464–482.
- [9] Shaari, N.Z.K., Abd Rahman, N., Sulaiman, N.A., and Mohd Tajuddin, R., 2017, Thin film composite membranes: Mechanical and antifouling properties, *MATEC Web Conf.*, 103, 06005.
- [10] Swain, B., 2017, Recovery and recycling of lithium: A review, *Sep. Purif. Technol.*, 172, 388–403.
- [11] Jamalludin, M.R., Harun, Z., Basri, H., Yunos, M.Z., and Shohur, M.F., 2013, Performance studies of polysulfone-based membrane: Effect of silica morphology, *Appl. Mech. Mater.*, 372, 8–12.
- [12] Jamalludin, M.R., Harun, Z., Hubadillah, S.K., Basri, H., Ismail, A.F., Othman, M.H.D., Shohur, M.F., and Yunos, M.Z., 2016, Antifouling polysulfone membranes blended with green SiO₂ from rice husk ash (RHA) for humic acid separation, *Chem. Eng. Res. Des.*, 114, 268–279.
- [13] Arthanareeswaran, G., and Starov, V., 2011, Effect of solvents on performance of polyethersulfone ultrafiltration membranes: Investigation of metal ion separations, *Desalination*, 267 (1), 57–63.
- [14] Harun, Z., Jamalludin, M.R., Basri, H., Shohur, M.F., Rosman, N., and Yunos, M.Z., 2013, The effect of synthetic silica on ultrafiltration PSF membrane, *J. Teknol.*, 65 (4), 121–125.
- [15] Shaari, N.Z.K., Sulaiman, N.A., and Abd Rahman, N., 2019, Thin film composite membranes: Preparation, characterization, and application towards copper ion removal, *J. Environ. Chem. Eng.*, 7 (1), 102845.
- [16] Shaari, N.Z.K., Abd Rahman, N., and Mohd Tajuddin, R., 2012, Thin film composite membrane with hybrid membrane as the barrier layer:

- Preparation and characterization, 2012 *IEEE Colloquium on Humanities, Science and Engineering (CHUSER)*, Kinabalu, Malaysia, 3-4 December 2012, 615–620.
- [17] de Lima, S.P.B., de Vasconcelos, R.P., Paiva, O.A., Cordeiro, G.C., de Moraes Chaves, M.R., Filho, R.D.T., de Moraes Rego Fairbairn, E., 2011, Production of silica gel from residual rice husk ash, *Quim. Nova*, 34 (1), 71–75.
- [18] Chik, N.S.I., Shaari, N.Z.K., Ramlee, N.A., and Abdul Manaf, M.R., 2022, Extraction of silica from rice husk ash and its effect on the properties of the integral membrane, *ASM Sci. J.*, 17, 1–13.
- [19] Setyawan, N., Hoerudin, H., and Wulanawati, A., 2019, Simple extraction of silica nanoparticles from rice husk using technical grade solvent: Effect of volume and concentration, *IOP Conf. Ser.: Earth Environ. Sci.*, 309, 012032.
- [20] Sulaiman, N.A., Shaari, N.Z.K., and Abdul Rahman, N., 2016, Removal of Cu(II) and Fe(II) ions through thin film composite (TFC) with hybrid membrane, *J. Eng. Sci. Technol.*, 11, 36–49.
- [21] Chik, N.S.I., and Shaari, N.Z.K., 2022, Effect of rice husk ash gel on the properties of integral membrane from a blend of polysulfone/chitosan/polyvinyl alcohol, *AIP Conf. Proc.*, 2610, 020010.
- [22] Ahmad, A.L., Yusuf, N.M., and Ooi, B.S., 2012, Preparation and modification of poly (vinyl) alcohol membrane: Effect of crosslinking time towards its morphology, *Desalination*, 287, 35–40.
- [23] Geetha, D., Ananthiand, A., and Ramesh, P.S., 2016, Preparation and characterization of silica material from rice husk ash – An economically viable method, *Res. Rev.: J. Pure Appl. Phys.*, 4 (3), 20–26.
- [24] Patel, K.G., Misra, N.M., and Shettigar, R.R., 2016, Preparation and characterization of silica gel from wheat straw, *Int. J. Chem. Eng. Appl.*, 7 (5), 344–347.
- [25] Ravi, S., and Selvaraj, M., 2014, Incessant formation of chain-like mesoporous silica with a superior binding capacity for mercury, *Dalton Trans.*, 43 (14), 5299–5308.
- [26] Alias, S.S., Harun, Z., Manoh, N., and Jamalludin, M.R., 2020, Effects of temperature on rice husk silica ash additive for fouling mitigation by polysulfone–RHS ash mixed-matrix composite membranes, *Polym. Bull.*, 77 (8), 4043–4075.
- [27] Nandiyanto, A.B.D., Oktiani, R., and Ragadhita, R., 2019, How to read and interpret FTIR spectroscopy of organic material, *Indones. J. Sci. Technol.*, 4 (1), 97–118.
- [28] Reyes-Ortega, F., Parra-Ruiz, F.J., Averick, S., Rodríguez, G., Aguilar, M.R., Matyjaszewski, K., and San Román, J., 2013, Smart heparin-based bioconjugates synthesized by a combination of ATRP and click chemistry, *Polym. Chem.*, 4 (9), 2800–2814.
- [29] Ruan, D.S., Li, Y.L., Wang, L., Su, D., and Hou, F., 2010, Fabrication of silicon oxycarbide fibers from alkoxide solutions along the sol–gel process, *J. Sol-Gel Sci. Technol.*, 56 (2), 184–190.
- [30] Tian, S., Ren, W., Li, G., Yang, R., and Wang, T., 2017, A theoretical analysis of pore size distribution effects on shale apparent permeability, *Geofluids*, 2017, 7492328.
- [31] Reino Olegário da Silva, D.A., Bosmuler Zuge, L.C., and de Paula Scheer, A., 2020, Preparation and characterization of a novel green silica/PVA membrane for water desalination by pervaporation, *Sep. Purif. Technol.*, 247, 116852.
- [32] Xu, H.P., Yu, Y.H., Lang, W.Z., Yan, X., and Guo, Y.J., 2015, Hydrophilic modification of polyvinyl chloride hollow fiber membranes by silica with a weak *in situ* sol–gel method, *RSC Adv.*, 5 (18), 13733–13742.

Synthesis of Hydroxyapatite-Polyethylene Glycol with *In-Situ* Method Using Calcium Oxide from Blood Shells (*Anadara granosa*)

Novesar Jamarun^{1*}, Nabila Ayyu Trycahyani¹, Syukri Arief¹, Upita Septiani¹, and Vivi Sisca²

¹Department of Chemistry, Andalas University, Limau Manis, Padang 25163, Indonesia

²Department of Biology Education, Institute of Education YPM Bangko, Jl. Jenderal Sudirman, Meranging, Jambi 37313, Indonesia

* **Corresponding author:**

email: novesarjamarun@sci.unand.ac.id

Received: October 21, 2022

Accepted: January 23, 2023

DOI: 10.22146/ijc.78538

Abstract: Hydroxyapatite ($\text{Ca}_{10}(\text{PO}_4)_6(\text{OH})_2$, HAp) is a calcium phosphate-based biomaterial that is widely used in bone implants due to its similarity in composition with the constituent elements of bone. However, HAp still has poor mechanical properties, so research was carried out to improve the mechanical properties such as reduced brittleness, less fracture resistance, and a denser structure of HAp by synthesizing composites with PEG. This study used PEG as a filler and HAp as a matrix. HAp was synthesized from blood clam shells (*Anadara granosa*) using the sol-gel method. HAp-PEG composite was synthesized using the in-situ method with various HAp concentrations of 40, 50, 60, 70, and 80%. FTIR characterization showed the presence of functional groups PO_4^{3-} and CO_2^{3-} , which indicated the presence of HAp. Analysis of the XRD pattern showed a crystal size of 24.194 nm. SEM-EDX showed the needle-shaped HAp-PEG composite HAp crystal morphology and obtained a Ca/P ratio of 1.87. Analysis of DTA results showed a weight loss of 65.72% in the composite at a temperature > 200 °C. A degradation test was also carried out to see the percentage of the HAp-PEG composite to be degraded, and the optimum degraded composite with increasing days had a concentration of 70%.

Keywords: hydroxyapatite; HAp-PEG composite; in-situ method; blood shells

■ INTRODUCTION

According to the Pharmaceutical and Medical Technology Center (PTFM), BPPT needs around 120,000 bones each year with a value of around Rp 600 billion. Based on data from the statistics center in 2018, bone implants needed in Indonesia are around Rp 27 trillion, and this data has continued to increase since 2016. This report shows that Indonesia's need for bone implants is very high. As a complex system and the most important constituent part of the human body, which consists of hydroxyapatite (HAp) and type 1 collagen fibrils (70% HAp, 20% collagen, and 10% water), if there is damage to the bone, it needs to be repaired [1-2].

One way to overcome this problem is to use bone graft material to replace bone. One of the requirements for the replacement material in human bones is that it is biocompatible. It does not cause a rejection reaction from

the human immune system because it is considered a foreign object [2-3]. Bioceramic material that is often used in biomedical applications is synthetic HAp, $\text{Ca}_{10}(\text{PO}_4)_6(\text{OH})_2$, as bone graft material [3]. Due to the similarity of composition and mineral phase in bone, having excellent biocompatibility, ability to assist cell function, and osteoconductivity, HAp is used as one of the alternative materials for bone graft material [4].

HAp is a bioceramic material with strong chemical bonds, bioactive with high bioaffinity [5-6]. Calcium phosphate is the main constituent of HAp, also contained in bone. HAp, as a biomaterial, can be synthesized from various sources, including limestone, eggshells, shells, or bones. This study synthesized HAp from blood clam shells (*Anadara granosa*) with a CaCO_3 content of 97–99%. Clams are marine biota that lives in mud or on the sand of the ocean. Indonesian people consume blood clams shells as culinary food and handicrafts. The

processing of blood clam shell waste is limited, so the clams shell waste is increasing and accumulating. Based on previous research, the blood clams shells have the main content of CaCO_3 as a source of calcium oxide. The results of Insani et al.'s research [7] stated that the CaO content in blood clams shells was 98%, and the phase with an intensity of 26° and crystal size of 7.79 nm.

HAp as a bone implant material still has several weaknesses, namely its low mechanical properties. According to Ryabenkova et al. [8], an essential condition for a material to be substituted for bone is its ability to bind to living bone or its host in the body. Therefore, to adjust its properties such as biocompatibility, mechanics, and solubility to control the composition, as well as the morphology, organic changes were carried out such as the use of organic compounds in bone implants, one of the methods carried out in this study was the synthesis of HAp composites with polyethylene glycol (PEG) [9]. HAp binds directly through the natural bone conversation mechanism so that it can accelerate bone formation on the implantation surface, but it is fragile. Then it needs to be compiled with biopolymers such as PEG, which is a biocompatible flexible, hydrophilic polymer, nontoxic, and has high tenacity and toughness [10]. In addition, PEG also has corrosion resistance and good chemical and thermal stability. However, PEG also has the disadvantage of having low thermal conductivity. For this reason, the synthesis of HAp-PEG composite is expected to increase the advantages of PEG and HAp so that a composite is formed with the ability as a suitable bone implant material and can be applied in the medical world.

Previous research found that using PEG as a composite material with HAp significantly affected particle size; the particle size of HAp decreased with increasing concentration of PEG in the composite. In addition, it was also found that there was a higher absorption rate than with the use of HAp alone. The temperature of the synthesis also influences the use of PEG as a composite with HAp because the nature of PEG is volatile, and when heated, it hardens quickly. Still, at room temperature, it becomes soft again [11-12]. This paper reports that HAp-PEG composite with a concentration of 70 wt.% has more optimum results in

terms of degradation ability compared to other concentrations, has a hexagonal structure and a crystal size of 24.194 nm, and had needle-shaped crystals, indicating the presence of HAp and agglomerated PEG crystals.

■ EXPERIMENTAL SECTION

Materials

The materials used in this study were blood clam shells collected from the beach, ammonium hydroxide NH_4OH (Merck), diammonium hydrogen phosphate NH_2HPO_4 (Merck), nitric acid HNO_3 p.a (Merck), PEG 6000, Phosphate-buffered saline (PBS, pH = 7.4), filter paper, and aquadest.

Instrumentation

The tools used in this research are mortar, pestle, grinder (Fritsch Pulveristte 16), furnace (Thermo Insight), hot plate, analytical balance, aluminum foil, oven (Labtech), pH indicator, and the necessary laboratory glassware. The characterization tools used are FTIR (FTIR Spectrometer Frontier PerkinElmer), XRD (PANalytical X'Pert PRO), DTA (Shimadzu dtg-60 & Shimadzu ta-60), and SEM EDX (Thermofisher Quatro S).

Procedure

Preparation of CaO powder

The blood clam shells (1.6 g) were cleaned, washed, dried, and ground using a grinder. The mashed blood clam shells were then calcined for 5 h at 900°C to obtain CaO powder [13].

HAp synthesis using sol-gel method

A total of 4.2 g of CaO powder was dissolved in 75 mL of 2 M HNO_3 , then stirred using a stirrer at a temperature of 65°C for 15 min at a speed of 250 rpm; the $\text{Ca}(\text{NO}_3)_2$ solution formed was then filtered. The $\text{Ca}(\text{NO}_3)_2$ filtrate was added with NH_4OH solution until pH 10 was obtained and sol of $\text{Ca}(\text{OH})_2$ was formed. The $\text{Ca}(\text{OH})_2$ sol that has been received is then added drop by drop, a 250 mL solution of 0.18 M $(\text{NH}_4)_2\text{HPO}_4$, then heated at 60°C while stirring using a stirrer for 5 h to form a HAp sol. The HAp sol was then aged for 24 h to

create a gel. The HAp gel was then filtered, then dried using an oven for 5 h at 110 °C [4].

Synthesis of HAp-PEG in-situ

A total of 4 g of PEG was dissolved in 15 mL of distilled water and stirred using a stirrer. In a separate container, 1.6 g of CaO is dissolved in 28 mL of 2 M HNO₃; check the pH of the solution. The dissolved CaO is then added to the PEG solution and stirred using a stirrer until homogeneous. After being homogeneous, this solution was added to the PEG solution while still being mixed, and then checked the pH and added NH₄OH to pH 10. A total of 2.2583 g (NH₄)₂HPO₄ is dissolved with NH₄OH and then mixed; the homogeneous solution is added dropwise into the previous solution then, check the pH of the solution and adjust the pH to pH 10 by adding NH₄OH. After all, were dissolved, they were heated using an oven at a temperature of 60 °C for 24 h. Heating using an oven at a temperature of 60°C because if it is more than 60 °C, it will cause damage to the HAp-PEG composite product that has been formed. The same thing was done for variations in the concentration of HAp on this HAp-PEG composite, with variations in concentrations of 40, 50, 60, 70, and 80% [11,14].

Preparation PBS solution pH 7.4

As much as 8 g of NaCl, 2.38 g of NH₂HPO₄, and 0.19 g of KH₂PO₄ were dissolved in distilled water until the volume is 1 L, then the pH of the solution was measured using a pH meter, and 0.1 M NaOH was added into the solution so that the pH reaches 7.4 [12,15].

Characterization

The product was characterized using an FTIR tool to identify the functional groups of the synthesized composite with measurements in the wave number range of 400–4000 cm⁻¹. XRD tool to determine the structure and crystal size of the synthesized HAp-PEG composite. SEM-EDS tool to determine the surface morphology and determine the Ca/P ratio in the resulting product. DTA tool to determine weight changes in composites related to changes in combustion temperature. The degradation test was carried out by immersing the product in a PBS solution for 14 d, and the product was weighed once every 2 d periodically within that period [16].

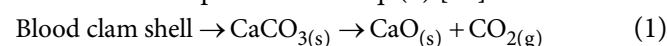
RESULTS AND DISCUSSION

Effect of HAp Concentration on HAp-PEG Composites

Effect synthesis of the HAp-PEG composite was carried out with various concentrations of 40, 50, 60, 70, and 80%, so there were some differences in the resulting product as seen in Table 1. The resulting product is generally white in the form of plates before being heated. The product in the form of a white gel indicates that HAp has been formed in the composite.

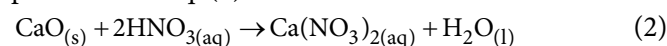
Preparation of CaO from *Anadara granosa*

HAp (Ca₁₀(PO₄)₆(OH)₂) was synthesized from *A. granosa*, because of the high CaCO₃ content, which was as much as 98.7%. CaCO₃ contained in this *A. granosa* is the primary source of calcium in the synthesis of HAp. The cleaned and mashed *A. granosa* were then calcined at 900 °C for 5 h. This calcination process aims to remove organic compounds and reduce CaCO₃ compounds; during this calcination process, a decomposition reaction also occurs, where CaCO₃ become CaO as presented in Eq. (1) [17].

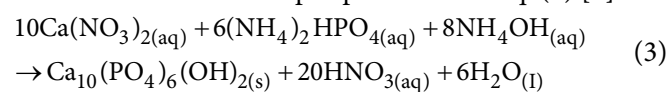


Analysis of HAp Synthesis Results and HAp-PEG Composites

HAp was synthesized using the sol-gel method. The calcined CaO was dissolved with HNO₃ to precipitate unnecessary compounds and form nitrate salts. The solution is then stirred until homogeneous so that unnecessary metals can be dissolved; the reaction is presented in Eq. (2).













Then NH₄OH was added to the Ca(NO₃)₂ solution to form a Ca(OH)₂ sol with a pH of 10; pH 10 is the optimum pH for HAp formation. Sol Ca(OH)₂ then added a solution of (NH₄)₂HPO₄ to form a white gel. The reaction for the formation of HAp is presented in Eq. (3) [8].



The HAp-PEG composite was synthesized with several variations of the concentration of HAp as a matrix

Table 1. Effect of HAp concentration on HAp-PEG composite with various concentrations of 40, 50, 60, 70, and 80%

Concentration variation	Observation before heating	Picture	Observation after heating	Mass (g)	Picture
40%	Gel form and white		Formed a solid that breaks easily but is soft, and there are few cracks	15.4732	
50%	Gel form and white		A solid is formed which breaks easily, and there are more cracks on the composite surface	16.9764	
60%	Gel form and white		Formed solids that break easily, dry, and quite hard	18.8505	
70%	Gel form and white		Formed a solid that breaks easily, dry there are many cracks on the surface, but hard	19.5421	
80%	Gel form and white		Formed solids break easily, dry, and have many cracks on the surface	19.7893	

on PEG. Concentration variations used were 40, 50, 60, 70, and 80%, chosen to see the HAp concentration's effect on the composite formed with the addition of PEG. The analysis showed that the variation of the concentration of HAp 70 wt.% on the HAp-PEG composite showed optimum results [10].

HAp-PEG Composite FTIR Analysis

The results of the FTIR analysis of the HAp-PEG composite for various concentrations of HAp 40, 50, 60, 70, and 80%, as well as pure PEG, are shown in Fig. 1. Fig. 1 shows the FTIR spectrum analysis in the wave range 400–4000 cm^{-1} . Based on the FTIR spectrum results, the absorption occurs at wavenumbers 1027, 1030, 1031, and 1032 cm^{-1} at each concentration (40, 50, 60, 70, and 80%) which indicates the presence of phosphate vibration. In addition, apatite carbonate also showed absorption at wavenumbers of 1430 and 1433 cm^{-1} . FTIR analysis showed that there were characteristics of typical absorption of HAp, namely phosphate, carbonate, and -OH, which were

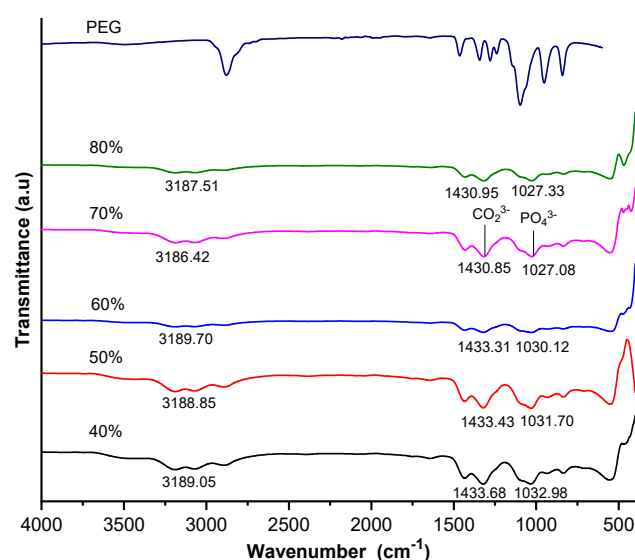


Fig 1. FTIR Spectrum of HAp-PEG composite with various concentrations of 40, 50, 60, 70, and 80 wt.% and PEG 6000

formed by marked PO_4 and PO_3 vibrational peaks from PO_4^{3-} , the appearance of CO vibrational peaks from CO_2

and the presence of -OH absorption bands [3,8,11].

HAp-PEG Composite X-Ray Analysis

The results of the X-ray analysis on the HAp-PEG composite with a concentration of 70 wt.% are shown in Fig. 2. Fig. 2 shows the diffraction pattern of HAp; the diffraction pattern of HAp formed follows the diffraction standard of HAp (ICSD #97849). XRD results prove the presence of HAp in the HAp-PEG composite. In addition to the diffraction pattern of HAp, this X-ray analysis also shows the diffraction pattern of PEG; this is due to the formation of HAp-PEG composite so that the crystallinity of PEG decreases [18].

Scherrer's calculations can determine the crystal size of the formed HAp-PEG composite.

$$L = \frac{k\lambda}{\beta \cos\theta} \quad (4)$$

With the description, L is the crystal size (nm); k is a constant (0.9); λ is the X-ray wavelength; β is FWHM (Full Width at Half Maximum) at 2θ (θ is the Bragg angle [7,19]). Based on the Scherrer equation, it is known that the crystal size of HAp in 70% HAp-PEG composite is 24.194 nm.

HAp-PEG Composite SEM-EDS Analysis

The results of the surface morphology analysis of the HAp-PEG composite with a concentration of 70% magnification of 40,000 \times are shown in Fig. 4. Fig. 4 shows the surface morphology of the HAp-PEG composite with needle-shaped crystals, indicating HAp

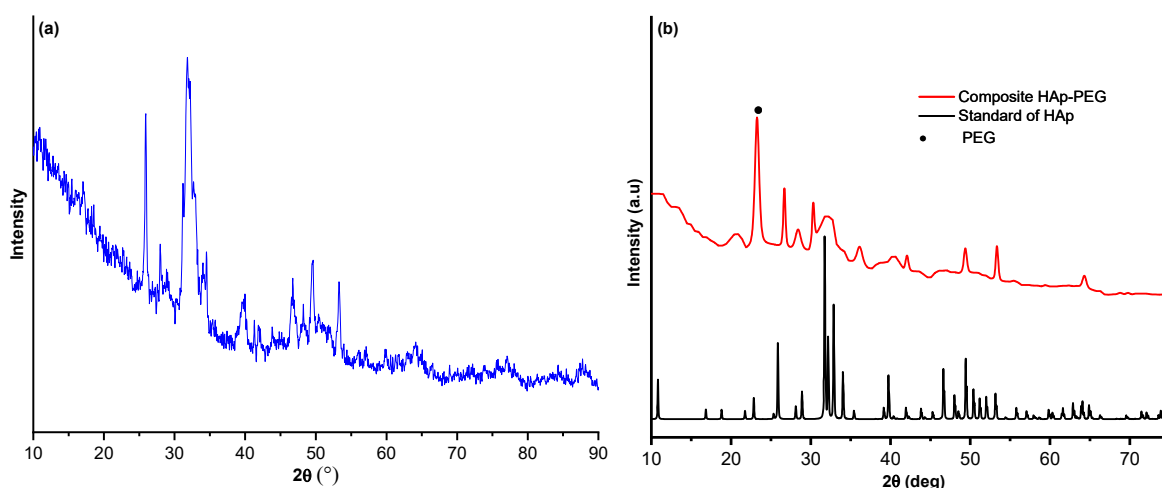


Fig 2. (a) X-ray diffraction of HAp. (b) X-ray diffraction pattern of HAp-PEG composite with a concentration of 70 wt.%

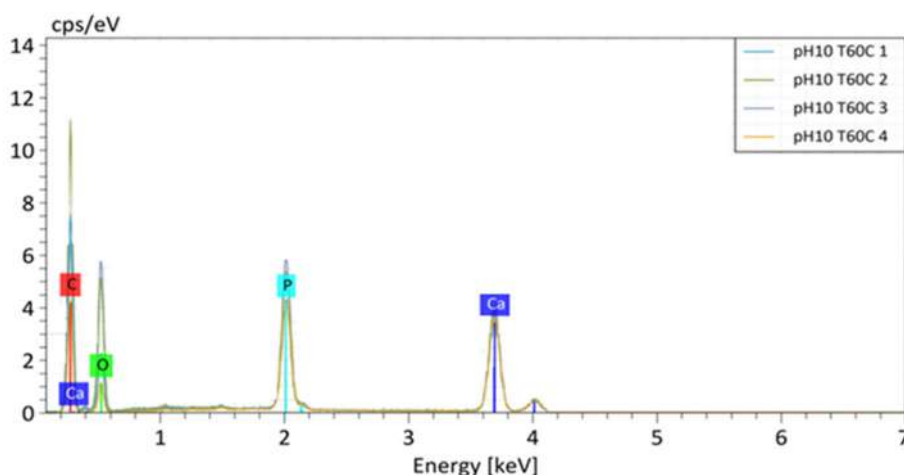


Fig 3. Composition of 70 wt.% HAp-PEG composite through EDS analysis

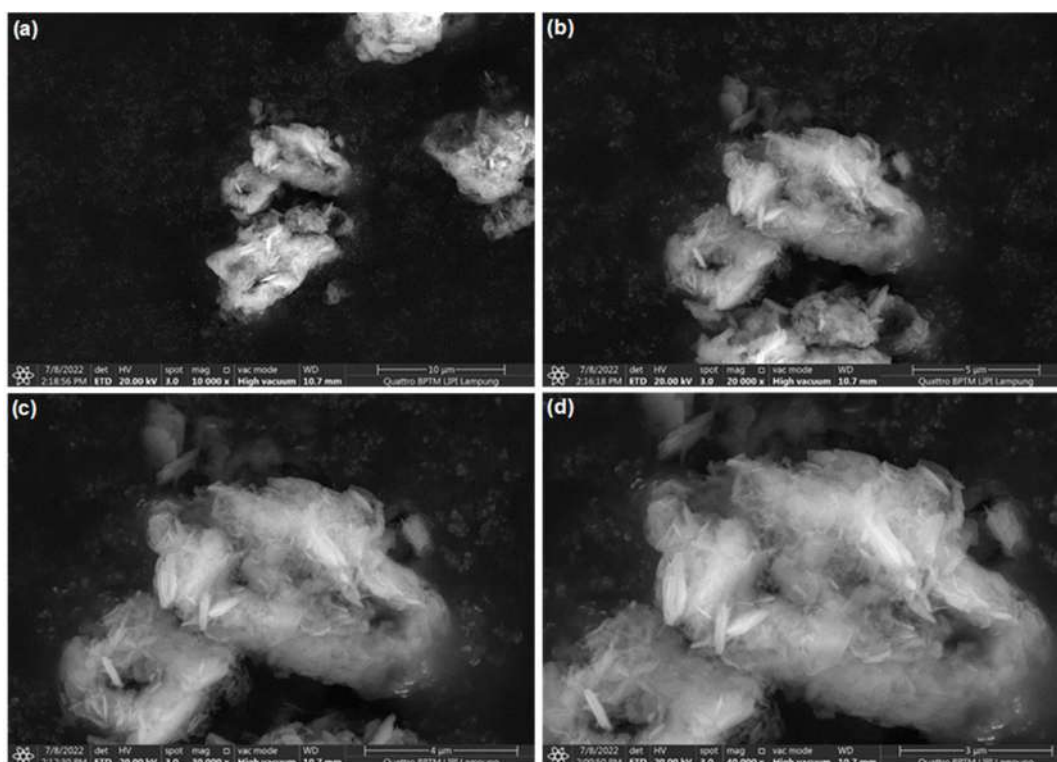


Fig 4. Surface morphology of 70 wt.% HAp-PEG composite on SEM characterization (a) 10,000× magnification (b) 20,000× magnification (c) 30,000× magnification (d) 40,000× magnification

crystals with particles size 5.1 nm. The results shown related to the morphology of the HAp-PEG composite can be influenced by the temperature when carrying out the reaction and the temperature during drying, pH, and the concentration of HAp and PEG in the composite.

To determine the Ca/P Ratio in HAp-PEG composites through SEM-EDS measurements. The composition of the compound in the HAp-PEG composite can be seen in Fig. 3. The compounds contained are C, O, Ca, and P, with the Ca/P ratio value obtained through the EDS measurement of 1.87. The value of the Ca/P ratio obtained is greater than the theoretical Ca/P ratio of 1.67; this indicates that more calcium phosphate is formed than pure Hap [7,19-21].

TGA-DTA Analysis of HAp-PEG Composites

The Hap-PEG composite 70% was analyzed using TGA-DTA at a temperature of 0–900 °C, which can be seen in Fig. 5. The results of the TGA-DTA analysis shown in the temperature range of 50–100 °C resulted in a mass reduction of 8.52% accompanied by an

endothermic reaction as shown in Fig. 5 shown on the DTA chart. Then at a temperature of 200–340 °C, a significant mass reduction occurred as much as 65.72% and was indicated by an exothermic reaction in a very sharp DTA pattern. The reaction is thought to occur due to the decomposition of organic compounds PEG used in the study. While at a temperature of 340–400 °C, a mass

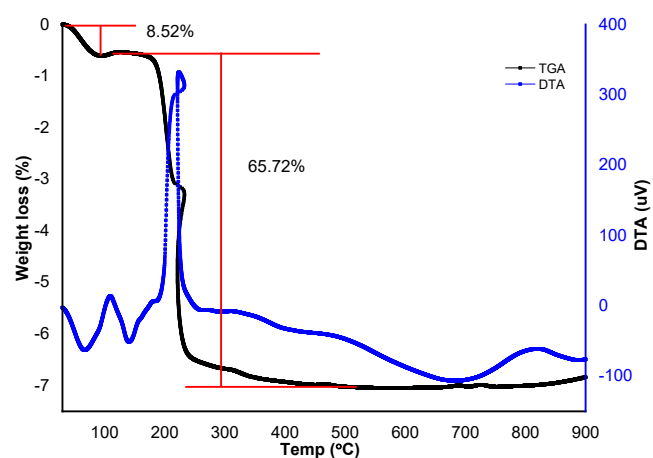


Fig 5. Results of TGA/DTA analysis of HAp-PEG composite 70% at a temperature of 0–900 °C

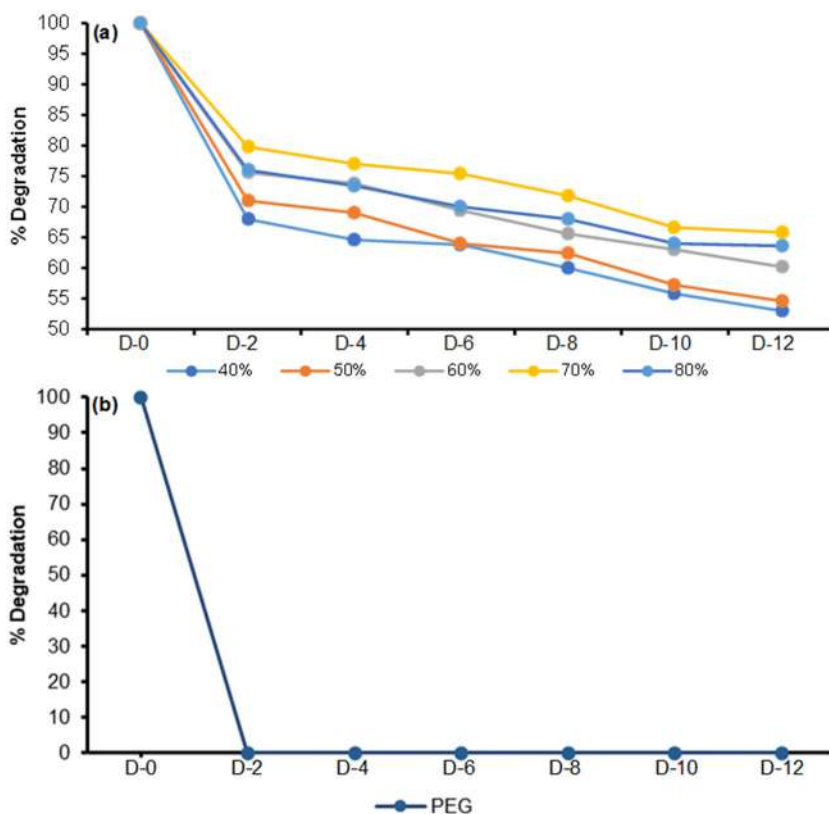


Fig 6. Percent degradation of (a) HAp-PEG composites and (b) PEG with increasing days

reduction is not as significant as 0.31%, accompanied by an endothermic reaction. At temperatures over 400 °C, no mass loss was identified, resulting in a total mass reduction of 74.55% [22-23].

Degradation Test

The ability to form HAp-PEG composite composition on bone was evaluated by immersing it in SBF solution for 14 d. This test can be seen in Fig. 6. Fig. 6 shows a graph of the percent degradation of the HAp-PEG composite. The X-axis shows the degradation testtime of 14 d and is weighed every 2 d, and the Y-axis is the percent degradation. The degradation graph shows the highest proportion of degradation values on the second day, where the weight reduction was significant and on the following day, there was a decrease in weight, and the degradation values slowly then remained constant on the 10th day. The percentage of weight loss in the composite is in line with the increase in PEG. This is in line with the faster degradation test on PEG, as shown in Fig. 6. This indicates that PEG, which is degraded first on

the surface of the HAp-PEG and HAP composites, helps inhibit degradation [24-25]. The interface is a space for water and solvent. High concentrations of HAP will cause an increase in the interface and degradation values.

Measurement of the percentage of degradation of the HAp-PEG composite can be determined by following the following equation:

$$D(\%) = \frac{W_d}{W_0} \times 100\% \quad (5)$$

with the explanation that W_0 and W_d are the percentages of combined weight before and after degradation [9,15].

CONCLUSION

The research results concluded that the HAp composite from blood clam shells (*Anadara granosa*) with PEG had been successfully synthesized using the *in situ* method. HAp-PEG Composite with a concentration of 70 wt.% has more optimum results in terms of degradation ability compared to other concentrations; this is seen from the results of the FTIR measurements

that have been obtained. HAp-PEG Composite 70 wt.% has a hexagonal structure and a crystal size of 24.194 nm according to ICSD #97849 standard. SEM-EDX characterization showed that the HAp-PEG composite sample had needle-shaped crystals, indicating the presence of HAp and agglomerated PEG crystals. The TGA/DTA analysis results showed a weight loss of 65.72% HAp-PEG composite at a temperature higher than 200 °C. The use of PEG for HAp composites also affects the mechanical properties of HAp, such as reduced brittleness, less fracture resistance and a denser structure, meanwhile, if HAp is disturbed it tends to be brittle and easily broken. Still, it does not entirely change the characteristics of HAp, the modification with PEG influenced the physical properties and water adsorption. HAp composites with PEG have the potential to be used as biomedical implant materials.

■ ACKNOWLEDGMENTS

This research was financially supported by the Ministry of Education, Culture, Research, and Technology of the Republic of Indonesia (*Direktorat Jenderal Pendidikan Tinggi, Kementerian Pendidikan dan Kebudayaan Indonesia*) through the national competitive grant [Grant number 086/E5/PG.02.00.PT/2022].

■ AUTHOR CONTRIBUTIONS

Novesar Jamarun collected the experimental data, Vivi Sisca and Nabiila Ayyu Trycahyani drafted the manuscript, and Novesar Jamarun, Syukri Arief, and Upita Septiani developed the idea and corrected the manuscript. All authors read and approved the final manuscript.

■ REFERENCES

- [1] Zhao, C., Liu, W., Zhu, M., Wu, C., and Zhu Y., 2022, Bioceramic-based scaffolds with antibacterial function for bone tissue engineering, *Bioact. Mater.*, 18, 383–398
- [2] Arjunan, A., Baroutaji, A., Praveen, A.S., Robinson, J., and Wang, C., 2020, "Classification of Biomaterial Functionality" in *Encyclopedia of Smart Materials*, Volume 1, Eds. Olabi, A.G., Elsevier, Oxford, 86–102.
- [3] You, B.C., Meng, C.E., Mohd Nasir, N.F., Mohd Tarmizi, E.Z., Fhan, K.S., Kheng, E.S., Abdul Majid, M.S., and Mohd Jamir, M.R., 2022, Dielectric and biodegradation properties of biodegradable nano-hydroxyapatite/starch bone scaffold, *J. Mater. Res. Technol.*, 18, 3215–3226.
- [4] Siregar, A., Jamarun, N., Sisca, V., Yulia Eka, P., 2020, Hydroxiapatites modification with magnesium using calcium from blood blood skin (*Tegillarca granosa*) and test of antibiacy activity, *Rev. Educ.*, 388 (4), 66–73.
- [5] Abere, D.V., Ojo, S.A., Oyatogun, G.M., Paredes-Epinosa, M.B., Niluxsshun, M.C.D., and Hakami, A., 2022, Mechanical and morphological characterization of nano-hydroxyapatite (nHA) for bone regranation: A mini review, *Biomed. Eng. Adv.*, 4, 100056.
- [6] Baladi, M., Amiri, M., Mohammadi, P., Salih Mahdi, K., Golshani, Z., Razavi, R., Salavati-Niazari, M., 2023, Green sol-gel synthesis of hydroxyapatite nanoparticles using lemon extract as capping agent and investigation of its anticancer activity against human cancer cell lines (T98, and SHSY5), *Arabian J. Chem.*, 16 (4), 104646.
- [7] Insani, P.M., and Rahmatsyah, R., 2021, Analysis of the structural pattern of Calcium Carbonate (CaCO₃) on the shells of blood clams (*Anadara granosa*) in Bukit Kerang, Aceh Tamiang Regency, *JTAF*, 9 (1), 23–32.
- [8] Ryabenkova, R., Pinnock, A., Quadros, R.A., Goodchild, R.L., Möbus, G., Crawford, A., Hatton, P.V., and Miller, C.A., 2017, The relationship between particle morphology and rheological properties in injectable nano-hydroxyapatite bone graft substitutes, *Mater. Sci. Eng., C*, 75, 1083–1090.
- [9] Oladele, I.O., Agbabiaka, O.G., Adediran, A.A., Akinwekomi, A.D., and Balogun, A.O., 2019, Structural performance of poultry eggshell derived hydroxyapatite based high density polyethylene bio-composites, *Heliyon*, 5 (10), e02552.
- [10] Abdian, N., Etminanfar, M., Sheykholeslami, S.O.R., Hamishehkar, H., and Khalil-Allafi, J., 2023, Preparation and characterization of

- chitosan/hydroxyapatite scaffolds containing mesoporous SiO₂-HA for drug delivery application, *Mater. Chem. Phys.*, 301, 127672.
- [11] Moeini, S., Mohammadi, M.R., and Simchi, A., 2017, *In-situ* solvothermal processing of polycaprolactone/hydroxyapatite nanocomposites with enhanced mechanical and biological performance for bone tissue engineering, *Bioact. Mater.*, 2 (3), 146–155.
- [12] Chaturvedi, S., Ayaz, S., and Shah, K., 2021, Validated UV spectrophotometric method for *in-vitro* dissolution studies in phosphate buffer pH 7.4, *Int. J. Pharm. Sci. Res.*, 12 (4), 2417–2421.
- [13] Azis, Y., Jamarun, N., Arief, S., and Nur, H., 2015, Facile synthesis of hydroxyapatite particles from cockle shells (*Anadara granosa*) by hydrothermal method, *Orient. J. Chem.*, 31 (2), 1099–1105.
- [14] Monte, J.P., Fontes, A., Santos B.S., and Pereira, G.A.L., 2023, Recent advances in hydroxyapatite/polymer/silver nanoparticles scaffolds with antimicrobial activity for bone regeneration, *Mater. Lett.*, 338, 134027.
- [15] Frasnelli, M., Cristofaro, F., Sglavo, V.M., Dirè, S., Callone, E., Ceccato, R., Bruni, G., Cornaglia, A.I., and Visai, L., 2017, Synthesis and characterization of strontium-substituted hydroxyapatite nanoparticles for bone regeneration, *Mater. Sci. Eng., C*, 71, 653–662.
- [16] Jamarun, N., Yuwan, S., Juita, R., and Rahayuningsih, J., 2015, Synthesis and characterization carbonate apatite from bukit Tui limestone Padang Indonesia, *J. Appl. Chem.*, 4 (2), 542–549.
- [17] Zahir, M.H., Rahman, M.M., Irshad, K., and Rahman, M.M., 2019, Shape-stabilized phase change materials for solar energy storage: MgO and Mg(OH)₂ mixed with polyethylene glycol, *Nanomaterials*, 9 (12), 1773.
- [18] Jamarun, N., Azharman, Z., Arief, S., Sari, T.P., Asril, A., and Elfina, S., 2015, Effect of temperature on synthesis of hydroxyapatite from limestone, *Rasayan J. Chem.*, 8 (1), 133–137.
- [19] Trakoolwannachai, V., Kheolamai, P., and Ummartyotin, S., 2019, Characterization of hydroxyapatite from eggshell waste and polycaprolactone (PCL) composite for scaffold material, *Composites, Part B*, 173, 106974.
- [20] Talaei, H., Fallah-Mehrjardi, M., and Hakimi, F., 2018, Polyethylene glycol-(*N*-methylimidazolium) hydroxide-grafted γ -Fe₂O₃@Hap: A novel nanomagnetic recyclable basic phase-transfer catalyst for the synthesis of tetrahydrobenzopyran derivatives in aqueous media, *J. Chin. Chem. Soc.*, 65 (5), 523–530.
- [21] Adamu, D.B., Zereffa, E.A., Segne, T.A., Razali, M.H., and Lemu, B.R., 2023, Synthesis and characterization of bismuth-doped hydroxyapatite nanorode for fluoride removal, *Environ. Adv.*, 12, 100360.
- [22] Jamarun, N., Azharman, Z., and Septiani, U., 2016, Effect of firing for synthesis of hydroxyapatite by precipitation method, *Orient. J. Chem.*, 32 (4), 2095–2099.
- [23] Hartatiek, H., Utomo, J., Noerjannah, L.I., Rohmah, N.Z., and Yudyanto, Y., 2021, Physical and mechanical properties of hydroxyapatite/polyethylene glycol nanocomposites, *Mater. Today: Proc.*, 44, 3263–3267.
- [24] Nurlidar, F., and Kobayashi, M., 2019, Succinylated bacterial cellulose induce carbonated hydroxyapatite deposition in a solution mimicking body fluid, *Indones. J. Chem.*, 19 (4), 858–864.
- [25] Senra, M.R., de Lima, R.B., de Holanda Saboya Souza, D., Marques, M.F.V., and Monteino, S.N., 2020, Thermal characterization of hydroxyapatite or carbonated hydroxyapatite hybrid composites with distinguished collagens for bone graft, *J. Mater. Res. Technol.*, 9 (4), 7190–7200.

Novel Metal Coordination Complexes Based on 4-Aminophenol: Spectroscopic Analysis and Antibacterial Test

Husna Syaima¹, Sentot Budi Rahardjo^{2*}, Anisa Nurul Hanifa²,
Ariffah Ana Fathonah², and Ratna Setyaningsih³

¹Department of Chemistry, Faculty of Mathematics and Natural Sciences, Universitas Mulawarman, Samarinda 75123, Indonesia

²Department of Chemistry, Faculty of Mathematics and Natural Sciences, Universitas Sebelas Maret, Jl. Ir. Sutami 36A, Kentingan, Surakarta 57126, Indonesia

³Department of Biology, Faculty of Mathematics and Natural Sciences, Universitas Sebelas Maret, Jl. Ir. Sutami 36A, Kentingan, Surakarta 57126, Indonesia

* **Corresponding author:**

email: sentotbr@staff.uns.ac.id

Received: October 31, 2022

Accepted: February 24, 2023

DOI: 10.22146/ijc.78757

Abstract: The aims of this research are to synthesize and determine the formula, characteristics, and complex structure of Cu(II) and Co(II) with 4-aminophenol and to investigate their antibacterial activity. The complexes were synthesized by refluxing a solution of CuSO₄·5H₂O and CoSO₄·7H₂O, respectively, with 4-aminophenol in methanol for 1 h. The products were characterized using UV-Vis spectroscopy, atomic absorption spectroscopy, thermal analysis, conductivity, FTIR, and magnetic moment. The formation of the complex was indicated by shifting of maximum wavelength of the metal solution toward shorter, i.e., 817 to 421 nm for Cu(II) and 566 to 450 nm for Co(II). From the characterization, the proposed formulas of the complexes are [Cu(4-aminophenol)₄]SO₄ and [Co(4-aminophenol)₄(H₂O)₂]SO₄·5H₂O forming square planar and octahedral geometry, respectively. Both complexes are paramagnetic with negligible antibacterial activity against *Staphylococcus aureus*, *Staphylococcus epidermidis*, *Escherichia coli*, and *Pseudomonas aeruginosa*.

Keywords: cobalt; copper; complex; 4-aminophenol

■ INTRODUCTION

4-Aminophenol is a derivative of phenol with an amine group in the para position, which is commonly used as antipyretics, analgesic drugs, and synthetic materials in various fields such as petroleum, photography as a redox reagent, rubber, developer, chemical inhibitor, and others [1]. The 4-aminophenol is a strong analgesic and weak anti-inflammatory compound which is very toxic. Reducing toxicity and increasing the activity of the compound is ably done by modifying the molecule as well as forming metal complexes. The 4-aminophenol can be used as ligands because it has amine (NH₂) and hydroxy (OH) groups that can act as electron donors to bond with metals.

Metal complexes are compounds consisting of a central metal ion with a ligand donating its lone pair of electrons to the central metal ion [2]. The central metal ion is surrounded by two or more molecules or ions, called ligands, that form a coordinating covalent bond with the central metal ion. Metal complexes have attracted attention in various applications in inorganic chemistry and have been used in the field of pharmacy, biology, medicine, clinics, industry, and others [3-4]. In addition, transition metal complexes and ligands as active drugs have been widely studied due to the possibility that complex compounds may have different pharmacological activities [5]. In designing effective complex compounds, the choice of metal ion structure and ligand is an important factor [6]. Transition metal

complexes of Cu, Co, Ni, Zn, and Ag with ligands are usually used for pharmaceutical applications as antibacterial, anticancer, and antioxidant [7-8]. Copper is widely used in the synthesis of complex compounds because it is proven to have high antibacterial power and low toxicity, so Cu(II) ions are used as an antibacterial substitute for silver [9]. Another transition metal that has been widely used is Co(II). In the complex compound prepared by Mishra et al. [10], the N and O groups of the ligands bind to metal ions Co(II), Cu(II), Ni(II), Zn(II), and Cd(II). Herrera et al. [11] synthesized a complex of Co(II), Ni(II), and Cr(III) with 2-thiozoline-2-thiol and showed better antibacterial activity. Al-Zaidi et al. [12] synthesized Co(II) with 1-(4-(4(diethylamino)-2-hydroxybenzylidene)amino)phenyl)ethanone oxime ligand and the results showed improved antibacterial properties compared to the ligand and its complex ion. Prajapati et al. [13] synthesized Co(II) with 2-[(E)-(2-hydroxybenzylidene)amino]benzoic acid and showed good antibacterial activity.

Based on the explanation above, 4-aminophenol has the potential to be ligands coordinating with Cu(II) and Co(II). Based on our knowledge, both complexes with identical structure never been synthesized before. Herein, the $[\text{Cu}(4\text{-aminophenol})_4]\text{SO}_4\cdot\text{H}_2\text{O}$ and $[\text{Co}(4\text{-aminophenol})_4(\text{H}_2\text{O})_2]\text{SO}_4\cdot 5\text{H}_2\text{O}$ complexes have been successfully synthesized and characterized. The complexes were also tested for antibacterial activity against *Staphylococcus aureus*, *Staphylococcus epidermis*, *Escherichia coli*, and *Pseudomonas aeruginosa*.

■ EXPERIMENTAL SECTION

Materials

The $\text{CoSO}_4\cdot 7\text{H}_2\text{O}$, $\text{CuSO}_4\cdot 5\text{H}_2\text{O}$, $\text{CuCl}_2\cdot 2\text{H}_2\text{O}$, $\text{FeSO}_4\cdot 7\text{H}_2\text{O}$, $\text{CoCl}_2\cdot 6\text{H}_2\text{O}$, 4-aminophenol, and solvent (methanol, DMF, and DMSO) are purchased from Merck. All chemicals were used without treatment.

Instrumentation

The molar absorptivity and electronic transition of both complexes' solutions were estimated using a double-beam UV-Vis spectroscopy (Shimadzu PC 1601). The complex formula was estimated by measuring the metal

content of the complex using an Atomic Absorption Spectrophotometer (AAS, Shimadzu AA-665). The presence or absence of water molecules in the complexes was determined using Thermal Gravimetry Analysis/Differential Scanning Calorimetry instrument (TG/DSC, Shimadzu 50) with a heating rate of 10 °C/min. Electrical conductivity of the Cu(II) and Co(II) complexes and some known metal salts solution in DMF and DMSO, respectively, at 25 °C using a conductivity meter (Jenway CE 4071). Infrared spectra of 4-aminophenol and the complexes were measured as KBr pellets in the frequency range of 4000–450 cm^{-1} using Fourier-transform infrared spectrophotometer (FTIR, Prestige-21 Shimadzu). The magnetic properties of the powder Cu(II) and Co(II) complexes can be determined moment with Magnetic Susceptibility Balance (MSB, Auto Sherwood Scientific 10169) and corrected using Pascal's constant.

Procedure

Synthesis of Co(II) complex

The Co(II) complex was synthesized by dissolving the 4-aminophenol (0.436 g) in 10 mL methanol. The metal $\text{CoSO}_4\cdot 7\text{H}_2\text{O}$ (0.281 g) was also dissolved in 10 mL methanol. The ligand solution was heated and stirred with a magnetic stirrer and then added dropwise into the metal solution was put into the ligand. The solution was refluxed for 1 h at 60 °C. The solution is then concentrated until it reaches half of the initial volume. The solution is allowed to stand (crystallize) until a precipitate is formed. The precipitate formed was washed with acetone and dried under a vacuum.

Synthesis of Cu(II) complex

The Cu(II)-4-aminophenol complex was synthesized in a ratio of 1:4 by dissolving $\text{CuSO}_4\cdot 5\text{H}_2\text{O}$ (0.249 g, 0.1 mmol) in 10 mL and 4-aminophenol (0.436 g, 0.4 mmol) in 10 mL methanol. The 4-aminophenol ligand solution was heated on a hot plate while stirring using a magnetic stirrer then a $\text{CuSO}_4\cdot 5\text{H}_2\text{O}$ metal solution was added dropwise into the 4-aminophenol ligand solution. The mixed solution was then refluxed for 1 h at 67 °C. The resulting solution was evaporated and concentrated until a precipitate was

formed. Then the precipitate was filtered using filter paper and then dried.

Antibacterial test

Antibacterial activity of Cu(II), Co(II), 4-aminophenol, Cu(II)-4-aminophenol, and Co(II)-4-aminophenol complex against *S. aureus* ATCC 25923, *S. epidermis* ATCC 12228, *E. coli* ATCC 25922, and *P. aeruginosa* ATCC 27853 was tested using paper disc diffusion method. The inhibition of bacteria was shown as the diameter of the clear zone in the test samples. The three test samples, namely metal $\text{CuSO}_4 \cdot 5\text{H}_2\text{O}$, ligand 4-aminophenol, Cu(II)-4-aminophenol complex were made with various concentrations (ppm): 125, 250, 500, and 1000. Positive controls used were commercial antibiotics vancomycin, chloramphenicol, and meropenem 30 $\mu\text{g}/\text{disk}$ and the negative control used was DMSO (the solvent).

RESULTS AND DISCUSSION

Indication of the Formation of Metal Complexes

The change in color from brass (4-aminophenol ligand solution in methanol) to blackish brown color (complex solution in methanol) indicated the formation of the cobalt complex. The shift in the absorption of the maximum wavelength of $\text{CoSO}_4 \cdot 7\text{H}_2\text{O}$ (566 nm) towards a smaller wavelength (450 nm) can be seen in Fig. 1. The shift of the maximum wavelength indicates the formation of complexes between Co(II) and 4-aminophenol ligands. Water molecules as coordinated ligands on Co(II) being replaced by 4-aminophenol. Similarly, Co(II)-nicotinamide complex that was synthesized by Rahardjo et al. [14] also experienced a shift towards a lower wavelength from 512 nm (cobalt salt solution) to 506 nm (complex solution).

Meanwhile, the formation of the copper complex was indicated by a color change from brown (4-aminophenol solution) to black solution. The synthesis product was black precipitates (0.396 g; 64.39%). Fig. 2 shows a shift in the maximum wavelength absorption (λ_{max}) of $\text{CuSO}_4 \cdot 5\text{H}_2\text{O}$ (817 nm) towards a lower wavelength in the Cu(II)-4-aminophenol complex (421 nm). The shift in wavelength indicates the formation of Cu(II)-4-aminophenol complex. It also proves that 4-aminophenol

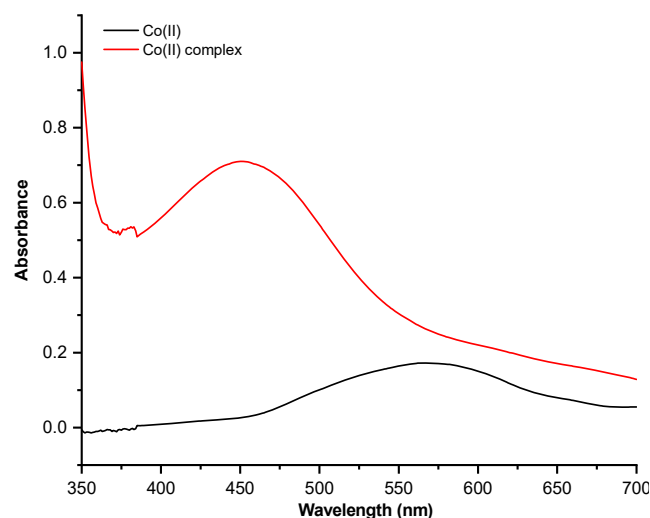


Fig 1. UV-vis spectra of Co(II) and its complex in methanol

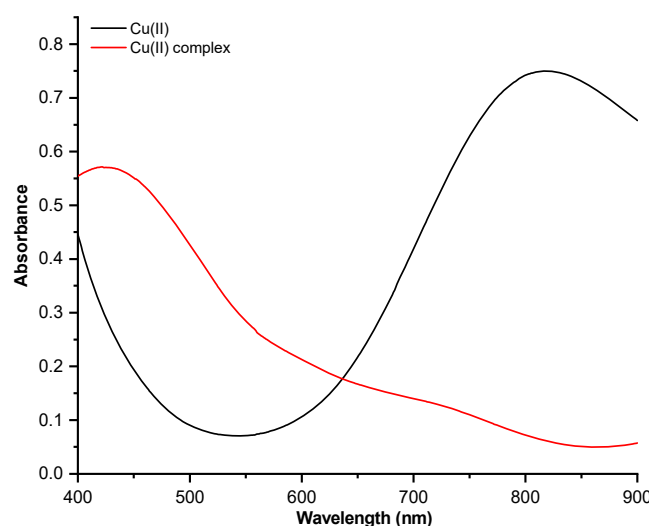


Fig 2. UV-vis spectra of Cu(II) and its complex in methanol

has a stronger ligand field energy than H_2O so that it is able to substitute H_2O positions. Other syntheses of copper complexes also experienced a maximum wavelength shift, as in the $\text{Na}_2[\text{Cu}((E)\text{-}2\text{-}(2\text{-hydroxy-}3\text{-methoxybenzylimidazolium) acetic acid})_2]$ complex a shift occurred from 700 nm to 380 nm [15] and the $\text{Cu}(\text{Indal-4-aminoantipyrine})\text{Cl}_2$ from 850 nm to 380 nm [16].

Atomic Absorption Spectrophotometer (AAS)

The results of the measurement of copper and cobalt content experimentally with AAS in Cu(II)-4-

aminophenol were $10.59 \pm 0.22\%$ and $8.62 \pm 0.20\%$, respectively (Table 1). The results of the measurement of copper and cobalt content are compared with theoretical Cu levels in various possible complex formulas as shown in Table 1, it can be estimated that the complex compound formula Cu(II)-(4-aminophenol) is Cu(4-aminophenol)₄SO₄(H₂O)_n (n = 0, 1, or 2) and Co(4-aminophenol)₄SO₄(H₂O)_n (n = 5, 6, or 7).

Thermal Analysis

The thermogram of the Cu(II)-4-aminophenol complex in Fig. 3 shows the occurrence of a mass shift of the complex as much as 3.12% at a temperature of 30–155 °C equivalent to the release of one H₂O molecule (theoretical calculation: 2.93%). Therefore, the empirical formula of Cu(II) complex is Cu(4-aminophenol)₄(SO₄)(H₂O). For Co(II) complex, the thermogram shows a twofold decrease in mass (Fig. 4). The first decrease occurred at a temperature of 40–135 °C and the second decrease occurred at a temperature of 135–185 °C. At a temperature of 40–135 °C there is a decrease in mass of 13.90% which is equivalent to five H₂O molecules (theoretical calculation: 13.205%). The second decrease was reduced by 6.06% equivalent to the release of two H₂O molecules (theoretical calculation: 5.74%). According to Himawati et al. [17], the decrease at a temperature of 30–130 °C water molecules as crystal water, not as a ligand, whereas according to Prajapti et al. [13], reducing mass at a temperature of 150–250 °C is water coordinated with metals. The empirical formula of cobalt complex with 4-aminophenol is Co(4-aminophenol)₄(SO₄)(H₂O)₇.

Molar Conductivity

The molar conductivity of the standard solution in Table 2 shows that the more ions produced in the solution, the greater the value of molar conductivity.

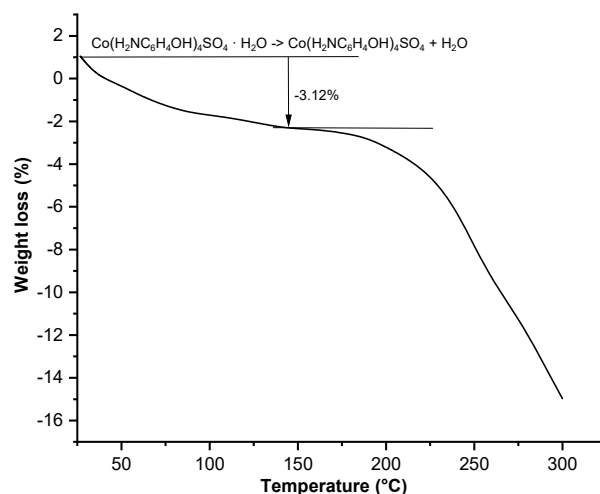


Fig 3. Thermogram of Cu(II) complex

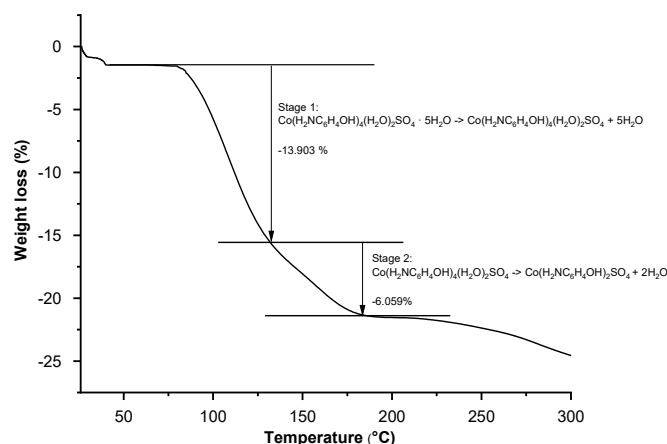


Fig 4. Thermogram of Co(II) complex

Table 1. Proposed formula of the complex based on AAS result

Proposed Empirical Formula	Theoretical metal content (%Cu or %Co)	AAS Result (%)
Cu(4-aminophenol) ₄ SO ₄	10.73	
Cu(4-aminophenol) ₄ (SO ₄)(H ₂ O)	10.41	10.59
Cu(4-aminophenol) ₄ (SO ₄)(H ₂ O) ₂	10.11	
Co(4-aminophenol) ₄ (SO ₄)(H ₂ O) ₅	8.66	
Co(4-aminophenol) ₄ (SO ₄)(H ₂ O) ₆	8.42	8.62
Co(4-aminophenol) ₄ (SO ₄)(H ₂ O) ₇	8.22	

Table 2. Average molar conductivity of the complexes and metal salts

Solvent	Compounds	Average molar conductivity (S cm ² /mol)	Number of ions	Average molar conductivity of the complex
DMF	CoSO ₄ ·7H ₂ O	10	2	[Cu(4-aminophenol) ₄]SO ₄ ·H ₂ O = 16 S cm ² /mol
	CuSO ₄ ·5H ₂ O	16	2	
	CuCl ₂ ·2H ₂ O	28	3	
DMSO	FeSO ₄ ·7H ₂ O	6	2	[Co(4-aminophenol) ₄ (H ₂ O) ₂]SO ₄ ·5H ₂ O = 10 S cm ² /mol
	CoSO ₄ ·7H ₂ O	10	2	
	CuCl ₂ ·2H ₂ O	32	2	
	CoCl ₂ ·6H ₂ O	86	3	

By comparing the value of the molar conductivity of the complex sample solution with the molar conductivity of the standard solution, it can be seen the number of ions produced in the sample solution. The molar conductivity of Cu(II)-4-aminophenol complex solution in DMF measured by electrical conductivity is close to the value of the electrical conductivity of the CuSO₄·5H₂O solution, which indicates the number of ions in the complex is 2. This indicates that the complex solution is an electrolyte with a ratio of cation and anion charges. in a 1:1 ratio. Thus, the sulfate in the complex does not act as a ligand but as a counter ion. Therefore, the possible complex formula for Cu(II)-4-aminophenol is [Cu(4-aminophenol)₄]SO₄·H₂O.

The molar conductivity of the Co(II)-4-aminophenol complex solution in DMSO is similar to the value of the molar conductivity of the CoSO₄·7H₂O solution, which both have a value of 10. This indicates that the number of ions contained by the Co(II)-4-aminophenol complex is two ions. This shows that the ratio of the total charge of cations and anions in the Co(II)-4-aminophenol complex is 1:1, so the formula for the Co(II)-4-aminophenol complex is [Co-(4-aminophenol)₄(H₂O)₂]SO₄·5H₂O with SO₄²⁻ as the counter ion.

FTIR

The functional groups that bind to metal central ions can be estimated through FTIR absorption. OH-phenol is at an absorption range of 3531–3640 cm⁻¹, H₂O is at 3200–3570 cm⁻¹ (broad) [18], and the shift of C–N absorption from 1612 to 1607 cm⁻¹, as seen in Fig. 5,

indicating the formation of Cu(II) complex [19]. This also occurred in the Cu(II) with 1,3,4-thiadiazolethiosemicarbazone, which showed a shift in NH₂ absorption from 3264 to 3246 cm⁻¹ and from 3152 to 3134 cm⁻¹ and C–N absorption from 1605 to 1599 cm⁻¹ [20]. Cu(II) complex with Schiff based-on glycine also showed a shift in C–N absorption from 1641 to 1600 cm⁻¹, which indicates the coordination of nitrogen atom to copper [21]. In this research, NH₂ absorption in the ligand and [Cu(4-aminophenol)₄]SO₄ shifts in a smaller absorption value from 3352 and 3287 cm⁻¹, respectively. This indicates the coordination of the nitrogen atom of the –NH₂ in 4-aminophenol on the Cu(II). The hydroxyl (O–H) group does not appear in the spectra, it is probably due to overlapping with the NH₂ group. This also is supported by the appearance of

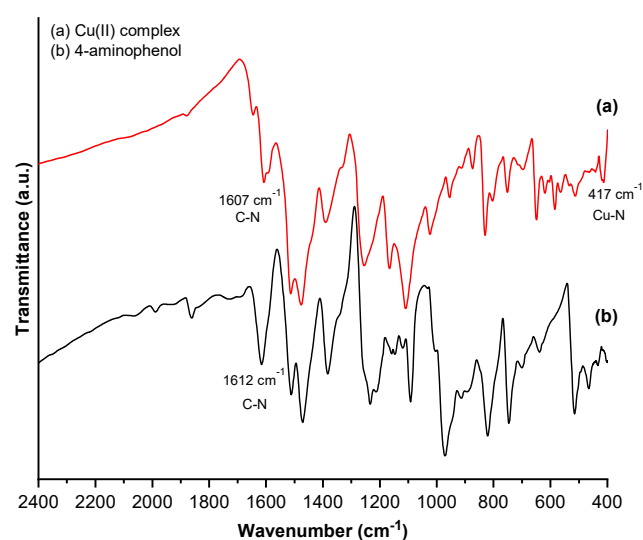


Fig 5. FTIR spectra of 4-aminophenol and Cu(II) complex

Cu–N absorption at 417 cm^{-1} . A new absorption at 414 cm^{-1} indicates the presence of metal bonds with the NH_2 (Cu–N) also happened at Batool et al. [22].

In Co(II) complex, NH_2 and C–N absorption shifted toward smaller from 3342 (4-aminophenol) to 3282 cm^{-1} (complex) and 1385 to 1384 cm^{-1} (Fig. 6). A similar case also happened to $[\text{Co}(\text{Phen})_2(\text{H}_2\text{O})_2]\text{Cl}_2\cdot\text{H}_2\text{O}$, C–N absorption shift from 328 to 1314 cm^{-1} [23]. Absorption of water molecules does not appear. However, the presence of absorption at 524 cm^{-1} indicates the presence of Co–N bonds. This shows that in the complex $[\text{Co}(4\text{-aminophenol})_4(\text{H}_2\text{O})_2]\text{SO}_4\cdot 5\text{H}_2\text{O}$, the cobalt ion binds to the nitrogen atom of NH_2 and the oxygen atom of H_2O .

UV-Vis

$[\text{Cu}(4\text{-aminophenol})_4]\text{SO}_4\cdot\text{H}_2\text{O}$ showed an absorption at 417 nm (23981 cm^{-1}), as revealed in Fig. 1. Copper complexes that have electronic absorption in the region of 20366 and 20202 cm^{-1} have ${}^2\text{B}_{1g}\rightarrow{}^2\text{E}_{1g}$ transitions and have a square planar geometry [24]. Thus the complex of $[\text{Cu}(4\text{-aminophenol})_4]\text{SO}_4\cdot\text{H}_2\text{O}$ is estimated to have square planar geometry. The Co(II) complex, $[\text{Co}(4\text{-aminophenol})_4(\text{H}_2\text{O})_2]\text{SO}_4\cdot 5\text{H}_2\text{O}$ showed one absorption peak at a wavelength of 450 nm ($22,222\text{ cm}^{-1}$). Co(II) complex with Schiff base salicylidenic ligand at a maximum wavelength of 470 nm ($21,276\text{ cm}^{-1}$) has an electronic transition of ${}^4\text{T}_{1g}(\text{F})\rightarrow{}^4\text{T}_{1g}(\text{P})$ and has octahedral geometry [25]. Thus, $[\text{Co}(4\text{-aminophenol})_4(\text{H}_2\text{O})_2]\text{SO}_4\cdot 5\text{H}_2\text{O}$ is also estimated to have octahedral geometry. Electronic spectral data of $[\text{Cu}(4\text{-aminophenol})_4]\text{SO}_4\cdot\text{H}_2\text{O}$ and $[\text{Co}(4\text{-aminophenol})_4(\text{H}_2\text{O})_2]\text{SO}_4\cdot 5\text{H}_2\text{O}$ are shown in Table 3.

Magnetism

The results of the measurement of the effective magnetic moment (μ_{eff}) of $[\text{Cu}(4\text{-aminophenol})_4]\text{SO}_4\cdot\text{H}_2\text{O}$ and $[\text{Co}(4\text{-aminophenol})_4(\text{H}_2\text{O})_2]\text{SO}_4\cdot 5\text{H}_2\text{O}$ is 1.79 and 5.30 BM , respectively. $[\text{Cu}(4\text{-aminophenol})_4]\text{SO}_4\cdot\text{H}_2\text{O}$ has similar magnetic properties to other Cu(II) complexes in the range $1.70\text{--}2.0\text{ BM}$, which show paramagnetic characteristics with one unpaired electron [19,26–28]. The result of $[\text{Co}(4\text{-aminophenol})_4(\text{H}_2\text{O})_2]\text{SO}_4\cdot 5\text{H}_2\text{O}$ is similar to the effective magnetic moment value of the copper complex according to $[\text{Co}(\text{Nicotinamide})_2(\text{H}_2\text{O})_2]\text{Cl}_2$, which was reported by Rahardjo et al. [14] was 5.3 BM and Obaid et al. [29] was 5.25 . The high spin octahedral Co(II) geometry has an effective magnetic moment value of $4.7\text{--}5.3\text{ BM}$ [24]. The significantly higher moment magnetic of octahedral Co(II) complexes than that of spin-only value (μ_{s} , 3.87 BM) for three unpaired electrons is due to the orbital contribution to the magnetic moment [30–31]. The proposed structures of the Cu(II) and Co(II) complexes are shown in Fig. 7.

$[\text{Cu}(4\text{-aminophenol})_4]\text{SO}_4\cdot\text{H}_2\text{O}$ and $[\text{Co}(4\text{-aminophenol})_4(\text{H}_2\text{O})_2]\text{SO}_4\cdot 5\text{H}_2\text{O}$ is 1.79 and 5.30 BM , respectively. $[\text{Cu}(4\text{-aminophenol})_4]\text{SO}_4\cdot\text{H}_2\text{O}$ has similar magnetic properties to other Cu(II) complexes in the range $1.70\text{--}2.0\text{ BM}$, which show paramagnetic characteristics with one unpaired electron [19,26–28]. The result of $[\text{Co}(4\text{-aminophenol})_4(\text{H}_2\text{O})_2]\text{SO}_4\cdot 5\text{H}_2\text{O}$ is similar to the effective magnetic moment value of the copper complex according to $[\text{Co}(\text{Nicotinamide})_2(\text{H}_2\text{O})_2]\text{Cl}_2$, which was reported by Rahardjo et al. [14] was 5.3 BM and Obaid et al. [29] was 5.25 . The high spin octahedral Co(II) geometry has an effective magnetic moment value of $4.7\text{--}5.3\text{ BM}$ [24]. The significantly higher moment magnetic of octahedral Co(II) complexes than that of spin-only value (μ_{s} , 3.87 BM) for three unpaired electrons is due to the orbital contribution to the magnetic moment [30–31]. The proposed structures of the Cu(II) and Co(II) complexes are shown in Fig. 7.

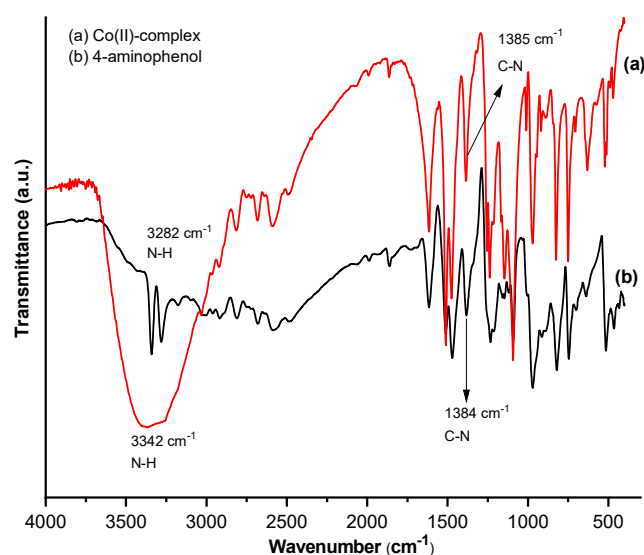


Fig 6. FTIR spectra of 4-aminophenol and Co(II) complex

Table 3. Electronic spectral data of $[\text{Cu}(4\text{-aminophenol})_4]\text{SO}_4\cdot\text{H}_2\text{O}$ and $[\text{Co}(4\text{-aminophenol})_4(\text{H}_2\text{O})_2]\text{SO}_4\cdot 5\text{H}_2\text{O}$

Compounds	λ_{max} (nm)	Absorbance	ν (cm^{-1})	ϵ ($\text{L mol}^{-1}\text{ cm}^{-1}$)
$\text{CuSO}_4\cdot 5\text{H}_2\text{O}$	794	0.146	12595	91.074
$\text{CoSO}_4\cdot 7\text{H}_2\text{O}$	566	0.170	12592	35.000
$[\text{Cu}(4\text{-aminophenol})_4]\text{SO}_4\cdot\text{H}_2\text{O}$	417	0.777	23981	795.350
$[\text{Co}(4\text{-aminophenol})_4(\text{H}_2\text{O})_2]\text{SO}_4\cdot 5\text{H}_2\text{O}$	450	0.710	22222	830.000

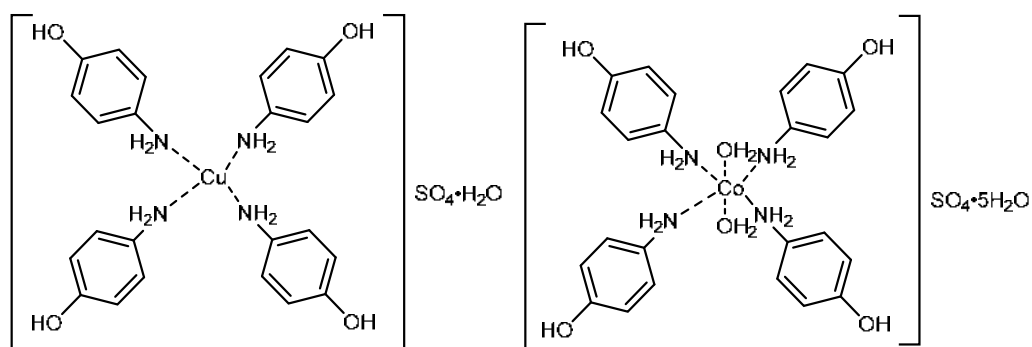


Fig 7. Proposed structures of Cu(II) and Co(II) complexes

Antibacterial Test

$[\text{Cu}(\text{4-aminophenol})_4]\text{SO}_4\cdot\text{H}_2\text{O}$ and $[\text{Co}(\text{4-aminophenol})_4(\text{H}_2\text{O})_2]\text{SO}_4\cdot 5\text{H}_2\text{O}$ do not show antibacterial activity against *S. aureus* ATCC 25923, *S. epidermis* ATCC 12228, *E. coli* ATCC 25922 and *P. aeruginosa* ATCC 27853.

CONCLUSION

Copper and cobalt complexes are successfully synthesized with estimated formulas $[\text{Cu}(\text{4-aminophenol})_4]\text{SO}_4\cdot\text{H}_2\text{O}$ and $[\text{Co}(\text{4-aminophenol})_4(\text{H}_2\text{O})_2]\text{SO}_4\cdot 5\text{H}_2\text{O}$. Both complexes are paramagnetic and estimated to form square planar and octahedral geometry, respectively. No antibacterial activity was observed against *S. aureus*, *S. epidermis*, *E. coli*, and *P. aeruginosa*.

ACKNOWLEDGMENTS

The authors express gratitude to PNBPN UNS 2022 for financial support.

AUTHOR CONTRIBUTIONS

Husna Syaima, Sentot Budi Rahardjo, Anisa Nurul Hanifa, and Ariffah Ana Fathonah conceived and planned the experiment. Anisa Nurul Hanifa and Ariffah Ana Fathonah contributed to sample preparation and conducted the experiment. Husna Syaima, Sentot Budi Rahardjo, Anisa Nurul Hanifa, and Ariffah Ana Fathonah contributed to the interpretation of the results of characterization of complexes. Ratna Setyaningsih supervised and analyzed the result of antibacterial activity. Husna Syaima and Sentot Budi Rahardjo took the

lead in writing the manuscript. All authors agreed to the final version of this manuscript.

REFERENCES

- [1] Singh, M., Sahu, A., Mahata, S., Singh, P.K., Rai, V.K., and Rai, A., 2019, Efficient electrochemical determination of *p*-aminophenol using a novel tricomponent graphene-based nanocomposite, *New J. Chem.*, 43 (37), 14972–14978.
- [2] Barzinjy, A.A.A., 2017, Comparative crystal field studies of some ligand of Cr^{3+} complexes, *Eurasian J. Sci. Eng.*, 3 (1), 109–116.
- [3] Grundhoefer, J.P., Hardy, E.E., West, M.M., Curtiss, A.B., and Gorden, A.E., 2019, Mononuclear Cu(II) and Ni(II) complexes of bis (naphthalen-2-ol) Schiff base ligands, *Inorg. Chim. Acta*, 484, 125–132.
- [4] Karabansannavar, S., Allolli, P., Shaikh, I.N., and Kalshetty, B.M., 2017, Synthesis, characterization and antimicrobial activity of some metal complexes derived from thiazole Schiff bases with *in-vitro* cytotoxicity and DNA cleavage studies, *Indian J. Pharm. Educ. Res.*, 51 (3), 490–502.
- [5] Zangrando, E., Islam, M.T., Islam, M.A.A.A., Sheikh, M.C., Tarafder, M.T.H., Miyatake, R., Zahan, R., and Hossain, M.A., 2015, Synthesis, characterization and bioactivity of nickel(II) and copper(II) complexes of a bidentate NS Schiff base of *s*-benzyl dithiocarbamate, *Inorg. Chim. Acta*, 427, 278–284.
- [6] Ding, P., Wang, Y., Kou, H., Li, J., and Shi, B., 2019, Synthesis of heterobinuclear Cu(II)-Ni(II) complex:

- Structure, CT-DNA interaction, hydrolytic function and antibacterial studies, *J. Mol. Struct.*, 1196, 836–843.
- [7] Gul, Z., Din, N.U., Khan, E., Ullah, F., and Nawaz Tahir, M., 2020, Synthesis, molecular structure, antimicrobial, anti-oxidant, and enzyme inhibition activities of 2-amino-6-methylbenzothiazole and its Cu(II) and Ag(I) complexes, *J. Mol. Struct.*, 1199, 126956.
- [8] Tania, L., Wijaya, K., and Trisunaryanti, W., 2014, Sintesis Cu(II)/silika dengan metode sol-gel sebagai antibakteri terhadap *Escherichia coli* dan *Staphylococcus aureus*, *BIMIPA*, 24 (2), 122–135.
- [9] Syaima, H., Rahardjo, S.B., and Suciningrum, E., 2017, Synthesis and elucidation structure of tetrakis-diphenylaminecopper(II) chloride hexahydrate, *J. Phys.: Conf. Ser.*, 909, 012080.
- [10] Mishra, N., Gound, S.S., Mondal, R., Yadav, R., and Pandey, R., 2019, Synthesis, characterization and antimicrobial activities of benzothiazole-imino-benzoic acid ligands and their Co(II), Ni(II), Cu(II), Zn(II) and Cd(II) complexes, *Results Chem.*, 1, 100006.
- [11] Herrera, K.M.S., Ferreira, L.S., Braga, A.V., Souza, J.P., Andrade, J.T., Soares, A.C., Soares, L.F., Chagas, R.C.R., and Ferreira, J.M.S., 2019, Synthesis, characterization and antimicrobial activity of Cr(III), Co(II) and Ni(II) complexes with 2-thiazoline-2-thiol derivative ligands against bacteria and yeasts of clinical importance, *An. Acad. Bras. Cienc.*, 91 (4), e20181077.
- [12] Al-Zaidi, B.H., Hasson, M.M., and Ismail, A.H., 2019, New complexes of chelating Schiff base: Synthesis, spectral investigation, antimicrobial, and thermal behavior studies, *J. Appl. Pharm. Sci.*, 9 (04), 045–057.
- [13] Prajapati, K.N., Brahmabhatt, M.P., Vora, J.J., and Prajapati, P.B., 2019, Synthesis, catalysis and biological study of transition metal(II) chelates with ONO-tridentate Schiff base ligand, *J. Pharm. Chem. Biol. Sci.*, 7 (2), 110–124.
- [14] Rahardjo, B., Wijanarko, D.M., Astuti, R., and Martina, A.A., 2018, Synthesis and characterization of diaquadinicotinamide cobalt(II) chloride, *AIP Conf. Proc.*, 2014, 020010.
- [15] De, A., Ray, H.P., Jain, P., Kaur, H., and Singh, N., 2020, Synthesis, characterization, molecular docking and DNA cleavage study of transition metal complexes of *o*-vanillin and glycine derived Schiff base ligand, *J. Mol. Struct.*, 1199, 126901.
- [16] Nair, M.S., Arish, D., and Johnson, J., 2016, Synthesis, characterization and biological studies on some metal complexes with Schiff base ligand containing pyrazolone moiety, *J. Saudi Chem. Soc.*, 20, S591–S598.
- [17] Himawati, A.W., Kusumaningsih, T., and Rahardjo, S.B., 2020, Cu(II)-3-aminoacetanilide complex: Synthesis and antibacterial activity test, *AIP Conf. Proc.*, 2296, 020067.
- [18] Nandiyanto, A.B.D., Oktiani, R., and Ragadhita, R., 2019, How to read and interpret FTIR spectroscopy of organic material, *Indones. J. Sci. Technol.*, 60, 4 (1), 97–118.
- [19] Venugopal, N., Krishnamurthy, G., Bhojyanaik, H.S., Madhukar Naik, M., and Sunilkumar, N., 2020, Synthesis, characterization, and biological activity of Cu(II) and Co(II) complexes of novel N^1, N^2 -bis(4-methyl quinolin-2-yl)benzene-1,2-diamine: CuO and CoO nanoparticles derived from their metal complexes for photocatalytic activity, *Inorg. Nano-Met. Chem.*, 51 (8), 1117–1126.
- [20] Takroni, K.M., Farghaly, T.A., Harras, M.F., and El-Ghamry, H.A., 2020, Synthesis, structure elucidation, DNA binding and molecular docking studies of novel copper(II) complexes of two 1,3,4-thiadiazolethiosemicarbazone derivatives, *Appl. Organomet. Chem.*, 34 (10), e5860.
- [21] Sevgi, F., Bagkesici, U., Kursunlu, A.N., and Guler, E., 2018, Fe(III), Co(II), Ni(II), Cu(II) and Zn(II) complexes of Schiff bases based-on glycine and phenylalanine: Synthesis, magnetic/thermal properties and antimicrobial activity, *J. Mol. Struct.*, 1154, 256–260.
- [22] Batool, S.S., Gilani, S.R., Zainab, S.S., Tahir, M.N., Harrison, W.T.A., Haider, M.S., Syed, Q., Mazhar, S., and Shoaib, M., 2020, Synthesis, Synthesis,

- crystal structure, thermal studies and antimicrobial activity of a mononuclear Cu(II)-cinnamate complex with *N,N,N',N'*-tetramethylethylenediamine as co-ligand, *Polyhedron*, 178, 114346.
- [23] Tamiru, G., Abebe, A., Abebe, M., and Liyew, M., 2019, Synthesis, structural investigation and biological application of new mono-and binuclear cobalt (II) mixed-ligand complexes containing 1, 10-phenanthroline, acetamide and ethylenediamine, *Ethiop. J. Sci. Technol.*, 12 (1), 69–91.
- [24] Revathi, N., Sankarganesh, M., Dhavethu Raja, J., Vinoth Kumar, G.G., Sakthivel, A., and Rajasekaran, R., 2020, Bio-active mixed ligand Cu(II) and Zn(II) complexes of pyrimidine derivative Schiff base: DFT calculation, antimicrobial, antioxidant, DNA binding, anticancer and molecular docking studies, *J. Biomol. Struct. Dyn.*, 39 (8), 3012–3024.
- [25] Kafi-Ahmadi, L., and Shirmohammadzadeh, L., 2017, Synthesis of Co(II) and Cr(III) salicylidenic Schiff base complexes derived from thiourea as precursors for nano-sized Co_3O_4 and Cr_2O_3 and their catalytic, antibacterial properties, *J. Nanostruct. Chem.*, 7 (2), 179–190.
- [26] Bakare, S.B., 2019, Cu(II), Co(II), Ni(II), Mn(II) and Zn(II) Schiff base complexes of 3-hydroxy-4-[*N*-(2-hydroxynaphthylidene)-amino]-naphthalene-1-sulfonic acid: Synthesis, Spectroscopic, thermal, and antimicrobial studies, *Pol. J. Chem. Technol.*, 21 (3), 26–34.
- [27] El-Sawaf, A.K., El-Essawy, F., Nassar, A.A., and El-Samanody, E.S.A., 2018, Synthesis, spectral, thermal and antimicrobial studies on cobalt(II), nickel(II), copper(II), zinc(II), and palladium(II) complexes containing thiosemicarbazone ligand, *J. Mol. Struct.*, 1157, 381–394.
- [28] Olanrewaju, A.A., Fabiyi, F.S., Ibeji, C.U., Kolawole, E.G., and Gupta, R., 2020, Synthesis, spectral, structure and computational studies of novel transition metal(II) complexes of (*Z*)-((dimethylcarbamoithioyl)thio)((1,1,1-trifluoro-4-(naphthalen-2-yl)-4-oxobut-2-EN-2yl)oxy), *J. Mol. Struct.*, 1211, 128057.
- [29] Obaid, S.M.H., Sultan, J.S., and Al-Hamdani, A.A.S., 2020, Synthesis, characterization and biological efficacies from some new dinuclear metal complexes for base 3-(3,4-dihydroxy-phenyl)-2-[(2-hydroxy-3-methylperoxy-benzylidene)-amino]-2-methyl propionic acid, *Indones. J. Chem.*, 20 (6), 1311–1322.
- [30] Aryasetiawan, F., and Karlsson, K., 2019, Modern theory of orbital magnetic moment in solids, *J. Phys. Chem. Solids*, 128, 87–108.
- [31] Ayuel, K., and Zakaria, A., 2018, Orbital and spin contributions to magnetic hyperfine fields of the 3D transition metal ions, *J. Magn. Magn. Mater.*, 457, 142–147.

Development of a Point-of-Use Drinking Water Purifier Using Aluminum Oxide-Based Flocculent-Disinfectant Composite

Patricia Namate^{1,2}, Feleke Zewge², and Eyobel Mulugeta^{3*}

¹Basic Sciences Department, Lilongwe University of Agriculture and Natural Resources, P.O. Box 219, Lilongwe, Malawi

²African Centre of Excellence for Water Management, Addis Ababa University, P.O. Box 1176, Addis Ababa, Ethiopia

³Bio and Emerging Technology Institute, Ministry of Innovation and Technology, P.O. Box 5954, Addis Ababa, Ethiopia

* Corresponding author:

email: eyoya2005@gmail.com

Received: November 8, 2022

Accepted: March 10, 2023

DOI: 10.22146/ijc.79024

Abstract: One in every three people in the world still lacks access to clean drinking water. Aside from microbiological pollution, high fluoride content in drinking water is one of the most serious problems in African countries. This study aimed to contribute to the availability of clean water by developing a point-of-use drinking water purifier using an aluminum oxide-based flocculent-disinfectant composite. Batch experiments were conducted to determine factors affecting fluoride removal efficiency (FRE) and E. coli log reduction efficiency. AO of 75 mg/L, 800 mg/L alum, lime (35% alum dose), and 1.5 mg/L Ca(OCl)₂ doses achieved 95% FRE and 5 log₁₀ reductions of E. coli using 15 mg/L as initial fluoride concentration ($[F^-]_0$), and 10⁵ CFU/100 mL E. coli concentration. $[F^-]_0$ affected FRE but showed no effect on E. coli log reduction. The optimum pH of the solution for both FRE and E. coli log reduction was found to be in the range of 4–8. Three prototypes in powder form were developed. The prototypes were tested on real water samples from the Ethiopian Rift Valley, and the results were found to be within the drinking water standards, thus indicating the capability of the developed products to purify contaminated water for human consumption.

Keywords: fluoride; aluminum oxide; water purifier; E. coli

■ INTRODUCTION

While access to safe drinking water remains critical to human survival, the majority of the world population lacks access to it [1]. For example, estimates in 2017 indicated that 785 million people worldwide lacked access to basic drinking water supply and sanitation, with around 144 million of these individuals depending on contaminated water resources. Duke et al. [2] also pointed out that even people with “improved” water sources, such as household connections, public standpipes, and boreholes, are still at risk of consuming microbiologically and chemically contaminated water. In Africa, the spread of deadly waterborne diseases such as dental and skeletal fluorosis, diarrhea, dysentery, typhoid, and cholera are linked to a lack of access to clean water and poor sanitation [3]. Naik [4] pointed out that less than 50% of the rural communities in Africa have access to both safe

water and sanitation. The authors further acknowledged that the continent continues to suffer from the problem of acute water scarcity, clean water deficit, and crises.

Countries within the African Great Rift Valley Region are at high risk of consuming contaminated water. For example, studies have indicated that fluoride concentration is exceptionally high in countries within the East African Great Rift Valley Region [5]. In some countries, such as Malawi [6], Ethiopia [7], and Tanzania [8], the hydrochemical characteristics of groundwater are highly associated with high fluoride concentration above the recommended level. In Ethiopia, about eight million people consume water containing fluoride concentration above 1.5 mg/L, that is permissible limits established by the WHO [9]. Zewge [9] reported that the daily intake of fluoride concentration above 1.5 mg/L is linked to dental and

skeletal fluorosis. Similar cases are reported in countries such as Sudan, Nigeria, Kenya, Tanzania, and Malawi, with a great occurrence of dental and skeletal fluorosis in the majority of populations [10-12].

The most prevalent household water treatment processes include chlorination, filtration, solar disinfection, boiling, coagulation, and flocculation [3]. These are effective at reducing microbial contamination. Various technologies have also been developed worldwide, including in Ethiopia, to treat water sources with high fluoride concentration [8,13]. The coagulation, precipitation on $Al_2(SO_4)_3$, CaO, and CaCl₂, adsorption on activated alumina, aluminum-based adsorbents, bentonite, ion exchange with synthetic resins, and bone char are the most extensively employed fluoride removal techniques in developing countries [14-15]. In rural Ethiopia, some of these techniques have proven to be inefficient in removing exceptionally high fluoride levels in the Central Rift Valley region [10]. Therefore, activated alumina and bone char have been proposed in the region.

Coagulant/disinfection products (CDPs) have the distinct benefit of offering microbial quality improvement, turbidity reductions, and a post-treatment free chlorine residual (FCR) among the various available point of use (POU) techniques (e.g., boiling, household chlorination, and ceramic filtration). These are readily available sachets that contain at least two main active ingredients (typically in powdered form), namely a coagulant (e.g., aluminum or ferric salt) and a disinfectant (i.e., chlorine variant). Examples include the PUR product, which is a small sachet containing powdered ferric sulfate (a flocculent) and calcium hypochlorite (a disinfectant), Bishan Gari as well as Aquatabs products [16]. The Bishan Gari water purifier has the following advantages, according to Bogale [16]: a longer shelf life than liquid chlorine, a small volume that makes it simpler to carry and store, it is locally made, and inexpensive. The downside of the Bishan Gari water purifier include that it does not reduce fluoride levels to below 1.5 mg/L for water sources with high fluoride concentration, and people do not like the smell of the treated water.

The combination of aluminum sulfate and lime

in water purifiers also reduces fluoride levels in drinking water. The insoluble aluminum hydroxide flocs formed during this process are responsible for the co-precipitation of the fluoride ions, a technique called Nalgonda [14]. However, this method is not suitable for treating water with high total dissolved solids (TDS) and raw water fluoride concentration exceeding 10 mg/L. In addition, the aforementioned water purifiers generate a lot more sludge after treatment since the technologies consume more aluminum sulfate dose to reduce the fluoride to its permissible level, and some of the water purifiers do not effectively treat turbid water. Hence, there is a need to look for a solution to minimize the amount of sludge produced after treatment and also to effectively treat turbid water.

Therefore, POU water treatment technologies with a combination of coagulants and disinfectants are among the technologies used to empower people and communities which use unimproved water sources and water sources with high fluoride concentration to improve water quality by treating it at home [12,17-18]. Research conducted by Mulugeta et al. [19] compared the performance of commercially available activated alumina (AA) and aluminum oxide (AO) synthesized in the laboratory. It showed that the fluoride removal capacity of AO synthesized in the lab was twice that of the commercially available aluminium oxide, such as activated alumina and pseudo-boehmite. These defluoridation technologies occur at the source, and therefore during transportation and storage of drinking water, there might be a high risk of microbial contamination together with fluoride contamination. Therefore, there is a need to look for technologies to remove both fluoride and microbes. Therefore, the objectives of this study were (a) to conduct batch fluoride and bacterial removal experiments using the synthesized AO, aluminum sulfate, calcium hypochlorite, and lime under optimized conditions, (b) to test the composite on actual water samples from the Ethiopian Rift Valley region, and (c) to develop a prototype household water purifier using aluminum oxide-based flocculent-disinfectant composite.

■ EXPERIMENTAL SECTION

Materials

The reagents and chemicals utilized were received without any treatment. The materials used in this study were anhydrous sodium fluoride (99.0% NaF, BDH Chemicals Ltd, Poole, England); aluminium sulfate ($\text{Al}_2(\text{SO}_4)_3 \cdot 14\text{H}_2\text{O}$, which was purchased from Awash Melkasa Aluminium Sulfate and Sulfuric Acid Factory, Ethiopia); sodium hydroxide, calcium hypochlorite, and sodium thiosulfate (99% purity, Merck, Germany); the lime was purchased from Senkele Lime Factory, Ethiopia. Total ionic strength adjustment buffer (TISAB) was prepared following the recommended procedure, except for the ethylenediaminetetraacetic acid (EDTA) that was substituted with cyclohexanediaminetetraacetic acid (CDTA). The Ethiopian Health and Nutrition Research Institute (EHNRI) provided a permanent *E. coli* stock culture. *E. coli* cells used in this study were prepared from the permanent culture.

Instrumentation

The instruments used in the present study were A pH/ISE meter (Orion Model EA 940 Expandable Ion Analyzer, USA) fitted with a combination ion selective fluoride electrode (Orion Model 96-09, USA) used to measure the concentration of fluoride; muffle furnace (Carbolite, ELF Model, UK); turbidity meter (Thermo Scientific Orion AQ4500 Turbidimeter, USA); UV-vis spectrophotometer (ThermoFisher Scientific, USA) and portable conductivity/TDS meter (HACH, HQ1140, USA).

Procedure

E. coli enumeration

Before and after treatment, the concentration of viable *E. coli* bacteria was determined using the pour plate method, as described in standard method 9215B [20]. The following formula in Eq. (1) was applied to the *E. coli* count.

$$\frac{\text{CFU}}{100} \text{ mL} = \frac{\text{Average count}}{\text{Volume of the sample}} \times 100 \quad (1)$$

where CFU is the Colony Forming Unit

Analysis of fluoride

The fluoride stock solution was prepared by dissolving 2.21 g of anhydrous sodium fluoride in deionized water and filling up to 1000 mL with deionized water. The fluoride solutions used during the batch process were made by diluting the stock solution. The pH/ISE meter was calibrated using standard solutions containing fluoride concentration of 0.5, 1.0, 5.0, 10.0, and 20.0 mg/L before each trial. An equal volume of TISAB was added to each sample before measuring the fluoride concentration. All samples were filtered through a 0.2 μm filter paper for fluoride analysis. All tests were carried out at room temperature.

Chlorine measurement

Calcium hypochlorite was used to produce a 1% chlorine stock solution. The chlorine solutions used during the batch process were made by diluting the stock solution. The chlorine and residual chlorine concentrations were measured by the *N,N*-diethyl-*p*-phenylenediamine (DPD) method [21].

Synthesis of aluminum oxide (AO)

AO was synthesized using the standard method developed by Mulugeta and his research colleagues [15]. The precursor material was aluminum sulfate (alum). AO was prepared by mixing 100 g of $\text{Al}_2(\text{SO}_4)_3 \cdot 14\text{H}_2\text{O}$ in 500 mL of distilled water while stirring with a magnetic stirrer until complete dissolution. NaOH (2 M) was used to adjust the pH. The precipitate (AO) was dried by exposure to sunlight. The AO was activated by heating it at 300 °C in a furnace for 1 h. It was then thoroughly washed with deionized water to remove excess Na_2SO_4 . The AO material was sun-dried again and crashed into powder with a mortar and pestle.

Batch experiments

All batch tests were performed in a 500 mL beaker containing 500 mL of fluoride-spiked distilled water and *E. coli* under constant mixing conditions on a magnetic shaker at room temperature. The sample solution was regularly removed from the beaker. The residual fluoride concentration was determined immediately after adding an equal amount of TISAB to a 10 mL sample

solution. Chlorination was stopped with a quencher of 50 μL of 10% sodium thiosulfate. All tests were conducted in triplicate, and the mean values were used. The fluoride removal efficiency (FRE) was determined using Eq. (2).

$$\% \text{ FRE} = \left(\frac{C_0 - C_t}{C_0} \right) \times 100 \quad (2)$$

where C_0 and C_t are the initial and at any time (t) fluoride concentration in solution (mg/L), respectively. The removal efficiency of *E. coli* was expressed as the \log_{10} reduction value of bacteria using Eq. (3).

$$\text{LRV} = \log_{10} \frac{N_t}{N_0} \quad (3)$$

where, LRV = log reduction value of bacteria counts at time t ; N_0 = initial bacterial concentration at time 0, N_t = final bacterial concentration after a treatment time t .

Optimization of operation parameters

Batch operation parameters were optimized by varying one parameter at a time and allowing the rest to remain constant. The effect of dose on fluoride removal efficiency and *E. coli* log reduction was studied by varying doses of aluminum sulfate (700, 800, 900, 1000, and 1100 mg/L), AO (45, 75, 105, 135 and 165 mg/L), lime (35% alum dose), and calcium hypochlorite (0.5, 1.0, 1.5, 2.0, 2.5, 3.0, 3.5 and 4.0 mg/L) at constant initial fluoride concentration of 15 mg/L and approximately 10^5 CFU/100 mL *E. coli* concentration.

The contact time effect was studied by changing time (10, 20, 30, 40, 50, 60, 70, 80, 90, 100, 110, and 120 min). The effect of initial fluoride concentration ($[F^-]_0$) was studied by varying the fluoride concentration (5, 10, 15, 20, 25, and 30 mg/L). The pH effect was examined by changing the initial pH of the solution (3, 4, 5, 6, 7, 8, 9, and 10). The effect of initial *E. coli* concentration was investigated by spiking the water with different *E. coli* concentrations (10^4 , 10^5 , 10^7 , and 10^8 CFU/100 mL).

Testing the composite with actual water samples

Actual water samples were collected from six different sites within the Ethiopian Rift Valley, namely the Bora district (Tube, Tejitu, Dolessa), the Adami Tulu Jido Kombolcha (ATJK) district (Germama, Anano), and the Dugda district (Serity) in 30 L plastic Jerri cans. The

samples for *E. coli* analysis were collected in sterilized bottles. The Jerri cans were labeled for identification before being adequately stored and transferred to the laboratory. The optimized dose from the batch experiments was tested on these water samples. Water samples were analyzed for different parameters before and after treatment. Methods of water quality analysis were done according to standard methods for examining water and wastewater specified by the American Public Health Association [20]. The water samples were analyzed for the following parameters: turbidity, pH, electrical conductivity (EC), fluoride, *E. coli*, alkalinity, sulfate, aluminum, residual chlorine, and chloride. The obtained values were compared against the WHO drinking water standards to evaluate their suitability for drinking purposes.

Development of a prototype household water purifier

Batch experiments were conducted on actual water samples to optimize a combination of four materials that can effectively treat 10 L of water samples. The water purifier prototype was developed based on batch experiments conducted on actual water samples. Three prototypes were developed as high, medium, and low dose for treating 10 L water samples with 5, 10, and 15 mg/L fluoride concentration, respectively. A dose of 75 mg/L AO, 800 mg/L alum, 15% lime, and 2 mg/L $\text{Ca}(\text{OCl})_2$ was used to develop a low-dose prototype to treat water with fluoride concentration ≤ 5 mg/L. A dose of 85 mg/L AO, 850 mg/L alum, 15% lime, and 2 mg/L $\text{Ca}(\text{OCl})_2$, was used to develop a medium dose prototype to treat water that contains fluoride concentration ≤ 10 mg/L. A dose of 95 mg/L AO, 900 mg/L alum, 15% lime, and 2 mg/L $\text{Ca}(\text{OCl})_2$ was used to develop a high-dose prototype to treat water that contains fluoride concentration ≤ 15 mg/L. The high, medium and low doses weigh 11.9, 10.6, and 9.9 g, respectively. Finally, the materials were packed in a single sachet for POU water treatment. The developed prototypes were tested on water samples from the Ethiopian Rift Valley. The treated water samples were analyzed for turbidity, pH, electrical conductivity, fluoride, *E. coli*, alkalinity, sulfate, aluminum, residual chlorine, and chloride.

■ RESULTS AND DISCUSSION

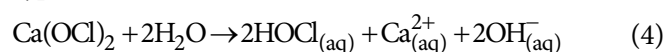
Optimization of Process Parameters

The effect of dose

Fluoride removal efficiency increased with an increase in dosage from 83.2 to 95.7%, as shown in Table 1. This is attributed to the increased production of higher amounts of precipitates and aluminum hydroxides, which increased the fluoride removal efficiency [22]. There was no improvement in the percent fluoride removal at higher dosages than 75 mg/L AO, 280 mg/L lime, and 800 mg/L alum due to the presence of excess precipitates compared to fluoride ions, assuming that the amount of aluminum complex per fluoride ion stays constant. Higher alum/AO doses could lead to the wastage of chemicals without significantly increasing the amount of fluoride removed.

This dosage of 75 mg/L AO, 800 mg/L alum, and 280 mg/L lime is adequate to lower the fluoride levels in drinking water to 1.5 mg/L. Similar results were obtained by Shimelis et al. [23] on the removal of fluoride from water using aluminum hydroxide. After a dose of 1.6 g/L, there was no significant change in fluoride removal; hence that dose was considered the optimum dose. Various combinations of AO and alum did not produce efficient *E. coli* log reduction, as shown in Table 2. The various combinations only reduced *E. coli* in the range of 0.0021

to 0.0091 log, corresponding to 2 to 9% *E. coli* removal. As such, a dose of 75 mg/L AO and 800 mg/L alum was selected for further dose optimization with calcium hypochlorite. The dose of 75 mg/L AO, 800 mg/L alum, and 280 mg/L lime was combined with different concentrations of calcium hypochlorite in the range of 0.5 to 4 mg/L. There was a slight increase in fluoride removal after adding calcium hypochlorite, as shown in Table 3. The reaction in Eq. (4) occurs when calcium hypochlorite is added to water.



The calcium ion in the solution reacts with fluoride to form calcium fluoride (CaF_2), according to Eq. (5).



Calcium fluoride is insoluble and is left like a precipitate. This contributes to fluoride removal via precipitation [24]. Calcium hypochlorite disinfects water through an inactivation process that causes damage to the cell membrane and cell wall of *E. coli* [25].

After adding calcium hypochlorite to water, hypochlorous acid (HOCl^-) is formed. Proteins and peptidoglycan bound to the cell wall and the cell membrane are the initial points of attack for chlorine disinfection [26]. After the cell wall and membrane damage, HOCl^- can penetrate the cell wall and reach the

Table 1. Fluoride removal efficiency (%) for various combinations of alum, AO, and 280 mg/L lime

AO (mg/L)	Alum (mg/L)				
	700	800	900	1000	1100
45	83.2 ± 0.71	85.7 ± 0.81	90.1 ± 0.08	91.2 ± 0.07	92.1 ± 0.45
75	85.8 ± 0.43	92.1 ± 0.51	93.2 ± 0.56	93.9 ± 0.73	94.1 ± 0.18
105	87.1 ± 0.63	92.5 ± 0.54	92.9 ± 0.54	94.1 ± 1.12	94.9 ± 0.38
135	89.7 ± 0.71	93.1 ± 0.87	93.7 ± 0.76	94.5 ± 0.34	95.2 ± 0.41
165	90.7 ± 0.98	94.7 ± 0.53	94.8 ± 0.34	95.1 ± 0.28	95.7 ± 0.37

Table 2. \log_{10} reduction (10^2 CFU/100 mL) of *E. coli* for various combinations of alum, AO, and 280 mg/L lime

AO (mg/L)	Alum (mg/L)				
	700	800	900	1000	1100
45	0.21 ± 0.05	0.24 ± 0.01	0.29 ± 0.01	0.33 ± 0.04	0.40 ± 0.05
75	0.31 ± 0.05	0.41 ± 0.05	0.51 ± 0.04	0.68 ± 0.04	0.60 ± 0.10
105	0.35 ± 0.10	0.52 ± 0.04	0.56 ± 0.01	0.59 ± 0.01	0.61 ± 0.05
135	0.40 ± 0.10	0.67 ± 0.04	0.72 ± 0.04	0.83 ± 0.04	0.87 ± 0.01
165	0.60 ± 0.01	0.73 ± 0.02	0.08 ± 0.05	0.90 ± 0.05	0.91 ± 0.05

cytoplasm, followed by reactions with purine and pyrimidine bases of the nucleic acids, whereby thymidine deoxyguanosine and uridine monophosphate are preferred targets. There was an increase in log reduction for *E. coli* with an addition of calcium hypochlorite (Table 3). An increase in the dose of calcium hypochlorite led to an increase in log₁₀ reduction of *E. coli*. A low concentration of calcium hypochlorite produces low HOCl⁻ concentrations. As a result, at low concentrations, microbial inactivation is low due to its inability to reach the cytoplasm and cause damage to the DNA [27]. A 0.5 mg/L of Ca(OCl)₂ only achieved 1 log₁₀ reduction (about 90%) of *E. coli*. In contrast, higher chlorine concentrations cause a larger impairment of the cell wall and membrane, enabling HOCl to penetrate the cell wall and react with nucleic acids. This results in high-level DNA damage to the bacterial cells, impeding DNA amplification, even for short amplicons [26]. This is why 4 mg/L of Ca(OCl)₂ achieved a 6.7 log₁₀ (99.9999%) reduction of *E. coli*. These results agree with a previous study by Owoseni et al. [21] on the survival of *E. coli* collected from secondary effluents of two wastewater treatment facilities in the Eastern Cape Province of South Africa with different chlorine concentrations. The bacteria log reduction ranged from 1 to 5 at low calcium hypochlorite concentrations (0.5 to 1.5 mg/L). At higher calcium hypochlorite concentrations (2 to 4 mg/L), the bacteria log reduction ranged from 6.0 to 6.7.

The residual chlorine concentration was in the range of 0.09 to 1.72 mg/L. Residual chlorine is defined as the concentration of chlorine species present in water after

the oxidant demand has been met [28]. The report from the Centers for Disease Control and Prevention indicates that the presence of residual chlorine in drinking water indirectly implies the absence of disease-causing organisms, secondly, it indicates that the water is protected against recontamination during transportation and storage at home [29]. The free chlorine level in drinking water correlates with the absence of most disease-causing organisms and hence serves as a measure of water potability. The WHO recommends that free chlorine residual range of 0.2–0.5 mg/L is maintained at all points in the water supply for locations with little risk of cholera or associated epidemics [30]. Since 1.5 mg/L of calcium hypochlorite produced 5 log reduction for *E. coli*, which is a good performance. The residual chlorine concentration was 0.48 mg/L, which is enough to protect water from recontamination and is within the WHO permissible limits. The dose of 1.5 mg/L Ca(OCl)₂, 75 mg/L AO, 800 mg/L alum, and 280 mg/L lime was selected as an optimum dose for further experiments.

Effect of contact time

Fig. 1(a) shows that fluoride removal was fast within the first 15 min. Fluoride removal attains almost an equilibrium condition after 60 min. This indicates that all active sites for binding fluoride ions are occupied quickly [31]. A contact time of 30 min is enough to remove 90% of fluoride in a solution with the dose of 75 mg/L AO, 800 mg/L alum, 35% lime, and 1.5 mg/L calcium hypochlorite. This shows that a contact time more than 30 min does not affect fluoride removal. Similar

Table 3. Fluoride removal efficiency (%) and *E. coli* log reduction with 75 mg/L AO, 800 mg/L alum, 280 mg/L lime, and different concentrations of calcium hypochlorite at 15 mg/L of fluoride and 10⁵ CFU/100 mL

Concentration of Ca(OCl) ₂ (mg/L)	Fluoride removal efficiency (%)	Log ₁₀ reduction for <i>E. coli</i>	Residual chlorine
0.5	94.31 ± 0.06	1.0 ± 0.07	0.09 ± 0.04
1.0	95.11 ± 0.09	2.7 ± 0.05	0.12 ± 0.03
1.5	95.32 ± 0.27	5.0 ± 0.50	0.48 ± 0.10
2.0	96.56 ± 0.13	6.0 ± 0.05	0.60 ± 0.06
2.5	96.71 ± 0.11	6.1 ± 0.10	0.92 ± 0.07
3.0	97.22 ± 0.24	6.2 ± 0.70	1.21 ± 0.01
3.5	97.31 ± 0.56	6.4 ± 0.90	1.50 ± 0.02
4.0	97.89 ± 0.70	6.7 ± 0.40	1.72 ± 0.09

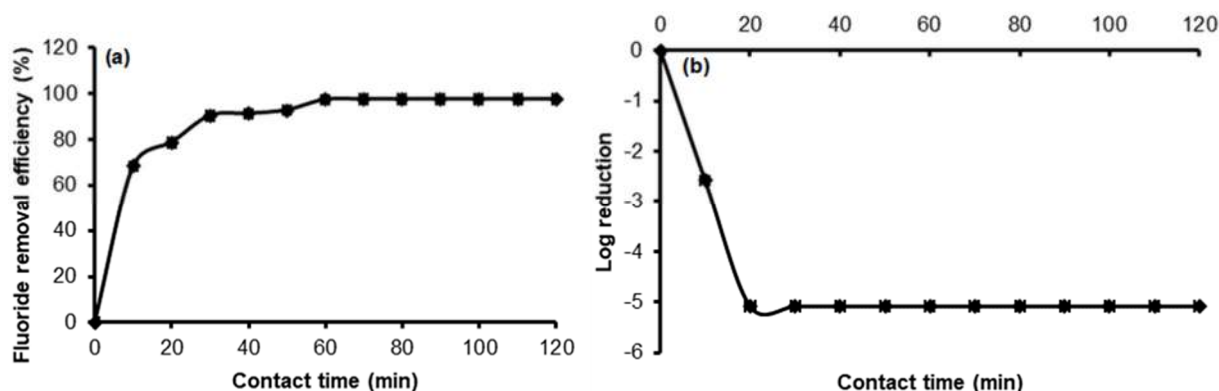


Fig 1. The effect of contact time on (a) fluoride removal and (b) *E. coli* log reduction ($[F^-] = 15$ mg/L, pH = 6.7, *E. coli* = 10^5 CFU/100 mL, AO = 75 mg/L, alum = 800 mg/L, lime = 280 mg/L and $Ca(OCl)_2 = 1.5$ mg/L)

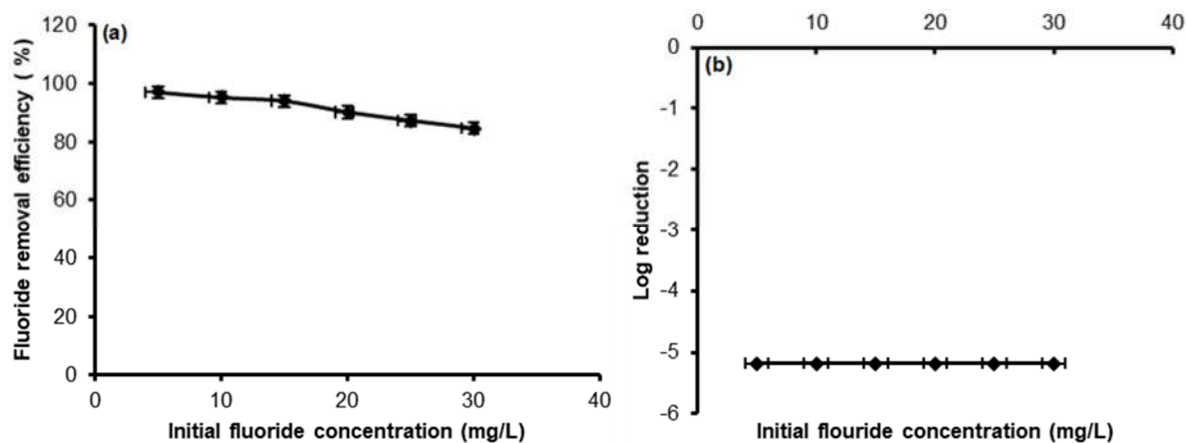


Fig 2. The effect of $[F^-]_0$ on (a) F^- removal efficiency, (b) *E. coli* log reduction (contact time = 30 min, pH = 6.7, *E. coli* = 10^5 CFU/100 mL, AO = 75 mg/L, alum = 800 mg/L, lime = 280 mg/L and $Ca(OCl)_2 = 1.5$ mg/L)

results were observed by Zewge [9] for the removal of fluoride from water using a combined aluminum sulfate/hydroxide process. Fig. 1(b) shows a 2.5 \log_{10} reduction of *E. coli* bacteria after 10 min of exposure. *E. coli* reductions of 5 \log_{10} were achieved within 20 min. After 20 min, there was no significant change in *E. coli* log reduction. The results agree with previous research findings by Owoseni et al. [21] on the inactivation of *E. coli* using calcium hypochlorite. The results showed that 5 \log_{10} *E. coli* reduction was achieved within 20 min and that after 20 min, there was no significant difference in *E. coli* log reduction. This shows that more than 20 min of contact time does not affect *E. coli* inactivation. Because the reactions involved *E. coli* log reduction and fluoride removal, 30 min was enough to reduce the fluoride concentration to 1.5 mg/L and achieve 5 *E. coli* log

reduction. Therefore, a contact time of 30 min was selected as the optimum contact time for further experiments.

Effect of initial fluoride concentration

The findings were plotted as fluoride removal efficiency versus initial concentration of fluoride (Fig. 2(a)) and *E. coli* log reduction versus $[F^-]_0$ (Fig. 2(b)). Maximum fluoride removal occurred at lower fluoride concentration, as shown in Fig. 2(a). For a given amount of coagulant level, fluoride removal is high at low fluoride concentration because there are more aluminum oxide complexes for fluoride ions [32]. As fluoride concentration increases, the binding potential of aluminum oxide reaches saturation, resulting in a decline in fluoride removal. This is attributed to the intensive use of all active sites on the complex's surface,

and the incoming fluoride ion from the water being repelled by repulsive forces [33]. These results are in line with Hussein and Vegi [31], who found that the fluoride removal efficiency reduced from 93 to 78% with the increase in $[F^-]_0$ from 8 to 25 mg/L. Initial fluoride concentration did not significantly affect *E. coli* log reduction, as shown in Fig. 2(b). Fluoride is toxic to bacteria, fungi, plants, and animals at high concentrations [34]. To overcome this problem of fluoride toxicity, *E. coli* bacteria developed fluoride resistance mechanisms. *E. coli* has a class of regulatory RNAs, or riboswitches, that bind to fluoride and regulate gene expression in response to this anion. Riboswitches are metabolite or ion-sensing structured RNA motifs typically found in the noncoding regions of specific mRNAs. They regulate the expression of neighboring protein-coding regions via various mechanisms, including transcription termination, translation blockade, and alternative splicing [35]. This explains why fluoride concentration did not affect *E. coli* log reduction.

Effect of pH

The fluoride removal process, which involves the hydrolysis of alum and the preferential adsorption of fluoride ions onto aluminum oxide undergoing precipitation, is highly dependent on the pH of the solution.

The percentage of fluoride removal increases as the pH of the solution increases from 3 to 8, and the

maximum fluoride removal is observed at pH 6 to 7 (Fig. 3(a)). $Al(OH)_3$ is responsible for fluoride removal. The $Al(OH)_3$ floc is believed to adsorb F^- strongly, and the formation of this precipitate is optimal in a pH range of 6 to 7 [36]. Below the pH of 5, there is insufficient aluminum hydroxide to precipitate $Al(OH)_3$ since aluminum species such as Al^{3+} , $Al(OH)^{2+}$ and $Al(OH)_2^+$ are prevalent [37]. When the pH was raised to 10, the percentage of fluoride removal gradually decreased because soluble $Al(OH)_4^-$ is the predominant species that repel the fluoride ions. This is consistent with the findings of [38], who also found that the maximum fluoride removal using aluminum oxide was achieved with a pH range of 6 to 7. The populations of *E. coli* were reduced by about 1 and 5 \log_{10} CFU/100 mL in a pH range of 3 to 10, with a maximum log reduction achieved at 5–6 (Fig. 3(b)). pH is an essential factor that influences the efficiency of disinfection. When calcium hypochlorite is added to water, Eq. (4) occurs:

Hypochlorous acid dissociates to produce the hypochlorite ion, as shown in Eq. (6).



Hypochlorous acid is more reactive than hypochlorite ion and a more powerful disinfectant and oxidant [27]. A higher pH allows for more hypochlorite ions, resulting in less hypochlorous acid in the water [39]. Low pH allows for the formation of fewer hypochlorite

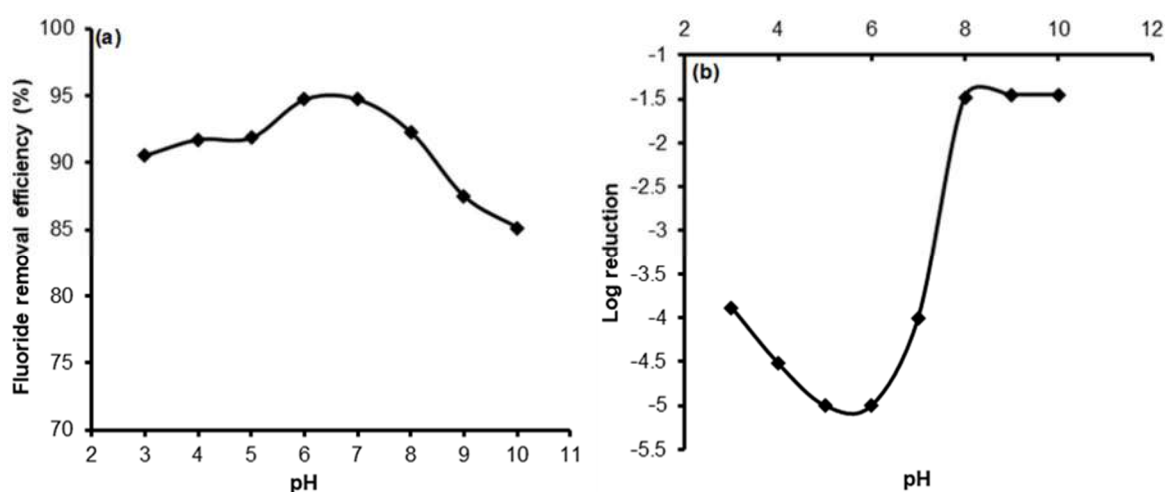


Fig 3. The pH effect on (a) fluoride removal and (b) *E. coli* log reduction ($[F^-] = 15$ mg/L, contact time = 15 min, *E. coli* = 10^5 CFU/100 mL, AO = 75 mg/L, alum = 800 mg/L, lime = 280 mg/L and $Ca(OCl)_2 = 1.5$ mg/L)

ions and more hypochlorous acid. Hypochlorous acid is the most effective type of free chlorine residual, i.e., chlorine that is accessible to kill microbes in water, whereas hypochlorite ions are far less effective disinfectants. As a result, disinfection is more efficient at low pH (with high amounts of hypochlorous acid in water) than at high pH (with high amounts of hypochlorite ions in water) [40]. This explains why *E. coli* concentrations were lower in the acidic medium compared to the primary media. These findings are consistent with Owoseni et al. [21], who showed that maximal log reduction of *E. coli* with calcium hypochlorite was attained in pH solutions ranging from 3 to 7.

Effect of initial *E. coli* concentration

The initial *E. coli* concentration did not affect fluoride removal (Fig. 4(a)). This might be attributed to the fact that there is no competition between *E. coli* and fluoride ions for the binding site. The log reduction rate decreased as *E. coli* concentration increased (Fig. 4(b)). At initial concentrations of 10^4 and 10^5 CFU/100 mL, 5 and 6 \log_{10} reduction was achieved. At initial concentrations of 10^7 and 10^8 CFU/100 mL, the \log_{10} reduction was reduced to 2.

More calcium hypochlorite or more extended treatment periods will be needed to destroy the same proportion of *E. coli* cells at very high cell concentrations (10^8 CFU/100 mL and more). The *E. coli* concentration

effect seen here may be attributed to the concentration of molecules available to interact with *E. coli* cells [27]. For the inactivation of *E. coli*, there is a need for direct interaction between a given concentration of hypochlorite in a solution and bacterial cell membranes [21]. This suggests that a saturation point is reached at high *E. coli* concentrations where enough bioactive molecules are required to associate with prominent receptor locations within the cell. The concentration of hypochlorite ions available to kill *E. coli* cells becomes very limited at high *E. coli* concentrations, and hence a higher reduction rate is not achieved [27]. These results are in line with those of Liang et al. [41], who argued that the initial *E. coli* concentration affects the log inactivation of *E. coli*.

Testing the Composite with Actual Water Samples

The concentrations of Fluoride and *E. coli* before and after treatment are shown in Table 4. The FRE was in the range of 77.5 to 89.1%. Treated water samples from Serity, Tejitu, Germama, and Anano had fluoride concentration that were above the acceptable WHO drinking water standard. The reduced fluoride removal efficiency could be attributed to the alkalinity of the water samples. Alkalinity includes hydroxides, carbonates, and bicarbonate. Carbonate has a high affinity for $\text{Al}(\text{OH})_3$. The observed decrease in fluoride removal may be attributed to the rivalry for aluminum hydroxide complexes between the carbonate and fluoride anion [36].

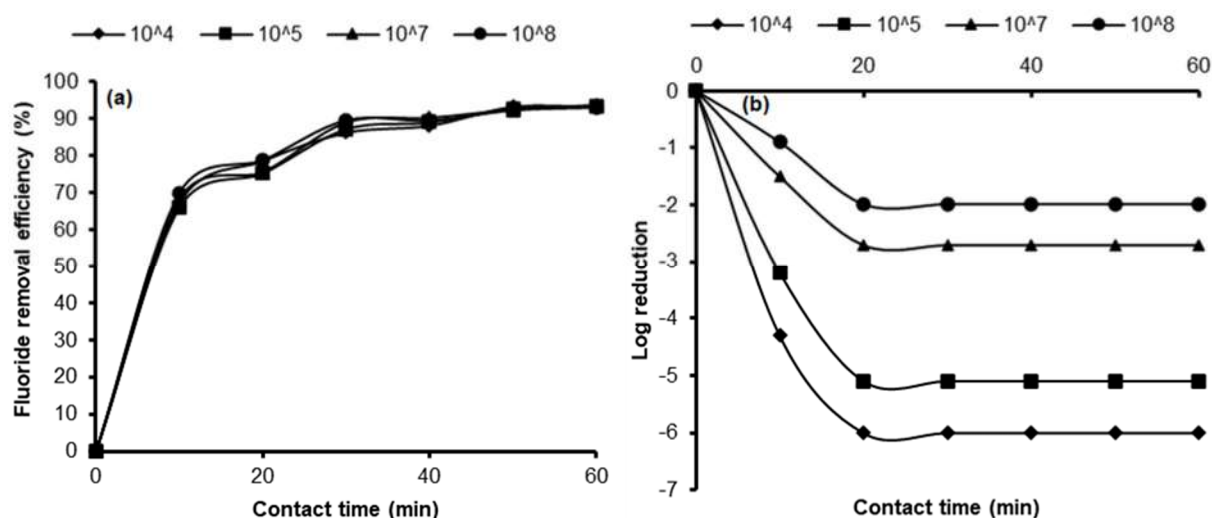


Fig. 4. The effect of initial *E. coli* concentration on (a) fluoride removal and (b) *E. coli* log reduction

Table 4. Concentrations of different water quality parameters for actual water samples

Drinking water quality parameters	Tube		Serity		Dollessa	
	RW	TW	RW	TW	RW	TW
Fluoride (mg/L)	3.67 ± 0.10	0.4 ± 0.01	12.3 ± 0.34	1.6 ± 0.08	5.55 ± 0.23	0.97 ± 0.12
pH	7.55 ± 0.12	7.20 ± 0.10	8.10 ± 0.34	7.24 ± 0.3	8.19 ± 0.40	6.62 ± 0.20
EC (µs/cm)	410 ± 0.79	546 ± 0.50	770 ± 0.90	836 ± 1.50	530 ± 1.03	767 ± 1.00
TDS (mg/L)	205 ± 1.22	273 ± 1.50	385 ± 1.72	458.5 ± 0.50	265 ± 2.33	383.5 ± 2.16
<i>E. coli</i> (CFU/100 mL)	1.9×10 ⁵ ± 13.0	19 ± 2.12	1.6×10 ⁵ ± 10	0	1.77×10 ⁵ ± 21	0
Turbidity (NTU)	58 ± 0.17	5 ± 0.09	3.3 ± 0.01	<1 ± 0.01	<1 ± 0.03	<1 ± 0.01
Alkalinity as CaCO ₃ (mg/L)	739 ± 0.81	-	821 ± 0.91	-	856 ± 0.12	-
Aluminum (mg/L)	0.01 ± 0.01	0.14 ± 0.01	0.01 ± 0.001	0.15 ± 0.01	0.01 ± 0.001	0.04 ± 0.005
Chloride (mg/L)	1.19 ± 0.01	2.35 ± 0.10	1.20 ± 0.12	3.10 ± 0.05	0.40 ± 0.03	1.27 ± 0.20
Sulfate (mg/L)	87 ± 0.89	135 ± 1.00	98 ± 0.91	140 ± 1.50	50 ± 0.70	117 ± 1.50
Residual Chlorine (mg/L)	-	0.08 ± 0.01	-	0.39 ± 0.04	-	0.33 ± 0.01
Drinking water quality parameters	Tejitu		Germama		Anano	
	RW	TW	RW	TW	RW	TW
Fluoride (mg/L)	9.63 ± 0.31	1.63 ± 0.03	15.1 ± 0.09	2.8 ± 0.03	10.5 ± 0.24	2.36 ± 0.67
pH	8.10 ± 0.12	7.32 ± 0.01	8.01 ± 0.45	7.16 ± 0.01	7.66 ± 0.82	6.90 ± 0.01
EC (µs/cm)	700 ± 1.33	836 ± 2.00	1115 ± 1.61	1335 ± 1.50	1101 ± 1.23	1348 ± 1.50
TDS (mg/L)	350 ± 1.21	418 ± 1.50	557.5 ± 1.83	667 ± 1.50	550.5 ± 0.21	674 ± 2.00
<i>E. coli</i> (CFU/100 mL)	1.98×10 ⁵ ± 23	0	1.08×10 ⁵ ± 17	87 ± 4	1.3×10 ⁴ ± 12	0
Turbidity (NTU)	<1 ± 0.01	<1 ± 0.02	59 ± 0.12	7 ± 0.02	<1 ± 0.01	<1 ± 0.01
Alkalinity as CaCO ₃ (mg/L)	809 ± 0.21	-	791 ± 0.21	-	784 ± 0.01	-
Aluminum (mg/L)	0.01 ± 0.002	0.06 ± 0.005	0.02 ± 0.002	0.06 ± 0.001	0.01 ± 0.002	0.18 ± 0.005
Chloride (mg/L)	0.90 ± 0.21	2.10 ± 0.20	1.43 ± 0.02	3.97 ± 0.08	0.82 ± 0.02	2.70 ± 0.10
Sulfate (mg/L)	67 ± 0.45	127 ± 1.00	56 ± 2.12	97 ± 1.50	30 ± 0.21	73 ± 0.50
Residual Chlorine (mg/L)	-	0.44 ± 0.02	-	0.12 ± 0.01	-	0.42 ± 0.01

Note: RW: Raw water. TW: Treated water

A similar interfering role of alkalinity due to carbonate ions on fluoride removal by activated carbon was also reported [42].

Treated water from Tube and Germama had *E. coli* concentration that was above the WHO drinking water standard. The residual chlorine of these water samples was 0.08 and 0.12 mg/L, respectively, which is below WHO drinking water standards. This could be attributed to the turbidity of the water samples. The turbidity of these water samples was 58 and 59 NTU for Tube and Germama, respectively. Turbidity contains organic compounds [43]. The organic compounds in turbidity are known to react with hypochlorite, increasing the chlorine demand and thereby reducing *E. coli* log reduction. In addition, organic and inorganic particles contained in turbidity protect microorganisms from free chlorine

disinfection, a phenomenon recognized as 'particle association' [39]. The stabilization of cell membranes protects by restricting access to critical components for cellular inactivation and microbial inactivation [44]. These results align with the findings of Léziart et al. [45], where *E. coli* log reduction reduced from 4 log reduction to 1 log due to turbidity. It was discovered that total organic carbon interferes with preserving free chlorine residual. To preserve adequate chlorine disinfection performance, the turbidity of the raw water is suggested to be 1 to 5 NTU or a high dose of coagulant and chlorine is required. The results show that the actual water samples require a high dose of calcium hypochlorite to meet the drinking water standard for a turbid water sample. On the other hand, aluminum, chloride, sulfate, pH, alkalinity, and total dissolved solids were within the

permissible limits. To meet the drinking water standards, batch experiments were conducted to find the dose that could effectively treat actual water samples with high fluoride concentration and high turbidity. The results showed that the water samples were alkaline, and hence the lime dose was reduced and $\text{Ca}(\text{OCl})_2$ concentration increased from 1.5 to 2.0 mg/L to effectively reduce *E. coli* concentration. A dose of 95 mg/L AO, 900 mg/L alum, 15% lime, and 2 mg/L calcium hypochlorite effectively treated the actual water samples with up to 15 mg/L fluoride and 58 NTU turbidity.

Development of a Prototype

The prototypes were developed to be used as follows: (1) Mix contents in 10 L of water, (2) Stir the well for 5 min and let the water stand for 25 min, (3) Use a clean

cloth to filter the treated water and dispose of the filtered floc, (4) The water is ready to use.

The developed prototypes were tested on actual water samples to assess their suitability for drinking purposes. The water quality parameters for treated water were within the WHO drinking water standards, as shown in Tables 5, 6 and 7). Residual chlorine concentrations were 0.29 to 0.46 mg/L, that lies within the recommended concentration. This means that the treated water can be protected against recontamination.

CONCLUSION

The results showed that the dose of 75 mg/L AO, 800 mg/L alum, 35% lime, and 1.5 mg/L calcium hypochlorite effectively achieved 95% fluoride removal and 5 log₁₀ reduction of *E. coli*. A contact time of 30 min

Table 5. Concentrations of raw and treated water by the high dose developed POU prototype

Drinking water quality parameters	Germama		Serty	
	RW	TW	RW	TW
Fluoride (mg/L)	15.1 ± 0.01	1.45 ± 0.12	12.3 ± 0.12	1.03 ± 0.9
pH	8.01 ± 0.16	7.12 ± 0.05	8.1 ± 0.23	7.11 ± 0.05
Electrical conductivity (µs/cm)	1115 ± 0.23	1410 ± 0.70	770 ± 0.26	920 ± 1.20
Total dissolved solids (mg/L)	558 ± 0.76	705 ± 1.40	385 ± 0.23	460 ± 1.20
<i>E. coli</i> (CFU/ 100 mL)	1.08×10 ⁵ ± 12	0	1.6×10 ⁵ ± 21	0
Turbidity (NTU)	59 ± 1.20	<1 ± 0.01	3.3 ± 0.01	<1 ± 0.01
Alkalinity as CaCO ₃ (mg/L)	841 ± 1.23	-	831 ± 0.47	-
Aluminum (mg/L)	0.02 ± 0.01	0.1 ± 0.01	0.01 ± 0.001	0.18 ± 0.02
Sulfate (mg/L)	56 ± 0.92	107 ± 0.15	98 ± 0.72	133 ± 0.93
Chloride (mg/L)	1.43 ± 0.54	4.83 ± 0.0	1.2 ± 0.24	3.4 ± 0.07
Residual chlorine (mg/L)	-	0.40 ± 0.01	-	0.42 ± 0.01

Table 6. Concentrations of raw and water treated by the medium dose developed POU prototype

Drinking water quality parameters	Anano		Tejitu	
	RW	TW	RW	TW
Fluoride (mg/L)	10.5 ± 0.13	1.07 ± 0.50	9.63 ± 0.02	0.79 ± 0.05
pH	8.2 ± 0.12	6.89 ± 0.50	8.1 ± 0.30	7.12 ± 0.01
Electrical conductivity (µs/cm)	1040 ± 0.23	1270 ± 1.20	700 ± 0.19	911 ± 1.50
Total dissolved solids (mg/L)	520 ± 0.34	635 ± 1.31	350 ± 0.45	455.5 ± 1.50
<i>E. coli</i> (CFU/100 mL)	1.3×10 ⁴ ± 1	0	1.98×10 ⁵ ± 10	0
Turbidity (NTU)	<1 ± 0.01	<1 ± 0.01	<1 ± 0.01	<1 ± 0.01
Alkalinity as CaCO ₃ (mg/L)	784 ± 0.021	-	809 ± 0.21	-
Aluminum (mg/L)	0.01 ± 0.001	0.2 ± 0.003	0.01 ± 0.001	0.1 ± 0.005
Sulfate (mg/L)	30 ± 0.21	97 ± 1.3	67 ± 0.45	109 ± 1.2
Chloride (mg/L)	0.82 ± 0.02	3 ± 0.02	0.9 ± 0.21	2.58 ± 0.01
Residual chlorine (mg/L)	-	0.44 ± 0.02	-	0.46 ± 0.01

Table 7. Concentrations of raw and water treated by the low dose developed POU prototype

Drinking water quality parameters	Tube	
	RW	TW
Fluoride (mg/L)	3.67 ± 0.10	0.39 ± 0.01
pH	7.55 ± 0.12	6.56 ± 0.50
Electrical conductivity (µs/cm)	410 ± 0.79	765 ± 1.50
Total dissolved solids (mg/L)	205 ± 1.22	382 ± 1.50
<i>E. coli</i> (CFU/100 mL)	1.9×10 ⁵ ± 13	0
Turbidity (NTU)	58 ± 0.43	2 ± 0.01
Alkalinity as CaCO ₃ (mg/L)	739 ± 0.81	-
Aluminum (mg/L)	0.01 ± 0.001	0.16 ± 0.003
Sulfate (mg/L)	87 ± 0.89	147 ± 1.50
Chloride (mg/L)	1.19 ± 0.01	2.77 ± 0.20
Residual chlorine (mg/L)	-	0.29 ± 0.01

was enough to achieve 90% fluoride removal and 5 log reduction of *E. coli*. Fluoride concentration showed an impact on fluoride removal as high fluoride concentration resulted in reduced fluoride removal efficiency. On the other hand, fluoride concentration did not significantly affect *E. coli* log reduction. The pH of raw water showed an impact on both fluoride removal and *E. coli* log reduction. Maximum fluoride removal was achieved at pH 6 to 7. Maximum *E. coli* log reduction was achieved at pH 6 to 7. Acidic pH values also achieved high log reduction. Initial *E. coli* concentration did not show any effect of fluoride removal, but it impacted *E. coli* log reduction. Water samples from the Ethiopian Rift Valley required a high dose of alum, AO, calcium hypochlorite, and a low dose of lime because of the alkalinity and organic matter associated with turbidity. Three prototypes were developed for treating water samples with a fluoride concentration ≤ 15 mg/L. The POU prototypes were tested on water samples from Rift Valley. The treated water was analyzed for fluoride, pH, EC, TDS, *E. coli*, alkalinity, aluminum, sulfate, turbidity, residual chlorine, and chloride. The obtained values were compared with the WHO drinking water standards. All parameters were within the permissible limits. The developed products effectively treat water with fluoride concentration above 10 mg/L and turbidity above 5 NTU, thus indicating the capability of the developed products to purify contaminated water for human consumption.

■ ACKNOWLEDGMENTS

We would like to sincerely thank the World Bank Group for providing research fund through the Africa Centre of Excellence for Water Management (ACEWM), Addis Ababa University, for awarding the scholarship for Patricia Namate to pursue her MSc studies. We would also like to thank the communities around the sampling areas for their dedicated support during the data collection.

■ AUTHOR CONTRIBUTIONS

All authors have participated in (a) conception and design, or analysis and interpretation of the data; (b) drafting the article or revising it critically for important intellectual content; and (c) approval of the final version.

■ REFERENCES

- [1] Immurana, M., Iddrisu, A.A., Mohammed, Z., and Toby Joseph Mathew, K.K., 2022, Access to basic drinking water and sanitation in Africa: Does financial inclusion matter?, *Cogent Social Sci.*, 8 (1), 2057057.
- [2] Duke, W.F., Nordin, R.N., Baker, D., and Mazumder, A., 2016, The use and performance of BioSand filters in the Artibonite Valley of Haiti: a field study of 107 households, *Rural Remote Health*, 6 (3), 570.
- [3] Admasie, A., Abera, K., and Feleke, F.W., 2022, Household water treatment practice and associated factors in rural households of Sodo Zuria District, Southern Ethiopia: Community-based cross-sectional, *Environ. Health Insights*, 16, 11786302221095036.
- [4] Naik, P.K., 2016, The water crisis in Africa: Myth or reality?, *Int. J. Water Resour. Dev.*, 33 (2), 326–339.
- [5] Kut, K.M.K., Sarswat, A., Srivastava, A., Pittman, C.U., and Mohan, D., 2016, A review of fluoride in African groundwater and local remediation methods, *Groundwater Sustainable Dev.*, 2-3, 190–212.
- [6] Mapoma, T.W.H., Xie, X., Zhang, L., Nyirenda, M.T., Maliro, A., and Chimutu, D., 2016, Hydrochemical characteristics of rural community groundwater supply in Blantyre, southern Malawi, *J. Afr. Earth. Sci.*, 114, 192–202.

- [7] Tekle-Haimanot, R., Melaku, Z., Kloos, H., Reimann, C., Fantaye, W., Zerihun, L., and Bjorvatn, K., 2006, The geographic distribution of fluoride in surface and groundwater in Ethiopia with an emphasis on the Rift Valley, *Sci. Total Environ.*, 367 (1), 182–190.
- [8] Nyangi, M.J., Chebude, Y., and Kilulya, K.F., 2020, Fluoride removal efficiencies of Al-EC and Fe-EC reactors: Process optimization using Box–Behnken design of the surface response methodology, *Appl. Water Sci.*, 10 (9), 214.
- [9] Zewge, F., 2016, Combined aluminum sulfate/hydroxide process for fluoride removal from drinking water, *Bull. Chem. Soc. Ethiop.*, 30 (3), 391–401.
- [10] Malago, J., Makoba, E., and Mazuka, A.N.N., 2017, Fluoride levels in surface and groundwater in Africa: A review, *Am. J. Water Sci. Eng.*, 3 (1), 1–17.
- [11] Dey, S., and Giri, B., 2016, Fluoride fact on human health and health problems: A review, *Med. Clin. Rev.*, 2 (1), 2.
- [12] Demelash, H., Beyene, A., Abebe, Z., and Melese, A., 2019, Fluoride concentration in groundwater and prevalence of dental fluorosis in Ethiopian Rift Valley: Systematic review and meta-analysis, *BMC Public Health*, 19 (1), 1298.
- [13] Ayalew, A.A., 2023, Comparative adsorptive performance of adsorbents developed from kaolin clay and limestone for de-fluoridation of groundwater, *S. Afr. J. Chem. Eng.*, 44, 1–13.
- [14] Dubey, S., Agrawal, M., and Gupta, A.B., 2018, Advances in coagulation technique for the treatment of fluoride-contaminated water: A critical review, *Rev. Chem. Eng.*, 35 (1), 109–137.
- [15] Mulugeta, E., Zewge, F., Johnson, A.C., and Chandravanshi, B.S., 2013, A high-capacity aluminum hydroxide-based adsorbent for water defluoridation, *Desalin. Water Treat.*, 52 (28-30), 5422–5429.
- [16] Bogale, G.G., 2020, Hotspots of unimproved sources of drinking water in Ethiopia: Mapping and spatial analysis of Ethiopia demographic and health survey data 2016, *BMC Public Health*, 20 (1), 878.
- [17] Holtslag, H., and Mekonta, L., 2014, HWTS in Ethiopia: The State of Art and Ideas to Scale Up, *Internal Report*, Millenium Water Alliance, Addis Ababa, Ethiopia.
- [18] Sharma, S., and Bhattacharya, A., 2017, Drinking water contamination and treatment techniques, *Appl. Water Sci.*, 7 (3), 1043–1067.
- [19] Mulugeta, E., Zewge, F., Johnson, C.A., and Chandravanshi, B.S., 2014, Aluminum hydro(oxide)-based (AO) adsorbent for defluoridation of drinking water: Optimisation, performance comparison, and field testing, *Water SA*, 41 (1), 121–128.
- [20] Bridgewater, L., American Public Health Association, American Water Works Association, and Water Environment Federation, 2012, *Standard Methods for the Examination of Water and Wastewater*, 22nd Ed., Eds. Rice, E.W., and Bridgewater, L., American Public Health Association, Washington DC, USA.
- [21] Owoseni, M.C., Olaniran, A.O., and Okoh, A.I., 2017, Chlorine tolerance and inactivation of *Escherichia coli* recovered from wastewater treatment plants in the Eastern Cape, South Africa, *Appl. Sci.*, 7 (8), 810.
- [22] Dargahi, A., Atafar, Z., Mohammadi, M., Azizi, A., Almasi, A., and Ahagh, M.M., 2016, Study of the efficiency of alum coagulant in fluoride removal from drinking water, *Int. J. Pharm. Technol.*, 8 (3), 16772–16778.
- [23] Shimelis, B., Zewge, F., and Chandravanshi, B.S., 2006, Removal of excess fluoride from water by aluminum hydroxide, *Bull. Chem. Soc. Ethiop.*, 20 (1), 17–34.
- [24] Wang, L., Zhang Y., Sun N., Sun W., Hu Y., and Tang H., 2019, Precipitation methods using calcium-containing ores for fluoride removal in wastewater, *Minerals*, 9 (9), 511.
- [25] Mizozoe, M., Otaki, M., and Aikawa, K., 2019, The mechanism of chlorine damage using enhanced green fluorescent protein-expressing *Escherichia coli*, *Water*, 11 (10), 2156.
- [26] Dodd, M.C., 2012, Potential impacts of disinfection processes on elimination and deactivation of antibiotic resistance genes during water and wastewater treatment, *J. Environ. Monit.*, 14 (7), 1754–1771.

- [27] Erkmen, O., 2010, Antimicrobial effects of hypochlorite on *Escherichia coli* in water and selected vegetables, *Foodborne Pathog. Dis.*, 7 (8), 953–958.
- [28] Vargas, T.F., Baía, C.C., Machado, T.L.S., Dórea, C.C., and Bastos, W.R., 2021, Decay of free residual chlorine in wells water of northern Brazil, *Water*, 13 (7), 992.
- [29] CDC, 2012, *Global WASH-Related Diseases and Contaminants*, Center for Diseases Control and Prevention, Atlanta, Georgia, USA.
- [30] WHO, 2019, *Results of Round Two of the WHO International Scheme to Evaluate Household Water Treatment Technologies*, World Health Organization, Geneva, Switzerland.
- [31] Hussein, I.A., and Vegi, M.R., 2020, Defluoridation of drinking water using coalesced and un-coalesced mica, *Appl. Water Sci.*, 10 (2), 64.
- [32] Alemu, S., Mulugeta, E., Zewge, F., and Chandravanshi, B.S., 2014, Water defluoridation by aluminium oxide–manganese oxide composite material, *Environ. Technol.*, 35 (15), 1893–1903.
- [33] Getachew, T., Hussein, A., and Rao, V.M., 2015, Defluoridation of water by activated carbon prepared from banana (*Musa paradisiaca*) peel and coffee (*Coffea arabica*) husk, *Int. J. Environ. Sci. Technol.*, 12 (6), 1857–1866.
- [34] Li, S., Smith, K.D., Davis, J.H., Gordon, P.B., Breaker, R.R., and Strobel, S.A., 2013, Eukaryotic resistance to fluoride toxicity mediated by a widespread family of fluoride export proteins, *Proc. Natl. Acad. Sci.*, 110 (47), 19018–19023.
- [35] Breaker, R.R., 2009, Riboswitches: From ancient gene-control systems to modern drug targets, *Future Microbiol.*, 4 (7), 771–773.
- [36] Emamjomeh, M.M., and Farzadkia, M.F., 2016, *Fluoride Removal by Electrocoagulation (EC) Process: Aluminium Chemistry and Speciation*, Proceedings of 47th The IRES International Conference, St. Petersburg, Russia.
- [37] Hu, C.Y., Lo, S.L. and Kuan, W.H., 2003, Effects of co-existing anions on fluoride removal in electrocoagulation (EC) process using aluminum electrodes, *Water Res.*, 37 (18), 4513–4523.
- [38] Waghmare, S.S., and Arfin, T., 2015, Fluoride removal from water by aluminium based adsorption: A review, *J. Biol. Chem. Chron.*, 2 (1), 1–11.
- [39] Chahal, C., van den Akker, B., Young, F., Franco, C., Blackbeard, J., and Monis, P., 2016, “Chapter Two - Pathogen and Particle Associations in Wastewater: Significance and Implications for Treatment and Disinfection Processes” in *Advances in Applied Microbiology*, Volume 97, Eds., Sariaslani, S., and Michael Gadd, G., Academic Press, Cambridge, USA, 63–119.
- [40] US Environmental Protection Agency, 2009, *Drinking Water Contaminants, National Primary Drinking Water Regulations*, U.S Government Publishing Office, Washington DC., USA.
- [41] Liang, Z., Chan, W.L., Tian, X., Lai, A.C.K., Lee, P.K.H., and Chan, C.K., 2022, Inactivation of *Escherichia coli* in droplets at different ambient relative humidities: Effects of phase transition, solute and cell concentrations, *Atmos. Environ.*, 280, 119066.
- [42] Sano, H., Omine, K., Prabhakaran, M., Darchen, A., and Sivasankar, V., 2018, Groundwater fluoride removal using modified mesoporous dung carbon and the impact of hydrogen-carbonate in borehole samples, *Ecotoxicol. Environ. Saf.*, 165, 232–242.
- [43] Stange, C., Sidhu, J.P.S., Toze, S., and Tiehm, A., 2019, Comparative removal of antibiotic resistance genes during chlorination, ozonation, and UV treatment, *Int. J. Hyg. Environ. Health*, 222 (3), 541–548.
- [44] Li, Y., Song, Y., Huang, Z., Mei, L., Jiang, M., Wang, D., and Wei, Q., 2023, Screening of *Staphylococcus aureus* for disinfection evaluation and transcriptome analysis of high tolerance to chlorine-containing disinfectants, *Microorganisms*, 11 (2), 475.
- [45] Léziart, T., Dutheil de la Rochere, P.M., Cheswick, R., Jarvis, P., and Nocker, A., 2019, Effect of turbidity on water disinfection by chlorination with the emphasis on humic acids and chalk, *Environ. Technol.*, 40 (13), 1734–1743.

Robust Biocomposite Film of Polylactic Acid and Ferroferric Oxide as a Radar Absorbing Material

Raffles Sinaga¹, Wida Banar Kusumaningrum², Yana Taryana³, Widya Fatriasari², Zuratul Ain Abdul Hami⁴, Lisman Suryanegara^{2*}, Holilah Holilah², and Yudi Darma^{1**}

¹Department of Physics, Faculty of Mathematics and Natural Sciences, Institut Teknologi Bandung, Jl. Ganesha No. 10, Bandung 40132, Indonesia

²Research Center for Biomass and Bioproducts, National Research and Innovation Agency, Cibinong 16911, Indonesia

³Research Center for Electronics and Telecommunication, National Research and Innovation Agency, Bandung 40135, Indonesia

⁴School of Materials & Mineral Resources Engineering, Universiti Sains Malaysia, Nibong Tebal Pulau Pinang 14300, Malaysia

* Corresponding author:

email: lisman.suryanegara@brin.go.id; yudi@itb.ac.id**

Received: November 11, 2022

Accepted: March 6, 2023

DOI: 10.22146/ijc.79089

Abstract: The polymer/ferroferric oxide (Fe_3O_4) foam and aerogel composites generally exhibit superior radar absorptivity performance. However, these composites have poor mechanical and thermal properties. This study manufactured a polylactic acid (PLA)/ Fe_3O_4 bio-composite and evaluated the radar absorptivity, thermal, and mechanical properties of radar-absorbing material. The composites were prepared using a solvent casting method to mix PLA and Fe_3O_4 at varying concentrations, followed by evaporation, oven drying, and hot pressing into a film. Thermogravimetric analysis showed that the decomposition temperature of the PLA/ Fe_3O_4 -5% composite occurred at around 306 °C, which shifted to a lower decomposition temperature of PLA. The addition of 25 wt.% Fe_3O_4 improved the tensile modulus of neat PLA from 2.92 to 3.55 GPa. The vector network analyzer demonstrated that the addition of Fe_3O_4 at 25% improved the reflection loss of PLA from -5.17 to -25.83 dB at a thickness of 3 mm, with energy absorbed by 99.74% at frequency position 10.58 GHz. These results demonstrated that PLA/ Fe_3O_4 composites have great potential in radar-absorbing practical applications.

Keywords: radar absorptivity; thermal properties; mechanical properties; reflection loss; PLA/ Fe_3O_4 biocomposites

■ INTRODUCTION

Nowadays, radar absorbing materials (RAM) have been massively developed in military equipment stealth applications to minimize reflected electromagnetic waves to the radar system [1-2]. Therefore, RAM, with its high absorptivity, ultra-thin, superior tensile strength, and good thermal stability, has attracted considerable research interest [3-4]. The basic principle of microwave absorption is to convert microwave energy into heat energy through various absorption mechanisms. Microwave absorbers were generally manufactured from carbon-based materials, conductive polymer-based materials, ceramics, and magnetic materials [5]. Various composites, including solid films, foams, and aerogels, were designed

to enhance the absorptivity performance of radar waves. Foam or aerogel is one of the lightest materials because it is filled with air in the pores or internal cavities, generally prepared through freeze drying [6].

Feroferic oxide (Fe_3O_4) is a magnetic material with excellent permeability and complex permittivity, the parameters that govern the significance of microwave absorption. Other advantages of Fe_3O_4 are high saturation magnetization value, high curie temperature, facile synthesis, and low cost [7-8]. Recently, researches have been directed toward increasing the microwave absorption of pure Fe_3O_4 particles, mainly based on particle sizes, including micro-spheres [9], nano-spheres [10], and nanocrystals

[11]. The Fe₃O₄ micro-sphere synthesized by a simple chemical at 90 °C showed a reflection loss value of -45.2 dB at 4.67 GHz; meanwhile, Fe₃O₄ nano-spheres and nanocrystals each showed a reflection loss (RL) of -21.2 dB at 5.6 and 8.16 GHz. However, Fe₃O₄ as an absorbent material has some limitations, including a rapid decrease in the value of the permeability at microwave frequencies, large density, ease of oxidation, and impedance mismatch, which hinders the effective performance of microwave absorbers [12].

The radar absorptivity performance of foam and aerogel composites manufactured from Fe₃O₄ dispersion in a polymer matrix has been evaluated in several previous studies. The foam and aerogel composites showed higher radar absorption values, low density, and good flexibility. Phadtare et al. [13] reported superior radar absorption performance of a Fe₃O₄/divinylbenzene/ethyl hexyl acrylate foam composite with an RL value of -23 dB at 9.3 GHz frequency position in 15 wt.% Fe₃O₄ filler concentration. In another study, Jiang et al. reported an RL value of -26.45 dB for the melamine/Fe₃O₄ foam composite at the frequency of 7.76 GHz with a filler ratio of 30 wt.% [14]. The large internal cavity will cause multi-reflection and polarization loss; therefore, more radar energy is trapped in the composite. The large internal cavity provides a larger surface area, which facilitates impedance matching and polarization loss through multi-reflections, causing attenuation of the radar wave in the material. These foam and aerogel composites have limitations in a broader of applications.

Poly(lactic acid) (PLA) is a bio-based polymer with excellent mechanical and thermal properties compared with synthetic polymers such as polyethylene. Notably, PLA is one of the most commonly used biopolymers for various applications because of its ease of processing [15]. PLA has been prepared with various types of inorganic fillers for numerous applications, one of which is to improve thermal and mechanical properties [16]. PLA is a biodegradable plastic that has great potential to replace petroleum-based fuel plastics due to its high stiffness and strength [17].

The objective of this study is to evaluate the radar absorptivity, thermal and mechanical properties of

PLA/Fe₃O₄ composites. The composites were prepared by mixing PLA and 5 to 25 wt.% Fe₃O₄ by solvent casting. The radar absorption performance of PLA/Fe₃O₄ composites was evaluated using a Vector Network Analyzer (VNA). Meanwhile, the thermal and mechanical properties of the composites were determined using thermogravimetric analysis and a universal testing machine, respectively. In addition, the morphological, crystal structure, and magnetic properties of the film composite were also investigated using Scanning Electron Microscope (SEM), X-ray Diffraction (XRD), and vibrating sample magnetometer (VSM).

■ EXPERIMENTAL SECTION

Materials

PLA 4043D was supplied by Natureworks Co., Minnetonka, MN (USA). Dichloromethane (DCM, ≥ 99.0%), ammonia solution 25%, and iron (III) chloride hexahydrate (FeCl₃·6H₂O) were purchased from Merck KGaA, Germany. Ferrous sulfate heptahydrate (FeSO₄·7H₂O, ≥ 99.0%) was supplied by HiMedia Laboratories Pvt.Ltd., India.

Instrumentation

The surface morphology of Fe₃O₄, neat PLA, and PLA/Fe₃O₄ composites was observed under SEM (JEOL JSM-IT200, Japan) operating at 3.0 kV. The sample of Fe₃O₄ was gold-coated to improve conductivity before observation. The crystal structure of the samples was evaluated by XRD (Shimadzu 7000, Japan) with an X-ray tube of Cu operating at 30.0 mA and 40.0 kV. The XRD pattern of samples was recorded in the interval of 10° to 80° at a speed of 2°/min. The degree of crystallinity (X_c) is calculated using the formula [19]:

$$X_c = \frac{\text{area of crystalline peaks}}{\text{area of all peaks (crystalline + amorphous)}} \times 100\%$$

The thermal stability of neat PLA and PLA/Fe₃O₄ composites was evaluated using PerkinElmer TGA 4000, USA. The samples were immersed in a closed aluminum pan. Temperature programs were from 25 to 600 °C at a temperature increase speed of 10 °C/min under a nitrogen condition. The heating scan of the specimens was used to estimate thermal parameters such as

decomposition temperature (T_d), temperature for 50% weight loss (T_{50}), and residual weight (remaining Fe_3O_4 content) at 600 °C. A universal testing machine (Shimadzu AGS-X series 10kN, Japan) was used to investigate the mechanical properties of the samples. The tensile testing samples were fabricated using a mini-jet pro to obtain a dumbbell-shaped tensile bar (ASTM D638-14 type V). The sample gauge length, width, and thickness were approximately 30, 3, and 3 mm, respectively, measured by a caliper when gripped. The crosshead rate was set at 1 mm/min. All data on mechanical properties were recorded in the 5 measurements. The magnetic hysteresis loops were investigated by a vibrating sample magnetometer (VSM250 Deking Magnet Ltd) with an applied magnetic field of 1 tesla under ambient temperature. The sample dimensions prepared were 5 × 5 × 1 mm (length-width-thick). The radar absorption of the samples was analyzed using the waveguide method at a frequency of 8.0 to 12.0 GHz using a vector network analyzer (VNA) Anritsu MS46322A, Japan, at room temperature. The sample, which measured 30 × 30 × 3 mm (length, width, thickness) was placed on the port and coated with a metal reflector. The complex permeability and air transmittance were measured to calibrate the instrument, which found results of $\mu'' = \epsilon'' = 1$ and $\mu' = \epsilon' = 0$. The reflection loss was calculated using line transmitting theory by adhering to the processes outlined in prior publications [20].

Procedure

The preparation of Fe_3O_4 particles was carried out following the procedure of the previous study [18]. A slight modification was made by extending the stirring time of 5.406 g (0.02 mol) $\text{FeCl}_3 \cdot 6\text{H}_2\text{O}$ and 2.701 g (0.01 mol) $\text{FeSO}_4 \cdot 7\text{H}_2\text{O}$ from 30 min to 2 h. PLA (described in Table 1) was dissolved in a beaker using DCM under stirring for 4 h. The Fe_3O_4 particles were added gradually to the PLA solution after the PLA was completely dissolved, and the stirring was kept going for another 4 h. The PLA/ Fe_3O_4 mixture was poured and dispersed on trays, and the dichloromethane solvent was evaporated at ambient temperature for 12 h before oven drying for 8 h at 80 °C. The dried mixture was cut into small

Table 1. The composition of the samples

Sample name	Fe_3O_4 (g)	PLA (g)	DCM (mL)
Neat PLA	0	10	100
PLA/ Fe_3O_4 -5%	0.5	9.5	100
PLA/ Fe_3O_4 -10%	1.0	9.0	100
PLA/ Fe_3O_4 -15%	1.5	8.5	100
PLA/ Fe_3O_4 -20%	2.0	8.0	100
PLA/ Fe_3O_4 -25%	2.5	7.5	100

pieces of around 5 × 5 mm and hot-pressed at a temperature of 155 °C with a pressure of 50 MPa for 10 min to obtain a PLA/ Fe_3O_4 composite film of 3 × 3 cm with various thickness.

RESULTS AND DISCUSSION

Morphological Analysis

The morphology of Fe_3O_4 is shown in Fig. 1(a). The SEM image shows Fe_3O_4 is a microparticle with an irregular shape with an average size of fewer than 5 μm . The previous co-precipitation method produced similar findings [18]. In the Fe_3O_4 particle preparation process, several factors influence particle size and particle distribution: stirring speed, ambient temperature, and solution, the concentration of ammonia solution, and the Fe^{2+} and Fe^{3+} reagents used [21].

The fracture morphology of neat PLA and PLA/ Fe_3O_4 composites observed using SEM is shown in Fig. 1(b-g). It can be seen from the figure that the pure PLA fracture surface is caused by the insoluble PLA portion and the appearance of pores due to DCM evaporation. The addition of more fillers results in the formation of agglomerates. Fe_3O_4 particles were visible in the fine-grained composite, which spread uniformly in the PLA matrix with a diameter smaller than 5 μm even in the Fe_3O_4 concentration of 25 wt.%. At 5 wt.% Fe_3O_4 concentration, there were no obvious cracks or holes on the fracture surface of the composite, which means that good interfacial interactions occur between the PLA matrix and Fe_3O_4 particles. With the addition of Fe_3O_4 concentration in the composite, the holes or cracks are more clearly visible, which means that the interfacial interaction is getting weaker.

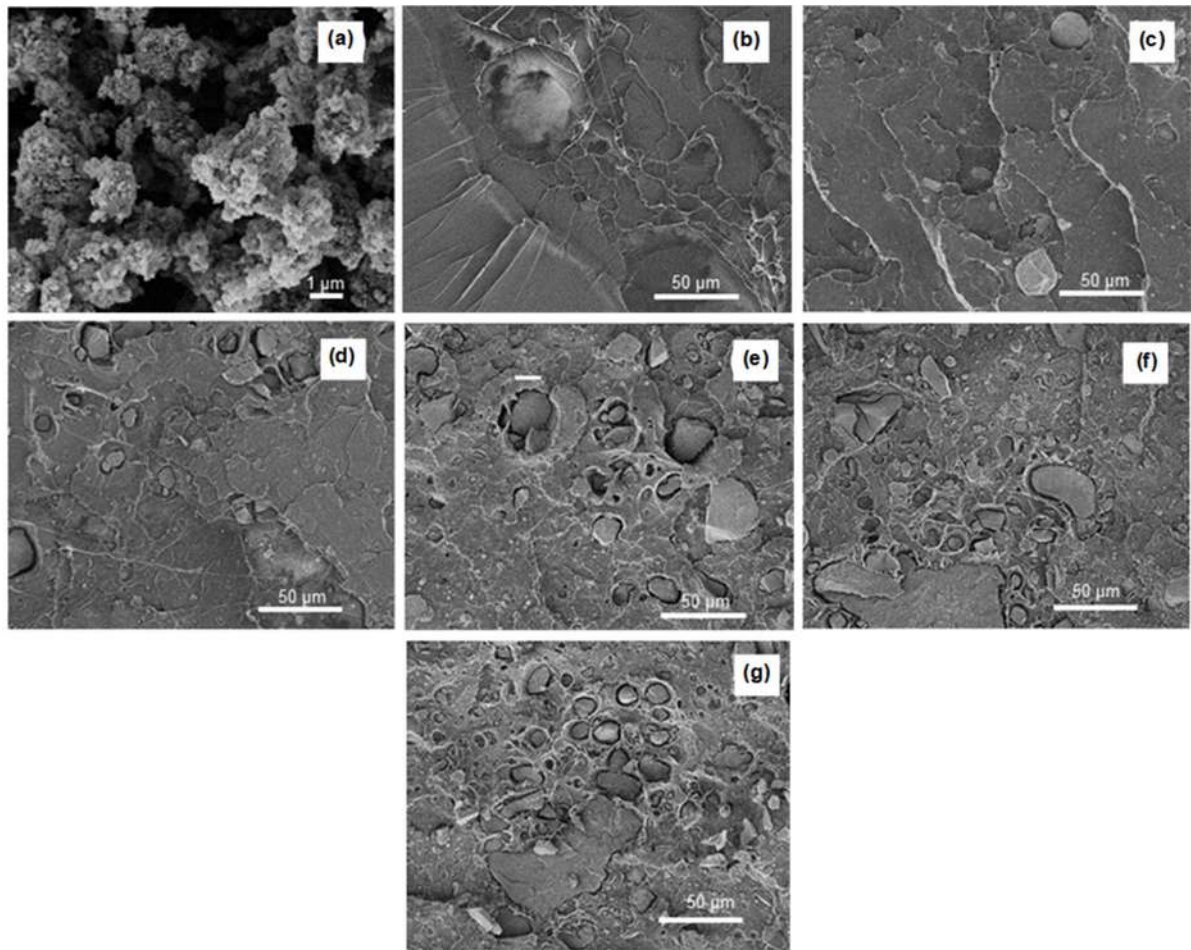


Fig 1. SEM images of morphology: (a) Fe_3O_4 particles; fracture of all composites: (b) Neat PLA, (c) PLA/ Fe_3O_4 -5%, (d) PLA/ Fe_3O_4 -10%, (e) PLA/ Fe_3O_4 -15%, (f) PLA/ Fe_3O_4 -20%, and (g) PLA/ Fe_3O_4 -25%

XRD Analysis

The diffraction peaks in the XRD pattern of Fe_3O_4 , neat PLA, and PLA/ Fe_3O_4 composites are shown in Fig. 2. The six diffraction peaks of Fe_3O_4 crystal at 2θ values are 30.3742, 35.6851, 43.3585, 53.8291, 57.5713, and 62.9956, according to the values of the index Miller of (220), (311), (400), (422), (511) and (440) crystal planes from the inverted cubic spinal structure of Fe_3O_4 (JCPDS 65-3107) [22-23]. These peaks indicated that the prepared Fe_3O_4 formed spinal structures, and no characteristic impurity peaks were detected in the XRD pattern.

Fig. 2 shows neat PLA exhibits large diffraction peaks at 2θ values of 16.52 and 32, which correspond to (200/110) and (203) according to a previous study [24]. When Fe_3O_4 particles were added, all composites displayed

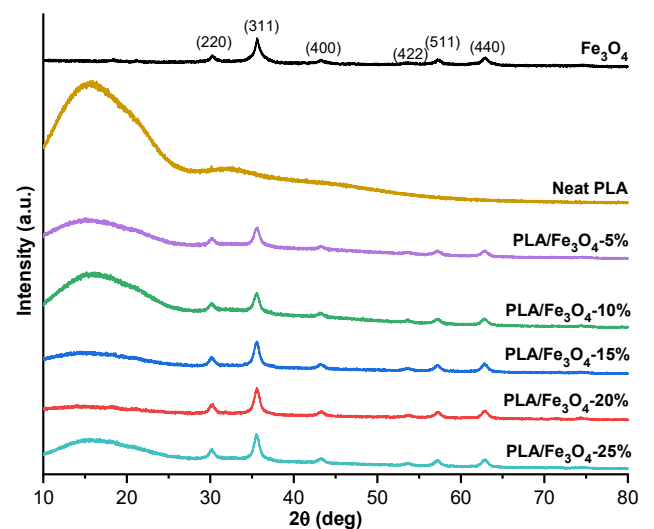


Fig 2. XRD patterns of Fe_3O_4 , neat PLA, and PLA/ Fe_3O_4 composites

broad diffraction peaks similar to the neat PLA peaks. The intensity of the PLA diffraction peaks did not increase with adding more Fe_3O_4 in the composite, although those shrunk and widened. The Fe_3O_4 addition may have prevented the development of numerous crystals and the organization of PLA molecular sequences, but it did not affect the crystal structure of PLA. Based on the calculation, X_c of neat PLA, PLA/ Fe_3O_4 -5%, PLA/ Fe_3O_4 -10%, PLA/ Fe_3O_4 -15%, PLA/ Fe_3O_4 -20%, and PLA/ Fe_3O_4 -25%, respectively, is 28.90, 32.69, 33.27, 34.48, 35.62, and 37.56%.

The Thermal Stability of PLA/ Fe_3O_4 Composites

The TGA test was used to investigate the effect of Fe_3O_4 on the thermal stability of PLA. Fig. 3 shows the weight loss of PLA and PLA/ Fe_3O_4 composites at varying Fe_3O_4 content as a function of temperature. The T_d , T_{50} , and residual Fe_3O_4 content at 600 °C are listed in Table 2. Based on the thermogram, we can see that neat PLA has thermal stability up to a degradation onset temperature of about 320 °C. Then, the decomposition temperature occurs at around 349 °C. After reaching it, the sample weight decreases drastically by a single-stage decomposition until the maximum rated temperature of 380 °C. The weight loss of the PLA continues to decrease slowly until the final test temperature, where the residual weight is 0.178%. The interactions between volatile organic compounds are primarily responsible for keeping the char structure firm. This thermal behavior is typical for polylactic acid polymers [25-26].

The presence of 10 wt.% Fe_3O_4 on the PLA could maintain thermal stability up to a temperature of 280 °C. The decomposition temperature of the PLA/ Fe_3O_4 -10% composite occurred at around 293 °C, which shifted to a lower decomposition temperature of PLA. Interestingly,

the addition of a higher Fe_3O_4 concentration did not significantly change the decomposition temperature of the PLA composite. After the decomposition temperature, the weight of all composites dropped drastically until around 30 to 50% of the sample weight remained at 300 °C. The weight loss of the PLA composites continued decreasing slowly until the final test temperature. The visible changes were in the remaining weight of each composite, where the final weight was determined based on the concentration of Fe_3O_4 . Considering the physicochemical properties and the chemical structure of the Fe_3O_4 , it can be assumed that the observed reduction in thermal stability is related to two simultaneous mechanisms. A similar effect is observed in the case of thermal stability of the other PLA/inorganic-filler composites, where the presence of copper slag contributes to a reduction in the decomposition temperature of PLA [25].

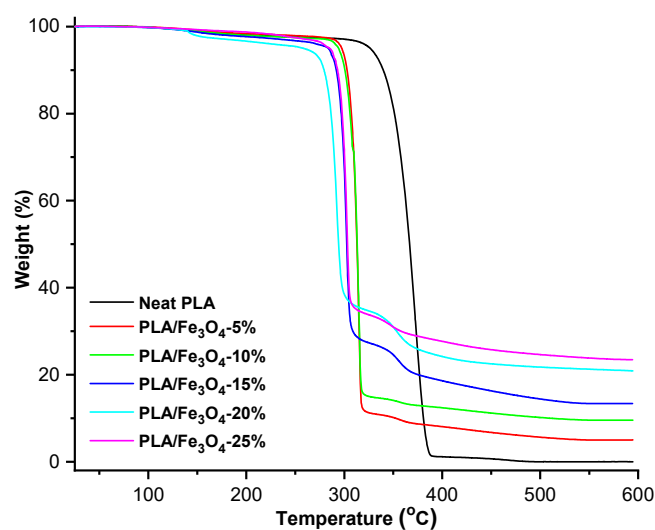


Fig 3. Thermogravimetric curves of neat PLA and PLA/ Fe_3O_4 composites with different Fe_3O_4 contents (wt.%)

Table 2. TGA results of neat PLA and PLA/ Fe_3O_4 composites

Samples	T_d (°C)	$T_{0.50}$ (°C)	Residual weight (%)
Neat PLA	349.16	365.13	0.178
PLA/ Fe_3O_4 -5%	306.14	312.92	5.020
PLA/ Fe_3O_4 -10%	304.23	312.36	9.707
PLA/ Fe_3O_4 -15%	297.14	303.32	13.390
PLA/ Fe_3O_4 -20%	258.23	288.22	20.896
PLA/ Fe_3O_4 -25%	295.85	302.41	23.355

The Mechanical Properties of PLA/Fe₃O₄ Composites

A tensile test was used to evaluate the influence of Fe₃O₄ addition on the mechanical characteristics of PLA. Table 3 and Fig. 4 present the mean and standard deviation of the mechanical properties of all the samples. The table and figure clearly show the tensile modulus of PLA improved with an increase of Fe₃O₄ content while the tensile strength and strain at break decreased. The addition of 5 wt.% Fe₃O₄ improved the modulus from 2.92 to 3.09 GPa. Furthermore, the composite stiffness increased significantly with the addition of a higher Fe₃O₄ concentration. The composite reached the highest stiffness of 3.55 GPa at a 25 wt.% Fe₃O₄ content.

It is clearly shown that added Fe₃O₄ deteriorated the composite strength compared to neat PLA. The decrease in tensile strength of PLA occurred after the addition of 5 wt.% Fe₃O₄ content from 67.57 to 57.94 MPa. Therefore, we could see that the strength remains almost constant between 5 to 25 wt.% Fe₃O₄ content. This decrease in the tensile strength of the composites was caused by poor interface adhesion between Fe₃O₄ particles and PLA. The weakened ion-dipole interaction between the ferrite cation and oxygen atom in the PLA carbonyl group also affects to decrease of tensile strength. The strain at the break value of neat PLA increased almost two times with the addition of 5% by weight of Fe₃O₄ from 3.52 to 5.21%. Then it decreased with the addition of Fe₃O₄ filler and reached 2.08% for 5 wt.% filler content. A decrease in elongation at break with the addition of Fe₃O₄ to polymers is commonly observed in thermoplastic composites. In brief, the mechanical properties of these composites depend on the following factors: the adhesion between the PLA matrix and the Fe₃O₄ filler, the ratio of the Fe₃O₄ filler to the PLA polymer, the size of the Fe₃O₄ filler, the type

and characteristics of the filler, and the degree of crystallinity of the matrix [16]. Decreased interphase stress results in reduced bond strength of the polymer structure. In addition, low adhesion between the matrix and filler results in cavities at the filler matrix interface resulting in a change in the strength value [27]. The tensile modulus value describes the stiffness of a material that allows it to withstand loads without shape deformation. High tensile strength and modulus values are needed for large loads [28].

Magnetic Property Analysis of PLA/Fe₃O₄ Composites

The hysteresis loops of neat PLA and PLA/Fe₃O₄ composite are shown in Fig. 5(a). The magnetic properties such as saturation magnetization (M_s), remanence magnetization (M_r), and coercive field (H_c) are listed in Table 4. A magnet attraction test was performed to determine the magnetic response of neat PLA and PLA/Fe₃O₄ composite. Neat PLA has no response,

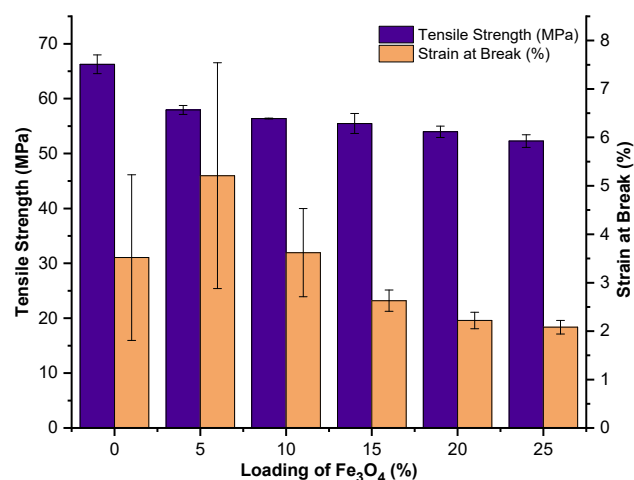


Fig 4. The graphs of tensile strength and strain at break depend on variations in Fe₃O₄ loading

Table 3. Mechanical properties of neat PLA and PLA/Fe₃O₄ composites

Samples	Tensile modulus (GPa)	Tensile strength (MPa)	Strain at break (%)
Neat PLA	2.92 ± 0.13	66.27 ± 1.70	3.52 ± 1.71
PLA/Fe ₃ O ₄ -5%	3.09 ± 0.05	57.94 ± 0.81	5.21 ± 2.33
PLA/Fe ₃ O ₄ -10%	3.16 ± 0.06	56.37 ± 0.08	3.62 ± 0.91
PLA/Fe ₃ O ₄ -15%	3.41 ± 0.06	55.48 ± 1.82	2.63 ± 0.22
PLA/Fe ₃ O ₄ -20%	3.53 ± 0.14	53.97 ± 1.04	2.22 ± 0.17
PLA/Fe ₃ O ₄ -25%	3.55 ± 0.07	52.28 ± 1.16	2.08 ± 0.14

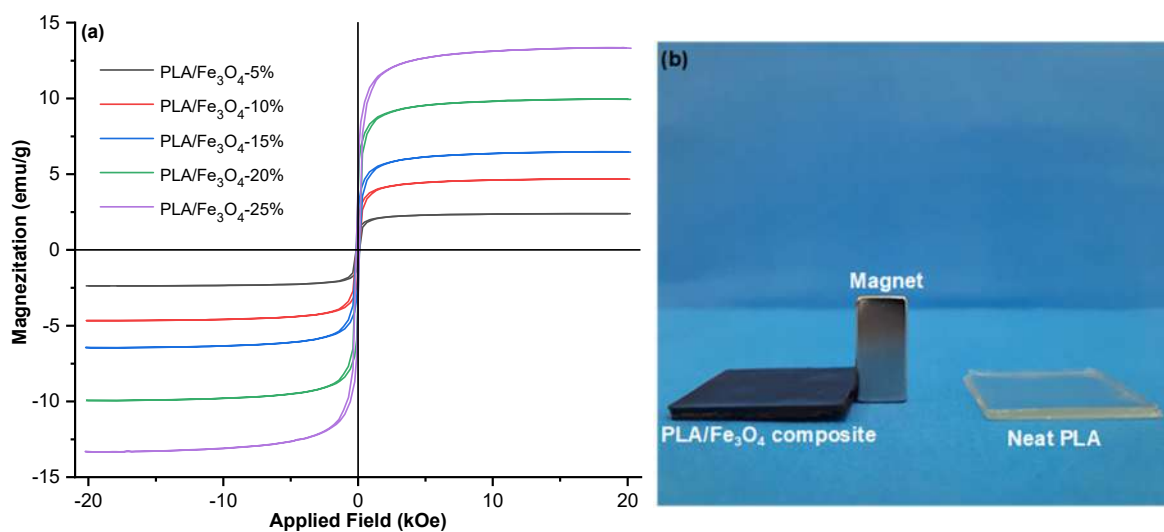


Fig 5. (a) Magnetic properties of PLA/Fe₃O₄ composites with a Fe₃O₄ content, (b) Comparison of magnet attraction by neat PLA and PLA/Fe₃O₄ composite

Table 4. Magnetic parameter of PLA/Fe₃O₄ composites

Samples	M _s (emu/g)	M _r (emu/g)	H _c (kOe)
Neat PLA	-	-	-
PLA/Fe ₃ O ₄ -5%	2.39	0.16	20.199
PLA/Fe ₃ O ₄ -10%	4.68	0.31	20.161
PLA/Fe ₃ O ₄ -15%	6.46	0.41	20.215
PLA/Fe ₃ O ₄ -20%	9.94	0.63	20.223
PLA/Fe ₃ O ₄ -25%	13.31	0.84	20.250

while PLA/Fe₃O₄ composite provides a magnetic response, as shown in Fig. 5(b).

The addition of 5 wt.% Fe₃O₄ into PLA resulted in magnetic properties of the PLA composite with a M_s of 2.39 emu/g and a M_r value of 0.16 emu/g (Table 4). The M_s and M_r values of the composite increased proportionally with the increase in Fe₃O₄ concentration. At 25 wt.% Fe₃O₄ content, the maximum M_s and M_r obtained were 13.31 and 0.84 emu/g, respectively. All composites' coercivity did not change significantly and remained almost constant with increasing Fe₃O₄ content. It shows that the coercive behavior is not controlled by the content of Fe₃O₄ particles but instead by the type of magnetic particles. The trend of increasing M_s and M_r due to the addition of magnetic filler is following previous studies [29].

Radar Absorption Performance of PLA/Fe₃O₄ Composite

The radar absorption performance of the samples is

described by the RL value. Fig. 6 shows the RL curve of neat PLA and PLA/Fe₃O₄ composites, while the reflectivity, energy absorbed, and the position of the maximum absorption frequency is presented in Table 5. Although neat PLA resulted in an RL value of 5.17 dB, PLA is not categorized as a radar-absorbing material. The radar absorption value that appears from the neat PLA is perhaps due to the component of carbon atoms in PLA, trapped air, and sample thickness. However, when PLA was combined with Fe₃O₄ at the same thickness, the radar absorption behavior increased significantly as the Fe₃O₄ concentration increased. The addition of 5 wt.% Fe₃O₄ improved the RL of PLA from -5.17 to -15.75 dB, with energy absorbed of 97.32% at frequency position 10.78 GHz. Furthermore, the RL of composites increased proportionally with the increase of Fe₃O₄ concentration. The composite at 25 wt.% Fe₃O₄ reached the highest RL of -25.83 dB, with energy absorbed 99.74% at 10.58 GHz and thickness of 3 mm.

As a magnetic loss absorber, the saturation magnetization of material will affect the radar absorption performance. The radar absorption intensity will grow as the saturation magnetization value increases. The addition of Fe₃O₄ magnetic material to PLA enhances the saturation magnetization of the composite, increasing the absorption performance of radar signals, as demonstrated in Tables 5 and 6. A comparison of the

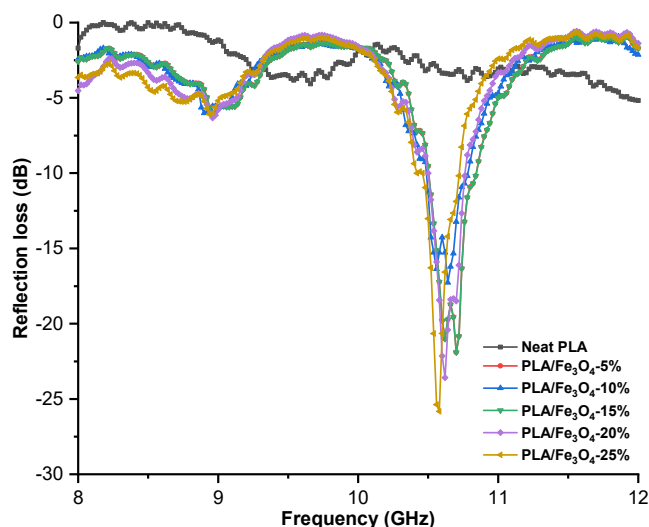


Fig 6. Radar absorption properties (thickness = 3 mm) of neat PLA and PLA/Fe₃O₄ composites. In set shows the zoom-out of the reflection loss graph at 10 to 11 GHz

reflectivity of composites of Fe₃O₄ in various polymer matrices is presented in Table 6. The RL value of the Fe₃O₄ in the PLA matrix is superior to other Fe₃O₄ composites. With a load of only 25 wt.% Fe₃O₄, PLA composite can absorb radar 72% higher than Poly(3,2-ethylenedioxythiophene) (PEDOT) composite at 80 wt.%

Fe₃O₄ content. It can be concluded that the magnetic properties of Fe₃O₄ remained superior in the PLA polymer.

CONCLUSION

The radar absorption, thermal, and mechanical properties of PLA/Fe₃O₄ biocomposite have been successfully evaluated. The vector network analyzer measurements showed that the highest reflection loss of -25.83 dB occurred in PLA composites with a Fe₃O₄ concentration of 25 wt.%, about 399% higher than neat PLA. The TGA measurement revealed that Fe₃O₄ in various concentrations was able to maintain the thermal stability of neat PLA up to 280 °C. However, the decomposition temperature of all composites shifted to a lower temperature of neat PLA. The addition of 25 wt.% of Fe₃O₄ in PLA increased the tensile modulus of neat PLA from 2.92 to 3.55 GPa, while the tensile strength and the strain at the break did not change significantly. Based on these results, PLA/Fe₃O₄ biocomposites offer great promise in a wide range of radar absorption applications due to their good RL and thermo-mechanical properties.

Table 5. The reflectivity, energy absorbed, and the position of the maximum absorption frequency of neat PLA and PLA/Fe₃O₄ composites

Samples	Reflectivity (dB)	Energy absorbed (%)	Frequency position (GHz)
Neat PLA	-5.17	69.59	12.00
PLA/Fe ₃ O ₄ -5%	-15.72	97.32	10.66
PLA/Fe ₃ O ₄ -10%	-17.27	98.03	10.64
PLA/Fe ₃ O ₄ -15%	-21.90	99.35	10.70
PLA/Fe ₃ O ₄ -20%	-23.58	99.56	10.62
PLA/Fe ₃ O ₄ -25%	-25.83	99.74	10.58

Table 6. The reflectivity of Fe₃O₄ in various polymer matrices reported in several studies

Polymer matrix	Fe ₃ O ₄ loading (wt.%)	Maximum absorption (dB)	Frequency position (GHz)	Thickness (mm)	Ref.
Poly(3,2-ethylenedioxythiophene) (PEDOT)	80	-15	9	2.8	[30]
Polypyrrole	50	-22.4	12.9	2.3	[31]
divinylbenzene (DVB), and ethyl hexyl acrylate (EHA)	15	-23	9.3	3	[13]
Polyaniline	62.5	-24.7	14.8	2.0	[32]
Polyethylene	10	-24.3	9	4	[33]
PLA/Fe ₃ O ₄ -25%	25	-25.83	10.58	3	This work

■ ACKNOWLEDGMENTS

This study was supported by Research Center for Biomass and Bioproducts, National Research and Innovation Agency (BRIN), Indonesia. This work is also partly supported by the Ministry of Education, Culture, Research, and Technology of the Republic of Indonesia year 2021–2022 and the ITB research program in 2022. Rafles Sinaga gratefully acknowledges the financial support from *Lembaga Pengelola Dana Pendidikan* (LPDP), Ministry of Finance, Republic of Indonesia.

■ AUTHOR CONTRIBUTIONS

Rafles Sinaga conducted the conceptualization, data curation, formal analysis, investigation, methodology, and writing–original draft. Wida Banar Kusumaningrum conducted the conceptualization, investigation, project administration and resources. Yana Taryana conducted data curation, formal analysis, investigation, and methodology. Widya Patriasari conducted a review, and formal analysis. Zuratul Ain Abdul Hami conducted a review, methodology, formal analysis. Holilah conducted formal analysis, investigation, methodology, and writing–original draft. Yudi Darma conducted conceptualization, supervision, and writing–original draft. Lisman Suryanegara conducted the conceptualization, data curation, formal analysis, funding acquisition, investigation; methodology, project administration, resources, supervision, and writing–original draft.

■ REFERENCES

- [1] Wang, H., Xiu, X., Wang, Y., Xue, Q., Ju, W., Che, W., Liao, S., Jiang, H., Tang, M., Long, J., and Hu, J., 2020, Paper-based composites as a dual-functional material for ultralight broadband radar absorbing honeycombs, *Composites, Part B*, 202, 108378.
- [2] Jayalakshmi, C.G., Inamdar, A., Anand, A., and Kandasubramanian, B., 2019, Polymer matrix composites as broadband radar absorbing structures for stealth aircrafts, *J. Appl. Polym. Sci.*, 136 (14), 47241.
- [3] Liu, R., Miao, M., Li, Y., Zhang, J., Cao, S., and Feng, X., 2018, Ultrathin biomimetic polymeric $\text{Ti}_3\text{C}_2\text{T}_x$ MXene composite films for electromagnetic interference shielding, *ACS Appl. Mater. Interfaces*, 10 (51), 44787–44795.
- [4] Saini, L., Gupta, V., Patra, M.K., Jani, R.K., Shukla, A., Kumar, N., and Dixit, A., 2021, Impedance engineered microwave absorption properties of Fe-Ni/C core-shell enabled rubber composites for X-band stealth applications, *J. Alloys Compd.*, 869, 159360.
- [5] Adebayo, L.L., Soleimani, H., Yahya, N., Abbas, Z., Wahaab, F.A., Ayinla, R.T., and Ali, H., 2020, Recent advances in the development of Fe_3O_4 -based microwave absorbing materials, *Ceram. Int.*, 46 (2), 1249–1268.
- [6] Sambyal, P., Iqbal, A., Hong, J., Kim, H., Kim, M.K., Hong, S.M., Han, M., Gogotsi, Y., and Koo, C.M., 2019, Ultralight and mechanically robust $\text{Ti}_3\text{C}_2\text{T}_x$ hybrid aerogel reinforced by carbon nanotubes for electromagnetic interference shielding, *ACS Appl. Mater. Interfaces*, 11 (41), 38046–38054.
- [7] Wu, N., Liu, C., Xu, D., Liu, J., Liu, W., Shao, Q., and Guo, Z., 2018, Enhanced electromagnetic wave absorption of three-dimensional porous $\text{Fe}_3\text{O}_4/\text{C}$ composite flowers, *ACS Sustainable Chem. Eng.*, 6 (9), 12471–12480.
- [8] Zhang, K., Zhang, Q., Gao, X., Chen, X., Wang, Y., Li, W., and Wu, J., 2018, Effect of absorbers' composition on the microwave absorbing performance of hollow Fe_3O_4 nanoparticles decorated CNTs/graphene/C composites, *J. Alloys Compd.*, 748, 706–716.
- [9] Ni, S., Sun, X., Wang, X., Zhou, G., Yang, F., Wang, J., and He, D., 2010, Low temperature synthesis of Fe_3O_4 micro-spheres and its microwave absorption properties, *Mater. Chem. Phys.*, 124 (1), 353–358.
- [10] Wang, G., Chang, Y., Wang, L., Liu, L., and Liu, C., 2013, Facile preparation and microwave absorption properties of Fe_3O_4 nanoparticles, *Mater. Res. Bull.*, 48 (3), 1007–1012.
- [11] Ni, S., Lin, S., Pan, Q., Yang, F., Huang, K., and He, D., 2009, Hydrothermal synthesis and microwave absorption properties of Fe_3O_4 nanocrystals, *J. Phys. D. Appl. Phys.*, 42, 055004.
- [12] Li, Y., Li, X., Li, Q., Zhao, Y., and Wang, J., 2022,

- Low-energy-consumption fabrication of porous TPU/graphene composites for high-performance microwave absorption and the influence of Fe₃O₄ incorporation, *J. Alloys Compd.*, 909, 164627.
- [13] Phadtare, V.D., Parale, V.G., Lee, K.Y., Kim, T., Puri, V.R., and Park, H.H., 2019, Flexible and lightweight Fe₃O₄/polymer foam composites for microwave-absorption applications, *J. Alloys Compd.*, 805, 120–129.
- [14] Jiang, S., Qian, K., Yu, K., Zhou, H., Weng, Y., and Zhang, Z., 2021, Study on ultralight and flexible Fe₃O₄/melamine derived carbon foam composites for high-efficiency microwave absorption, *Chem. Phys. Lett.*, 779, 138873.
- [15] Murariu, M., and Dubois, P., 2016, PLA composites: From production to properties, *Adv. Drug Delivery Rev.*, 107, 17–46.
- [16] Zhao, X., Liu, J., Li, J., Liang, X., Zhou, W., and Peng, S., 2022, Strategies and techniques for improving heat resistance and mechanical performances of poly(lactic acid) (PLA) biodegradable materials, *Int. J. Biol. Macromol.*, 218, 115–134.
- [17] Suryanegara, L., Fatriasari, W., Zulfiana, D., Anita, S.H., Masruchin, N., Gutari, S., and Kemala, T., 2021, Novel antimicrobial bioplastic based on PLA-chitosan by addition of TiO₂ and ZnO, *J. Environ. Health Sci. Eng.*, 19 (1), 415–425.
- [18] Valenzuela, R., Fuentes, M.C., Parra, C., Baeza, J., Duran, N., Sharma, S.K., Knobel, M., and Freer, J., 2009, Influence of stirring velocity on the synthesis of magnetite nanoparticles (Fe₃O₄) by the coprecipitation method, *J. Alloys Compd.*, 488 (1), 227–231.
- [19] Qu, M., Wang, H., Chen, Q., Wu, L., Tang, P., Fan, M., Guo, Y., Fan, H., and Bin, Y., 2022, A thermally-electrically double-responsive polycaprolactone – thermoplastic polyurethane/multi-walled carbon nanotube fiber assisted with highly effective shape memory and strain sensing performance, *Chem. Eng. J.*, 427, 131648.
- [20] Rezazadeh, N., Kianvash, A., and Palmeh, P., 2018, Microwave absorption properties of double-layer nanocomposites based on polypyrrole/natural rubber, *J. Appl. Polym. Sci.*, 135 (34), 46565.
- [21] Bhattacharya, S., Roychowdhury, A., Das, D., and Nayar, S., 2015, Multi-functional biomimetic graphene induced transformation of Fe₃O₄ to ε-Fe₂O₃ at room temperature, *RSC Adv.*, 5 (109), 89488–89497.
- [22] Yang, Y., Mao, X., Li, R., Zhang, M., Li, T., Wen, L., and Qin, L., 2022, Transformation of organonitrogen-encapsulated MOFs into N-doped Fe₃O₄@C nanopolyhedron via CVD super-assembly for photochemical oxidation, *Adv. Funct. Mater.*, 33 (3), 2210265.
- [23] Koesnarpadi, S., Santosa, S.J., Siswanta, D., and Rusdiarso, B., 2017, Humic acid coated Fe₃O₄ nanoparticle for phenol sorption, *Indones. J. Chem.*, 17 (2), 274–283.
- [24] Yu, B., Wang, M., Sun, H., Zhu, F., Han, J., and Bhat, G., 2017, Preparation and properties of poly (lactic acid)/magnetic Fe₃O₄ composites and nonwovens, *RSC Adv.*, 7 (66), 41929–41935.
- [25] Barczewski, M., Hejna, A., Aniśko, J., Andrzejewski, J., Piasecki, A., Mysiukiewicz, O., Bąk, M., Gapiński, B., and Ortega, Z., 2022, Rotational molding of polylactide (PLA) composites filled with copper slag as a waste filler from metallurgical industry, *Polym. Test.*, 106, 107449.
- [26] Barczewski, M., Mysiukiewicz, O., Matykiewicz, D., Skórczewska, K., Lewandowski, K., Andrzejewski, J., and Piasecki, A., 2020, Development of polylactide composites with improved thermomechanical properties by simultaneous use of basalt powder and a nucleating agent, *Polym. Compos.*, 41 (7), 2947–2957.
- [27] Zhao, G., Liu, H.Y., Cui, X., Du, X., Zhou, H., Mai, Y.W., Jia, Y.Y., and Yan, W., 2022, Tensile properties of 3D-printed CNT-SGF reinforced PLA composites, *Compos. Sci. Technol.*, 230, 109333.
- [28] Fan, W., Yuan, L., D’Souza, N., Xu, B., Dang, W., Xue, L., Li, J., Tonoy, C., and Sun, R., 2018, Enhanced mechanical and radar absorbing properties of carbon/glass fiber hybrid composites

- with unique 3D orthogonal structure, *Polym. Test.*, 69, 71–79.
- [29] Sukthavorn, K., Phengphon, N., Nootsuwan, N., Jantaratana, P., Veranitisagul, C., and Laobuthee, A., 2021, Effect of silane coupling on the properties of polylactic acid/barium ferrite magnetic composite filament for the 3D printing process, *J. Appl. Polym. Sci.*, 138 (38), 50965.
- [30] Yan, L., Wang, X., Zhao, S., Li, Y., Gao, Z., Zhang, B., Cao, M., and Qin, Y., 2017, Highly efficient microwave absorption of magnetic nanospindle-conductive polymer hybrids by molecular layer deposition, *ACS Appl. Mater. Interfaces*, 9 (12), 11116–11125.
- [31] Li, Y., Chen, G., Li, Q., Qiu, G., and Liu, X., 2011, Facile synthesis, magnetic and microwave absorption properties of Fe₃O₄/polypyrrole core/shell nanocomposite, *J. Alloys Compd.*, 509 (10), 4104–4107.
- [32] Zhang, B., Du, Y., Zhang, P., Zhao, H., Kang, L., Han, X., and Xu, P., 2013, Microwave absorption enhancement of Fe₃O₄/polyaniline core/shell hybrid microspheres with controlled shell thickness, *J. Appl. Polym. Sci.*, 130 (3), 1909–1916.
- [33] Ting, T.H., 2020, Synthesis, characterization of Fe₃O₄/polymer composites with stealth capabilities, *Results Phys.*, 16, 102975.

Visible-Light-Induced Photodegradation of Methylene Blue Using Mn,N-codoped ZrTiO₄ as Photocatalyst

Akhmad Syoufian^{1*} and Rian Kurniawan²

¹Department of Chemistry, Faculty of Mathematics and Natural Sciences, Universitas Gadjah Mada, Sekip Utara, Yogyakarta 55281, Indonesia

²Institute of Chemical Technology, Universität Leipzig, Linnéstr. 3, 04103 Leipzig, Germany

* Corresponding author:

email: akhmadsyoufian@ugm.ac.id

Received: November 19, 2022

Accepted: April 3, 2023

DOI: 10.22146/ijc.79261

Abstract: Composites of manganese and nitrogen-codoped zirconium titanate (Mn,N-codoped ZrTiO₄) had been synthesized by the sol-gel method as a visible-light responsive photocatalyst for the photodegradation of methylene blue (MB). Synthesis was conducted at 25 °C using titanium(IV) isopropoxide, zirconium oxide, urea, and manganese(II) chloride. Mn,N-codoped ZrTiO₄ containing fixed 10% nitrogen dopant (w_N/w_{Ti}) with various Mn dopant contents (2, 4, 6, 8, and 10% w_{Mn}/w_{Ti}) and calcination temperatures (500, 700, and 900 °C) had been investigated. All of the Mn,N-codoped ZrTiO₄ exhibit a band gap within the visible range (2.51 to 2.74 eV). Photodegradation of MB was performed under visible light illumination for 120 min. The highest activity was achieved up to 7.7 $\mu\text{g L}^{-1} \text{min}^{-1}$, which was obtained from Mn,N-codoped ZrTiO₄ calcined at 500 °C containing 6% Mn and 10% N dopants.

Keywords: Mn,N-codoped ZrTiO₄; band gap; methylene blue; photodegradation; visible-light

■ INTRODUCTION

Methylene blue (MB) is a synthetic dye and is widely used in the textile, pharmaceutical, paper, printing, paint, and food industries [1]. MB is an azo dye that will form quaternary ammonium cation when dissolved in water and has a high chrome content [2]. The presence of MB in the environment can cause various negative impacts, such as reducing the transmission of sunlight and solubility of oxygens, affecting photosynthetic activity in the aquatic ecosystem, which also reduces the diversity, and decreases the aesthetics of the ecosystem [3]. Due to the high aromatic content and stability properties of MB, biological treatment is not effective in degrading the dye. This ineffectiveness is associated with the presence of azo compounds, which are resistant to aerobic and anaerobic degradations. When azo is reduced, it will produce colorless aromatic amine compounds, which are potentially carcinogenic [4-5]. The development of technology for MB removal with a total contaminant destruction system is necessary. Therefore, the oxidation

of MB to H₂O and CO₂ via photocatalysis is an interesting subject to study.

The photodegradation process can occur in the presence of a photocatalyst, i.e., a semiconductor that can be activated by absorbing photons and accelerating a reaction without being consumed. By absorbing photons with energy equal to or greater than the semiconductor band gap, photocatalysis is carried out on the semiconductor photocatalyst to produce an electron-hole [6]. The photo-induced electrons and holes react with oxygen, water, and hydroxyl group to generate reactive oxygen species, such as hydroxyl radicals ($\bullet\text{OH}$) and superoxide radical anions ($\bullet\text{O}_2^-$) with strong oxidation abilities [7]. The weaknesses of a semiconductor photocatalyst are its limit of application, such as low usage in visible light, wide band gap, and high recombination rate of photo-induced electrons and holes [8]. Therefore, various elements, such as noble metals and transition metals, as well as non-metals and metalloids, are doped into the photocatalyst to enhance the photodegradation performance [9].

Titanium oxide or titania (TiO_2) is widely used as a photocatalyst because of its attractive properties, such as non-toxicity, low cost, strong oxidizing, and biological and chemical inertness [10]. TiO_2 has broad band gaps, 3.0 eV for the rutile phase and 3.2 eV for the anatase phase, which causes limited light absorption, thus making TiO_2 effective as a photocatalyst in spectrum ultraviolet region (4–5% of solar light) and very low activity in visible light (~45% of solar spectrum) [11]. Therefore, previous research has reported visible-light-active TiO_2 by incorporating different dopants, which involve metal (Mn, Fe, and Ni) [12–15] and non-metal (C, N, F, and S) [16–21]. The metal dopant can improve the separation of electrons and holes on the surface of the photocatalyst. Another semiconductor, such as zirconium oxide or zirconia (ZrO_2), has very limited photocatalytic properties, but the addition of another oxide, such as TiO_2 , ZnO and SnO_2 , has a beneficial effect on their photocatalytic activity [22]. The addition of ZrO_2 into TiO_2 in ZrTiO_4 composite can increase the surface area because ZrO_2 inhibits the phase transition of anatase to rutile and crystallite growth in TiO_2 [23].

In this work, manganese and nitrogen codoped ZrTiO_4 composites were prepared by the sol-gel method. The sol-gel method was chosen because it has numerous benefits, such as a simple synthesis process at ambient temperature under atmospheric pressure, does not require a complicated setup, low cost, and is eco-friendly [24]. TiO_2 was grown on the surface of ZrO_2 to form a material with higher thermal stability. Both metal and nonmetal dopants, i.e., Mn and N, were incorporated into the ZrTiO_4 to enhance the photodegradation ability of the material in visible light. Mn was selected as a dopant due to its photocatalytic-activity improvement to TiO_2 in visible-light region and its similar six-fold ionic radius to Ti ion ($\text{Mn}^{4+} = 0.53 \text{ \AA}$; $\text{Ti}^{4+} = 0.60 \text{ \AA}$) [12]. Meanwhile, nitrogen was also selected as a dopant because it reduces the recombination rate of photogenerated charges in TiO_2 and shifts the light absorption ability of TiO_2 to the visible-light region, thus improving the photocatalytic activity as well [17]. Codoping, both Mn and N into ZrTiO_4 , should further elevate the photocatalytic activity of the composite. Various Mn dopant contents and

calcination temperatures were applied to understand the influence of Mn,N codoping and crystal structure on the photocatalytic activity of the ZrTiO_4 composite.

■ EXPERIMENTAL SECTION

Materials

Titanium(IV) tetraisopropoxide (TTIP) (97%, Sigma Aldrich) and ZrO_2 powder (Jiaozou Huasu) were chosen as TiO_2 precursor and supporting material, respectively. Manganese(II) chloride ($\text{MnCl}_2 \cdot 4\text{H}_2\text{O}$) (Merck) and urea ($\text{CH}_4\text{N}_2\text{O}$) (PA, Merck) were chosen as the dopant sources. Methylene blue (MB) (Thermo Fisher Scientific India Pvt. Ltd.) was used as a test dye for a photodegradation experiment to determine the activity of composites. Absolute ethanol (PA, Merck) and demineralized water (Jaya Sentosa) were used as solvents.

Instrumentation

Fourier transform infrared spectrophotometer (FTIR) Thermo Nicolet iS10 was used to identify the vibrational spectra of functional groups in the materials. The crystalline structure of the materials was analyzed using an X-ray powder diffractometer (XRD) Analytical X'Pert PRO MRD with Cu $K\alpha$ radiation ($\lambda = 1.54 \text{ \AA}$, 40 kV, 30 mA). The morphology of the materials was observed by using a scanning electron microscope equipped with an energy-dispersive X-ray spectrometer (SEM-EDX) JSM-6510LA. The band gap of materials was determined from the absorption spectra using specular reflectance UV-Vis spectrometer (SR-UV) Shimadzu UV-1700 Pharmaspec. The concentration of MB was measured using a spectrophotometer UV-Vis Thermo Scientific Genesys 50.

Procedure

Synthesis and characterization of Mn,N-codoped ZrTiO_4

Mn,N-codoped ZrTiO_4 was synthesized by the sol-gel method at room temperature. TTIP as Ti precursor (2.5 mL) was dissolved in 25 mL of absolute ethanol and stirred for 10 min. Various amounts of $\text{MnCl}_2 \cdot 4\text{H}_2\text{O}$ (2, 4, 6, 8, and 10% ($w_{\text{Mn}}/w_{\text{Ti}}$)), 1 g of ZrO_2 , and 86.6 mg of urea (10% ($w_{\text{N}}/w_{\text{Ti}}$)) were mixed in 25 mL of

demineralized water. The aqueous suspension was added to the TTIP solution dropwise under mild stirring. Then, the mixture was stirred for 30 min and then separated by centrifugation at 2000 rpm for 1 h. The solid was aged in the air for 48 h before being heated at 80 °C for 24 h. Composites with various Mn contents were calcined at 500 °C for 4 h under atmospheric conditions. Additionally, a composite with 6% of Mn content was calcined at 700 and 900 °C to observe the effect of calcination temperature. The composites are labeled as xMn-N-ZT-y, where x is the percentage of Mn content and y is the calcination temperature (°C). All composites were characterized using XRD, FTIR, SRUV, and SEM-EDX.

Photodegradation of methylene blue

About 15 mg of Mn,N-codoped ZrTiO₄ were added into 30 mL of 4 mg L⁻¹ aqueous MB solution. The mixture was stirred under visible light irradiation for 120 min. Photodegradation of MB in visible light irradiation has been investigated using a LIFE MAX 30W/765 PHILIPS TLD Lamp. After the photodegradation process, the photocatalyst was separated by centrifugation. For comparison, the same procedure was also done for TiO₂ and ZrO₂. The concentration of MB after photodegradation was determined by a UV-Visible spectrophotometer at the optimum wavelength of the MB solution (664 nm). Quantitative analysis of the photodegradation was calculated using the pseudo-first kinetic order model (Eq. (1) and (2)):

$$-\frac{dC}{dt} = k_{\text{obs}}C \quad (1)$$

$$\ln C = -k_{\text{obs}}t + \ln C_0 \quad (2)$$

where k_{obs} is the observed rate constant for the photodegradation, C is the concentration of MB after degradation, C_0 is the initial concentration of MB, and t is the irradiation time [25]. The percentage of MB degradation was calculated following this calculation (Eq. (3)):

$$\% \text{MB degradation} = \frac{C_i - C_f}{C_i} \times 100\% \quad (3)$$

where C_i and C_f are the initial and the final concentration of MB (mg L⁻¹), respectively [26].

RESULTS AND DISCUSSION

The morphology of the composites was characterized by SEM-EDX. SEM images of ZrO₂, TiO₂, and 6Mn-N-ZT-500 composite are shown in Fig. 1. The surface of 6Mn-N-ZT-500 appears to be rougher and coarser than pure TiO₂ and ZrO₂, which indicates the deposition of TiO₂ on the ZrO₂ surface. Agglomeration is also formed in 6Mn-N-ZT-500 due to dopant incorporation. For higher dopant concentrations, agglomeration of dopant ions takes place at isolated locations, and thus surface starts charging [27]. There is no formation of any nanostructure-like nanorods or nanowires. It was also reported that the incorporation of dopants with different concentrations plays an important role in surface morphology [28].

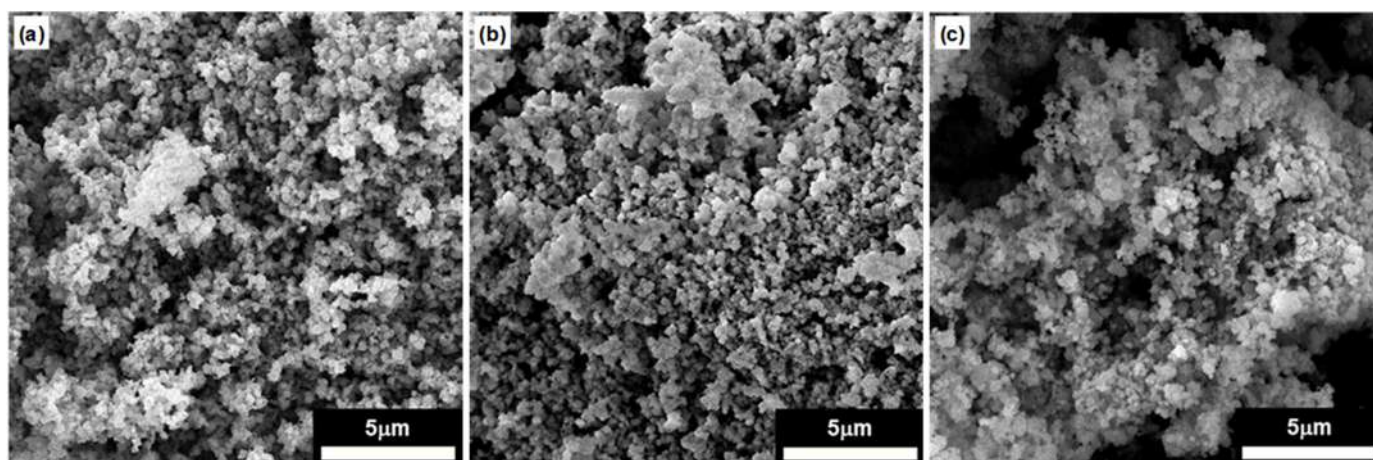


Fig 1. SEM images of (a) TiO₂ 500 °C, (b) ZrO₂ 500 °C and (c) 6Mn-N-ZT-500

The elemental mass percentage on the localized surface of the taken SEM images is summarized in Table 1. Manganese (Mn) was detected on the surface of the 6Mn-N-ZT-500, confirming the successful Mn doping. On the other hand, nitrogen (N) was not detected. It is possible that the amount of N was too low, so the amount of energy given off by X-rays after hitting the surface will be insufficient to adequately measure its proportion. Also, some elements are not easily detected (i.e., nitrogen, boron, and beryllium), and others (i.e., hydrogen, helium, and lithium) are not detectable at all, leading at times to materials misidentification due to low atomic number [29-30].

The diffraction pattern of Mn,N-codoped $ZrTiO_4$ with various Mn contents is shown in Fig. 2. Diffraction patterns of all Mn-N-ZT-500 display anatase and tetragonal structure but no rutile structure. Reflexes

observed at $2\theta = 25^\circ$ (101) and 48° (200) correspond to the anatase TiO_2 pattern according to ICDD: 00-001-0562, while reflexes observed at $2\theta = 30^\circ$ (101) and 51° (112) correspond to tetragonal ZrO_2 pattern according to ICDD: 01-079-1763. The absence of rutile is possibly caused by the presence of ZrO_2 , which can prevent the transformation of anatase to rutile in the TiO_2 structure. No shift of pattern is observed as the Mn content increases.

Reflexes of anatase (101) and tetragonal (101) were chosen as a comparison for average crystallite size (D). The crystallite size was calculated using Scherrer's equation [31]. Table 2 summarizes the calculated crystallite size of various Mn-N-ZT-500. No significant change is observed in both the crystallite size of anatase and tetragonal as the amount of Mn dopant increases. Mn doping causes no alteration to the crystal structure of

Table 1. Elemental surface composition of TiO_2 500 °C, ZrO_2 500 °C, and 6Mn-N-ZT-500

Material	% Mass					Total
	Zr	Ti	O	Mn	N	
TiO_2 500 °C	-	50.60	49.40	-	-	100
ZrO_2 500 °C	71.46	-	28.54	-	-	100
6Mn-N-ZT-500	31.35	29.58	38.35	0.72	-	100

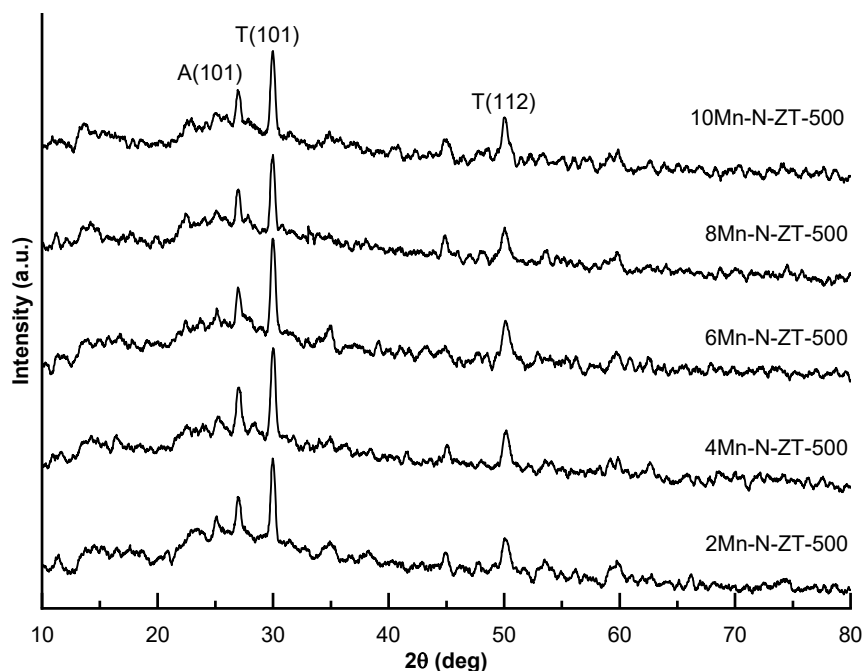


Fig 2. Diffraction patterns of Mn,N-codoped $ZrTiO_4$ with various Mn contents whereas A and T represent anatase and tetragonal crystal phases

Table 2. Crystal phase of various dopant Mn in composites

Material	Crystal phase	D (nm)
2Mn-N-ZT-500	Anatase	24
	Tetragonal	26
4Mn-N-ZT-500	Anatase	22
	Tetragonal	24
6Mn-N-ZT-500	Anatase	27
	Tetragonal	23
8Mn-N-ZT-500	Anatase	24
	Tetragonal	25
10Mn-N-ZT-500	Anatase	25
	Tetragonal	24

Mn,N-codoped $ZrTiO_4$. The amount of Mn-doped into Mn-N-ZT was too low, therefore, no changes can be detected properly by the X-ray powder diffraction.

Diffraction patterns of 6Mn-N-ZT calcined at 700 and 900 °C are displayed in Fig. 3. Both 6Mn-N-ZT-700 and 6Mn-N-ZT-900 exhibit rutile patterns in TiO_2 structure. A reflex at $2\theta = 27^\circ$ (110) corresponds to rutile TiO_2 according to ICDD: 03-065-1118. The intensity of the anatase reflex is lower than rutile in 6Mn-N-ZT-700, while the anatase reflex almost disappeared in 6Mn-N-ZT-900. The increasing calcination temperature beyond 500 °C causes the transformation of the crystalline phase from anatase to rutile [32].

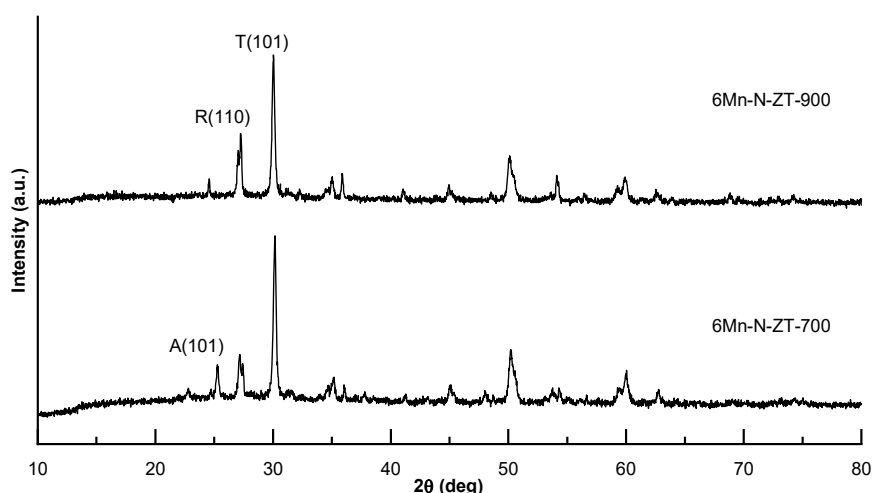
Crystallite sizes of anatase TiO_2 , rutile TiO_2 and tetragonal ZrO_2 in both 6Mn-N-ZT-700 and 6Mn-N-ZT-900 composites were calculated to observe any changes at

different calcination temperatures. The (110) reflex of rutile was chosen to calculate the crystallite size. Table 3 summarizes the crystallite size of 6Mn-N-ZT-700 and 6Mn-N-ZT-900. The increasing crystallite size of rutile as the increasing calcination temperature indicates that higher calcination temperature beyond 700 °C promotes anatase-to-rutile phase transformation, in which it is higher than pristine TiO_2 (around 500 °C). The presence of ZrO_2 in the composite inhibits the crystallization of TiO_2 .

Fig. 4 shows FTIR spectra of Mn-N-ZT-500 composite with various Mn contents; additionally, 6Mn-N-ZT calcined at 700 and 900 °C. FTIR spectra of all composites show hydroxyl ($-OH$) stretching vibration around $3300-3700\text{ cm}^{-1}$ and bending vibration around 1650 cm^{-1} [12]. The vibration at 1430 cm^{-1} indicates the presence of the O–N band that confirms the N atom in the TiO_2 network [33]. The vibration at the O–N bond plays an important role in the photocatalytic activity due

Table 3. Crystallite size of 6Mn-N-ZT calcined at 700 and 900 °C

Material	Crystal phase	D (nm)
6Mn-N-ZT-700	Anatase	59
	Rutile	46
	Tetragonal	35
6Mn-N-ZT-900	Rutile	69
	Tetragonal	38

**Fig 3.** Diffraction patterns of 6Mn-N-ZT calcined at 700 and 900 °C whereas A, R and T represent anatase, rutile, and tetragonal crystal phases, respectively

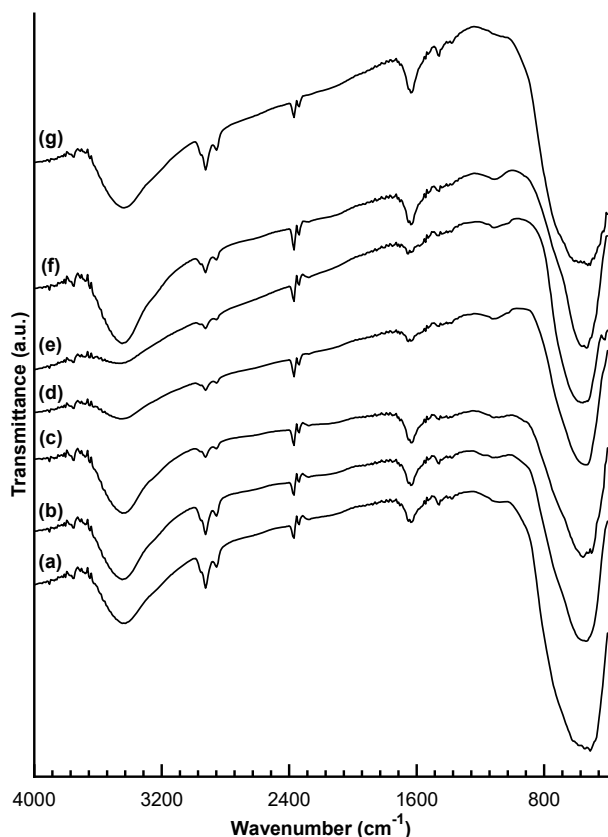


Fig 4. FTIR spectra of (a) 2Mn-, (b) 4Mn-, (c) 6Mn-, (f) 8Mn-, and (g) 10Mn-N-ZT-500, along with 6Mn-N-ZT (d) -700 and (e) -900

to the higher amount of surface-adsorbed water and hydroxyl groups [20]. An absorption spectrum at 1441 cm^{-1} region indicates the presence of Mn dopant in the composites [34]. At the low wavenumber region, the absorption belonged to the vibration of Ti-O-Ti, Mn-O-Ti, and Mn-O are found around $400\text{--}700\text{ cm}^{-1}$ [35]. Sharp peaks observed around 500 cm^{-1} correspond to the stretching vibration of Zr-O of the ZrO_2 phase [36]. Absorption spectra of Mn-O did not show any significant changes with the increasing Mn dopant content. The absorption intensity of the hydroxyl group decreases significantly as the calcination temperature increases beyond $500\text{ }^\circ\text{C}$. This is mainly due to the removal of water molecules from the sample and particle growth [36].

Fig. 5 presents the UV-Vis absorption spectral profiles of Mn-N-ZT composite with various Mn dopant contents and calcination temperatures, alongside TiO_2 $500\text{ }^\circ\text{C}$ and ZrO_2 $500\text{ }^\circ\text{C}$ as references. The calculated band gaps of Mn-N-ZT composites are summarized in Table 4. As shown in Fig. 5, the absorption edge of Mn-N-ZT-500 shifts to a longer wavelength as Mn dopant content increases from 2 up to 6%, but it shifts back to a shorter wavelength beyond 6 up to 10%. The pattern is similar to the band gap trends in Table 4.

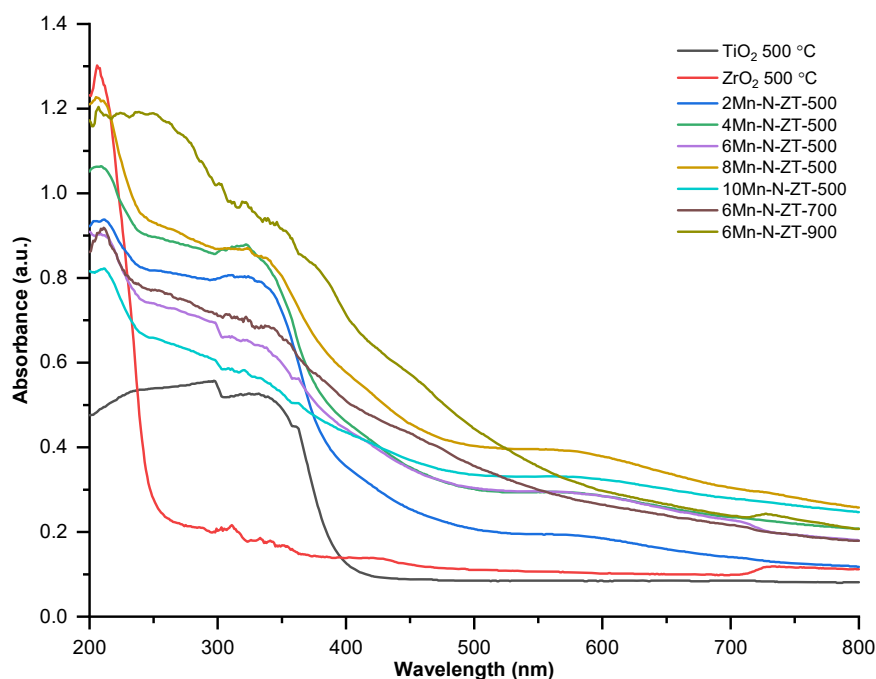


Fig 5. UV-Vis absorption spectra of various Mn-N-ZT with TiO_2 $500\text{ }^\circ\text{C}$ and ZrO_2 $500\text{ }^\circ\text{C}$

Table 4. The calculated band gap of various Mn-N-ZT

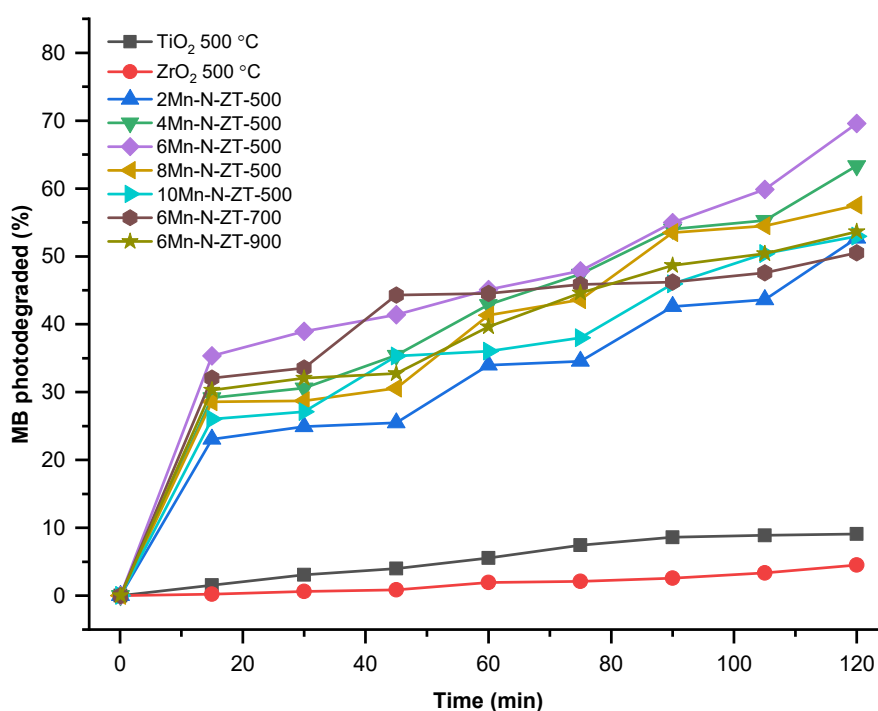
Materials	Band gap (eV)
TiO ₂ 500 °C	3.20
ZrO ₂ 500 °C	4.91
2Mn-N-ZT-500	2.74
4Mn-N-ZT-500	2.67
6Mn-N-ZT-500	2.64
8Mn-N-ZT-500	2.71
10Mn-N-ZT-500	2.73
6Mn-N-ZT-700	2.51
6Mn-N-ZT-900	2.68

The addition of Mn dopants reduces the band gap to 2.64 eV until it reaches the optimum Mn content (6%). An excessive amount of metal dopants on the surface of TiO₂ can cause semiconductor-semiconductor heterojunction between the metal oxide and TiO₂ [37]. The band gap of 6Mn-N-ZT-700 (2.51 eV) is lower than 6Mn-N-ZT-500 (2.64 eV), while the band gap of 6Mn-N-ZT-900 is slightly higher (2.68 eV). High calcination temperature promotes the phase transformation of anatase to rutile in TiO₂. Rutile is the polymorph with the narrowest bandgap but mostly expresses up to an order of magnitude lower photocatalytic activity than anatase [38]. The band gap of 6Mn-N-ZT-900 is higher than 6Mn-N-

ZT-700 due to the sintering of Mn at high calcination temperature, thus canceling the doping effect of Mn. All Mn-N-ZT composites possess a band gap in the range of visible light spectrum (less than 3.10 eV).

Fig. 6 shows the MB photodegradation percentage for various Mn-N-ZT at various times under visible light irradiation. All Mn-N-ZT composites display superior MB photodegradation percentage at 120 min compared to TiO₂ 500 °C (9%) and ZrO₂ 500 °C (5%). The percentage of MB degraded increases as the Mn dopant content increases to 6%, reaching up to 70% of MB 4 mg L⁻¹ solution after 120 min irradiation. MB photodegradation percentage falls down as the amount of Mn dopant rises beyond 6%. The decline of MB photodegradation percentage also occurs in 6Mn-N-ZT-700 compared to 6Mn-N-ZT-500 and -900. Detailed photocatalytic activity of the composites represented as observed rate constant (k_{obs}) is shown in Fig. 7.

Based on k_{obs} data of all Mn-N-ZT-500 in Fig. 7, the photocatalytic activity increases up to 7.7 $\mu\text{g L}^{-1} \text{min}^{-1}$ as the Mn dopant content increases up to 6%, then it declines to 5.4 $\mu\text{g L}^{-1} \text{min}^{-1}$ as the Mn dopant content increases beyond 6%. It appears that the composite may agglomerate at higher dopant concentrations; therefore,

**Fig 6.** Percentage of photodegraded MB over time for various Mn-N-ZT

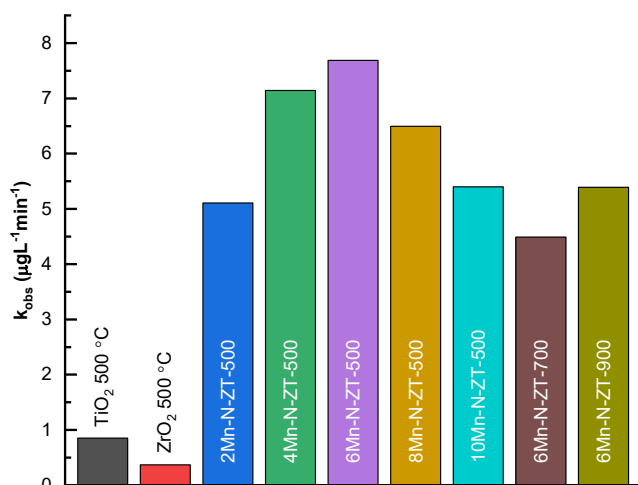


Fig 7. Summary of observed rate constant (k_{obs}) for various Mn-N-ZT

its surface is not fully exposed during photocatalysis [39]. The trend is similar to the band gap of Mn-N-ZT-500 with the increasing Mn contents. It indicates that the band gap constitutes the photodegradation properties of Mn-N-ZT-500. It is well known that the photocatalytic performance of a photocatalyst greatly depends on its electronic band structure because the band gap narrowing simultaneously weakens the redox power, either lowering the level of the conduction band or lifting the level of the valence band or both, which is detrimental to the photocatalytic capability [40]. On the contrary, 6Mn-N-ZT-700, with the lowest band gap, displays the lowest photocatalytic activity among other composites. The low band gap of 6Mn-N-ZT-700 and -900 is due to the presence of a rutile phase in the structure. The rutile phase is also known to demote the photocatalytic activity of TiO₂. The photocatalytic activity of all Mn-N-ZT composites under visible-light irradiation is significantly greater than TiO₂ 500 °C and ZrO₂ 500 °C. This phenomenon indicates that the coupling of ZrO₂-TiO₂ and codoping of Mn and N effectively improve photocatalytic performance.

CONCLUSION

Mn,N-codoped ZrTiO₄ composites with visible light photocatalytic properties have been prepared by the sol-gel method. The presence of Mn on the surface of the

composite was confirmed by EDX analysis. Codoping with nitrogen and manganese shifts the band gap of the ZrTiO₄ composite down to 2.51 eV (6% Mn, 10% N, and calcination at 500 °C). The Mn,N-codoped ZrTiO₄ with 6% Mn and 10% N calcined 500 °C was able to degrade MB 4 mg L⁻¹ solution up to 70% after 120 min irradiation under visible-light illumination, with observed rate constant (k_{obs}) of 7.7 $\mu\text{g L}^{-1} \text{min}^{-1}$. The Mn,N-codoped ZrTiO₄ is a potential photocatalyst for the photodegradation of methylene blue in an aqueous solution.

REFERENCES

- [1] Siddeeg, S.M., Tahooun, M.A., Mnif, W., and Ben Rebah, F., 2019, Iron oxide/chitosan magnetic nanocomposite immobilized manganese peroxidase for decolorization of textile wastewater, *Processes*, 8 (1), 5.
- [2] Zhu, C., Feng, Q., Ma, H., Wu, M., Wang, D., and Wang, Z., 2018, Effect of methylene blue on the properties and microbial community of anaerobic granular sludge, *BioResources*, 13 (3), 6033–6046.
- [3] Khan, I., Saeed, K., Zekker, I., Zhang, B., Hendi, A.H., Ahmad, A., Ahmad, S., Zada, N., Ahmad, H., Shah, L.A., Shah, T., and Khan, I., 2022, Review on methylene blue: Its properties, uses, toxicity and photodegradation, *Water*, 14 (2), 242.
- [4] Chung, K.T., Fulk, G.E., and Andrews, A.W., 1981, Mutagenicity testing of some commonly used dyes, *Appl. Environ. Microbiol.*, 42 (4), 641–648.
- [5] Nasrullah, A., Khan, H., Khan, A.S., Man, Z., Muhammad, N., Khan, M.I., and Abd El-Salam, N.M., 2015, Potential biosorbent derived from *Calligonum polygonoides* for removal of methylene blue dye from aqueous solution, *Sci. World J.*, 2015, 562693.
- [6] Yin, X., Liu, L., and Ai, F., 2021, Enhanced photocatalytic degradation of methylene blue by WO₃ nanoparticles under NIR light irradiation, *Front. Chem.*, 9, 683765.
- [7] Han, M., Zhu, S., Lu, S., Song, Y., Feng, T., Tao, S., Liu, J., and Yang, B., 2018, Recent progress on the

- photocatalysis of carbon dots: Classification, mechanism and applications, *Nano Today*, 19, 201–218.
- [8] Huang, Z., Gao, Z., Gao, S., Wang, Q., Wang, Z., Huang, B., and Dai, Y., 2017, Facile synthesis of S-doped reduced TiO_{2-x} with enhanced visible-light photocatalytic performance, *Chin. J. Catal.*, 38 (5), 821–830.
- [9] Koe, W.S., Lee, J.W., Chong, W.C., Pang, Y.L., and Sim, L.C., 2019, An overview of photocatalytic degradation: photocatalysts, mechanisms, and development of photocatalytic membrane, *Environ. Sci. Pollut. Res.*, 27 (3), 2522–2565.
- [10] Zhang, J., Xiao, X., and Nan, J., 2010, Hydrothermal-hydrolysis synthesis and photocatalytic properties of nano-TiO₂ with an adjustable crystalline structure, *J. Hazard. Mater.*, 176 (1–3), 617–622.
- [11] Reda, S.M., Khairy, M., and Mousa, M.A., 2020, Photocatalytic activity of nitrogen and copper doped TiO₂ nanoparticles prepared by microwave-assisted sol-gel process, *Arabian J. Chem.*, 13 (1), 86–95.
- [12] Sudrajat, H., Babel, S., Ta, A.T., and Nguyen, T.K., 2020, Mn-doped TiO₂ photocatalysts: Role, chemical identity, and local structure of dopant, *J. Phys. Chem. Solids*, 144, 109517.
- [13] Valero-Romero, M.J., Santaclara, J.G., Oar-Arteta, L., van Koppen, L., Osadchii, D.Y., Gascon, J., and Kapteijn, F., 2019, Photocatalytic properties of TiO₂ and Fe-doped TiO₂ prepared by metal organic framework-mediated synthesis, *Chem. Eng. J.*, 360, 75–88.
- [14] Ganesh, I., Gupta, A.K., Kumar, P.P., Sekhar, P.S.C., Radha, K., Padmanabham, G., and Sundararajan, G., 2012, Preparation and characterization of Ni-doped TiO₂ materials for photocurrent and photocatalytic applications, *Sci. World J.*, 2012, 127326.
- [15] Umar, K., Aris, A., Ahmad, H., Parveen, T., Jaafar, J., Majid, Z.A., Reddy, A.V.B., and Talib, J., 2016, Synthesis of visible light active doped TiO₂ for the degradation of organic pollutants—methylene blue and glyphosate, *J. Anal. Sci. Technol.*, 7 (1), 29.
- [16] Negi, C., Kandwal, P., Rawat, J., Sharma, M., Sharma, H., Dalapati, G., and Dwivedi, C., 2021, Carbon-doped titanium dioxide nanoparticles for visible light driven photocatalytic activity, *Appl. Surf. Sci.*, 554, 149553.
- [17] Khan, T.T., Rafiqul Bari, G.A.K.M., Kang, H.J., Lee, T.G., Park, J.W., Hwang, H.J., Hossain, S.M., Mun, J.S., Suzuki, N., Fujishima, A., Kim, J.H., Shon, H.K., and Jun, Y.S., 2021, Synthesis of N-doped TiO₂ for efficient photocatalytic degradation of atmospheric NOx, *Catalysts*, 11 (1), 109.
- [18] Yu, W., Liu, X., Pan, L., Li, J., Liu, J., Zhang, J., Li, P., Chen, C., and Sun, Z., 2014, Enhanced visible light photocatalytic degradation of methylene blue by F-doped TiO₂, *Appl. Surf. Sci.*, 319, 107–112.
- [19] Cravanzola, S., Cesano, F., Gaziano, F., and Scarano, D., 2017, Sulfur-doped TiO₂: Structure and surface properties, *Catalysts*, 7 (7), 214.
- [20] Cheng, X., Yu, X., Xing, Z., and Yang, L., 2016, Synthesis and characterization of N-doped TiO₂ and its enhanced visible-light photocatalytic activity, *Arabian J. Chem.*, 9, S1706–S1711.
- [21] Piątkowska, A., Janus, M., Szymański, K., and Mozia, S., 2021, C-, N- and S-doped TiO₂ photocatalysts: A review, *Catalysts*, 11 (1), 144.
- [22] Długosz, O., Szostak, K., and Banach, M., 2020, Photocatalytic properties of zirconium oxide–zinc oxide nanoparticles synthesised using microwave irradiation, *Appl. Nanosci.*, 10 (3), 941–954.
- [23] Zare, M.H., and Mehrabani-Zeinabad, A., 2022, Photocatalytic activity of ZrO₂/TiO₂/Fe₃O₄ ternary nanocomposite for the degradation of naproxen: characterization and optimization using response surface methodology, *Sci. Rep.*, 12 (1), 10388.
- [24] Chandra, U., 2017, *Recent Applications in Sol-Gel Synthesis*, IntechOpen, Rijeka.
- [25] Syoufian, A., and Nakashima, K., 2008, Degradation of methylene blue in aqueous dispersion of hollow titania photocatalyst: Study of reaction enhancement by various electron scavengers, *J. Colloid Interface Sci.*, 317 (2), 507–512.
- [26] Hidayat, R., Wahyuningsih, S., Fadillah, G., and Ramelan, A.H., 2022, Highly visible light photodegradation of RhB as synthetic organic dye pollutant over TiO₂-modified reduced graphene

- oxide, *J. Inorg. Organomet. Polym. Mater.*, 32 (1), 85–93.
- [27] Muzammil, P., Basha, S.M., and Muhammed, G.S., 2020, Structural and magnetic properties of Fe-doped GaN by sol-gel technique, *J. Supercond. Novel Magn.*, 33 (9), 2767–2771.
- [28] Feng, Z.H., Liu, B., Yuan, F.P., Yin, J.Y., Liang, D., Li, X.B., Feng, Z., Yang, K.W., and Cai, S.J., 2007, Influence of Fe-doping on GaN grown on sapphire substrates by MOCVD, *J. Cryst. Growth*, 309 (1), 8–11.
- [29] Wolfgong, W.J., 2016, “Chemical Analysis Techniques for Failure Analysis: Part 1, Common Instrumental Methods” in *Handbook of Materials Failure Analysis with Case Studies from the Aerospace and Automotive Industries*, Eds. Makhlof A.S.H., and Aliofkhaezraei, M., Butterworth-Heinemann, Boston, 279–307.
- [30] Titus, D., James Jebaseelan Samuel, E., and Roopan, S.M., 2019, “Nanoparticle Characterization Techniques” in *Green Synthesis, Characterization and Applications of Nanoparticles*, Eds., Shukla, Ashutosh K., and Iravani, S., Elsevier, Amsterdam, Netherlands, 303–319.
- [31] Holzwarth, U., and Gibson, N., 2011, The Scherrer equation versus the 'Debye-Scherrer equation', *Nat. Nanotechnol.*, 6 (9), 534–534.
- [32] Chauhan, R., Kumar, A., and Chaudhary, R.P., 2012, Structural and optical characterization of Zn doped TiO₂ nanoparticles prepared by sol-gel method, *J. Sol-Gel Sci. Technol.*, 61 (3), 585–591.
- [33] Natarajan, T.S., Mozhiarasi, V., and Tayade, R.J., 2021, Nitrogen doped titanium dioxide (N-TiO₂): synopsis of synthesis methodologies, doping mechanisms, property evaluation and visible light photocatalytic applications, *Photochem*, 1 (3), 371–410.
- [34] Sakthisharmila, P., Sivakumar, N., and Mathupriya, J., 2021, Synthesis, characterization of Mn, Fe doped ZrO₂ composites and its applications on photocatalytic and solar catalytic studies, *Mater. Today: Proc.*, 47, 2159–2167.
- [35] Muslim, M.I., Kurniawan, R., Pradipta, M.F., Trisunaryanti, W., and Syoufian, A., 2021, The effects of manganese dopant content and calcination temperature on properties of titania-zirconia composite, *Indones. J. Chem.*, 21 (4), 882–890.
- [36] Horti, N.C., Kamatagi, M.D., Nataraj, S.K., Wari, M.N., and Inamdar, S.R., 2020, Structural and optical properties of zirconium oxide (ZrO₂) nanoparticles: effect of calcination temperature, *Nano Express*, 1 (1), 010022.
- [37] Sze, S.M., and Ng, K.K., 2006, *Physics of Semiconductor Devices*, 3rd Ed., Wiley-Interscience, Hoboken, New Jersey, US.
- [38] Žerjav, G., Žižek, K., Zavašnik, J., and Pintar, A., 2022, Brookite vs. rutile vs. anatase: What's behind their various photocatalytic activities?, *J. Environ. Chem. Eng.*, 10 (3), 107722.
- [39] Zakria, H.S., Othman, M.H.D., Kamaludin, R., Sheikh Abdul Kadir, S.H., Kurniawan, T.A., and Jilani, A., 2021, Immobilization techniques of a photocatalyst into and onto a polymer membrane for photocatalytic activity, *RSC Adv*, 11 (12), 6985–7014.
- [40] Chu, S., Wang, Y., Wang, C., Yang, J., and Zou, Z., 2013, Bandgap modulation of polyimide photocatalyst for optimum H₂ production activity under visible light irradiation, *Int. J. Hydrogen Energy*, 38 (25), 10768–10772.

Phytochemical Analysis and Cytotoxic Activities of Hantap Leaves (*Sterculia coccinea* Jack) Extract

Yuliet Yuliet^{1*}, Agustinus Widodo¹, Khildah Khaerati¹, and Joni Tandj²

¹Department of Pharmacy, Faculty of Mathematics and Natural Sciences, Tadulako University, Jl. Sukarno-Hatta Km 9, Palu 94148, Indonesia

²Department of Pharmacy, College of Pharmacy and Natural Sciences Pelita Mas, Jl. Wolter Monginsidi No. 106 A, Palu 94111, Indonesia

* **Corresponding author:**

email: yuliet_susanto@yahoo.com

Received: November 23, 2022

Accepted: April 20, 2023

DOI: 10.22146/ijc.79362

Abstract: Hantap (*Sterculia coccinea* Jack) has been used traditionally for various health issues, including cancer treatment. The therapeutic effects of natural ingredients are often attributed to their chemical constituents. This study aimed to analyze the phytochemical contents and cytotoxic activities of *S. coccinea* leaves on HeLa and MCF-7 cancer cell lines. The quantitative phytochemical analysis was carried out following standard laboratory procedures. Phytochemical compounds were identified using LC-MS/MS QTOF. The MTT assay PrestoBlue™ Cell Viability Reagent test method was used to test cytotoxic activity in the cell culture. Extraction was carried out by the maceration method using 96% ethanol as solvent. The quantitative analysis revealed that tannins were the major phytochemical constituent in the highest percentage of 72.16%, followed by alkaloids, flavonoids, and steroids, with values of 30.80, 28.66, and 2.85%, respectively. Saponins were present in the lowest percentage of 1.15%. The ethanolic extract exhibited moderate cytotoxicity on HeLa and MCF-7 cells with IC₅₀ values of 591.00 and 578.10 µg/mL, respectively. Identification using LC-MS/MS showed the suspected compounds 5,7-dihydroxy-3-(4'-hydroxybenzyl)chromone as homoisoflavanones and kaempferide-3-O-α-L-rhamnosyl-7-O-α-L-rhamnoside from flavonol triglycosides. These results may contribute to the study on the use of leaves extract of *S. coccinea* for developing a chemoprevention agent.

Keywords: cytotoxicity; hantap leaves; HeLa; MTT assay; MCF-7

■ INTRODUCTION

Cancer is one of the most prominent and still incurable diseases worldwide, including in Indonesia. A report has shown that approximately 10 million people die from cancer each year, with 70% occurring in developing or Low-Middle-Income Countries (LMICs), such as Indonesia [1-2]. The International Agency for Research on Cancer (IARC) predicts that by 2040, there will be around 29.5 million new cases and 16.3 million deaths from cancer in the world [3]. According to Basic Health Research, the prevalence of tumors/cancer in Indonesia increased from 1.4 per 1000 in 2013 to 1.79 per 1000 population in 2018 [4]. Based on GLOBOCAN 2020 data, the highest cancer cases in the country are breast and

cervical cancers [5]. Several efforts have been made to cancer treatment, including surgery, radiation, monoclonal antibodies, and chemotherapy [6]. However, these treatments also have side effects such as cardiotoxicity, renal toxicity, and myelotoxicity [7-9]. Various problems in cancer therapy trigger the development of new drugs from natural compounds due to their advantages in therapeutic management, including relatively minor side effects. The existence of these side effects causes serious problems, leading people to the selection of other alternatives to treat cancer with herbal medicines. Therefore, there is a significant scientific and commercial interest in discovering new natural anticancer agents [10-11].

Medicinal plants or herbs can be used as complementary medicine alternatives. This approach combines conventional or medical services with traditional and only alternative treatment. Herbal medicine has been used as an alternative or complementary medicine for breast, cervical, and cervical cancers around the world [10,12]. In Indonesia, reports have shown that 61.8% of cancer patients with cervical cancer use herbal medicine in addition to conventional treatment [13]. Various studies have been conducted to discover new compounds that can serve as chemopreventive agents. Chemoprevention involves the use of synthetic or natural chemical compounds to prevent carcinogenesis, inhibit the development of cancer cells, reduce pain, and improve healing [14]. Therefore, chemotherapeutic agents are potential to be used as anticancer compounds in chemoprevention. Many natural compounds in plants, such as vincristine, vinblastine, taxol, and camptothecin, exhibit anticancer activity [15].

One of the plants commonly used by the Donggala community as traditional medicine is hantap leaves (*Sterculia coccinea* Jack). Leaves are boiled and drunk to treat various cancers, such as breast, brain, blood (leukemia), uterine, cervical, and prostate cancers [16]. However, there is still limited information on its potential as an anticancer. In a previous study, coumarin compounds (stercularin) isolated from plants of the same genus, *Sterculia diversifolia*, showed a cytotoxic effect with an LD₅₀ of 8.00 µg/mL and anticancer activity against PC-3 cell lines with IC₅₀ 3.92 ± 0.20 µg/mL [17]. Other studies have also demonstrated an anticancer effect on three human cancer cell lines, namely MCF-7, HepG2, and HeLa, of the stercufoetin compound isolated from the leaves of *Sterculia foetida* L [18]. Based on the chemotaxonomic approach, plants from the same genus or family may also have compounds with similar structures and biological activity [19]. Many natural compounds in plants are known to have cytotoxic activity against cancer cells [20-21]. The chemical content in *S. coccinea* leaves is suspected of contributing to the anticancer effect. Therefore, this study aims to investigate the cytotoxic activity of *S. coccinea* leaf extract against breast (MCF-7) and cervical (HeLa) cancer cells and to

determine the secondary metabolite levels contained in these extracts contributing to their cytotoxic effects. The results are expected to become scientific information for the development of *S. coccinea* plants as anticancer-standardized herbal medicinal ingredients.

■ EXPERIMENTAL SECTION

Materials

Chemicals and reagents required for cell culture and molecular biology grade in this study were purchased from Thermo Fisher Scientific. These included PrestoBlue™ Cell Viability Reagent, Roswell Park Memorial Institute Medium (RPMI), Fetal Bovine Serum (FBS), Trypsin-EDTA, and Trypan Blue. The pro-analyst solvents used for phytochemical analysis, including ethanol, methanol, chloroform, acetonitrile, and formic acid were purchased from Sigma Aldrich. Subsequently, HeLa and MCF-7 cells were obtained from the Central Laboratory of Padjadjaran University, Bandung. All other reagents were purchased from Merck.

Instrumentation

The tools used included analytical balance (Shimadzu), plate 96 wells (Thermo MicroWell), water bath, Erlenmeyer (Pyrex), oven (Memmert), beaker (Pyrex), blender (Miyako), rotary evaporator (Heidolph), micropipette (Thermo Fisher Scientific), biosafety cabinet, CO₂ incubator (Thermo Fisher Scientific), microscope (Olympus CX33), and Multimode reader (Thermo Fisher Scientific). LCMS/MS data were acquired using an Acquity UPLC I-Class/Xevo G2-XS, QT, USA) and column ACQUITY UPLC BEH C8 1.7 µm 2.1 × 50 mm.

Procedure

Sample preparation and extract

The used plant parts were leaves collected in Palu, Central Sulawesi, and identified at the Plant Biosystematics Laboratory, Department of Biology, Faculty of Mathematics and Natural Sciences, Tadulako University with No. 340/UN 28.1.28/BIO/2021. The leaf powder of *S. coccinea* plants, weighing 2.8 kg, was extracted using the maceration method using 96%

ethanol solvent with ± 28 L. Extract process was carried out for 1×24 h and occasionally stirred and filtered. The maceration in the form of the liquid extract was collected, and the dregs were maceration for 5×24 h with the same solvent. All the macerate was collected and evaporated with a vacuum vaporizer until a thick extract was obtained and weighed, followed by the calculation of the percent yield.

Phytochemical analysis

A quantitative phytochemical test of the ethanol extract of *S. coccinea* leaves was performed according to standard laboratory methods of the Integrated Research and Testing Laboratory Universitas Gadjah Mada (saponins and steroids) and the Pakuan University Service Laboratory (alkaloids, flavonoids, and tannins). The test procedures were conducted as follows:

Determination of total alkaloids. The 50 mg sample was dissolved with aqua distillate, and 2 mL of the solution was pipetted. This was followed by the addition of 2 mL of phosphate buffer solution pH 4.7 and 2 mL of bromocresol green (BCG), as well as 3 mL of chloroform for the extraction process, three times each. The chloroform layer formed was taken and put into a 10 mL test tube, and 10 mL of chloroform was added. The solution was tested with a spectrophotometer with a wavelength of 430 nm, with Atropine as the standard. Subsequently, concentration series of 50, 100, 150, 200, and 250 ppm were made. The standard solution was made by pipetting 2 mL of a certain concentration and adding 2 mL phosphate buffer pH 4.7, with 2 mL BCG solution, and extracting with 3 mL chloroform three times. The chloroform layer formed was put into a 10 mL test tube, and chloroform to 10 mL was added. The resulting solution was tested using a spectrophotometer with a wavelength of 430 nm [22].

Determination of total flavonoids. A total of 10 mg of the sample was dissolved in 10 mL aqua distillate. Approximately 0.5 mL of test solution was pipetted and mixed with 1.5 mL of 96% ethanol, 0.1 mL of 10% aluminum chloride, and 0.1 mL of sodium acetate in a total volume of 2.8 mL. The mixture was homogenized and incubated for 30 min at room temperature, followed by testing with a spectrophotometer at a wavelength of

430 nm. A total of 10 mg of quercetin was dissolved in methanol in a 10 mL volumetric flask to obtain a concentration of 1,000 ppm. Subsequently, 100, 200, 300, 400, and 500 μ L of the solution was pipetted into a 5 mL scale test tube with methanol to obtain a concentration of 20, 40, 60, 80, and 100 ppm. The standard solution was made by mixing 0.5 mL of the solution with 1.5 mL of 96% ethanol, 0.1 mL of 10% aluminum chloride, 0.1 mL of sodium acetate, and 2.8 mL of distilled water. The mixture was homogenized and incubated for 30 min at room temperature, followed by testing using a spectrophotometer at a wavelength of 430 nm [23].

Determination of total tannins. A total of 10 mg of the sample was dissolved with the aqua distillate in a 10 mL volumetric flask. Approximately 1 mL of test solution was pipetted and added with 0.5 mL Folin Ciocalteu, 1 mL Na_2CO_3 20%, and distilled water up to 10 mL. The mixture was homogenized and incubated for 30 min at room temperature, followed by testing using a spectrophotometer at a wavelength of 430 nm. Subsequently, 50 mg of tannic acid was dissolved with the aqua distillate in a 50 mL volumetric flask to obtain a concentration of 1,000 ppm. A total of 100, 200, 300, 400, and 500 μ L of the solution was pipetted into a 5 mL scale test tube and equilibrated with aqua distillate to obtain the concentrations of 20, 40, 60, 80, and 100 ppm. To prepare the standard solution, 1 mL of the diluted solution was pipetted and mixed with 0.5 mL Folin Ciocalteu, 1 mL of 20% Na_2CO_3 , and 10 mL of aqua distillate 10 mL. The mixture was homogenized and incubated for 30 min at room temperature, followed by testing using a spectrophotometer at a wavelength of 740 nm [24].

Determination of total saponins. Approximately 50 mg of the sample was weighed and 2 mL of 25% H_2SO_4 was added. The mixture was autoclaved for 120 min at 110 $^\circ\text{C}$, followed by extraction with ether. Subsequently, the filtrate was dried, and 1 mL of water was added. The solution was extracted by vortex for 5 min, and 50 μ L of anisaldehyde was added, shaken, and allowed to stand for 10 min. A total of 2 mL of 50% sulfuric acid was added and heated in a water bath at

60 °C for 10 min. The volume was adjusted to 10 mL by adding water with a measuring flask and diluted 5 times. The absorption was read at a wavelength of 435 nm. For the preparation of the standard saponin curve from Quillaja bark, the standard of saponins was weighed at 10 mg and added to 5 mL of water. The solution was extracted by vortex for 5 min, added with 50 µL of anisaldehyde, shaken, and allowed to stand for 10 min before adding 2 mL of 50% sulfuric acid. The solution was heated in a water bath at 60 °C for 10 min, and a water volume of 10 mL was added using a measuring flask. The standard curve was prepared by diluting the solution to 200, 100, 50, 25, 12.5, and 6.25 µL. Finally, the absorption was read at a wavelength of 435 nm [25].

Determination of total steroids. A total of 50 mg of the sample was weighed and placed in a microtube. Subsequently, 1 mL of ethanol was added, and the mixture was vortexed for 30 s and sonicated for 60 min. The sample was macerated for 24 h at room temperature and centrifuged. This was followed by the application of 1 and 2 µL of the supernatant on a silica gel 60 F254 plate, including a beta-sitosterol comparator. The plate was entered into the saturated chamber with the mobile phase toluene: ethyl acetate (80:20) and expanded to limit, removed, and dried. Spraying was carried out using Lieberman Burchard reagent, and the mixture was heated at 110 °C for 2 min. The sample spotting was 1 and 2 µL, with a propagation distance of 8 cm. The R_f beta-sitosterol was found to be 0.55, and a 1,000 g/mL (60% purity) solution was used as the standard [22]. Different concentrations of standard beta-sitosterol (0.12, 0.24, 0.48, 0.72, and 0.96 µg/mL) solution were prepared identically as that of the sample to construct a standard curve. The interpretation of the TLC plate with a densitometer was carried out by scanning the maximum wavelength and measuring the area under the curve (AUC). The steroid content in the sample extract was calculated by linear regression between AUC and the content of the standard beta-sitosterol curve [26].

Identification of phytochemical compounds ethanoic extract by LC-MS/MS

A sample of 1 µL was injected into the column using a gradient elution method with water-formic acid 0.1%

(v/v) as solvent A, acetonitrile-formic acid 0.1% (v/v) as solvent B, and a flowing rate of 0.3 mL/min with a 17 min gradient elution. All parameters, namely column, mobile phase, and MS detection, were optimized to obtain the best separation conditions with a suitable run time. The optimal conditions of analysis were as follows: column temperature 40 °C, sample temperature 20 °C, acquisition start time, 0.00–17.00 min start mass, full scan 100.00–1,200.00 *m/z*, scan time 0.100 s; acquisition mode, ESI (+). The fragmentor capillary was set at 2 kV, cone 30 V, source temperature 120 °C, desolvation temperature 500 °C, cone gas flow 50 L/h, and desolvation gas flow 1000 L/h. The UNIFI software was used to process the LC-MS/MS data files.

Cytotoxic activity assay

Cytotoxic preparation and testing followed the Central Laboratory, Padjajaran University test protocol. The cytotoxic activity of *S. coccinea* leaves extract was evaluated against HeLa and MCF-7 cells using Presto Blue Cell Viability reagent. Cisplatin was used as the standard drug [27] and extracts were dissolved with 2% DMSO in PBS and serially diluted to obtain different concentrations of 7.81, 15.6, 31.25, 62.5, 125, 250, 500, and 1,000 µg/mL. In 96 well plates, 10 µL of suspension cells with a density of 170,000 cells/mL were added and incubated at 37 °C in a 5% (v/v) CO₂ incubator for 24 h. The cells were treated with 100 µL various concentrations of extract as well as positive control and incubated for 48 h. After incubation, the culture medium was removed, and the cells were washed with PBS. The medium was immediately replaced by 10 µL Presto Blue reagent in a 90 µL RPMI medium and was incubated for 1–2 h until a color change was observed. Subsequently, the absorbance was measured at a wavelength of 570 nm. The experiment was performed in triplicate using a 19 µM concentration of cisplatin for the test. The results of the cytotoxic test on HeLa and MCF-7 cancer cells showed that the absorption data was searched for a linear regression relationship between the concentration log and the percent of living cells leading to the equation $y = bx + a$. The IC₅₀ was calculated by substituting the value 50 for Y to obtain the value of x, and the value of IC₅₀ was taken as the antilog of x.

Data analysis

The quantitative phytochemical results were presented in a descriptive method, while the cytotoxicity examination was analyzed and graphed using Graph Pad.

RESULTS AND DISCUSSION

Medicinal plants were found useful in managing several diseases, including cancer [28]. *S. coccinea* leaves were one of the medicinal plants used empirically by a tribe in Donggala, Central Sulawesi, for the treatment of breast and cervical cancers [29]. In this study, ethanolic extract from the maceration process resulted in a yield of 15.7%, which was an important value in extract manufacture. The yield value showed the effectiveness of the extract process, which was influenced by the sample particle size, extract method, extract time, and the type of solvent used [30].

Phytochemical Analysis

A quantitative phytochemical analysis was carried out on the ethanolic extract of *S. coccinea* leaves using the standard methods for alkaloids, flavonoids, saponins, tannins, and steroids. The results of the phytochemical analysis obtained from ethanolic extract were presented in Table 1. Phytochemicals are important for human health and can potentially treat various diseases. According to Effendi [16], the results of the chemical identification of *S. coccinea* leaves powder showed the presence of tannins, steroids, and alkaloids. Several active compounds, such as flavonoids, alkaloids, saponins, tannins, and steroids, were shown to possess anticancer effects [31]. Therefore, a quantitative analysis of the phytochemical of the extract was conducted to determine the levels of secondary metabolites contributing to the anticancer effect.

Table 1. Total alkaloids, flavonoids, saponins, tannins, and steroids on *S. coccinea* leaves extract

No	Type of analysis	Result (%)
1	Alkaloids	30.80
2	Flavonoids	28.66
3	Saponins	1.15
4	Tannins	72.16
5	Steroids	2.85

The ethanol extract was found to contain total alkaloids, which were quantified using the linear regression equation $y = 0.0012x + 0.1982$ ($R^2 = 0.9990$) of the atropine standard curve. Total flavonoids were quantified using linear regression equation $y = 0.0074x + 0.0055$ ($R^2 = 0.9992$) of the standard quercetin curve. Moreover, total tannins and saponins were determined, respectively, by applying the linear regression equation $y = 0.0086x + 0.0132$ ($R^2 = 0.9993$) of the tannic acid standard curve and $y = 9.4416 \times 10^{-4}x - 0.0038$ ($R^2 = 0.9996$) of the Quillaja bark.

The results of the quantitative analysis in Table 1 showed that tannins had the highest levels, followed by alkaloids and flavonoids. Steroids and saponins were present in small amounts. The determination of the levels of secondary metabolites in the leaf extract showed that the most numerous groups of phenolic compounds were tannins and flavonoids, with values of 72.16 and 28.66% w/w. Previous studies showed that phenolics and flavonoids were the most important secondary metabolites in the genus *Sterculia* [32].

Identification of Phytochemical Compounds in Ethanol Extract of Hantap Leaves by LC-MS/MS

Analysis of the secondary metabolite profile of *S. coccinea* leaves extract was performed using LC-MS/MS. The results showed that the extract contained at least five compounds in Table 2, but only two compounds belonging to the flavonoid group. The LC-MS/MS spectrum is shown in Fig. 1. This study supported the results of quantitative phytochemical analysis of the leaves extract that phenolic compounds, including flavonoids, were present in large enough quantities. This was also confirmed by the study by El-Sherei et al. [33] on the genus *Sterculia*, indicating the presence of various flavonoid compounds, mostly as flavones and flavonol glycosides.

Cytotoxic Activity Assay

Previous studies showed that *S. coccinea* leaves ethanolic extract had a very strong antioxidant activity, with an IC_{50} of 6.48 $\mu\text{g/mL}$ and moderate cytotoxic activity (LC_{50} 591.56 $\mu\text{g/mL}$), as demonstrated by the

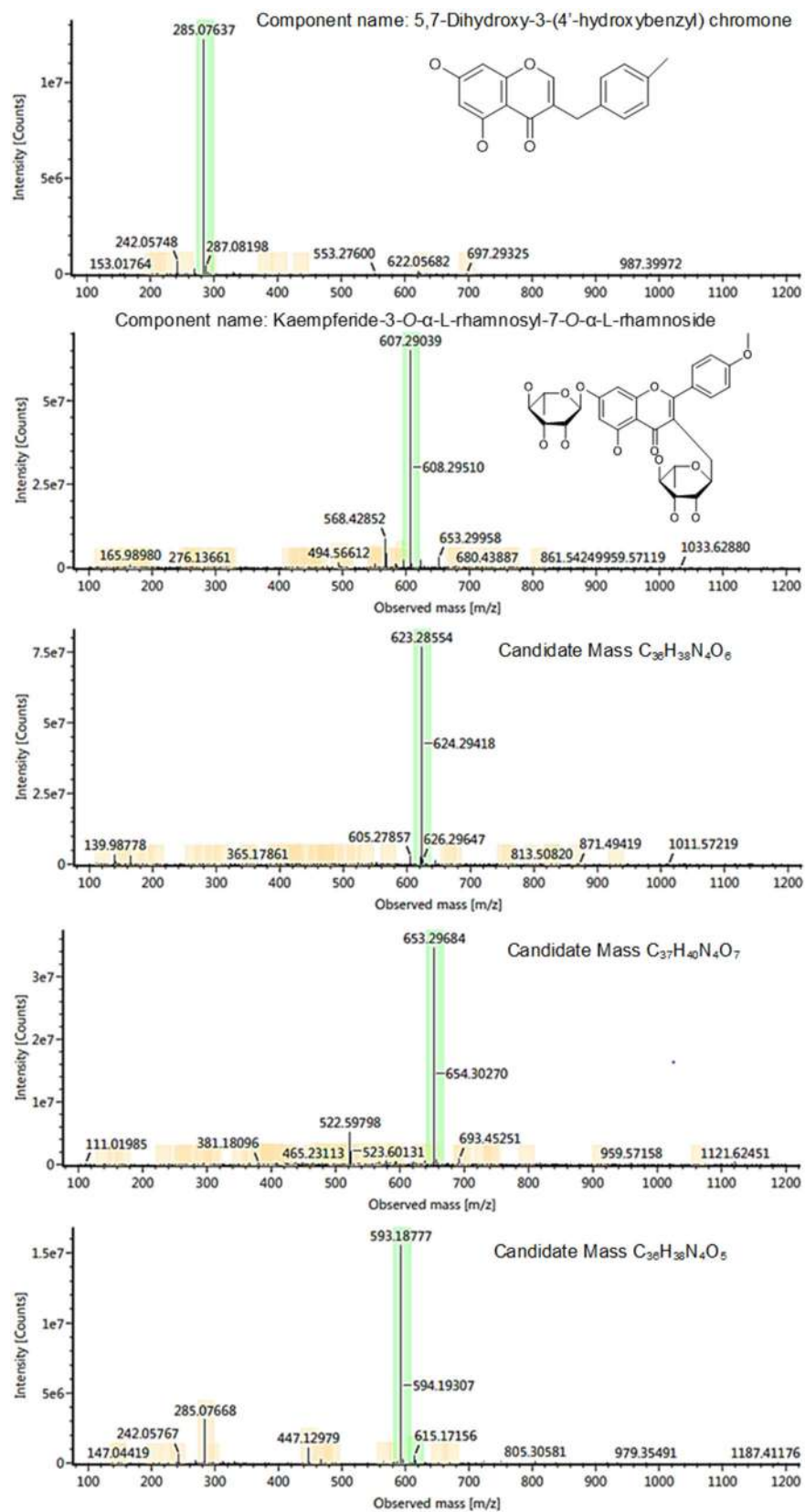
Fig 1. Mass spectrum of *S. coccinea* leaves extract

Table 2. LC-MS/MS profile of *S. coccinea* leaves extract

Component name	Formula	Observed m/z	Observed RT (min)	Mass error (mDA)	Class
5,7-Dihydroxy-3-(4'-hydroxybenzyl)chromone	C ₁₆ H ₁₂ O ₅	285.0764 [M+H]	5.73	0.60	homoisoflavanones
Kaempferide-3-O- α -L-rhamnosyl-7-O- α -L-rhamnoside	C ₂₈ H ₃₂ O ₁₄	593.1878 [M+Na]	4.18	1.30	flavonol triglycosides
Candidate mass C ₃₆ H ₃₈ N ₄ O ₆	C ₃₆ H ₃₈ N ₄ O ₆	623.2855 [M+H]	10.74	-0.90	nd
Candidate mass C ₃₇ H ₄₀ N ₄ O ₇	C ₃₇ H ₄₀ N ₄ O ₇	653.2968 [M+H]	11.20	-0.10	nd
Candidate mass C ₃₆ H ₃₈ N ₄ O ₅	C ₃₆ H ₃₈ N ₄ O ₅	607.2904 [M+H]	11.00	-1.10	nd

Note: nd = not determined

Brine Shrimp Lethality Test (BSLT) method [29]. The cytotoxic potential was further examined using the MTT assay method with ELISA at a wavelength of 570 nm. Cytotoxic potential in cancer cells was calculated based on the percentage of living cells through the absorbance data of the cells. Subsequently, a correlation curve of the log concentration versus the percentage value of live cells was made, and the IC₅₀ value was calculated. The examination was carried out on MCF-7 and HeLa cancer cells, and the magnitude of cytotoxic potential was described by the lower IC₅₀ values. In this study, the IC₅₀ value was used as a cytotoxicity parameter, indicating the cytotoxicity of a compound to cells. The natural material was considered very toxic when the IC₅₀ value was 10–100 $\mu\text{g/mL}$, moderate 100–1,000 $\mu\text{g/mL}$, and non-toxic when the IC₅₀ value was > 1,000 $\mu\text{g/mL}$ [34].

According to the results in Fig. 2, the leaves extract had IC₅₀ < 1,000 $\mu\text{g/mL}$ in MCF-7 and HeLa cancer cells, which was classified as moderate cytotoxicity.

Based on the results, the IC₅₀ criteria for *S. coccinea* leaves extract exhibited moderate cytotoxicity and had chemopreventive potential. This showed that *S. coccinea* leaf extract could not be used as an anticancer but to prevent the growth or further development of cancer cells. The moderate cytotoxic of *S. coccinea* leaves extract was found to inhibit the growth of cancer cells and increase the percentage of cell death at graded concentrations. This indicated the positive effect of *S. coccinea* leaves on inhibiting cancer cell growth.

The results of the identification of LCMS/MS indicated the presence of a class of flavonoids, which mostly contributed to the chemopreventive activity.

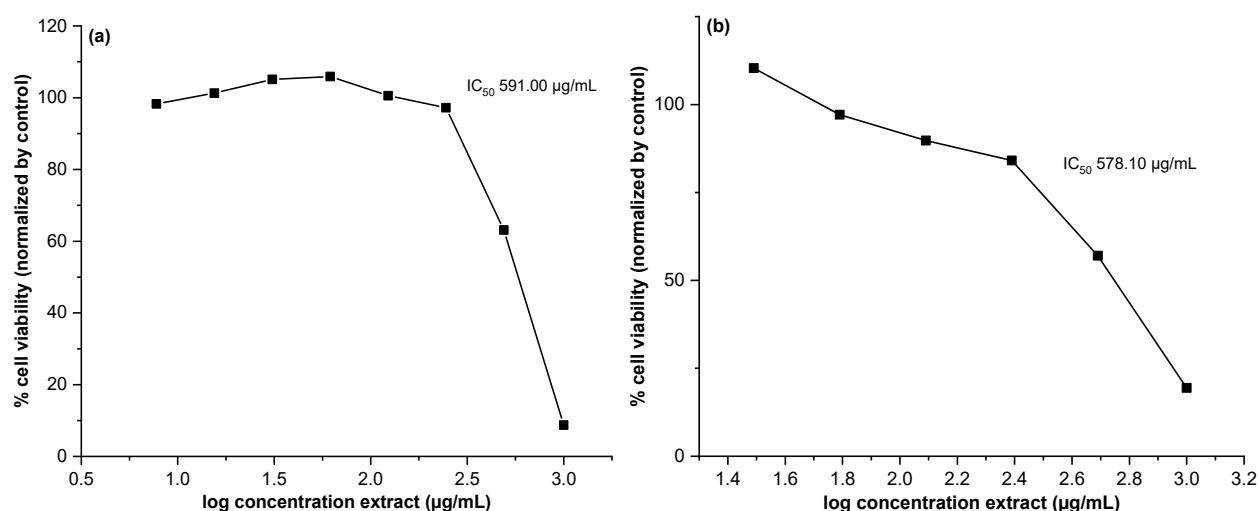


Fig 2. Cytotoxicity against HeLa and MCF-7 cell proliferation (a) HeLa treated with *S. coccinea* leaves extract showing an IC₅₀ value of 591.00 $\mu\text{g/mL}$ (b). MCF-7 treated with *S. coccinea* leaves extract an IC₅₀ value of 578.10 $\mu\text{g/mL}$

Flavonoids, especially 5,7-dihydroxy-3-(4'-hydroxybenzyl) chromone and kaempferide-3-O- α -L-rhamnosyl-7-O- α -L-rhamnoside, have the potential as anticancer by in vivo testing and clinical trials up to phase II with various mechanisms of action, namely carcinogen inactivation, antiproliferative, stop the cell cycle, induce apoptosis, promotion of differentiation, inhibiting angiogenesis, antioxidant, and modulating multidrug resistance [35-37]. The results of the phytochemical analysis test showed the presence of other classes of compounds in the leaf extract, such as tannins, alkaloids, saponins, and steroids which contributed to the chemopreventive effect. Tannin can inhibit cancer promotion, progression, proliferation, and angiogenesis, induction of cell cycle arrest and apoptosis, and inhibition of cancer cell migration, invasion, and colony formation [38]. Alkaloids were also found to possess potential chemopreventive properties due to induction cell cycle arrest, increased cell apoptosis, disruption of redox homeostasis, inhibition of angiogenesis, inhibition of PI-3K/Akt signaling pathways and modulation of ER stress, and autophagy [39-40]. Several studies have reported the role of saponins and steroids in cancer and the mechanism of actions, including apoptosis stimulation, mainly on its intrinsic pathway, cell-cycle arrest, antioxidant activity, and cellular invasion inhibition [41-42].

This study suggests that *S. coccinea* leaves extract has the potential as a natural source of chemopreventive. However, further study is needed to understand the underlying mechanisms of chemoprevention action and identify the compounds that are responsible for such activity. The limitation of this study is that LC-MS/MS analysis did not detect all the components of the chemical content contained in *S. coccinea* leaves extract. This shows the need for further investigation to determine all the components of secondary metabolites and isolate bioactive compounds in the leaf extract. The evaluation of the cytotoxicity of this compound against normal cell lines will also be carried out to obtain the selectivity index.

■ CONCLUSION

This study showed that *S. coccinea* leaves extract contained important phytochemicals, such as tannins

(72.16%), alkaloids (30.80%), flavonoids (28.66%), steroids (2.85%), and saponins (1.15%). The results of identification with LCMS/MS revealed that there were at least 5 compounds with 2 flavonoid compounds. *S. coccinea* leaves extract also exhibited moderate cytotoxicity on HeLa and MCF-7 cancer cells. However, further studies were recommended to investigate the active compound for potential anticancer activity and confirm the mechanism of action.

■ ACKNOWLEDGMENTS

The authors gratefully acknowledge Tadulako University for the funding through Competitive research DIPA Faculty, Postgraduate, PSDKU Tojo Una-Una, and University Ministry of Education, Culture, Research, and Technology Tadulako University with contracts No. 751w/UN28.2/PL/2022. The authors sincerely thank the facilities and technical support from Advanced Characterization Laboratories Serpong, Indonesian Institute of Sciences through E-Layanan Sains, Lembaga Ilmu Pengetahuan Indonesia, and Central Laboratory Padjajaran University.

■ AUTHOR CONTRIBUTIONS

Yuliet: study design, data interpretation, data collection, data analysis, original manuscript writing, revision, manuscript finalization and administration. Khildah Khaerati: data acquisition, data analysis, and data collection. Agustinus Widodo and Joni Tandil: data analysis and interpretation. All the authors have contributed equally.

■ REFERENCES

- [1] Kristina, S.A., Endarti, D., and Aditama, H., 2022, Prediction of productivity costs related to cervical cancer mortality in Indonesia 2018, *Malays. J. Med. Sci.*, 29 (1), 138-144.
- [2] The Global Cancer Observatory, 2020, *Cancer Incident in Indonesia*, Vol. 858, International Agency for Research on Cancer, Lyon, France.
- [3] Islam, S.M.S., Purnat, T.D., Phuong, N.T.A., Mwingira, U., Schacht, K., and Fröschl, G., 2014, *Non Communicable Diseases (NCDs) in developing*

- countries: A symposium report, *Global. Health*, 10 (1), 81.
- [4] Ministry of Health of Republic Indonesia, 2018, *Laporan Nasional Riskesdas 2018*, Ministry of Health of Republic Indonesia, Jakarta.
- [5] Sung, H., Ferlay, J., Siegel, R.L., Laversanne, M., Soerjomataram, I., Jemal, A., and Bray, F., 2021, Global cancer statistics 2020: GLOBOCAN estimates of incidence and mortality worldwide for 36 cancers in 185 countries, *Ca-Cancer J. Clin.*, 71 (3), 209–249.
- [6] American Cancer Society, 2018, *Global Cancer-Facts & Figures*, 4th Ed., American Cancer Society, Atlanta.
- [7] Kurtin, S., 2012, Myeloid toxicity of cancer treatment, *J. Adv. Pract. Oncol.*, 3 (4), 209–224.
- [8] Lameire, N., 2014, Nephrotoxicity of recent anti-cancer agents, *Clin. Kidney J.*, 7 (1), 11–22.
- [9] Chen, Z., and Ai, D., 2016, Cardiotoxicity associated with targeted cancer therapies, *Mol. Clin. Oncol.*, 4 (5), 675–681.
- [10] Greenwell, M., and Rahman, P.K.S.M., 2015, Medicinal plants: Their use in anticancer treatment, *Int. J. Pharm. Sci. Res.*, 6 (10), 4103–4112.
- [11] Meiyanto, E., and Larasati, Y.A., 2019, The chemopreventive activity of Indonesia medicinal plants targeting on hallmarks of cancer, *Adv. Pharm. Bull.*, 9 (2), 219–230.
- [12] George, B.P, Chandran, R., and Abrahamse, H., 2021, Role of phytochemicals in cancer chemoprevention: Insights, *Antioxidants*, 10 (9), 1455.
- [13] Radji, M., Aldrat, H., Harahap, Y., and Irawan, C., 2010, Penggunaan obat herbal pada pasien kanker serviks, *JIFI*, 8 (1), 33–39.
- [14] Cragg, G.M., and Pezzuto, J.M., 2016, Natural products as a vital source for the discovery of cancer chemotherapeutic and chemopreventive agents, *Med. Princ. Pract.*, 25 (Suppl. 2), 41–59.
- [15] Dave, A., Parande, F., Park, E.J., and Pezzuto, J.M., 2020, Phytochemicals and cancer chemoprevention, *J. Cancer Metastasis Treat.*, 6, 46.
- [16] Effendi, N., 2012, Standarisasi simplisia daun hantap (*Sterculia coccinea* Jack) asal kabupaten Donggala propinsi Sulawesi Tengah sebagai bahan baku sediaan fitofarmaka, *J. Sainsmat*, 1 (1), 23–32.
- [17] Rabbi, F., Zada, A., Adhikari, A., Nisar, A., and Khalil, S.K., 2021, Chemical constituent with cytotoxicity from *Sterculia diversifolia*, *J. Asian Nat. Prod. Res.*, 23 (9), 899–905.
- [18] Pham, N.K.T., Nguyen, T.D., Doan, T.D.C., Ha, T.D., Tran, N.M.A., Tran, T.D., and Nguyen, T.P., 2021, Stercufoetin A, new oleanane-type triterpenoid from the leaves of *Sterculia foetida* L., *Nat. Prod. Res.*, 35 (7), 1226–1231.
- [19] Liu, K, Abdullah, A.A., Huang, M., Nishioka, T., Altaf-Ul-Amin, M., and Kanaya, S., 2017, Novel approach to classify plants based on metabolite-content similarity, *BioMed Res. Int.*, 2017, 5296729.
- [20] Pourahmad, J., Salimi, A., and Seydi, E., 2016, "Role of oxygen free radicals in cancer development and treatment" in *Free Radicals and Diseases*, Eds. Ahmad, R., IntechOpen, Rijeka, Croatia.
- [21] Lichota, A., and Gwozdziński, K., 2018, Anticancer activity of natural compounds from plant and marine environment, *Int. J. Mol. Sci.*, 19 (11), 3533.
- [22] Lianah, L., Nur Khasanah, R.A., Pranatami, D.A., and Krisantini, K., 2021, Phytochemical screening and cytotoxic evaluation of *Bauhinia scandens* leaf extracts using HeLa and T47D cell lines, *Biodiversitas*, 22 (2), 913–919.
- [23] Fakhruddin, N., Khairunnisa, S.Y., Azzahra, A., and Ajiningtyas, R.J., 2016, Study of radical scavenger activity, total phenol and flavonoid contents of *Artocarpus altilis* leaves extracts, *Int. J. Pharm. Clin. Res.*, 8 (5), 352–356.
- [24] Anbukkarasi, M., Dhamotharan, R., and Janarthanam, B., Studies on phytochemical screening, tannins content and antibacterial activity from leaf and callus extracts of *Memecylon umbellatum*, *Asian J. Pharm. Clin. Res.*, 10 (5), 265–269.
- [25] Hardianto, M.A., and Widiyanto, S., 2022, *In vitro* anthelmintic activity of *Limonia acidissima*, L. leaves aqueous extract on *Haemonchus contortus* (Rudolphi, 1803), *Proceedings of the 7th International Conference on Biological Science*

- (ICBS 2021), Atlantis Press, 73–77.
- [26] Sutar, N.G., and Patil, P.P., 2020, A HPTLC densitometric method for the determination of β -sitosterol in *Perguleria daemia* leaf and stem extract, *Int. J. Pharm. Sci. Res.*, 11 (4), 1698–1704.
- [27] Aldossary, S.A., 2019, Review on pharmacology of cisplatin: Clinical use, toxicity and mechanism of resistance of cisplatin, *Biomed Pharmacol. J.*, 12 (1), 7–15.
- [28] Alnuqaydan, A.M., Almutary, A.G., Alshehri, O.Y., Henidi, H.A., Alajlan, A.M., Al Tamim, A., Rather, M.Y., and Rah, B., 2022, Evaluation of the cytotoxic activity of *Tamarix articulata* and its anticancer potential in prostate cancer cells, *J. Appl. Pharm. Sci.*, 12 (2), 89–108.
- [29] Cahyani, R., Susanto, Y., and Khumaidi, A., 2017, Aktivitas antioksidan dan sitotoksik ekstrak etanol daun hantap (*Sterculia coccinea* Jack.), *Nat. Sci.: J. Sci. Technol.*, 6 (1), 11–21.
- [30] Mohamad, M., Ali, M.W., Ripin, A., and Ahmad, A., 2013, Effect of extraction process parameters on the yield of bioactive compounds from the roots of *Eurycoma longifolia*, *J. Teknol.*, 60 (1), 51–57.
- [31] Bibi, T., Ahmad, M., Bakhsh Tareen, R., Mohammad Tareen, N., Jabeen, R., Rehman, S.U., Sultana, S., Zafar, M., and Yaseen, G., 2014, Ethnobotany of medicinal plants in district Mastung of Balochistan province-Pakistan, *J. Ethnopharmacol.*, 157, 79–89.
- [32] Prastiwi, R., Dewanti, E., Fadliani, I.N., Aqilla, N., Salsabila, S., and Ladeska, V., 2020, The nephroprotective and antioxidant activity of *Sterculia rubiginosa* Zoll. Ex Miq. leaves, *Pharmacogn. J.*, 12 (4), 843–849.
- [33] El-Sherei, M.M., Ragheb, A.Y., Kassem, M.E.S., Marzouk, M.M., Mosharrafa, S.A., and Saleh, N.A.M., 2016, Phytochemistry, biological activities and economical uses of the genus *Sterculia* and the related genera: A review, *Asian Pac. J. Trop. Dis.*, 6 (6), 492–501.
- [34] Gad, S.C., 2015, "Alternatives to *In vivo* Studies in Toxicology" in General, Applied and Systems Toxicology, Eds. Ballantyne, B., Marrs, T.C., Syversen, T., Casciano, D.A., and Sahu, S.C., Wiley, Chichester, 15–47.
- [35] Nath, L.R., Gorantla, J.N., Joseph, S.M., Antony, J., Thankachan, S., Menon, D.B., Sankar, S., Lankalapalli, R.S., and Anto, R.J., 2015, Kaempferide, the most active among the four flavonoids isolated and characterized from *Chromolaena odorata*, induces apoptosis in cervical cancer cells while being pharmacologically safe, *RSC Adv.*, 5 (122), 100912–100922.
- [36] Abotaleb, M., Samuel, S.M., Varghese, E., Varghese, S., Kubatka, P., Liskova, A., and Büsselberg, D., 2019, Flavonoids in cancer and apoptosis, *Cancers*, 11 (1), 28.
- [37] Gupta, D., and Guliani, E., 2022, Flavonoids: Molecular mechanism behind natural chemoprotective behavior-A mini review, *Biointerface Res. Appl. Chem.*, 12 (5), 5983–5995.
- [38] Baer-Dubowska, W., Szafer, H., Majchrzak-Celińska, A., and Krajka-Kuźniak, V., 2020, Tannic acid: Specific form of tannins in cancer chemoprevention and therapy-old and new applications, *Curr. Pharmacol. Rep.*, 6 (2), 28–37.
- [39] Ballout, F., Habli, Z., Monzer, A., Rahal, O.N., Gali-Muhtasib, H., and Fatfat, M., 2019, "Anticancer Alkaloids: Molecular Mechanisms and Clinical Manifestations" in *Bioactive Natural Products for the Management of Cancer: From Bench to Bedside*, Eds. Sharma, A.K., Springer, Singapore, 1–35.
- [40] Tilaoui, M., Ait, Mouse, H., and Zyad, A., 2021, Update and new insights on future cancer drug candidates from plant-based alkaloids, *Front. Pharmacol.*, 12, 719694.
- [41] Elekofehinti, O.O., Iwaloye, O., Olawale, F., and Ariyo, E.O., 2021, Saponins in cancer treatment: Current progress and future prospects, *Pathophysiology*, 28 (2), 250–272.
- [42] Hou, Y., Shang, C., Meng, T., and Lou, W., 2021, Anticancer potential of cardiac glycosides and steroid-azole hybrids, *Steroids*, 171, 108852.

Pharmacological Properties of *Genista sagittalis* L. (Fabaceae) Grown in Turkey

Pelin Şenel¹, Bleda Can Sadıkoğulları¹, Elif Çepni Yüzbaşıoğlu², Gülnur Mertoğlu Elmas³, Dilek Oral⁴, Ayşegül Gölcü^{1*}, and Ayşe Daut Özdemir^{1**}

¹Department of Chemistry, Faculty of Sciences and Letters, Istanbul Technical University, 34469 Istanbul, Turkey

²Department of Molecular Biology and Genetics, Faculty of Science, Istanbul University, Vezneciler, 34134 Istanbul, Turkey

³Department of Forest Industrial Engineering, Forest Faculty, Istanbul University-Cerrahpasa, 34473 Istanbul, Turkey

⁴Department of Forest Botany, Forest Faculty, Istanbul University-Cerrahpasa, 34473 Istanbul, Turkey

* **Corresponding author:**

email: aysgolcu@itu.edu.tr*

daut@itu.edu.tr**

Received: November 28, 2022

Accepted: April 14, 2023

DOI: 10.22146/ijc.79477

Abstract: The genus *Genista* L. (Family: Fabaceae) is a plant having several traditional uses for treating common ailments such as diabetes, ulcer, and respiratory diseases. In this current study, the composition of essential oil and the biological activities of *Genista sagittalis* L. (Fabaceae) from Kocaeli: Yuvacık Dam Basin have been studied. A total of fourteen components were identified in the essential oil. The identified compounds belonged to straight-chain alkane, aromatic ether, and terpenoid derivatives. The antibacterial activity analyses demonstrated that *G. sagittalis* flower extract only had low activity against *P. mirabilis* and *P. aeruginosa* with MICs 1 to 2 mg/mL, as the peduncle extract showed strong anti-QS activity at 1.3 mg/mL. To the best of our knowledge, the current work is the first to report the antimicrobial and anti-quorum sensing activity of *G. sagittalis* growing in Turkey. Double-stranded DNA binding affinity investigations of the flower and peduncle ethanol extracts indicate that there are interactions with double-stranded DNA and related binding constants (K_b) were found as $1.97 \times 10^3 \pm 0.37$ and $3.68 \times 10^2 \pm 0.44$ for the flower and peduncle extract, respectively.

Keywords: antibacterial; anti-quorum sensing; DNA binding; Fabaceae; *Genista sagittalis*; plant extracts

■ INTRODUCTION

The genus *Genista* L., being a genus of the Fabaceae family, contains about 100 species (such as *G. anglica* L., *G. pilosa* L., *G. sagittalis* L., *G. tenera* (Jacq. ex Murray) Kuntze, *G. tinctoria* L., etc.) and has been used generally as folk medicine in Mediterranean area in the treatment of diabetes, ulcer, respiratory diseases and also in rheumatic disorders [1]. Apart from these kinds of medicinal uses, the genus *Genista* L. is also known for its yellow pigment property [2]. *Genista* species are also characterized by their flavonoid and isoflavonoid content [3], acting as primary antioxidants or free radical scavengers [4-5]. One of its species, *Genista sagittalis* L. (Syn. *Chamaespartium sagittale* (L.) P.E. Gibbs, *Genistella sagittalis* (L.) Gams) is native to West, South of Europe, and Northwestern Turkey [6-9]. It is a naturalized species

in the Czech Republic [10-11], Poland [12], and Lithuania [13]. The distribution of this species in Turkey has emerged with its population determined in the Yuvacık Dam Basin of Kocaeli province by Efe et al. [8]. *Genista sagittalis* usually grows in maquis habitats, in oak or conifer forests, shrub fields, dry grasslands, slopes, and mountain slopes at 1050–1600 m (rarely 2360 m) in South and Central Europe, in open woodland, maquis scrub, and rocky slopes at 450–850 m in Kocaeli. It was recommended by the International Union for Conservation of Nature (IUCN) [14] as the Red data category EN due to road construction works and livestock grazing in Turkey [8].

Genista sagittalis plant, which can be grown to a height of 10–50 cm from the soil surface, has leaf-like branches, semi-shrub, procumbent, rhizome or

caespitose. Young shoots with straight and silky hairs, later glabrous. Leaves are $0.5\text{--}2.2 \times 0.5\text{--}1.0$ cm, linear to elliptic, entire, pubescent beneath, and subglabrous above. It blooms in April–May. The number of flowers in the terminal inflorescence is variable between 4–25. Calyx hairy, 0.5–0.7 cm; Corolla yellow, glabrous, standard 1–1.2 cm; wings 0.9–1 cm; keel 0.9–1.1 cm; and legume fruit, hairy, $1.5\text{--}2.0 \times \text{ca. } 0.5$ cm. The number of seeds in the legume fruit ranges between 1 and 5. Olive green or blackish. *G. sagittalis* differs from other *Genista* species in that its shoots are winged and thornless. Illustrations of the plant's habitus, stem-wing, flower, calyx, corolla parts, fruit, seed, and root are given in detail by Efe et al. [8].

According to the literature reviewed, the investigations related to *G. sagittalis* are limited. The investigations have been mainly done on the flavonoid and isoflavonoid contents of *G. sagittalis* blooming aerial parts performed by liquid chromatography [15-17] and it is an antioxidant property [5]. Callus cultures of *G. sagittalis* have been established with the objective of producing high amounts of isoflavones of phytoestrogen activity [18]. And some other investigations are related to their morphology [19-20].

Plant extracts have their own importance as they are considered as most urgent biomolecule sources that can be screened due to the fact that not only various active pharmaceutical compounds have been isolated and characterized but also used as bioactive compounds in drug initiatives [21-22]. For this purpose, the extraction of such biomolecules by medicinal plants has been carried out using various solvents and different types of extraction methods. The plant extracts, which are widely known as therapeutic among the public, have attracted the attention of some researchers today, and they have been evaluated in a number of bio-analytical experiments in order to take the research to a further level. Today, many drugs targeting deoxyribonucleic acid (DNA) are both in use and in phase. There are many different types of these drugs that treat by different mechanisms. However, due to the serious side effects of these types of drugs, scientists continue their research to develop different types of drugs (with less toxic side effects).

As it is known, DNA, playing an important role in the transmission of genetic information, is one of the clear targets for drug development research. The majority of structure-specific molecules, such as intercalators and groove binders currently available on the market and in the literature, bind to DNA by non-covalent interaction. The first of these non-covalent types of attachment is intercalation, in which an insertion occurs between the base pairs of double-stranded DNA (dsDNA) and the small molecule through strong intermolecular forces, causing the DNA bases to rupture irreversibly in hydrogen bonds. The second is the groove binding, where the small molecule binds to the small or large groove of dsDNA. The third is external binding on the dsDNA surface, primarily through hydrogen-bonding interactions with the phosphodiester backbone and small molecules. Our research group has so far examined the interaction of different chemical structures (for example, drug molecules, some newly synthesized ligands, bioactive metal complexes and structures isolated from plants) with fish sperm and/or calf thymus dsDNA by spectroscopic, voltammetric, viscosimetric, and theoretical ways [23-27].

In the present work, investigations are done on the essential oil part while alcoholic extracts of the flower and



Fig 1. *Genista sagittalis* near Serinlik locality in Kocaeli-Turkey

peduncle parts of *G. sagittalis* collected from Kocaeli province-Turkey (Fig. 1). We analyzed the essential oil chemical profilings by using gas chromatography coupled to mass spectrometry (GC-MS) and, we tried for the first time the interaction of the flower and peduncle extracts of *G. sagittalis* with dsDNA by using UV-Vis spectroscopy and cyclic voltammetry (CV) techniques. In both techniques, we obtained the binding constants (K_b) of these extracts to dsDNA with reproducible results. Furthermore, to the best of our knowledge, the current work is the first to report the antimicrobial and anti-quorum sensing (anti-QS) activity of *G. sagittalis* extracts growing in Turkey.

■ EXPERIMENTAL SECTION

Materials

The materials used in this study were, sodium chloride (NaCl) (99.9% purity, Merck), synthetic double-stranded DNA (99.9% purity, Merck, Germany), and tris(hydroxymethyl) aminomethane hydrochloride ($C_4H_{12}ClNO_3$) (99.9% purity, Merck, Germany), used without further purification. Solvents used in this study, dichloromethane, ethyl alcohol, *n*-hexane, and methanol, were distilled before use.

Two Gram-positive (*Staphylococcus aureus* 29213, *Staphylococcus epidermidis* 12228) and three Gram-negative (*Chromobacterium violaceum* 12472, *Proteus mirabilis* 14153, *Pseudomonas aeruginosa* 27853) bacteria were used for antibacterial analysis. *C. violaceum* 12472 was also used to determine anti-QS activity. Production of the purple violacein pigment in wild type strain of *C. violaceum* (CV12472) relies on an intact quorum-sensing mechanism [28]. For strains' growth Luria-Bertani (LB) broth (1% tryptone, 0.5% yeast extract, 0.5% NaCl) at 28 °C, and 200 rpm was used.

A stock solution of 230 μ M dsDNA containing 0.2 M Tris-HCl and 150 mM NaCl (pH 7.4), is stable for one week and should be stored at 4 °C. The ratio of absorbance at 260 and 280 nm is used to assess the purity of the related solution, which gives $A_{260}/A_{280} = 1.92$ value. The molarity of dsDNA was calculated using $\epsilon = 6600 \text{ M}^{-1} \text{ cm}^{-1}$ [29]. In the UV-Vis spectroscopic studies, extracts 1 and 2 (same amounts for both extracts

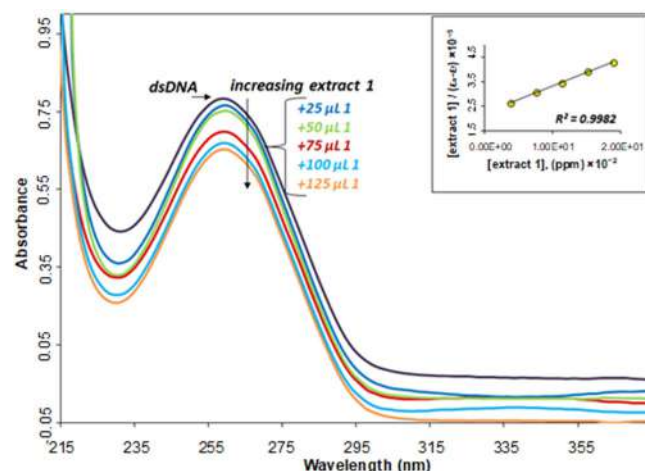


Fig 2. UV absorption titration of dsDNA (30 ppm) with extract 1 (25–125 μ L) in Tris-HCl buffer. (The arrow shows how absorbance decreased and not shifted ($\lambda_{\text{max}} = 260 \text{ nm}$) as the concentration of extract 1 increased, and binding constants (K_b) were determined from the inset)

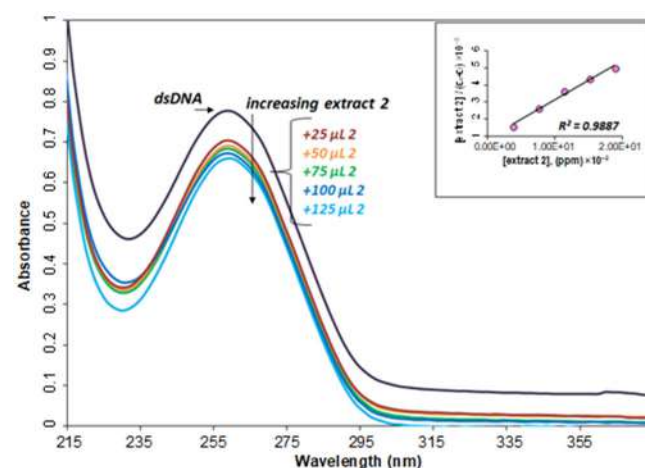


Fig 3. UV absorption titration of dsDNA (30 ppm) with extract 2 (25–125 μ L) in Tris-HCl buffer. (The arrow shows how absorbance decreased and not shifted ($\lambda_{\text{max}} = 260 \text{ nm}$) as the concentration of extract 2 increased, and binding constants (K_b) were determined from the inset)

in the range of 25–125 μ L) were added separately (with different experiments) at increasing concentrations onto the 30 ppm dsDNA solution. The absorption spectra of dsDNA + extract 1 or 2 solutions were recorded (Fig. 2 and 3). All experimental methods were repeated three times, and the binding constants based on the results are reported as relative standard deviation (RSD) values from the mean. In the voltammetric experiments, the

cyclic voltammograms of the prepared dsDNA + extract **1** or **2** solutions were recorded in the direction of oxidation by adding extract **1** or **2** (in the range of 12.5–75 µL) solution at increasing concentrations onto the 10 ppm dsDNA solution. In voltammetric measurements, dsDNA diluted with the acetate buffer solution with a pH of 4.8 has been used as dsDNA stock solution.

Instrumentation

The instruments used in this study were UV-VIS spectrophotometer (A T80 + UV-Vis spectrophotometer) and GC-MS (Thermo Trace GC Ultra with an HP Innwax column (30 m–0.25 mm–0.25 µm) and Thermo Trace DSQ). The prepared solutions were recorded against the blank and Tris-HCl (pH: 7.4) buffer solution. The GC-MS studies were performed at TUBITAK Marmara Research Center. Column conditions were as follows: 60 °C (3 min isothermal), heated to 220 °C at a rate of 3 °C/min, and 5 min (isothermal) at 220 °C. Inlet temperature: 175 °C; injection mode: splitless; carrier flow: 1 mL/min; transfer line temperature: 200 °C; with a mass range of 40–450 *m/z*, ion source temperature: 200 °C, incubation time: 30 min, and incubation temperature: 60 °C.

The voltammetric recordings were performed using an Autolab potentiostat/galvanostat (PGSTAT 302 N, Eco Chemie, the Netherlands), a BAS 100 W (BioanalyticalSystem, USA) potentiometer, and a glassy carbon electrode (BAS; U: 3 mm diameter). The General Purpose Electrochemical System (GPES) and Nova 2.2 software packages were used to control experimental conditions. An Ag/AgCl reference electrode (BAS; 3 M KCl in all experiments), a platinum wire counter electrode, and a 10 mL single-chamber standard cell with three electrodes were the triple electrode systems used.

Procedure

Fieldwork

Flower and peduncle samples of *G. sagittalis* (Fig. 1) were collected from Kocaeli province in May 2018. The location information where the samples were collected is given below.

Kocaeli: Yuvacık Dam Basin, between Camidüzü-Örnekköy, near Serinlik locality, on the upper side of the

road, on the side of the path, south, shrubland, 510 m, 40°39'02"N, 30°00'16' E.

In this study, the following taxa were accompanied at the location where the plant samples were collected: *Quercus petraea* (Mattuschka) Liebl. subsp. *iberica* (Steven ex M.Bieb.) Krassiln., *Tilia tomentosa* Moench, *Arbutus unedo* L., *Rosa canina* L., *Cistus creticus* L., *Erica arborea* L., and *Genista tinctoria* L. The study area was visited during the flowering period of *Genista sagittalis*. Individuals of this plant in the location detailed above were determined and identified in the area, and in order to be used in this study, inflorescence samples in the terminal part of the branches were collected in paper bags.

Extraction procedure

The collected inflorescence samples of the plant *G. sagittalis* were separated into two groups flowers and peduncles. Both groups were air dried in the shade indoors and ground into powder in 50 mesh size. The samples were extensively extracted with 300 mL of methanol in a Soxhlet apparatus. The yield percentages of the ethanol extracts were 10.78 and 7.38% as dry matter, respectively. The obtained extracts are then re-extracted with a separatory funnel containing 300 mL of cyclohexane. The crude flower and peduncle extracts were concentrated in vacuo to dryness at 40 °C.

For DNA binding experiments: the dry matter percentages of the flowers and peduncle of the ground samples were approximately 1.87 and 1.87%, respectively. Extractions of the flower and peduncle parts were performed with 20 mL of 70% ethanol, for 30 min in a water bath, at 60 °C. The ethanol extracts were then cooled and centrifuged at 4,500 rpm for 15 min to obtain an overhead liquid [5]. The yield percentages of ethanol extracts were 9.35 and 5.75% as dry matter, respectively. In this study, extracts **1** and **2** are denoted as the flower and peduncle extracts, respectively.

Isolation of essential oil

The essential oil of air-dried powdered 300 g *G. sagittalis* was obtained by hydrodistillation using a Clevenger-type apparatus.

Minimal inhibition concentration (MIC) analysis

A modified broth dilution assay in 96 well-microplate, described in detail in a previous paper of our group [30], has been used in the antibacterial activity analysis. Briefly, the stock solutions were prepared at 50 mg/mL in methanol from methanolic extracts of flower and peduncle parts of *G. sagittalis*. The extracts were added to each well in a total volume of 200 μ L with final concentrations of 0.25–2 mg/mL from the stock solution for assay. The bacterial suspensions were adjusted to optic density 600 0.1. Ampicillin (200 μ g/mL) and kanamycin (100 μ g/mL) were used as standard antibiotics. Covered plates were mixed carefully and incubated at 28 °C, 200 rpm for 24 h. The absorbance of each well was measured at 600 nm using an Epoch microplate spectrophotometer (Biotek, USA). All tests were performed in triplicate. The MIC was defined as the lowest concentration that inhibits the growth of microorganisms.

Anti-QS analysis

Anti-QS activity was analyzed by a modified broth dilution assay [30] in 96 well-microplate previously described using sub-MIC concentrations (1.0–1.9 mg/mL) with CV12472 biosensor strain. Kanamycin (100 μ g/mL) was used as a standard antibiotic. Covered plates were mixed thoroughly and incubated at 28 °C, 200 rpm for 24 h. The absorbance of each well was measured at 600 nm using an Epoch microplate spectrophotometer (Biotek, USA) to confirm the growth of bacterial cultures. QS activity was measured by quantitative analyses of violacein production [31]. A 200 μ L CV1472 culture sample from each well was

transferred to a microcentrifuge tube and centrifuged at 13,000 rpm for 10 min to precipitate insoluble violacein. Supernatants were discarded, and 200 μ L DMSO was added to the pellets and vortexed vigorously until a uniform resuspension was achieved. Removing of cell lysates from these resuspensions was immediately done with centrifugation at 13,000 rpm for 10 min. After centrifugation, the absorbance of the supernatant, which is added to a 96-well microplate, was measured at 585 nm with a microplate spectrophotometer.

Statistical analysis

For antibacterial and anti-QS analyses, values were calculated with Excel software (Microsoft Office). One-way ANOVA and Tukey's test were used for statistical analyses, and the results are expressed as the mean \pm SD. Statistical significance levels were shown as * $p < 0.05$, ** $p < 0.01$ and *** $p < 0.001$.

RESULTS AND DISCUSSION

Chemical Composition of the Essential Oil

The GC-MS analysis of *G. sagittalis* oil detected 14 components, accounting for 9.88% of the total oil which is listed in Table 1. The main identified compounds were straight-chain alkanes ethers (7.51%), aromatic ethers and esters (1.43%) and terpenoids (0.94%). The representative gas chromatogram of *G. sagittalis* essential oil is given in Fig. 4.

Interaction with dsDNA

It is known that the mechanisms of action of some antitumor and antimalarial drugs include interactions with dsDNA. Alkylating agents (e.g., bendamustine,

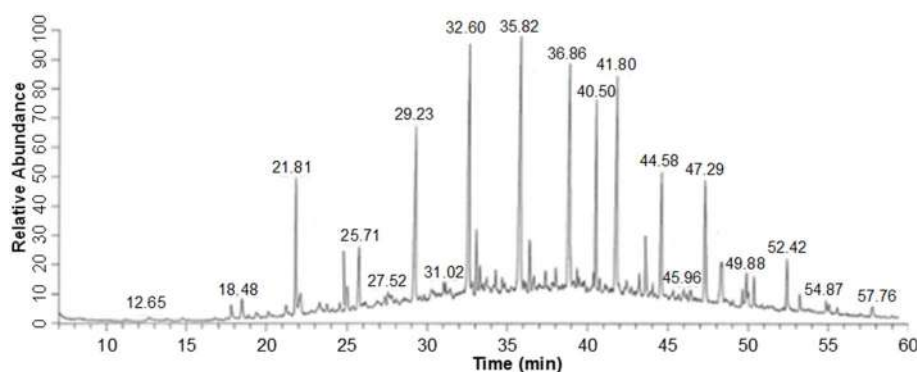


Fig 4. Gas chromatogram of *G. sagittalis* essential oil part

Table 1. Composition of the essential oil of *Genista sagittalis* from Kocaeli (Turkey)

Peak number	Classification	Component	Retention time/min	Area %	SI/RSI ^a
1	p-menthane monoterpene	α -terpinenyl acetate	21.81	0.78	911/938
2	straight-chain alkane	octadecane	25.71	0.31	850/858
3	straight-chain alkane	nonadecane	29.22	0.86	879/904
4	straight-chain alkane	eicosane	32.59	1.45	889/897
5	aromatic ether	1,2-dimethoxy-4-(1-propenyl)-(Isoeugenyl methyl ether)benzene	33.06	0.45	798/824
6	straight-chain alkane	heneicosane	35.79	1.50	874/904
7	sesquiterpene	hexahydrofarnesyl acetone (6,10,14-trimethyl-2-pentadecanone)	36.41	0.16	785/887
8	straight-chain alkane	hexatriacontane	38.83	1.11	880/926
9	aromatic ether	4-methoxy-6-(2-propenyl)-1,3-benzodioxole (Myristicin)	40.50	0.67	902/933
10	straight-chain alkane	tricosane	41.77	1.06	872/941
11	straight-chain alkane	heptacosane	44.56	0.53	845/887
12	straight-chain alkane	nonacosane	47.29	0.50	810/838
13	aromatic ester	2-cyclohexylethyl isobutylphthalate	48.30	0.31	690/837
14	straight-chain alkane	pentatriacontane	52.42	0.19	795/860

^aSI/RSI Search index/Reverse search index

carmustine, chlorambucil, cyclophosphamide, chlormethine, dacarbazine, fotemustine, lomustine, melphalan, streptozocin, temozolomide), platinum compounds (e.g., carboplatin, cisplatin, nedaplatin, oxaliplatin), antitumor antibiotics (e.g., bleomycin, doxorubicin, mithramycin), and various other substances (e.g., chloroquine) have been reported. Based on the interaction of small molecular weight ligand molecules with DNA, several short-term methods have been developed that can be applied to the discovery of naturally occurring agents that function through this mechanism. Doxorubicin, which is among the drug molecules known to interact with DNA through intercalation, decreases the peak current of DNA in the study conducted with High-Performance Liquid Chromatography (HPLC). Daunomycin and ethidium bromide, which are known to interact strongly with DNA, also showed similar properties [32-33]. In this context, the wide diversity in the binding mode between plant extracts and dsDNA has taken its place in the literature due to the following factors, with the idea of obtaining similar analytical signals [34]. These are $[DNA]/[plant\ extract]$ concentration ratio and buffer medium. This study is based

on $[DNA] = [plant\ extract]$ at pH 7.4 media.

DNA-Binding Study with UV Spectroscopy

UV-Vis absorption titration was used to determine the binding constants (K_b) and interaction of extracts **1** and **2** with dsDNA. In fact, the interaction of dsDNA with any molecule depends on the structure of that molecule. In studies conducted by some scientific groups, DNA interaction percentages with different plant extracts are given [21,35-37]. For example, the interaction of 52 methanolic and 51 dichloromethane crude plant extracts with herring sperm DNA has been made according to the HPLC method and was evaluated in terms of decreasing the peak absorbance values in HPLC by Correa et al. [35]. In the UV-Vis spectroscopic studies, the interaction of extracts **1** and **2** with dsDNA was investigated by examining the absorption spectra of the mixture solutions prepared at the appropriate concentration. Some solutions were prepared by adding increasing amounts of extract solutions (25–125 μ L) to dsDNA solution at a certain concentration prepared from a stock solution. The UV-Vis spectra obtained from these data are given in Fig. 2 and 3. The data

obtained from the spectrum clearly revealed that the information about the extract **1** or **2** - DNA interaction type and the K_b , which indicates the binding strength of the extracts to dsDNA, were calculated based on the titration data. The K_b also known as the intrinsic binding constant for two extracts with dsDNA can be obtained by monitoring the changes in absorbance between 215–375 nm and displayed as the slope of the graph, where $[\text{extract}]/(\varepsilon_a - \varepsilon_f)$ plotted against the molarity of extract according to the following “Benesi-Hildebrand” equation (Eq. 1) [38];

$$\frac{[\text{extract}]}{(\varepsilon_a - \varepsilon_f)} = \frac{[\text{extract}]}{(\varepsilon_b - \varepsilon_f)} + \frac{1}{K_b \times (\varepsilon_a - \varepsilon_f)} \quad (1)$$

where ε_a is the apparent extinction coefficient obtained by the calculation of $A_{\text{obsd}}/[\text{DNA}]$, ε_f is extinction coefficient of the DNA in its free form, ε_b is extinction coefficient for the DNA in the fully bound form and $[\text{extract}]$ is the increasing extract concentration. The high value of K_b obtained for extracts suggests a strong binding of two compounds to dsDNA. K_b values were found as $1.97 \times 10^3 \pm 0.37$ and $3.68 \times 10^2 \pm 0.44$ for extracts **1** and **2**, respectively. As a result, when extract **1** was added at increasing concentrations on 30 ppm dsDNA solution, a decrease in the absorbance value (hypochromic effect) of dsDNA was observed (% Hypo \pm RSDa = 16.73 ± 0.46). No red or blue shift was observed at the maximum wave value of dsDNA ($\lambda_{\text{max}} = 260$ nm). This situation was the same in the experiments performed with extract **2** solutions and the % Hypo \pm RSD for extract **2** was found to be 14.54 ± 0.39 . The formula “(% Hypo = % Hypochromism = $(A_0 - A)/A_0$)” was used in percent hypo calculations. All tests were performed in triplicate and are expressed as mean and relative standard deviation.

Voltammetric Studies

Voltammetry is an advantageous technique that provides high sensitivity, inexpensive, simple usage, rapid results, and compatibility with microfabrication technology. Due to the small sample requirement, it has been widely used in biological and chemical analyses. Electrochemical methods of DNA interaction of small molecules such as drugs are possible in two ways: (i) the signal change of the electroactive bases (guanine or

adenine, or both) is measured and interpreted according to these changes; (ii) necessary calculations are made by measuring the intensity of the peak currents in the oxidation and/or reduction direction of small molecules (before and after the interaction with DNA) [23-24,39]. In this study, extract **1** or **2** was separately added to the dsDNA solution of a certain concentration, and the changes in the peak current and peak potential of dsDNA were interpreted. The cyclic voltammograms of 10 ppm dsDNA (black) with increasing amounts of extract **1** and extract **2** in pH 4.8 acetate buffer have been given in Fig. 5 and 6.

The typical cyclic voltammograms (anodic direction) of 10 ppm dsDNA at GCE in pH 4.8 acetate buffer have two sharp oxidation that belongs to the dGuo and dAdo at 1.05 and 1.33 V, respectively. The interaction between extract **1** or extract **2** and dsDNA was evaluated after applying different incubation times from 3 to 15 min and cyclic voltammograms were recorded. The decrease in peak current intensities of both guanine and adenine, after activation with extract **1** or extract **2**, is clear evidence that these extracts interact over both bases. On the other hand, no oxidation peak was

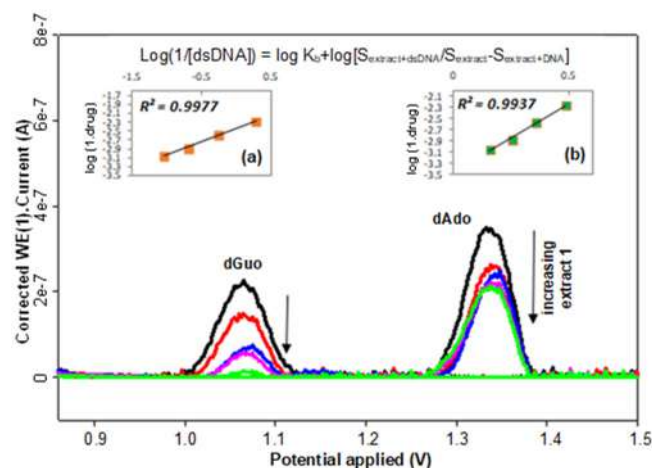


Fig 5. Cyclic voltammograms of 10 ppm dsDNA (black) with increasing amounts of extract **1** (12.5–75 μL) in pH 4.8 acetate buffer. (The arrow shows how the peak current decreased as the concentration of extract **1** increased, and binding constants (K_b) for dGuo (a) and dAdo (b) bases were determined from the slopes of the graphs)

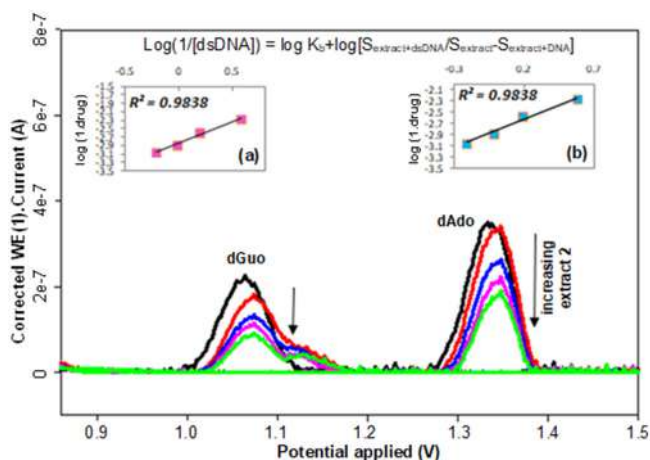


Fig 6. Cyclic voltammograms of 10 ppm dsDNA (black) with increasing amounts of extract 2 (12.5–75 µL) in pH 4.8 acetate buffer. (The arrow shows how the peak current decreased as the concentration of extract 2 increased, and binding constants (K_b) for dGuo (a) and dAdo (b) bases were determined from the slopes of the graphs)

observed in either extract 1 or extract 2 under these conditions. Based on these data, the K_b of each compound was calculated by Eq. 2 [40].

$$\log \frac{1}{[\text{extract}]} = \log K_b + \log \frac{S_{\text{dsDNA}} + \text{extract}}{S_{\text{dsDNA}} - (S_{\text{dsDNA}} + \text{extract})} \quad (2)$$

The terms used in the equation are as follows; [extract]: increasing extract concentration, $S_{\text{dsDNA-extract}}$: current signal received from dsDNA after interaction with

extract, and S_{dsDNA} : current signal received from the dsDNA alone extract [40]. The K_b and $\log K_b$ values calculated from these data are shown in Table 2. The two techniques have K_b values close to each other.

Antibacterial and Anti-QS Activities

The antimicrobial activity of alkaloid extract of *G. vuralii* A. Duran & Dural has been previously reported against *S. aureus*, *B. subtilis* and *Candida krusei* [41]. Antibacterial activities of genistin, isosalipurpol and koaburaside isolated from *G. numidica* Spach aerial parts were investigated in a recent study [42]. They were reported that these compounds have antibacterial activity against *S. aureus*, *S. epidermidis*, *P. aeruginosa* and *Enterococcus faecalis* with MICs ranging from 31.2 to 125 µg/mL, while 80% MeOH extract of the plant did not exhibit antibacterial activity. In our study, the growth of any of the bacteria species was not inhibited by *G. sagittalis* peduncle extract. However, the antibacterial activity of *G. sagittalis* flower extract was determined against *P. aeruginosa* 27853 and *P. mirabilis* 14153 with MICs 1 to 2 mg/mL (Table 3). Additionally, anti-QS activity was observed for peduncle extract at 1.3 mg/mL. Violacein production was reduced to $68.53 \pm 0.14\%$ (** $p < 0.01$) by the concentration of the extract. According to our results, *G. sagittalis* flower extract has low antibacterial activity against certain pathogens, while

Table 2. Voltammetric binding constant data for extracts

25 °C Compound 1	$K_b \pm \text{RSD}^a$		$\log K_b \pm \text{RSD}^a$	
	dGuo	dAdo	dGuo	dAdo
extract 1	$2.75 \times 10^2 \pm 0.41$	$2.82 \times 10^3 \pm 0.27$	2.44 ± 0.39	3.45 ± 0.35
extract 2	$6.76 \times 10^2 \pm 0.21$	$7.24 \times 10^2 \pm 0.33$	2.83 ± 0.43	2.86 ± 0.19

^a All tests were performed in triplicate and are expressed as mean and relative standard deviation

Table 3. Determination of the antibacterial activity of *G. sagittalis* methanol extracts (mg/mL)

	Flower extract (extract 1)	Peduncle extract (extract 2)	Growth inhibition %	Amp (200 µg/mL)	Kn (100 µg/mL)
<i>S. aureus</i> 29213	ND	ND	ND	+	+
<i>S. epidermidis</i> 12228	ND	ND	ND	+	+
<i>P. aeruginosa</i> 27853	2	ND	$17.33 \pm 0.94^{***}$	+	-
<i>P. mirabilis</i> 14153	1	ND	$11.17 \pm 2.32^*$	+	+
<i>C. violaceum</i> 12472	ND	ND	ND	-	+

ND: Not detected, Amp: Ampicillin, Kn: Kanamycine, +: Inhibition effect determined, -: Inhibition effect not determined,

* $p < 0.05$, ** $p < 0.01$, *** $p < 0.001$

the peduncle extract showed strong anti-QS activity. However, to fully comprehend the processes underlying its antibacterial and anti-QS actions, more research is required.

■ CONCLUSION

Knowing that plants are a vital part of the world's natural heritage, and they have an important contribution to primary healthcare, this study presents the biological activities of *Genista sagittalis* L. (Fabaceae) from Kocaeli: Yuvacık Dam Basin in Turkey with the essential oil composition. The results demonstrated that a total of fourteen components were identified in the essential oil part. The antibacterial activity analyses demonstrated that *G. sagittalis* flower extract only had low activity against *P. mirabilis* and *P. aeruginosa* with MICs 1 to 2 mg/mL, as the peduncle extract showed strong anti-QS activity at 1.3 mg/mL. Additionally, dsDNA binding affinity investigations of the flower and peduncle ethanol extracts indicate that there are interactions with adenine and guanine bases. These results may offer new perspectives for pharmaceutical applications of *Genista sagittalis* and that further studies will enlighten the different applications and properties of this plant to scientists.

■ ACKNOWLEDGMENTS

The authors wish to thank to Istanbul Technical University, Faculty of Sciences and Letters, Department of Chemistry for experimental conditions (Lab L-105 and L2-111 belonging to Prof. Gölçü and Dr. Özdemir respectively) and to Dr. Kübra Erkan Türkmen from Hacettepe University for providing the bacterial strain CV12472. The authors would like to thank the support of the grant of Istanbul Technical University (Scientific Research Projects Unit) under the THD-2023-44771 project.

■ AUTHOR CONTRIBUTIONS

Pelin Şenel and Elif Çepni Yüzbaşıoğlu conducted bioanalytical and microbiological studies, respectively. Bleda Can Sadıkoğulları and Gülnur Mertoğlu Elmas supervised experimental studies. Dilek Oral collected plant material. Ayşegül Gölçü and Ayşe Daut Özdemir

supervised, wrote and revised the manuscript. All authors agreed to the final version of this manuscript.

■ REFERENCES

- [1] Grafakou, M.E., Barda, C., Tomou, E.M., and Skaltsa, H., 2021, The genus *Genista* L.: A rich source of bioactive flavonoids, *Phytochemistry*, 181, 112574.
- [2] Schmidt-Przewozna, K., and Zajaczek, K., 2022, Influence of flavonoid dyes on the color and pro - health benefits of linen fabrics, *J. Nat. Fibers*, 19 (15), 11165–11180.
- [3] Simões, M.A.M., Pinto, D.C.G.A., Neves, B.M.R., and Silva, A.M.S., 2020, Flavonoid profile of the *Genista tridentata* L., a species used traditionally to treat inflammatory processes, *Molecules*, 25 (4), 812.
- [4] Sharifi-Rad, J., Quispe, C., Imran, M., Rauf, A., Nadeem, M., Gondal, T.A., Ahmad, B., Atif, M., Mubarak, M.S., Sytar, O., Zhilina, O.M., Garsiya, E.R., Smeriglio, A., Trombetta, D., Pons, D.G., Martorell, M., Cardoso, S.M., Razis, A.F.A., Sunusi, U., Kamal, R.M., Rotariu, L.S., Butnariu, M., Docea, A.O., and Calina, D., 2021, Genistein: An integrative overview of its mode of action, pharmacological properties, and health benefits, *Oxid. Med. Cell. Longevity*, 2021, 3268136.
- [5] Hanganu, D., Olah, N.K., Benedec, D., Mocan, A., Crisan G., Vlase, L., Popica, I., and Oniga I., 2016, Comparative polyphenolic content and antioxidant activities of *Genista tinctoria* L. and *Genistella sagittalis* (L.) Gams (Fabaceae), *Pak. J. Pharm. Sci.*, 29 (Suppl. 1), 301–307.
- [6] Tutin, T.G., 1968, "*Chamaespartium* Adans" in *Flora Europaea Volume 2, Rosaceae to Umbelliferae*, Eds. Tutin, T.G., Heywood, V.H., Burges, N.A., Moore, D.M., Valentine, D.H., Walters, S.M., and Webb, D.A., Cambridge University Press, Cambridge, UK, 205.
- [7] Talavera, S., 1999, "*Chamaespartium* Adans" in *Flora Iberica, Leguminosae-Cytiseae, Vol. 7, part 2*, Real Jardin. Botánico, Madrid, Spain, 88, 128–133.
- [8] Efe, A., Özhatay, E., Aksoy, N., and Oral, D.D., 2009, *Chamaespartium* Adans. (Leguminosae): A

- new record for the flora of Turkey, *Turk. J. Bot.*, 33 (6), 453–456.
- [9] POWO (Plants of the World Online), *Genista sagittalis* L., Royal Botanic Gardens, KEW, <https://powo.science.kew.org/taxon/urn:lsid:ipni.org:names:496318-1>, accessed on March 1st, 2022.
- [10] Danihelka, J., Chrtek, J., and Kaplan, Z., 2012, Checklist of vascular plants of the Czech Republic, *Preslia*, 84, 647–811.
- [11] Pyšek, P., Danihelka, J., Sádlo, J., Chrtek, J., Chytrý, M., Jarošík, V., Kaplan, Z., Krahulec, F., Moravcová, L., Pergl, J., Štajerová, K., and Tichý, L., 2012, Catalogue of alien plants of the Czech Republic (2nd edition): Checklist update, taxonomic diversity and invasion patterns, *Preslia*, 84, 155–255.
- [12] Kalita, M., and Małek, W., 2017, Molecular phylogeny of *Bradyrhizobium* bacteria isolated from root nodules of tribe Genisteae plants growing in southeast Poland, *Syst. Appl. Microbiol.*, 40 (8), 482–491.
- [13] Gudžinskas, Z., and Taura, L., 2020, New alien plant species recorded in South Lithuania, *Botanica*, 26 (2), 170–183.
- [14] IUCN, 2001, *IUCN Red List Categories and Criteria, Version 3.1*, IUCN Species Survival Commission, Gland, Switzerland and Cambridge, UK.
- [15] Hanganu, D., Vlase, L., and Olah, N.K., 2010, Phytochemical analysis of isoflavons from some *Fabaceae* species extracts, *Not. Bot. Horti Agrobot. Cluj-Napoca*, 38 (1), 57–60.
- [16] Kiss, B., Popa, D.S., Hanganu, D., Pop, A., and Loghin, F., 2010, Ultra-performance liquid chromatography method for the quantification of some phytoestrogens in plant material, *Rev. Roum. Chim.*, 55 (8), 459–465.
- [17] Tero-Vescan, A., Vari, C.E., and Vlase, L., 2014, Alkaloid content of some potential isoflavonoids sources (native *Genista* species). Long-term safety implications, *Farmacía*, 62 (6), 1109–1117.
- [18] Łuczkiwicz, M., and Głód, D., 2003, Callus cultures of *Genista* plants—*in vitro* material producing high amounts of isoflavones of phytoestrogenic activity, *Plant Sci.*, 165 (5), 1101–1108.
- [19] Käss, E., and Wink, M., 1995, Molecular phylogeny of the Papilionoideae (family Leguminosae): RbcL gene sequences versus chemical taxonomy, *Bot. Acta*, 108 (2), 149–162.
- [20] Teixeira, G., and Pereira, A.L., 2004, Winged stems in *Pterospartum tridentatum*: Morphoanatomical study, *Acta Bot. Gallica*, 151 (1), 103–109.
- [21] Desmarchelier, C., Mongelli, E., Coussio, J., and Ciccía, G., 1996, Studies on the cytotoxicity, antimicrobial and DNA-binding activities of plants used by the Ese'ejas, *J. Ethnopharmacol.*, 50 (2), 91–96.
- [22] Haspłova, K., Hudecova, A., Miadokova, E., Magdolenova, Z., Galova, E., Vaculcikova, L., Gregan, F., and Dusinska, M., 2011, Biological activity of plant extract isolated from *Papaver rhoeas* on human lymphoblastoid cell line, *Neoplasma*, 58 (5), 386–391.
- [23] Alizadeh, N., Şenel, P., Erdoğan, T., and Gölcü A., 2022, Elucidation of binding interactions and mechanism of rivastigmine tartrate with dsDNA via multi-spectroscopic, electrochemical, and molecular docking studies, *J. Mol. Struct.*, 1268, 133736.
- [24] Şenel, P., Cetinkaya, A., Kaya, S.I., Erdoğan, T., Topal, B.D., Gölcü, A., and Ozkan, S.A., 2022, Spectroscopic, electrochemical, and some theoretical studies on the interactional of neuraminidase inhibitor zanamivir with double helix deoxyribonucleic acid, *J. Mol. Struct.*, 1262, 133029.
- [25] Waihenya, S., Şenel, P., Osonga, F.J., Erdoğan, T., Altay, F., Gölcü, A., and Sadık, O.A., 2021, Mechanism of interactions of dsDNA binding with Apigenin and its sulfamate derivatives using multispectroscopic, voltammetric, and molecular docking studies, *ACS Omega*, 6 (8), 5124–5137.
- [26] Yılmaz, Z.T., Odabaşoğlu, H.Y., Şenel, P., Adımcılar, V., Erdoğan, T., Özdemir, A.D., Gölcü, A., and Odabaşoğlu M., 2020, A novel 3-((5-methylpyridin-2-yl) amino) isobenzofuran-1(3*H*)-one: Molecular structure describe, X-ray diffractions and DFT calculations, antioxidant activity, DNA binding and molecular docking studies, *J. Mol. Struct.*, 1205, 127585.
- [27] Cheraghi, S., Şenel, P., Topal, B.B., Agar, S., Majidian,

- M., Yurtsever, M., Atici, E.B., Gölcü, A., and Ozkan, S.A., 2023, Elucidation of DNA-eltrombopag binding: Electrochemical, spectroscopic and molecular docking techniques, *Biosensors*, 13 (3), 300.
- [28] McLean, R.J.C., Pierson, L.S., and Fuqua, C., 2004, A simple screening protocol for the identification of quorum signal antagonists, *J. Microbiol. Methods*, 58 (3), 351–360.
- [29] de Farias, S.T., Furtado, A.N.M., dos Santos Junior, A.P., and José, M.V., 2023, Natural history of DNA-dependent DNA polymerases: Multiple pathways to the origins of DNA, *Viruses*, 15 (3), 749.
- [30] Yılmaz, Z.T., Odabaşoğlu, H.Y., Şenel, P., Yüzbaşıoğlu, E.Ç., Erdoğan, T., Özdemir, A.D., Gölcü, A., Odabaşoğlu, M., and Büyükgüngör, O., 2023, Identification of a 3-(5-methyl-2-thiazolylamino)phthalide as a new minor groove agent, *J. Biomol. Struct. Dyn.*, 41 (9), 4048–4064.
- [31] Blosser, R.S., and Gray, K.M., 2000, Extraction of violacein from *Chromobacterium violaceum* provides a new quantitative bioassay for *N*-acyl homoserine lactone autoinducers, *J. Microbiol. Methods*, 40 (1), 47–55.
- [32] Small, H., 2023, Bayesian history of science: The case of Watson and Crick and the structure of DNA, *Quant. Sci. Stud.*, 4 (1), 209–228.
- [33] Noer, J.B., Hørsdal, O.K., Xiang, X., Luo, Y., and Regenber, B., 2022, Extrachromosomal circular DNA in cancer: History, current knowledge, and methods, *Trends Genet.*, 38 (7), 766–781.
- [34] Pezzuto, J.M., Che, C.T., McPherson, D.D., Zhu, J.P., Topcu, G., Erdelmeier, C.A.J., and Cordell, G.A., 1991, DNA as an affinity probe useful in the detection and isolation of biologically active natural products, *J. Nat. Prod.*, 54 (6), 1522–1530.
- [35] Correa, Y.M, Niño, J., and Mosquera, O.M., 2007, DNA interaction of plant extracts from Colombian flora, *Pharm. Biol.*, 45 (2), 111–115.
- [36] Doğan, H.H., and Arslan, E., 2015, Biological activities and DNA interactions of *Amanita ovoidea*, *Pharm. Biol.*, 53 (9), 1386–1390.
- [37] Zhao, L., Zhao, X., Ma, Y., Zhang, Y., and Wang D., 2020, DNA binding characteristics and protective effects of yellow pigment from freshly cut yam (*Dioscorea opposita*), *Molecules*, 25 (1), 175.
- [38] Benesi, H.A., Hildebrand, J.H., 1949, A spectrophotometric investigation of the interaction of iodine with aromatic hydrocarbons, *J. Am. Chem. Soc.*, 71 (8), 2703–2707.
- [39] Beyazit, N., Kaya, K., Şenel, P., Özdemir, A.D., and Gölcü, A., 2019, Crystal structure and DNA binding properties of khellin oxime, *J. Mol. Struct.*, 1197, 450–457.
- [40] Şenel, P., Agar, S., İş, Y.S., Altay, F., Gölcü, A., and Yurtsever, M., 2022, Deciphering the mechanism and binding interactions of Pemetrexed with dsDNA with DNA-targeted chemotherapeutics via spectroscopic, analytical, and simulation studies, *J. Pharm. Biomed. Anal.*, 209, 114490.
- [41] Erdemoğlu, N., Ozkan, S., Duran, A., and Tosun, F., 2009, GC-MS analysis and antimicrobial activity of alkaloid extract from *Genista vuralii*, *Pharm. Biol.*, 47 (1), 81–85.
- [42] Boutaghane, N., Magid, A.A., Abedini, A., Cafolla, A., Djeghim, H., Gangloff, S.C., Voutquenne-Nazabadioko, L., and Kabouche, Z., 2019, Chemical constituents of *Genista numidica* Spach aerial parts and their antimicrobial, antioxidant and antityrosinase activities, *Nat. Prod. Res.*, 33 (12), 1734–1740.

The Addition of Copper Nanoparticles to Mineral Trioxide Aggregate for Improving the Physical and Antibacterial Properties

Muhammad Akram Fakhri¹, Bambang Rusdiarso¹, Siti Sunarintyas², and Nuryono Nuryono^{1*}

¹Department of Chemistry, Faculty of Mathematics and Natural Sciences, Universitas Gadjah Mada, Sekip Utara, Yogyakarta 55281, Indonesia

²Department of Biomaterial, Faculty of Dentistry, Universitas Gadjah Mada, Jl. Denta 1, Sekip Utara, Yogyakarta 55281, Indonesia

* **Corresponding author:**

email: nuryono_mipa@ugm.ac.id

Received: November 28, 2022

Accepted: May 25, 2023

DOI: 10.22146/ijc.79491

Abstract: The physical and antibacterial properties of mineral trioxide aggregate (MTA) have been improved by adding copper nanoparticles (CuNP). The CuNP colloid was synthesized by reacting $\text{CuCl}_2 \cdot 2\text{H}_2\text{O}$ and NaBH_4 as the reducing agent using $\text{C}_6\text{H}_8\text{O}_6$ as the capping agent. The Cu(II) concentration was varied by 3.0, 6.0, and 9.0 mM to produce CuNP-3, CuNP-6, and CuNP-9 colloids, respectively. The CuNP colloids were characterized with a UV-Vis spectrophotometer and TEM. MTA was hydrated with CuNP at a mass-to-volume ratio of 2:1 to produce Cu-MTA-3, Cu-MTA-6, and Cu-MTA-9, respectively. All products were characterized with XRD and SEM-EDX. The compressive strength, pH, Ca ion release, and solubility were measured, and antibacterial activity was tested. The results showed a spherical shape of the synthesized CuNP with a particle size of ~ 28.08 nm. Adding CuNP-9 to hydrated MTA increased the compressive strength, pH, Ca ion release, and solubility, with the value of 4.78 ± 0.38 MPa; 9.01 ± 0.03 ; 1718 ± 63 ppm, and $22.48 \pm 0.37\%$, respectively. The highest antibacterial activity occurred for Cu-MTA-9, with an inhibition zone of 10.15 ± 0.47 mm against *S. aureus* and 11.93 ± 1.16 mm against *P. aeruginosa*. The findings show a potential application of the product for endodontic materials containing antibacterial agents.

Keywords: antibacterial; copper nanoparticles; physical properties; MTA

■ INTRODUCTION

Inflammation in the dental root canal is one of the problems often found in dental and oral health [1], and mineral trioxide aggregate (MTA) is alternative endodontic material to solve the problem by treating the root canal of teeth [2]. MTA is divided into white mineral trioxide aggregate (WMTA) and gray mineral trioxide aggregate (GMTA). WMTA contains a small amount of iron oxide, so it does not cause discoloration of the teeth [3]. MTA meets the criteria as an endodontic material but has some low physical properties compared to other materials. MTA compressive strength is lower than biodentine in 1 to 28 d [4], and biodentine has a pH value of 12, while MTA has a lower pH [5].

Additionally, MTA does not show higher antibacterial properties against *S. aureus* bacteria, which

are lower than other endodontic materials, namely AH-26 sealer [6]. Smart paste Bio and AH-Plus have higher antibacterial properties than MTA against *P. aeruginosa* [7]. Therefore, modifications of MTA are needed to improve the physical and antibacterial properties.

Copper nanoparticles (CuNP) have been widely reported to be able to act as antibacterial, for example, against *S. aureus* [8] and *P. aeruginosa* [9]. Nazer et al. [10] reported the addition of copper to Portland cement increases the pH of cement. Additionally, the Portland cement strength increased with copper addition because copper binds the material in the pores of the cement during the hydration process [11]. As MTA contains similar components to cement [12], the mechanical and antibacterial properties can be improved by modifying the metal and oxide nanoparticles. Yuliatun et al. [13]

reported the addition of SrO 5% and hydroxyapatite 6% increased the compressive strength of MTA from 2.21 to 18.01 MPa and improved the adhesion between dentin surface and MTA. Lim and Yoo [14] reported the modification of MTA with calcium fluoride (CaF_2) to give antibacterial activity against *Enterococcus faecalis*, *Porphyromonas endodontalis*, and *Porphyromonas gingivalis*. Bolhari et al. [15] improved the antibacterial activity of MTA by mixing MTA with fluorohydroxyapatite against *E. faecalis*. However, the effect of the modification on the mechanical properties was not investigated.

This paper reports the effect of CuNP addition on the hydrated MTA's physical properties and antibacterial activity. It included the synthesis of CuNP colloid and hydration of MTA using CuNP colloid as the hydrating liquid. The compressive strength and antibacterial activity against *S. aureus* and *P. aeruginosa* are also evaluated.

■ EXPERIMENTAL SECTION

Materials

Materials used for the synthesis of CuNP and Cu-MTA included copper(II) chloride dihydrate ($\text{CuCl}_2 \cdot 2\text{H}_2\text{O}$) p.a. (Pudak), L-ascorbic acid ($\text{C}_6\text{H}_8\text{O}_6$) p.a. (Merck), sodium borohydride (NaBH_4) p.a. (Merck). A sample of MTA was purchased from Maarc Dental. Chloramphenicol (Merck) was used as a positive control of the antibacterial agent, and bacteria of *P. aeruginosa* ATCC 27853 and *S. aureus* ATCC 29213 were provided by Laboratory of Microbiology, Universitas Gadjah Mada.

Instrumentation

CuNPs were characterized by a UV-Visible spectrophotometer (Genesys 10S). The morphology and the particle size of CuNP-6 were analyzed with Transmission Electron Microscope (TEM, JEOL JEM-1400). MTA before and after hydration, Cu-MTA-6 and Cu-MTA-9, were characterized with an X-ray Diffractometer (XRD, Shimadzu 6000, equipped with monochromatic Cu K α radiation operated at 30 kW, $\lambda = 1.54 \text{ \AA}$) and scanned in the range of $3^\circ \leq 2\theta \leq 90^\circ$ with a scan speed of $3^\circ/\text{min}$ (a scan step degree of 0.02°) and scanning electron microscope-energy dispersive X-ray (SEM EDX, JSM-6510LA). The compressive strength of the pellets was

measured with a universal testing machine (UTM, Zwick BL-GR5500N) at the initial conditions: a force of 0.01 N, pre-load speed of 300 mm/min, and a test speed of 10 mm/min. The pH was measured with a pH meter (Inolab ph7110) while atomic absorption spectroscopy (AAS, ContraAA300 Analytik Jena) was used to determine the concentration of Ca(II) ions released from the MTA.

Procedure

Synthesis of copper nanoparticles

The precursor of $\text{CuCl}_2 \cdot 2\text{H}_2\text{O}$ (7.7, 15.4, and 23.0 mg) was dissolved in 7.5 mL of deionized water to produce Cu(II) solution with various concentrations (3, 6, and 9 mM). L-ascorbic acid (142.7 mg) was dissolved in 3.0 mL of deionized water, and then the solution was added to the Cu(II) solution and stirred with a magnetic stirrer for one hour at room temperature (25°C). After that, NaBH_4 solids (3.4, 6.8, and 10.2 mg) were dissolved in 4.5 mL of deionized water and then added to the Cu(II) solutions with the various concentrations (3, 6, and 9 mM), and the solutions were stirred for 15 min at room temperature. The colloids of CuNP formed were successively labeled CuNP-3, CuNP-6, and CuNP-9. All CuNP colloids were characterized with a UV-Visible spectrophotometer. The morphology and particle size of CuNP-6 were analyzed with TEM.

Synthesis of Cu-MTA

MTA sample (1.00 g) was mixed with 0.50 mL of CuNP-3 colloid (the mass-to-volume ratio of 2:1). The mixture was stirred until it began to form a Cu-MTA-3 hard solid. Similar work was carried out for the CuNP-6 and CuNP-9 colloids to produce Cu-MTA-6 and Cu-MTA-9 solids, respectively, and hydration of MTA using deionized water was also performed. The products were characterized with XRD and SEM EDX.

Compressive strength testing

The four samples were (1) hydrated MTA; (2) Cu-MTA-3; (3) Cu-MTA-6; and (4) Cu-MTA-9 molded pellet tubes with sizes (diameter = 4 mm, thickness/height = 6 mm) on the mold as per ISO 9917-1. Pellets were stored in an airtight container at room temperature for 14 d. The compressive strength of the pellets was measured with a Universal Testing Machine.

Measurement of pH and Ca(II) ions release

The four samples of freshly hydrated MTA have formed pellets (diameter = 4 mm, height = 3 mm) and were then allowed to stand for 14 d at room temperature in an airtight container. The sample (60 mg) was immersed in 2.5 mL of demineralized water, which was replaced every 1, 3, and 7 d. The pH of the filtrate was measured with a pH meter, and Ca(II) ions concentrations were determined with AAS.

Solubility

The hydrated MTA sample used to identify the pH change and Ca(II) ions release was soaked for 7 d, separated from the filtrate, and dried in an oven at 50 °C for 6 h. The dried samples were weighed, and the difference in mass before and after immersion was calculated. The mass difference indicates the mass loss of the component from the sample [16]. The solubility of the sample was calculated using Eq. (1).

Solubility =

$$\frac{\text{mass difference of the sample} - \text{evaporating hydrate mass}}{\text{sample mass before soaking}} \times 100\% \quad (1)$$

Antibacterial test

Four MTA samples were pelleted (diameter = 4 mm; thickness = 3 mm) and allowed to stand for 14 d in an airtight container. *S. aureus* bacteria were inoculated into sterile aqueducts and homogenized with a vortex, and 100 microliths were taken and put into the medium on a petri dish. The MTA sample was fed into the substrate in a saucer with tweezers. Disc paper was taken, and then a positive control (chloramphenicol) of 10 microliths was transferred to the disc paper. Disc paper was inserted into the substrate, and Petri dishes were covered with a seal and incubated for 24 h. The same work was performed for samples of Cu-MTA-3, Cu-MTA-6, and Cu-MTA-9, as

well as *P. aeruginosa* bacteria. Observations and measurements of antibacterial activity were carried out the next day. Antibacterial activity was calculated by measuring the diameter of the inhibitory power of bacteria in a saucer with calipers or rulers. The test was conducted at the Microbiology Laboratory, Faculty of Biology, Universitas Gadjah Mada.

RESULTS AND DISCUSSION

Characteristics of CuNP

The precursor used to prepare CuNP colloids was a blue color Cu(II) solution obtained by dissolving $\text{CuCl}_2 \cdot 6\text{H}_2\text{O}$. Adding an L-ascorbic acid and NaBH_4 solution to the Cu(II) solution changes the solution to yellow-brown, as seen in Fig. 1.

The results of synthesized CuNP were brownish-yellow colloids, similar to the results reported previously [17]. The intensity increases as the concentration of CuNP increases (from left to right), indicating a higher concentration of CuNP. The absorbance of the CuNP colloids is presented in Fig. 2. All the maximum wavelengths in a 300–305 nm range align with previous research [18]. An increase of Cu(II) concentrations from 3.0 to 6.0 mM increases the absorbance significantly, and the increase from 6.0 to 9.0 mM slightly increases the absorbance. Therefore, 6.0 mM was chosen as the representation for TEM characterization.

Characterization was continued to identify the morphology of CuNP with TEM, and CuNP-6 is the representative sample to know the particle size. The result can be seen in Fig. 3. The TEM image showed that the main morphology of CuNP-6 tends to be spherical, and based on Fig. 3(a), particle size can be measured by taking and analyzing 45 points in the TEM image using

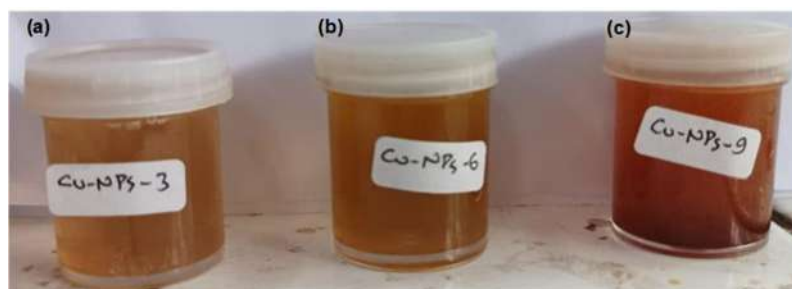


Fig 1. CuNP images synthesized from Cu(II) solution with a concentration of (a) 3.0 mM, (b) 6.0 mM, and (c) 9.0 mM

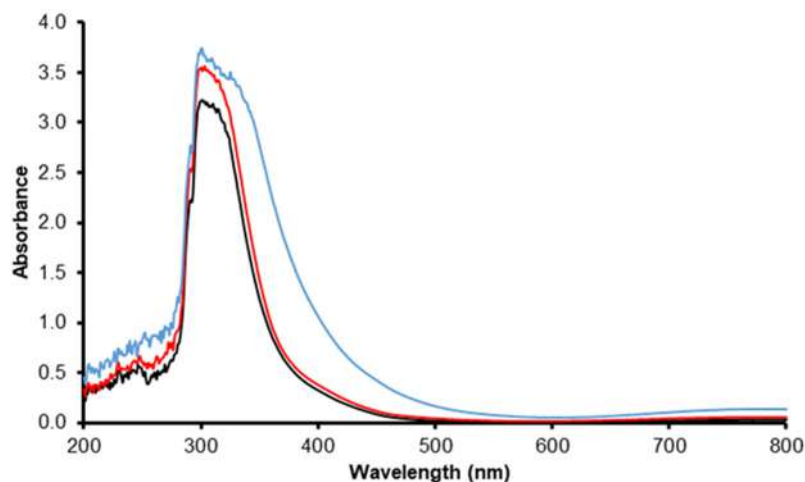


Fig 2. UV-Visible Spectra of CuNP colloids

ImageJ and OriginPro software. The histogram of the CuNP-6 particle size distribution is presented in Fig. 3(b), with an average of 28.08 nm.

Characteristics of MTA-CuNP

For hydration, 1 g of MTA powder was mixed with 0.5 mL of CuNP colloid (the mass-to-volume ratio of 2:1). It follows the hydration procedure for any commercial MTA. Characterization with the XRD instrument was performed on MTA, hydrated MTA, Cu-MTA-6, and Cu-MTA-9, and the patterns are presented in Fig. 4. Referring Crystallography Open Database (COD) and the value of 2θ , five components, namely C_2S , C_3S , C_3A , CaO , and Ta_2O_3 for MTA, and the presence of CuNPs for Cu-MTA can be obtained and presented in Table 1. Products of the hydration include calcium silicate hydrate (C-S-H),

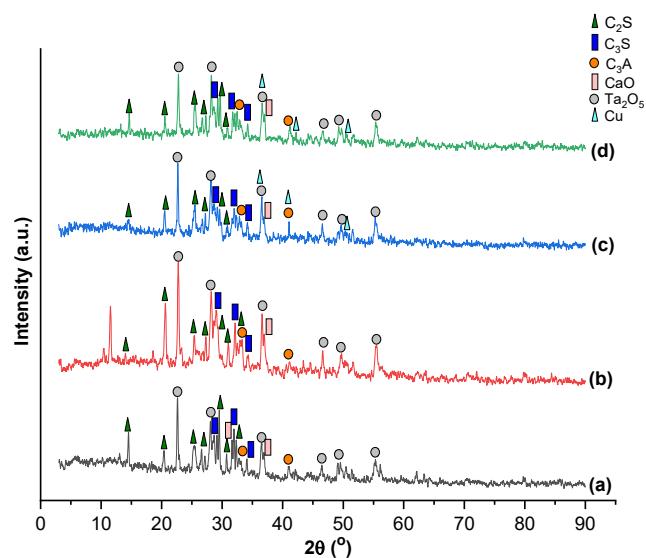


Fig 4. XRD pattern of (a) MTA, (b) Hydrated MTA, (c) Cu-MTA-6, and (d) Cu-MTA-9

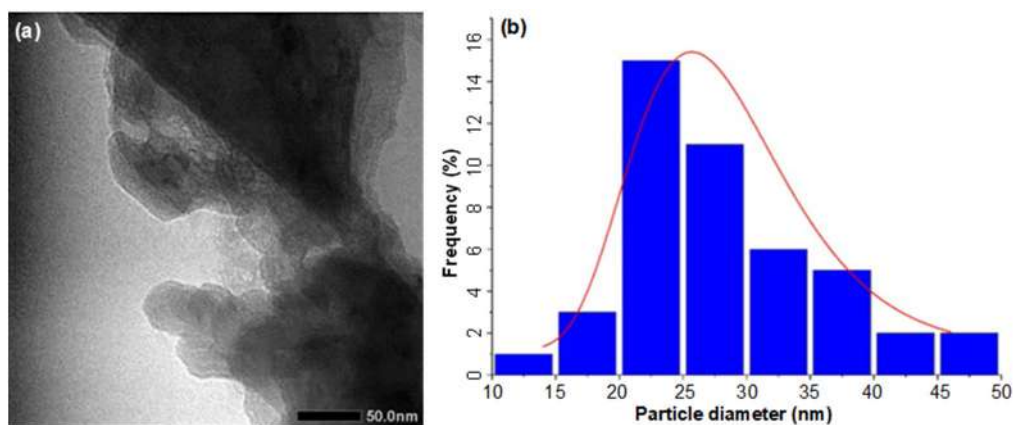


Fig 3. (a) TEM image and (b) particle size distribution histogram of CuNP-6

Table 1. Value 2θ peaks of XRD patterns

Composition	2θ (°)			
	Non-hydrated MTA	Hydrated MTA	Cu-MTA-6	Cu-MTA-9
C ₂ S (COD 00-210-3316)	14.54	14.06	14.52	14.64
	20.40	20.64	20.48	20.56
	27.18	27.32	27.24	27.30
	29.54	29.32	29.56	29.68
	30.78	31.04	30.92	30.96
C ₃ S (COD 00-154-0704)	29.20	29.06	29.16	29.24
	32.00	32.14	32.04	32.10
	34.12	34.30	34.24	34.28
C ₃ A (COD 00-901-4359)	33.12	33.30	32.92	32.98
	40.96	40.62	41.04	41.14
CaO (COD 00-900-6701)	36.84	37.00	36.94	37.04
Ta ₂ O ₅ (COD 00-153-1068)	22.66	22.76	22.70	22.80
	28.06	28.16	28.16	28.20
	36.58	36.60	36.56	36.62
	46.52	46.62	46.54	46.56
	49.58	49.70	49.68	49.74
Cu (JCPDS 01-089-2838)	55.32	55.50	55.28	55.36
			36.64	37.00
			41.10	41.30
		50.62	50.64	

calcium hydroxide (CH), monosulfate phase, and ettringite ($3\text{CaO}\cdot\text{Al}_2\text{O}_3\cdot 3\text{CaSO}_4\cdot 31\text{H}_2\text{O}$), supporting the previous report [19]. The peaks of CuNP are too low and are covered by the peaks of other components because the CuNP used is so tiny that the intensity is small and difficult to identify.

The intensity of C₂S and C₃S peaks in hydrated MTA, Cu-MTA-6, and Cu-MTA-9 is lower than in non-hydrated MTA. It is probable the water forms hydrated C₂S and C₃S that reduce the crystallinity [20]. Adding CuNP to the MTA (in Cu-MTA-6 and Cu-MTA-9 samples) reduces the intensity of C₂S and C₃S because the nanoparticles can provide more nucleation additional sites for the crystallization of calcium silicate hydrate and calcium hydroxide, which are hydration products replacing C₂S and C₃S [21].

Characterization was followed by an analysis of MTA, hydrated MTA, Cu-MTA-3, Cu-MTA-6, and Cu-MTA-9 samples using SEM-EDX instruments, as shown in Fig. 5. SEM images of MTA (Fig. 5(a)) still show a large

enough space when compared to MTA hydrated (Fig. 5(b)) because C-S-H formed during hydration strengthens and makes the strong interaction between particles [22]. The addition of CuNP makes the sample density increase since a small-sized CuNP (~28.08 nm) can fill the empty pores of the MTA, as seen in Cu-MTA-3 (Fig. 5(c)), Cu-MTA-6 (Fig. 5(d)), and Cu-MTA-9 (Fig. 5(e)). The sample density increases as the concentration of CuNP increases, indicating more CuNP can fill the space in the pores of the MTA sample. Testing continued using EDX, which showed the percentage of the composition of the elements in the sample in Table 2. The presence of CuNP, which is difficult to be confirmed with XRD, can be overcome with EDX data. CuNP of 1.87 to 2.95% of the mass can be found in Cu-MTA samples.

Compressive strength testing is one of the basic tests to be carried out because compressive strength indicates the MTA setting reaction and stability [23]. The results of compressive strength tests on the MTA,

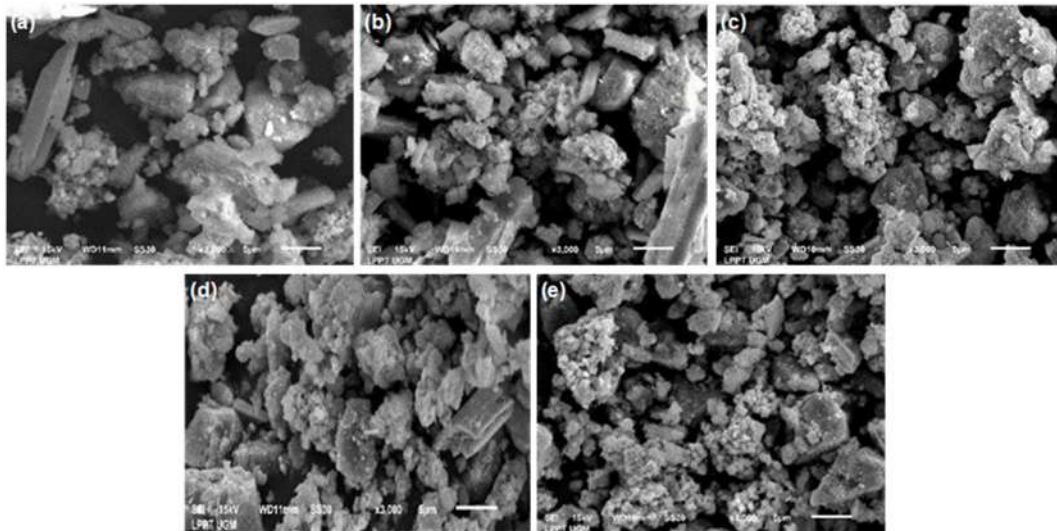


Fig 5. SEM image of 3000× magnification at (a) MTA, (b) MTA hydrated, (c) Cu-MTA-3, (d) Cu-MTA-6, and (e) Cu-MTA-9

Table 2. Mass percentage composition of all samples

Element	Mass (%)				
	MTA	MTA hydrated	Cu-MTA-3	Cu-MTA-6	Cu-MTA-9
O	34.54	34.00	38.99	45.21	39.19
Al	0.36	0.32	0.79	0.88	0.87
Si	1.25	0.79	3.40	3.33	3.33
Ca	27.41	9.77	21.24	25.12	21.35
Ta	36.44	55.00	33.71	22.67	31.81
Cu	-	-	1.87	2.79	2.95

Table 3. Compressive strength of samples after hydration for 14 days

Sample name	Compressive strength (MPa)
MTA	3.87±0.13
Cu-MTA-3	4.04±0.65
Cu-MTA-6	4.42±0.22
Cu-MTA-9	4.74±0.38

Cu-MTA-3, Cu-MTA-6, and Cu-MTA-9 are found in Table 3.

Table 3 shows that adding CuNP to the MTA increases the material's compressive strength, per previous research [24]. Adding copper to Portland cement can improve the cement's strength because the pores in the cement are filled with copper, which functions as a binder to the material during the hydration process [10]. The addition of nanoparticles to cement strengthens the structure of the cement because the nanoparticles act as

pore fillers, so there is a significant increase in cement density [25]. The rise in CuNP concentration causes the compressive strength value to be higher because more CuNP fills the pores in the MTA so that the density of the MTA increases. The results of the SEM-EDX analysis in Fig. 5 support the compressive strength because they show a greater morphological density of the sample as the increase of added CuNP concentrations.

The pH change was evaluated to determine the MTA's and Cu-MTA's alkalinity, which affects antibacterial properties [26]. The pH change in various hydration periods is presented in Table 4.

The highest pH is generated when the soaking of the sample is carried out on the first day, then decreases further and stabilizes at the alkaline pH from day 3 to 7. The obtained results follow the previous research [27-28]. The decrease in pH is relatively low to lead to a stable pH

Table 4. Result of pH test on MTA and Cu-MTA samples

Sample name	Days		
	1	3	7
MTA	8.55±0.05	7.96±0.16	7.83±0.01
Cu-MTA-3	9.01±0.03	8.19±0.03	8.13±0.01
Cu-MTA-6	8.73±0.09	8.07±0.07	8.03±0.07
Cu-MTA-9	8.68±0.09	8.02±0.10	7.94±0.05

the overtime the MTA material, and the variation of Cu-MTA will experience an increase in mechanical properties, causing the release of hydroxide ions into the environment to be reduced until it begins to stabilize [28]. The pH value obtained is already alkaline, so it is expected to be able to contribute to antibacterial properties.

The diffusion of Ca(II) ions from MTA, Cu-MTA-3, Cu-MTA-6, and Cu-MTA-9 was evaluated because calcium is the main component in MTA, namely C_2S , C_3S , C_3A , and CaO [22]. The test results are shown in Fig. 6. It can be seen that the highest release of Ca(II) ions for all samples occurs on the first day of immersion and then decreases on the next day, and it follows previous research [28]. The diffusion of Ca(II) ions correlates with the pH value because in forming hydration products in the form of C-S-H, $Ca(OH)_2$ compounds are also produced, which will be ionized and are responsible for the diffusion of Ca(II) ions, and the resulting pH value. An increase in the concentration of Ca(II) ions leads to a higher resulting pH value [27]. This can be proved by comparing Table 4 and

Fig. 6, which have similarities in the sample order. Material Cu-MTA-3 has the highest diffusion of Ca(II) ions because using CuNP accelerates the hydration process, resulting in more hydration products, especially $Ca(OH)_2$ [21], so there is an increase in Ca cations from the MTA material. This reason also can be applied to Cu-MTA-6 and Cu-MTA-9. Both variations have more CuNP concentrations that can cover the pores where Ca(II) ions come out. This statement can be proven by the SEM-EDX image (Fig. 5), which shows that the presence of CuNP in MTA increases the density (small pores). The lost calcium is used to prevent dental demineralization, accelerate tooth mineralization, and repair and regenerate bone damage [29].

Solubility testing aims to evaluate the stability of MTA and Cu-MTA samples in an aqueous solution. The solubility of MTA, Cu-MTA-3, Cu-MTA-6, and Cu-MTA-9 samples are presented in Table 5.

The solubility of Cu-MTA samples is higher than MTA because CuNP can accelerate the hydration resulting in more $Ca(OH)_2$ as a hydration product. One of the ionization results of $Ca(OH)_2$ is the Ca(II) cation which is the main constituent component of the MTA, so when the Ca(II) is released from the MTA, it increases in the solubility of the Cu-MTA. The study results follow the results obtained from pH testing and diffusion of Ca(II) ions. High solubility values not only have a negative

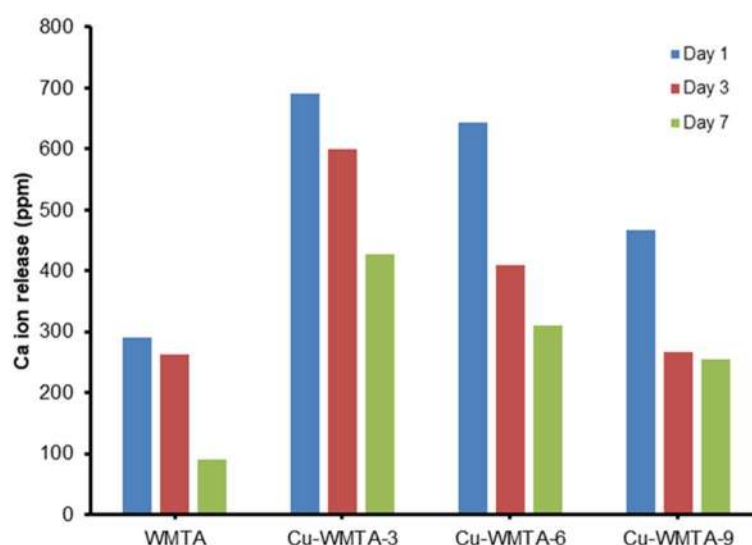
**Fig 6.** Diagram of Ca(II) ion released from MTA samples after various days of hydration

Table 5. The solubility of MTA samples after 14 days of hydration

Sample name	Solubility	
	Mass (mg)*	Percentage (%)**
MTA	10.19±0.53	17.00±0.96
Cu-MTA-3	14.05±0.57	22.48±0.37
Cu-MTA-6	12.06±0.28	20.68±0.61
Cu-MTA-9	11.29±0.24	19.08±0.54

*the mass of the initial sample minus the mass of the final sample (after soaking)

**Percentage of the dissolved mass to the mass of the initial sample

impact on the teeth but also have some positive benefits. $\text{Ca}(\text{OH})_2$ can reduce inflammatory processes, dissolve dead dental tissue, and heal periapical tissue in the teeth [30].

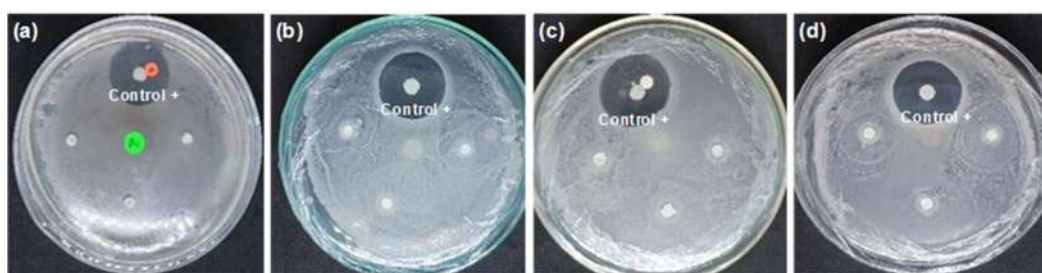
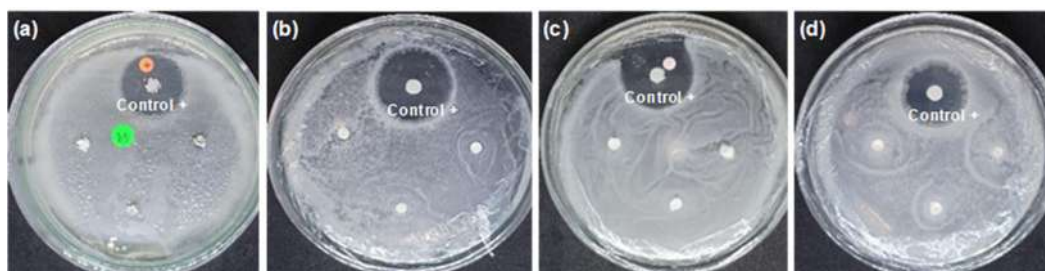
The antibacterial properties test aims to evaluate the effect of adding CuNP with various concentrations on the MTA antibacterial activity. The bacteria investigated are *S. aureus*, a Gram-positive bacteria, and *P. aeruginosa*, a Gram-negative bacteria. Both are found in teeth [31]. The results of testing the antibacterial properties, presented as inhibition zones, of MTA, Cu-MTA-3, Cu-MTA-6, and Cu-MTA-9 can be seen in Fig. 7 for *S. aureus* bacteria and Fig. 8 for *P. aeruginosa* bacteria. Observations were made on MTA samples on the 7th day after hydration.

The inhibition zone diameters of the antibacterial test presented in Fig. 7 and 8 were measured using calipers, and the result is summarized in Table 6.

Table 6 shows that MTA does not have inhibitory capability against both *S. aureus* and *P. aeruginosa* bacteria. There is no component in MTA acting as the antibacterial agent, and the pH of MTA is around 8 and 9 (Table 4). Both bacteria, *S. aureus*, and *P. aeruginosa*, still grow in the pH range of 4.0 to 9.8 [32-33]. CuNP, an antibacterial agent [34], is still active even though combined with MTA. The antibacterial performance mechanism is probably different from MTA modified with CaF_2 [14] and fluorohydroxiapatite [15], in which the higher pH leads to bacterial death. The CuNP on the MTA surface may interact with the bacterial cells causing bacterial cell leakage and leading to lysed and death [35].

Table 6. The results of the measurement of the inhibition zone of the MTA and Cu-MTA samples

Sample name	Inhibition zone (mm)	
	<i>S. aureus</i>	<i>P. aeruginosa</i>
MTA	0	0
Chloramphenicol	25.17±1.31	27.00±1.41
Cu-MTA-3	8.30±0.53	8.42±0.78
Cu-MTA-6	9.20±0.25	9.74±0.88
Cu-MTA-9	10.15±0.47	11.93±1.16

**Fig 7.** Inhibition zone of *S. aureus* tested with (a) MTA; (b) Cu-MTA-3; (c) Cu-MTA-6; (d) Cu-MTA-9**Fig 8.** Inhibition zone of *P. aeruginosa* tested with (a) MTA; (b) Cu-MTA-3; (c) Cu-MTA-6; (d) Cu-MTA-9

Yadav et al. [34] reported that CuNP interacts with DNA and the protoplasm of bacterial cells, causing DNA damage, and bacteria cannot carry out cell metabolism.

■ CONCLUSION

Copper nanoparticles have been successfully synthesized by reacting the precursors of $\text{CuCl}_2 \cdot 2\text{H}_2\text{O}$, the protective agent of L-ascorbic acid, and NaBH_4 , as a reducing agent, to produce spherical CuNP with the particle size of ~28.08 nm. Hydration of MTA with CuNP colloid improved the compressive strength, pH, Ca(II) ions release, solubility, and antibacterial properties. Using CuNP colloid prepared from 9.0 mM Cu(II) solution increased the compressive strength from 4 to 4.74 MPa and showed antibacterial activity with the inhibitor zone diameters of 10.15 mm for *S. aureus* bacteria and 11.93 mm for *P. aeruginosa*. The modified MTA is the potential to be implemented for endodontic material containing antibacterial agents.

■ ACKNOWLEDGMENTS

The authors would like to thank the Research Directorate, Universitas Gadjah Mada, through the research grant *Penelitian Dasar Unggulan Perguruan Tinggi* (PDUPT), contract number: 1651/UN1/DITLIT/Dit-Lit/PT.01.03/2022 for the financial support.

■ REFERENCES

- [1] Napitupulu, R.L.Y., Adhani, R., and Erlita, I., 2019, Hubungan perilaku menyikat gigi, keasaman air, pelayanan kesehatan gigi terhadap karies di MAN 2 Batola, *Dentin*, 1 (3), 17–22.
- [2] Bachtiar, Z.A., 2016, Perawatan saluran akar pada gigi permanen anak dengan bahan gutta percha, *Jurnal PDGI*, 2 (65), 60–67.
- [3] Patel, N., Patel, K., Baba, S.M., Jaiswal, S., Venkataraghavan, K., and Jani, M., 2014, Comparing gray and white mineral trioxide aggregate as a repair material for furcation perforation: An *in vitro* dye extraction study, *J. Clin. Diagn. Res.*, 8 (10), ZC70–ZC73.
- [4] Butt, N., Talwar, S., Chaudhry, S., Nawal, R.R., Yadav, S., and Bali, A., 2017, Comparison of physical and mechanical properties of mineral trioxide aggregate and biodentine, *Indian J. Dent. Res.*, 25 (6), 692–697.
- [5] Kaur, M., Singh, H., Dhillon, J.S., Batra, M., and Saini, M., 2017, MTA versus biodentine: Review of literature with a comparative analysis, *J. Clin. Diagn. Res.*, 11 (8), ZG01–ZG05.
- [6] Mohammadi, Z., Giardino, L., Palazzi, F., and Shalavi, S., 2012, Antibacterial activity of a new mineral trioxide aggregate-based root canal sealer, *Int. Dent. J.*, 62 (2), 70–73.
- [7] Gürel, M., Demiryürek, E.Ö., Özyürek, T., and Gülhan, T., 2016, Antimicrobial activities of different bioceramic root canal sealers on various bacterial species, *Int. J. Appl. Dent. Sci.*, 2, 19–22.
- [8] Akhidime, D., Saubade, F., Benson, P., Butler, J., Olivier, S., Kelly, P., Verran, J., and Whitehead, K., 2018, The antimicrobial effect of metal substrates on food pathogens, *Food Bioprod. Process.*, 113, 68–76.
- [9] Ghasemian, E., Naghoni, A., Rahvar, H., Kialha, M., and Tabaraie, B., 2015, Evaluating the effect of copper nanoparticles in inhibiting *Pseudomonas aeruginosa* and *Listeria monogtogenes* biofilm formation, *Jundishapur J. Microbiol.*, 8 (5), e17430.
- [10] Nazer, A., Payá, J., Borrachero, M.V., and Monzó, J., 2016, Use of ancient copper slags in Portland cement and alkali activated cement matrices, *J. Environ. Manage.*, 167, 115–123.
- [11] Liu, S., Li, Q., and Zhao, X., 2018, Hydration kinetics of composite cementitious materials containing copper tailing powder and graphene oxide, *Materials*, 11 (12), 2499.
- [12] Saghiri, M.A., Kazerani, H., Morgano, S.M., and Gutmann, J.L., 2020, Evaluation of mechanical activation and chemical synthesis for particle size modification of white mineral trioxide aggregate, *Eur. Endod. J.*, 5 (2), 128–133.
- [13] Yuliatun, L., Kunarti, E.S., Widjijono, W., and Nuryono, N., 2022, Enhancing compressive strength and dentin interaction of mineral trioxide aggregate by adding SrO and hydroxyapatite, *Indones. J. Chem.*, 22 (6), 1651–1662.
- [14] Lim, M., and Yoo, S., 2022, The antibacterial activity of mineral trioxide aggregate containing calcium fluoride, *J. Dent. Sci.*, 17 (2), 836–841.

- [15] Bolhari, B., Sooratgar, A., Pourhajibagher, M., Chitsaz, N., and Hamraz, I., 2021, Evaluation of the antimicrobial effect of mineral trioxide aggregate mixed with fluorohydroxyapatite against *E. faecalis* *in vitro*, *Sci. World J.*, 2021, 6318690.
- [16] Pushpa, S., Maheshwari, C., Maheshwari, G., Sridevi, N., Duggal, P., and Ahuja, P., 2018, Effect of pH on solubility of white mineral trioxide aggregate and biodentine: An *in vitro* study, *J. Dent. Res. Dent. Clin. Dent. Prospects*, 12 (3), 201–207.
- [17] Cerda, J.S., Gomez, H.E., Nunez, G.A., Rivero, I.A., Ponce, Y.G., and Lopez, L.Z.F., 2017, A green synthesis of copper nanoparticles using native cyclodextrins as stabilizing agents, *J. Saudi Chem. Soc.*, 21 (3), 341–348.
- [18] Suprpto, S., Handoyo, C.A.H., Senja, P.A., Ramadhan, VB, and Ni'mah, Y.L., 2020, synthesis of copper nanoparticles using *Chromolaena odorata* (L.) leaf extract as a stabilizing agent, *Indones. J. Chem. Anal.*, 3 (1), 9–16.
- [19] Camilleri, J., 2007, Hydration mechanism of mineral trioxide aggregate, *Int. Endod. J.*, 40 (6), 462–470.
- [20] Akhavan, H., Mohebbi, P., Firouzi, A., and Noroozi, M., 2015, X-ray Diffraction analysis of ProRoot mineral trioxide aggregate hydrated at different pH values, *Iran. Endod. J.*, 11 (2), 111–113.
- [21] Wang, X., 2017, Effects of Nanoparticles on the Properties of Cement-Based Materials, *Dissertation*, Civil Engineering Iowa State University, Iowa, US.
- [22] Altan, H., and Tosun, G., 2016, The setting mechanism of mineral trioxide aggregate, *J. Istanbul Univ. Fac. Dent.*, 50 (1), 65–72.
- [23] Sobhnamayan, F., Adl, A., Shojaee, N.S., Sedigh-Shams, M., and Zarghami, E., 2017, Compressive strength of mineral trioxide aggregate and calcium-enriched mixture cement mixed with propylene glycol, *Iran. Endod. J.*, 12 (4), 493–496.
- [24] Akbari, M., Zebarjad, S.M., Nategh, B., and Roubani, R., 2013, Effect of nano-silica on setting time and physical properties of mineral trioxide aggregate, *J. Endod.*, 39 (11), 1448–1451.
- [25] Nazari, A., and Riahi, S., 2011, Effects of CuO nanoparticles on compressive strength of self-compacting concrete, *Sādhanā*, 36 (3), 371–391.
- [26] Farrugia, C., Baca, P., Camilleri, J., and Arias Moliz, M.T., 2017, Antimicrobial activity of ProRoot MTA in contact with blood, *Sci. Rep.*, 7, 41359.
- [27] Abu Zeid, S.T.H., Alothmani, O.S., and Yousef, M.K., 2015, Biodentine and mineral trioxide aggregate: An analysis of solubility, pH changes, and leaching element, *Life Sci. J.*, 12 (4), 18–23.
- [28] Wibowo, M.W.A., Yunita, A.I., Mukaromah, L., Kartini, I., and Nuryono, N., 2022, Effect of titania and silver nanoparticles on the tensile strength of cement-like mineral trioxide aggregate, *Mater. Sci. Forum*, 1068, 183–188.
- [29] Al-Sanabani, J.S., Madfa, A.A., and Al-Sanabani, F.A., 2013, Application of calcium phosphate materials in dentistry, *Int. J. Biomater.*, 2013, 876132.
- [30] Dewiyani, S., 2011, Calcium hydroxide as intracanal dressing for teeth with apical periodontitis, *Dent. J.*, 44 (1), 12–16.
- [31] Yamin, I.F., and Natsir, N., 2014, Bakteri dominan di saluran akar gigi nekrosis, *Dentofasial*, 13 (2), 113–116.
- [32] Valero, A., Pérez-Rodríguez, F., Carrasco, E., Fuentes-Alventosa, J.M., García-Gimeno, R.M., and Zurera, G., 2009, Modelling the growth boundaries of *Staphylococcus aureus*: Effect of temperature, pH and water activity, *Int. J. Food Microbiol.*, 133 (1-2), 186–194.
- [33] Klein, S., Lorenzo, C., Hoffmann, S., Walther, J.M., Storbeck, S., Piekarski, T., Tindall, B.J., Wray, V., Nimtz, M., and Moser, J., 2009, Adaptation of *Pseudomonas aeruginosa* to various conditions includes tRNA-dependent formation of alanyl-phosphatidylglycerol, *Mol. Microbiol.*, 71 (3), 551–565.
- [34] Yadav, L., Tripathi, R.M., Prasad, R., Pudake, R.N., and Mittal, J., 2017, Antibacterial Activity of Cu Nanoparticles against *E. coli*, *Staphylococcus aureus* and *Pseudomonas aeruginosa*, *Nano Biomed. Eng.*, 9 (1), 9–14.
- [35] Brooks, G.F., Carroll, K.C., Butel, JS, and Morse, S.A., 2007, *Medical Microbiology*, McGraw-Hill Medical, New York, US.

Adsorption Isotherms for CBY 3G-P Dye Removal from Aqueous Media Using TiO₂ Degussa, Fe₂O₃, and TiO₂/DPC

Shireen Abdulmohsin Azeez, Fadhela Muhammad Hussein, and Rasha Wali Mohi Al-Saedi*

Department of Chemistry, College of Science, Mustansiriya University, Baghdad 10052, Iraq

* Corresponding author:

email:

rwmal_saedi2@uomustansiriya.edu.iq

Received: December 2, 2022

Accepted: March 7, 2023

DOI: 10.22146/ijc.79706

Abstract: The adsorption of Cibacron Brilliant Yellow (CBY) 3-GP dye onto TiO₂ Degussa, Fe₂O₃, and TiO₂ anatase/Diphenylcarbide in aqueous solution was studied with respect to temperature, contact time, and pH. The CBY 3-GP adsorption at equilibrium increased as the initial dye concentration increased for TiO₂/DPC, while it decreased for TiO₂ Degussa; however, it increased the initial dye concentration. The best removal efficiency was obtained at 1 mg for TiO₂/DPC, TiO₂ Degussa, and the amount of adsorption decreases with the rising of temperature. The negative ΔH° reveals the adsorption is exothermic and extremely negative ΔS° for TiO₂ Degussa. The negative value for ΔS° indicates a regular increase of the randomness at the TiO₂/DPC and Fe₂O₃ solution interface during adsorption. The intraparticle diffusion, pseudo-first- and second-order kinetic models were used. The Langmuir, Temkin, Freundlich, and Dubbin adsorption models were examined to describe the equilibrium isotherms. The usage of TiO₂ Degussa and TiO₂/DPC indicates that the equilibrium sorption was favorable.

Keywords: CBY dye; adsorption models; TiO₂ Degussa; Fe₂O₃; kinetic study; dynamic data

■ INTRODUCTION

Due to their beneficial properties, such as strong interaction with the substrate, bright color, water-fastness, simple application techniques, and lower energy consumption required for the dyeing process, numerous highly reactive dyes, such as Cibacron Brilliant Yellow 3G-P (CBY) have been used in dyeing processes [1]. These characteristics reduce the water's clarity discharge since relatively small volumes of highly reactive dyes may result in ugly water discoloration and can have a very negative effect on waterways and biological systems. Therefore, the color removal from the effluents of the dye and textile industries is of great environmental significance. For the purpose of removing dye from wastewater effluents before release, a variety of wastewater treatment applications for processes such as chemical oxidation, coagulation, adsorption, filtering, and electrolysis have been made. The removal of colored materials, particularly dye, has been attempted using a variety of procedures that can be broadly categorized as physical, chemical, or biological treatment strategies, with varying degrees of

success. The notable techniques are membrane separation, photodegradation, ozonation, adsorption, coagulation/flocculation, and biodegradation [2]. Because of its effectiveness, adsorption becomes one of the most well-known wastewater treatment techniques. Due to its operational importance in terms of technology, environment, and biology, adsorption is typically thought of as a significant separation process. Aqueous solutions, wastewater, and huge quantities of potable water are processed using a separation method that prioritizes the removal of low concentrations of contaminants [3].

One of the biggest threats to humanity is water contamination, which is linked to rapid industrialization and has generated a lot of research overall [4]. Due to their non-biodegradable characteristics, organic, and synthetic dyes—contaminant effluents removed from various food and textile industries—are one of the main sources of environmental contamination [5]. The most common method for removing dissolved organics from water is the adsorption process. For the removal of dye,

a variety of unconventional, affordable adsorbents has been tried. Peat-activated sludge, organic peel waste, tree fern [6], and minerals are a few of these. Additionally, the removal of color using activated carbon is made from unconventional sources such as sawdust, rice husk, and coir pith [7]. Therefore, it is essential to develop workable techniques to decrease the pollution brought on by Zn^{2+} discharges and to lower the dangers connected with its environmental presence. Industrial effluents can be treated in a variety of ways to remove heavy metal ions, which include ion exchange, solvent extraction, biodegradation, and adsorption [8]. Adsorption, however, is widely acknowledged as one of the most efficient methods for removing pollutants because of its low cost, ease of handling, low reagent usage, and potential for recovering value-added components through desorption and regeneration of adsorbent [9].

The most determinants of adsorption are greater adsorption ability implied by a larger surface area. The internal diffusion and mass transfer limitations to the penetration of the adsorbate into the adsorbent are decreased with smaller particle sizes (i.e., nearly complete adsorption capacity can be reached, and equilibrium is easier to achieve). The adsorption will be more thorough the longer the period of time.

Adsorption will be easier for substances with low solubility in water than for those with high solubility. Additionally, because non-polar compounds have a weaker affinity for water, they will be easier to remove than polar substances. The pH has an effect on a species' level of ionization. This then has an influence on adsorption.

Because the adsorbate molecules have higher vibrational energies and are, therefore, more likely to desorb from the surface, increasing the temperature generally reduces adsorption slightly. All of the applications that are relevant to us, however, take place in isothermal conditions. Various compounds that are particulate and have one dimension smaller than 100 nm in size make up the diverse class of materials known as nanoparticles (NPs) [10]. These materials can be 0D, 1D, 2D, or 3D, depending on the overall shape [11]. When researchers found that a substance's size could affect its physiochemical characteristics, such as its optical

capabilities, they realized the significance of these materials. Semiconductor NPs have broad bandgaps, which led to a considerable change in their characteristics when the bandgap was tuned. Because of this, they are critical elements of photocatalysis, photo optics, and electronic devices. As an example, due to their optimal bandgap and band edge locations, a number of semiconductor NPs are discovered to be highly effective in water-splitting applications [12].

In this work, TiO_2 Degussa, Fe_2O_3 , and TiO_2 anatase/Diphenylcarbide (DPC) were used for the adsorption of CBY dye in an aqueous solution. The adsorption of CBY was first studied in a batch system by examining the effect of CBY concentration, contact time, and temperature, in several adsorption models Freundlich, Temkin, Dubbin, and Langmuir. Also, the kinetic data were evaluated in the adsorption process. Thermodynamic parameters were investigated that the adsorption of CBY on TiO_2 Degussa, TiO_2 /DPC, and Fe_2O_3 .

■ EXPERIMENTAL SECTION

Materials

The materials used in this study were ($C_{25}H_{15}Cl_3N_9Na_3O_{10}S_3$, Fig. 1) CBY 3G-P (Sigma Aldrich (USA)), titanium(IV) *i*-propoxide ($Ti(OiPr)_4$, 99.9% purity), Fe_2O_3 , and TiO_2 Degussa were acquired from Sigma Aldrich (USA). Ethyl alcohol (EtOH Merck), DPC, HNO_3 (BDH. Co, LTD), sodium hydroxide NaOH (99% purity GCC, UK), and HCl (BDH) were purchased from other companies.

Instrumentation

The instrumentations used in this study were X-ray diffraction spectroscopy (D5000 XRD6000, Shimadzu, Japan), scanning electron microscopy (INSPECT S50 FEL, USA), atomic force microscopy (Sartorius Arium 611), and transmission electron microscopy TEM (Germany).

Procedure

Preparation of TiO_2 /DPC

$Ti(OiPr)_4$ in ethanol was used to dissolve TiO_2 before being mixed with distilled water at a molar ratio

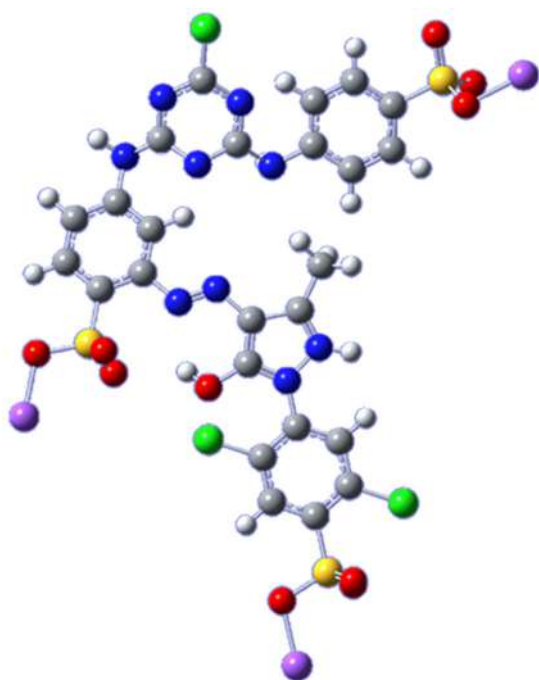


Fig 1. The chemical structure of CBY. Grey, white, blue, green, yellow, red, and purple color represent carbon, hydrogen, nitrogen, chlorine, sulfur, oxygen, and sodium atom, respectively

of TTIP:H₂O = 1:4 to produce the sol-gel TiO₂. HNO₃ was employed to change the pH and restrain the solution's hydrolysis process. The obtained solutions were stirred slowly and continuously for 40 min at room temperature. The gels were dried for 1.5 h at 500 °C to completely evaporate water and organic material in order to produce NPs [13]. Following ball milling [14], the resultant dry powders were subjected to a 2 h calcination process at 400 °C to produce TiO₂ nanocrystals. As for creating TiO₂/DPC, add 0.1 mol of DPC that has been dissolved in ethanol and 1.0 mol of the TiO₂ NPs solution that has been prepared previously. The mixture was stirred at room temperature for 30 min while it is separated by a centrifuge for 15 min, and then washed several times with water and ethanol to get rid of any extra residue. The material was taken, aged for 24 h, and then dried at 90 °C for 4 h before being stored for further analysis.

Adsorption experiments

The appropriate quantity (1 g) of CBY was dissolved in a liter of deionized water to create a stock solution at a

concentration of 1 g/L. The stock solution was diluted with deionized water to create the working solutions, which were then given the proper concentration.

Erlenmeyer flasks containing 50 mL solution of 3G-P using TiO₂ Degussa, or TiO₂/DPC or Fe₂O₃ as adsorbent. The effect of various parameters, including solution pH 3–9, contact time 15–150 min, initial CBY concentration 2.18–10.9 mg/L, adsorbent dosage 1–5 mg, and temperature 15–90 °C was investigated. The pH of solutions was adjusted using 0.1 M HCl and/or 0.1 M NaOH. After each test, the adsorbent was separated from the aqueous solution, and the residual CBY in the aqueous solution was determined using absorption spectrometry. Double-beam UV-visible spectrophotometer was used to determine the concentrations of CBY dye in the solution. The concentration of the residual dye was measured at a maximum for the dye solution (428 nm) by taking samples at predetermined intervals, centrifuging them, and checking the supernatant for any remaining CBY. Based on a mass balance calculation, Eq. (1), the amount of adsorbed CBY (mg/g) was determined [15].

$$q_e = \frac{(C_0 - C_e)V}{M} \quad (1)$$

where C_e is the final or equilibrium concentration of CBY in the solution (mg/L), V is the volume of the solution (L), and W is the mass of TiO₂ Degussa, or TiO₂/DPC or Fe₂O₃ (g), q_e is the equilibrium adsorption capacity per gram weight of the adsorbent, and C_0 is the initial concentration of CBY in the solution (mg/L).

The flasks were shaken at 298 K for 2 h at a steady speed of 200 rpm. During the current investigation, the effects of factors such as the initial concentration and adsorbent dose were evaluated.

Effect of CBY initial concentration and contact time. The dye solutions were placed in an isothermal water bath shaker at initial concentrations of 2.18, 4.36, 6.55, 8.73, and 10.9 mg/L. For 24 h, the water bath shaker's temperature and rotational speed were set at 25 °C and 200 rpm, respectively.

Effect of temperatures. By varying the adsorption temperatures at 15, 30, 45, 60, 75, and 90 °C by adjusting the water bath shaker's temperature controller, the effect

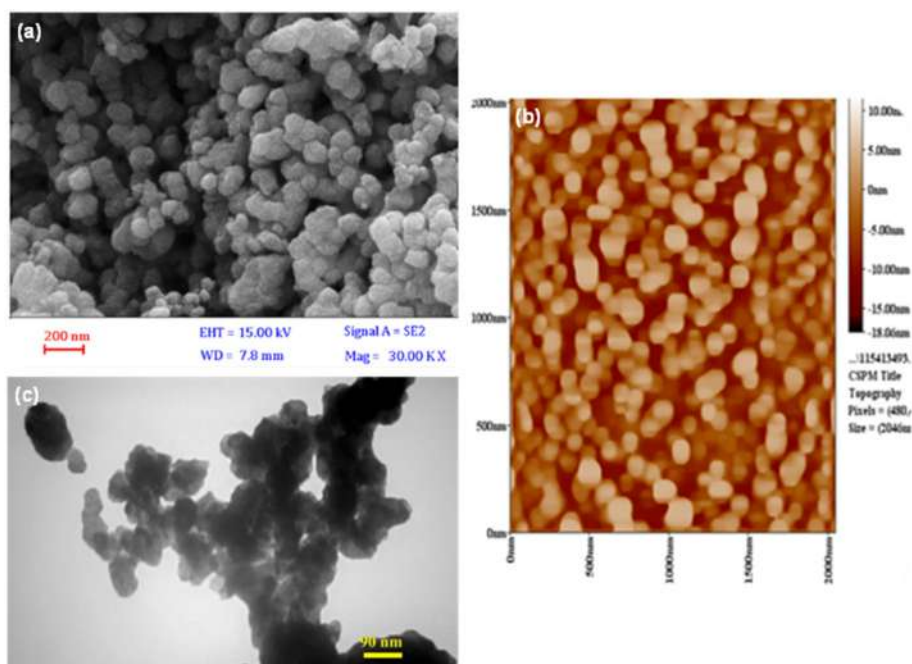


Fig 2. (a) SEM of TiO_2/DPC nanoparticle, (b) AFM of TiO_2/DPC nanoparticle, and (c) TEM of TiO_2/DPC nanoparticle

of temperatures on the adsorption process was investigated. The pH of the solution and other variables were left unchanged.

■ RESULTS AND DISCUSSION

Characterization of Adsorbents

The TiO_2 Degussa P25 crystallites are composed of 80% anatase and 20% rutile. Because of its inexpensive nature, great chemical stability, and reactivity, TiO_2 catalyst provides unique properties for a variety of environmental applications. Due to the wide surface area of the adsorption site, TiO_2 has good sorption properties. When there is a large concentration of hydroxyl groups (OH) on the surface of TiO_2 , the contaminants can be adsorbed onto the material [16-17].

The group of iron-oxide minerals includes Fe_2O_3 crystals, which have a hexagonal shape and exhibit paramagnetic properties. Fe_2O_3 oxide can be activated under visible irradiation due to its small band gap (2.3 eV). Moreover, they have a powerful catalytic effect, are widely and simply accessible, and are incredibly ecologically friendly. Fe_2O_3 catalyst has the advantages of strong toxicity resistance and high catalytic activity [18].

Fig. 2(a) shows the SEM morphology images of TiO_2/DPC . The results indicate that the fine TiO_2/DPC has a spherical shape with dispersion nanoparticles the particle size of the TiO_2/DPC nanoparticle is 67 nm. The characteristic of TiO_2/DPC nanoparticles is determined by AFM as shown in Fig. 2(b), the particles size of TiO_2/DPC is 94.9 nm, while TEM images of sol-gel derived nanoparticles are shown in Fig. 2(c) is spherical and having diameter 37 nm. The band gap energy (E_g) of TiO_2/DPC is 2.1 eV which is smaller than the value of 3.2 eV for the bulk TiO_2 .

Semiconductor NPs are materials that have properties that fall between those of metals and nonmetals. Substantial changes to their electrical and optical characteristics with a change in particle size. Due to their broad bandgaps, semiconductor NPs have demonstrated considerable changes in their characteristics when the bandgap is tuned. In light of this, they are finding use in photocatalysis, photo-optics, and electric devices [19].

Effect of Contact Time and Initial Concentration of Adsorbate

By varying the concentration of CBY solutions

between 2.18, 4.36, 6.55, 8.73, and 10.9 mg/L, it was possible to study the effect of increasing CBY concentrations on the adsorption onto TiO₂/DPC, TiO₂ Degussa, and Fe₂O₃ as shown in Fig 3. For TiO₂/DPC at 75 min, the CBY adsorption increased from 4.69 to 13.33 mg/g as the initial dye concentration increased from 1.6 to 9.17 mg/L. The results indicate that when CBY concentrations rise, so does the amount of adsorption, and they become constant. This occurs because the availability of CBY molecules at the interface rises with increased CBY concentration, which in turn improves the adsorption while decreasing from 2.25 to 0.078 mg/g for TiO₂ Degussa at 90 min. However, increased from 13 to 30.6 mg/g as the initial dye concentration. This phenomenon was due to an increase in the driving force of the concentration gradient as an increase in the initial dye concentration, then decreased to 2.3 mg/g for Fe₂O₃ at 60 min. Due to a large number of available surface sites, CBY was quickly adsorbed; however, as the process progressed toward equilibrium, it became difficult for CBY to interact with TiO₂ Degussa or Fe₂O₃ surface when all of the accessible sites were occupied, leading to saturated adsorption. Repulsion between the solute molecules and the bulk phases developed as a result of the difficulty in filling the remaining surface of sites [20].

Effect of pH

Adsorption isotherm of CBY onto TiO₂/DPC, TiO₂ Degussa, and Fe₂O₃ at different pH was recorded at pH 3 was more in compression pH at range 3, 4, 7, and 9. Since it was found that changing from an acidic to a basic medium's higher pH value considerably lowered the adsorption density of CBY. However, the adsorption increased with decreased pH to a value of around 3. As the pH is decreased, the positive charge on the surfaces of TiO₂/DPC and Fe₂O₃ increases. CBY is a non-ionic molecule that is easily adsorbed onto TiO₂/DPC, Fe₂O₃, and TiO₂ Degussa at a lower pH. The adsorption capabilities were greater in the acidic and neutral pH ranges and the lowest in the alkaline pH ranges. Whereas, at higher pH 9, Since the adsorbents are negatively charged, electrostatic repulsion reduces the rate of the sorption process. It is also understood that increasing pH

results in an increase in hydroxyl ions, which reduces the adsorption capacities, the experimental data of the pH effect is in Table 1.

Effect of Adsorbent Weight

By using various concentrations of TiO₂/DPC, TiO₂ Degussa, and Fe₂O₃ ranging from 1 to 5 mg, q_e is CBY dye adsorbed amount on TiO₂/DPC, TiO₂ Degussa, and Fe₂O₃. The results showed in Table 2, in which the best-adsorbed amount was obtained at 1 mg for TiO₂/DPC and TiO₂ Degussa. The reason for this is that as the dosage of the adsorbent was increased, the adsorption

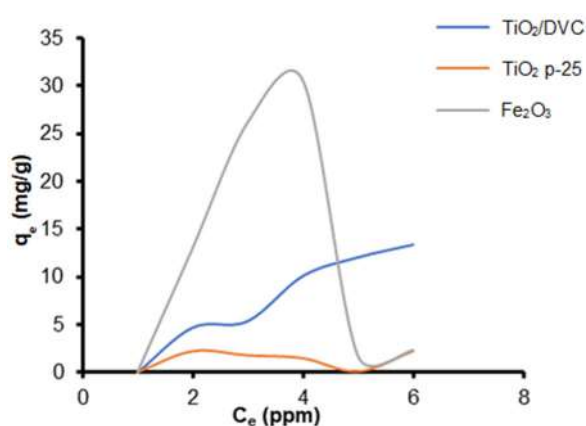


Fig 3. Adsorption effect of CBY solutions onto TiO₂/DPC, TiO₂ Degussa and Fe₂O₃

Table 1. Effect of solution pH on CBY adsorption (adsorbent TiO₂/DPC, TiO₂ Degussa, and Fe₂O₃), 75 min

Adsorbent	pH 3	pH 4	pH 7	pH 9
	q _e (mg/g)			
TiO ₂ Degussa	6.06	3.98	8.18	0.90
TiO ₂ /DPC	0.63	0.56	0.46	0.46
Fe ₂ O ₃	13.1	9.62	1.21	2.42

Table 2. Different quantities of TiO₂/DPC, TiO₂ Degussa, and Fe₂O₃ with the amount of adsorption

Weight (mg)	TiO ₂ /DPC	TiO ₂ Degussa	Fe ₂ O ₃
	q _e (mg/g)		
1	8.80	7.00	4.00
2	6.90	2.60	4.60
3	4.67	2.00	0.20
4	3.50	3.70	0.10
5	2.80	1.60	3.28

capability decreased, creating 2 mg of Fe_2O_3 the best-adsorbed amount. The interference and collision of active adsorbent sites at larger adsorbent dosages or the inability of the CBY dye in the solution to establish bonds with the accessible and active sites on the adsorbent to explain this result surfaces of TiO_2/DPC , TiO_2 Degussa, and Fe_2O_3 [21-22].

Effect Temperatures on CBY Adsorption

The results of a study of the effect of temperature on CBY adsorption at 15, 30, 45, 60, 75, and 90 °C can be used to indicate the exothermic nature of adsorption in detail. The increased tendency of the CBY to escape from the surface of TiO_2/DPC , TiO_2 Degussa, and Fe_2O_3 may be the cause of the decrease in adsorption as the temperature rises. Adsorption decreases when the temperature rises because the CBY's binding forces to the surface are reduced [23].

Increasing the temperature has improved the diffusion of dye molecules across the sample's exterior and internal boundary layers since it has reduced the viscosity of the solution [24]. Additionally, at higher temperatures, more dye molecules are mobile because they have more energy to interact with the adsorbent's active sites, allowing the dye to enter the pores of the adsorbent [25].

Effect of Temperature on Thermodynamic Parameters

From 15 to 55 °C, the influence of temperature on CBY adsorption on TiO_2/DPC , TiO_2 Degussa, and Fe_2O_3 (Fig 4) was studied. Eq. (2) and (3) can be used to get the Gibbs energy, G^0 (J/mol).

$$\Delta G^0 = \Delta H^0 - T\Delta S^0 \quad (2)$$

$$\Delta G^0 = -RT \ln K_c \quad (3)$$

The ability of the adsorbent to hold the adsorbate and the amount of mobility of the adsorbate within the solution are both represented by K_c , the equilibrium constant [26]. Eq. (4) or (5) can be used to determine the K_c , which is the ratio of the equilibrium concentration of the dye bound to the adsorbent to the equilibrium CBY concentration in solution (C_e) according to the Van't Hoff in Eq. (5) [27-28].

$$K_c = q_e/C_e \quad (4)$$

$$\ln K_c = \Delta S^0/R - \Delta H^0/RT \quad (5)$$

The slope and intercept of a linear plot between $\ln K_c$ and $1/T$ can be used to determine the values of ΔH^0 (J/mol) and ΔS^0 (J/mol K).

Thermodynamic parameters are shown in Table 3, with temperatures ranging from 15 to 55 °C. The possibility of the process and the spontaneous nature of the adsorption are indicated by the negative value of G^0 at various temperatures. Usually, the enthalpy of adsorption changes. The exothermic and physical nature of the adsorption is indicated by the negative ΔH^0 (-29074.0 J/mol). Additionally, the CBY adsorption process' slightly negative ΔS^0 indicates a regular rise in

Table 3. Thermodynamic parameters of CBY adsorption onto TiO_2 Degussa, TiO_2/DPC , and Fe_2O_3

Materials	ΔH (J/mol)	ΔS (J/mol K)	ΔG (J/mol)
$\text{TiO}_2(\text{P25})$	-29074.0	-56.2	-11762.2
TiO_2/DPC	34503.1	-21.3	41058.3
Fe_2O_3	75054.6	-25.9	83054.3

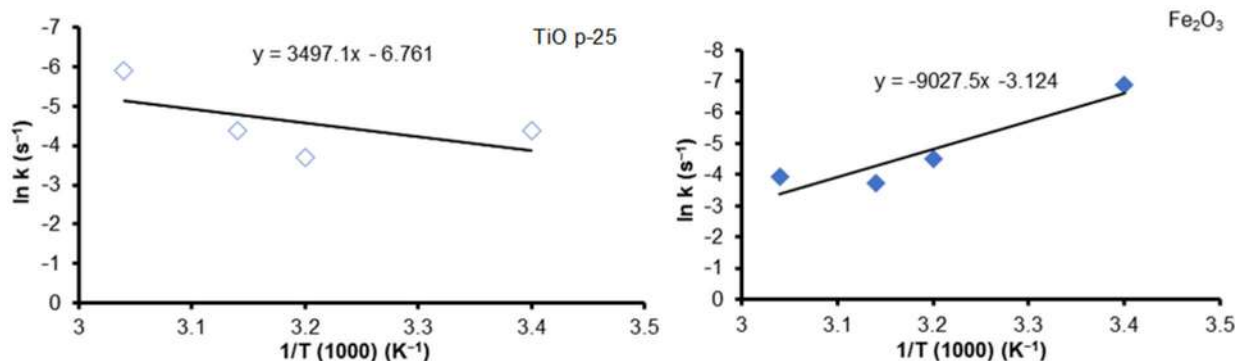


Fig 4. Effect of temperature on CBY adsorption onto TiO_2 Degussa, Fe_2O_3

the randomness at the TiO₂(P25) solution interface throughout adsorption. State exothermic adsorption of CBY and reduced randomness at the boundary layer between TiO₂(P25) and aqueous solution, indicating exothermic adsorption of CBY on the adsorbent and destroyed active sites of TiO₂(P25) surface.

Table 3 also displays the rising temperature, as shown by the positive value of ΔG^0 at various temperatures. Usually, the variation of the adsorption enthalpy.

The positive ΔH^0 (34503.1 and 75054.6 J/mol) indicates that the adsorption is chemical in nature and endothermic. Additionally, the CBY adsorption process' slightly negative ΔS^0 value shows a consistent rise in randomness at the interface of the TiO₂/DPC or Fe₂O₃ solution during adsorption. This suggests that the CBY dye was adsorbed in this condition by an endothermic process.

At higher temperatures for dye, the surface coverage increased. This can be related to the development of additional active sites or the enhanced penetration of reactive dyes into microspores at higher temperatures. Several publications have observed endothermic adsorption of reactive dyes on various types of adsorbents, resulting in the creation of more than one molecular layer on the surface of TiO₂/DPC [29].

The following isotherms were used to fit the data: Freundlich, Temkin, and Langmuir [30].

Langmuir adsorption isotherm

The model presupposes homogeneous adsorption energies on the surface and a lack of adsorptive transmigration in the surface plane. These suppositions led Langmuir to represent Eq. (6) and (7):

$$\frac{1}{q_e} = \frac{1}{q_0} + \frac{1}{q_0 K_L q_e} \quad (6)$$

$$C_e/q_e = 1/q_{\max} K_L + C_e/q_{\max} \quad (7)$$

where q_0 is the highest monolayer coverage capacity (mg/g), K_L = Langmuir isotherm constant (L/mg), C_e is the adsorbate's equilibrium concentration (mg/L), and q_e = the number of substances adsorbent at equilibrium (mg/g).

The values of q_{\max} and K_L were calculated using the slope and intercept of the Langmuir plot of $1/q_e$ vs $1/C_e$ and R_L , the separation factor (also known as the equilibrium

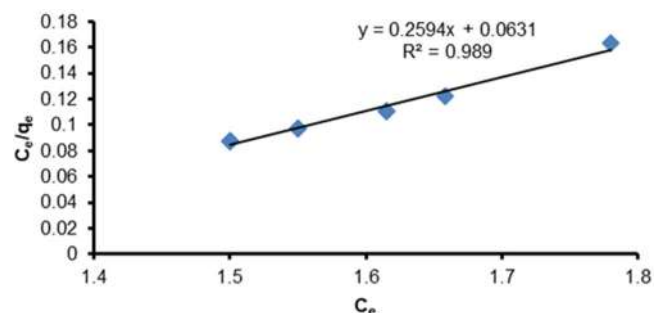


Fig 5. Linear Langmuir adsorption isotherm TiO₂ Degussa

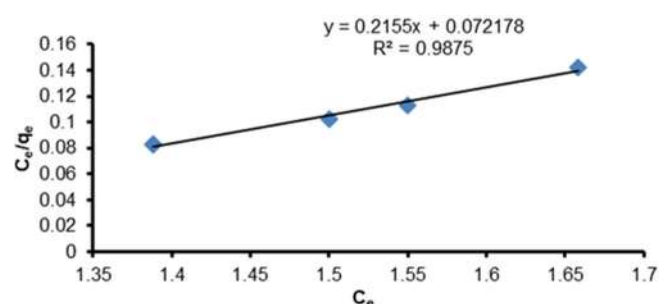


Fig 6. Linear Langmuir adsorption isotherm TiO₂/DPC

parameter), which is a dimensionless constant.

$$RL = \frac{1}{1 + (1 + K_L C_e)} \quad (8)$$

where K_L is a constant relating to adsorption energy (Langmuir Constant), initial concentration C_0 , and R_L value indicates whether the adsorption is favorable or unfavorable. The estimated data show that the Langmuir isotherm is favorable since the R_L is larger than 0 but less than 1 according to the data. The K_L from this research work is 4.1109, and 2.9855 L/mg, as R_L values are 0.10038, and 0.0520 for TiO₂ Degussa, and TiO₂/DPC indicating that the equilibrium sorption was favorable. When it comes to Fe₂O₃, Langmuir adsorption is not applicable.

Fig. 5 and 6 display a linear Langmuir adsorption isotherm. The slope and intercept of the linear plot of C_e/q_e vs C_e were used to compute the values of q_m and K_L of the Langmuir adsorption isotherm, indicating that it is the Langmuir equation for TiO₂ Degussa that best fits the experimental data.

Freundlich adsorption isotherm

These data often fit the empirical equation proposed by Freundlich (Eq. (9)),

$$\ln q_e = \ln K_f + 1/n \ln C_e \quad (9)$$

where K_f = Freundlich isotherm constant (mg/L), q_e = the number of materials adsorbed per gram of adsorbent at equilibrium (mg/g), n is the adsorption intensity, and C_e is the equilibrium adsorbate concentration (mg/L). While $1/n$ is a function of the strength of adsorption in the adsorption process, the constant K_f is a rough indicator of adsorption capacity. The value of $1/n$ is below one for TiO_2 Degussa, and TiO_2/DPC and Fe_2O_3 it indicates normal adsorption. The constants k and n change with temperature in order to account for the empirical finding that the quantity adsorbed rises more slowly is needed to saturate the surface. While the sorbent-sorbate system's K_f and n properties must be determined by data fitting, the smaller $1/n$, the greater the expected heterogeneity, even though linear regression is commonly employed to create the parameters of kinetic and isotherm models. An isotherm of linear adsorption results from this expression.

Temkin isotherm

This isotherm has a component that explicitly accounts for the interactions between the adsorbent and adsorbate. By neglecting the extremely low and high concentration values, the model assumes that the heat of adsorption of all molecules in the layer will decrease linearly rather than logarithmically with coverage. By graphing the amount sorbed q_e versus $\ln C_e$ and calculating the constants from the slope and intercept, it was possible to demonstrate that, as predicted by the equation, the derivation is characterized by a uniform distribution of binding energies. Eq. (10) and (11) provide the model.

$$B = RT/b_T \quad (10)$$

$$q_e = B \ln A_T + B \ln C_e \quad (11)$$

where T = temperature at 298 K, A_T = Temkin isotherm equilibrium binding constant (L/g), R = universal gas constant (8.314 J/mol/K), b_T = Temkin isotherm constant, and B = heat of sorption constant (J/mol). The following values, which are a measure of the heat of sorption and indicate a physical adsorption process, are taken from the Temkin plot in Fig. 7, 8, and 9 [31].

Dubinin-Radushkevich isotherm model

On a heterogeneous surface, the Dubinin-Radushkevich isotherm is typically used to express the

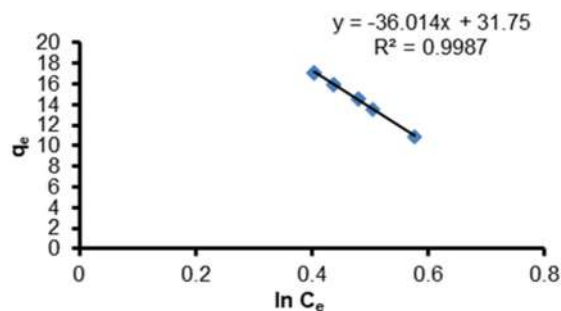


Fig 7. Temkin adsorption isotherm using TiO_2 Degussa

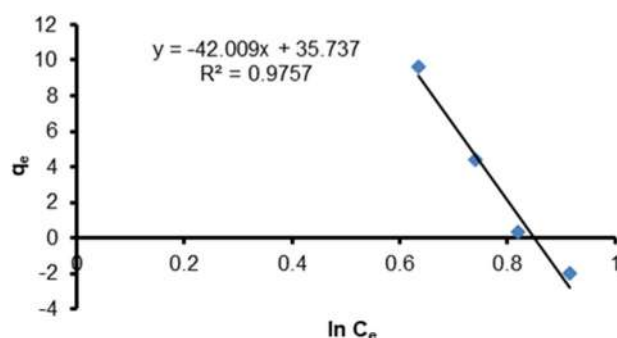


Fig 8. Temkin adsorption isotherm using Fe_2O_3

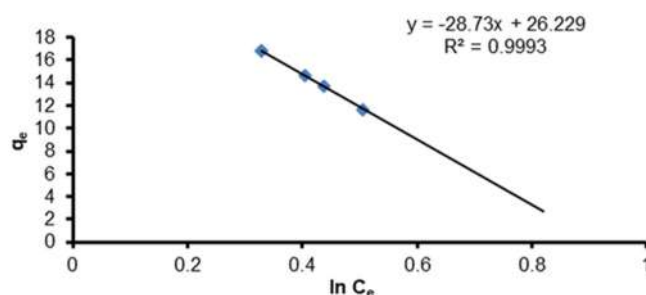


Fig 9. Temkin adsorption isotherm using TiO_2/DPC

adsorption mechanism [32]. The results from the intermediate range of concentrations and high solute activity have generally been well fit by the model (Eq. (12)).

$$\ln q_e = \ln q_s - K_{ad} \varepsilon^2 \quad (12)$$

where q_e = amount of adsorbate in the adsorbent at equilibrium (mg/g), K_{ad} = Dubinin-Radushkevich isotherm constant (mol^2/kJ^2), and q_s = theoretical isotherm saturation capacity (mg/g). The method was typically used to differentiate between the physical and chemical adsorption of metal ions with its mean free energy, ε per molecule of adsorbate, which can be calculated by the relationship (Eq. (13)).

$$\varepsilon = RT \ln(1 + 1/C_e) \quad (13)$$

where R , T , and C_e stand for the equilibrium adsorbate concentrations (mg/L), the gas constant in J/mol K, and the absolute temperature (K), respectively. When adsorption data at various temperatures are represented as a function of the logarithm of quantity adsorbed ($\ln q_e$) vs. ε^2 the square of potential energy, the Dubinin-Radushkevich isotherm model's temperature dependence is one of the model's distinct features. The characteristic curve is also known as the curve on which all acceptable data will lie [33]. Eq. (13) was used to determine constants like q_s and K_{ad} from Fig. 10, 11, and 12. From the linear plot of the Dubinin-Radushkevich model, q_s was determined to be 1.436 mg/g, K_{ad} was determined 3×10^{-7} the $R^2 = 0.997$ for TiO_2/DPC , while Fe_2O_3 and TiO_2 Degussa do not apply (Table 4).

The results of isotherm parameters (Langmuir, Freundlich, Temkin, and Dubinin-Radushkevich) applied in this study for the following in Table 5.

The parameter results in Table 5 Langmuir model using TiO_2/DPC , TiO_2 Degussa, and Fe_2O_3 . The active site can only adsorb one molecule, thus the K_L value for all adsorption systems displays a relatively low value, indicating weak interaction between the molecules of the absorbent and adsorbate. TiO_2/DPC and TiO_2 Degussa have relatively high correlation values ($R^2 > 0.80$) than Fe_2O_3 .

Table 5 displays the parameters of the Freundlich model when TiO_2/DPC , TiO_2 Degussa, and Fe_2O_3 adsorbents. Freundlich isotherm is a good representation of TiO_2/DPC and TiO_2 Degussa P25 adsorption systems than the Fe_2O_3 adsorption system; this is confirmed by the R^2 value of higher than 0.80, the adsorption process takes place on a heterogeneous surface in a multilayer form with weak interactions between the adsorbent and adsorbate.

The parameter results from the Temkin model using TiO_2/DPC , TiO_2 Degussa, and Fe_2O_3 . A comparatively low value between the molecules of the absorbent and the adsorbate is shown by the AT value for all adsorption systems. Physical interaction only involves more interaction weak, correlation coefficient value ($R^2 > 0.80$), for TiO_2/DPC , TiO_2 Degussa, and Fe_2O_3 are suitable with Temkin isotherm.

While results Dubinin-Radushkevich model using TiO_2/DPC , TiO_2 Degussa, and Fe_2O_3 have small β values. Influenced by pore volume for β value. The highest maximal binding energy value is impacted by the greater pore volume. TiO_2/DPC , TiO_2 Degussa adsorption system, and TiO_2 have the best correlation coefficient values ($R^2 > 0.80$), indicating that they have the greatest

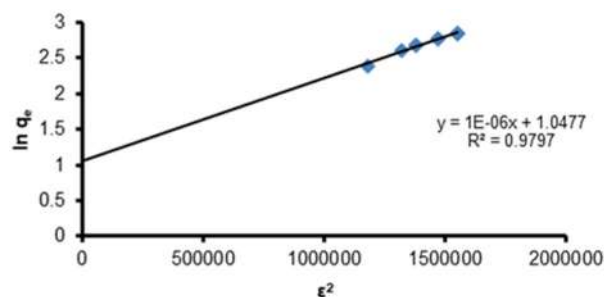


Fig 10. Dubinin-Radushkevich adsorption isotherm using TiO_2 Degussa

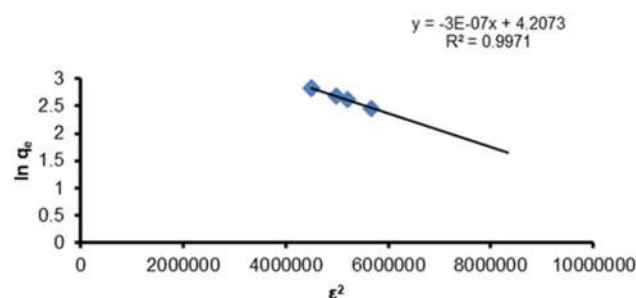


Fig 11. Dubinin-Radushkevich adsorption isotherm using TiO_2/DPC

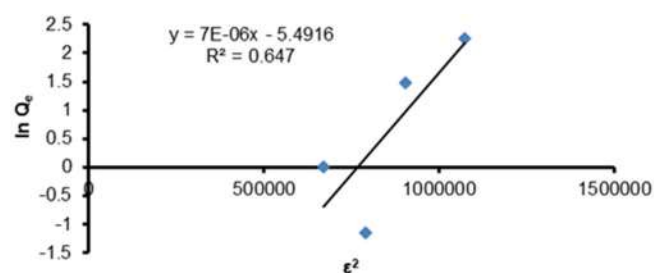


Fig 12. Dubinin-Radushkevich adsorption isotherm using Fe_2O_3

Table 4. Dubinin-Radushkevich adsorption isotherm constants

Material	K_{ad}	q_s	R^2
TiO_2/DPC	3×10^{-7}	1.436	0.997
TiO_2 Degussa	-1×10^{-6}	2.851	0.979
Fe_2O_3	-7×10^{-6}	4.120×10^{-3}	0.647

Table 5. Isotherm parameters (Langmuir, Temkin, Freundlich, and Dubinin-Radushkevich)

Langmuir isotherm parameters				
Adsorbent	K_L (L/mg)	RL	R^2	Note
TiO ₂ /DPC	2.9850	0.05200	0.987	$0 < RL < 1$ favorable adsorption
TiO ₂ Degussa	4.1109	0.10038	0.978	$R^2 > 0.80$, monolayer adsorption
Fe ₂ O ₃	-0.4920	1.0000	0.407	Linear adsorption process, $RL = 1$. (Depending on the amount adsorbed and the concentration adsorbed) $R^2 < 0.80$ does not suggest monolayer adsorption
Freundlich isotherm parameters				
Adsorbent	$1/n$	n	R^2	Note
TiO ₂ /DPC	-2.014	-0.496	0.993	$n < 1$, chemical interaction between adsorbate molecules $R^2 > 0.80$, multilayer adsorption
TiO ₂ Degussa	-2.557	-0.390	0.988	
Fe ₂ O ₃	-9.960	-0.100	0.615	
Temkin isotherm parameters				
Adsorbent	A_T (L/g)	B_T (J/mol)	R^2	Note
TiO ₂ /DPC	0.334	-83.304	0.993	$B_T < 8$ kJ/mol, physical interaction between adsorbate molecules
TiO ₂ Degussa	0.414	-66.486	0.998	$R^2 > 0.80$, uniform distribution adsorbate to the adsorbent surface
Fe ₂ O ₃	0.427	-56.998	0.979	
Dubinin-Radushkevich isotherm parameters				
Adsorbent	B (mol ² /kJ ²)	E (kJ/mol)	R^2	Note
TiO ₂ /DPC	0.3×10^{-6}	1291.088	0.997	$E > 8$ kJ/mol, chemical interaction between adsorbate molecules
TiO ₂ Degussa	1×10^{-6}	707.107	0.979	$R^2 > 0.80$, micro pore size is existing in the adsorbent surface
Fe ₂ O ₃	7×10^{-6}	267.265	0.647	

correlation coefficient, while Fe₂O₃ has the correlation coefficient is low ($R^2 = 0.647$). Temkin model was discovered to have the best fit because it had the greatest regression value.

Kinetic of sorption

Kinetic models have been used to analyze the mechanism of sorption and potential rate-controlling processes in order to select the appropriate operating parameters for full-scale batch operation [34]. The models utilized were pseudo-first-order, pseudo-second-order, and zeroth-order kinetic models.

Pseudo-first-order model. The -first-order rate expression based on solid capacity is generally expressed as follows Eq. (14) and (15):

$$\ln(q_e - q_t) = \ln q_e - k_1 t \quad (14)$$

$$\ln(C_0 - C_t) = \ln C_0 - k_1 t \quad (15)$$

where q_t is the amount adsorbed at time t (mg/g), C_t is the concentration at the time, q_e is the amount of CBY

adsorbed at equilibrium (mg/g), k_1 is the rate constant of first-order adsorption (1/min), and C_0 is the initial concentration. From the $\ln(q_e - q_t)$ against t straight-line plot, the value of the adsorption rate constant k_1 for the CBY adsorption onto (TiO₂ Degussa, TiO₂/DPC, or Fe₂O₃) was calculated (Fig. 13, 14, and 15). The data were fitted with correlation coefficients, showing that the first-order equation is followed by the rate of removal of CBY.

The findings were poorly correlated, showing that the rate of removal of CBY onto TiO₂ Degussa, TiO₂/DPC, or Fe₂O₃ is not followed by the second-order equation.

Pseudo-second-order model. With the use of the following Eq (16), the second-order kinetic rate was investigated.

$$\frac{t}{C_t} = \frac{1}{k_2 q_e^2} + \frac{1}{q_e} \quad (16)$$

where k_2 , C_t , and q_e stand for the rate constant, the concentration at a given time 't' and the amount adsorbed at equilibrium, respectively. By displaying the

graph of t/C_t versus t . With the use of the following equation, the second-order kinetic rate was investigated. The value of $k_2 = 1.06 \times 10^{-5}$ g/mg min, $q_e = 416.66$ mg/g and $R^2 = 0.4138$ for TiO₂/DPC (Fig. 16); $k_2 = 0.0618 \times 10^{-5}$ g/mg min, $Q_e = 1666.66$ mg/g, and $R^2 = 0.5728$ for TiO₂ Degussa (Fig. 18); and $K_2 = 0.24 \times 10^{-5}$ g/mg min, $Q_e = 1000$ mg/g, and $R^2 = 0.2134$ for Fe₂O₃ (Fig. 17) were calculated. The CBY adsorption onto TiO₂ Degussa, TiO₂/DPC, and Fe₂O₃ was in loose agreement with the total rate of CBY adsorption on to TiO₂ Degussa, TiO₂/DPC, and Fe₂O₃, according to the obtained kinetic adsorption data, which appeared to be controlled by the physicochemical process.

The pseudo-first-order model, which is often relevant over the first stage of an adsorption process, is predicated on the idea that the rate of change in solute uptake with time is perfectly proportional to the difference in saturation concentration and the amount of solid uptake with time. When adsorption occurs through diffusion through the interface, it is usually seen that kinetics follows this pseudo-first-order rate equation, and the intercept of $\ln(q_e - q_t)$ vs t plots would therefore be equal to \ln of empirically obtained q_e to fit the experimental value, the pseudo-first-order equation usually does not provide a good fit over the entire range of adsorption time.

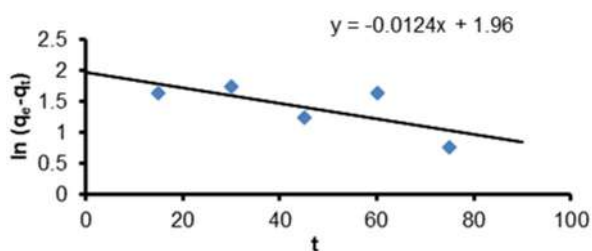


Fig 13. Pseudo-first-order of CBY adsorption onto TiO₂ Degussa

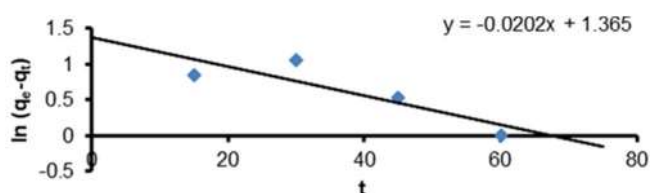


Fig 14. Pseudo-first-order of CBY adsorption onto TiO₂/DPC

The pseudo-second-order kinetic model predicts behavior over the whole adsorption range under the assumption that chemisorption is the rate-limiting step;

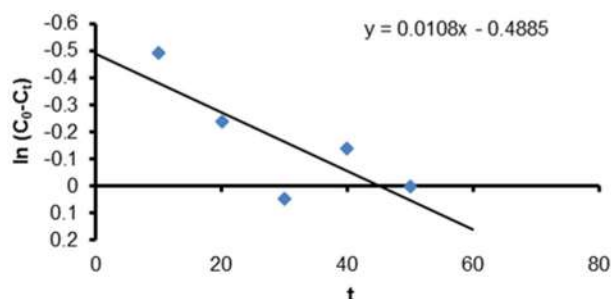


Fig 15. Pseudo-first-order of CBY adsorption onto Fe₂O₃

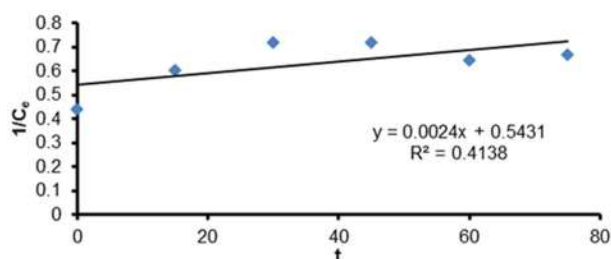


Fig 16. Pseudo-second-order of CBY adsorption onto TiO₂/DPC

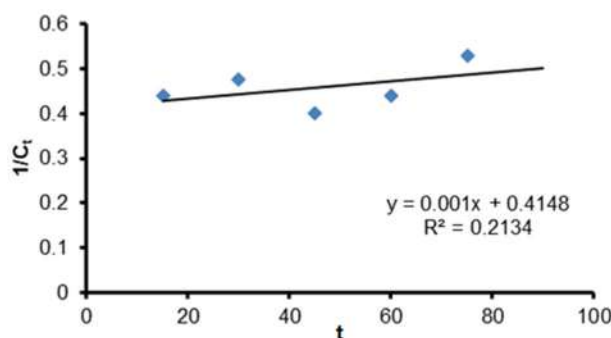


Fig 17. Pseudo-second-order of CBY adsorption onto Fe₂O₃

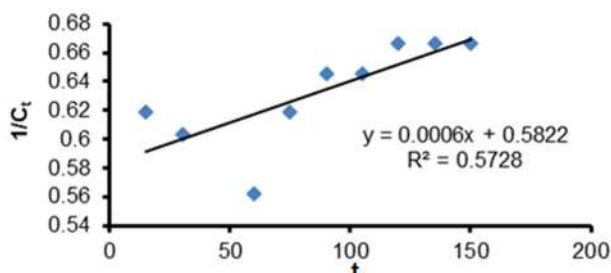


Fig 18. Pseudo-second-order of CBY adsorption onto TiO₂ Degussa

Table 6. Rate constants and correlation coefficients for models studied of the kinetic equations

Adsorbents	Pseudo-zeroth-order		Pseudo-first-order		Pseudo-second-order	
	K (mg g/min)	R ²	K ₁ (1/min)	R ²	K ₂ (g/mg min) × 10 ⁻⁵	R ²
TiO ₂ /DPC	0.434	0.452	0.0202	0.817	1.060	0.413
TiO ₂ Degussa	0.904	0.357	0.0124	0.737	0.062	0.573
Fe ₂ O ₃	-0.711	0.163	0.0108	0.634	0.213	0.213

the adsorption rate is determined by adsorption capacity rather than adsorbate concentration. This model has several advantages over the Lagergren first-order model, one of which is the ability to compute the equilibrium adsorption capacity.

According to studies, values of $R^2 > 0.8$ show a strong fit between the data and the model, while values of $R^2 < 0.5$ indicate a weak correlation between the predictor variable and the response variable, based on Table 6, it is expected that is suitable for pseudo-first-order according to the values of R^2 .

■ CONCLUSION

Adsorption was influenced by some operational factors, including temperature, initial concentration, pH, and contact time. The study of the CBY dye's adsorption to the TiO₂/DPC, TiO₂ Degussa, and Fe₂O₃ materials revealed that as the concentration of CBY increases, more CBY molecules are available at the interface, which improves the adsorption. It can be inferred that electrostatic repulsion plays a significant role in this system, given that the amount of adsorption increases with increasing CBY concentration. This was caused by an increase in initial dye concentration reducing pH, which increased the driving force of the concentration gradient. The increased tendency of the CBY to escape from the surfaces of TiO₂/DPC, TiO₂ Degussa, and Fe₂O₃ may be the cause of the decrease in adsorption as the temperature rises. Demonstrate the viability of the procedure and the spontaneous nature of the adsorption at various temperatures. The CBY adsorption process' negative result for ΔS^0 implies a regular rise in randomness at the interface of the adsorbent throughout adsorption. The TiO₂ Degussa Langmuir equation provides the experimental data with the best match compared to the other isotherm. The CBY adsorption

onto the adsorbent surfaces was confirmed by the obtained kinetic adsorption data, proving that the pseudo-first-order equation is really followed by the rate of CBY removal from these surfaces. The study's findings were well-explained by Freundlich, Langmuir, Temkin, and Dubbin-Radushkevich. The experimental results had the best fit with the Langmuir equation. The kinetic data showed that a pseudo-first-order equation was in control of the adsorption process. Thermodynamic investigations showed that the adsorption of CBY on the adsorbent was both endothermic and chemical in nature, as well as exothermic and occurring spontaneously.

■ REFERENCES

- [1] Khan, T.A., Singh, V.V., and Kumar, D., 2004, Removal of some basic dyes from artificial textile wastewater by adsorption on Akash Kinari coal, *J. Sci. Ind. Res.*, 63 (4), 355–364.
- [2] Khamparia, S., and Jaspal, D.K., 2017, Adsorption in combination with ozonation for the treatment of textile waste water: A critical review, *Front. Environ. Sci. Eng.*, 11 (1), 8.
- [3] Nwodika, C., and Onukwuli, O.D., 2017, Adsorption study of kinetics and equilibrium of basic dye on kola nut pod carbon, *Gazi Univ. J. Sci.*, 30 (4), 86–102.
- [4] Shahabuddin, S., Khanam, R., Khalid, M., Sarih, N.M., Ching, J.J., Mohamad, S., and Saidur, R., 2018, Synthesis of 2D boron nitride doped polyaniline hybrid nanocomposites for photocatalytic degradation of carcinogenic dyes from aqueous solution, *Arabian J. Chem.*, 11, 1000–1016.
- [5] Zhou, X., Zheng, P., Wang, L., and Liu, X., 2019, Preparation of sulfonated poly(arylene ether

- nitrile)-based adsorbent as a highly selective and efficient adsorbent for cationic dyes, *Polymers*, 11 (1), 32.
- [6] Onur, I., Demir, I., Yuceer, A., and Cinar, O., 2017, Isotherm and kinetic modelling of azo dyes adsorption, *Eur. J. Eng. Nat. Sci.*, 2 (1), 210–216.
- [7] Malik P.K., 2003, Use of activated carbons prepared from sawdust and rice-husk for adsorption of acid dyes: A case study of Acid Yellow 36, *Dyes Pigm.*, 56 (3), 239–249.
- [8] Qasem, N.A.A., Mohammed, R.H., and Lawal, D.U., 2021, Removal of heavy metal ions from wastewater: A comprehensive and critical review, *npj Clean Water*, 4 (1), 36.
- [9] Baskar, A.V., Bolan, N., Hoang, S.A., Sooriyakumar, P., Kumar, M., Singh, L., Jasemizad, T., Padhye, L.P., Singh, G., Vinu, A., Sarkar, B., Kirkham, M.B., Rinklebe, J., Wang, S., Wang, H., Balasubramanian, R., and Siddique, K.H.M., 2022, Recovery, regeneration and sustainable management of spent adsorbents from wastewater treatment streams: A review, *Sci. Total Environ.*, 822, 153555.
- [10] Joudeh, N., and Linke, D., 2022, Nanoparticle classification, physicochemical properties, characterization, and applications: A comprehensive review for biologists, *J. Nanobiotechnol.*, 20 (1), 262.
- [11] Byakodi, M., Shrikrishna, N.S., Sharma, R., Bhansali, S., Mishra, Y., Kaushik, A., and Gandhi, S., 2022, Emerging 0D, 1D, 2D, and 3D nanostructures for efficient point-of-care biosensing, *Biosens. Bioelectron.*: X, 12, 100284.
- [12] Hisatomi, T., Kubota, J., and Domen, K., 2014, Recent advances in semiconductors for photocatalytic and photoelectrochemical water splitting, *Chem. Soc. Rev.*, 43 (22), 7520–7535.
- [13] Bokov, D., Turki Jalil, A., Chupradit, S., Suksatan, W., Javed Ansari, M., Shewael, I.H., Valiev, G.H., and Kianfar, E., 2021, Nanomaterial by sol-gel method: Synthesis and application, *Adv. Mater. Sci. Eng.*, 2021, 5102014.
- [14] Thangavelu, K., Annamalai, R., and Arulnandhi, D., 2013, Preparation and characterization of nanosized TiO₂ powder by sol-gel precipitation route, *Int. J. Emerging Technol. Adv. Eng.*, 3 (1), 636–639.
- [15] Ahmad, M.A., Herawan, S.G., and Yusof, A.A., 2014, Equilibrium, kinetics, and thermodynamics of remazol brilliant blue R dye adsorption onto activated carbon prepared from pinang frond, *Int. Scholarly Res. Not.*, 2014, 184265.
- [16] Xiao, G., Su, H., and Tan, T., 2015, Synthesis of core-shell bioaffinity chitosan-TiO₂ composite and its environmental applications, *J. Hazard. Mater.*, 283, 888–896.
- [17] El Mouchtari, E.M., Daou, C., Rafqah, S., Najjar, F., Anane, H., Piram, A., Hamade, A., Briche, S., and Wong-Wah-Chung, P., 2020, TiO₂ and activated carbon of *Argania spinosa* tree nutshells composites for the adsorption photocatalysis removal of pharmaceuticals from aqueous solution, *J. Photochem. Photobiol., A*, 388, 112183.
- [18] Wang, N., Ye, C., Xie, H., Yang, C., Zhou, J., and Ge, C., 2021, Fe₂O₃ enhanced high-temperature arsenic resistance of CeO₂-La₂O₃/TiO₂ catalyst for selective catalytic reduction of NO_x with NH₃, *RSC Adv.*, 11 (16), 9395–9402.
- [19] Tiwari, A.P., and Rohiwal, S.S., 2019, “Synthesis and Bioconjugation of Hybrid Nanostructures for Biomedical Applications” in *Hybrid Nanostructures for Cancer Theranostics*, Eds. Ashok Bohara, R., and Thorat, N., Elsevier, Amsterdam, Netherlands, 17–41.
- [20] Ahmad, M.A., and Alrozi, R., 2011, Removal of malachite green dye from aqueous solution using rambutan peel-based activated carbon: Equilibrium, kinetic and thermodynamic studies, *Chem. Eng. J.*, 171 (2), 510–516.
- [21] Fan, T., Liu, Y., Feng, B., Zeng, G., Yang, C., Zhou, M., Zhou, H., Tan, Z., and Wang, X., 2008, Biosorption of cadmium(II), zinc(II) and lead(II) by *Penicillium simplicissimum*: Isotherms, kinetics and thermodynamics, *J. Hazard. Mater.*, 160 (2-3), 655–661.
- [22] Tamjidi, S., and Esmaeili, H., 2019, Chemically modified CaO/Fe₃O₄ nanocomposite by sodium

- dodecyl sulfate for Cr(III) removal from water, *Chem. Eng. Technol.*, 42 (3), 607–616.
- [23] Singh, K., Kumar, A., Awasthi, S., Pandey, S.K., and Mishra, P., 2019, Adsorption mechanism of carboxymethyl cellulose onto mesoporous mustard carbon: Experimental and theoretical aspects, *Colloids Surf., A*, 581, 123786.
- [24] Alkan, M., Doğan, M., Turhan, Y., Demirbaş, Ö., and Turan, P., 2008, Adsorption kinetics and mechanism of maxilon blue 5G dye on sepiolite from aqueous solutions, *Chem. Eng. J.*, 139 (2), 213–223.
- [25] Zghal, S., Jedidi, I., Cretin, M., Cerneaux, S., and Abdelmouleh, M., 2023, Adsorptive removal of Rhodamine B dye using carbon graphite/CNT composites as adsorbents: Kinetics, isotherms and thermodynamic study, *Materials*, 16 (3), 1015.
- [26] Banerjee, S., and Chattopadhyaya, M.C., 2017, Adsorption characteristics for the removal of a toxic dye, tartrazine from aqueous solutions by a low cost agricultural by-product, *Arabian J. Chem.*, 10 (Suppl. 2), S1629–S1638.
- [27] Bhattacharyya, K.G., and Sarma, A., 2003, Adsorption characteristics of the dye, Brilliant Green, on Neem leaf powder, *Dyes Pigm.*, 57 (3), 211–222.
- [28] Aljeboree, A.M., Alshirifi, A.N., and Alkaim, A.F., 2017, Kinetics and equilibrium study for the adsorption of textile dyes on coconut shell activated carbon, *Arabian J. Chem.*, 10, S3381–S3393.
- [29] Abdoul, H.J., Yi, M., Prieto, M., Yue, H., Ellis, G.J., Clark, J.H., Budarin, V.L., and Shuttleworth, P.S., 2023, Efficient adsorption of bulky reactive dyes from water using sustainably-derived mesoporous carbons, *Environ. Res.*, 221, 115254.
- [30] Habeeb, O.A., Ramesh, K., Ali, G.A.M., Yunus, R.M., and Olalere, O.A., 2017, Kinetic, isotherm and equilibrium study of adsorption capacity of hydrogen sulfide-wastewater system using modified eggshells, *IJUM Eng. J.*, 18 (1), 13–25.
- [31] Inyinbor, A.A., Adekola, F.A., and Olatunji, G.A., 2016, Kinetics, isotherms and thermodynamic modeling of liquid phase adsorption of Rhodamine B dye onto *Raphia hookerie* fruit epicarp, *Water Resour. Ind.*, 15, 14–27.
- [32] Hu, Q., and Zhang, Z., 2019, Application of Dubinin–Radushkevich isotherm model at the solid/solution interface: A theoretical analysis, *J. Mol. Liq.*, 277, 646–648.
- [33] Foo, K.Y., and Hameed, B.H., 2010, Insights into the modeling of adsorption isotherm systems, *Chem. Eng. J.*, 156 (1), 2–10.
- [34] Cáceres-Jensen, L., Rodríguez-Becerra, J., Garrido, C., Escudey, M., Barrientos, L., Parra-Rivero, J., Domínguez-Vera, V., and Loch-Arellano, B., 2021, Study of sorption kinetics and sorption–desorption models to assess the transport mechanisms of 2,4-dichlorophenoxyacetic acid on volcanic soils, *Int. J. Environ. Res. Public Health*, 18 (12), 6264.

Supplementary Data

This supplementary data is a part of a paper entitled “GC-MS and Bioassay-Guided Isolation of Xanthenes from *Mammea siamensis*”.

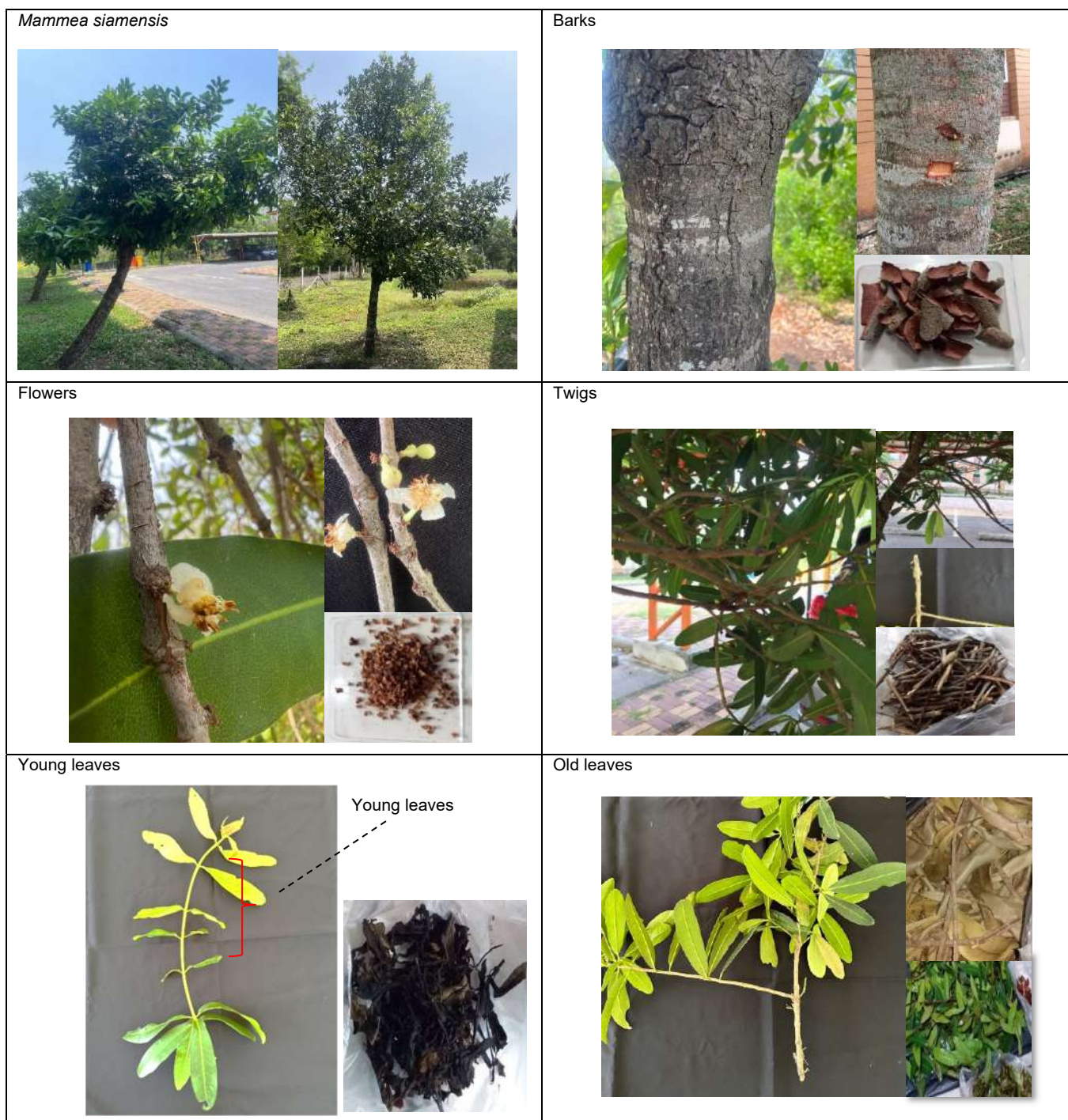
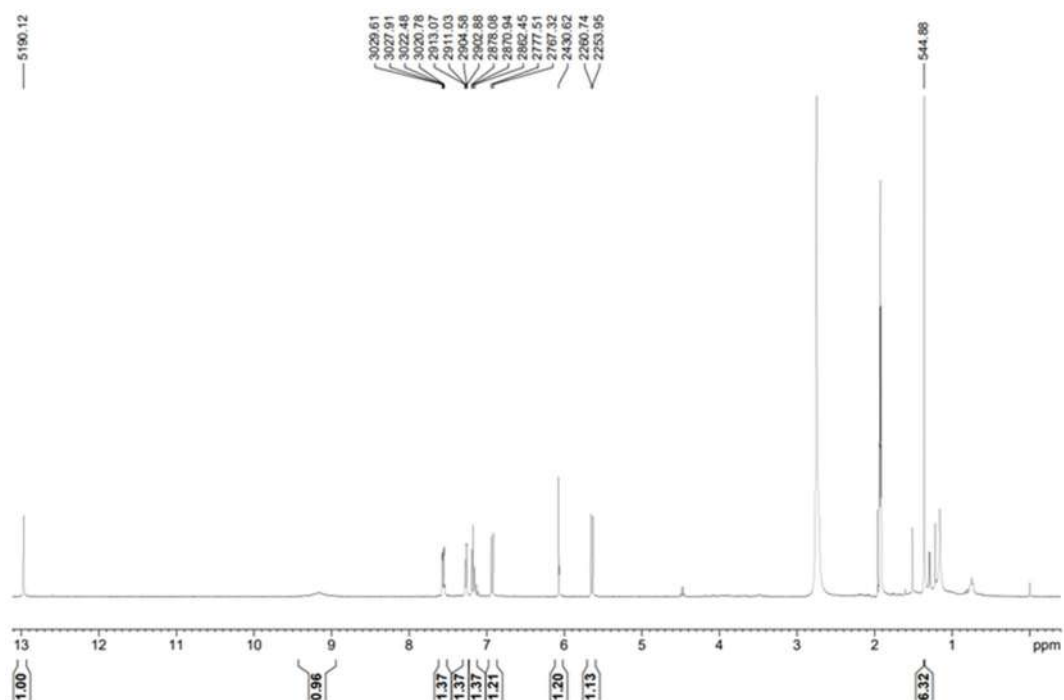
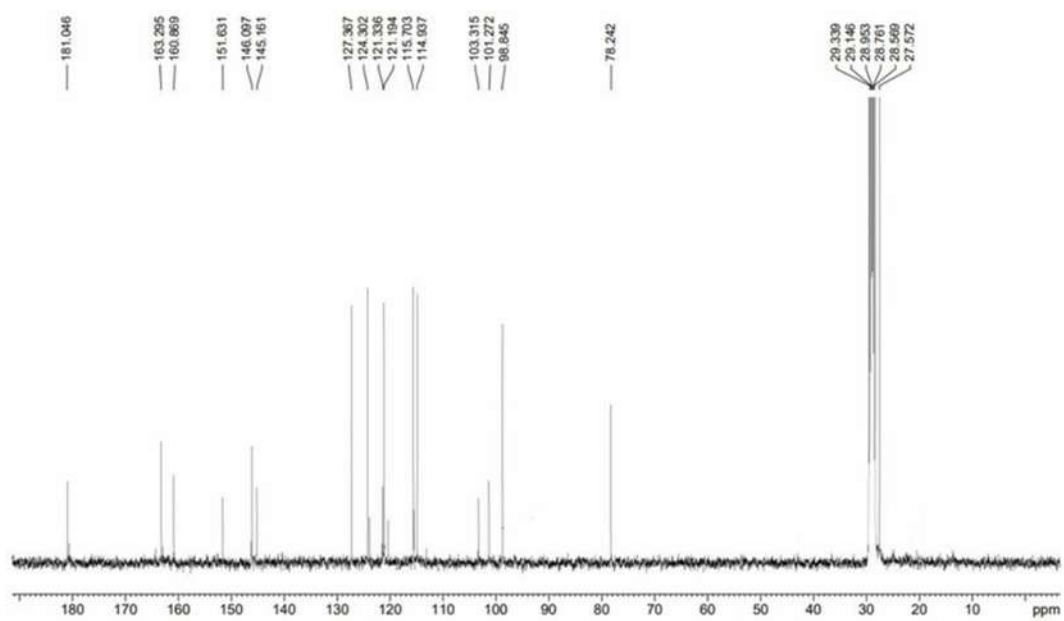


Fig S1. Pictures of *Mammea siamensis* plant and its parts

Fig S2. $^1\text{H-NMR}$ of compound 1 in acetone- d_6 Fig S3. $^{13}\text{C-NMR}$ of compound 1 in acetone- d_6

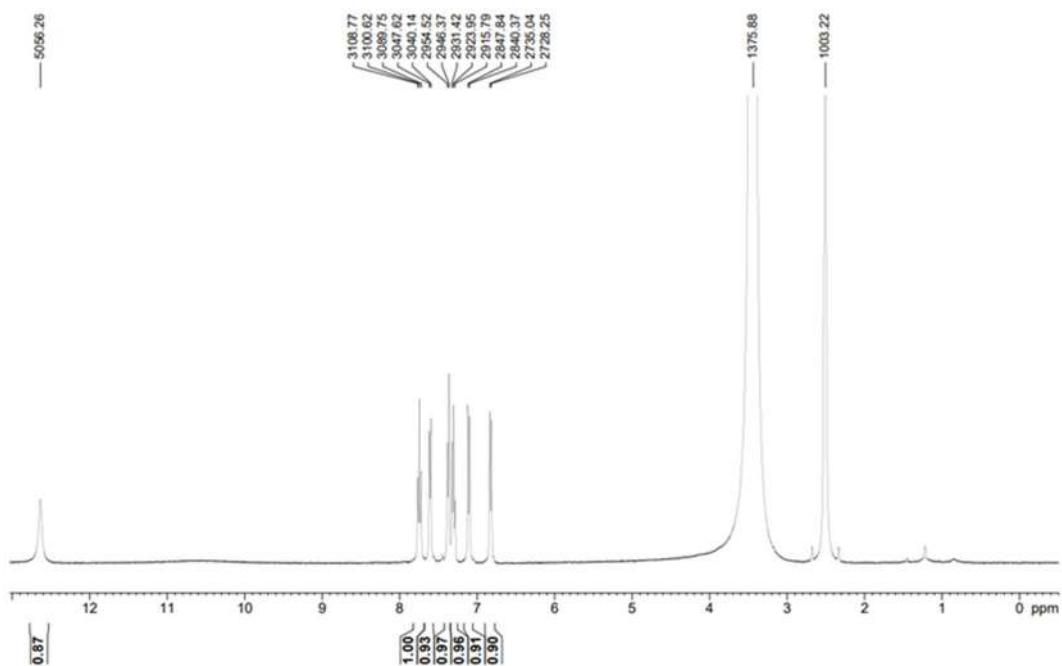


Fig S4. $^1\text{H-NMR}$ of compound 2 in $\text{DMSO-}d_6$

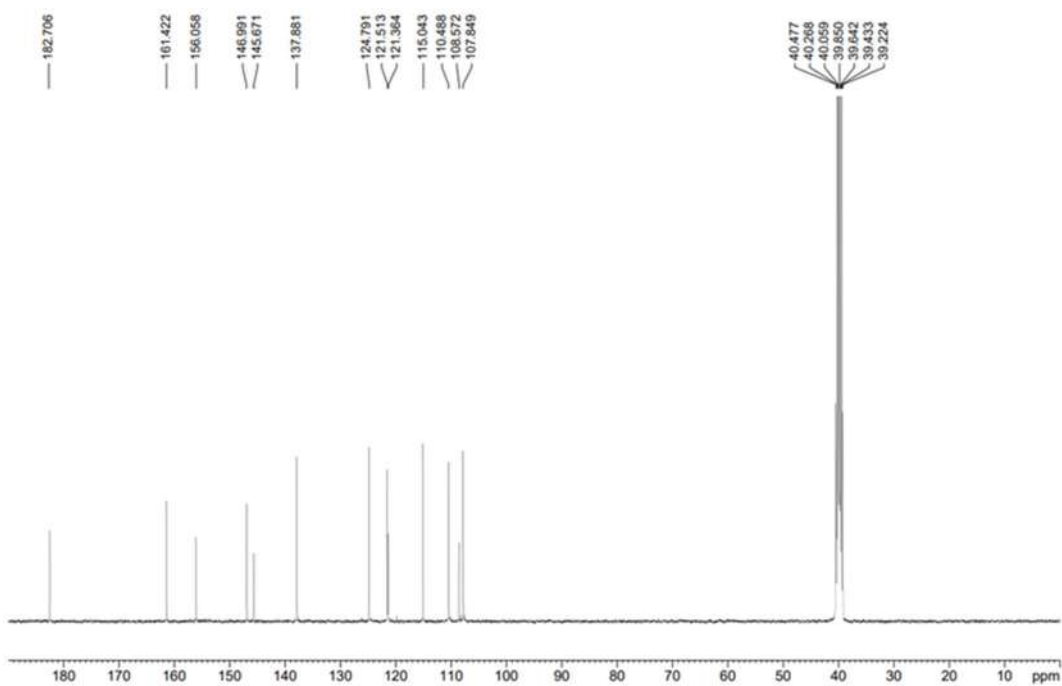


Fig S5. $^{13}\text{C-NMR}$ of compound 2 in $\text{DMSO-}d_6$

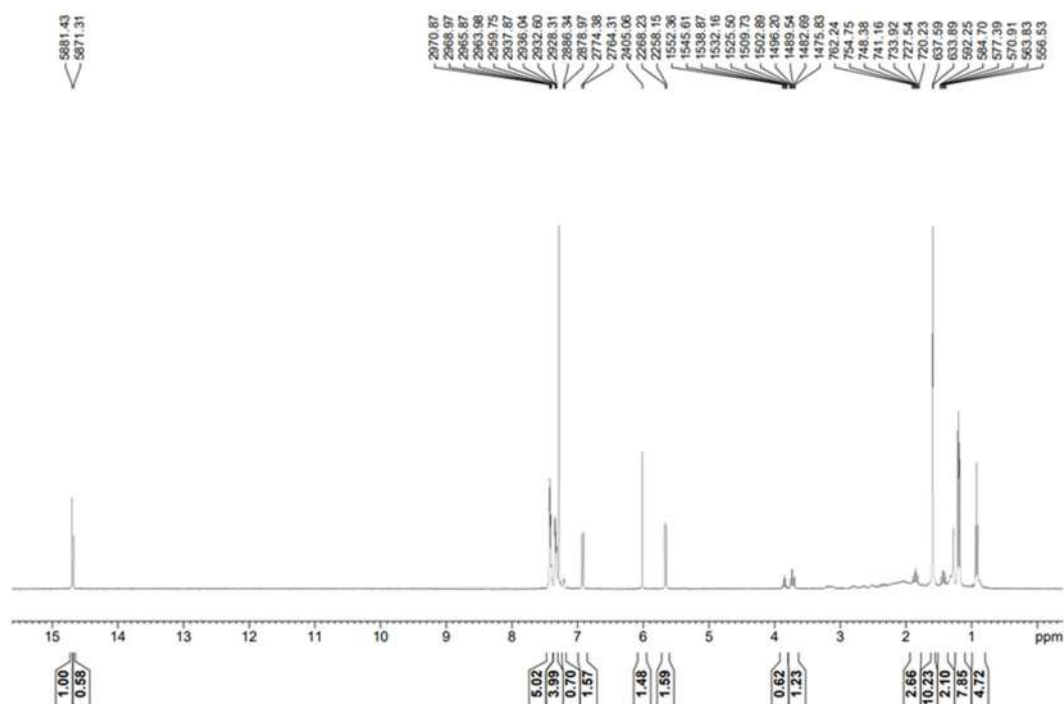
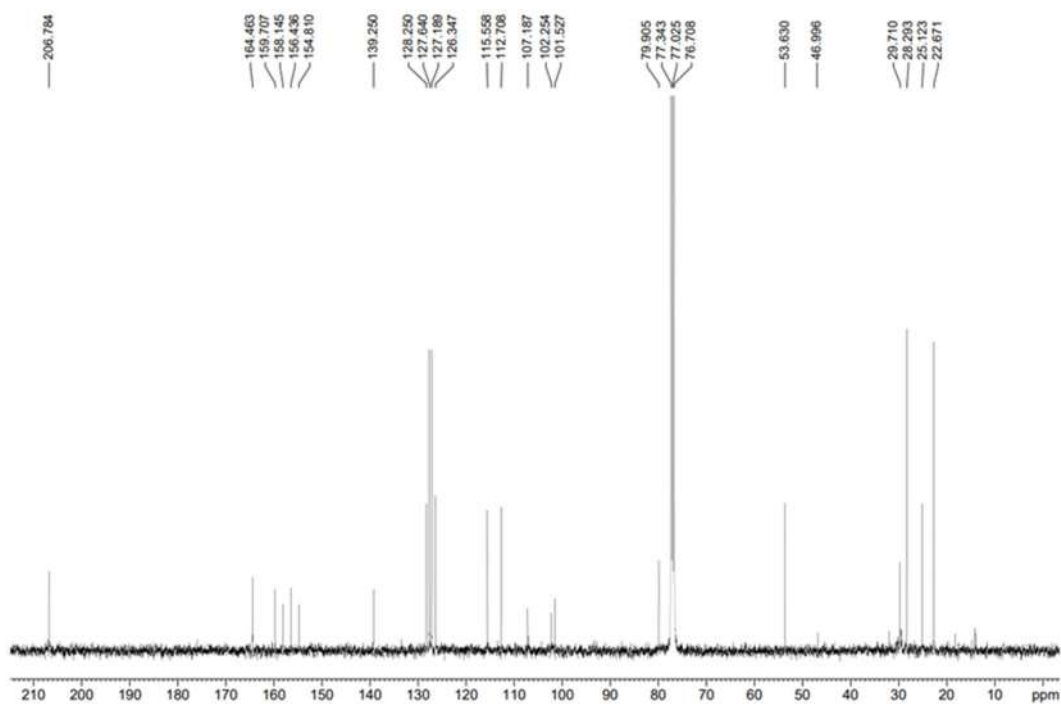
Fig S6. ¹H-NMR of a mixture of compounds 3 and 4 in CDCl₃Fig S7. ¹³C-NMR of a mixture of compounds 3 and 4 in CDCl₃

Table S1. Relative constituents from barks, flowers, twigs, leaves and young leaves of *Mammea siamensis* detected by GC-MS data

Compounds	RT (min)	Relative content (%)				
		Barks	Flowers	Twigs	Leaves	Young leaves
Phenolic derivatives						
2,4-Di- <i>tert</i> -butylphenol	7.19	0.2	-	0.4	0.2	0.6
Methyl di- <i>tert</i> -butylhydroxyhydrocinnamate	9.61	0.2	-	0.3	0.2	-
Methyl 2-ethylhexylphthalate	10.06	0.3	-	0.4	-	0.7
4-Hexylphenol	11.48	-	-	-	-	0.2
5-Hydroxy-2,2,10-trimethyl-6-(2-methylbutanoyl)-2 <i>H</i> ,8 <i>H</i> -benzo[1,2- <i>b</i> :3,4- <i>b'</i>]dipyran-8-one	11.90	0.4	2.6	-	-	0.8
2-Methoxy-3,8-dioxocephalotax-1-ene	12.02	0.6	2.2	-	0.1	1.3
<i>bis</i> (2-Ethylhexyl) phthalate	12.25	-	3.5	2.0	0.9	3.6
2-Amino- α -[2-chlorophenyl]cinnamic acid	12.28	10.5	7.9	1.0	-	4.9
5-Hydroxy-2-(4-hydroxyphenyl)-3,6,7-trimethoxy-4 <i>H</i> -1-benzopyran-4-one	12.50	0.8	-	-	-	-
1-Phenyl-2-(2-phenyl-4 <i>H</i> -1-benzopyran-4-yl)-ethanone,	13.13	-	-	-	-	0.1
1,2,3,4-Tetrahydro-6-methoxy-1,1,4,4-tetramethyl-5-(phenylethenyl)anthracene	13.54	7.7	11.4	3.0	0.8	6.8
1-Hydroxy-3,5,8-trimethoxy-4-(3'-methyl-2'-but-2'-enyl)-xanthone	13.68	2.6	8.4	-	-	4.6
(+)-11,12- <i>trans</i> -10,11-Dihydro-12-hydroxy-4-propyl-6,6,11-trimethyl-2 <i>H</i> ,6 <i>H</i> ,12 <i>H</i> -benzo[1,2- <i>b</i> :3,4: <i>b'</i> :5,6- <i>b''</i>]tripyrans-2-one	13.74	6.5	-	-	-	1.8
Calanolide A	13.85	-	7.1	-	-	0.8
3,5- <i>bis</i> (1,1-Dimethylethyl)-1,2-benzenediol	14.92	-	-	-	-	0.5
9-Methoxy-tetrahydropyrano[2,3- <i>f</i>]isobenzofuran-8-one-2,spiro,2'-hydroxy-4',7'-dimethoxybenzofuran-3'-ol	16.17	-	-	-	-	2.1
Fatty acid and terpenoid derivative						
Caryophyllene	6.73	-	-	-	0.6	0.4
Alloaromadendrene	6.99	-	-	-	-	0.4
Farnesene	7.15	-	-	-	-	0.4
γ -Murolene	7.30	-	-	-	-	0.3
Cadinene	7.42	-	-	-	-	0.3
Caryophyllene oxide	7.60	-	-	-	-	0.5
Hexadecane	7.68	0.4	-	0.6	-	1.2
Deacetyl-coralloidin-B	7.83	-	-	-	-	0.4
α -Humulene epoxide II	7.92	-	-	0.7	0.3	1.7
Muurola-4,10(14)-dien-1- β -ol	7.99	-	-	-	-	0.4
10,10-Dimethyl-2,6-dimethylene-bicyclo[7.2.0]undecan-5 β -ol	8.07	-	4.6	-	-	1.5
Octadecane	8.80	0.2	-	0.4	0.3	0.7
Neophytadiene	9.02	-	-	-	1.0	-
<i>n</i> -Hexadecanoic acid	9.67	-	5.0	-	2.0	2.2
Eicosane	9.82	-	-	-	-	0.2
<i>E</i> -15-Heptadecenal	10.24	-	-	-	-	0.6
<i>Cis</i> -9, <i>trans</i> -12 methyl linoleate	10.30	0.3	-	1.4	0.3	3.4

Table S1. Relative constituents from barks, flowers, twigs, leaves and young leaves of *Mammea siamensis* detected by GC-MS data (*Continued*)

Compounds	RT (min)	Relative content (%)				
		Barks	Flowers	Twigs	Leaves	Young leaves
Fatty acid and terpenoid derivative						
Methyl 10-octadecenoate	10.37	-	-	-	-	4.3
Phytol	10.39	-	-	-	2.3	3.3
Methyl stearate	10.42	0.6	2.6	1.3	0.9	1.8
9,12-Octadecadienoic acid	10.52	-	-	-	-	1.2
Methyl docosanoate	12.13	-	-	-	-	0.5
(5 α)-Androstane-3,17-dione	12.36	6.2	7.3	1.0	-	3.0
Furosardonin A	12.39	-	-	-	-	2.0
Methyl tetracosanoate	12.91	-	-	-	-	0.4
(4aS,10aS)-7-Isopropyl-1,1,4a-trimethyl-1,2,3,4,4a,5,6,9,10,10a-decahydrophenanthrene	13.22	-	-	-	-	0.3
3- β -Chloro-5-cholestene	16.37	-	-	-	-	2.6
Stigmasterol	16.45	-	9.3	-	1.3	5.8
Inophyllum D	16.69	-	-	-	-	1.4
(3-methyl)-stigmast-5-en-3-ol	17.01	3.3	-	-	4.1	7.7
α -Amyrin	17.99	-	-	-	0.8	1.1

GC-MS and Bioassay-Guided Isolation of Xanthenes from *Mammea siamensis*

Wiyarat Kumutanat¹, Sakchai Hongthong^{1,2}, Sariyarach Thanasansurapong^{2,3},
Naowarat Kongkum⁴, and Napasawan Chumnanvej^{5*}

¹Division of Chemistry and Multidisciplinary Research in Chemistry (MulRiC) Laboratory, Faculty of Science and Technology, Rajabhat Rajanagarindra University, Chachoengsao 24000, Thailand

²Center of Excellence for Innovation in Chemistry (PERCH-CIC), Department of Chemistry, Faculty of Science, Mahidol University, Bangkok 10400, Thailand

³National Nanotechnology Center, NSTDA, 111 Thailand Science Park, Klong Luang, Pathum Thani 12120, Thailand

⁴Division of Chemistry, Faculty of Science and Technology, Surindra Rajabhat University, Surin 32000, Thailand

⁵Department of Fundamental Science and Physical Education, Faculty of Science at Sriracha, Kasetsart University, Chonburi 20230, Thailand

* **Corresponding author:**

tel: +66-38354580

email: srcnwh@ku.ac.th

Received: December 9, 2022

Accepted: March 21, 2023

DOI: 10.22146/ijc.79987

Abstract: *Mammea siamensis* (Miq.) T. Anders. (Calophyllaceae) plants have long been employed as an active integral composition in Thai traditional medicine. Additionally, phenylcoumarins and triterpenes were reported as major components in phytochemical research. This work explored the various parts of *M. siamensis*; barks, flowers, twigs, leaves, and young leaves; to determine their bioactive compounds. By using the GC-MS and bioassay guidance, two xanthenes, 6-deoxyisojacareubin (**1**) and 1,5-dihydroxyxanthone (**2**), together with a mixture of phenylcoumarins, mammea A/AA cyclo D (**3**) and mammea A/AB cyclo D (**4**) have been isolated from the methanolic extract of young leaves. Their structures were identified by means of spectroscopic technique and by comparison with literature data. In particular, the current study was the first exposed report of xanthenes **1** and **2** from the genus *Mammea*. Furthermore, compounds **1** and **2** and the methanolic young leaf extract had high antioxidant efficiency on DPPH and ABTS assays. The young leaf extract provided mild toxicity on the brine shrimp lethality test (BSLT) with LC_{50} value of $93.11 \pm 1.37 \mu\text{g/mL}$. In addition, the isolated compounds **1** and **2** were non-toxicity in BSLT assay. Therefore, the young leaf extract and the purified constituents **1** and **2** should be further studied and developed for using in pharmaceutical industries.

Keywords: antioxidant activity; *Mammea siamensis*; phenylcoumarins; toxicity; xanthenes

■ INTRODUCTION

Medicinal plants are employed as ingredients in several traditional remedies due to their phytochemical metabolites, such as terpenoids, flavonoids, alkaloids, and polyphenols. These significant bioactive components revealed diverse efficiency, for example, anticancer [1-3], antioxidant [3-5], antimicrobial [4-6], and antileishmanial activities [5,7]. Accordingly, various Thai medicinal plants are famous for acting as active elements

in several folk medicines, including *Mammea siamensis* [8-9].

The genus *Mammea* belongs to the family Guttiferae, recently assigned to the Calophyllaceae [10]. This genus consists of approximately 75 species overspreading throughout the tropics in Africa, Central America, Madagascar, and tropical Asia. Three species, *M. brevipes*, *M. harmandii*, and *M. siamensis*, have been reported in Thailand [11].

M. siamensis (Miq.) T. Anders, named “Saraphi”, is a Thai botanical medicine. Its flowers have long been traditionally employed as an active, integral composition in Thai herbal prescriptions as a heart tonic and promoting of appetite [12-13]. Several parts of this plant, such as flowers [12,14], twigs [15], seeds [16-18], and barks [19], have been phytochemically investigated. For example, many bioactive compounds separated from the methanol extract of *M. siamensis* flowers showed potent cytotoxic activity, such as mammeasin A and surangin B [20]. The extensive literature review has investigated only one phytochemical constituent from *M. siamensis* leaves. Proanthocyanidin, a condensed tannin, has been isolated from 95% ethanol extract of the leaves, and it showed molluscicidal activity at its sufficient concentration [21]. In particular, the prior reports determined higher effectiveness of shoot or young leaves than mature leaves in various bioactivities, anticancer [1,22], antioxidant, and total phenolic contents [23-24]. In the present work, gas chromatography-mass spectrometry (GC-MS) analytical method and bioactivity evaluation, antioxidative activity and *in vivo* toxicity on brine shrimp lethality assays were performed to examine bioactive compounds from the leaf, young leaf (first 3-5 leaves) [25-26], twig, bark and flower extracts of *M. siamensis*. As guided by such techniques, the methanolic young leaf extract was further investigated, leading to the isolation of two bioactive xanthenes, 6-deoxyisojacareubin (**1**) and 1,5-dihydroxyxanthone (**2**) and a mixture of mammea A/AA cyclo D (**3**) and mammea A/AB cyclo D (**4**). Their structures were identified by NMR and mass spectroscopic data, with this work providing the first report of compounds **1** and **2** from the medicinal plant in *Mammea* genus. Furthermore, these two isolated compounds were tested for their antioxidative ability and *in vivo* toxicity using brine shrimp lethality assay and the results were discussed.

■ EXPERIMENTAL SECTION

Materials

The barks, flowers, twigs, leaves, and young leaves of *Mammea siamensis* were collected in February 2019 from Chachoengsao province, Thailand. The plant materials were identified by SH and a voucher specimen with the

plant code RRU-SH-009 was collected at the Faculty of Science and Technology, Rajabhat Rajanagarindra University, Chachoengsao, Thailand.

Instrumentation

The ^1H -, ^{13}C -, and 2D-NMR spectra were recorded with a Bruker Ascend™ 400 spectrometer in acetone- d_6 (CD_3COCD_3), dimethyl sulfoxide- d_6 (CD_3SOCD_3) and chloroform- d (CDCl_3) (were acquired from Merck, Germany) solutions by using an internal standard as either tetramethylsilane (TMS) or residual non-deuterated solvent peak. High-resolution mass spectra were recorded with a Bruker micro TOF spectrometer. Agilent 5977B GC/MSD was employed for GC-MS technique evaluation. Analytical purposes were performed by using silica gel 60 PF₂₅₄-pre-coated TLC aluminum sheets of (20 × 20 cm, layer thickness of 0.2 mm, Merck, Germany). Spraying with 12% H_2SO_4 in ethanol or anisaldehyde reagent and visualization under ultraviolet light were used for chemical composition monitoring. Column chromatography was implemented using Merck silica gel 60 (60–200 μm or 70–230 mesh ASTM) and Merck Sephadex LH-20. Distillation technique was employed for solvent preparation prior to use in extraction, chromatography, and crystallization processes. Analytical grade solvents, ethanol and methanol, were obtained from Fisher Scientific Korea Ltd.

Procedure

Extraction

The air-dried powdered materials from the barks, flowers, twigs, leaves and young leaves of *M. siamensis* (10 g each) were macerated at room temperature with methanol (200 mL × 7 d × triplicates) for each extraction. Removal of the solvents under reduced pressure and subsequent freeze-drying were performed after filtration. Then the crude methanol extracts were obtained and kept at -4°C until further analysis.

GC-MS analysis

GC-MS analysis was implemented by employing an Agilent 5977B GC/MSD with an HP5MS column (30 m × 0.25 mm × 0.25 mm) under Helium as carrier gas with a flow rate of 1.3 mL/min. Samples were

analyzed in the column held at an initial temperature of 50 °C for 3 min after injection. Then, increasing temperature was carried out to 280 °C at a program rate of 10 °C/min and then held for 20 min. The injections were performed at 250 °C in splitless mode. The pressure was 10 psi, the run time was 37.5 min, and the temperatures of injector and detector were 250 °C. Before submission to GC-MS analysis, each crude extract (2.0 mg) was dissolved in 1 mL of methanol and subjected to exhaustive filtration. The isolated constituents were examined to compare with the authentic samples by referring to their retention times and mass weights available in GC-MS NIST library.

Antioxidant activity

The free radical scavenging ability of the extracts and the isolated compounds were evaluated on the basis of DPPH and ABTS free radical scavenging assays.

The DPPH inhibition of each sample was determined according to the modified procedure [27]. Briefly, varied concentrations of the samples; 6.25, 12.5, 25, 50, and 100 µg/mL; were prepared by dissolution and dilution in methanol. To analyze, 0.2 mM DPPH solution in methanol (4 mL) was mixed with the sample solutions (1 mL) and the mixtures were shaken intensely. Instantaneously, incubation of the reaction mixtures at room temperature was operated in the absence of light for 30 min before the absorbance measurement at 517 nm. All assays were executed in triplicate to afford accurate data. The percentage of DPPH free radical inhibition was determined by using Eq. (1):

$$\text{Percentage of DPPH inhibition} = \left(\frac{A_0 - A_1}{A_0} \right) \times 100 \quad (1)$$

where A_0 and A_1 correspond to the absorbance at 517 nm of the DPPH radical in control and in the presence of samples, respectively. Additionally, the 50% inhibitory concentration (IC_{50}) value indicating the least sample concentration inhibiting 50% of free radicals was calculated. The quercetin and butylated hydroxytoluene (BHT) solutions were employed as reference antioxidants.

For ABTS assay, the procedure was modified according to the literature [28]. In brief, 7 mM ABTS solution (10 mL) was added to 2.45 mM potassium

persulfate ($K_2S_2O_8$, 176 µL) and the mixture was immediately kept in the dark condition at room temperature for 12–16 h prior to use. Subsequently, the ABTS working solution was prepared to obtain the appropriate absorbance of 0.700 ± 0.020 at 734 nm by dilution with 95% ethanol. Then, 100 µL of the sample solutions with different concentrations: 6.25, 12.5, 25, 50, and 100 µg/mL, were mixed with 900 µL of the ABTS working solution and the reaction was allowed to leave for 6 min at room temperature. Ethanol was set as the standard blank for absorbance measurement at 734 nm. Quercetin and BHT were used as references. The Eq. (2) evaluated the percentage of free radical inhibition of the extracts:

$$\text{Percentage of ABTS inhibition} = \left(\frac{A_0 - A_1}{A_0} \right) \times 100 \quad (2)$$

where A_0 is the absorbance of the control and A_1 is the absorbance of the tested sample or standard after treatment.

In vivo toxicity on brine shrimp lethality assay

The prepared extracts and the isolated compounds were examined by employing the brine shrimp lethality test (BSLT) [29]. Briefly, brine shrimp cysts (0.25 g) were hatched in an Erlenmeyer flask containing 1 L of well-aerated artificial seawater (26.29 g of NaCl, 0.74 g of KCl, 0.99 g of $CaCl_2$, 2.86 g of $MgCl_2$, and 3.94 g of $MgSO_4 \cdot 7H_2O$, with adjusted pH 7.8) under lighted conditions for 48 h. The extracts were prepared by dissolving in 1% v/v of DMSO in artificial seawater in concentrations ranging from 62.5, 125, 250, 500, and 1000 µg/mL. Simultaneously, more than 30 *Artemia* larvae were transferred from the hatching flask into each concentration of sample during the preparation to avoid dilution from transferring larvae medium to the test samples. Also, potassium dichromate ($K_2Cr_2O_7$) solution with the same preparation was employed as a positive control in 6.25, 12.5, 25, 50, and 100 µg/mL concentrations. All experiments were determined in triplicate by only dividing 10 nauplii per sample tube. Furthermore, nauplii was examined as blank in 1% v/v of DMSO in artificial seawater. Then, the incubation of all samples was investigated under proper light for 24 h at room temperature. The percentage lethality was

evaluated from the counted alive nauplii by utilizing Eq. (3):

$$\% \text{ Mortality} = \left(\frac{\text{Total nauplii} - \text{Alive nauplii}}{\text{Total nauplii}} \right) \times 100 \quad (3)$$

The data were processed using a Probit analysis program to calculate the lethal concentration of half of the test organisms (LC₅₀).

Extraction, purification, and spectroscopic data of isolated compounds

Air-dried and finely powdered young leaves (1.5 kg) of *M. siamensis* were macerated with methanol (4 L × 7 d × triplicates) at room temperature. Then, the methanolic crude extract (34.9 g) was obtained by filtration and solvent removal under reduced pressure, respectively. A vacuum liquid column chromatography (VCC) technique was employed to isolate the pure compounds. Gradient elution of EtOAc–hexane solution (0, 10, 20, 40, 60, 80, 100%, 2 L each) followed by MeOH–EtOAc solution (10, 20, 50, 100%, 1 L each) was conducted for VCC. Based on TLC characteristics, the fractions (1 L each) were collected and combined to yield seven fractions (F1–F7). Fraction F3 (1.3 g) was purified employing silica gel column chromatography (Si-gel CC) with the gradient solvent system elution of EtOAc–hexane (0–100%) and MeOH–EtOAc (0–100%) to provide subfractions F3.1–F3.4. Sephadex LH-20 was presented for gel filtration of subfraction F3.2 (242.0 mg) to isolate a pure constituent, xanthone **1** (6.0 mg), together with a mixture of mammea A/AA cyclo D (**3**) and mammea A/AB cyclo D (**4**) (4.2 mg) in the ratio of 1:2. After purification of fraction F4 (2.3 g) using Si-gel CC with MeOH-CH₂Cl₂ (0–100%), gradient as eluent, subfractions F4.1–F4.4 were obtained. Chromatography of subfraction F4.2 (177.0 mg) was performed on Sephadex LH-20 with MeOH elution to afford compound **2** (18.0 mg).

6-Deoxyisojacareubin (1). A yellowish solid; m.p. 220.1–222.0 °C; UV (MeOH) λ_{max} (log ε) 329 (3.78), 267 (4.23), 251 (4.27) nm; IR (KBr) ν_{max} 3467, 3402, 3023, 2978, 1651, 1619, 1573, 1485, 1344, 1278, 1159, 1114, 762 cm⁻¹; ¹³C-NMR (acetone-*d*₆, 100 MHz) and ¹H-NMR (acetone-*d*₆, 400 MHz) data, see Table 2; HR-EI-MS *m/z* 311.0907 [M+H]⁺ (calc. for C₁₈H₁₅O₅, 311.0914).

1,5-Dihydroxyxanthone (2). A brownish solid; m.p. 198.2–199.0 °C; UV (MeOH) λ_{max} (log ε) 370 (3.94), 312 (4.15), 348 (4.88) nm; IR (KBr) ν_{max} 3424, 1651, 1611, 1579, 1497, 1462, 1279, 1240, 1144, 1067, 793, 724 cm⁻¹; ¹³C-NMR (DMSO-*d*₆, 100 MHz) and ¹H-NMR (DMSO-*d*₆, 400 MHz) data, see Table 2; HR-EI-MS *m/z* 288.0428 [M]⁺ (calc. for C₁₃H₈O₄, 288.0423).

A mixture of mammea A/AA cyclo D (3) and mammea A/AB cyclo D (4). (ratio 1:2 by ¹H-NMR data); ¹³C-NMR (CDCl₃, 100 MHz): 206.7 (C-1^{''}), 164.4 (C-5), 159.6 (C-2), 156.4 (C-4), 154.9 (C-10b), 153.1 (C-6a), 139.3 (C-1[']), 128.8 (C-4[']), 127.6 (C-3['], C-5[']), 127.2 (C-2['], C-6[']), 126.3 (C-9), 115.0 (C-10), 112.7 (C-3), 107.2 (C-6), 102.0 (C-4a), 101.0 (C-10a), 79.9 (C-8), 53.6 (C-2^{''}), 28.7 (C-1^{''}, C-2^{''}), 25.5 (C-3^{''}), 22.7 (C-4^{''}, C-5^{''}) for **3**; 211.5 (C-1^{''}), 164.4 (C-5), 159.7 (C-2), 157.8 (C-10b), 156.4 (C-4), 154.4 (C-6a), 139.2 (C-1[']), 128.2 (C-4[']), 127.6 (C-3['], C-5[']), 127.1 (C-2['], C-6[']), 126.3 (C-9), 115.5 (C-10), 112.7 (C-3), 107.3 (C-6), 102.0 (C-4a), 101.5 (C-10a), 79.8 (C-8), 46.6 (C-2^{''}), 28.6 (C-1^{''}, C-2^{''}), 25.5 (C-3^{''}), 16.8 (C-4^{''}), 11.6 (C-5^{''}) for **4**; ¹H-NMR (CDCl₃, 400 MHz): 14.10 (1H, *s*), 7.43 (3H, *m*, H-3['], H-4['], H-5[']), 7.35 (2H, *m*, H-2['], H-6[']), 6.92 (1H, *d*, 10.0, H-10), 6.03 (1H, *s*, H-3), 5.67 (1H, *d*, 10.0, H-9), 3.00 (2H, *d*, 7.2, H-2^{''}), 2.26 (1H, *m*, H-3^{''}), 1.60 (6H, *s*, H-1^{''}, H-2^{''}), 0.98 (6H, *d*, 6.8, H-4^{''}, H-5^{''}) for **3**; 14.54 (1H, *s*), 7.31 (3H, *m*, H-3['], H-4['], H-5[']), 7.24 (2H, *m*, H-2['], H-6[']), 6.81 (1H, *d*, 10.0, H-10), 5.91 (1H, *s*, H-3), 5.55 (1H, *d*, 10.0, H-9), 3.67 (2H, *sextet*, 6.6, H-2^{''}), 1.69 (1H, *m*, H-3^{''}), 1.48 (6H, *s*, H-1^{''}, H-2^{''}), 1.26 (1H, *m*, H-3^{''}), 1.12 (3H, *d*, 6.9, H-5^{''}), 0.84 (3H, *t*, 7.3, H-4^{''}) for **4**; HR-EI-MS *m/z* 404.1631 [M]⁺ (calc. for C₂₅H₂₄O₅, 404.1624).

RESULTS AND DISCUSSION

After extraction of several parts of *M. siamensis*; barks, flowers, twigs, leaves, and young leaves, with methanol as the eluent followed by filtration and evaporation under reduced pressure, each crude extract was analyzed using GC-MS and the constituents are shown in Fig. 1. The tentative scanning of the GC-MS chromatogram of barks, flowers, twigs, leaves, and young leaves revealed the signal of several phenolic components by comparison with the NIST database (see

Supplementary information). After comparison of GC-MS chromatograms, it was indicated that various phenolic components were contained in crude methanol extract of the leaves and young leaves. Antioxidant

activities in both DPPH and ABTS radical scavenging assays evaluated in the extracts from various parts of *M. siamensis* are summarized in Table 1.

As shown in Table 1, the antioxidant activity of the

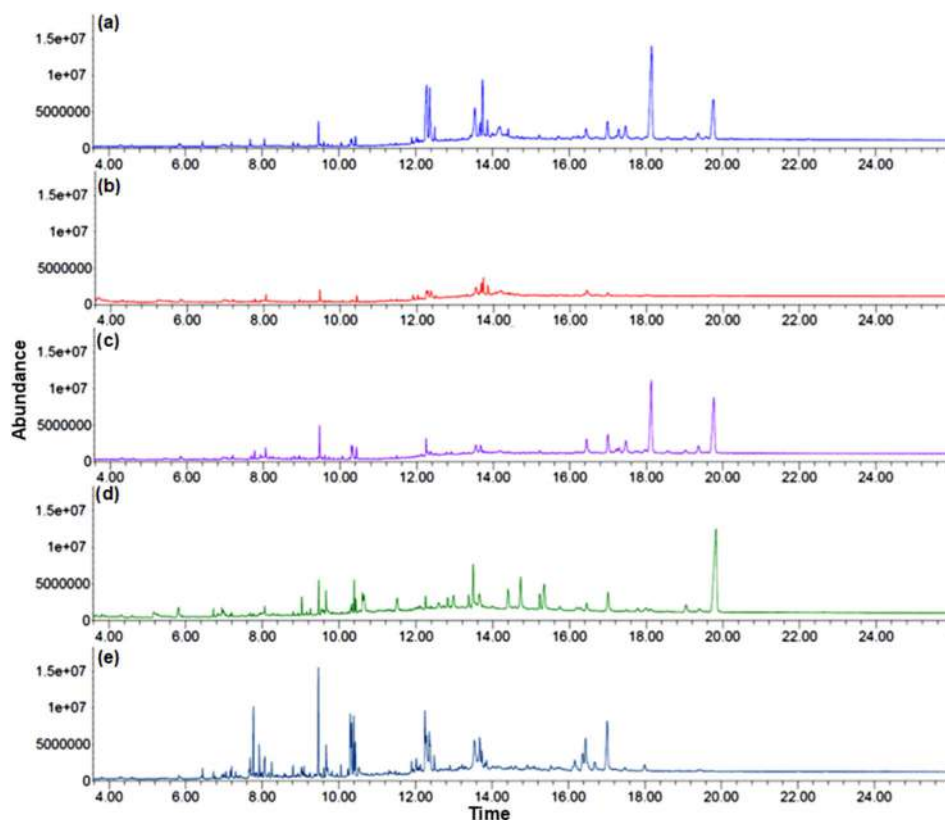


Fig 1. Total ion GC-MS chromatograms of different extracts from *M. siamensis*, (a) barks, (b) flowers, (c) twigs, (d) leaves, and (e) young leaves

Table 1. Antioxidant activity and *in vivo* toxicity on BSLT of *M. siamensis* extracts and isolated compounds **1** and **2**

Sample	IC ₅₀ (µg/mL)		LC ₅₀ (µg/mL)
	DPPH assay	ABTS assay	BSLT assay
Bark extract	55.11 ± 2.18	103.69 ± 1.21	>100
Flower extract	50.38 ± 2.90	69.58 ± 0.88	70.14 ± 0.79
Twig extract	53.91 ± 0.55	76.67 ± 1.23	76.59 ± 1.27
Leave extract	66.31 ± 1.24	47.71 ± 0.67	8.37 ± 1.22
Young leaf extract	59.04 ± 1.92	47.22 ± 1.09	93.11 ± 1.37
1	78.16 ± 1.32	40.42 ± 0.59	> 100
2	70.16 ± 0.97	38.86 ± 1.66	> 100
Quercetin	14.02 ± 0.86	14.02 ± 0.86	ND
BHT	ND	23.23 ± 1.50	ND
K ₂ Cr ₂ O ₇	ND	ND	12.62 ± 0.72

IC₅₀ and LC₅₀ results are average of three independent experiments ± standard deviation. Quercetin and BHT were used as positive controls for the antioxidant assay and K₂Cr₂O₇ was used as positive control for BSLT assay. ND = not determined

extracts exhibited free radical scavenging activity with IC_{50} values ranging from 50.38 ± 2.90 to $66.31 \pm 1.24 \mu\text{g/mL}$ for DPPH assay and from 47.22 ± 1.09 to $103.69 \pm 1.21 \mu\text{g/mL}$ for ABTS assay. The results indicated strong effective antioxidant ability of whole parts according to the literature [30]; at lower than $50 \mu\text{g/mL}$ of IC_{50} values shows very strong antioxidant properties, strong antioxidant characterization is exhibited as IC_{50} values of $50\text{--}100 \mu\text{g/mL}$, IC_{50} values of moderate ability are provided at $100\text{--}150 \mu\text{g/mL}$, and weak efficiency shows the IC_{50} value of $150\text{--}200 \mu\text{g/mL}$. Furthermore, the toxicity assay based on the BSLT at different concentrations (Table 1) revealed that all the extracts except from the barks showed toxicity at LC_{50} ranging from 8.37 ± 1.22 to $93.11 \pm 1.37 \mu\text{g/mL}$ [31-32]. Based on the antioxidant results of the extracts, the young leaf extract provided free radical scavenging activity apparently in both DPPH and ABTS assays at 59.04 ± 1.92 and $47.22 \pm 1.09 \mu\text{g/mL}$, respectively. Additionally, the cytotoxic effect in BSLT from the young leaf extract afforded mild toxicity with LC_{50} value of $93.11 \pm 1.37 \mu\text{g/mL}$.

In accordance with the combination of GC-MS profiling and the biological activities of the various parts of *M. siamensis* extracts, the young leaf extract exhibited more interesting efficiency than the others; therefore, it was chosen to isolate its attractively bioactive constituents. After the isolation and purification by chromatography techniques, compounds **1** and **2** along with a mixture of coumarins **3** and **4** were obtained (Fig. 2). All compounds were elucidated and identified based on spectroscopic techniques.

Compound **1** was obtained as a yellowish solid. The molecular formula $C_{18}H_{14}O_5$ was determined by HR-EI-

MS at m/z 311.0907 $[M+H]^+$ (calc. for $C_{18}H_{15}O_5$, 311.0914). Its ^1H and ^{13}C -NMR data are summarized in Table 2. The ^{13}C -NMR and DEPT135 spectra analysis identified 17 signals for 18 carbons, 2 methyls, 6 methines and 10 quaternary carbons. The ^1H -NMR spectrum exhibited low-field broad signals at δ 12.11 and 9.14 ppm, indicating the hydroxyl chelated group at C-1 and free hydroxyl group at C-5, respectively. Three aromatic protons at δ 7.67 (1H, dd, $J = 7.8, 1.6$ Hz), 7.35 (1H, dd, $J = 7.8, 1.6$ Hz), and 7.30 (1H, t, $J = 7.8$ Hz) ppm indicated the presence of the ABC-type aromatic protons H-8, H-6, and H-7, respectively. A singlet signal at δ 6.19 (1H) ppm was assigned to the aromatic proton H-2. A sharp singlet at δ 1.50 (CH_3 -14 and CH_3 -15) ppm and a pair of doublets at δ 7.09 (1H, H-11) and 5.75 (1H, H-12) ppm with coupling constant of 10.1 Hz suggested the presence of a 2,2-dimethylchromene ring. To confirm the structure of **1**, the chemical shifts of each carbon and proton were deduced based on the 2D NMR information (COSY, HMQC, and HMBC correlations), along with comparisons of the data to those in the literature [33-35]. Thus, compound **1** was identified as 6-deoxyisojacareubin.

Compound **2** was a brownish solid with a molecular formula of $C_{13}H_8O_4$ associated with the HR-EI-MS m/z 288.0428 (calc. for $[M]^+$, 288.0423). The comparison between ^{13}C and DEPT135 NMR spectra indicated 13 signals for 13 carbons, 4 methine carbons, and 9 quaternary carbons, as summarized in Table 2. The ^1H -NMR spectrum of **2** showed the characteristics of a chelated hydroxyl proton at C-1 and of a free hydroxyl group at C-5 at δ 12.62 (1H, s) and δ 10.55 (1H, s) ppm, respectively. The aromatic protons at δ 7.70 (1H, dd, $J = 8.3, 8.3$ Hz, H-3), 7.05 (1H, d, $J = 8.3$ Hz, H-4), and

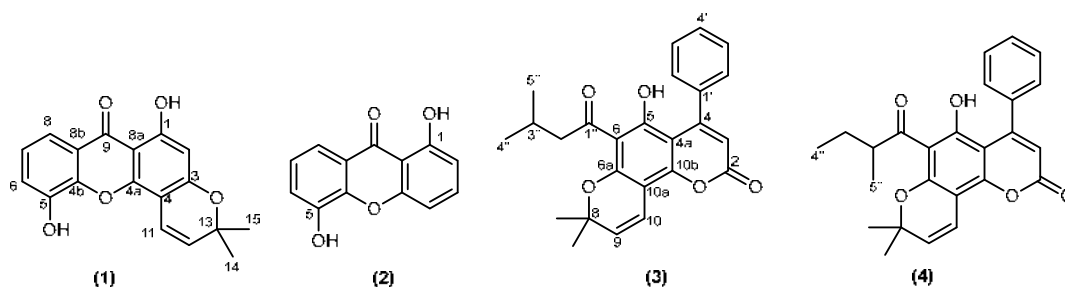


Fig 2. Structures of compounds **1**–**4** isolated from young leaves of *M. siamensis*

Table 2. ^{13}C (100 MHz) and ^1H -NMR (400 MHz) data of compounds **1** and **2**

Position	1 ^a		2 ^b	
	δ_{C}	δ_{H} (mult., <i>J</i> (Hz))	δ_{C}	δ_{H} (mult., <i>J</i> (Hz))
1	164.20 (C)		161.00 (C)	
2	99.80 (CH)	6.19 (s)	110.50 (CH)	6.77 (d, 8.3)
3	161.90 (C)		137.40 (C)	7.70 (dd, 8.3, 8.3)
4	102.20 (C)		107.60 (C)	7.05 (d, 8.3)
4a	152.50 (C)		155.80 (C)	
4b	147.00 (C)		146.00 (C)	
5	147.10 (C)		146.40 (C)	
6	122.20 (CH)	7.35 (dd, 7.8, 1.6)	121.00 (CH)	7.55 (d, 7.7)
7	125.70 (CH)	7.30 (t, 7.8)	124.90 (CH)	7.25 (dd, 7.7, 7.7)
8	116.90 (CH)	7.67 (dd, 7.8, 1.6)	114.60 (CH)	8.33 (d, 7.7)
8a	122.60 (C)		121.30 (C)	
8b	104.40 (C)		108.90 (C)	
9	182.00 (C=O)		182.10 (C=O)	
11	115.90 (CH)	7.09 (d, 10.1)		
12	129.50 (CH)	5.75 (d, 10.1)		
13	79.20 (C)			
14	28.40 (CH ₃)	1.50 (s)		
15	28.40 (CH ₃)	1.50 (s)		
1-OH		12.11 (s)		12.62 (s)
5-OH		9.14 (br. s)		10.55 (br. s)

^aThe spectral data were recorded in deuterated acetone (CD_3COCD_3). ^bThe spectral data were recorded in deuterated dimethyl sulfoxide (CD_3SOCD_3). Carbon types were deduced by DEPT135 experiment. mult. = multiplicity

6.77 (1H, d, *J* = 8.3 Hz, H-2) ppm were assigned to be 1,2,3-trisubstituted benzene ring A. The three aromatic signals at δ 8.33 (1H, d, *J* = 7.7 Hz, H-8), 7.55 (1H, d, *J* = 7.7 Hz, H-6), and 7.25 (1H, dd, *J* = 7.7, 7.7 Hz, H-7) ppm were also indicated as 1,2,3-trisubstituted benzene ring C. In addition, the chemical structure of compound **2** was evaluated using 2D (COSY, HMQC, and HMBC correlations) NMR spectroscopy. Finally, the data were intensively compared with the literature data [36]. Hence, compound **2** was identified as 1,5-dihydroxyxanthone.

Although compounds **3** and **4** were isolated as the mixture, their chemical structural identification was determined using the ^1H and ^{13}C -NMR data together with HR-EI-MS data and comparison to the human metabolome database (HMDB). The ^1H and ^{13}C chemical shifts of each compound were clearly identified by comparing them with the previous report by Verotta, L. and co-workers [37]. Based on the intensive comparison

of the spectroscopic data of the mixture with the literature data, the mixture of coumarins **3** and **4** was identified as mammea A/AA cyclo D and mammea A/AB cyclo D, respectively (see supplementary information).

The GC-MS chromatograms of the methanolic extracts of young leaves and leaves were identified to contain compounds **1** and **2** by comparing the molecular mass and retention time of each pure isolated compound, as shown in Fig. 3. This result might indicate that both compounds are the remarkably important secondary metabolites for the plant leaves.

The biological activities of the isolated compounds **1** and **2** were examined by using DPPH and ABTS radical scavenging assays along with *in vivo* toxicity in the BSLT assay. Both compounds exhibited strong antioxidant characteristics in DPPH assay with IC_{50} values of 78.16 ± 1.32 and 70.16 ± 0.97 $\mu\text{g/mL}$, respectively [30].

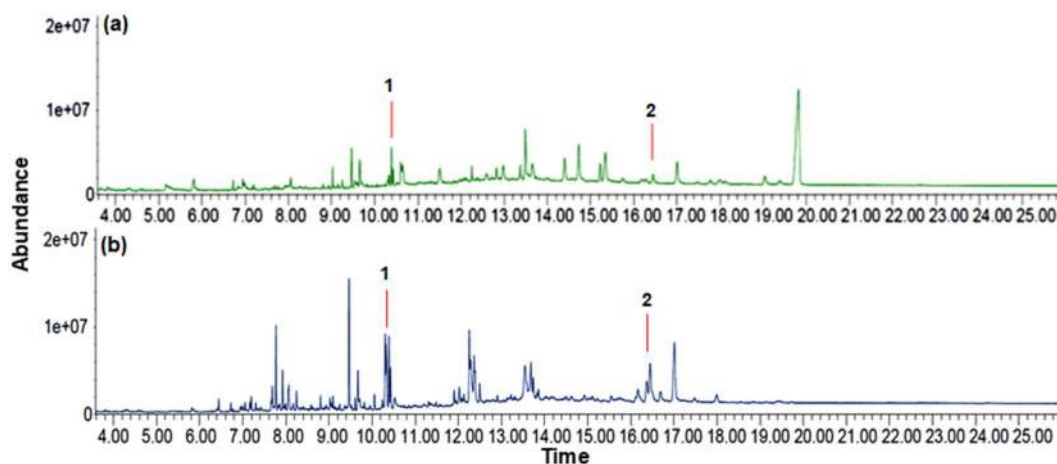


Fig 3. GC-MS chromatograms of compounds **1** and **2** in crude extracts, (a) leaves; (b) young leaves

In ABTS assay, the IC_{50} values of **1** and **2** were 40.42 ± 0.59 and 38.86 ± 1.66 $\mu\text{g/mL}$, respectively, which also showed very strong antioxidative levels [30]. After comparing the data, compounds **1** and **2** have the coordinately antioxidative results. In addition, they were non-toxic in BSLT with LC_{50} values > 100 $\mu\text{g/mL}$ [31]; thus, both compounds were not active regarding *in vivo* toxicity. This result agreed with the toxicity of the related xanthone derivatives, 1,7-dihydroxyxanthone and 1-hydroxy-5-methoxyxanthone, previously isolated from seed of *M. siamensis* [16].

According to the previous study, the crude extracts and isolated compounds from several parts of *M. siamensis* were evaluated for biological cytotoxicity [14,16-17,20] and antibacterial activity [38], and most of them revealed coumarins being the major constituents [17,39-40]. However, xanthenes are a small group of phytochemical constituents in *M. siamensis*. To the best of our precedent search from SciFinder database, we first found xanthone derivatives **1** and **2** isolated from *Mammea* plants in the present study.

■ CONCLUSION

Mammea siamensis is an important medicinal plant containing notable bioactive compounds. Based on GC-MS and bioassay-guided isolation screening, the present study isolated two naturally occurring xanthone derivatives, 6-deoxyisojacareubin (**1**) and 1,5-dihydroxyxanthone (**2**), together with a mixture of

phenylcoumarins, namely mammea A/AA cyclo D (**3**) and mammea A/AB cyclo D (**4**) from the methanolic young leaf extract of *M. siamensis*. The structures of the two isolated compounds were confirmed based on spectroscopic data and comparison with the literature. Furthermore, isolation of the secondary metabolites **1** and **2** has not been previously reported from this plant or the *Mammea* genus. Additionally, both isolated constituents provided efficient scavenging activity on DPPH and ABTS radicals, whereas they were no *in vivo* toxicity based on the brine shrimp lethality assay. Hence, isolated constituents, **1** and **2**, and the young leaf extract should be further studied for employment in anti-aging cosmetics and pharmaceutical industries in traditional plant-based medicines.

■ ACKNOWLEDGMENTS

We acknowledge the Division of Chemistry and Multidisciplinary Research in Chemistry (MulRiC) Laboratory, Faculty of Science and Technology, Rajabhat Rajanagarindra University, and Research and Development Institute Rajabhat Rajanagarindra University to Wiyarat Kumutanat. We also thank the Faculty of Science at Sriracha, Kasetsart University, Thailand, for partial financial support to Napasawan Chumnanvej, respectively. We also thank the Center of Excellence for Innovation in Chemistry (PERCH-CIC) and the Office of the Higher Education Commission and Mahidol University under the National Research

Universities Initiative for spectroscopic measurements. We also thank Dr. Andrew Warner, Kasetsart University, Thailand, for native English proofreading.

■ AUTHOR CONTRIBUTIONS

Wiyarat Kumutanat, Sakchai Hongthong, Sariyarach Thanasansurapong, and Napasawan Chumnanvej conducted the experiment in isolation of the isolated compounds and analysis using GC-MS spectrometry. Naowarat Kongkum and Napasawan Chumnanvej conducted the experiment of DPPH and ABTS radical scavenging inhibition and *in vivo* toxicity by BSLT assay. Napasawan Chumnanvej and Wiyarat Kumutanat wrote and revised the manuscript. All authors agreed to the final version of this manuscript.

■ REFERENCES

- [1] Ghanadian, M., Ali, Z., Khan, I.A., Balachandran, P., Nikahd, M., Aghaei, M., Mirzaei, M., and Sajjadi, S.E., 2020, A new sesquiterpenoid from the shoots of Iranian *Daphne mucronata* Royle with selective inhibition of STAT3 and Smad3/4 cancer-related signaling pathways, *DARU J. Pharm. Sci.*, 28 (1), 253–262.
- [2] Aghaei, M., Mirzaei, M., Ghanadian, M., Fallah, M., and Mahboodi, R., 2021, 6-Methoxylated flavonoids: Jacein, and 3-demethyljacein from *Centaurea schmidii* with their endoplasmic reticulum stress and apoptotic cell death in breast cancer cells along with *in-silico* analysis, *Iran. J. Pharm. Res.*, 20 (2), 417–432.
- [3] Shalaby, E.A., Shanab, S.M.M., Hafez, R.M., and El-Ansary, A.E., 2023, Chemical constituents and biological activities of different extracts from ginger plant (*Zingiber officinale*), *Chem. Biol. Technol. Agric.*, 10 (1), 14.
- [4] Dyshlyuk, L.S., Fotina, N.V., Milentyeva, I.S., Ivanova, S.A., Izgarysheva, N.V., and Golubtsova, Y.V., 2024, Antimicrobial and antioxidant activity of *Panax ginseng* and *Hedysarum neglectum* root crop extracts, *Braz. J. Biol.*, 84, e256944.
- [5] Kefi, S., Essid, R., Papetti, A., Abid, G., Bouslama, L., Aouani, E., Tabbene, O., and Limam, F., 2023, Antioxidant, antibacterial, and antileishmanial potential of *Micromeria nervosa* extracts and molecular mechanism of action of the bioactive compound, *J. Appl. Microbiol.*, 134 (2), lxad007.
- [6] Sakyiamah, M.M., Gordon, P.K., Bolah, P., Baffour, P.K., Ehun, E., Quasie, O., Kumadoh, D., Archer, M.A., Mintah, S.O., and Appiah, A.A., 2023, Assessment of the phytochemical composition and antimicrobial properties of *Tapinanthus bangwensis* leaves hosted by the branches of *Persea americana*, *BMC Complementary Med. Ther.*, 23 (1), 34.
- [7] Abdeyazdan, S., Mohajeri, M., Saberi, S., Mirzaei, M., Ayatollahi, S.A., Saghaei, L., and Ghanadian, M., 2022, Sb(V) kaempferol and quercetin derivative complexes: Synthesis, characterization and antileishmanial activities, *Iran. J. Pharm. Res.*, 21 (1), e128379.
- [8] Sukkasem, K., Panthong, S., and Itharat, A., 2016, Antimicrobial activities of Thai traditional remedy “Kheaw-Hom” and its plant ingredients for skin infection treatment in chickenpox, *J. Med. Assoc. Thailand*, 99 (Suppl. 4), S116–S123.
- [9] Streinrut, L., Itharat, A., and Ruangnoo, S., 2011, Free radical scavenging and lipid peroxidation of Thai medicinal plants used for diabetic treatment, *J. Med. Assoc. Thailand*, 94 (Suppl. 7), S178–S182.
- [10] Lemus, C., Smith-Ravin, J., and Marcelin, O., 2021, *Mammea americana*: A review of traditional uses, phytochemistry and biological activities, *J. Herb. Med.*, 29, 100466.
- [11] Byrne, C., Parnell, J.A.N., and Chayamarit, K., 2018, Systematics of the Thai Calophyllaceae and Hypericaceae with comments on the Kiehmeyeroideae (Clusiaceae), *Thai Forest Bull., Bot.*, 46 (2), 162–216.
- [12] Luo, F., Manse, Y., Chaipech, S., Pongpiriyadacha, Y., Muraoka, O., and Morikawa, T., 2023, Structures of Mammeasins P and Q, coumarin-related polysubstituted benzofurans, from the Thai medicinal plant *Mammea siamensis* (Miq.) T. Anders.: Anti-proliferative activity of coumarin constituents against human prostate carcinoma cell line LNCaP, *Pharmaceuticals*, 16 (2), 231.

- [13] Sangkaruk, R., Rungrojsakul, M., Tima, S., and Anuchapreeda, S., 2017, Effect of Thai Saraphi flower extracts on WT1 and Bcr/Abl protein expression in leukemic cell lines, *Afr. J. Tradit., Complementary Altern. Med.*, 14 (2), 16–24.
- [14] Ninomiya, K., Shibatani, K., Sueyoshi, M., Chaipech, S., Pongpiriyadacha, Y., Hayakawa, T., Muraoka, O., and Morikawa, T., 2016, Aromatase inhibitory activity of geranylated coumarins, Mammeasins C and D, isolated from the flowers of *Mammea siamensis*, *Chem. Pharm. Bull.*, 64 (7), 880–885.
- [15] Prachywarakorn, V., Mahidol, C., and Ruchirawat, S., 2006, Siamenols A–D, four new coumarins from *Mammea siamensis*, *Chem. Pharm. Bull.*, 54 (6), 884–886.
- [16] Laphookhieo, S., Promnart, P., Syers, J.K., Kanjana-Opas, A., Ponglimanont, C., and Karalai, C., 2007, Coumarins and xanthenes from the seeds of *Mammea siamensis*, *J. Braz. Chem. Soc.*, 18 (5), 1077–1080.
- [17] Rungrojsakul, M., Katekunlaphan, T., Saiai, A., Ampasavate, C., Okonogi, S., Sweeney, C.A., and Anuchapreeda, S., 2016, Down-regulatory mechanism of mammea E/BB from *Mammea siamensis* seed extract on Wilms' tumor 1 expression in K562 cells, *BMC Complementary Altern. Med.*, 16 (1), 130.
- [18] Rungrojsakul, M., Saiai, A., Ampasavate, C., Anuchapreeda, S., and Okonogi, S., 2016, Inhibitory effect of mammea E/BB from *Mammea siamensis* seed extract on Wilms' tumour 1 protein expression in a K562 leukaemic cell line, *Nat. Prod. Res.*, 30 (4), 443–447.
- [19] Ngo, N.T.N., Nguyen, V.T., Vo, H.V., Vang, O., Duus, F., Ho, T.D.H., Pham, H.D., and Nguyen, L.H.D., 2010, Cytotoxic coumarins from the bark of *Mammea siamensis*, *Chem. Pharm. Bull.*, 58 (11), 1487–1491.
- [20] Luo, F., Sugita, H., Muraki, K., Saeki, S., Chaipech, S., Pongpiriyadacha, Y., Muraoka, O., and Morikawa, T., 2021, Anti-proliferative activities of coumarins from the Thai medicinal plant *Mammea siamensis* (Miq.) T. Anders. against human digestive tract carcinoma cell lines, *Fitoterapia*, 148, 104780.
- [21] Balza, F., Abramowski, Z., Towers, G.H.N., and Wiriyaichitra, P., 1989, Identification of proanthocyanidin polymers as the piscicidal constituents of *Mammea siamensis*, *Polygonum stagninum* and *Diospyros diepenhorstii*, *Phytochemistry*, 28 (7), 1827–1830.
- [22] El-Amier, Y.A., Soliman, H.M., ElHalawany, E.F., and El-Nabawy, B.S., 2022, Chemical characterization of *Reichardia tingitana* methanolic extract and evaluation of its antioxidant and anticancer activity, *Egypt. J. Chem.*, 65 (132), 933–940.
- [23] Maisarah, A.M., Nurul Amira, B., Asmah, R., and Fauziah, O., 2013, Antioxidant analysis of different parts of *Carica papaya*, *Int. Food Res. J.*, 20 (3), 1043–1048.
- [24] Liu, H.Y., Liu, Y., Mai, Y.H., Guo, H., He, X.Q., Xia, Y., Li, H., Zhuang, Q.G., and Gan, R.Y., 2021, Phenolic content, main flavonoids, and antioxidant capacity of instant sweet tea (*Lithocarpus litseifolius* [Hance] Chun) prepared with different raw materials and drying methods, *Foods*, 10 (8), 1930.
- [25] Sumartini, S., Ratrinia, P.W., and Hutabarat, R.F., 2022, The effect of mangrove types and leave maturity on the mangrove leaves (*Sonneratia alba*) and (*Rhizophora mucronata*) tea powder, *IOP Conf. Ser.: Earth Environ. Sci.*, 967, 012018.
- [26] Dorkbuakaew, N., Ruengnet, P., Pradmeeteekul, P., Nimkamnerd, J., Nantitanon, W., and Thitipramote, N., 2016, Bioactive compounds and antioxidant activities of *Camellia sinensis* var. *assamica* in different leave maturity from Northern Thailand, *Int. Food Res. J.*, 23 (5), 2291–2295.
- [27] Mistriyani, M., Riyanto, S., Windarsih, A., and Rohman, A., 2021, Antioxidant activities and identification of an active compound from rambutan (*Nephelium lappaceum* L.) peel, *Indones. J. Chem.*, 21 (2), 259–267.
- [28] Hidayati, M.D., Ersam, T., Shimizu, K., and Fatmawati, S., 2017, Antioxidant activity of *Syzygium polynthum* extracts, *Indones. J. Chem.*, 17 (1), 49–53.

- [29] Wickramaratne, M.N., Punchihewa, J.C., and Wickramaratne, D.B.M., 2016, *In-vitro* alpha amylase inhibitory activity of the leaf extracts of *Adenantha pavonina*, *BMC Complementary Altern. Med.*, 16 (1), 466.
- [30] Priska, M., Peni, N., and Carvalho, L., 2019, Phytochemicals screening and antioxidant effectiveness of garlic (*Allium sativum*) from Timor Island, *Biosaintifika*, 11 (1), 1–7.
- [31] Mkgara, M., and Mpenda, F.N., 2022, Antimicrobial and cytotoxicity activities of medicinal plants against *Salmonella gallinarum* isolated from chickens, *Vet. Med. Int.*, 2022, 2294120.
- [32] Clemen-Pascual, L.M., Macahig, R.A.S., and Rojas, N.R.L., 2022, Comparative toxicity, phytochemistry, and use of 53 Philippine medicinal plants, *Toxicol. Rep.*, 9, 22–35.
- [33] Guo, P.J., Chen, T., Zheng, L., Peng, S., Lv, K.Q., Wang, W.Q., and Xuan, L.J., 2022, Two new xanthenes from *Hypericum japonicum* and their lipid-lowering activities, *Phytochem. Lett.*, 49, 40–44.
- [34] Hano, Y., Matsumoto, Y., Sun, J.Y., and Nomura, T., 1990, Structures of three new isoprenylated xanthenes, cudraxanthenes E, F, and G, *Planta Med.*, 56 (4), 399–402.
- [35] Sabphon, C., Sermboonpaisarn, T., and Sawasdee, P., 2012, Cholinesterase inhibitory activities of xanthenes from *Anaxagorea luzonensis* A. Gray, *J. Med. Plants Res.*, 6 (21), 3781–3785.
- [36] Teh, S.S., Ee, G.C.L., and Mah, S.H., 2013, Chemical constituents and new xanthone derivatives from *Mesua ferrea* and *Mesua congestiflora*, *Asian J. Chem.*, 25 (15), 8780–8784.
- [37] Verotta, L., Lovaglio, E., Vidari, G., Finzi, P.V., Neri, M.G., Raimondi, A., Parapini, S., Taramelli, D., Riva, A., and Bombardelli, E., 2004, 4-Alkyl- and 4-phenylcoumarins from *Mesua ferrea* as promising multidrug resistant antibacterials, *Phytochemistry*, 65 (21), 2867–2879.
- [38] Canning, C., Sun, S., Ji, X., Gupta, S., and Zhou, K., 2013, Antibacterial and cytotoxic activity of isoprenylated coumarin mammea A/AA isolated from *Mammea africana*, *J. Ethnopharmacol.*, 147 (1), 259–262.
- [39] Morikawa, T., Luo, F., Manse, Y., Sugita, H., Saeki, S., Chaipech, S., Pongpiriyadacha, Y., Muraoka, O., and Ninomiya, K., 2020, Geranylated coumarins from Thai medicinal plant *Mammea siamensis* with testosterone 5 α -reductase inhibitory activity, *Front. Chem.*, 8, 00199.
- [40] Luo, F., Manse, Y., Chaipech, S., Pongpiriyadacha, Y., Muraoka, O., and Morikawa, T., 2022, Phytochemicals with chemopreventive activity obtained from the Thai medicinal plant *Mammea siamensis* (Miq.) T. Anders.: Isolation and structure determination of new prenylcoumarins with inhibitory activity against aromatase, *Int. J. Mol. Sci.*, 23 (19), 11233.

The Effect of Thermal Treatment on the Characteristics of Porous Ceramic-Based Natural Clay and Chitosan Biopolymer Precursors

Suriati Eka Putri^{1,2}, Ahyar Ahmad^{3,4*}, Indah Raya³, Rachmat Triandi Tjahjanto⁵, Rizal Irfandi⁶, Harningsih Karim⁷, Susilo Sudarman Desa⁸, and Abd Rahman⁹

¹Doctoral Program, Department of Chemistry, Faculty of Mathematics and Natural Sciences, Hasanuddin University, Jl. Perintis Kemerdekaan Km. 20, Makassar 90245, Indonesia

²Department of Chemistry, Faculty of Mathematics and Natural Science, Universitas Negeri Makassar, Jl. Daeng Tata, Makassar 90244, Indonesia

³Department of Chemistry, Faculty of Mathematics and Natural Sciences, Hasanuddin University, Jl. Perintis Kemerdekaan Km. 20, Makassar 90245, Indonesia

⁴Research and Development Centre for Biopolymers and Bioproducts, LPPM, Hasanuddin University, Jl. Perintis Kemerdekaan Km. 20, Makassar 90245, Indonesia

⁵Department of Chemistry, Faculty of Mathematics and Natural Sciences, Brawijaya University, Jl. Veteran, Malang 65145, Indonesia

⁶Department of Biology Education, Faculty of Teacher Training and Education, Universitas Puangrimanggalatung, Jl. Sultan Hasanuddin, Madukkeleng, Sengkang 90915, Indonesia

⁷Department of Pharmacy, School of Pharmacy YAMASI, Makassar 90244, Indonesia

⁸School of Bio-Chemical Engineering and Technology, Sirindhorn International Institute of Technology, Thammasat University, Pathum Thani 12120, Thailand

⁹Inorganic Chemistry, King Fahd University of Petroleum & Minerals, Academic Belt Road, Dhahran 31261, Saudi Arabia

* Corresponding author:

tel: +62-8984917549

email: ahyarahmad@gmail.com

Received: December 19, 2022

Accepted: April 18, 2023

DOI: 10.22146/ijc.80375

Abstract: This study was conducted to determine the role of thermal treatment on the crystallinity and pore characteristics of porous ceramic, which was prepared from natural clay (NC) and chitosan (CS) biopolymer using the gel casting method. CS was used as an environmentally friendly pore-forming agent. The applied temperature treatment was based on thermal analysis (TGA/DTA) results and followed a sintering temperature of 900 to 1100 °C. The results showed that at sintering temperatures from 900 to 1000 °C, the crystallinities of the ceramic decrease (from 76.06 to 74.06%) and the crystallite size decreases (from 35.71 to 34.47 nm) while the lattice strain increases (calculated from the Full Width at Half Maximum (β) of the diffraction peak). The highest porosity of ceramic occurred at a sintering temperature of 1000 °C of 37.82 ± 0.19 , but the formation of heterogeneous microstructure was observed. The resulting pore size for all temperature treatments was almost mesoporous (19.1 Å). Based on the results obtained, it is emphasized that the sintering temperature can be used to adjust the porosity and microstructure of porous ceramics.

Keywords: porous ceramic; gel casting; sintering; clay

■ INTRODUCTION

Porous ceramics have undergone substantial research for a variety of crucial applications, such as gas/liquid

filtration, thermal insulation, catalyst support, and drug delivery [1-3]. This is due to several properties possessed by porous ceramics, such as their high melting point, low

thermal conductivity, good chemical inertness, and high specific surface area [4]. Several methods are used to prepare porous ceramic, such as pore-forming agent [5], freeze casting [6-7], gel casting [8-10], foam gel casting [11], sacrificial templating [12], and particle stacking [13]. The gel casting method is the most often utilized of the aforementioned techniques due to its benefits of a simple operating process. However, the industry is reluctant to use the gel casting technique because the most commonly used gel is acrylamide (AM), which is a neurotoxin. Thus, several previous researchers have utilized natural polymers in the fabrication of porous ceramics such as egg white [14-15], rice flour [16-17], cassava starch [18-19], sodium alginate [20], and chitosan (CS) [20-21].

In addition, gel casting of porous ceramics also uses raw materials, which are generally used including synthetic oxides such as alumina, zirconia, nitride, and titania, along with polymers that act as gelling agents and also pore templates [22-24]. These raw materials can be quite expensive, making them unsuitable for large-scale manufacture. At the moment, porous ceramics made from natural minerals, particularly clays, have attracted a lot of attention due to their abundance, good chemical resistance, good mechanical properties, and thermal stability [25-26]. Porous ceramic-based clay can also be used in some of the previously described porous ceramic applications [27]. In this study, we tried to develop the use of natural clay (NC) as a raw material and CS as a gelling agent and pore template.

The selection of CS as a pore template is due to it being renewable that is quite abundant in nature and is environmentally friendly [28]. Several previous studies have reported the use of CS as a pore template in the production of porous ceramics by gel casting. Salomão and Brandi [29] succeeded in producing a new porous filamentous using alumina-CS, and the resulting ceramic can be applied to the process of catalysis, filtration, support for biological tissue growth, and thermal insulation. Further research developing a cylindrical porous ceramic using a different raw material, namely aluminum hydroxide, the obtained results show a fairly high porosity (up to 84%) and a specific surface area (up to 7 m²/g) [30]. The optimum conditions for the use of CS as a gelling agent

have been reported by Bengisu and Yilmaz [31] using alumina and zirconia as the raw materials, obtaining the optimum pH for gelification of CS in the slurry at pH 4, reaction temperature 55 °C, the acetic acid concentration of 1 wt.%, and CS concentration of 10 wt.%.

With this perspective, this study has successfully employed NC and CS to prepare an environmentally porous ceramic membrane that has not been previously reported. The porosity of the ceramic body comes from the thermal degradation of CS, which can be easily decomposed in the temperature range of 219–505 °C [30]. A previous study has shown that the sintering temperature significantly affects the characteristics of porous ceramics. Salomão and Brandi [29] reported that thermal treatment affects mechanical strength, porosity, specific surface area and microstructure of gel casting porous ceramics with alumina and CS as raw materials. For instance, low-temperature sintering can make ceramic materials more porous and increase the pore size [32]. However, with a high sintering temperature, the mechanical properties can be improved [33]. The effect of thermal treatment on the microstructure and porosity of porous ceramics based on NC and CS is described in this work due to the major impact of the sintering temperature treatment.

■ EXPERIMENTAL SECTION

Materials

The materials used in this study consist of NC obtained from South Sulawesi (was slightly ground and sieved to pass 60 Mesh, then characterized using XRF, SAA with BET method, and PSA, the characterization results shown in Table 1), CS powder from our previous study [34] (the characteristic shown in Table 1), alumina (Merck, Germany CAS number 1344-28-1), carboxymethyl cellulose (CMC) food grade as a dispersant, and CH₃COOH (99% purity Merck, Germany).

Instrumentation

The instruments used in this study involved furnace (Nabertherm LT 5/14/B410), X-ray fluorescence (XRF, Thermo Fischer Scientific), X-ray diffractometer (XRD,

Table 1. Raw materials used in this study

Natural clay	
Chemical analysis (using XRF; wt.%)	SiO ₂ : 59.33; Al ₂ O ₃ : 2.77; Fe ₂ O ₃ : 0.77; CaO: 0.30; TiO ₂ : 3.84; ZrO ₂ , NiO, CuO, ZnO, and etc < 0.70
Specific surface area (BET method; m ² g ⁻¹)	17.02
Particle size (using PSA; μm)	4.34
Chitosan	
Molecular weight (kDa)	302.40
Particle size (using PSA; μm)	1.22
Polydispersity Index	0.51
Deacetylation degree (%)	93.81
Loss of ignition (%)	0.71
Moisture regains (%)	8.75
Viscosity (mPa.s)	155.31

Shimadzu 7000), particle size analyzer (PSA, Malvern Panalytical), TGA/DTA (Hitachi STA7300), surface area analyzer (SAA, type Quantachrome Nova 4200e), and scanning electron microscope (SEM, JEOL-6000PL).

Procedure

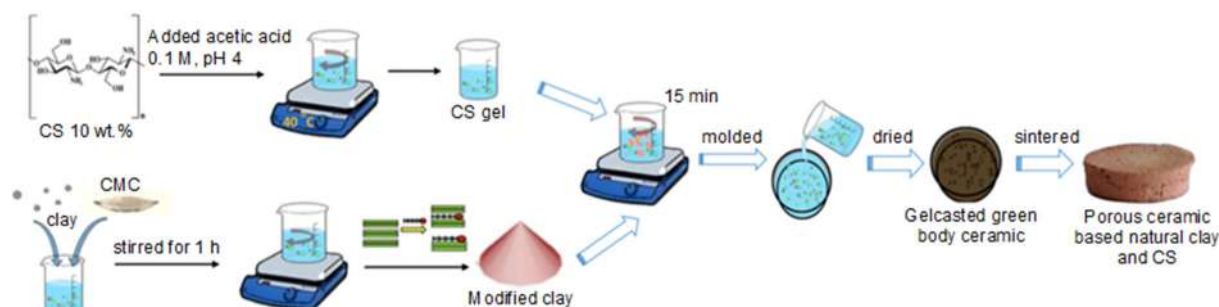
Specimen preparation

Porous ceramic-based NC and CS were fabricated by the gel casting method. The CS gel (10 wt.% in 0.1 M acetic acid solution, pH 4) was stirred at 40 °C for 2 h until the polymer was completely dissolved [30]. Furthermore, the formation of organoclay through clay modification with CMC (hereinafter referred to as modified clay (MC)) facilitates the interaction between clay and CS [35]. The raw material (clay and alumina with a ratio of 1:1 wt.%, the addition of alumina aims to restrain the rate of thermal expansion of silica, which is the main content in NC [36]) and 0.1 wt.% of CMC dispersant were added to 1.5 mL of distilled water, stirred for 1 h. The CS solution and MC solution were mixed and stirred for 15 min to

produce a slurry, and then a 25 × 25 × 120 mm³ PVC mold was used to pour into and permitted to dry in an air atmosphere for 12 h. The gelled ceramics were molded; the resulting ceramic body is called gel casted green body ceramic. Then sintered with the heating rate based on the results from the analysis of thermal using TGA/DTA with sintering temperature variations of 900, 1000, and 1100 °C for 3 h. An illustration of specimen preparation is shown in Fig. 1.

Determination of heat treatment parameters in gel casted green body ceramic

TG-DTA studies on the Hitachi STA7300 were used to simultaneously determine the heat treatment parameters of gel casted green body ceramic. Gel casted green body ceramic were ground into powder and weighed about 3.9 mg on an alumina crucible for comprehensive thermal analysis and then heated to 1000 °C in a static air environment after being isothermally heated at 30 °C for 10 min under airflow (8 L/min). The alumina was

**Fig 1.** The illustration of specimen preparation

employed as the reference material, and the heating rate was 50 °C /min.

Characterizations of specimen

The phase of the specimen was characterized by XRD with Cu K α radiation ($\lambda = 1.5405 \text{ \AA}$). The average crystallite size was determined by the Debye-Scherrer equation. Mass shrinkage is determined by calculating the ratio of the difference between the mass of the specimen before and after sintering to the mass before sintering. The bulk density and apparent porosity were measured by the Archimedes principle according to the ASTM C373-88.

The pore characteristic of the specimen, including surface area, pore volume, and pore distribution, was determined by nitrogen adsorption using SAA at a temperature of 250 °C with outgas time of 3 h and bath temperature of 273 K. Brunauer-Emmet-Teller (BET) was used to calculate the specific textural properties such as surface area and pore volume. Using the t-plot approach, the total adsorbed gas at relative pressure $P/P_0 = 0.99$ was used to represent the total pore volume, and the pore

distribution was based on Barret-Joyner-Halenda (BJH) analysis.

SEM was used to examine the specimen's microstructures, which qualitatively indicated a grain size of 60 mesh; the quantitative analysis was also examined with energy dispersive analysis (EDX), and phase quantification was obtained from SEM-EDX maps by processing EDX area maps using Image JED-2300 software.

RESULTS AND DISCUSSION

TGA-DTA of Gel Casted Green Body Ceramic

TGA-DTA was used in the determination of heat treatment parameters, including the sintering temperature of gel casted green body ceramic, to explain the process that occurs in the sintering process so that a thermal analysis of clay and CS, along with CMC, is also carried out. The results are shown in Fig. 2. To simplify the analysis, the thermal properties of green body ceramic based on the TGA-DTA curve are divided into three stages.

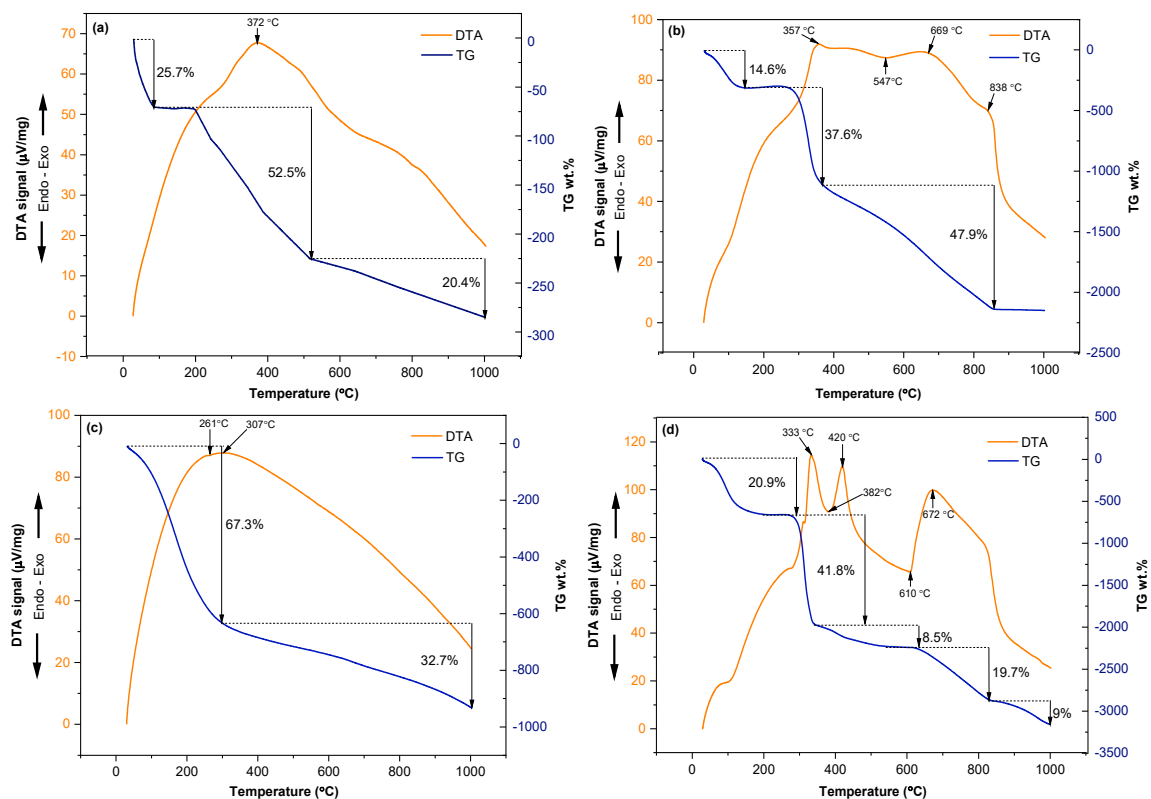


Fig 2. TGA-DTA curves of (a) gel casted green body ceramic, (b) CS, (c) clay, and (d) CMC

The first stage is the temperature increased from room temperature to 100 °C, and the mass of the green body decreased by about 25.7 wt.%, showing the removal of free and physically adsorbed water from the specimen's surface as well as the release of related water. In addition, it also indicates the evaporation of residual water in the CS polymer, which is in curve Fig. 2(b). There is also a reduction in mass at a temperature of 100 °C [37].

The second stage starts from 200 to 500 °C, the mass of the green body reduced to 52.5 wt.%. It is estimated that the hydration process of raw NC material occurs, which is in curve Fig. 2(c). There is also a reduction in mass at room temperature to 300 °C; this phenomenon is followed by a broad exothermic peak at 201 °C corresponding to the dehydroxylation of kaolinite into meta kaolinite [38]. Furthermore, curve Fig. 2(b). there was a decrease in mass at the temperature range of 200 to 400 °C, indicating the loss of the acetyl group that was still contained in the chitosan; the acetyl group had π bonding which is a weaker and more reactive bond so it was easier to break first. This phenomenon is followed by the exothermic peak at 357 °C, on the DTA curve [39]. It is estimated that at this stage, the formation of pores on the green body ceramic has started to occur.

The last stage is when the mass of the green body reduced to 20.5 wt.% from 500 to 1000 °C. This is due to the occurrence of degradation and decomposition of the CS chain, this is evidenced by the reduction in mass on the TGA curve of the CS thermogram (Fig. 2(b)), and there are also several small peaks which indicate the process of degradation and decomposition of various polymer units [39]. Thus, in this temperature range, it is suspected that the polymer network of CS will be burning out so that the formation of pores occurs optimally. In

addition, at temperatures between 800 and 1000 °C, a massive DTA peak is visible; this is a result of the phase change from meta kaolin to Al-Si spinel [40].

In the sintering process, the mass reduction of CMC is only 20.9% at temperatures of 100 to 300 °C, which indicates water decomposition; at temperatures of 300 to 400 °C indicates CMC decomposition with a mass reduction of about 41.8%. Furthermore, mass reduction is not so significant at temperatures above 400 °C, which indicates the decomposition of cross-link bonds in CMC and confirms the occurrence of curing behavior in porous ceramic bodies [41]. In this study, CMC acts as a dispersant in the ceramic body so that its presence is bound to each other with the matrix and binder of the specimen [11]. Thus, based on the thermal properties of the green body ceramic, the thermal treatment applied to the porous ceramic specimen is shown in Fig. 3.

X-ray Diffraction Investigations

The gel casted green body ceramics was sintered with various sintering temperatures (900, 1000, and 1100 °C) and the mineral phases were identified by XRD (Fig. 4). The SiO₂ crystalline phase that appears for all specimens is quartz (JCPDS 46-1212) and cristobalite (JCPDS 39-1425), while the mullite phase is only found in specimens at a temperature treatment of 900 °C at 25.97° which corresponding to the plane of primary mullite phase [42]. In addition, there is also a corundum phase for all specimens. Corundum increases steadily in its amount, while quartz increases and the amount of corundum nearly disappears at 1000 °C; it is in contrast to the results of the previous study because the sintering temperature carried out in this study is lower than that which been done previously [40]. The appearance of

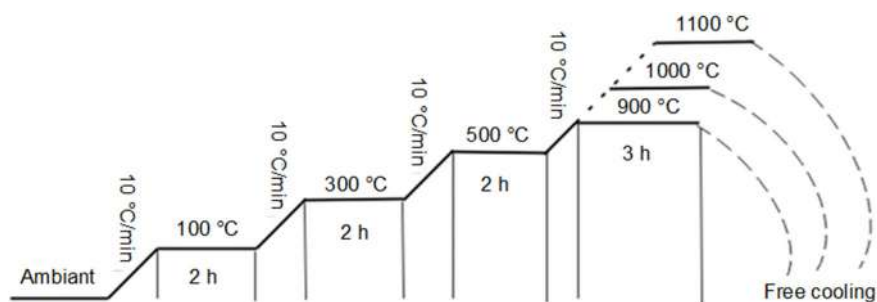


Fig 3. Thermal treatment applied in porous ceramic production

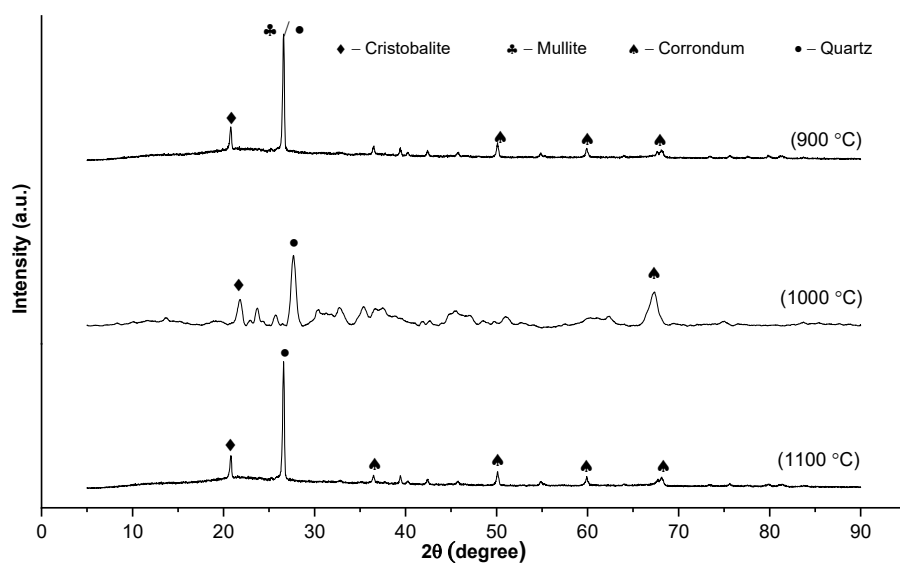


Fig 4. XRD patterns of the specimen with different sintering temperature

corundum peaks in all specimens indicates that not all alumina reacts with kaolinite in the clay to form mullite. The reason for failure to complete mullitization might be due to alumina size with large granular (18.64 μm) as raw material [25]. The results prove that the final phase compositions depend greatly on the treating temperatures.

The crystallinity of the specimen was determined by the Segal method. The weight fraction of the amorphous (x_A) component over different temperatures, was determined from Eq. (1) [43],

$$x_A (\%) = 100 - (1 - x_c) \quad (1)$$

where x_c is the crystallinity of the specimen given by Eq. (2) [43-44],

$$x_c (\%) = 100 \frac{I_{\text{crystal}}}{I_{\text{crystal}} + I_{\text{amorphous}}} \quad (2)$$

where I_{crystal} and $I_{\text{amorphous}}$ correspond to the intensity of the integrated for all crystalline peaks and the amorphous scattering, respectively. The crystallinity of the specimen with different sintering temperatures is plotted in Fig. 5(b). Due to the microcline phase melting at a higher sintering temperature of 1000 $^{\circ}\text{C}$, the crystallinity reduces, and the microstructure is typical of the sintering liquid phase. It was associated with the disappearance of the mullite phase (Fig. 4) due to the complete dissolution in the glass melt. This is agreed with the results of previous

studies [45-46]. However, the crystallinity increased at 1100 $^{\circ}\text{C}$, by reforming the diffraction peak; it was also known that the crystal diffraction peak and full width at half maxima (FWHM) did not change with increasing sintering temperature. Sintering temperature up to 1100 $^{\circ}\text{C}$ does not change the crystal phase but only causes an increase in the intensity of the diffraction peak [47].

Furthermore, the crystallite size (D) and the strain (ϵ) were obtained from three samples based on different thermal treatments. From the maximum peak FWHM amount, the crystallite size of specimens is calculated using the Debye-Scherrer equation as Eq. (3) [48], which takes from six data by taking the six dominant peaks as shown in Fig. 4 and the result is plotted in Fig. 5(a);

$$D = \frac{0.9\lambda}{\beta \cos \theta} \quad (3)$$

where β is the full width at half-maximum (FWHM) of the diffraction peak, λ (1.5406 \AA) is the X-ray wavelength radiation of $\text{Cu K}\alpha$, and θ is the Bragg angle. Based on the Debye-Scherrer equation, shown in Table 2, the crystallite size of specimens decreased by the increasing sintering temperature from 900 to 1000 $^{\circ}\text{C}$ but increased homogeneously at 1100 $^{\circ}\text{C}$. This finding is different from the results of several previous studies, which revealed that the crystallite size increased with increasing sintering temperature with the same sintering temperature from 800 to 1000 $^{\circ}\text{C}$ [47,49-50]. This anomalous behavior can

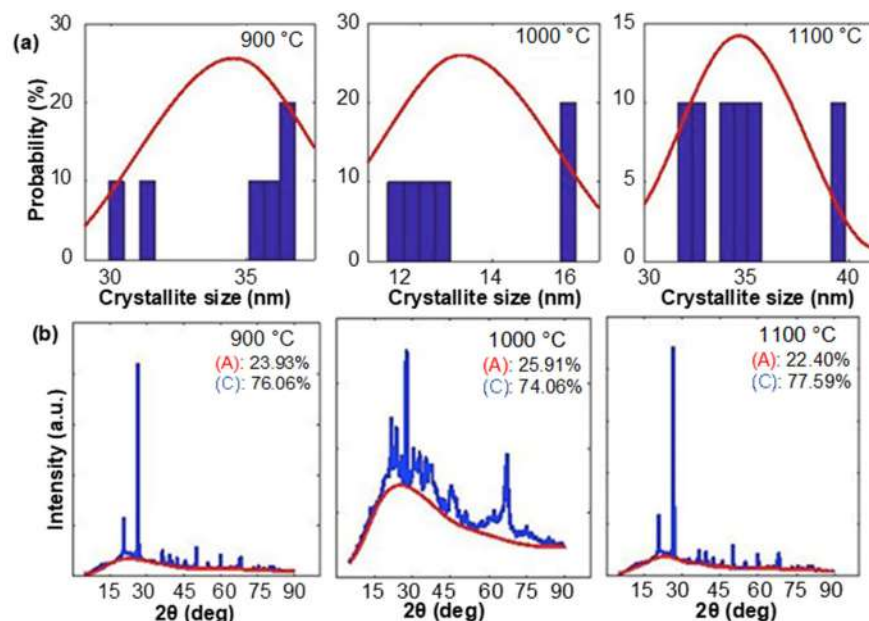


Fig 5. The evaluation of (a) the crystallite size of the specimens and (b) crystallinity with (A) amorphous and (C) crystalline phases

Table 2. The relationship between crystallite size and microstrains of the specimens

900 °C		1000 °C		1100 °C	
Crystallite size (nm)	Strain ($\times 10^{-3}$)	Crystallite size (nm)	Strain ($\times 10^{-3}$)	Crystallite size (nm)	Strain ($\times 10^{-3}$)
31.45	6.63	16.34	12.16	33.87	6.18
35.61	4.60	15.93	9.89	32.96	4.98
36.38	3.40	12.45	9.98	35.07	3.44
36.78	2.42	11.56	7.60	39.84	2.24
35.71	2.12	12.35	5.89	34.47	2.19
29.87	2.26	11.07	6.16	31.67	2.13

be explained by assuming that a high defect concentration is produced during densification at 1000 °C; it can be attributed to the low crystallinity of the specimen at a sintering temperature of 1000 °C (Fig. 5) and associated rapid particle deformation [51]. In order to confirm the structural parameters of the specimens, the Williamson-Hall was also used to determine the strain using Eq. (4) [52]. The microstrains can be caused by dislocations, anti-phase domain borders, deformation faulting, or homogeneous crystal lattice distortion [53].

$$\beta_{hkl} \cos \theta = \frac{\kappa \alpha}{D} + (4\epsilon \sin \theta) \quad (4)$$

When using the Williamson-Hall calculation method, it is presumed that the strain is constant throughout the crystallographic space and that the material's

characteristics are independent of space [44]. Based on Table 2, the strain has a positive value, indicating the strain tensile present during the sintering process of gel casted green body ceramics. Thus, the crystallite coalescence occurs as a consequence of the destroying-rebuilt oxygen-metallic cation of quartz and corundum, regardless of the phase transition of quartz to cristobalite [54]. As previously mentioned, the crystal size increases with a sintering temperature of 1100 °C. It can be seen from the decrease in FWHM of the diffraction peak with the sintering temperature, indicating an increase in the crystallization process by eliminating defects such as crystal growth and coalescence. The findings are in agreement with the previous studies [47,55].

Pore Parameters of Sintered Specimens

Mass shrinkage, bulk density and apparent porosity

The effect of thermal treatment on the mass shrinkage, bulk density and apparent porosity of the sintered specimens are shown in Table 3. As the sintering temperature increased from 900 to 1000 °C, the mass shrinkage of specimens increased and decreased at 1100 °C. The mass shrinkage increased as a result of the interconnectedness of the kaolin grains in the specimen body becoming weirder with an increase in sintering temperature [56]. However, at the sintering temperature of 1100 °C, mass shrinkage decreased due to forming a large amount of glassy phase, supported by XRD data (Fig. 4); grain merging was not completed due to the very high intensity of quartz peaks.

Similar results were observed for apparent porosity and bulk density; as the sintering temperature increased from 900 to 1000 °C, porosity increased while density decreased. As the sintering temperature was 1100 °C, the porosity decreased, and density decreased. It means the mixture of kaolinite and corundum sinter maximally when fired at 1000 °C; it can also be learned from the highest mass shrinkage occurred at these conditions and

the porosity of the porous ceramic is dependent on the temperature treatment. The density and porosity with various sintering temperatures were not so much different, and it was connected to the minor mass decrease. The results obtained are different from previous studies, which produce a regular trendline of the effect of the sintering temperature on density and porosity [56]. This is presumably because this study did not control the amount of alumina mixture as the raw material. Moreover, the resulting porosity is almost the same as the porous ceramic synthesized by conventional methods [33]. The findings suggest that by varying the sintering temperature, the bulk density and apparent porosity should be controllable.

Surface area, pore volume, and pore distribution

The surface area, pore volume, and pore distribution of the specimens were analyzed using the BET and BJH methods, shown in Fig. 6. As it is shown in the N₂ adsorption-desorption isotherms curves of specimens (Fig. 6(a)), no obvious hysteresis loops exist. After analyzing the BET data, the adsorption isotherm of the specimens is included in one of the types of adsorption isotherms discussed by Brunauer et al. [57],

Table 3. Mass shrinkage, bulk density, and apparent porosity with different sintering temperatures

Sintering temperature (°C)	Apparent porosity (%)	Bulk density (g/cm ³)	Mass shrinkage (%)
900	30.14 ± 0.14	10.61 ± 0.01	4.18 ± 0.03
1000	37.82 ± 0.19	8.64 ± 0.03	5.74 ± 0.05
1100	29.96 ± 0.15	12.27 ± 0.01	4.01 ± 0.05

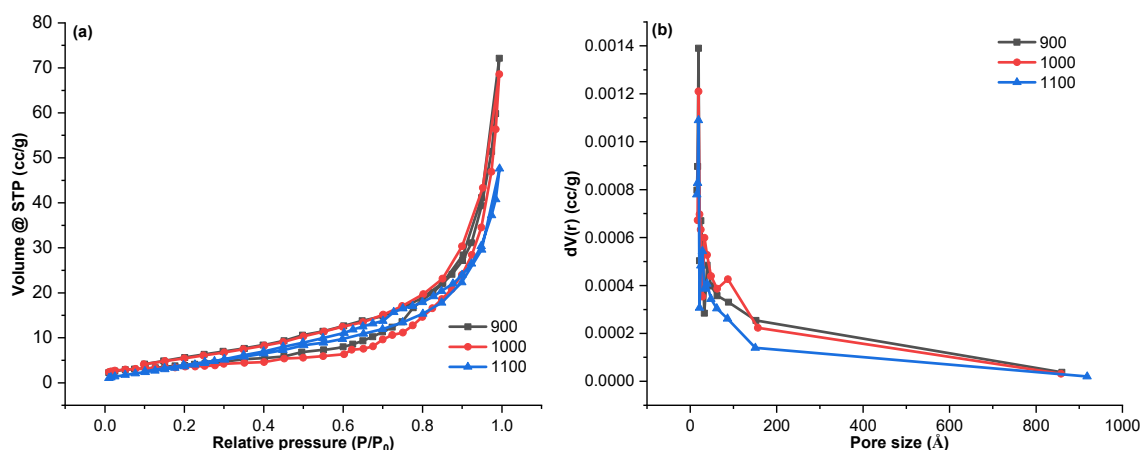


Fig 6. (a) Isotherm of adsorption-desorption curves and (b) pore size distribution of specimens

which is included in type III. This particular isotherm is convex to the axis of the relative pressure and does not show adsorption limiting $P/P_0 = 1$. When the adsorbate interacts more with the adsorbed layer than the adsorbent surface, type III isotherms are created.

The value of the surface area of the specimens increased from a temperature of 900 °C to a temperature of 1000 °C and decreased at a temperature of 1100 °C, while the volume and pore distribution of the specimens were not much different. The largest surface area occurs at a sintering temperature of 1000 °C, which is 17.27 m²/g. The same results were observed by Akhtar et al. [58], which uses diatomite as a raw material; at temperatures above 1000 °C the surface area of the specimen decreases, which is associated with the formation of a melting phase at temperatures above 1000 °C which promotes liquid phase sintering. However, the surface area of the resulting porous ceramics is larger than that of the porous alumina

ceramics synthesized by the freeze-drying [59] and wet-spun fibers method that also uses CS as a pore template [30]. During the sintering process, the grains agglomerate, resulting in a decrease in the pore volume, and the surface area of the ceramic powder decreases drastically [60-61]. The resulting pore distribution ranges from 19.1 Å, with the result that the porous ceramic is close to the mesoporous character. The pore characteristics of the specimens are summarized in Table 4.

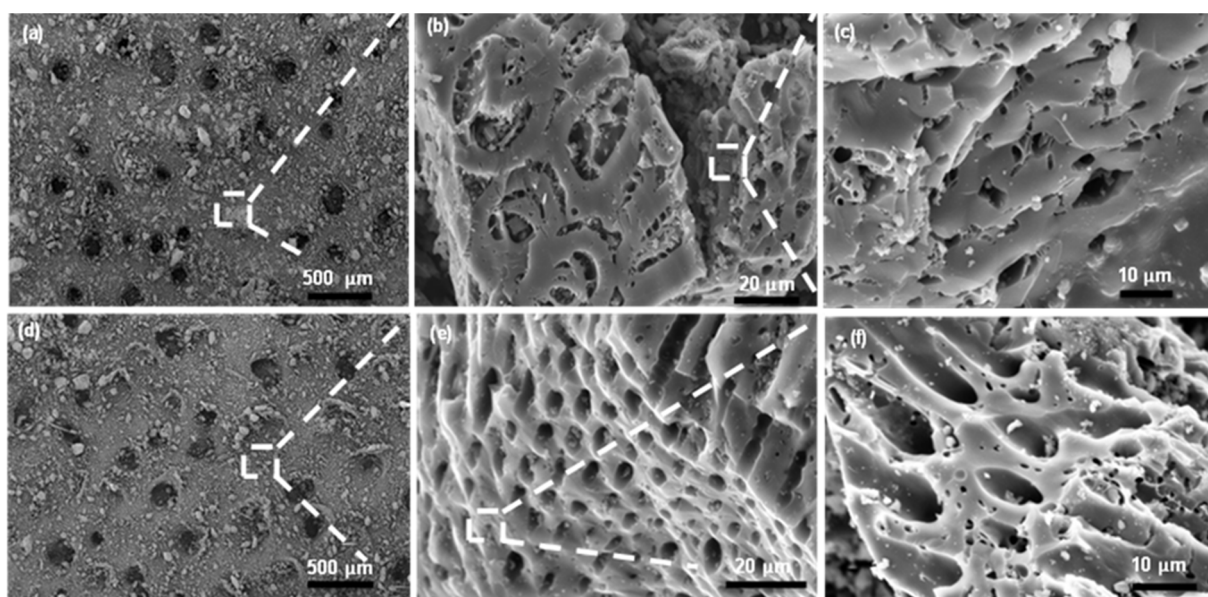
Surface morphology of specimens

The SEM photographs for the fracture surface of specimens with various sintering temperatures are shown in Fig. 7. It was obvious that the specimens made through the gel casting method had complex microstructures, with large spherical pores containing microscopic cellular pores on their inside walls. The

Table 4. Pore characteristics of porous ceramic-based NC and CS correspond to Fig. 6

Sintering temperature (°C)	Surface area (m ² /g)			Volume @STP (cc/g)			Pore distribution (Å)	
	^a BET	^b Micro	^c Meso	^d Total	^e Micro	^f Meso	Micro	Meso
900	15.2204	14.1493	1.0711	0.1116	0.0004	0.1111	19.0929	45.0112
1000	17.2752	9.0612	8.2140	0.0736	0.0041	0.0695	19.1011	37.2112
1100	12.5215	2.6483	9.8732	0.1061	0.0020	0.1041	19.1012	27.0001

^aBET surface area; ^bMicropore surface area evaluated by *t*-plot method; ^cMesopore surface area calculated using $S_{BET} - S_{micro}$; ^dTotal pore volume at $P/P_0 \sim 0.99$; ^eMicropore volume calculated by *t*-plot method; ^fMesopore volume calculated using $V_{total} - V_{micro}$; ^gPore distribution based on BJH analysis



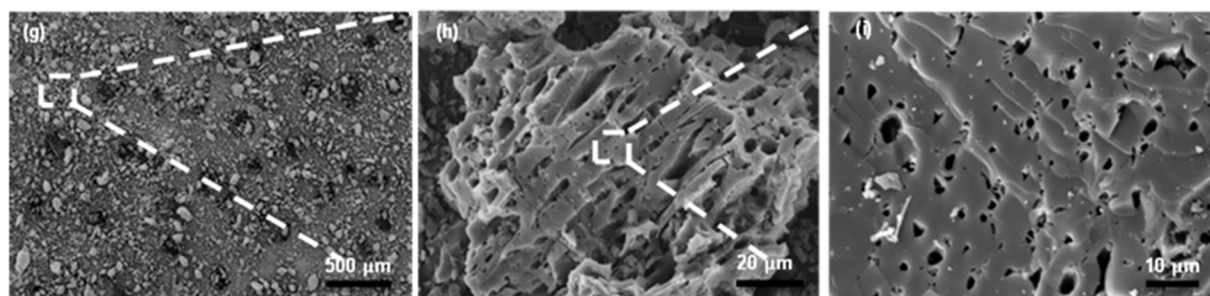


Fig 7. SEM images of the specimens with various sintering temperatures: 900 °C (a, b and c), 1000 °C (d, e and f), and 1100 °C (g, h and i)

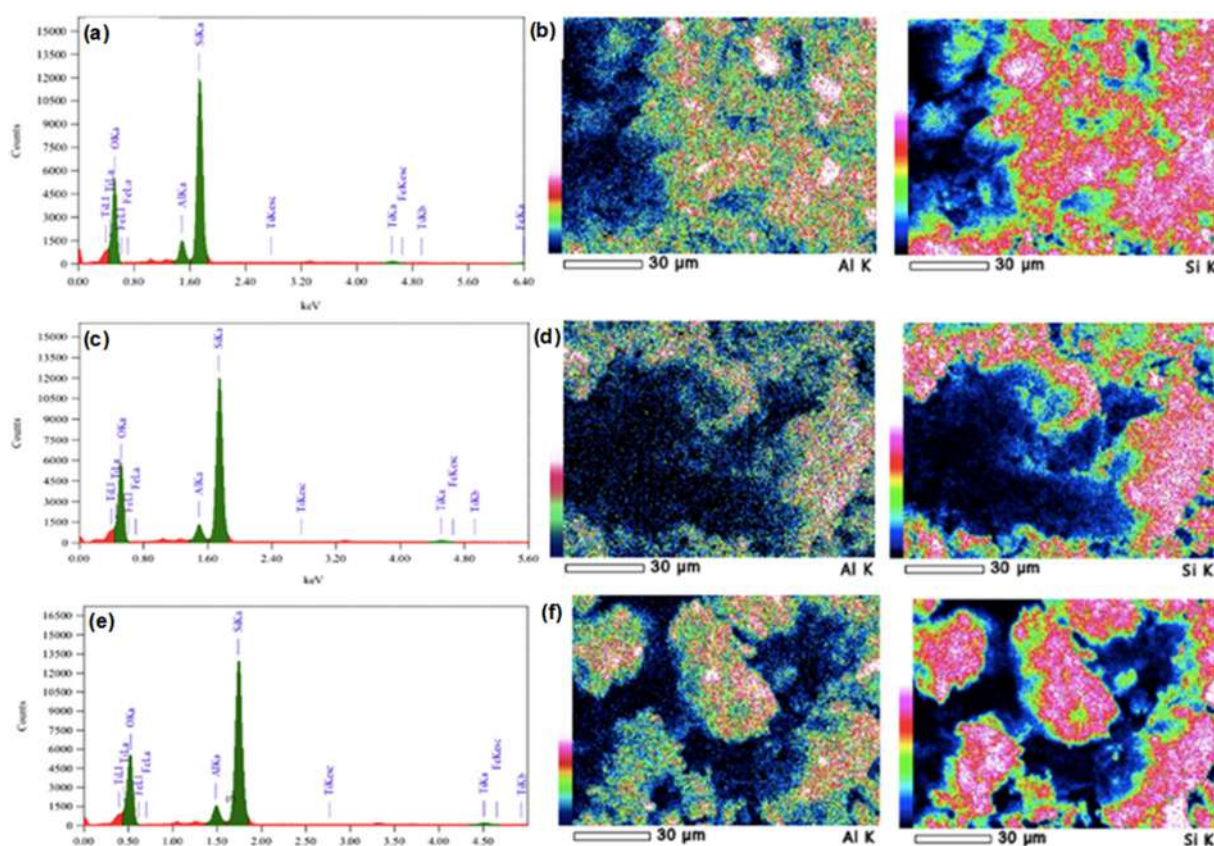


Fig 8. EDS elemental mapping of the specimens for sintering temperatures (a, b) 900 °C, (c, d) 1000 °C, and (e, f) 1100 °C

process of gelification produced large spherical pores, while the removal of CS and aggregation of quartz particles produced small cellular pores in internal walls [56]. It may be explained by mass shrinkage and porosity, which increase with increasing sintering temperature, that the number of small pores reduces as the sintering temperature increases from 900 to 1000 °C, as shown in Table 3. But when the sintering temperature is as high as 1100 °C, the porosity decreases drastically (Fig. 7(g, h, and

i)), presumably due to the glass phases being less viscous and easy to flow, so they could fill most of the pores formed by burning the gel CS polymer and thereby dramatically reduce porosity. A similar result was observed by Liu et al. [40] reporting when the sintering temperature was increased, the large particles did not seem to fully fuse with each other, thus causing the porosity to decrease. Besides, Yang et al. [56] also observed at a certain high temperature, the growth and

Table 5. Elemental analysis of the specimens corresponds to Fig. 8 (a, c, and e)

Element	Compound	Mass (%) of element			Mol (%) of compounds		
		900 °C	1000 °C	1100 °C	900 °C	1000 °C	1100 °C
O K	-	52.06	52.02	52.25	-	-	-
Al K	Al ₂ O ₃	4.50	4.17	3.79	8.50	7.88	7.17
Si K	SiO ₂	41.24	41.31	42.09	88.22	88.38	90.04
Ti K	TiO ₂	1.17	1.38	1.02	1.95	2.30	1.71
Fe K	Fe ₂ O ₃	1.04	1.12	0.85	1.34	1.44	1.09

interconnection of kaolinite grains on the raw material were not uniform, causing the porosity to decrease. Surface morphology showing homogeneous pore distribution observed at a sintering temperature of 1000 °C which is shown in Fig. 7(d, e, and f).

To observe the distribution of Si and Al elements (which are the main constituents of NC) in sintered ceramics, an EDS mapping analysis was also carried out on the specimens, which is shown in Fig. 8. The results obtained showed an incomplete solid-state reaction, where the distribution of Si and Al elements was unevenly distributed equally. If it is associated with the pore size of the specimens in Table 4, where the smallest pore size occurs at a sintering temperature of 1000 °C, as shown in Fig. 8(d), the distribution of Al and Si elements is the most uneven among other treatments. It indicates that grain merging was not completed so grain growth was not completed during the sintering process, which only for 3 h, thus, the pores formed were smaller than other specimens [60]. The mass (%) of Si and mole (%) of compounds SiO₂ increases with increasing sintering temperature. Different results were observed for the element Al and its compounds showing the mass (%), and mole (%) decreased with increasing sintering temperature, as shown in Table 5.

■ CONCLUSION

Porous ceramics were formed by the gel casting method using NC and CS. Pore development was mostly brought about by CS's thermal degradation. The crystallinities of the ceramic decreased (76.06 to 74.06%) at sintering temperatures 900 to 1000 °C while the crystallite size decreased and the lattice strain increased. The apparent porosity increased (30.14 to 37.82%) at sintering temperature from 900 to 1000 °C. However, the

apparent porosity decrease became 29.96% when the sintering temperature increased to 1100 °C, as indicated by the formation of heterogeneous microstructure was observed. The resulting pore size for all temperature treatments was almost mesoporous (19.1 Å). The findings imply that the sintering temperature can be used to continually regulate the microstructure behavior of porous ceramics based on NC and CS.

■ ACKNOWLEDGMENTS

The researcher would like to thank the Chemical Physics Laboratory of Hasanuddin University and Research Laboratory of Universitas Negeri Makassar that have supported and assisted in conducting the research.

■ AUTHOR CONTRIBUTIONS

Suriati Eka Putri conducted the experiment and wrote the manuscript, Ahyar Ahmad and Indah Raya revised the manuscript, Rachmat Triandi Tjahjanto and Rizal Irfandi did proofread the manuscript, Abd Rahman conducted the TGA/DTA and XRD analysis, Susilo Sudarman Desa conducted the BET and BJH calculations, Harningsih Karim did the grammar check process. All authors agreed to the final version of this manuscript.

■ REFERENCES

- [1] Gopi, S., Pius, A., and Thomas, S., 2020, *Handbook of Chitin and Chitosan: Composites and Nanocomposites from Chitin and Chitosan, Manufacturing and Characterisations*, vol. 2, Elsevier, Amsterdam, Netherlands.
- [2] Aouadja, F., Bouzerara, F., Guvenc, C.M., and Demir, M.M., 2021, Fabrication and properties of novel porous ceramic membrane supports from the

- (Sig) diatomite and alumina mixtures, *Bol. Soc. Esp. Ceram. Vidrio*, 61 (5), 531–540.
- [3] Guo, W., Hu, T., Qin, H., Gao, P., and Xiao, H., 2021, Preparation and in situ reduction of Ni/SiC_xO_y catalysts supported on porous SiC ceramic for ethanol steam reforming, *Ceram. Int.*, 47 (10, Part A), 13738–13744.
- [4] Han, L., Deng, X., Li, F., Huang, L., Pei, Y., Dong, L., Li, S., Jia, Q., Zhang, H., and Zhang, S., 2018, Preparation of high strength porous mullite ceramics via combined foam-gelcasting and microwave heating, *Ceram. Int.*, 44 (12), 14728–14733.
- [5] Manap, N.R.A., and Jais, U.S., 2009, Influence of concentration of pore forming agent on porosity of SiO₂ ceramic from rice husk ash, *Mater. Res. Innovations*, 13 (3), 382–385.
- [6] de Moraes Santos, L.N.R., de Melo Cartaxo, J., Silva, J.R.S., Rodrigues, A.M., de Andrade Dantas, E.L., de Sousa, F.B., de Araújo Neves, G., and Menezes, R.R., 2021, High porous ceramics with isometric pores by a novel saponification/gelation/freeze-casting combined route, *J. Eur. Ceram. Soc.*, 41 (14), 7111–7118.
- [7] Nishihora, R.K., Rachadel, P.L., Quadri, M.G.N., and Hotza, D., 2018, Manufacturing porous ceramic materials by tape casting—A review, *J. Eur. Ceram. Soc.*, 38 (4), 988–1001.
- [8] Wang, X., Xie, Y., Peng, C., Wang, R., Zhang, D., and Feng, Y., 2019, Porous alumina ceramic via gelcasting based on 2-hydroxyethyl methacrylate dissolved in *tert*-butyl alcohol, *Trans. Nonferrous Met. Soc. China*, 29 (8), 1714–1720.
- [9] Putri, S.E., Pratiwi, D.E., Tjahjanto, R.T., Mardiana, D., and Subaer, S., 2018, On the effect of acrylamide and methylenecacrylamid ratio on gelcasted ceramic pore character, *J. Chem. Technol. Metall.*, 53 (5), 841–844.
- [10] Hooshmand, S., Nordin, J., and Akhtar, F., 2019, Porous alumina ceramics by gel casting: Effect of type of sacrificial template on the properties, *Int. J. Ceram. Eng. Sci.*, 1 (2), 77–84.
- [11] Dong, J., Wei, J., Han, L., Li, X., Han, B., and Yan, W., 2022, Preparation of porous halloysite nanotube ceramics with high porosity and low thermal conductivity by foam-gelcasting, *Ceram. Int.*, 48 (2), 2441–2448.
- [12] Lukacs, V.A., Stanculescu, R., Curecheriu, L., Ciomaga, C.E., Horchidan, N., Cioclea, C., and Mitoseriu, L., 2020, Structural and functional properties of BaTiO₃ porous ceramics produced by using pollen as sacrificial template, *Ceram. Int.*, 46 (1), 523–530.
- [13] Wei, J., Han, B., Wei, Y., Li, N., and Miao, Z., 2021, Influence of phase evolution and thermal decomposition kinetics on the properties of zircon ceramic, *Ceram. Int.*, 47 (19), 27285–27293.
- [14] Fakhruddin, A.K., and Mohamad, H., 2018, Effect of glutinous rice flour and dried egg white in fabrication of porous cordierite by gel casting method, *Cerâmica*, 64 (370), 242–247.
- [15] He, X., Su, B., Zhou, X., Yang, J., Zhao, B., Wang, X., Yang, G., Tang, Z., and Qiu, H., 2011, Gelcasting of alumina ceramics using an egg white protein binder system, *Ceram.-Silik.*, 55 (1), 1–7.
- [16] Wan, W., Huang, C., Yang, J., and Qiu, T., 2014, Study on gelcasting of fused silica glass using glutinous rice flour as binder, *Int. J. Appl. Glass Sci.*, 5 (4), 401–409.
- [17] Kanlai, K., Wasanapiarnpong, T., Wiratphinthu, B., and Serivalsatit, K., 2018, Starch consolidation of porous fused silica ceramics, *J. Met., Mater. Miner.*, 28 (1), 71–76.
- [18] Luchese, C.L., Spada, J.C., and Tessaro, I.C., 2017, Starch content affects physicochemical properties of corn and cassava starch-based films, *Ind. Crops Prod.*, 109, 619–626.
- [19] Putri, S.E., Pratiwi, D.E., Tjahjanto, R.T., Hasri, H., Andi, I., Rahman, A., Ramadani, A.I.W.S., Ramadhani, A.N., Subaer, S., and Fudholi, A., 2022, The renewable of low toxicity gelcasting porous ceramic as Fe₂O₃ catalyst support on phenol photodegradation, *Int. J. Des. Nat. Ecodyn.*, 17 (4), 503–511.
- [20] Salomão, R., Cardoso, P.H., and Brandi, J., 2014, Gelcasting porous alumina beads of tailored shape and porosity, *Ceram. Int.*, 40 (10, Part B), 16595–16601.

- [21] Brandi, J., Ximenes, J.C., Ferreira, M., and Salomão, R., 2011, Gelcasting of alumina-chitosan beads, *Ceram. Int.*, 37 (4), 1231–1235.
- [22] Wu, J.M., Ma, Y.X., Chen, Y., Cheng, L.J., Chen, A.N., Liu, R.Z., Li, C.H., Shi, Y.S., and Lin, J.P., 2019, Preparation of Si₃N₄ ceramics by aqueous gelcasting using non-toxic agar powder as gelling agent without cooling crosslink process, *Ceram. Int.*, 45 (16), 20961–20966.
- [23] Putri, S.E., Pratiwi, D.E., Triandi, R., Mardiana, D., and Side, S., 2018, Performance test of gelcasted porous ceramic as adsorbent of azo dyes, *J. Phys.: Conf. Ser.*, 1028, 012039.
- [24] Yao, Q., Zhang, L., Chen, H., Gao, P., Shao, C., Xi, X., Lin, L., Li, H., Chen, Y., and Chen, L., 2021, A novel gelcasting induction method for YAG transparent ceramic, *Ceram. Int.*, 47 (3), 4327–4332.
- [25] Liu, Y.F., Liu, X.Q., Li, G., and Meng, G.Y., 2001, Low cost porous mullite-corundum ceramics by gelcasting, *J. Mater. Sci.*, 36 (15), 3687–3692.
- [26] Georgiev, A., Yoleva, A., and Djambazov, S., 2018, Influence of brewery waste sludge containing diatomite on the physical properties and thermal conductivity of porous clay bricks, *J. Chem. Technol. Metall.*, 53 (6), 1117–1122.
- [27] Alves Xavier, L., de Oliveira, T.V., Klitzke, W., Mariano, A.B., Eiras, D., and Vieira, R.B., 2019, Influence of thermally modified clays and inexpensive pore-generating and strength improving agents on the properties of porous ceramic membrane, *Appl. Clay Sci.*, 168, 260–268.
- [28] Rajiv Gandhi, M., Viswanathan, N., and Meenakshi, S., 2010, Preparation and application of alumina/chitosan biocomposite, *Int. J. Biol. Macromol.*, 47 (2), 146–154.
- [29] Salomão, R., and Brandi, J., 2013, Filamentous alumina-chitosan porous structures produced by gelcasting, *Ceram. Int.*, 39 (7), 7751–7757.
- [30] Salomão, R., and Brandi, J., 2013, Macrostructures with hierarchical porosity produced from alumina-aluminum hydroxide-chitosan wet-spun fibers, *Ceram. Int.*, 39 (7), 8227–8235.
- [31] Bengisu, M., and Yilmaz, E., 2002, Gelcasting of alumina and zirconia using chitosan gels, *Ceram. Int.*, 28 (4), 431–438.
- [32] Bouazizi, A., Breida, M., Karim, A., Achiou, B., Ouammou, M., Calvo, J.I., Aaddane, A., Khiat, K., and Younssi, S.A., 2017, Development of a new TiO₂ ultrafiltration membrane on flat ceramic support made from natural bentonite and micronized phosphate and applied for dye removal, *Ceram. Int.*, 43 (1, Part B), 1479–1487.
- [33] Mouiya, M., Bouazizi, A., Abourriche, A., El Khessaimi, Y., Benhammou, A., El hafiane, Y., Taha, Y., Oumam, M., Abouliatim, Y., Smith, A., and Hannache, H., 2019, Effect of sintering temperature on the microstructure and mechanical behavior of porous ceramics made from clay and banana peel powder, *Results Mater.*, 4, 100028.
- [34] Putri, S.E., Ahmad, A., Raya, I., Tjahjanto, R.T., and Irfandi, R., 2022, Synthesis and antibacterial activity of chitosan nanoparticles from black tiger shrimp shell (*Penaeus monodon*), *Egypt. J. Chem.*, Article in Press.
- [35] Lei, M., Huang, W., Sun, J., Shao, Z., Duan, W., Wu, T., and Wang, Y., 2020, Synthesis, characterization, and performance of carboxymethyl chitosan with different molecular weight as additive in water-based drilling fluid, *J. Mol. Liq.*, 310, 113135.
- [36] Sembiring, S., Simanjuntak, W., Situmeang, R., Riyanto, A., and Karo-Karo, P., 2017, Effect of alumina addition on the phase transformation and crystallisation properties of refractory cordierite prepared from amorphous rice husk silica, *J. Asian Ceram. Soc.*, 5 (2), 186–192.
- [37] Szymańska, E., and Winnicka, K., 2015, Stability of chitosan—A challenge for pharmaceutical and biomedical applications, *Mar. Drugs*, 13 (4), 1819–1846.
- [38] Barry, K., Lecomte-Nana, G.L., Seynou, M., Faucher, M., Blanchart, P., and Peyratout, C., 2022, Comparative properties of porous phyllosilicate-based ceramics shaped by freeze-tape casting, *Ceramics*, 5 (1), 75–96.

- [39] Gámiz-González, M.A., Correia, D.M., Lanceros-Mendez, S., Sencadas, V., Gómez Ribelles, J.L., and Vidaurre, A., 2017, Kinetic study of thermal degradation of chitosan as a function of deacetylation degree, *Carbohydr. Polym.*, 167, 52–58.
- [40] Liu, Y.F., Liu, X.Q., Wei, H., and Meng, G.Y., 2001, Porous mullite ceramics from national clay produced by gelcasting, *Ceram. Int.*, 27 (1), 1–7.
- [41] Zhang, J., Tan, L., Dong, H., Qu, W., and Zhao, J., 2022, Curing behavior of sodium carboxymethyl cellulose/epoxy/MWCNT nanocomposites, *RSC Adv.*, 12 (20), 12427–12435.
- [42] Shin, C., Oh, S.H., Choi, J.H., Hwang, K.T., Han, K.S., Oh, S.J., and Kim, J.H., 2021, Synthesis of porous ceramic with well-developed mullite whiskers in system of Al_2O_3 -kaolin- MoO_3 , *J. Mater. Res. Technol.*, 15, 1457–1466.
- [43] de Oliveira, L.S., de Oliveira Melquiades, M., da Costa Pinto, C., Trichês, D.M., and de Souza, S.M., 2020, Phase transformations in a NiTiGe system induced by high energy milling, *J. Solid State Chem.*, 281, 121056.
- [44] Reddy, M.P., Shakoor, R.A., Mohamed, A.M.A., Gupta, M., and Huang, Q., 2016, Effect of sintering temperature on the structural and magnetic properties of MgFe_2O_4 ceramics prepared by spark plasma sintering, *Ceram. Int.*, 42 (3), 4221–4227.
- [45] Amir, N., Tahir, D., and Heryanto, H., 2023, Synthesis, structural and optical characteristics of Fe_3O_4 /activated carbon photocatalysts to adsorb pesticide waste, *J. Mater. Sci.: Mater. Electron.*, 34 (5), 445.
- [46] Lu, J., Li, Y., Zou, C., Liu, Z., and Wang, C., 2018, Effect of sintering additives on the densification, crystallization and flexural strength of sintered glass-ceramics from waste granite powder, *Mater. Chem. Phys.*, 216, 1–7.
- [47] Almasri, K.A., Sidek, H.A.A., Matori, K.A., and Mohd Zaid, M.H., 2017, Effect of sintering temperature on physical, structural and optical properties of wollastonite based glass-ceramic derived from waste soda lime silica glasses, *Results Phys.*, 7, 2242–2247.
- [48] Heryanto, H., and Tahir, D., 2021, The correlations between structural and optical properties of magnetite nanoparticles synthesised from natural iron sand, *Ceram. Int.*, 47 (12), 16820–16827.
- [49] Singh, L.K., Bhadauria, A., Jana, S., and Laha, T., 2018, Effect of sintering temperature and heating rate on crystallite size, densification behaviour and mechanical properties of Al-MWCNT nanocomposite consolidated via spark plasma sintering, *Acta Metall. Sin. (Engl. Lett.)*, 31 (10), 1019–1030.
- [50] Venkatesh, D., Siva Ram Prasad, M., Rajesh Babu, B., Ramesh, K.V., and Trinath, K., 2015, Effect of sintering temperature on the micro strain and magnetic properties of Ni-Zn nanoferrites, *J. Magn.*, 20 (3), 229–240.
- [51] Fauzi, F., Noviyanto, A., Fitriani, P., Wibowo, A., Sudiro, T., Aryanto, D., and Rochman, N.T., 2022, Silicon carbide/polysilazane composite: Effect of temperature on the densification, phase, and microstructure evolution, *Indones. J. Chem.*, 22 (2), 548–556.
- [52] Bindu, P., and Thomas, S., 2014, Estimation of lattice strain in ZnO nanoparticles: X-ray peak profile analysis, *J. Theor. Appl. Phys.*, 8 (4), 123–134.
- [53] Khotib, M., Soegijono, B., Zainal Alim Mas'ud, Z.A., and Nadjamoeddin, G.L., 2022, Growth, electronic structure, and electrochemical properties of cubic BaTiO_3 synthesized by low-pressure hydrothermal-assisted sintering, *Indones. J. Chem.*, 22 (1), 242–252.
- [54] Cavalheiro, A.A., de Oliveira, L.C.S., and dos Santos, S.A.L., 2017, "Structural Aspects of Anatase to Rutile Phase Transition in Titanium Dioxide Powders Elucidated by the Rietveld Method" in *Titanium Dioxide*, Eds. Janus, M., IntechOpen, Rijeka, Croatia, 63–81.
- [55] Saparuddin, D.I., Noor Hisham, N.A., Ab Aziz, S., Matori, K.A., Honda, S., Iwamoto, Y., and Mohd Zaid, M.H., 2020, Effect of sintering temperature on the crystal growth, microstructure and mechanical strength of foam glass-ceramic from waste materials, *J. Mater. Res. Technol.*, 9 (3), 5640–5647.

- [56] Yang, F., Li, C., Lin, Y., and Wang, C.A., 2012, Effects of sintering temperature on properties of porous mullite/corundum ceramics, *Mater. Lett.*, 73, 36–39.
- [57] Brunauer, S., Deming, L.S., Deming, W.E., and Teller, E., 1940, On a theory of the van der Waals adsorption of gases, *J. Am. Chem. Soc.*, 62 (7), 1723–1732.
- [58] Akhtar, F., Rehman, Y., and Bergström, L., 2010, A study of the sintering of diatomaceous earth to produce porous ceramic monoliths with bimodal porosity and high strength, *Powder Technol.*, 201 (3), 253–257.
- [59] Hu, S., Feng, B., Tang, X., and Zhang, Y., 2019, Porous alumina ceramics obtained by particles self-assembly combing freeze drying method, *Materials*, 12 (6), 897.
- [60] Aytimur, A., Koçyiğit, S., and Uslu, İ., 2014, Calcia stabilized ceria doped zirconia nanocrystalline ceramic, *J. Inorg. Organomet. Polym. Mater.*, 24 (6), 927–932.
- [61] Putri, S.E., Ahmad, A., Raya, I., Triandi, R., Natsir, H., Taba, P., and Karim, H., 2023, A review of the development of the gel casting method for porous ceramic fabrication, *Rasayan J. Chem.*, 16 (1), 48–60.

Investigation of Crystal Size Distribution in Purification of Terephthalic Acid from Polyester Textile Industry Waste by Reactive Crystallization

Bekti Marlana^{1,2*}, Hary Sulisty¹, and Rochmadi Rochmadi¹

¹Department of Chemical Engineering, Universitas Gadjah Mada, Jl. Grafika 2, Yogyakarta 55284, Indonesia

²Center for Standardization and Industrial Pollution Prevention Services, Jl. Kimangunsarkoro No. 6, Semarang 5013, Indonesia

* **Corresponding author:**

email: bektimarlena@mail.ugm.ac.id

Received: December 31, 2022

Accepted: March 29, 2023

DOI: 10.22146/ijc.80820

Abstract: The purification of terephthalic acid recovered from an alkali-reduction wastewater by reactive crystallization was investigated. The crude terephthalic acid was reacted with sodium hydroxide solution to form a salt of disodium terephthalate, then acidified with sulfuric acid to get the terephthalic acid with higher purity. The effects of time, pH, concentration, and flow rate of secondary feed solutions, temperature, and stirring rate on crystal size distribution (CSD) of terephthalic acid precipitate were investigated. The results showed that CSD was influenced by the concentration of reactants and the pH solution. On the other hand, time, temperature, flow rate of secondary solution, and stirring rate had no significant effects on the CSD, which the mean size of crystals $\pm 3 \mu\text{m}$. The mean size of crystals at solution pH 5, 4, and 3 were 6.03, 9.42, and 10.34 μm , respectively; meanwhile, at concentrations of 0.5, 0.3, and 0.1 M, were 7.57, 3.24, and 3.09 μm , respectively. The semi-batch reactive crystallization with double-feeding at constant pH and temperature resulted in monodispersed crystals. However, this method must be carried out more than once for terephthalic acid purification, intended for polyethylene terephthalate (PET) polymerization.

Keywords: crystal size distribution; purification; reactive crystallization; terephthalic acid

■ INTRODUCTION

Polyester is the most widely used synthetic fiber due to its low production cost and good fiber properties. Still, it has poor wear comfort because of its low moisture absorption and stain removal ability. Therefore, some approaches have been developed to improve the hydrophilicity of polyester fiber [1]. The strong alkaline treatment of polyester leads to the rupture of ester bonds. It increases the number of polar functional groups of alcohol and carboxylic acid on the fiber surface [2].

On the other hand, alkali treatment causes hydrolysis of the ester bond. The chain hydrolysis of polyethylene terephthalate (PET) with sodium hydroxide produces disodium terephthalate, which is highly soluble in water. This alkali process also causes changes in fabric weight, strength, wettability, and aesthetics [3]. The large amount of weight loss in this hydrolysis process is known as the weight reduction process.

The wastewater from this process has extreme characteristics such as a very alkaline pH (> 12.8) and a high organic concentration (COD of 20,000–100,000 mg/L) [4]. Therefore, some researchers have studied the recovery of terephthalic acid as one of the attractive treatments for this wastewater [5]. Terephthalic acid recovery is carried out by acidifying wastewater to precipitate the terephthalic acid. This method is known as precipitation or reactive crystallization. In this process, the formation of a crystal or solid product is initiated with high supersaturation conditions which are obtained from the chemical reaction between the soluble reactants [6]. Supersaturation is a driving force for nucleation which is the initial formation of a solid phase or crystal. The growth of the crystal increases the crystal size.

Industrially, crystalline product quality and properties are determined by the crystal size distribution (CSD), morphology, and purity [7-8]. Chemical

composition, as represented by the chemical purity and impurity levels, can change the crystal properties, such as the mechanical, electrical, thermal, and optical properties. Control of impurities is also essential in many industries, especially in the food and pharmaceutical industries, where product purity should reach the strict specifications required for human use [9]. The crystal size distribution (CSD) and crystal habit or morphology can change product and bulk properties such as dusting, dissolution rate, compressibility, and flowability [10]. They also influence the efficiency of downstream processes such as filtration, centrifugation, and drying [11].

The crystallization process control is important to acquire products with desired and reproducible properties. Poor product properties can cause extra processing steps, which will increase manufacturing costs and be time-consuming [12]. Obtaining the desired particle size can often be challenging due to the interaction among various process parameters. A series of techniques, including mathematical modeling tools, have been applied to predict and control particle size and distribution [13].

The CSD on crystallization can be predicted using the Population Balance Equation (PBE). PBE is an equation that represents the balance of the number of particles in a specific state. For a batch crystallizer or a semi-batch crystallizer with assumptions that the system is perfectly mixed and there is no net inflow or outflow of crystals. The PBE can be written in Eq. (1).

$$\frac{\partial n}{\partial t} = G \frac{\partial n}{\partial L} \quad (1)$$

Eq. (1) requires an initial condition and a boundary condition. The initial condition of $n(L, 0)$ for unseeded batch suspension crystallizer uses the size distribution of crystal at the time of the first appearance crystals. The boundary condition $n(0, t)$ is the nuclei population density (n_0) and is related to the nucleation rate (B), as shown in Eq. (2).

$$n(0, t) = n_0(t) = \frac{B(t)}{G(0, t)} \quad (2)$$

Nucleation kinetics and crystal growth rate cannot be predicted theoretically, and in practice, they must be measured and correlated empirically with environmental

conditions, such as concentration and temperature, using a power law model, as shown in Eq. (3) and (4).

$$B = k_N \Delta c^b \quad (3)$$

$$G = k_G \Delta c^g \quad (4)$$

where B is nucleation rate, k_N is nucleation rate constant, Δc is supersaturation, exponent b is an order of nucleation, G is crystal growth, k_G is growth rate constant, and exponent g is an order of growth. The value of the primary nucleation kinetic constant b varies in the range of 1–10 [14]. Meanwhile, the value of growth kinetic constant g , in general, is $1 \leq g \leq 2$, and $g > 2$ only for sparingly soluble compounds [6]. Studies of CSD on semi-batch reactive crystallization were conducted by single feed [15-17] or double feeds [18], as well as double feeds at constant pH by adding external acid or basic [19-20].

Studies on the purification and recovery of terephthalic acid from alkali weight reduction wastewater using reactive crystallization [5] and cooling crystallization [21] focused on terephthalic acid's purity. However, research on CSD of terephthalic acid using reactive crystallization, especially from recovery weight reduction wastewater, is still scarce.

It is assumed that at a constant pH, disodium terephthalate will react with sulfuric acid to form terephthalic acid, which increases the concentration of terephthalic acid in the solution. It is expected to increase the crystal growth rate and size. Thus, the work presented in this paper aimed to study the effect of the crystallization processes (time, pH, temperature, concentration, flow rate of secondary solutions, and stirring speed) on the crystal size distribution. The crystallization process was conducted in conditions of semi-batch, constant solution pH, and constant solution temperature (isothermal) by adjusting the feeding of the secondary solution of reactants.

■ EXPERIMENTAL SECTION

Materials

The weight-reduced wastewater was collected from a textile industry in Central Java Province, Indonesia. The weight-reduced wastewater was added with activated carbon and then acidified to pH 2 [5]. The

terephthalic acid precipitate was then filtered and dried to produce crude terephthalic acid, having the characteristics shown in Table 1.

Analytical grade chemicals used in reactive crystallization were sulfuric acid (Merck, 95–97%), charcoal activated (Merck), and sodium hydroxide (Merck, 99%).

Instrumentation

The semi-batch crystallization system with double-feeding reactants for the study of reactive crystallization of terephthalic acid is illustrated in Fig. 1. Experimental setup consisted of a reactor, a mechanical stirrer, two peristaltic pumps, and a pH meter. A glass beaker of 1 L

equipped with four baffles (0.1 of beaker diameter) and four blades of paddle impeller stirrer (0.3 of beaker diameter) was used as a reactor. The stirrer was driven by IKA RW 20 digital overhead stirrer. HI9890 pH meter was connected to a computer to monitor and save the data of pH and temperature during the process. A Cole Palmer water bath was used to maintain and control the process temperature. Masterflex C/L peristaltic pumps were employed to feed the secondary disodium terephthalate and sulfuric acid solutions to the reactor. The crystal size distribution was determined using a Particle Size Analyzer (PSA) Horiba Partica LA 960 V2.

Table 1. Characteristics of crude terephthalic acid

No	Parameter	Crude terephthalic acid	Unit	Method
1	Acid number	572.500 ± 7.500	mg KOH/g	Titration
2	Ash	229.900 ± 5.200	ppm (w/w)	Gravimetry
3	Moisture	6.160 ± 0.220	% (w/w)	Gravimetry
4	Alkali transparency T-400	73.350	%	Spectrophotometry
5	Mean size	21.335 ± 0.065	µm	Laser diffraction
6	Metal contents			
	Mn	2.890 ± 0.119	ppm (w/w)	Atomic absorption
	Ni	0.279 ± 0.219	ppm (w/w)	spectroscopy (AAS)
	Co	0.020 ± 0.001	ppm (w/w)	
	Cr	1.219 ± 0.462	ppm (w/w)	
7	Iron (Fe)	17.556 ± 4.239	ppm (w/w)	AAS
8	Color in 5% dimethylformamide	51.650	-	spectrophotometry

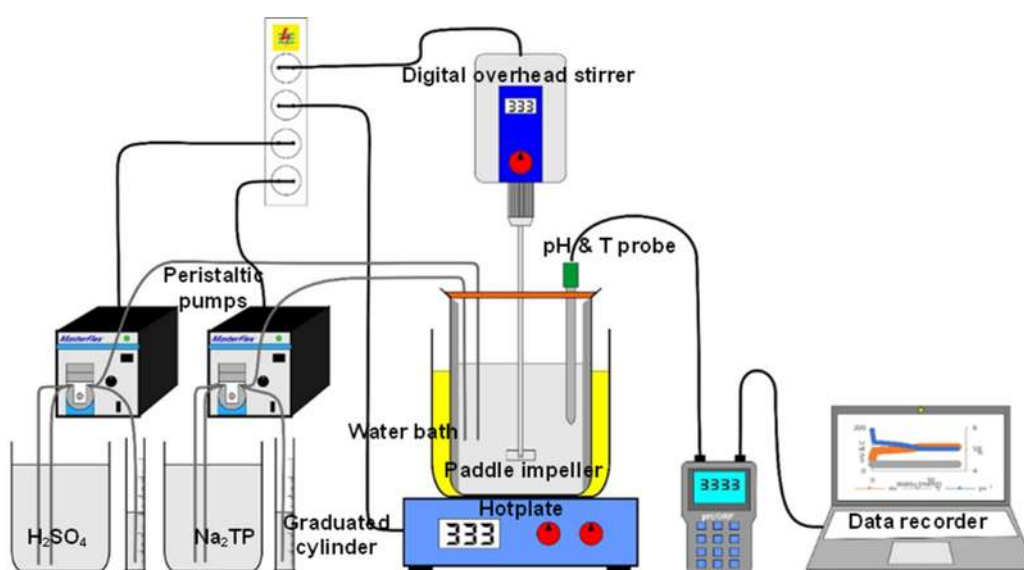


Fig 1. Experimental setup

Procedure

The amount of 400 mL of 0.06 M primary disodium terephthalate solution was put into a glass beaker with a volume of 1 L as a reactor. It was acidified with 0.5 M sulfuric acid solutions (approximately 50 mL) until the targeted pH was reached. At this point, initial time sampling was carried out by taking 25 mL of solution.

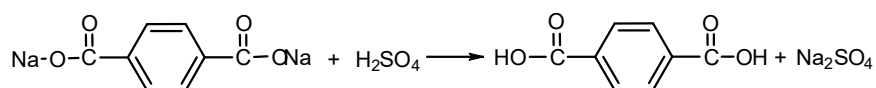
Secondary solutions of 0.5 M disodium terephthalate and 0.5 M sulfuric acid solutions were added continuously to the reactor (primary solution) using two peristaltic pumps in an equal amount between terephthalate and sulfuric acid. The addition of this second solution did not affect the pH of the solution due to an equimolar amount of terephthalate and sulfuric acid. The initial volume of the primary solution at the targeted pH was approximately 450 mL. The volume of sulfuric acid added at a feeding rate of 1 mL/min was 30 mL, and the volume of disodium terephthalate added was also 30 mL. The final total volume was 385 mL after subtracting the entire sample volume taken (125 mL). Samples were taken at 5, 10, 20, and 30 min after secondary solutions were charged into the primary solution. The pH and temperature of the reaction were monitored and manually controlled by manipulating the flow rate of the H₂SO₄ solution.

Each sample was filtered, and the precipitated terephthalic acid was oven-dried at 70 °C and then weighed (until constant). The dried sample was analyzed using a PSA, which shows the characteristic dimension of the crystals in the volume equivalent size.

RESULTS AND DISCUSSION

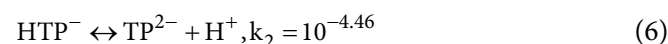
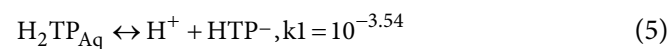
The Chemical Reaction of Disodium Terephthalate with Sulfuric Acid

The reaction of disodium terephthalate with sulfuric acid is shown in Scheme 1. Disodium terephthalate and sulfuric acid are ionic reactants in an aqueous solution, which essentially reacts very fast, producing a terephthalic acid precipitate [22]. The reactive crystallization mechanism consists of several steps. The first step is



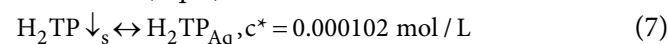
Scheme 1. The reaction of disodium terephthalate with sulfuric acid

terephthalic acid formation by reacting disodium terephthalate with sulfuric acid. The solution dissolves the terephthalic acid into ionic terephthalates (Eq. 5-6) [23].



where H₂TP, HTP⁻ and TP²⁻ indicate the neutral, dissociated, and twice dissociated forms of terephthalic acid, respectively. The neutral form is called free acid. The relative amounts of the three ions depend on the pH solution. The concentration of each species at equilibrium can be calculated by the fraction or alpha (α) by comparing its concentration with the total concentration of phthalate ions with the help of the dissociation constant [24].

Fig. 2 shows the speciation of terephthalic acid as a function of the pH solution. The two intersection points of these curves were pK₁ and pK₂. The free acid of terephthalic acid forms a precipitate when its concentration exceeds the solubility value at equilibrium conditions (Eq. 7).



The mass balance of total terephthalates in the solution was calculated from concentrations of terephthalate ions (HTP⁻ and TP²⁻) and free acid H₂TP using Eq. (8).

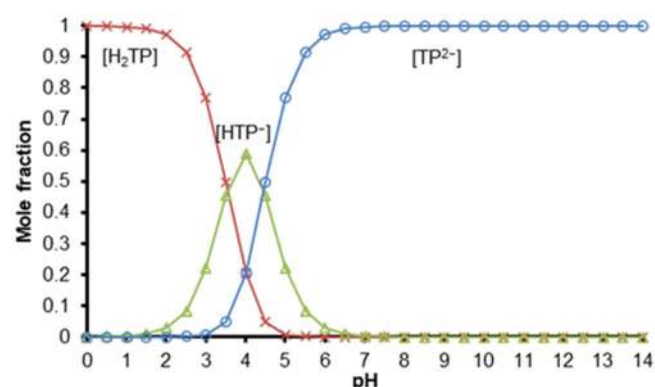


Fig 2. Mole fractions of ionic species of terephthalate as a function of solution pH

$$[\text{TP}_{\text{TOTAL}}] = [\text{TP}^{2-}] + [\text{HTP}^-] + [\text{H}_2\text{TP}] \quad (8)$$

The electroneutrality balance of all species in the solution was calculated using Eq. (9).

$$[\text{H}^+] = 2[\text{TP}^{2-}] + [\text{HTP}^-] + [\text{HSO}_4^-] + 2[\text{SO}_4^{2-}] + [\text{OH}^-] \quad (9)$$

Eqs. (5-9), together with measured pH data and total sodium concentration, were used to calculate the concentrations of terephthalate ions (TP^{2-} and HTP^-), free terephthalic acid (H_2TP) in the solution, and solid, with the assumption that the solution was an ideal solution at equilibrium and sulfuric acid was a strong acid.

The pH profiles, concentrations of terephthalic acid in solution, and terephthalic acid solid at the addition of sulfuric acid into 100 mL disodium terephthalate solution with the same concentration (0.45 M) are shown in Fig. 3.

Adding sulfuric acid decreased the solution pH and the concentration of disodium terephthalate. The gentle slope of the pH curve (red line) indicated the occurrence of spontaneous nucleation. Then, it was followed by the steep slope in which the solution was sensitive to pH (around $\text{pH} = 4$), where disodium terephthalate was equimolar to sulfuric acid. At this stage, adding a small amount of sulfuric acid (± 3 mL) drastically changed the pH from 4.64 to 2.85.

The terephthalic acid is sparingly soluble in water with a solubility of 0.000102 M. If the concentration of terephthalic acid exceeds the solubility value at equilibrium conditions, then the solid terephthalic acid forms. The solubility of terephthalic acid or concentration of terephthalic acid in the solution (H_2TP) curve (green line) was assumed constant regardless of the pH of the solution.

The supersaturation condition of terephthalic acid was the driving force of crystallization which consisted mainly of nucleation and crystal growth. The relationship between nucleation and growth and agglomeration or breakage of crystals certainly affected the final product of CSD [8].

CSD of Crude Terephthalic Acid

The CSD of crude terephthalic acid used in this experiment is shown in Fig. 4. The graph shows that CSD stretched from 0.5–700 μm , with two peaks located at 5.5 μm by 4.1% and 29.9 μm by 3.9%. It indicated that the

crude terephthalic acid had a very broad crystal size with a mean size of 26.83 μm .

CSD of Terephthalic Acid from Double Feed Semi-batch Reactive Crystallization at Constant pH and Temperature

The primary disodium terephthalate solution was acidified with sulfuric acid solutions until the targeted pH was reached. At this point, initial time sampling was carried out. Secondary disodium terephthalate and sulfuric acid solution were added equimolar by keeping the pH solution constant.

Adding an equimolar secondary solution of disodium terephthalate and sulfuric acid at constant pH was expected to increase the concentration of terephthalic acid in the reactor for crystal growth. The feeding time of secondary solutions at constant pH was conducted for 30 min.

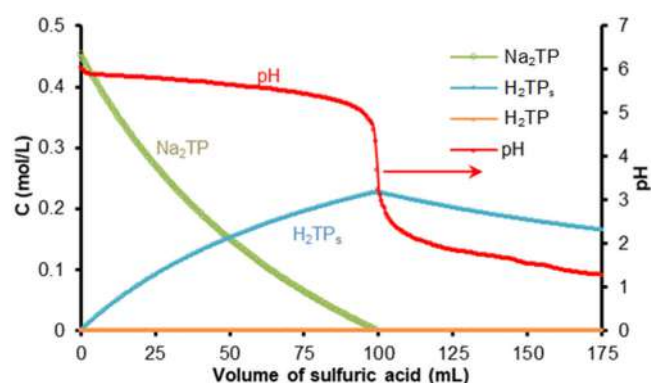


Fig 3. Equilibrium concentrations and pH of 0.45 M disodium terephthalate 100 mL with 0.45 M sulfuric acid additions

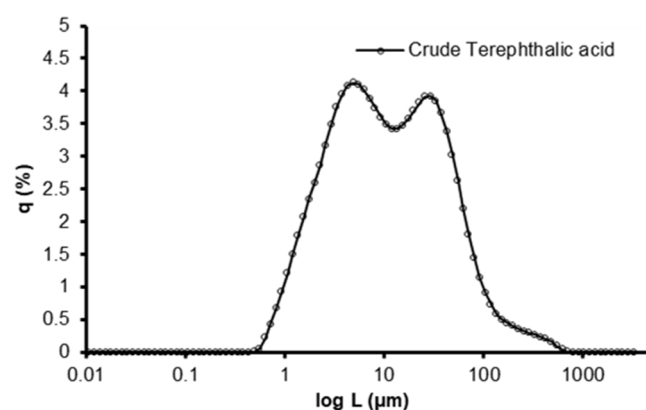


Fig 4. CSD of crude terephthalic acid

Effect of feeding time

The experiments were conducted at a solution pH of 5, at a concentration of a secondary solution of 0.5 M, and at a temperature of 30 °C at various feeding times.

The addition of secondary solutions (in equimolar reactants) increased the amount and number of crystals. Still, the size distribution was similar at various feeding times, from 0 to 30 min, as shown in Fig. 5. This means that feeding time did not influence the size of crystals. It was apparent that the crystallization process (nucleation and crystal growth) occurred very fast in the time scale of seconds; meanwhile, samples taken from the solution were within 5–10 min intervals. The short time scale of the crystallization process was probably due to the high supersaturation of terephthalic acid due to the low solubility of the terephthalic acid in water [25]. The high supersaturation caused the spontaneous primary nucleation to be more dominant than the growth of crystals.

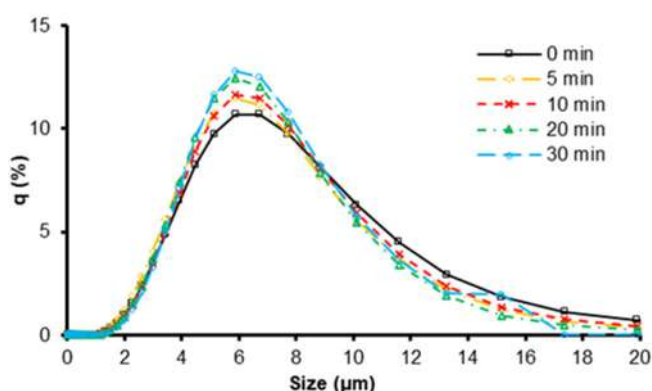


Fig 5. CSD of terephthalic acid at conditions of pH 5 and T 30 °C

Effect of solution pH

The solution pH was varied to 3, 4, and 5, as shown in Fig. 7. During the experiment, the feed rate was controlled manually at a fixed pH. Controlling the secondary solution feed rate was relatively easy at solution pH 5, compared to solution pH 4 and 3, which were sensitive to small fluctuations in the acid feed rate. It is illustrated in Fig. 6.

The fluctuations in the concentration of H^+ ions at pH 3, 4, and 5 were between 3.05–2.96, which equaled $CH^+ = 9.10^{-5}$ (g ion/L); between 4.12–3.88, which equaled $CH^+ = 2.4.10^{-5}$ (g ion/L), and between 5.02–4.99, which equaled $CH^+ = 3.10^{-7}$ (g ion/L).

As mentioned above, the terephthalic acid was dissociated in water, and the species of ion terephthalates was a function of the solution pH. Fig. 2 shows that the free acid from terephthalic acid began to increase at pH 5.5, increasing with the decrease in the solution pH. Therefore, decreasing the pH can increase

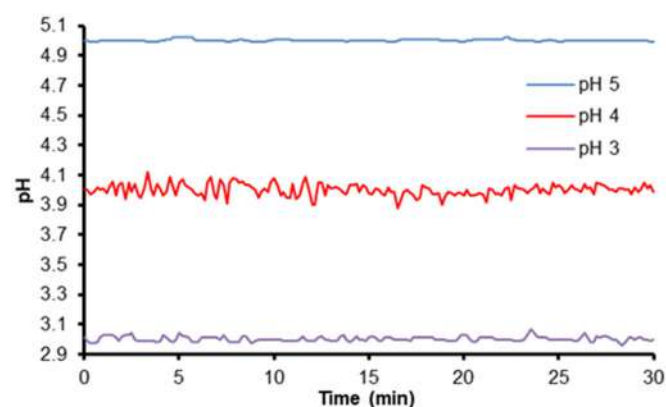


Fig 6. pH fluctuations during experiments

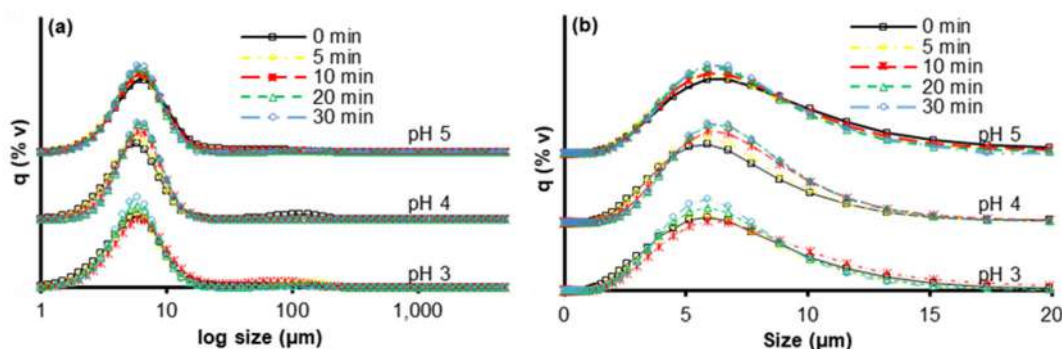


Fig 7. CSD of terephthalic acid at pH variations

the concentration of terephthalic acid as well as supersaturation. When the supersaturation was high, and the solubility was low, the crystallization process was dominated by nucleation, which produced fine crystals. On the other hand, a decrease in the pH of the solution can increase the accumulation of fine crystals [26-27]. Aggregation occurred because there were terephthalate ions (TP^{2-} and HTP^-) and undissociated terephthalate (H_2TP) when lattice crystals were formed so that the surface of the crystal was easily charged.

The logarithmic scale has a broader span of crystal size, as shown in Fig. 7(a). Because of this wide span, CSD in the logarithmic scale showed the presence of two peaks (bimodal) at pH solution of 4 and 3 in the early minutes of the experiments. The primary peak dominated the crystal distribution in a smaller size ($\pm 10 \mu m$), while the second peak appeared in a larger size ($\pm 130 \mu m$), but its frequency was relatively small. Meanwhile, the normal scale (Fig. 7(b)) showed a tendency to increase the number of crystals, indicated by an increase in the peak distribution concerning time.

Large-sized crystals at acidic pH probably came from the aggregation of terephthalic acid. Adding a secondary solution at a constant pH can reduce the accumulation towards a more uniform crystal distribution. It was indicated by the disappearance of the secondary peak (which is essentially small), leading to an increase in the height of the primary peak. Similar studies with double feeds at constant pH showed that changes in CSD indicated the occurrence of aggregation [20].

Fig. 8 shows that the mean crystal size of the terephthalic was increased as the pH solution decreased from 5 to 3. In this case, the pH solution = 5 was chosen for further experiments because it was more stable and easier to control the pH solution. A decrease in pH means that the rise of H^+ concentration (more acidic solution) essentially affected the saturated concentration of terephthalic acid and consequently influenced the size of the terephthalic crystal. Eqs. (3) and (4) can be used to describe this phenomenon.

The reactive crystallization by changing the solution pH (pH swing) was widely applied to produce a less soluble acid or base from a salt [8], usually applied for a

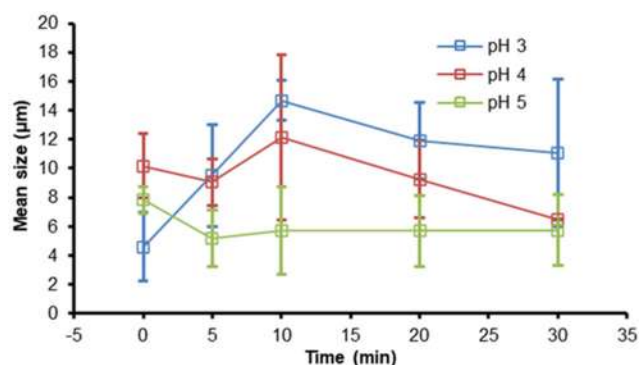


Fig 8. The mean size of terephthalic acid at variations of pH

single-feed semi-batch reactive crystallization [26]. In general, the acid solution produced fine crystals because of rapid nucleation and increased agglomeration. Meanwhile, the double-feed semi-batch crystallization at constant pH showed that pH variation contributed to aggregation [20] and morphology [19].

Effect of secondary solutions concentration

Higher secondary solution concentrations increased the crystal size of terephthalic acid, as presented in Fig. 9. A lower concentration of secondary solution produced a narrower distribution of terephthalic crystals; meanwhile, a higher concentration made a broadened distribution. The secondary solution concentrations affected mean crystal sizes. The concentrations of 0.5, 0.3, and 0.1 M resulted in a mean size of 7.13–8.75, 2.93–4.20, and 3.02–3.20 μm , respectively. A lower concentration led to a lower mean crystal size and variance coefficient, indicating a more uniform size.

A higher concentration of reactants (in secondary solutions) produced a higher terephthalic acid supersaturation condition, which was a driving force for nucleation followed by consecutive and rapid growth. After nucleation, followed by the growth of the crystal, the concentration of the solution decreased gradually, leading to saturated concentration, in which the growth rate stopped.

Similar results were obtained by Tai and Chen [20], reporting that under high supersaturation conditions, the crystal size increased due to the high growth rate. The experiment was conducted for the precipitation of

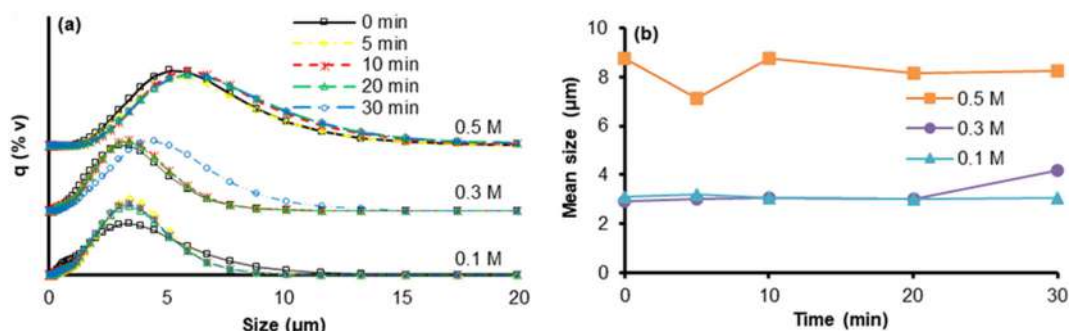


Fig 9. (a) Distribution and (b) size of crystals of terephthalic acid at the variation of secondary solution concentrations

calcium sulfite hemihydrate by using double feeds and operating at a constant pH. These conditions resulted in nucleation rates that were not too high, and supersaturation conditions controlled the crystal growth rate.

Different results were shown by Rewatkar et al. [15] regarding the precipitation of calcium oxalate and Caro et al. [16] regarding the precipitation of salicylic acid. These previous studies showed that the higher the reactant concentration was used, the finer the crystal size was obtained. However, these studies were carried out on single-feed reactive crystallization systems. Furthermore, a study on reactive crystallization conducted by Utomo et al. [28] comparing single feed and double feeds showed that the single feed system produced a smaller and wider crystal size distribution than the double feed systems.

Effect of feeding rate

The feeding rate affects the supersaturation. An increase in the feeding rate increases local supersaturation, increasing the nucleation rate.

The results showed that a feeding rate of 1 to 3 mL/min did not significantly affect the CSD of

terephthalic acid. It is shown in Fig. 10(a), where the CSDs overlapped. The feeding rate of 1, 2, and 3 mL/min resulted in a mean size of 2.92–3.76, 3.01–3.87, and 3.12–4.07 μm, respectively.

The same result was observed by Han and Louhi-Kultanen [17] and Tai and Chen [20], stating that increasing feed speed can increase supersaturation and nucleation. Still, if the supersaturation was high, then the effect of feed speed was small enough, so it was not significant to be analyzed further. To some extent, nucleation was challenging to be controlled by controlling the feeding rate, especially in unseeded operations [29].

Effect of temperature

The experiments were conducted under isothermal conditions at three temperature variations of 30, 50, and 70 °C.

The tendency of crystal distributions varies with time; at 30 °C, the peak tended to shift to the right; at 50 °C, it tended to increase, while at 70 °C, it had a very close value. Temperature affected the nucleation rate. The nucleation rate increased with increasing the temperature and the degree of supersaturation. In addition, the

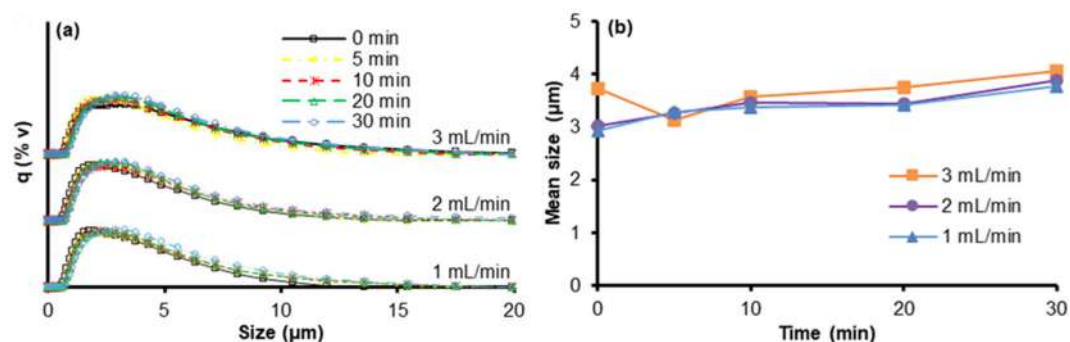


Fig 10. (a) Distribution and (b) mean size of crystals of terephthalic acid at the variation of feeding rates

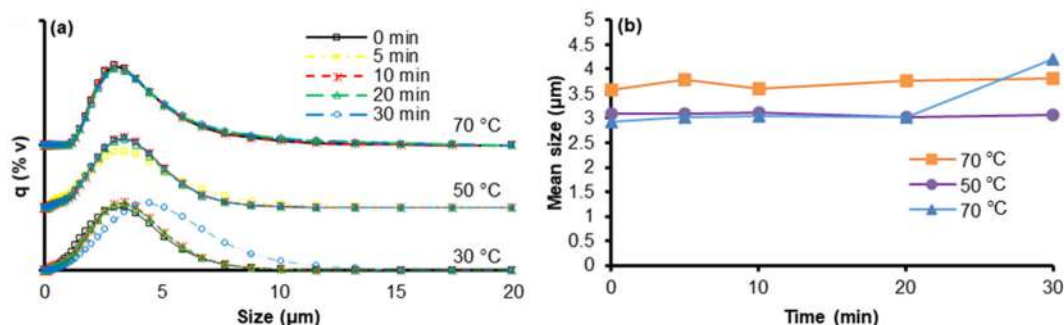


Fig 11. (a) Distribution and (b) mean size of crystals of terephthalic acid at variations of temperatures

solubility of terephthalic acid increased with increasing the solution temperature. The solubility of terephthalic acid in water from experiments at various temperatures compared to a previous study by Park and Sheehan [30] is presented in Fig. 12.

A higher temperature caused a higher terephthalic acid (saturated) solubility, consequently lowering the supersaturation conditions ($\Delta c = \text{initial concentration} - \text{saturated concentration}$). Finally, it decreased the nucleation and increased the crystal growth, producing a larger crystal size. However, Fig. 11(b) indicates that terephthalic acid precipitation temperature only significantly affected the crystal size. The competition between the increasing reaction rate and the solubility with the solution temperature was specific for each system [22]. The competition seems negligible for the reactive crystallization of terephthalic acid; therefore, the temperature significantly affected CSD.

Effect of the stirring rate

Theoretically, crystal growth is influenced by mass transfer rate, as confirmed by Eq. (4). One factor that affects the mass transfer rate is the stirring rate, besides

the solution properties.

This study conducted experiments at 120, 300, and 420 rpm stirring rates. Fig. 13(b) shows that the mean crystal size slightly decreased with the increase of stirring rate from 120 to 420 rpm, although it was not very significant. This result agreed with the research on the precipitation of hydroxyapatite by Tourbin et al. [31], which showed that crystal size increased at a stirring rate of 120–600 rpm. However, the results of Caro et al. [16] showed that crystal size increased at a stirring rate of 100–400 rpm and decreased at a stirring

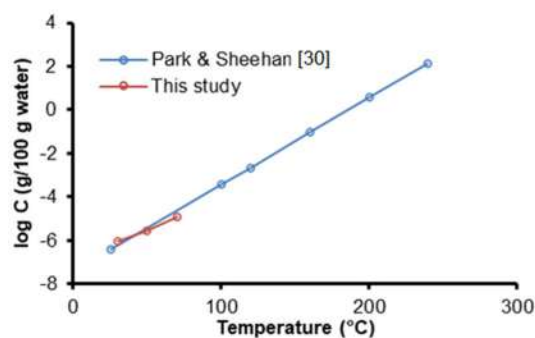


Fig 12. Terephthalic acid solubility at various temperatures

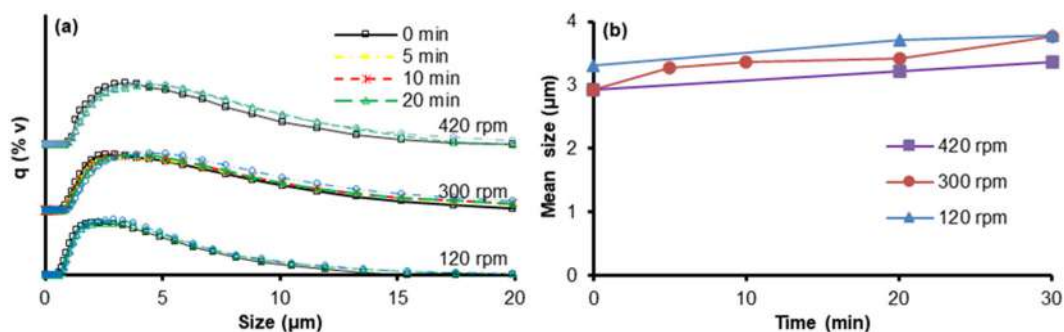


Fig 13. (a) Distribution and (b) mean size of crystals of terephthalic acid at the variation of stirrer stirring rates

Table 2. Characteristics of terephthalic acid by reactive crystallization

No	Parameter	Terephthalic acid	Standard	Unit	Method
1	Acid value	675.338	675 ± 2	mg KOH/g	Titrimetry
2	Ash content	31.047	max 15	ppm (w/w)	Gravimetry
3	Water content	0.028	max 0.15	% (w/w)	Gravimetry
4	Metals	1.115	10	ppm	
5	Fe	0.472	2	ppm	Atomic absorption
6	Co, Mo, Ni, Ti, Mg	0.643	max 1	ppm	spectroscopy
7	4-CarboxyBenzaldehyde (4-CBA)	73.141	max 25	ppm	Chromatography
8	<i>p</i> -Toluic acid	112.379	max 150	ppm	Chromatography
9	Color in 5% dimethylformamide	8.580	max 10	APHA	Spectro

speed of 800–1600 rpm.

Essentially, the rise of the stirring rate enhances the degree of turbulence, which increases the mass transfer rate and finally increases the crystal growth rate. However, the results showed that the stirring rate only slightly affected the crystal size distribution, where the mean crystal size remained as the stirring rate increased. It means that the crystal growth step did not control the overall crystallization process.

The semi-batch reactive crystallization with double-feeding reactants at constant pH and temperature forms nearly the same size crystals. It shows that this method can be used to obtain monodispersed crystals.

Purity of Terephthalic Acid

Terephthalic acid obtained from this experiment was characterized and compared to the standard of commercial terephthalic acid [32] to demonstrate its potential industrial application.

According to ASTM D7976 Standard for purified terephthalic acid, the terephthalic acid purity requirement for PET polymerization is a 4-CBA content of 25 ppm max [21]. The presence of 4-CBA impurities reduces the rate of polymerization in polyester production because the aldehyde functional group in 4-carboxy benzaldehyde cannot react with ethylene glycol in the polymerization process, which limits the polyester chain so that the molecular weight becomes low [33-34].

The results show that reactive purification still contains 4-CBA, which is still relatively high at 73 ppm, and ash content of 31.05 ppm (Table 2). Therefore, the purification of terephthalic acid using the reactive

crystallization method needs to be carried out more than once to meet the terephthalic acid requirements for PET polymerization.

CONCLUSION

The semi-batch reactive crystallization of terephthalic acid at constant pH and isothermal was conducted to study the effect of the crystallization processes (time, pH, temperature, concentration of secondary solutions, flow rate of secondary solutions, and stirring rate) on the CSD of terephthalic acid. The experimental results showed that the pH and concentration of reactants influenced CSD. The operational parameters of crystallization of time, temperature, flow rate, secondary solution, and stirring rate were found to have no significant effect on the mean crystal size of terephthalic acid. Crystallization of terephthalic acid was dominated by nucleation, which was reflected in the fine terephthalic acid crystal size. The semi-batch reactive crystallization with double-feeding reactants at constant pH and temperature forms nearly the same size crystals. However, purification by the reactive crystallization method needs to be carried out more than once to meet the TA requirements for PET polymerization.

ACKNOWLEDGMENTS

The authors thank *Kementerian Riset, Teknologi dan Pendidikan Tinggi via Saintek* Scholarship No. 3535 in 2018 for financial support. The authors also thank the Center for Standardization and Industrial Pollution Prevention Services and the Ministry of Industry for

providing research facilities.

■ AUTHOR CONTRIBUTIONS

Bekti Marlina was involved in conceptualization, methodology, formal analysis, data curation, writing of the draft, and visualization. Rochmadi contributed to conceptualization, methodology, resource acquisition, writing review, and editing and provided supervision. Hary Sulistyono participated in methodology, validation, writing review, and editing and provided supervision. All authors have carefully read and agreed to the final version of the manuscript.

■ REFERENCES

- [1] Cao, J., Meng, C., Cheng, X., and Pan, X., 2019, Surface alkali deweighting and dyeing of polyester fabric by one-bath and one-step process, *Surf. Innovations*, 7 (2), 104–111.
- [2] Gupta, D., Chaudhary, H., and Gupta, C., 2015, Topographical changes in polyester after chemical, physical and enzymatic hydrolysis, *J. Text. Inst.*, 106 (7), 690–698.
- [3] Hilal, N.M., Gomaa, S.H., and Elsisy, A.A., 2020, Improving dyeing parameters of polyester/cotton blended fabrics by caustic soda, chitosan, and their hybrid, *Egypt. J. Chem.*, 63 (6), 2381–2395.
- [4] Yang, B., Xu, H., Wang, J., Yan, D., Zhong, Q., and Yu, H., 2018, Performance evaluation of anaerobic baffled reactor (ABR) for treating alkali-decrement wastewater of polyester fabrics at incremental organic loading rates, *Water Sci. Technol.*, 77 (10), 2445–2453.
- [5] Chaonan, L., and Jihua, C., 2007, The study of the recovery of highly purified terephthalic acid from alkali weight-reduction wastewater, *Int. J. Environ. Pollut.*, 29 (4), 484–494.
- [6] Lewis, A.E., Seckler, M.M., Kramer, H., and Van Rosmalen, G., 2015, *Industrial Crystallization: Fundamentals and Applications*, Cambridge University Press, Cambridge, UK.
- [7] Lee, A.Y., Erdemir, D., and Myerson, A.S., 2019, "Crystals and Crystal Growth" in *Handbook of Industrial Crystallization*, Eds. Myerson, A.S., Erdemir, D., and Lee, A.Y., Cambridge University Press, Cambridge, UK, 32–75.
- [8] Nagy, Z.K., Fujiwara, M., and Braatz, R.D., 2019, "Monitoring and Advanced Control of Crystallization Processes" in *Handbook of Industrial Crystallization*, Eds. Myerson, A.S., Erdemir, D., and Lee, A.Y., Cambridge University Press, Cambridge, UK, 313–345.
- [9] Nicoud, L.H., and Myerson, A.S., 2019, "Influence of Impurities and Additives on Crystallization" in *Handbook of Industrial Crystallization*, Eds. Myerson, A.S., Erdemir, D., and Lee, A.Y., Cambridge University Press, Cambridge, UK, 115–135.
- [10] Suharso, S., Parkinson, G., and Ogden, M., 2007, effect of cetyltrimethylammonium bromide (CTAB) on the growth rate and morphology of borax crystals, *J. Appl. Sci.*, 7 (10), 1390–1396.
- [11] Karpiński, P.H., and Bałdyga, J., 2019, "Precipitation Processes" in *Handbook of Industrial Crystallization*, Eds. Myerson, A.S., Erdemir, D., and Lee, A.Y., Cambridge University Press, Cambridge, UK, 216–265.
- [12] Pitt, K., Peña, R., Tew, J.D., Pal, K., Smith, R., Nagy, Z.K., and Litster, J.D., 2018, Particle design via spherical agglomeration: A critical review of controlling parameters, rate processes and modelling, *Powder Technol.*, 326, 327–343.
- [13] Liu, F., Bagi, S.D., Su, Q., Chakrabarti, R., Barral, R., Gamekkanda, J.C., Hu, C., and Mascia, S., 2022, Targeting particle size specification in pharmaceutical crystallization: A review on recent process design and development strategies and particle size measurements, *Org. Process Res. Dev.*, 26 (12), 3190–3203.
- [14] Bałdyga, J., 2016, Mixing and fluid dynamics effects in particle precipitation processes, *KONA Powder Part. J.*, 33, 127–149.
- [15] Rewatkar, K., Shende, D.Z., and Wasewar, K.L., 2018, Reactive crystallization of calcium oxalate: Population balance modeling, *Chem. Biochem. Eng. Q.*, 32 (1), 11–18.

- [16] Caro, J.A., Woldehaimanot, M., and Rasmuson, Å.C., 2014, Semibatch reaction crystallization of salicylic acid, *Chem. Eng. Res. Des.*, 92 (3), 522–533.
- [17] Han, B., and Louhi-Kultanen, M., 2018, Real-time Raman monitoring of calcium phosphate precipitation in a semi-batch stirred crystallizer, *Cryst. Growth Des.*, 18 (3), 1622–1628.
- [18] Zhang, W., Zhang, F., Ma, L., Yang, J., Yang, J., and Xiang, H., 2019, Prediction of the crystal size distribution for reactive crystallization of barium carbonate undergrowth and nucleation mechanisms, *Cryst. Growth Des.*, 19 (7), 3616–3625.
- [19] Chen, P.C., Cheng, G.Y., Kou, M.H., Shia, P.Y., and Chung, P.O., 2001, Nucleation and morphology of barium carbonate crystals in a semi-batch crystallizer, *J. Cryst. Growth*, 226 (4), 458–472.
- [20] Tai, C.Y., and Chen, P.C., 1995, Crystal growth and agglomeration of calcium sulfite hemihydrate crystals, *Ind. Eng. Chem. Res.*, 34 (4), 1342–1351.
- [21] Slapnik, J., Kraft, G., Wilhelm, T., and Lobnik, A., 2019, Purification of Recycled Terephthalic Acid and Synthesis of Polyethylene Terephthalate, *The 1st International Conference on Circular Packaging*, Ljubljana, Slovenia, 151–159.
- [22] McDonald, M.A., Salami, H., Harris, P.R., Lagerman, C.E., Yang, X., Bommarius, A.S., Grover, M.A., and Rousseau, R.W., 2021, Reactive crystallization: A review, *React. Chem. Eng.*, 6 (3), 364–400.
- [23] Rezazadeh, A., Thomsen, K., Gavala, H.N., Skiadas, I.V., and Fosbøl, P.L., 2021, Solubility and freezing points of disodium terephthalate in water-ethylene glycol mixtures, *J. Chem. Eng. Data*, 66 (5), 2143–2152.
- [24] Christian, G.D., Dasgupta, P.K., and Schug, K.A., 2013, *Analytical Chemistry*, 7th Ed., John Wiley & Sons, Inc., Hoboken, New York, US.
- [25] Rehage, H., Semmel, M., and Kind, M., 2020, A dynamic model for process flowsheet simulation of semi-batch precipitation of sparingly soluble salts, *Comput. Chem. Eng.*, 137, 106818.
- [26] Amari, S., Sugawara, C., Kudo, S., and Takiyama, H., 2022, Investigation of operation strategy based on solution pH for improving the crystal quality formed during reactive crystallization of L-aspartic acid, *ACS Omega*, 7 (3), 2989–2995.
- [27] Sato, E., Seki, Y., and Takiyama, H., 2019, Control of reaction crystallization of organic compounds using the supersaturation profile, *J. Chem. Eng. Jpn.*, 52 (7), 599–604.
- [28] Utomo, J., Asakuma, Y., Maynard, N., Maeda, K., Fukui, K., and Tadé, M.O., 2010, Semi-batch reactive crystallisation of mono-ammonium phosphate: An experimental study, *Chem. Eng. J.*, 156 (3), 594–600.
- [29] Li, M., Shang, Z., and Hou, B., 2019, Optimizing the aspect ratio of cephalexin in reactive crystallization by controlling supersaturation and seeding policy, *Trans. Tianjin Univ.*, 25 (4), 348–356.
- [30] Park, C., and Sheehan, R.J., 2000, "Phthalic Acids and Other Benzenepolycarboxylic Acids" in *Kirk-Othmer Encyclopedia of Chemical Technology*, John Wiley & Son, New York.
- [31] Tourbin, M., Brouillet, F., Galey, B., Rouquet, N., Gras, P., Chebel, N.A., Grossin, D., and Frances, C., 2020, Agglomeration of stoichiometric hydroxyapatite: Impact on particle size distribution and purity in the precipitation and maturation steps, *Powder Technol.*, 360, 977–988.
- [32] Wiley-VCH, 2016, *Ullmann's Polymer and Plastics*, 1st Ed., Wiley-VCH, Weinheim, Germany.
- [33] Azarpour, A., Rezaei, N., and Zendejboudi, S., 2020, Product quality control in hydropurification process by monitoring reactor feed impurities: Dynamic mathematical modeling, *J. Ind. Eng. Chem.*, 92, 62–76.
- [34] Rao, P.N., Sabavath, G.K., and Paul, S.N., 2021, Impact of MTA blend % in melt spinning process and polyester properties, *SN Appl. Sci.*, 3 (2), 184.

Synthesis of Co(II), Ni(II), Cu(II), Pd(II), and Pt(IV) Complexes with 1⁴,1⁵,3⁴,3⁵-Tetrahydro-1¹H, 3¹H-4,8-diaza-1,3(3,4)-ditriazola-2,6(1,4)-dibenzenacyclooctaphane-4,7-dien-1⁵,3⁵-dithione, and the Thermal Stability of Polyvinyl Chloride Modified Complexes

Ali Mudher Abdulkareem Al-Khazraji*

Department of Chemistry, College of Education for Pure Science Ibn Al-Haitham, University of Baghdad, Baghdad, Iraq

* **Corresponding author:**

tel: +964-7724031983

email:

ali.m.ak@ihcoedu.uobaghdad.edu.iq

Received: January 13, 2023

Accepted: February 16, 2023

DOI: 10.22146/ijc.81272

Abstract: In the current endeavor, a new Schiff base of 1⁴,1⁵,3⁴,3⁵-tetrahydro-1¹H,3¹H-4,8-diaza-1,3(3,4)-ditriazola-2,6(1,4)-dibenzenacyclooctaphane-4,7-dien-1⁵,3⁵-dithione was synthesized. The new symmetrical Schiff base (Q) was employed as a ligand to produce new complexes comprising Co(II), Ni(II), Cu(II), Pd(II), and Pt(II) metal-ions at a ratio of 2:1 (Metal:ligand). There have been new ligands and their complexes validated by (FTIR), (UV-visible), ¹H-NMR, ¹³C-NMR, CHNS, and FAA spectroscopy, Thermogravimetric analysis (TG), Molar conductivity, and Magnetic susceptibility. The photostabilization technique to enhance the polymer was also used. The ligand Q and its complexes were mixed in 0.5% w/w of polyvinyl chloride in tetrahydrofuran (THF). The photo stabilization of polymer films was studied at 25 °C under irradiation of light λ 380–250 nm with intensity of 7.75 × 10⁻⁹ ein dm⁻³ s⁻¹. The photostabilization activity of these compounds was determined by monitoring the hydroxyl, carbonyl, and polyene indexes, weight loss method with irradiation time. The I_{CO}, I_{PO} and I_{OH} index values increased with irradiation time, this increase depends on the type of additives. The surface morphology for these films was studied during irradiation time. This project is highly intriguing for the ecosystem in regards to the decrease in the consumption of plastic.

Keywords: Schiff base; PVC; photostability; photodegradation; PVC films; weight loss

■ INTRODUCTION

Chemical compounds with at least two diversified atom types in the rings are known as hetero cycles [1]. Organic hetero cyclic encompass ringed blended rings without atoms and heteroatoms (N, O, and S). Most organic compounds have at least one heterocyclic sequence to make them the most predominant variety of compounds; hetero-atom presence provides heterocyclic compounds with numerous physical and chemical characteristics. Heterocycles are found in many organic ingredients such as vitamins, hormones [2], antibiotics [3], and pigments [4], and each of the main constituents are critical to human health. Therefore, we can conclude that the concept of biologically active molecules is becoming more widely discussed. Biologically active natural products are impeded by heterocyclic nitrogen, a synthetic compound. Chemically, triazole is part of the class of organic heterocyclic compounds called pyridazines [5]. It has two

carbon atoms at the non-adjacent site and belongs to a class of five unsaturated ring structure members with three atoms each; the isomer resembles the triazole.

The triazole ring is a planar geometry that possesses a resonance system through (6 π-electron) delocalized for carbon atoms and π-electron distortion system due to nitrogen atoms for both types (symmetrical and vicinal formula). Through the phenomenon of resonance in the five-ring system represented by the triazole ring, it adds to its high stability through the exchange of electrons and is known as tautomerism state by conjugate bonds with an π-electron with nitrogen atoms. In two unique tautomeric forms, 1,2,4-triazoles [6] are feasible; pharmaceutically, the 1,2,4-triazole-1H and 4-hydro-1,2,4-triazole is considered essential.

In sequence, for the amine and sulfur atom to take effect, soft, and hard nitrogen atoms must constitute an

exquisite ligand. This new Schiff base ligand interacts with the terephthaldehyde [7].

Additionally, considerable investigation into the coordination of divalent metal ions can be conducted using this newer Schiff base [8]. Metal transition complexes are the ongoing inspiration for us in our experiments. The polyvinyl chloride film [9] is judged for photodegradation to accurately assess newer compounds in a photostability operation to synthesize, characterize, and test the new ligand (Schiff base) and complexes. When it comes to nitrogen, neither soft nor hard instances must be attached to the same ligand. Terephthaldehyde and the new Schiff base [10] ligand, interact with each other. The coordination of various metal ions is also used to study the functioning of this novel Schiff base and its procedures. Metal transition complexes are an ongoing attraction for us in our research. The polyvinyl chloride film is judged for photodegradation to judge new compounds in a photostability [11] set-up to synthesize, characterize, and test the new ligand (Schiff base) and complexes through monitoring the degree of polymerization, weight loss, hydroxyl, carbonyl, and polyene index.

■ EXPERIMENTAL SECTION

Materials

All the chemicals used in this research were supplied by Sigma-Aldrich without any additional purification. Terephthalic acid, absolute EtOH, Carbon-disulfide CS_2 , Hydrazine hydrate 80%, Glacial acetic acid, Sulfuric acid, Potassium hydroxide KOH, Sodium bicarbonate NaHCO_3 , Diethyl ether, the metal salt $\text{CoCl}_2 \cdot 6\text{H}_2\text{O}$, $\text{CuCl}_2 \cdot 2\text{H}_2\text{O}$, $\text{NiCl}_2 \cdot 6\text{H}_2\text{O}$, $\text{PdCl}_2 \cdot 2\text{H}_2\text{O}$, and $\text{PtCl}_6 \cdot 6\text{H}_2\text{O}$ and Polyvinyl chloride $(\text{CH}_2\text{CHCl})_n$ were all obtained from Sigma-Aldrich.

Instrumentation

The instrumentations used in this study were The Fourier transform Infrared (FTIR) spectra ($400\text{--}4000\text{ cm}^{-1}$) recorded on a Shimadzu 8400 Spectrophotometer (Shimadzu Cooperation, Kyoto, Japan) using the KBr disc technique. Proton nuclear spectrum for Schiff base (Q) magnetic resonance ($^1\text{H-NMR}$, $^{13}\text{C-NMR}$) spectra

(400 MHz , 125 MHz) recorded on a Bruker DRX400 NMR Spectrometer (Bruker, Zürich, Switzerland) in $\text{DMSO-}d_6$ related to tetramethylsilane. Conductivity measurements were conducted with the WTW, USA. The chloride content was measured with the 686-Titro Processor-665 Dosim A-Metrohm/Swiss. Magnetic susceptibility measurements were conducted with the Bruker BM6 instrument. The electronic spectra used A Shimadzu-160 spectrophotometer ($200\text{--}900\text{ nm}$; Kyoto, Japan). The atomic absorption (A.A.) technique was performed using a Shimadzu PR-5 ORAPHIC PRINTER atomic absorption spectrophotometer. The melting point was determined by the Gallen Kamp Apparatus. The elemental analyses were performed on the Vario EL III Elementar instrument. A Digital Caliper, $1000\text{ mm}/40\text{-inch}$ Vogel, Germany was utilized to prepare PVC films. The morphology images of PVC films were recorded on the Meiji Techno Microscope (Meiji Techno, Tokyo, Japan), ($460\times$ magnification).

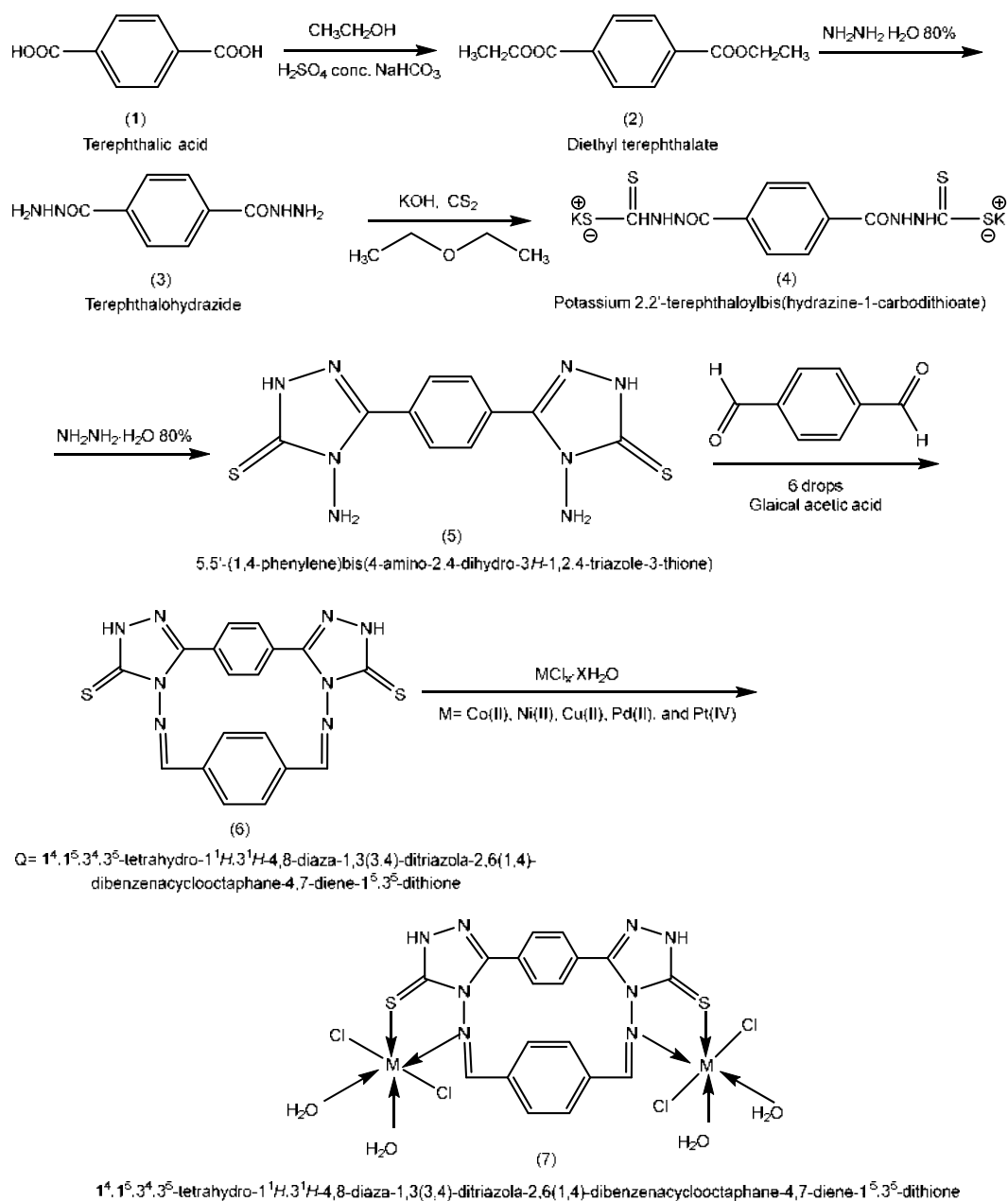
Procedure

Diethyl terephthalate synthesis – the initial step (2)

According to the following scheme, diethyl terephthalate was synthesized [12]; 5 g of Terephthalic acid 0.03 mmol was dissolved in 45 mL of EtOH. The insertion of 5 mL of concentrated H_2SO_4 rendered the reaction acidic. The reaction mixture was incubated under reflux for 6 h. To eliminate vacuum-filtered residual acid, the remaining alcohol is distilled- H_2O and cooled with a 10% saturated sodium chloride followed by a sodium bicarbonate solution. Eventually, the diethyl terephthalate crystal was assembled.

Terephthalohydrazide synthesis - the second step (3)

The present route was used to synthesize the terephthalohydrazide [13] Scheme 1: Two point three grams of Diethyl terephthalate 0.01 mmol was immersed in 20 mL of ethanol. The mixture was then heated and refluxed for 10 h after appending 80% of the stated amount of hydrazine (35 mL). The reaction was assessed using thin-layer chromatography (TLC), and vacuum-dried and filtered solids were produced. Utilizing a white crystal needle and ice-cold water, the product was obtained in the form of a powder.



Scheme 1. The general synthetic route for new Schiff bases and their complexes

Potassium 2,2'-terephthaloyl bis-ester (hydrazine-1-carbodithioate) synthesis - the third step (4)

The present route follows Scheme 1 for the synthesis of potassium 2,2'-terephthaloylbis(hydrazine-1-carbodithioate). Ethanol was used to dissolve potassium-hydroxide (KOH) (35 mL). Terephthalohydrazide and carbon disulfide (CS_2) were then inserted into the mixture, which was held at room temperature with stirring for 12 h. Diethyl ether (250 mL) had also been

inserted into the reaction and stirred for 10 min to cool down; diethyl ether was washed under vacuum after already being presented in a solid filter.

Synthesis of 5,5'-(1,4-phenylene)bis(4-amino-2,4-dihydro-3H-1,2,4-triazole-3-thione) - the fourth step (5)

The present route follows Scheme 1 to synthesize 5,5'-(1,4-phenylene)bis(4-amino-2,4-dihydro-3H-1,2,4-triazole-3-thione). Hydrazine hydrate 80% (35 mL) was

diluted with a compound (4) (0.0094 mmol). The blending has been overflowing for 6 h now. The greenish reaction abruptly changed color. In order to keep a perceive of the reaction, TLC was used. As an outcome, the tenor had already become acidic. Under vacuum, the precipitation was sprayed onto the compound.

Synthesis of 1⁴,1⁵,3⁴,3⁵-tetrahydro-1¹H,3¹H-4,8-diaza-1,3(3,4)-diazola-2,6(1,4)-dibenzenacyclooctaphane-4,7-diene-1⁵,3⁵-dithione (Q) - the fifth step (6)

Following Scheme 1, absolute ethanol was utilized to distribute and augment the concentration of compound (5) (0.0094 mmol) at a volume of 35 mL. Thereafter, terephthaldehyde was inserted (0.003 mmol). An acidic reaction was caused by the insertion of six drops of glacial acetic acid into the mixture. Under reflux, the mixtures were heated for approx. 10 h. To keep abreast of the reaction, TLC was used, and the eventual powder was filtered under vacuum.

Synthesis of the transition metal complex - the sixth step (7)

Transition metal complexes of Co(II), Cu(II), Ni(II), Pd(II), and Pt(IV) were synthesized from the metallic salts of CoCl₂·6H₂O, NiCl₂·6H₂O, CuCl₂·2H₂O, PdCl₂·2H₂O, and PtCl₆·6H₂O besides (Q), in 2:1 ratio of metal to ligand, following Scheme 1. It took 6 h of warming under reflux to finalize the reaction. The precipitate was filtered and eventually washed with distilled water.

Films preparation technique of polyvinyl chloride

The polymer polyvinyl chloride was dissolved by

tetrahydrofuran (THF) in a solution 0.5% w/v; after preparation, the solutions were poured into a glass frame, and small sinks with a capacity of 6 mL were created by attaching laboratory glass slides to a piece of ordinary glass to make this frame. As the solvent evaporated at 24 h, polymer films began to appear. These films have a thickness of around 40 μm, and are adhered to papers, with dimension holes of 2 × 2 cm.

RESULTS AND DISCUSSION

A new ligand from Schiff bases and their complexes are indicated by the information in Table 1, including experimental formula (C, H, N, and S), the ratio of metal to ligand, and the physical properties of the new ligand from Schiff base and their complexes. All complexes were soluble in DMSO-*d*₆.

The FTIR Spectra of the New Schiff Base (Q) and Their Complexes

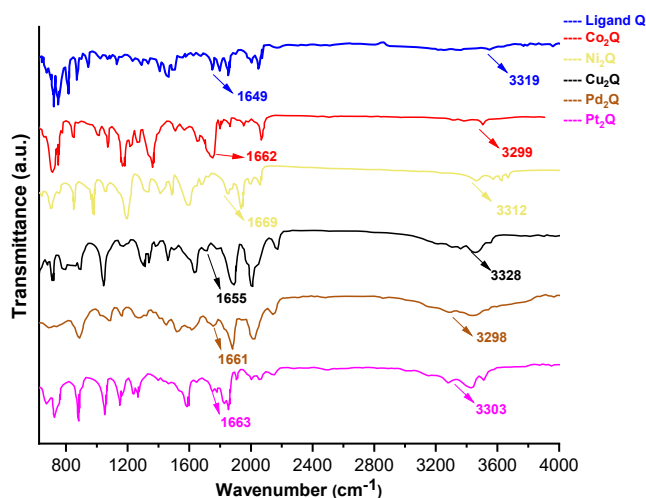
Diverse Schiff base ligands and their complexes were analyzed with FTIR spectrophotometry. Table 2 and Fig. 1 show the absorption variations for the ligand observed in the bands of N-H 3319 cm⁻¹ symmetry and asymmetry, CH=N 1649 cm⁻¹, and C=S 1120 cm⁻¹; the two groups of nitrogen and sulfur atoms observed the coordinate with a metal ion, although the complexes are revealed bands at 1662 cm⁻¹, for CH=N [14], and 1117 cm⁻¹ for C=S, the ligand-Metal coordinate is responsible for shifting (Q) intensity. It is also conspicuous that there are new bands in the metals (Metal-N), (Metal-O),

Table 1. The physical properties and analytical data of the new Schiff base (Q) and its complexes

Comp.	Experimental formula	Color	M.P °C	Yield %	M.wt g.mol ⁻¹	Micro elemental analysis found (calc.)				Metal content % found (calc.)
						C%	H%	N%	S%	
Q	C ₁₈ H ₁₂ N ₈ S ₂	Off-white	> 300	74	404.47	54.11 (53.45)	2.74 (2.99)	26.02 (27.70)	15.39 (15.85)	-
Co ₂ Q	C ₁₈ H ₂₄ Co ₂ Cl ₄ N ₈ S ₂ O ₆	Yellowish	> 305	68	771.8	35.02 (35.51)	3.14 (4.59)	12.36 (12.66)	5.98 (7.78)	11.21 (10.08)
Ni ₂ Q	C ₁₈ H ₂₂ Ni ₂ Cl ₄ N ₈ S ₂ O ₇	Dark Brown	285	71	785.4	27.37 (26.44)	2.99 (4.32)	12.94 (13.76)	6.43 (7.26)	10.41 (10.11)
Cu ₂ Q	C ₁₈ H ₂₀ Cu ₂ Cl ₄ N ₈ S ₂ O ₄	Yellowish	> 310	66	745	28.37 (27.91)	2.67 (3.83)	13.88 (12.79)	6.21 (6.73)	15.29 (14.40)
Pd ₂ Q	C ₂₀ H ₂₆ Pd ₂ Cl ₄ N ₈ S ₂ O	Light yellowish	> 315	73	812.8	26.93 (28.86)	1.86 (3.24)	12.33 (11.26)	6.29 (7.46)	21.43 (20.24)
Pt ₂ Q	C ₁₈ H ₂₄ Pt ₂ Cl ₈ N ₈ S ₂ O ₂	Dark yellowish	294	68	1122	31.32 (30.11)	1.87 (2.65)	9.08 (9.51)	6.47 (6.13)	32.05 (33.00)

Table 2. FTIR spectrum data for new Schiff base (Q) and their metal complexes are observed

Symbol	FTIR (ν , cm^{-1})						
	N-H	C=N	C=S	M-N	M-O	M-S	M-Cl
Q	3319	1649	1120	-	-	-	-
Co ₂ Q	3299	1662	1117	607	554	441	398
Ni ₂ Q	3312	1669	1109	612	542	448	390
Cu ₂ Q	3328	1655	1084	601	539	499	391
Pd ₂ Q	3298	1661	1099	598	547	472	388
Pt ₂ Q	3303	1663	1097	591	566	489	362

**Fig 1.** FTIR spectrum for Schiff base (Q) and their metal ion complexes

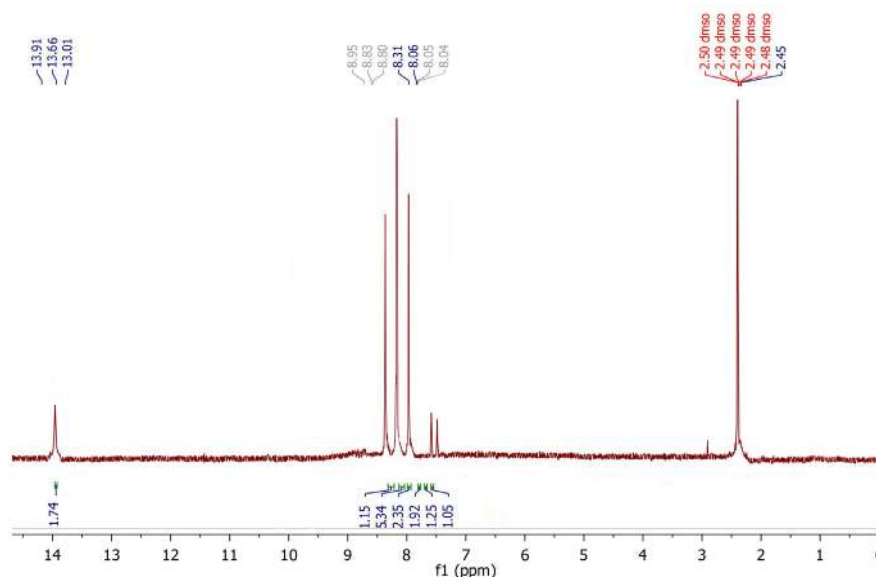
(Metal-S), and (Metal-Cl) in the range of 290–610 cm^{-1} .

NMR Spectra of Synthesized Compounds (Q)

Fig. 3 and Table 3 show the results of a ¹³C-NMR spectrum of (Q) spotted the signals at δ , ppm: 168 for CH=N (imine) [15], 161 for C=S thione group, 136 for C-C benzene ring; whereas in Fig. 2, and Table 3 showed the values of chemical shifts for the ¹H-NMR spectrum of (Q) spotted: 13.66 (1H, s, SH) thiol, 8.31 (4H, m, CH ar.) benzene ring, 7.93 (1H, m, CH=N) imine group.

The Ultra-Violet Spectra of the New Schiff Bases (Q) and Their Complexes

Schiff bases were dissolved in chloroform and their complexes were derived from a variety of bands as a consequence; Fig. 4, and Table 4 show the ligand (Q) with three bands of absorption at 242 nm, 41322 cm^{-1} , and 362 nm, 27624 cm^{-1} allocated to $\pi \rightarrow \pi^*$ and $n \rightarrow \pi^*$

**Fig 2.** The ¹H-NMR spectrum of Schiff base (ligand Q)

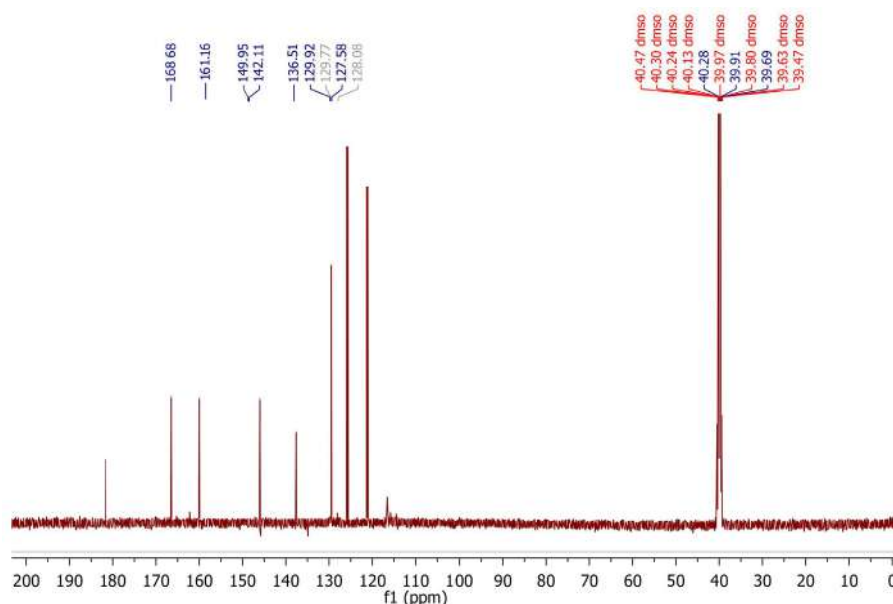


Fig 3. ^{13}C -NMR spectrum of Schiff base (ligand Q)

Table 3. Data for the new Schiff base (Q) is shown in (NMR data)

Symbol	^1H -NMR (500 MHz, $\text{DMSO-}d_6$, δ , ppm in Hz)
Q	13.66 (1H, s, SH) thioI, 8.31 (4H, m, CH ar.), 7.93 (1H, m, CH=N) imine
Symbol	^{13}C -NMR (125 MHz, $\text{DMSO-}d_6$, δ , ppm in Hz)
Q	168 (CH=N) (imine), 161 (C=S) thione, 136 (C-C) benzene ring

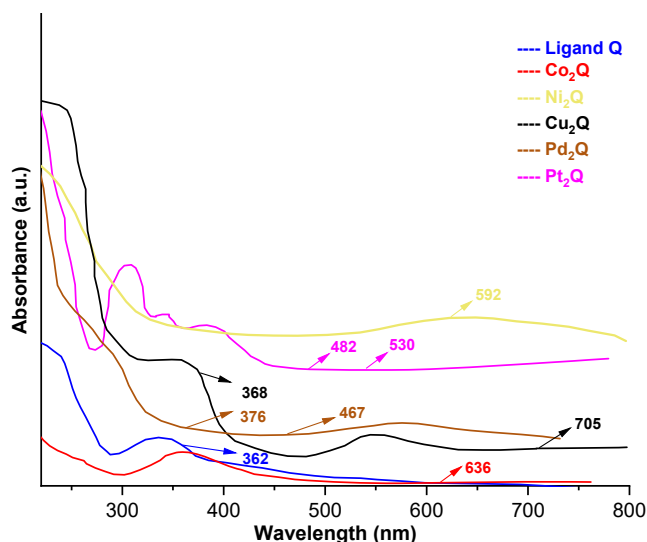


Fig 4. Electronic spectra of the ligand and their metal complexes

intra-ligand transition, and 421 nm, 23752 cm^{-1} for $n \rightarrow \pi^*$ whereas other complexes arranged to cobalt(II) complex two-bands at 636 nm, 15723 cm^{-1} and 498 nm, 20080 cm^{-1} ; nickel(II) complex two-bands at 592 nm, 16891 cm^{-1} and

472 nm, 21186 cm^{-1} for $[^3\text{A}_{2g} \rightarrow ^3\text{T}_{1g}]$ (F) ν_2 , and $[^3\text{A}_{2g} \rightarrow ^3\text{T}_{1g}]$ (P) ν_3 ; copper(II) complex $[^2\text{E}_g \rightarrow ^2\text{T}_{2g}]$ [L \rightarrow Cu] (C.T.); palladium(II) complex were assigned to 467 nm, 21413 cm^{-1} ; 376 nm, 26595 cm^{-1} ; and 305 nm, 32786 cm^{-1} for $[^1\text{A}_{1g} \rightarrow ^1\text{B}_{1g}]$, $[^1\text{A}_{1g} \rightarrow ^1\text{E}_{1g}]$ and [L \rightarrow Pd] (C.T.); platinum(IV) complex were assigned to 530 nm, 18867 cm^{-1} ; 482 nm, 20746 cm^{-1} ; and 433 nm, 23094 cm^{-1} $[^1\text{A}_{1g} \rightarrow ^3\text{T}_{1g}]$, $[^1\text{A}_{1g} \rightarrow ^3\text{T}_{2g}]$ and [L \rightarrow Pt] (C.T.).

Thermal Analysis (TG) of the New Schiff Base (Q) and Its Complexes

Fig. 5 and Table 5 imply the Schiff base ligand (Q)'s thermogravimetric TG curve and their complexes under nitrogen gas (N_2) in which temperatures ranged from 25 to 600 $^\circ\text{C}$ at a rate of 10 $^\circ\text{C}/\text{min}$. In TGA, oven moisture is blended with gravimetric analysis, and there is a modest oven rod that records the temperature and weight of the specimen over time until that weight is somewhat constant. As a result of its high sensitivity to exothermic and endothermic processes and the ability to

Table 4. Molar conductivity and magnetic-susceptibility of metal-complexes

Compound	λ_{\max} nm (ν , cm^{-1})	Assignment	Molar conductivity $\text{Ohm}^{-1} \text{cm}^2 \text{mol}^{-1}$	Magnetic susceptibility (B.M.) (calc.) found	Suggested geometry
Ligand Q	242 (41322)	$(\pi \rightarrow \pi^*)$	-	-	Octahedral geometry
	362 (27624)	$(n \rightarrow \pi^*)$			
Co ₂ Q	636 (15723)	$^4T_{1g} \rightarrow ^4A_{2g}$ (F)	10.65	(4.12) 4.22	Octahedral geometry
Ni ₂ Q	592 (16891)	$^3A_{2g} \rightarrow ^3T_{1g}$ (F)	12.77	(2.75)	Octahedral geometry
	472 (21186)	$^3A_{2g} \rightarrow ^3T_{1g}$ (P)		2.79	
Cu ₂ Q	705 368	$^2E_g \rightarrow ^2T_{2g}$ L \rightarrow Cu C.T.	11.39	(1.73) 1.80	Octahedral geometry
	Pd ₂ Q	467 (21413)		$^1A_{1g} \rightarrow ^1B_{1g}$	
Pt ₂ Q		376 (26595)	$^1A_{1g} \rightarrow ^1E_{1g}$	19.04	0.02
	530 (18867)	$^1A_{1g} \rightarrow ^3T_{1g}$	(0.06)		Octahedral geometry
	482 (20746)	$^1A_{1g} \rightarrow ^3T_{2g}$	0.11		

Table 5. Thermal decomposition data for the new Schiff base ligand and its complexes

Comp.	Molecular formula M.wt.	Steps	Temp. range of the decomposition (TG) °C	The suggested formula for loss	Mass loss %	
					Cal.	Found
Q	C ₁₈ H ₁₂ N ₈ S ₂ 404.47	1	0–220	C ₆ H ₄ , 2S	34.61	32.87
		2	220–405	2N, 2C=N-NH	27.19	27.01
		3	405–595	2N, C ₆ H ₄	25.71	24.66
Co ₂ Q	C ₁₈ H ₂₄ Co ₂ Cl ₄ N ₈ S ₂ O ₆ 771.8	1	0–190	2N, C ₆ H ₄ , 2H ₂ O	18.13	18.02
		2	190–390	2C ₂ N ₃ H, C ₆ H ₄	27.20	28.11
		3	390–595	4Cl, 4H ₂ O	27.72	26.15
Ni ₂ Q	C ₁₈ H ₂₂ Ni ₂ Cl ₄ N ₈ S ₂ O ₇ 785.4	1	0–229	C ₆ H ₄ , H ₂ O	11.96	10.09
		2	229–377	2N, 2S, 2C ₂ N ₃ H	28.77	27.38
		3	377–595	C ₆ H ₄ , 4Cl, 3H ₂ O	34.63	34.06
Cu ₂ Q	C ₁₈ H ₂₀ Cu ₂ Cl ₄ N ₈ S ₂ O ₄ 745	1	0–268	2C ₂ N ₃ H, C ₆ H ₄	28.18	28.66
		2	268–405	C ₆ H ₄ , 2S, 2N	22.55	20.82
		3	405–595	4H ₂ O, 3Cl	23.95	21.87
Pd ₂ Q	C ₂₀ H ₂₆ Pd ₂ Cl ₄ N ₈ S ₂ O 812.8	1	0–228	CH ₃ CH ₂ OH	5.65	6.02
		2	228–395	2S, 2N, 2C ₂ N ₃ H	27.80	26.24
		3	395–595	2C ₆ H ₄ , 2Cl, 4H ₂ O	36.29	34.98
Pt ₂ Q	C ₁₈ H ₂₄ Pt ₂ Cl ₈ N ₈ S ₂ O ₂ 1122	1	0–270	2H ₂ O, C ₆ H ₄	9.98	10.20
		2	270–350	2N-NH, 4N, 2S	15.86	14.54
		3	440–595	C ₆ H ₄ , 4Cl, 3H ₂ O	24.24	23.66

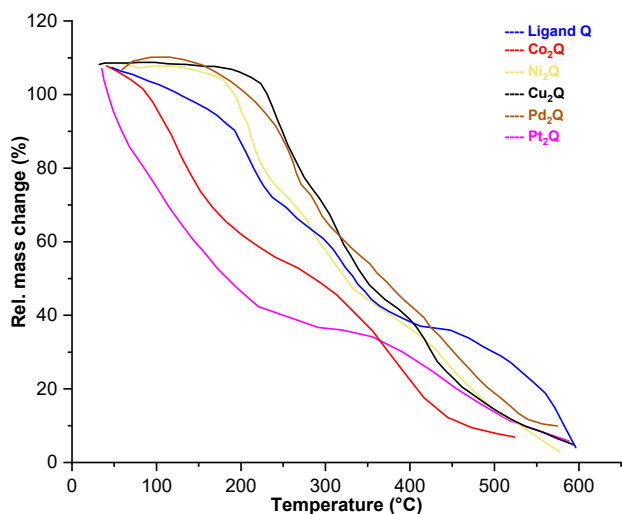


Fig 5. Thermogravimetric (TG) curve of ligands and their complexes by heating 10 °C/min under nitrogen gas

evaluate temperature-dependent variations in physical and chemical properties, heat capacity can be judged. Most weight losses happened during the later disintegration, and the final deterioration resulted in a weight loss of more than 60% overall. As a result, the thermal vaporization of volatile substances was revealed as the first stage in the decomposition of complexes after moisture evaporation. Depleting molecules from the complexes presumably caused the second stage of deterioration. The Schiff base ligand Q also shows two stages of decomposition and subsequent dehydration. The DTG curves similarly exhibited a slight peak affiliated with moisture loss, a steep summit with maximum temperature values as shown in Table 5 as well as a slight decrease associated with moisture loss, except for Pt₂Q, which had a large, broad peak between 600 and 800 °C. The break-down temperatures of all the combinations were virtually the same, ranging from 150 to 330 °C, proving their thermal stability. To validate the complexes' relative stability, the temperature at which deterioration began has been proposed. In contrast to the Pt₂Q complex, degradation persisted at temperatures above 800 °C.

Photostability

The photostability of the Schiff base and five metal complexes of Co(II), Ni(II), Cu(II), Pd(II), and Pt(IV) modified with polyvinyl chloride films was performed by

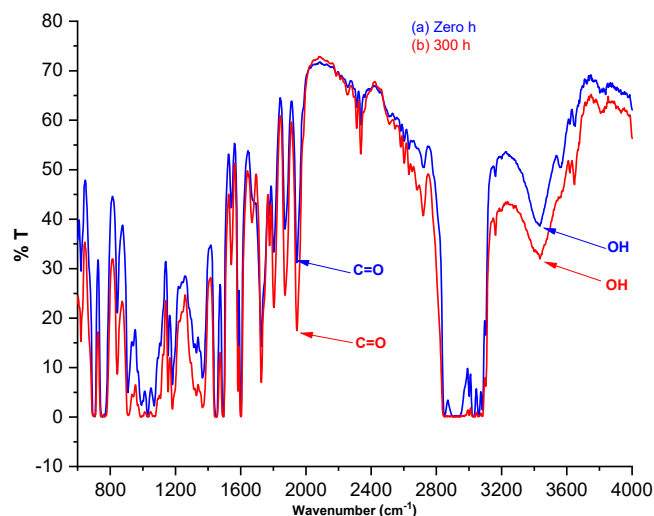


Fig 6. The FTIR spectra of a PVC film (a) before and (b) after 300 h of exposure

dissolving in tetrahydrofuran (THF) at 25 °C. It can be seen in the 3600–3200 cm⁻¹ band where a large-band occurs that weakens the band's strength in the FTIR spectrum; this is responsible for the formation of hydroxyl, carbonyl, and polyene groups [16] as shown in Fig. 6. I_{OH}, I_{CO}, I_{PO} indices are shown in Fig. 7–9 where the raying sensitivity period was comparative to PVC without addition and raises the exposure ray rate of I_{OH}, I_{CO}, and I_{PO}.

Fig. 7–9 show a significant rise in exposure ray rate of I_{OH}, I_{CO}, and I_{PO} indices compared to PVC films without the additament of sensitivity raying time, with the addition of metals such as copper, nickel and platinum(IV) which was inferred to be the majority effective photo-stabilizer.

PVC Films Molecular Average Weight Changes as an Outcome of Photolysis

A significant chain collapse at a distant place in the PVC chain caused a rapid decline in \overline{M}_v in Fig. 11, revealing that PVC degradation attributed to the reduced scale of PVC in Fig. 10. The \overline{M}_v versus exposure plot proves that the film was irradiated an extra 0.5% of the time. S is the actual population of chain scissors in Fig. 12, (Eq. (1)) [17].

$\overline{M}_v,0$ = M.wt viscosity means at the foremost of the experiment;

\overline{M}_v, t = M.wt viscosity on average during irradiation

$$S = \frac{\overline{Mv,0}}{\overline{Mv,t}} - 1 \quad (1)$$

Since cross-linking can determine the level of retrogradation premised on branching in Fig. 13, it thus indicates a rise in data. (α) via Eq. (2) are:

m = Primitive of M.wt

$$\alpha = \frac{m \times S}{\overline{Mv}} \quad (2)$$

The degree of retrograde rate (α) versus the time of radiation as shown in Fig. 14, the primary phases of PVC, grade assembly (D.P.) and the number of PVC monomeric unit (Eq. (3)) illustrates the degree of irradiation; Reverse polymerizing ($1/DP_n$) versus an inverted sample in front of a blank demonstrates an augmentation in radiation time ($1/DP_n$).

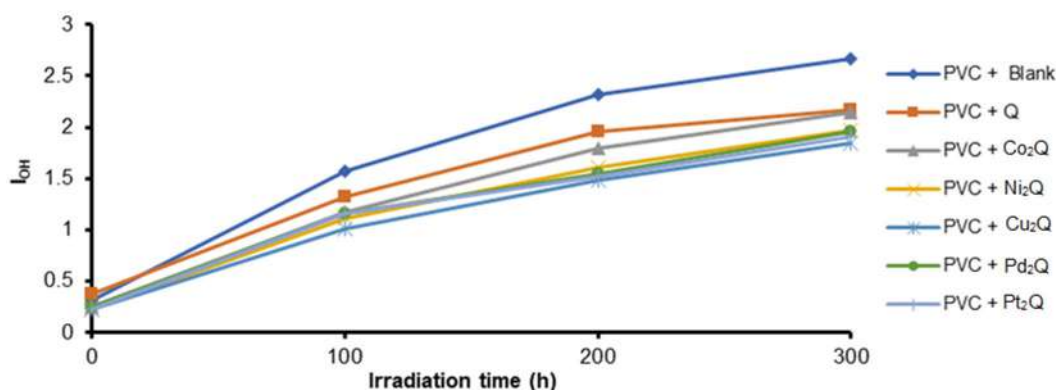


Fig 7. The relationship between (I_{OH}) and irradiation time for PVC films ($40 \mu\text{m}$) containing 0.5% additives

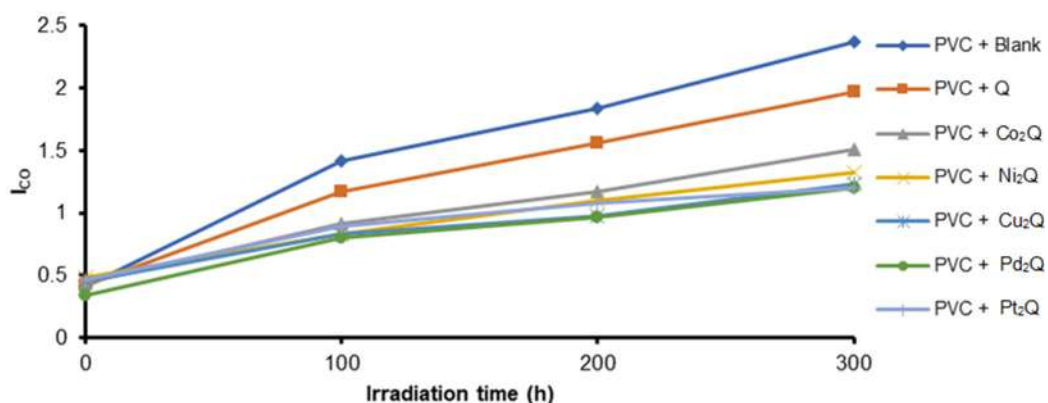


Fig 8. The relationship between (I_{CO}) and irradiation time for PVC films ($40 \mu\text{m}$) containing 0.5% additives

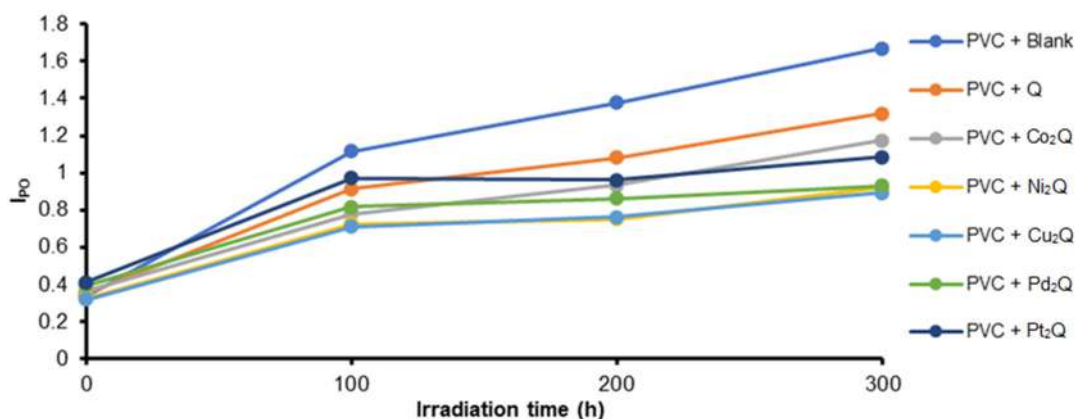


Fig 9. The relationship between (I_{PO}) and irradiation time for PVC films ($40 \mu\text{m}$) containing 0.5% additives

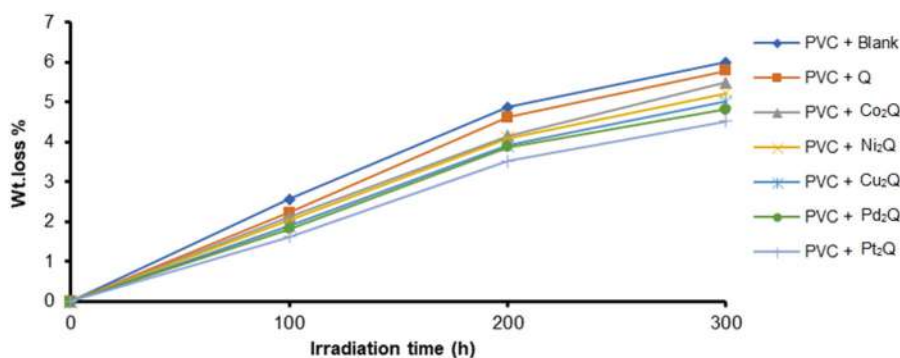


Fig 10. Variation of the weight loss of PVC films (40 μm) thickness containing 0.5% additives with the irradiation time

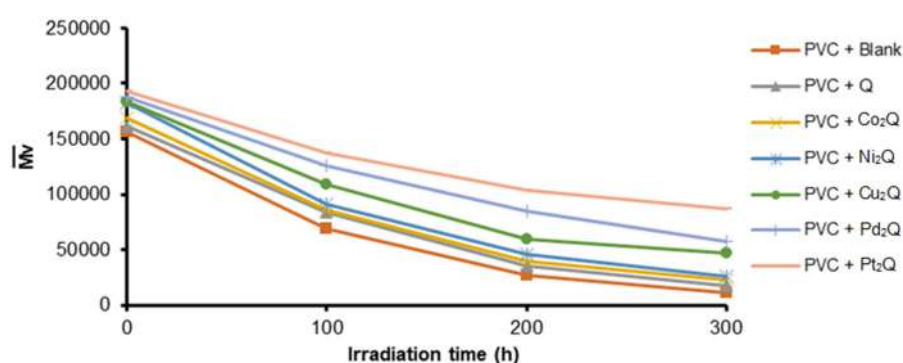


Fig 11. Variation of the M.wt. average for PVC films (40 μm) thickness containing 0.5% additives with the irradiation time

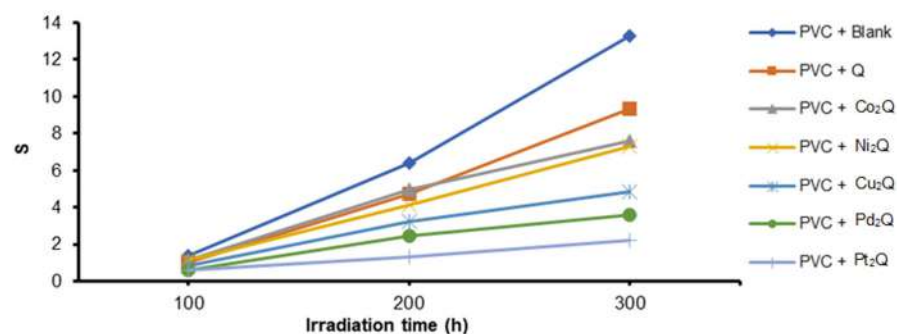


Fig 12. Variation of the Increase growth in the degree of branching (S) for PVC films (40 μm) thickness containing 0.5% additives with the irradiation time

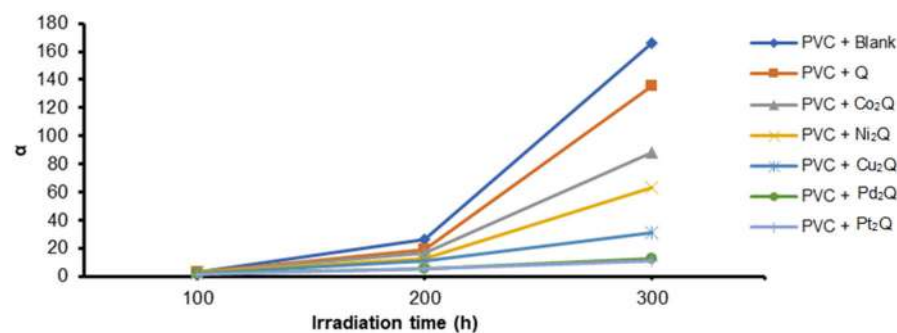


Fig 13. Variation of degree of degradation (α) for PVC films (40 μm) thickness containing 0.5% additives with the irradiation time

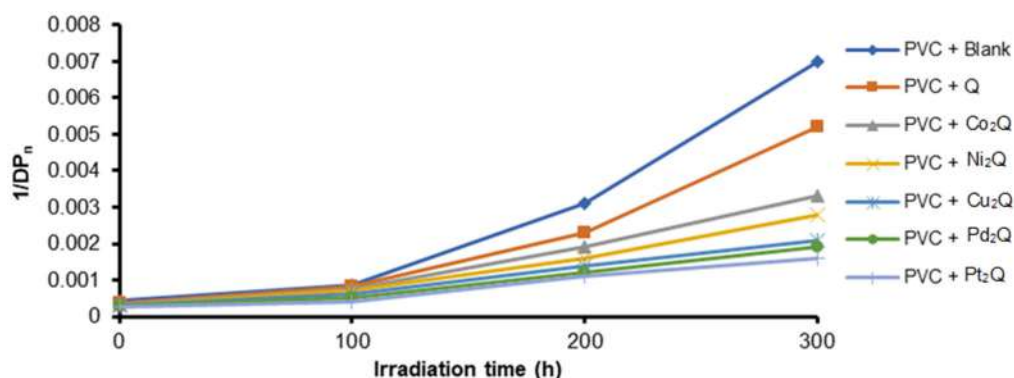


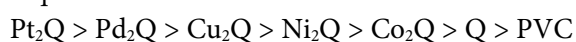
Fig 14. Variation of degree of polymerization ($1/DP_n$) for PVC films ($40 \mu\text{m}$) thickness containing 0.5% additives with the irradiation time

M_n = the molecular weight M.wt. average number

$$DP_n = X_n = \frac{M_n}{M_o} \quad (3)$$

It is calculated that the first-order-rate constant (K_d) [18] of all modified polymer films in these additive polymers are UV-light stable because photo-stabilizers [19] always have low K_d values. Photo-stabilizers, the category of additives in PVC films, have an influence on K_d values, which reduces in the order specified in Table 6.

The investigated photo-stabilizers stabilizing effectiveness was demonstrated to go in the following sequence:



Proposed Stabilization Mechanisms for PVC Additives

The 1,2,4-triazole-3-thione ring is crucial in photo-stabilization if ultra-violet (UV) light absorption results from radical scavenging and peroxide degeneration, absorption exposures cause the aromatic ring's UV energy to decrease [20] in PVC photography stability. There is a possibility that the complex of chromophores [21] will develop radical cavities due to the transmission energy amongst chelates and chromophore excitations being sustained. All this work on film stabilization use the resonance resonant suggested in Scheme 2. Polymer (C-C) bonds are degraded when exposed to UV light over an extended period. Because of the effects of photostabilization and photo degradation [22], the following procedure might lead to energy transmission in

Table 6. Photodecomposition rate constants (K_d) irradiation time for PVC films ($40 \mu\text{m}$) containing 0.5% additives

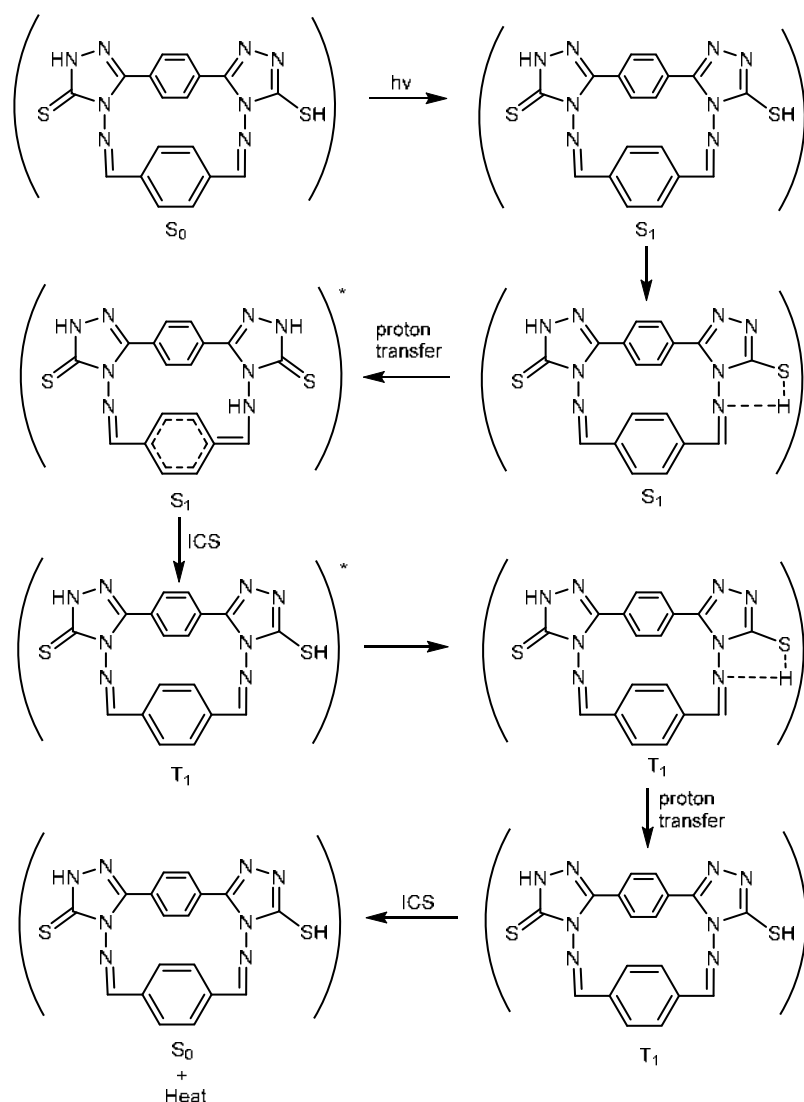
Compound	K_d (S^{-1})
PVC + Blank	6.221×10^{-3}
PVC + Q	5.361×10^{-3}
PVC + Co ₂ Q	3.319×10^{-3}
PVC + Ni ₂ Q	3.118×10^{-3}
PVC + Cu ₂ Q	2.729×10^{-3}
PVC + Pd ₂ Q	1.995×10^{-3}
PVC + Pt ₂ Q	1.257×10^{-3}

polymers that is highly ineffective. The energy is transferred between molecules of a photo-stabilizer (acceptor) [23] and a stimulating polymer molecule (donor) [24]. Intra molecular [23] energy exchange happens between the molecules of a polymer (acceptor) and another chromophore (donor).

Surface Morphology for PVC Photodegradation Evaluation

Individual polymer chains are visualized in their configuration and in some cases, single atoms can be observed. Although microscopic [25] techniques are widely used in the study of polymers and are very popular, little is known about their applications to the study of polymer degradation processes.

In UV-irradiated specimens, chain scission, branching and cross-linking [26], polyene fashioning, oxidation hydroxyl and hydroperoxide groups, and rearrangement processes are the main reactions. The



Scheme 2. The suggested mechanism of photostabilization of PVC by Q ligand through absorption of UV light and dissipation of light energy as heat

specimen surface is where oxidation reactions are primarily localized and are influenced by its morphology [27]. As a result of their sensitivity to light and the elevation activity of the intermediate free-radical [28] fashioning, photodegradation products can speed-up the further destruction of specimens. Exposure to specimens typically causes the specimens to become brittle and yellow, and the films to shrink. It was discovered that the deterioration and evolution of volatile products led to the fashioning of cracks and holes.

Microscopy visuals of PVC films exposed to 300 h of UV-lamp in the air are shown in Fig. 15 in order to begin

polymer decomposition, active free radicals can eliminate hydrogen atoms from macromolecules [29]; crack development was observed to increase with irradiation time in PVC films devoid of any additives; film embrittlement raises as photodegradation occurs in the presence of UV light; lighter cracks can be seen in PVC samples photodegraded with the additament of Cu(II) and Pt(IV) complexes. The chain scission reaction in photodegraded samples is directly linked to the formation of micro-cracks [30] on the polymer surface. It takes up more space than the original macromolecules when polymer bonds are damaged, resulting

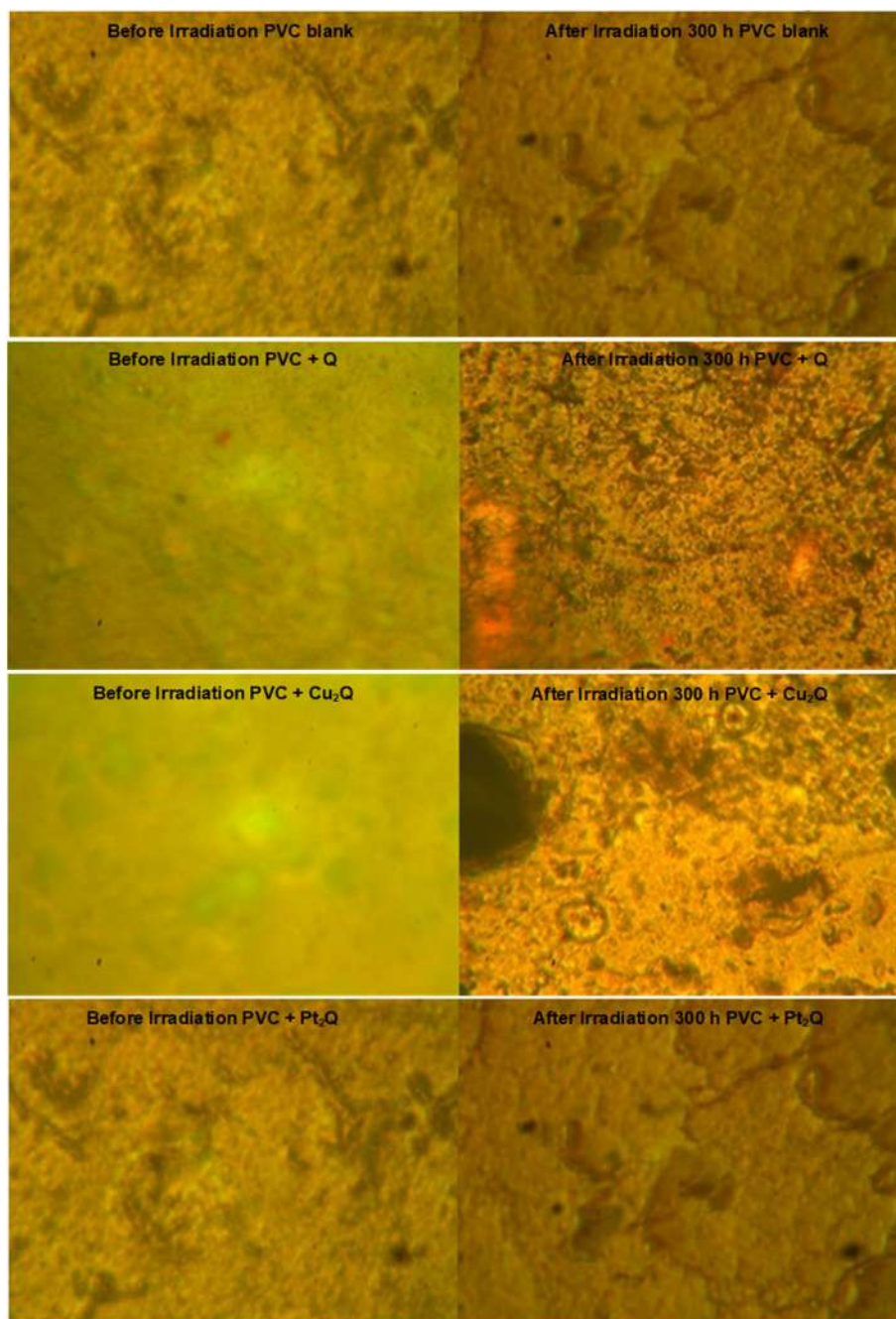


Fig 15. Surface morphologies (460× magnification) before and after 300 h of irradiation, microscopic images of PVC films (40 μm) blank and their complexes films were achieved

in more fragments. UV irradiated polymer film can be damaged by micro-cracks forming as a result of the strains and stresses [31] induced by this break-down of internal defects such as cracks or impurities that are frequently responsible for the formation of cracks; undegraded PVC film does not have a unique micro-structure; the films are smooth and without any visible structural flaws.

UV radiation of polymers often leave behind micro pores of varying shapes and sizes as the volatile [32] vapor degradation products exit; holes were shown in a photodegraded PVC film as an example, due to hydrogen abstraction and the main chain scission reaction [31] PVC's chemical structure is very simple, consisting of varying ethylene and chloride groups, due

to the voids and holes formed, the number of adsorbent surface and diffusion channels increases for the volatile, low molecular product, mainly HCl. As an outcome oxygen rapidly diffuses into the packing of the polymer, resulting in even more rapid oxidation of PVC films.

■ CONCLUSION

The Schiff bases ligand (Q) were synthesized by using a 2-amino-triazole derivative and 4-phenoxybenzaldehyde by using the procedure reported in the literature. The novel ligand (Q) evinced bi-dentate behaviour in all metal complexes namely cobalt(II), nickel(II), copper(II), palladium(II), and platinum(IV) metal ions that coordinate with thiol group and nitrogen of dimethyldiazene. The ratio between complexes and new ligand relying on 2:1 molar ratio; The identification of the ligand and their complexes utilize several spectroscopic analysis namely FTIR, ¹H-NMR, ¹³C-NMR and other techniques such as flame atomic absorption, magnetic susceptibility measurements, thermal analysis, C, H, N, and S elemental analyses and molar conductance. The outcomes revealed the the suggested complexes' structures that had an octahedral shape, except for palladium that had a tetrahedral geometry. The sequence of these complexes and ligands for photostabilization effectiveness is Pt₂Q > Pd₂Q > Cu₂Q > Ni₂Q > Co₂Q > Q > PVC blank. Fig. 10. showed that the rate of molecular weight reduction, weight loss, hydroxyl, carbonyl, and polyene groups was excellent and showed slight variation over time. The complex containing Pt-complex was more effective as a photo-stabilizer.

■ ACKNOWLEDGMENTS

We thank Baghdad and Mustansiriyah Universities for technical support.

■ AUTHOR CONTRIBUTIONS

Ali Mudher Abdulkareem Al-Khazraji conceived and designed the experiments, conducted the experiments, analyzed the data, wrote the paper, provided funds, and revised the paper. The author also discussed the findings and improved the final text of the paper.

■ REFERENCES

- [1] Numan, A.T., 2010, Synthesis and spectral studies for new Schiff base and its binuclear complexes with Zn^{II}, Cd^{II} and Hg^{II}, *Ibn Al-Haitham J. Pure Appl. Sci.*, 23 (2), 65–75.
- [2] Sellami, M., Bragazzi N.L., Slimani M., Hayes L., Jabbour G., De Giorgio A., and Dugué, B., 2019, The effect of exercise on glucoregulatory hormones: A countermeasure to human aging: Insights from a comprehensive review of the literature, *Int. J. Environ. Res. Public Health*, 16 (10), 1709.
- [3] Yang, L., Bajinka, O., Jarju, P.O., Tan, Y., Taal, A.M., and Ozdemir, G., 2021, The varying effects of antibiotics on gut microbiota, *AMB Express*, 11 (1), 116.
- [4] Maoka, T., 2020, Carotenoids as natural functional pigments, *J. Nat. Med.*, 74 (1), 1–16.
- [5] Dixit, D., Verma, P.K., and Marwaha, R.K., 2021, A review on 'triazoles': Their chemistry, synthesis and pharmacological potentials, *J. Iran. Chem. Soc.*, 18 (10), 2535–2565.
- [6] Al-Khazraji, A.M.A., and Al Hassani, R.A.M., 2020, Synthesis, characterization and spectroscopic study of new metal complexes form heterocyclic compounds for photostability study, *Syst. Rev. Pharm.*, 11 (5), 535–555.
- [7] Al-Khazraji, A.M.A., Al Hassani, R.A.M., and Ahmed, A., 2020, Studies on the photostability of polystyrene films with new metals complex of 1,2,4-triazole-3-thione derivate, *Sys Rev Pharm.*, 11 (5), 525–534.
- [8] Cordes, E.H., and Jencks, W.P., 1962, On the mechanism of Schiff base formation and hydrolysis, *J. Am. Chem. Soc.*, 84 (5), 832–837.
- [9] Endo, K., 2002, Synthesis and structure of poly(vinyl chloride), *Prog. Polym. Sci.*, 27 (10), 2021–2054.
- [10] Saad, H.A.R., Shakir, R.M., and Mahdi, M.H., 2018, Synthesis and thermal electro conductivity of some new triazole derivatives bearing azo or azomethain group, *Ibn Al-Haitham J. Pure Appl. Sci.*, 31 (3), 88–101.

- [11] Kryczyk-Poprawa, A., Kwiecień, A., and Opoka, W., 2019, Photostability of topical agents applied to the skin: A review, *Pharmaceutics*, 12 (1), 10.
- [12] Panwar, H., and Singh S., 2011, Synthesis and characterization of 3-aryl-5H,13aH-quinolino(3,2-f)(1,2,4)triazolo(4,3-b)(1,2-diaza-4-sulpho)azepines: *In vitro* antifungal and antibacterial activity, *Indones. J. Chem.*, 11 (2), 148–153.
- [13] Al-Mohammadi, N.A.H.A.H., Al-Fahdawi, A.S.M., and Al-Janabi, S.S.I., 2021, Design and characterization of new dinuclear macrocyclic dithiocarbamate complexes by the preparation of a free ligand derived from isopropylamine, *Iraqi J. Sci.*, 62 (1), 1–15.
- [14] Shekhawat, A., Singh, N., and Chundawat, N., 2022, Synthesis, characterization and biological activities of Schiff's base metal complexes derived from hydroxy trizene and aromatic aldehyde, *J. Sci. Res.*, 14 (1), 387–394.
- [15] Prakash, V., 2017, Applications of vanillin Schiff base ligands and their complexes: A review, *Int. J. Eng. Res. Sci.*, 3 (2), 36–47.
- [16] Chen, C., Chen, L., Yao, Y., Artigas, F., Huang, Q., and Zhang, W., 2019, Organotin release from polyvinyl chloride microplastics and concurrent photodegradation in water: Impacts from salinity, dissolved organic matter, and light exposure, *Environ. Sci. Technol.*, 53 (18), 10741–10752.
- [17] Cross, M.M., 1969, Polymer rheology: Influence of molecular weight and polydispersity, *J. Appl. Polym. Sci.*, 13 (4), 765–774.
- [18] Seo, H.J., Lee, J.W., Na, Y.H., and Boo, J.H., 2020, Enhancement of photocatalytic activities with nanosized polystyrene spheres patterned titanium dioxide films for water purification, *Catalysts*, 10 (8), 886.
- [19] Watheq, B., Yousif, E., Al-Mashhadani, M.H., Mohammed, A., Ahmed, D.S., Kadhom, M., and Jawad, A.H., 2020, A surface morphological study, poly(vinyl chloride) photo-stabilizers utilizing ibuprofen tin complexes against ultraviolet radiation, *Surfaces*, 3 (4), 579–593.
- [20] Ankamah, E., Sebag, J., Ng, E., and Nolan, J.M., 2019, Vitreous antioxidants, degeneration, and vitreo-retinopathy: Exploring the links, *Antioxidants*, 9 (1), 7.
- [21] Chamas, A., Moon, H., Zheng, J., Qiu, Y., Tabassum, T., Jang, J.H., Abu-Omar, M., Scott, S.L., and Suh, S., 2020, Degradation rates of plastics in the environment, *ACS Sustainable Chem. Eng.*, 8 (9), 3494–3511.
- [22] Yousif, E., Ahmed, D.S., Ahmed, A.A., Hameed, A.S., Muhamed, S.H., Yusop, R.M., Redwan, A., and Mohammed, S.A., 2019, The effect of high UV radiation exposure environment on the novel PVC polymers, *Environ. Sci. Pollut. Res.*, 26 (10), 9945–9954.
- [23] Minsker, K.S., Kolesov, S.V., Kulish E.I., Zaikov, G.E., 2019, "PVC Degradation in Blends with Other Polymers" in *Polymer Yearbook 13*, Eds. Pethrick, R.A., Zaikov, G., Tsuruta, T., and Koide, N., CRC Press, Boca Raton, Florida, 5–20.
- [24] Mohamed, N.A., and Al-Harby, N.F., 2021, Enhancement of the thermal stability of PVC filled with multiwalled carbon nanotubes using new antimicrobial itaconimido aryl 1,3,4-oxadiazoles, *Polym. Compos.*, 42 (3), 1245–1257.
- [25] Hendrickson, E., Minor, E.C., and Schreiner, K., 2018, Microplastic abundance and composition in western Lake Superior as determined via microscopy, Pyr-GC/MS, and FTIR, *Environ. Sci. Technol.*, 52 (4), 1787–1796.
- [26] Ainali, N.M., Bikiaris, D.N., and Lambropoulou, D.A., 2021, Aging effects on low-and high-density polyethylene, polypropylene and polystyrene under UV irradiation: An insight into decomposition mechanism by Py-GC/MS for microplastic analysis, *J. Anal. Appl. Pyrolysis*, 158, 105207.
- [27] Zhao, T., Cao, C., Wang, H., Shen, X., Lai, H., Zhu, Y., Chen, H., Han, L., Rehman, T., and He, F., 2021, Highly efficient all-polymer solar cells from a dithieno[3,2-f:2',3'-h] quinoxaline-based wide band gap donor, *Macromolecules*, 54 (24), 11468–11477.
- [28] Gao, Y., Zhou, D., Lyu, J., A, S., Xu, Q., Newland,

- B., Matyjaszewski, K., Tai, H., and Wang, W., 2020, Complex polymer architectures through free-radical polymerization of multivinyl monomers, *Nat. Rev. Chem.*, 4 (4), 194–212.
- [29] Jia, P., Hu, L., Shang, Q., Wang, R., Zhang, M., and Zhou, Y., 2017, Self-plasticization of PVC materials via chemical modification of mannich base of cardanol butyl ether, *ACS Sustainable Chem. Eng.*, 5 (8), 6665–6673.
- [30] Al-Salem, S.M., Behbehani, M.H., Al-Hazza'a, A., Arnold, J.C., Alston, S.M., Al-Rowaih A.A., Asiri, F., Al-Rowaih, S.F., and Karam, H., 2019, Study of the degradation profile for virgin linear low-density polyethylene (LLDPE) and polyolefin (PO) plastic waste blends, *J. Mater. Cycles Waste Manage.*, 21 (5), 1106–1122.
- [31] Vijayan, K., Muniyandi, M., and Munusamy, Y., 2021, Impact modified polyvinyl chloride based thermoplastic elastomers: effect of nitrile butadiene rubber and graphene oxide loading, *J. Eng. Sci.*, 17 (1), 51–74.
- [32] Apel, P.Y., 2019, Fabrication of functional micro- and nanoporous materials from polymers modified by swift heavy ions, *Radiat. Phys. Chem.*, 159, 25–34.

The Potential of *Clerodendrum paniculatum* Leaves Fraction as a 3-Chymotrypsin-Like (3CL) Protease Inhibitor of SARS-CoV-2

Muhammad Arba^{1*}, Arfan Arfan¹, Yamin Yamin¹, and Muhammad Sulaiman Zubair²

¹Faculty of Pharmacy, Halu Oleo University, Kendari 93232, Indonesia

²Faculty of Pharmacy, Tadulako University, Palu 94148, Indonesia

* **Corresponding author:**

email: muh.arba@uho.ac.id

Received: January 18, 2023

Accepted: March 3, 2023

DOI: 10.22146/ijc.81447

Abstract: We described the biological activity of the *Clerodendrum paniculatum* leaf fraction against the SARS-CoV-2 3-Chymotrypsin-like 3CL protease at the molecular level. This study applied LC-MS/MS to identify bioactive compounds from fractions, computational studies, and fluorescence resonance energy transfer (FRET) assays to ascertain their inhibitory activity. LC-MS/MS analysis of the three samples revealed that sample 1 contained 18 compound peaks. In samples 2 and 3, there were 23 and 25 compounds with different molecular weights, respectively. Docking's study identified that the alkaloids (komarovicine and roemerine) have lower binding energies than other metabolites and standard compounds, with values of -33.47 and -32.63 kJ/mol, respectively. Roemerine demonstrated excellent stability based on dynamic simulation results and confirmed its affinity for 3CL protease predicted by the MM-PBSA approach of -89.44 kJ/mol. The FRET method for testing 3CL protease activity revealed that sample 2 had an enzyme inhibitory activity of 94.3%, which was close to that of GC376 (98.19%). Meanwhile, samples 1 and 3 yielded satisfactory inhibition activity by 89.64% and 85.24%, respectively. The antiviral activity of *C. paniculatum* leaves was discovered for the first time by inhibiting the 3CL protease SARS-CoV-2, providing an excellent opportunity for its development as an anti-SARS-CoV-2.

Keywords: *Clerodendrum paniculatum*; COVID-19; molecular dynamics simulation; SARS-CoV-2; 3-chymotrypsin-like protease

■ INTRODUCTION

COVID-19 has been a pandemic since it first spread from the capital of Hubei Province, Wuhan, at the end of 2019 [1]. Coronavirus disease reduces the function of the human respiratory system owing to infection with SARS-CoV-2 and has spread worldwide [2]. Efforts to deal with this virus globally are being vigorously carried out [3]. However, the pathogen transmission rate is swift, and the effectiveness of therapy needs to be increased [4]. The therapeutic management of COVID-19 patients needs to be improved and limited [5]. Various clinical trials are underway, including remdesivir, lopinavir/ritonavir, favipiravir, and hydroxychloroquine combined with azithromycin as alternatives to solve this problem [6-8]. Several studies have shown ineffective results and adverse side effects associated with these drugs [9-10]. Based on

this information, new drug candidates to inhibit this coronavirus urgently need to improve treatment strategies for COVID-19 patients.

The search for SARS-CoV-2 inhibitors against critical targets such as papain-like protease, helicase, RNA-dependent RNA polymerase, uridine-specific endonuclease, and 3-Chymotrypsin-like proteases has become a focus of research due to their vital functions [11-13]. These targets are responsible for protein synthesis, viral replication, and viral infection [14-15]. The 3CL protease is a promising target. In addition to its role in viral replication, it is responsible for the conserved catalytic site cleavage mechanism in SARS-CoV-2 polyproteins 1a (pp1a) and 1ab (pp1ab) [16]. The translation of the coronavirus replication gene produces these two polyproteins. Pp1a modifies host cell factors

and aids in the preparation of cells for viral RNA synthesis, whereas pp1ab catalyzes and regulates viral RNA replication and transcription [17-18]. Viral replication can be completely inhibited by inhibiting this proteolytic process, virus replication can be completely stopped [19].

Natural products offer great opportunities in the pharmaceutical sector because they are lead compounds in various modern medicines [20]. Natural products contain unique compounds and diverse structures with pharmacological properties that contribute to drug discovery and development [21]. One of the natural products reported to be practical in traditional medicine and proven to have various biological activities is *C. paniculatum* [22]. In Indonesia, especially in the Central Buton Regency, Southeast Sulawesi Province, *C. paniculatum* is known as Kamena-mena. *C. paniculatum* has biological activity as antioxidant, anticancer, hepatoprotective, anti-inflammatory, antimicrobial, antimutagenic, antiaging, anthelmintic, hypolipidemic, and insecticidal [23-25]. There are few reports on the antiviral activity of this plant. Several families of *Clerodendrum*, such as *C. myricoides*, have antiviral activity against HIV and respiratory syncytial virus (RSV), which cause bronchitis and pneumonia [26]. In addition, based on *in silico* studies, oleanolic acid, and acetoside compounds from *C. serratum* were thought to inhibit the main proteases, NSP3 and NSP15 of SARS-CoV-2 [27]. Therefore, this study aimed to investigate the antiviral activity of the *C. paniculatum* leaf fraction through inhibition of the 3CL protease SARS-CoV-2 in an *in vitro* assay. Lastly, the mechanism at the molecular level of the identified compounds in this fraction was explained using LC-MS/MS combined with an *in silico* study to reveal its potential as an anti-COVID-19 agent.

■ EXPERIMENTAL SECTION

Materials

Fresh leaves of *C. paniculatum* were collected from the middle of the Masangka sub-district, Buton Tengah district, Southeast Sulawesi Province, Indonesia. Fresh leaves were washed with running water, stoned, and dried in the sun. The sample was covered with a black cloth to avoid direct contact with ultraviolet light during drying.

Procedure

Extraction

Dried *C. paniculatum* leaves were ground using an electric blender (SHARP®) at 240 W to obtain a fine powder. The maceration method was applied for the extraction process, in which 800 g of *C. paniculatum* leaf powder was immersed in 8 L ethanol. Maceration was carried out at room temperature for 3 × 24 h and filtered every 1 × 24 h with Whatman paper Number 1 [28]. A rotary evaporator was used to concentrate the filtrate at 40 °C to obtain a thick extract of 102 g.

Fractionation

A vacuum column chromatography method with a solvent gradient system was used for fractionation. The eluent was a mixture of *n*-hexane and ethyl acetate to obtain the polar, semipolar, and nonpolar fractions. The fractionation results were separated into three categories: samples 1, 2, and 3. Sample 1 was eluted with *n*-hexane: ethyl acetate (100:0 to 70:30 mL). Sample 2 was followed by solvent *n*-hexane: ethyl acetate at a ratio of 60:40 to 30:70 mL. Sample 3 was eluted with *n*-hexane: ethyl acetate at a ratio of 20:80 to 0:100 mL. Finally, the samples were cleaned with 100 mL ethanol.

LC-MS/MS analysis

Each *C. paniculatum* sample was injected into the column with a 1 mL aliquot at a flow rate of 0.3 mL/min. Instrument adjustments were as follows: gain time 0.00–16.00 min, initial mass 50.00–120.00 *m/z*, low collision energy, 6 eV; high energy 10–40 eV, ESI acquisition mode (+); capillary and conical voltages were set at 2 kV and 30 V. The cone and desolvation gas flow rates were 50 and 1000 L/h. The temperature was adjusted to 500 °C for desolvation, 120 °C for source, 40 °C for column, and 20 °C for sample. The resulting data were processed using UNIFI software (version 1.8, Waters Corporation, Milford, Massachusetts, MA, USA) and matched against a database of compounds based on molecular weight, molecular formula, and chemical structure.

Molecular docking stage

The crystal structure of the SARS-CoV-2 3CL protease with code 6M2N (<https://www.rcsb.org/>) was

chosen for the molecular docking stage [29]. First, the crystallized water molecules and bound ligands were removed from the receptor utilizing AutoDock Tools version 1.5.6 [30]. The protease structure was prepared by adding polar hydrogen atoms and Kollman charges. Finally, the protease was generated in the PDBQT format [31]. The 3D structures of all compounds identified in the LC/MS-MS analysis were collected from the PubChem database (<https://pubchem.ncbi.nlm.nih.gov/>). All compounds were released under restraint and assigned Gasteiger charges with the assistance of the AutoDock Tools program. The docking process utilized AutoDock Vina software [32]. The grid box area was arranged according to the position of baicalein (the reference ligand) on the protease. The grid coordinates were set at -32,981; -65,438; and 41,404 for the x, y, and z axes with an area length of 50 Å. The best compounds and their interactions with the 3CL protease from the docking results were analyzed using Discovery Studio Visualizer.

Molecular dynamic simulation

The best compounds from the docking results were subjected to molecular dynamics simulations using GROMACS 2016 software to determine their stability [33]. The AMBER99SB-ILDN and GAFF force fields for the protein and ligand, respectively, were used in the simulation [31,34]. ACPYPE was used to create parametric ligands [35]. The TIP3P water model was then applied to solve each system, with a minimum distance of 10 Å around the complex and neutralized with Na⁺ and Cl⁻ ions. Three phases were performed successively to complete the minimization step, each of which had conjugate gradients of 5,500 steps and the steepest descents of 500 steps. Every 50 ps, each complex was gradually heated to 310 K in an NVT ensemble with a time step of 0.0005 ps [36]. The system was relaxed using NPT's 500 ps equilibration steps, and production was run with a 2 fs timestep for a 100 ns simulation. The particle mesh Ewald method was used to mimic electrostatic interactions and rectify the 1.2 nm cut-off for van der Waals energy terms [37]. The stability of the complexes was verified by analyzing the root-mean-square deviation (RMSD), root-mean-square fluctuation (RMSF), radius gyration (Rg), and principal component analysis (PCA) parameters. The

complex's binding energy was calculated using the MM/PBSA method [38]. High-Performance Computing (HPC) hardware was used for the docking and dynamic simulations, with Intel (R) Core i5-8500 processor specifications @4.30 GHz (6 CPUs), 4096 MB RAM, 2 TB hard drive, 120 GB solid-state drive, and VGA Intel HD Graphics NVIDIA GeForce GTX 1080 Ti.

FRET-based in vitro assay on 3CL protease of SARS-CoV-2

The *in vitro* assay was performed following the procedure which was reported in our previous research [39]. Approximately 12 µL of dithiothreitol (0.5 M) was added to 6 mL of buffer to prepare the assay buffer. The dilution process was carried out by adding an assay buffer of 3.95 mL for the enzyme and 950 µL for the substrate. The sample was dissolved in DMSO at a concentration of 500 µM (200 µg/mL) in a 96-well microplate. The control inhibitor was GC376, a peptidomimetic made at the same concentration as the sample. Then, 12 µL of dithiothreitol with a concentration of 0.5 M was added to 6 mL of buffer to prepare the assay buffer. The dilution process was carried out by adding an assay buffer of 3.95 mL for the enzyme and 950 µL for the substrate. Ten microliters of the sample and control (GC376) were added to 30 µL of each enzyme (5 ng/µL) to produce a mixed volume of 40 µL. The mixture was then incubated at 25 °C for 30 min with gentle shaking. Finally, 10 µL of the substrate (250 µM) was added. The mixture was then incubated for 1 × 24 h and absorbance was measured at a wavelength 360/460 nm with a Synergy HTX-3 Multi-mode Reader (Winooski, Vermont, VT, USA).

RESULTS AND DISCUSSION

LC-MS/MS Analysis

LC-MS/MS succeeded in recognizing several compounds in the *C. paniculatum* fraction based on the molecular mass and similarity in retardation time in the database of UNIFI 1.8 software. In sample 1, 18 peaks were observed (Table 1). The results for samples 2 and 3 revealed 23 and 25 peaks, respectively (Table 2 and 3). Each peak indicated the presence of a compound with a specific molecular weight. The same compounds, such

as yohimbic acid and convolidine, were found in all the samples. However, compounds found in only one sample were also observed, such as 2,4-dihydroxy acetophenone

in sample 1, glycocitridine in sample 2, and 9,10,16-trihydroxy hexadecanoic acid, alpha-dihydrolysergol, and ajmaline in sample 3.

Table 1. The LC-MS/MS analysis of sample 1 of *C paniculatum*

Peak	<i>m/z</i>	Identified Compound
1	137.3090	-
2	197.4042	-
3	340.5990	Yohimbic acid/ Behenic acid
4	397.1448	-
5	453.6928	-
6	274.5595	-
7	288.5544	Testosterone
8	277.4959	Convolidine/Venlafaxine
9	279.5576	Roemerine
10	353.5950	Trichodesmine
11	313.6079	Heliotrine
12	299.6129	Komarovicine
13	429.5112	-
14	607.6002	-
15	152.3011	2,4-Dihydroxyacetophenone/2,6-Dihydroxyacetophenone/2-Mercaptopurine/6-Mercaptopurine/o-Anisic acid/Ribitol/Vanilin
16	405.7049	-

Table 2. The LC-MS/MS analysis of sample 2 of *C. paniculatum*

Peak	<i>m/z</i>	Identified Compound
1	274.5595	-
2	588.7282	-
3	340.5990	Yohimbic acid/Behenic acid
4	397.2072	-
5	274.5595	-
6	207.4622	-
7	277.4959	Convolidine/Venlafaxine
8	279.4951	Roemerine
9	291.5532	-
10	307.5475	Conviline/Foliosidine
11	293.5525	-
12	291.4908	Penbutolol
13	263.5013	Glycocitridine
14	299.5504	Komarovicine
15	293.4901	-
16	463.6904	-
17	295.5518	-
18	413.5778	Narcotine/ Solasodine
19	307.4850	Betaxolol/ Conviline
20	605.7879	-

Table 3. The LC-MS/MS analysis of sample 3 of *C. paniculatum*

Peak	m/z	Identified Compound
1	137.3090	-
2	207.3997	Salsolidine
3	197.3418	3,4-Dihydroxy-L-phenylalanine/Beclamide
5	397.2072	-
6	453.7552	-
7	281.4319	Coumarin 106/Cycloheximide
8	351.5331	Retrorsine
9	274.5595	-
10	288.5544	Testosterone
12	304.6111	9,10,16-Trihydroxyhexadecanoic acid/Tschimganin
14	322.6049	-
15	471.6886	-
16	324.6042	Glabranin/Quinine
17	569.7314	-
18	326.6036	Ajmaline/ <i>N</i> -Methylisothobainium
19	256.5665	alpha-Dihydrolysergol
20	313.5455	Heliotrine
21	639.5952	-
22	341.5987	-
23	152.3636	Ribitol
24	797.8255	-
25	131.6870	-

Molecular Docking Stage

The potential activity of the compounds analyzed by LC-MS/MS in inhibiting the 3CL protease of SARS-CoV-2 became one of our targets to accelerate the drug discovery process and predict the interaction between ligands and receptors at the molecular level. The molecular structures of baicalein, komarovicine, and roemerine are presented in Fig. 1. The docking study was applied by validating the docking process to the active site of this protease based on the RMSD parameters. The docking parameter had an RMSD of 0.723 Å (Fig. 2(a)) after the baicalein conformation from re-docking process was superimposed onto its X-ray conformation. Baicalein complexed with 3CL protease was chosen because it has drug-like characteristics that are commonly used as protease inhibitors. The docking results identified three compounds (komarovicine, roemerine, and solasodine) with lower binding energies than baicalein (-31.38 kJ/mol). These two compounds have binding energies similar to baicalein, namely coumarin-106 and

glabranin. Komarovicine has the lowest binding energy of -33.47 kJ/mol, followed by roemerine and solasodine at -32.63 and -32.21 kJ/mol, respectively.

In Baicalein, hydrogen bonds with Glu166 on the carbonyl group and Gly143 with hydroxyl groups on the

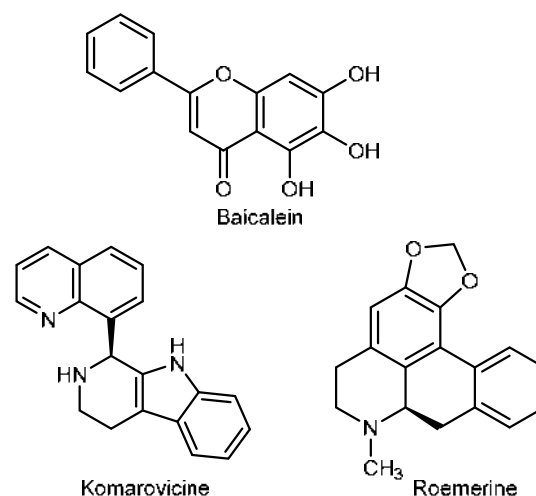


Fig 1. The molecular structures of baicalein and best-docked compounds

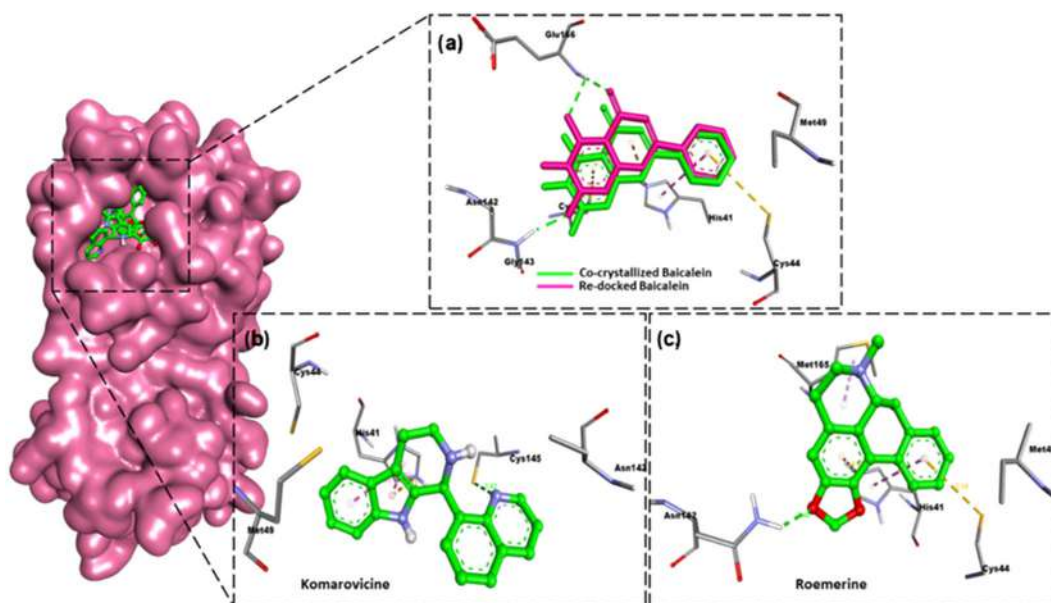


Fig 2. Molecular interactions of best compounds in the *C. paniculatum* fraction with 3CL protease of SARS-CoV-2. (a) overlay 3D conformation of co-crystallized and docked baicalein, 2D interactions of (b) komarovicine, and (c) roemerine with 3CL protease of SARS-CoV-2

chroman ring were observed. In addition, there is also a carbon-hydrogen bond with the Cys145 residue and a pi-donor hydrogen bond with the Asn142 residue. Hydrophobic interactions were formed at the His41 and Met49 residues (Fig. 2(a)). Meanwhile, komarovicine formed a hydrogen bond with Cys145 on the nitrogen atom of its quinoline ring (Fig. 2(b)). Interestingly, pi-donor hydrogen bonds with Asn142 residues and hydrophobic interactions with Cys44 and Met49 residues were observed in this compound. In roemerine, hydrogen bonds were formed at residues Glu166 with a carbon-hydrogen bond type and Asn 142, which is similar to

baicalein (Fig. 2(c)). This compound had hydrophobic interactions similar to those of other compounds but differed only in the Met165 residue.

Molecular Dynamics Simulation

The RMSD and RMSF analysis

RMSD analysis of the protease system and its ligands (baicalein, komarovicine, and roemerine) is presented in Fig. 3(a). The results show that the baicalein RMSD increased to 0.28 nm at 40–70 ns simulation time. A similar trend was also observed for roemerine at 80–90 ns, which moved higher to 0.32 nm but then decreased

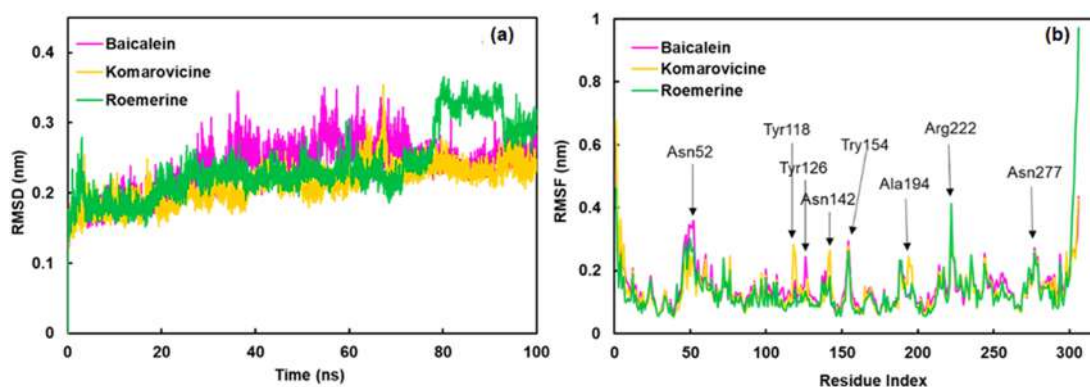


Fig 3. The plots of (a) RMSD of backbone atoms for protease complex, and (b) RMSF of backbone atoms for protease complex, during 100 ns of simulation

to 0.29 nm until the end of the simulation. Overall, komarovicin was relatively more stable than baicalein and roemerine, with a mean value of 0.237 nm.

RMSF analysis of the protease backbone region showed that all complexes had similar flexibilities (Fig. 3(b)). Several residues with high RMSF values included Asn52, Tyr118, Tyr126, Asn142, Tyr154, Ala194, Arg222, and Asn277. The Gln306 residue in the protease loop region showed very high peak fluctuations for roemerine at 0.97 nm and other compounds at 0.42 nm. Fluctuations in the Asn52 and Tyr126 residues of the baicalein complex were higher than those in the other two compounds, at 0.36 and 0.24 nm, respectively. Lastly, komarovicine showed more active fluctuations than other compounds, such as Try119, Asn142, and Ala194 residues, with 0.28, 0.26, and 0.24 nm, respectively.

Radius of gyration and principal component analysis

The compactness of the protease during the simulation was determined by measuring the Rg (Fig. 4(a)). Rg values in the low range indicated that the protease folded at a stable level. It can be seen in the graph that the protease complex with komarovicine and roemerine had similar compactness from the beginning to the end of the

simulation, with an average Rg value of ~2.225 nm. Unlike other compounds, the baicalein complex had a high Rg 2.25 nm at a simulation time of 40–100 ns.

We analyzed the overall essential dynamic patterns of the complex using PCA. Protein movement was recorded using two eigenvectors and visualized using a Cartesian plot (Fig. 4(b)). A stable complex can be identified from the smaller space occupied by the cluster during simulation. The roemerine complex occupied less space than the other complexes, but it appeared similar to the komarovicine complex. In contrast to the other complexes, baicalein demonstrated the most significant atomic movement of the protein.

Binding energy calculations

We analyzed the binding energies by applying the MM-PBSA method to compare the affinities of each complex system. The binding energies (ΔE_{BIND}) can be seen in Table 4.

The variables affecting the binding affinity of the complexes were investigated including the van der Waal energy (ΔE_{VDW}), electrostatic (ΔE_{ELE}), polar solvation (ΔE_{PB}), and solvent-accessible surface area energy (ΔE_{SASA}). Baicalein, as a standard, had a binding energy

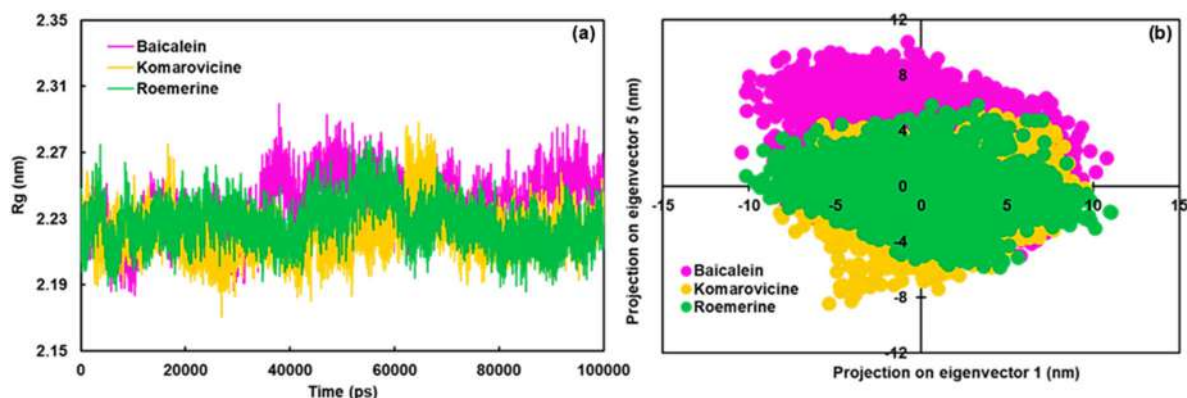


Fig 4. The plots of (a) radius of gyration of backbone atoms for protease complex, and (b) principal component analysis of the projected trajectory in 2D, during 100 ns of simulation

Table 4. Binding energy prediction by the MM-PBSA method*

Compounds	ΔE_{VDW}	ΔE_{ELE}	ΔE_{PB}	ΔE_{SASA}	ΔE_{BIND}
Baicalein	-143.66 ± 14.48	-43.60 ± 8.71	135.59 ± 14.61	-13.61 ± 0.74	-65.28 ± 15.99
Komarovicine	-71.13 ± 27.76	-12.17 ± 9.02	55.39 ± 43.62	-8.61 ± 2.78	-36.53 ± 41.93
Roemerine	-135.85 ± 16.20	-7.84 ± 6.40	67.47 ± 14.66	-13.21 ± 1.33	-89.44 ± 11.94

*All values are in kJ/mol

of -65.28 kJ/mol, which is higher than roemerine (-89.44 kJ/mol). Meanwhile, komarovicine showed higher energy than baicalein, with a value of -36.53 kJ/mol, due to the complex's lack of van der Waals interactions. These results demonstrated the ability of the *C. paniculatum* fraction to inhibit the 3CL protease of SARS-CoV-2. The analysis showed that the van der Waals energy had the most significant contribution to the binding affinity. On the other hand, the polar solvation energy is less favorable for complex systems.

In Vitro Inhibition Assay on 3CL Protease of SARS-CoV-2

Three sample fractions of *C. paniculatum* leaves (samples 1, 2, 3) were tested for their inhibitory ability against the 3CL protease enzyme from SARS-CoV-2 (Fig. 5). The measurement results for each sample were then compared with those of the positive control, GC376. This assay showed that all samples had similar inhibitory activities, but were slightly less active than GC376. This test was carried out by measuring the fluorescence intensity of the mixture (sample, substrate, and enzyme), where a lower intensity indicates the ability of the sample to inhibit 3CL protease activity. FRET is a vulnerable method for measuring molecular dissociation [40]. FRET works by transferring non-radiative energy from one excited fluorophore (donor) to a chromophore (acceptor), producing an absorption signal at a specific wavelength [41].

Interestingly, sample 2 inhibited the 3CL protease by 94.30%, which was close to the positive control's inhibition value of 98.19%. Based on these results, this enzyme could only change the substrate by 5.7% due to inhibition by sample 2. Sample 1 had 89.64%, a lower inhibitory activity than sample 2. Sample 3 had the lowest inhibitory activity (85.24%). The *C. paniculatum* leaves fraction inhibited the activity of 3CL protease and showed potential as an anti COVID-19 agent. The isolation of the active compounds and more detailed testing of this plant fraction are still auspicious for the development of COVID-19 drugs.

Several studies have reported the biological activity

of *C. paniculatum*; for example, Poriferasta-5,22E,25-trien-3 β -ol from its leaf inhibited 82% of Cucumber Mosaic Virus (CMV) activity at a concentration of 300 ppm [42]. Petroleum ether and chloroform extracts from this plant showed reduced inflammation in *in vitro* and *in vivo* assays at doses of 200 and 400 mg/kg compared to indomethacin (10 mg/kg) [43]. In addition, *C. paniculatum* root extract was highly antimutagenic in an *in vitro* assay against frameshift and base substitution mutations caused by nitrite-treated 1-aminopyrene [24]. The antiviral activity of *C. paniculatum* has not been extensively studied. However, the other families, such as *C. serratum*, which effectively inhibit yellow fever virus (EC_{50} = 15.9 mcg/mL) [44] and root extract of *C. myricoides*, can reduce the spread of human respiratory syncytial virus infection with EC_{50} = 0.21 mcg/mL [26]. Taraxero compounds from *Clerodendrum* spp. by computational studies with molecular dynamics were predicted to inhibit the main protease, RdRp, and spike protein of SARS-CoV-2 [45]. A docking study conducted by Erukainure et al. [46] revealed that the compound harpagide 5-O- β -D-glucopyranoside from *C. volubile* interacts and binds strongly at the initiation of translation and termination of mRNA sequence sites on the SARS-CoV-2 S-protein and ACE-2 receptor. To our knowledge, the *in vitro* assay of *C. paniculatum* against the SARS-CoV-2 protease in this study is the first to be reported.

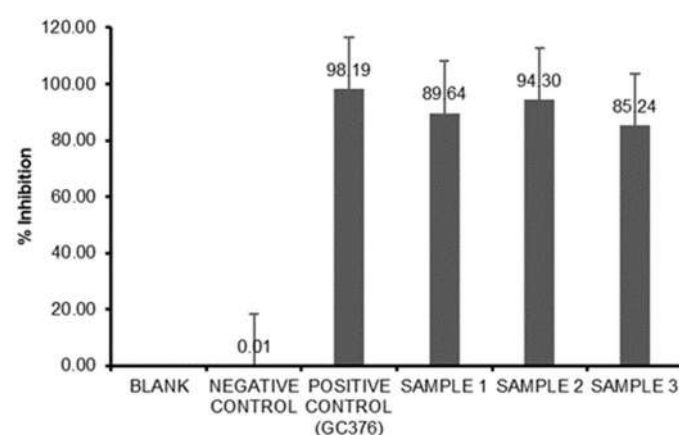


Fig 5. The percent inhibition activity of *C. paniculatum* fractions and GC376 against 3CL protease of SARS-CoV-2 by *in vitro* assay

■ CONCLUSION

LC-MS/MS and computational studies have identified potential compounds from the leaf fraction of *C. paniculatum* as 3CL protease inhibitors of SARS-CoV-2. Roemerine and komarovicine, which are alkaloid compounds from this plant, show a more optimistic binding energy prediction than baicalein. Roemerine was able to stabilize and bind strongly to proteases during simulation based on trajectory analysis of the backbone dynamics of the proteases. The *in vitro* assay successfully determined the potential of this plant fraction as a 3CL protease inhibitor of SARS-CoV-2. Sample 2 had an inhibitory activity of 94.30%, which was slightly lower than that of the positive control, GC376 (98.19%). Furthermore, samples 1 and 3 had perfect inhibitory activities of 89.64% and 85.24%, respectively.

■ ACKNOWLEDGMENTS

Muhammad Arba would like to thank the late Dr. Maywan Hariono for helping the *in vitro* assay.

■ AUTHOR CONTRIBUTIONS

Muhammad Arba conducted the experiment and wrote and revised the manuscript, Arfan conducted the MD simulation, Yamin conducted extraction and fractionation, Muhammad Sulaiman Zubair wrote and revised the manuscript. All authors agreed to the final version of this manuscript.

■ REFERENCES

- [1] Kumar, A., Singh, R., Kaur, J., Pandey, S., Sharma, V., Thakur, L., Sati, S., Mani, S., Asthana, S., Sharma, T.K., Chaudhuri, S., Bhattacharyya, S., and Kumar, N., 2021, Wuhan to world: The COVID-19 pandemic, *Front. Cell. Infect. Microbiol.*, 11, 596201.
- [2] Adil, M.T., Rahman, R., Whitelaw, D., Jain, V., Al-Taani, O., Rashid, F., Munasinghe, A., and Jambulingam, P., 2021, SARS-CoV-2 and the pandemic of COVID-19, *Postgrad. Med. J.*, 97 (1144), 110–116.
- [3] Djalante, R., Lassa, J., Setiamarga, D., Sudjatma, A., Indrawan, M., Haryanto, B., Mahfud, C., Sinapoy, M.S., Djalante, S., Rafliana, I., Gunawan, L.A., Surtiari, G.A.K., and Warsilah, H., 2020, Review and analysis of current responses to COVID-19 in Indonesia: Period of January to March 2020, *Prog. Disaster Sci.*, 6, 100091.
- [4] Aisyah, D.N., Mayadewi, C.A., Diva, H., Kozlakidis, Z., Siswanto, S., and Adisasmito, W., 2020, A spatial-temporal description of the SARSCoV-2 infections in Indonesia during the first six months of outbreak, *PLoS One*, 15 (12), e0243703.
- [5] Jensen, H.I., Ozden, S., Kristensen, G.S., Azizi, M., Smedemark, S.A., and Mogensen, C.B., 2021, Limitation of life-sustaining treatment and patient involvement in decision-making: a retrospective study of a Danish COVID-19 patient cohort, *Scand. J. Trauma, Resusc. Emerg. Med.*, 29 (1), 173.
- [6] Gottlieb, R.L., Vaca, C.E., Paredes, R., Mera, J., Webb, B.J., Perez, G., Oguchi, G., Ryan, P., Nielsen, B.U., Brown, M., Hidalgo, A., Sachdeva, Y., Mittal, S., Osiyemi, O., Skarbinski, J., Juneja, K., Hyland, R.H., Osinusi, A., Chen, S., Camus, G., Abdelghany, M., Davies, S., Behenna-Renton, N., Duff, F., Marty, F.M., Katz, M.J., Ginde, A.A., Brown, S.M., Schiffer, J.T., and Hill, J.A., 2022, Early remdesivir to prevent progression to severe Covid-19 in outpatients, *N. Engl. J. Med.*, 386 (4), 305–315.
- [7] Patel, T.K., Patel, P.B., Barvaliya, M., Saurabh, M.K., Bhalla, H.L., and Khosla, P.P., 2021, Efficacy and safety of lopinavir-ritonavir in COVID-19: A systematic review of randomized controlled trials, *J. Infect. Public Health*, 14 (6), 740–748.
- [8] Gautret, P., Lagier, J.C., Honoré, S., Hoang, V.T., Colson, P., and Raoult, D., 2021, Hydroxychloroquine and azithromycin as a treatment of COVID-19: Results of an open label non-randomized clinical trial revisited, *Int. J. Antimicrob. Agents*, 57 (1), 106243.
- [9] Salazar, E., Perez, K.K., Ashraf, M., Chen, J., Castillo, B., Christensen, P.A., Eubank, T., Bernard, D.W., Eagar, T.N., Long, S.W., Subedi, S., Olsen, R.J., Leveque, C., Schwartz, M.R., Dey, M., Chavez-East, C., Rogers, J., Shehabeldin, A., Joseph, D., Williams, G., Thomas, K., Masud, F., Talley, C., Dlouhy, K.G., Lopez, B.V., Hampton, C., Lavinder,

- J., Gollihar, J.D., Maranhao, A.C., Ippolito, G.C., Saavedra, M.O., Cantu, C.C., Yerramilli, P., Pruitt, L., and Musser, J.M., 2020, Treatment of coronavirus disease 2019 (COVID-19) patients with convalescent plasma, *Am. J. Pathol.*, 190 (8), 1680–1690.
- [10] Izcovich, A., Siemieniuk, R.A., Bartoszko, J.J., Ge, L., Zeraatkar, D., Kum, E., Qasim, A., Khamis, A.M., Rochweg, B., Agoritsas, T., Chu, D.K., McLeod, S.L., Mustafa, R.A., Vandvik, P., and Brignardello-Petersen, R., 2022, Adverse effects of remdesivir, hydroxychloroquine and lopinavir/ritonavir when used for COVID-19: Systematic review and meta-analysis of randomised trials, *BMJ Open*, 12 (3), e048502.
- [11] Mody, V., Ho, J., Wills, S., Mawri, A., Lawson, L., Ebert, M.C.C.J.C., Fortin, G.M., Rayalam, S., and Taval, S., 2021, Identification of 3-chymotrypsin like protease (3CLPro) inhibitors as potential anti-SARS-CoV-2 agents, *Commun. Biol.*, 4 (1), 93.
- [12] Osipiuk, J., Azizi, S.A., Dvorkin, S., Endres, M., Jedrzejczak, R., Jones, K.A., Kang, S., Kathayat, R.S., Kim, Y., Lisnyak, V.G., Maki, S.L., Nicolaescu, V., Taylor, C.A., Tesar, C., Zhang, Y.A., Zhou, Z., Randall, G., Michalska, K., Snyder, S.A., Dickinson, B.C., and Joachimiak, A., 2021, Structure of papain-like protease from SARS-CoV-2 and its complexes with non-covalent inhibitors, *Nat. Commun.*, 12 (1), 743.
- [13] Vlachakis, D., Papakonstantinou, E., Mitsis, T., Pierouli, K., Diakou, I., Chrousos, G., and Bacopoulou, F., 2020, Molecular mechanisms of the novel coronavirus SARS-CoV-2 and potential anti-COVID19 pharmacological targets since the outbreak of the pandemic, *Food Chem. Toxicol.*, 146, 111805.
- [14] Kanimozhi, G., Pradhapsingh, B., Singh Pawar, C., Khan, H.A., Alrokayan, S.H., and Prasad, N.R., 2021, SARS-CoV-2: Pathogenesis, molecular targets and experimental models, *Front. Pharmacol.*, 12, 638334.
- [15] Wu, C., Liu, Y., Yang, Y., Zhang, P., Zhong, W., Wang, Y., Wang, Q., Xu, Y., Li, M., Li, X., Zheng, M., Chen, L., and Li, H., 2020, Analysis of therapeutic targets for SARS-CoV-2 and discovery of potential drugs by computational methods, *Acta Pharm. Sin. B*, 10 (5), 766–788.
- [16] Gyebi, G.A., Ogunro, O.B., Adegunloye, A.P., Ogunyemi, O.M., and Afolabi, S.O., 2021, Potential inhibitors of coronavirus 3-chymotrypsin-like protease (3CL^{Pro}): An *in silico* screening of alkaloids and terpenoids from African medicinal plants, *J. Biomol. Struct. Dyn.*, 39 (9), 3396–3408.
- [17] Roe, M.K., Junod, N.A., Young, A.R., Beachboard, D.C., and Stobart, C.C., 2021, Targeting novel structural and functional features of coronavirus protease nsp5 (3CL^{Pro}, M^{Pro}) in the age of COVID-19, *J. Gen. Virol.*, 102 (3), 001558.
- [18] Malone, B., Urakova, N., Snijder, E.J., and Campbell, E.A., 2022, Structures and functions of coronavirus replication–transcription complexes and their relevance for SARS-CoV-2 drug design, *Nat. Rev. Mol. Cell Biol.*, 23 (1), 21–39.
- [19] Cannalire, R., Cerchia, C., Beccari, A.R., Di Leva, F.S., and Summa, V., 2022, Targeting SARS-CoV-2 proteases and polymerase for COVID-19 treatment: State of the art and future opportunities, *J. Med. Chem.*, 65 (4), 2716–2746.
- [20] Mathur, S., and Hoskins, C., 2017, Drug development: Lessons from nature, *Biomed. Reports*, 6 (6), 612–614.
- [21] Atanasov, A.G., Zotchev, S.B., Dirsch, V.M., Orhan, I.E., Banach, M., Rollinger, J.M., Barreca, D., Weckwerth, W., Bauer, R., Bayer, E.A., Majeed, M., Bishayee, A., Bochkov, V., Bonn, G.K., Braidy, N., Bucar, F., Cifuentes, A., D’Onofrio, G., Bodkin, M., Diederich, M., Dinkova-Kostova, A.T., Efferth, T., El Bairi, K., Arkells, N., Fan, T.P., Fiebich, B.L., Freissmuth, M., Georgiev, M.I., Gibbons, S., Godfrey, K.M., Gruber, C.W., Heer, J., Huber, L.A., Ibanez, E., Kijjoa, A., Kiss, A.K., Lu, A., Macias, F.A., Miller, M.J.S., Mocan, A., Müller, R., Nicoletti, F., Perry, G., Pittalà, V., Rastrelli, L., Ristow, M., Russo, G.L., Silva, A.S., Schuster, D., Sheridan, H., Skalicka-Woźniak, K., Skaltsounis, L., Sobarzo-Sánchez, E., Brecht, D.S., Stuppner, H., Sureda, A., Tzvetkov, N.T., Vacca, R.A., Aggarwal, B.B., Battino, M., Giampieri, F., Wink, M., Wolfender,

- J.L., Xiao, J., Yeung, A.W.K., Lizard, G., Popp, M.A., Heinrich, M., Berindan-Neagoie, I., Stadler, M., Daglia, M., Verpoorte, R., and Supuran, C.T., 2021, Natural products in drug discovery: Advances and opportunities, *Nat. Rev. Drug Discovery*, 20 (3), 200–216.
- [22] Shruthi, G., Joyappa, M.P., Chandrashekhar, S., Kollur, S.P., Prasad, M.N.N., Prasad, A., and Shivamallu, C., 2016, Bactericidal property of *Clerodendrum paniculatum* and *Saraca asoka* against multidrug resistant bacteria, restoring the faith in herbal medicine, *Int. J. Pharm. Sci. Res.*, 8 (9), 3863–3871.
- [23] Kopilakkal, R., Chanda, K., and Balamurali, M.M., 2021, Hepatoprotective and antioxidant capacity of *Clerodendrum paniculatum* flower extracts against carbon tetrachloride-induced hepatotoxicity in rats, *ACS Omega*, 6 (40), 26489–26498.
- [24] Phuneerub, P., Limpanasithikul, W., Palanuvej, C., and Ruangrunsi, N., 2015, *In vitro* anti-inflammatory, mutagenic and antimutagenic activities of ethanolic extract of *Clerodendrum paniculatum* root, *J. Adv. Pharm. Technol. Res.*, 6 (2), 48–52.
- [25] Prashith Kekuda, T.R., and Sudharshan, S.J., 2018, Ethnobotanical uses, phytochemistry and biological activities of *Clerodendrum paniculatum* L. (Lamiaceae): A comprehensive review, *J. Drug Delivery Ther.*, 8 (5), 28–34.
- [26] Umereweneza, D., Molel, J.T., Said, J., Atilaw, Y., Muhizi, T., Trybala, E., Bergström, T., Gogoll, A., and Erdélyi, M., 2021, Antiviral iridoid glycosides from *Clerodendrum myricoides*, *Fitoterapia*, 155, 105055.
- [27] Nallusamy, S., Mannu, J., Ravikumar, C., Angamuthu, K., Nathan, B., Nachimuthu, K., Ramasamy, G., Muthurajan, R., Subbarayalu, M., and Neelakandan, K., 2021, Exploring phytochemicals of traditional medicinal plants exhibiting inhibitory activity against main protease, spike glycoprotein, RNA-dependent RNA polymerase and non-structural proteins of SARS-CoV-2 through virtual screening, *Front. Pharmacol.*, 12, 667704.
- [28] Yamin, Y., Ruslin, R., Sartinah, A., Ihsan, S., Kasmawati, H., Suryani, S., Andriyani, R., Asma, A., Adjeng, A.N.T., and Arba, M., 2020, Radical scavenging assay and determination flavonoid and phenolic total of extract and fractions of Raghu bark (*Dracontomelon dao* (Blanco) Merr), *Res. J. Pharm. Technol.*, 13 (5), 2335–2339.
- [29] Su, H., Yao, S., Zhao, W., Li, M., Liu, J., Shang, W., Xie, H., Ke, C., Hu, H., Gao, M., Yu, K., Liu, H., Shen, J., Tang, W., Zhang, L., Xiao, G., Ni, L., Wang, D., Zuo, J., Jiang, H., Bai, F., Wu, Y., Ye, Y., and Xu, Y., 2020, Anti-SARS-CoV-2 activities *in vitro* of Shuanghuanglian preparations and bioactive ingredients, *Acta Pharmacol. Sin.*, 41 (9), 1167–1177.
- [30] Morris, G.M., Huey, R., Lindstrom, W., Sanner, M.F., Belew, R.K., Goodsell, D.S., and Olson, A.J., 2009, AutoDock4 and AutoDockTools4: Automated docking with selective receptor flexibility, *J. Comput. Chem.*, 30 (16), 2785–2791.
- [31] Arfan, A., Muliadi, R., Malina, R., Trinovitasari, N., and Asnawi, A., 2022, Docking and dynamics studies: Identifying the binding ability of quercetin analogs to the ADP-ribose phosphatase of SARS CoV-2, *Jurnal Kartika Kimia*, 5 (2), 145–151.
- [32] Trott, O., and Olson, A.J., 2010, AutoDock Vina: Improving the speed and accuracy of docking with a new scoring function, efficient optimization, and multithreading, *J. Comput. Chem.*, 31 (2), 455–461.
- [33] Abraham, M.J., Murtola, T., Schulz, R., Páll, S., Smith, J.C., Hess, B., and Lindahl, E., 2015, GROMACS: High performance molecular simulations through multi-level parallelism from laptops to supercomputers, *SoftwareX*, 1-2, 19–25.
- [34] Petrov, D., and Zagrovic, B., 2014, Are current atomistic force fields accurate enough to study proteins in crowded environments?, *PLoS Comput. Biol.*, 10 (5), e1003638.
- [35] Sousa da Silva, A.W., and Vranken, W.F., 2012, ACPYPE - AnteChamber PYthon Parser interfacE, *BMC Res. Notes*, 5 (1), 367.
- [36] Arba, M., Ruslin, R., Kalsum, W.U., Alroem, A., Muzakkar, M.Z., Usman, I., and Tjahjono, D.H., 2018, QSAR, molecular docking and dynamics studies of quinazoline derivatives as inhibitor of phosphatidylinositol 3-kinase, *J. Appl. Pharm. Sci.*, 8 (5), 1–9.

- [37] Wang, H., Gao, X., and Fang, J., 2016, Multiple staggered mesh Ewald: Boosting the accuracy of the smooth particle mesh Ewald method, *J. Chem. Theory Comput.*, 12 (11), 5596–5608.
- [38] Kumari, R., Kumar, R., and Lynn, A., 2014, *g-mmpbsa*—A GROMACS tool for high-throughput MM-PBSA calculations, *J. Chem. Inf. Model.*, 54 (7), 1951–1962.
- [39] Zubair, M.S., Maulana, S., Widodo, A., Pitopang, R., Arba, M., and Hariono, M., 2021, GC-MS, LC-MS/MS, docking and molecular dynamics approaches to identify potential SARS-CoV-2 3-chymotrypsin-like protease inhibitors from *Zingiber officinale* Roscoe, *Molecules*, 26 (17), 5230.
- [40] Liu, L., He, F., Yu, Y., and Wang, Y., 2020, Application of FRET biosensors in mechanobiology and mechanopharmacological screening, *Front. Bioeng. Biotechnol.*, 8, 595497.
- [41] Cihlova, B., Huskova, A., Böserle, J., Nencka, R., Boura, E., and Silhan, J., 2021, High-throughput fluorescent assay for inhibitor screening of proteases from RNA viruses, *Molecules*, 26 (13), 3792.
- [42] Musa, W., Hersanti, H., Zainuddin, A., and Tjokronegoro, R., 2009, The poriferasta compound-5,22e,25-trien-3-O β from *Clerodendrum paniculatum* leaf as inducer agent of systemic resistance on red chilli plant *Capsicum annuum* L from Cucumber Mosaic Virus (CMV), *Indones. J. Chem.*, 9 (3), 479–486.
- [43] Joseph, J., Bindhu, A.R., and Aleykutty, N.A., 2013, *In vitro* and *in vivo* antiinflammatory activity of *Clerodendrum paniculatum* Linn. leaves, *Indian J. Pharm. Sci.*, 75 (3), 376–379.
- [44] Joshi, B., Panda, S.K., Jouneghani, R.S., Liu, M., Parajuli, N., Leyssen, P., Neyts, J., and Luyten, W., 2020, Antibacterial, antifungal, antiviral, and anthelmintic activities of medicinal plants of Nepal selected based on ethnobotanical evidence, *Evidence-Based Complementary Altern. Med.*, 2020, 1043471.
- [45] Kar, P., Sharma, N.R., Singh, B., Sen, A., and Roy, A., 2021, Natural compounds from *Clerodendrum* spp. as possible therapeutic candidates against SARS-CoV-2: An *in silico* investigation, *J. Biomol. Struct. Dyn.*, 39 (13), 4774–4785.
- [46] Erukainure, O.L., Atolani, O., Muhammad, A., Katsayal, S.B., Ebhuoma, O.O., Ibeji, C.U., and MESAİK, M.A., 2022, Targeting the initiation and termination codons of SARS-CoV-2 spike protein as possible therapy against COVID-19: The role of novel harpagide 5-O- β -D-glucopyranoside from *Clerodendrum volubile* P Beauv. (Labiatae), *J. Biomol. Struct. Dyn.*, 40 (6), 2475–2488.

The Compounds of Tuna-Shredded (*Thunnus* sp.) Fortified Banana Blossom Extracts' Antioxidant Activity and Xanthine Oxidase Enzyme Inhibition Capacity: An *In Vitro-In Silico* Study

Heder Djamaludin^{1*}, Hardoko Hardoko¹, Muhammad Dailami², Vivi Nurhadianty³,
Mohammad Sholeh Uluwwi¹, Novaldo Yuri Muhammad¹, and Brighton Jorgi Tristany¹

¹Fish Product Technology Study Program, Faculty of Fisheries and Marine Science, Brawijaya University, Veteran Street, Malang 65145, Indonesia

²Aquaculture Study Program, Faculty of Fisheries and Marine Science, Brawijaya University, Veteran Street, Malang 65145, Indonesia

³Department of Chemical Engineering, Faculty of Engineering, Brawijaya University, M.T. Haryono 167 Street, Malang 65145, Indonesia

* **Corresponding author:**

email: hederdjamaludin@ub.ac.id

Received: January 18, 2023

Accepted: March 2, 2023

DOI: 10.22146/ijc.81448

Abstract: Tuna is one of the fish source of nutrition for humans because it contains high-quality protein and omega-3 fatty acids, which are beneficial for health. Tuna can be processed into various products, such as tuna-shredded. But it still has a drawback, i.e., the lower-fiber content. To enrich the fiber of tuna-shredded, fortification with banana blossoms can be developed as functional food such as preventing gout arthritis. The aims of this study were to develop a diversified product of tuna-shredded fortified banana blossoms and to determine the antioxidant activity in vitro and anti-arthritis gout through inhibition of the xanthine oxidase (XO) enzyme in silico. The method used was a simple, completely randomized design. The formulation of tuna-shredded used fortification and active compounds analyzed by LC-HRMS. The antioxidant activity was analyzed by the DPPH. Inhibition of the XO enzyme was analyzed by molecular docking in silico. The results showed that tuna-shredded extract contained 32 compounds, which had total phenolic was 0.00134 mg GAE/g, total flavonoid was 0.0006670 mg QE/g, and IC_{50} was 4.38 ppm. Ferulic acid had the potential to inhibit the XO enzyme with binding affinity was -9.70 kcal/mol through hydrogen bonds and hydrophobic interactions.

Keywords: anti-arthritis gout; antioxidant; in silico; in vitro; tuna-shredded

■ INTRODUCTION

Gout is a degenerative disease with a prevalence that increases with age. Gout is caused by the absence of uric acid in the joints, causing inflammation (causing pain). The presence and formation of monosodium urate (MSU) crystals in the joints cause severe pain. Hyperuricemia can be caused by impaired renal excretion or excess production of uric acid due to excessive production of foods high in purine content [1]. Patients with gout are at risk for chronic disease, cardiovascular disease, metabolic disorders, and psychosis [2].

During purine metabolism, hypoxanthine and xanthine are produced and then metabolized in the liver to uric acid. The reaction is catalyzed by the xanthine oxidase (XO) enzyme [3]. Humans lack uricase, an enzyme that degrades uric acid to soluble allantoin; therefore, uric acid is not degraded, leading to the accumulation of insoluble uric acid crystals in joints, bones, and many other organs such as the kidneys [4]. According to Kostalova et al. [3], XO is a key enzyme in the pathogenesis of arthritis gout, and its inhibition is very important in the management of this pathological condition.

Nonsteroidal anti-inflammatory drugs (NSAIDs), as well as systemic and intra-articular corticosteroids, are used to treat acute gout. In patients with gout who could not tolerate NSAIDs or systemic corticosteroids, oral colchicine is generally the treatment of choice. However, these various treatments have side effects, such as the occurrence of gastrointestinal and liver toxicity. Various risks of degenerative diseases require increased knowledge for each individual so that they can recognize early and be aware of the health problems they are experiencing, especially the diet and nutritional content of the food consumed [5].

Tuna (*Thunnus* sp.) meat contains a high nutritional value, i.e., protein and fat of 28.34% and 0.51%, respectively [6]. Tuna also contains omega-3 fatty acids such as eicosapentaenoic acid and docosahexaenoic acid [7], minerals and vitamins such as calcium, phosphorus, iron, sodium, vitamin A (retinol), and vitamin B (thiamin, riboflavin, and niacin) [8]. For the availability of food made from tuna, it can be processed into various processed products, one of which is tuna-shredded. Tuna-shredded is tuna meat that is chopped and dried with the addition of certain spices. This type of fish processing is one of the businesses of processing fish products. When compared with other traditional forms of processing, tuna-shredded has a relatively long shelf-life, which is still acceptable in storage for 50 d at room temperature [9]. As a processed fish product, tuna-shredded can be used as a side dish for consumers with degenerative disease conditions, including arthritis and gout. Polyunsaturated fatty acids and omega-3 contained in tuna meat can reduce the risk of arthritis gout. However, shredded fish still has a drawback, i.e., low fiber content. Where fiber can help fill the stomach and prevent obesity, obesity is one of the triggers for arthritis gout and other joint diseases [10].

Currently, dietary fiber is being studied comprehensively to understand its role in the prevention of degenerative diseases, such as arthritis gout, heart disease, obesity, diabetes, cancer, and others. The consumption of fiber-rich foods is rich in antioxidants and other nutrients that protect against cell damage and reduce inflammation throughout the body, including

joints [11]. Dietary fiber addition by fortification has several usages both from technological and nutraceutical perspectives. Dietary fiber is a necessary component of the human diet [12]. Fortification, especially dietary fiber fortification, may increase the proximate as well as the nutritional content of food products [13-14]. One of the ingredients that can be used as a source of fiber is banana (*Musa paradisiaca*) blossoms. The banana blossoms have great nutritional value and health benefits. Many *in vitro* studies have used parts of the banana plant, including banana blossoms, as other drugs in surgical dressings, pain relief, food and medicine, nanotechnology, induction of apoptosis, and cell cycles. The banana blossoms are also a good source of calories because it is rich in fiber and a good source of vitamin C [15]. Thus, the aims of this study were to develop a diversified product of tuna (*Thunnus* sp.) shredded fortified banana blossoms as a functional food and to determine the antioxidant activity *in vitro* and also anti-arthritis gout through inhibition of XO enzyme through molecular docking *in silico*.

■ EXPERIMENTAL SECTION

Materials

The raw materials used for producing tuna-shredded fortified with banana blossom, such as tuna (*Thunnus* sp.), banana blossom, and spices. The tuna used was obtained from the Probolinggo Regency, East Java Province and had the characteristics of clear eyes, bright red gills, a little slimy, the texture of the flesh is dense and elastic when touched with a finger, and measuring less than 50 cm long and about 2 kg. The banana blossom used is the type of kepok banana obtained from Bunul Market and Muharto Market, Malang City, East Java Province. The seasonings used include garlic, shallots, coriander powder, sugar, table salt, turmeric, galangal, bay leaf, lemongrass, lime leaves, coconut milk, and cooking oil. The materials for parameter testing include quercetin (Sigma-Aldrich), gallic acid (Sigma-Aldrich), Folin-Ciocalteu (Sigma-Aldrich), sodium carbonate (Sigma-Aldrich), sodium nitrite (Sigma-Aldrich), aluminum chloride (Sigma-Aldrich), acetic acid (Sigma-Aldrich), chloroform

(Sigma-Aldrich), potassium Iodide (Sigma-Aldrich), aquades, sodium thiosulfate (Sigma-Aldrich), tapioca flour (Cap Swan), filter paper Whatman No. 1 (Sigma-Aldrich), tissue, label paper, aluminum foil (Klin Pak 8 m × 30 cm) and plastic wrap (Cling Wrap 30 m × 30 cm). Materials for *in silico* analysis were XO P80457 (XDH_BOVIN, code: 1FIQ) and its resolution 2.5 Å obtained from Protein Data Bank <https://www.rcsb.org/>, allopurinol (ligand control) and active compounds of tuna-shredded fortified banana blossoms extract obtained from PubChem <https://pubchem.ncbi.nlm.nih.gov/>.

Instrumentation

The instrumentation used for LC-HRMS analysis consists of LC Alliance brand LC equipment 2996 (waters) with photodiode-array detector (PDA) 2996 (Waters) and MS type XEVOG2QTOF (Waters) equipment. LC-HRMS analysis using HPLC Thermo Scientific Dionex Ultimate 3000 RSLCnano with microflow meter. UV-Visible Spectrophotometer (Shimadzu UV-1601PC, Japan). The instrumentation used for *in silico* process is Acer TravelMate P633-M Laptop, Intel(R) Core™ i5-3230M CPU@2.60 GHz (4 CPUs), 4096 MB RAM Memory, Open Babel GUI, PyMOL, Discovery Studio Visualizer, and PyRx software.

Procedure

The process of making tuna-shredded fortified banana blossom

The process of making tuna-shredded refers to the method of Hardoko et al. [16]. Making tuna-shredded consists of 3 steps, i.e., making crushed banana blossom, preparing fish meat, and making seasonings. The banana blossom mash is made by washing and cleaning the banana blossom, removing the outer skin to leave a yellowish white inside, steaming for 15 min, and then blending it. The crushed banana blossom is squeezed using a filter cloth to reduce the water content so that the crushed banana blossom juice is ready to be used as an additional ingredient in the manufacture of shredded tuna. While the process of making banana blossom mash, tuna fish are weeded by removing the contents of the stomach, fins, head, and gills, and washed with running

water. Clean tuna is steamed for 30 min, cooled, and separated from the meat. The tuna meat is then shredded using a grater. While the shredding process is carried out, the seasoning is also prepared by weighing the required spices according to the tuna-shredded formulation (Table 1), mixing and mashing the spices with a blender so that a smooth seasoning is obtained. The spices are then mixed with coconut milk, grated fish meat, and crushed banana heart, then boiled until boiling or cooked. Furthermore, the stew of the shredded ingredients is filtered with a filter cloth and squeezed to obtain the residue of the shredded material. The remaining shredded juice is fried for about 5 min or until light brown. Abon, which has been light brown in color, is removed, and the oil is drained using a spinner in order to obtain a dry floss that is ready to be packaged and analyzed for its compounds.

Extraction of tuna-shredded and active compound analysis

The extraction process for tuna-shredded is carried out using the stratified maceration method. The maceration process begins with weighing the shredded 50 g and adding *n*-hexane solvent in a ratio of 1:5, and macerating at room temperature for 24 h. The maceration results were filtered with filter paper, and the residue was macerated at room temperature for 24 h with ethyl acetate solvent in a ratio of 1:5. The result of

Table 1. Formulation of tuna-shredded fortified banana blossom

Ingredients	Number
Tuna (g)	250
Banana Blossom (g)	175
Garlic (g)	11
Onion (g)	21
Coriander powder (g)	4
Sugar (g)	21
Salt (g)	16
Turmeric (g)	10
Galangal (g)	25
Bay leaves (g)	3
Lemongrass (g)	19
Lime leaves (g)	3
Coconut milk (mL)	25

maceration with ethyl acetate was filtered and the residue was macerated at room temperature for 24 h with ethanol solvent in a ratio of 1:5. Furthermore, the results of maceration with methanol were filtered through Whatman filter paper No.1 and the filtrate was taken to be evaporated at a temperature of 50 °C at a speed of 100 rpm until the solvent evaporated completely and a methanol extract of tuna-shredded was obtained for compound analysis using LC-HRMS. The mobile phase used was A: Water + 0.1% formic acid, B: acetonitrile + 0.1% formic acid. The column used is Hypersil GOLD aQ 50 × 1 mm × 1.9 particle size with flow rate 40 L/min. The mass spectrometry used was Thermo Scientific Q Exactive with a full scan at a resolution of 70,000, an analysis time of 30 min with positive and negative ion modes.

Analysis of total phenolic content

Total phenolic contents (TP) of the tuna-shredded fortified banana blossoms extract were determined using Folin-Ciocalteu (FC) assay. A 40 µL of properly diluted tuna-shredded fortified banana blossoms extract solution was mixed with 1.8 mL of FC reagent. The reagent was pre-diluted 10 times with distilled water. After standing for 5 min at room temperature, 1.2 mL of (7.5% w/v) sodium carbonate solutions were added. The solutions were mixed and incubated for 1 h at room temperature. Then, the absorbance was measured at 765 nm using a UV-Vis. A calibration curve was prepared using a standard solution of gallic acid (20, 40, 60, 80 and 100 mg/L, $R^2 = 0.997$). The total phenolic content was indicated as mg gallic acid equivalent per 1 g of extract weight (mg GAE/g) [17].

Analysis of total flavonoid content

The total flavonoid content (TF) of the tuna-shredded fortified banana blossoms was determined according to the colorimetric assay. A 1 mL of properly diluted tuna-shredded fortified banana blossoms extract was mixed with 4 mL of distilled water. At zero-time, 0.3 mL of (5% w/v) NaNO₂ was added. After 5 min, 0.3 mL of (10% w/v) AlCl₃ was added. At 6 min, 2 mL of 1 M solution of sodium hydroxide was added. After that, the volume was made up to 10 mL immediately by the addition of 2.4 mL of distilled water. The mixture was

shaken vigorously, and the absorbance of the mixture was read at 510 nm. A calibration curve was prepared using a standard solution of quercetin (20, 40, 60, 80, and 100 mg/L, $R^2 = 0.996$). The total flavonoid content was as mg equivalent of quercetin per 1 g of extract weight (mg QE/g) [17].

Analysis of antioxidant activity

The antioxidant activity of the tuna-shredded fortified banana blossoms extract was also studied through the evaluation of the free radical-scavenging effect on the 1,1-diphenyl-2-picrylhydrazyl (DPPH) radical. An aliquot (10 µL) of tuna-shredded fortified banana blossoms extract was mixed with 90 µL of distilled water and 3.9 mL of 25 mM DPPH methanolic solution. The mixture was thoroughly vortex-mixed and kept in the dark for 30 min. The absorbance was measured later, at 515 nm, against a blank of methanol without DPPH. Results were expressed as a percentage of inhibition of the DPPH radical. The percentage of inhibition of the DPPH radical was calculated according to the Eq. (1):

$$\% \text{ Inhibition of DPPH} = \frac{\text{Abs}_{\text{control}} - \text{Abs}_{\text{sample}}}{\text{Abs}_{\text{control}}} \times 100 \quad (1)$$

Abs_{control} is the absorbance of DPPH solution without extracts [18].

Analysis of pharmacokinetic (drug-likeness)

The drug-likeness analysis of the test compound/ligand is aimed at finding out whether the test compound/ligand complies with Lipinski's rule. The analysis was carried out online through the page <http://www.scfbio-iitd.res.in/software/drugdesign/lipinski.jsp> [19-21]. This stage is carried out before molecular docking *in silico* analysis.

Molecular docking

Molecular docking of the active compound obtained from the LC-MS results of tuna-shredded fortified banana blossoms with XO P80457 (XDH_BOVIN, code: 1FIQ) and its resolution 2.5 Å as a receptor using PyRx software. The XO enzyme as a receptor was obtained from <https://www.rcsb.org>. The test ligands used were obtained from the active compound content of tuna-shredded fortified banana

blossom and control ligands in the form of allopurinol. The 3D structure of the ligand was obtained from PubChem <https://pubchem.ncbi.nlm.nih.gov> in sdf format. Then, it is converted into pdb format using the Discovery Studio software. Receptor preparation was carried out by separating the C chain structure from the intact structure, then saving it in *.pdbqt format. After being stored, the water molecule was removed, and the natural ligand was separated from the enzyme chain C structure. The file was then saved in *.pdbqt format. The molecular docking process is carried out in the PyRx software, and the type of docking is blinded docking. After docking is complete, the results of several docking modes along with the value of binding affinity (kcal/mol), are obtained. Next, visualize the docking results in 2D and 3D using Discovery Studio software.

Analysis of toxicity and bioavailability

The test ligands with the best binding affinity were tested for toxicity predictions one by one using an online

toxicity test program accessed http://tox.charite.de/protox_II/ [22]. Ligands that showed non-toxic results were tested for bioavailability (ADME) using a program that can be accessed at <http://www.swissadme.ch/> [23].

Analysis of statistical

Data were analyzed using SPSS software. Analysis of variance (ANOVA) and Duncan's multiple range method were used to compare any significant differences. The difference was considered significant at a p -value < 0.05.

RESULTS AND DISCUSSION

The results of compound analysis using LC-HRMS from ethanol extract of tuna-shredded fortified with banana blossom identified 32 compounds divided into groups of phytochemical compounds (steroids, alkaloids, flavonoids, terpenoids, and phenolics), organic compounds, fatty acids, and amino acids. The detail of the compounds identified can be seen in Table 2.

Table 2. Identified compounds in tuna-shredded fortified banana blossom extracts

No.	Retention time (min.)	Molecule weight (g/mol)	Formula	Compound	Compound Group
1	2.409	436.22734	C ₂₄ H ₃₃ FO ₆	Flurandrenolide	Steroids
2	2.415	143.09410	C ₇ H ₁₃ NO ₂	DL-Stachydrine	Alkaloids
3	8.702	464.09450	C ₂₁ H ₂₀ O ₁₂	Quercetin-3β-D-glucoside	Flavonoids
4	13.51	286.08324	C ₁₆ H ₁₄ O ₅	Sakuranetin	Flavonoids
5	14.692	368.12517	C ₂₁ H ₂₀ O ₆	Curcumin	Flavonoids
6	17.016	218.16640	C ₁₅ H ₂₂ O	Nootkatone	Sesquiterpenoid
7	17.372	216.15096	C ₁₅ H ₂₀ O	(+)-ar-Turmerone	Sesquiterpenoid
8	20.483	120.05732	C ₈ H ₈ O	Acetophenone	Organic compound
9	7614	194.05744	C ₁₀ H ₁₀ O ₄	Ferulic acid	Phenolic
10	6.949	132.05712	C ₉ H ₈ O	trans-Cinnamaldehyde	Organic compound
11	2.422	145.10976	C ₇ H ₁₅ NO ₂	Acetylcholine	Organic compound
12	2.826	109.06384	C ₅ H ₇ N ₃	2-Amino-4-methyl pyrimidine	Organic compound
13	3.391	129.07855	C ₆ H ₁₁ NO ₂	L-Pipecolic acid	Organic compound
14	3.554	136.03800	C ₅ H ₄ N ₄ O	Hypoxanthine	Organic compound
15	3.559	109.05264	C ₆ H ₇ NO	4-Aminophenol	Phenolic
16	3.561	267.09593	C ₁₀ H ₁₃ N ₅ O ₄	Adenosine	Organic compound
17	8.54	195.19820	C ₁₃ H ₂₅ N	N-Cyclohexyl-N-methylcyclohexanamine	Organic compound
18	22.612	390.27559	C ₂₄ H ₃₈ O ₄	Bis(2-ethylhexyl)-phthalate	Organic compound
19	11.019	255.16155	C ₁₇ H ₂₁ NO	Diphenhydramine	Antihistamine
20	15.057	250.15611	C ₁₅ H ₂₂ O ₃	3,5-di-tert-Butyl-4-hydroxybenzoic acid	Phenolic
21	2.44	228.14672	C ₁₁ H ₂₀ N ₂ O ₃	Prolylleucine	Amino acid
22	2.248	203.11516	C ₉ H ₁₇ NO ₄	Acetyl-L-carnitine	Amino acid

23	2.743	117.07870	C ₅ H ₁₁ NO ₂	Valine	Amino acid
24	2.787	113.05866	C ₄ H ₇ N ₃ O	Creatinine	Amino acid
25	2.835	155.06894	C ₆ H ₉ N ₃ O ₂	L-Histidine	Amino acid
26	2.898	174.11104	C ₆ H ₁₄ N ₄ O ₂	DL-Arginine	Amino acid
27	3.56	204.08933	C ₁₁ H ₁₂ N ₂ O ₂	DL-Tryptophan	Amino acid
28	8.469	197.11992	C ₁₄ H ₁₅ N	Dibenzylamine	Aromatic amine
29	21.613	281.27083	C ₁₈ H ₃₅ NO	Oleamide	Fatty acid
30	21.826	255.25545	C ₁₆ H ₃₃ NO	Hexadecanamide	Fatty acid
31	22.386	283.28658	C ₁₈ H ₃₇ NO	Stearamide	Fatty acid
32	25.762	337.33315	C ₂₂ H ₄₃ NO	Erucamide	Fatty acid

Total Phenolic Content

Determination of the total phenolic content of extract tuna-shredded was performed using FC assay and analyzed by UV-Vis spectrophotometer at 765 nm. Phenolic contents react with the FC reagent and form complex blue compounds. The standard solution used was gallic acid, a phenolic compound derived from hydroxybenzoic acid. The total phenolic contents of tuna shredded extract are shown in Table 3.

The total phenolic content of tuna-shredded fortified banana blossoms extract was 0.00286 mg GAE/g. Each g of the extract was equivalent to 0.00286 mg of gallic acid—the presence of spices used in the processing of tuna-shredded act as a source of phenolic compounds. Sukisman et al. [24] reported that the total phenolic content in the spices for making shredded meat was 82.49 ± 0.19 mg GAE/g. Phenolic compounds contained in plants act as provide antioxidant activity to chelate redox-active metal ions and lipid-free radical chains and block the conversion of hydroperoxides to reactive oxyradicals [25]. The presence of total phenolic

contributes to antioxidant activity. As their free radical scavenging ability is induced by the hydroxyl (OH) group, thus the total phenolic content could be used as a basis for rapid screening of antioxidant activity.

Total Flavonoid Content

The tuna-shredded extract's total flavonoid content was analyzed by the complex formation between AlCl₃ with the keto group on the C-4 atom and the hydroxy group on the C-3 or C-5 atom from the flavone and flavanol groups. Quercetin was used as a standard for analyzing flavonoids' content since quercetin was a flavanol group with a keto group on the C-4 atom and the OH group on the C-3 and C-5 atoms. The results of total phenolic contents are shown in Table 4.

The total flavonoid content of tuna-shredded extract as mg equivalent per g of dry tuna-shredded was 0.0006670 mg QE/g (Table 4). This results in sync with the total phenolic content obtained. Another research has shown that phenolic content also contains amounts of flavonoid content [25]. Herbs, as spices ingredients in this research, were a major source of minerals, vitamins,

Table 3. Total phenolic content of extracts banana blossoms and tuna-shredded fortified banana blossoms extracts

No.	Sample	Total phenolic content (mg GAE/g)
1	Extract Banana Blossoms	0.00286
2	Extract Tuna-Shredded Fortified Banana Blossoms	0.00134

Table 4. Total flavonoid content of extracts banana blossoms and tuna-shredded fortified banana blossoms extracts

No.	Sample	Total flavonoid content (mg QE/g)
1	Extract Banana Blossoms	0.0006672
2	Extract Tuna-Shredded Fortified Banana Blossoms	0.0006670

and other essential nutrients. Most medicinal plants, including herbs, contain phenolic acids, flavonoids, and other phytochemicals. Flavonoids such as flavone, flavanol and condensed tannins are plant secondary metabolite compounds, the antioxidant activity of which depends on the presence of free OH group, especially 3-OH [26].

Antioxidant Activity

The antioxidant compound in a food product can inhibit or prevent the oxidation of lipids. Compounds that can be easily oxidized will cause food damage, causing rancidity. One of the parameters that can describe the percentage of a food ingredient's ability to inhibit free radical is by determining the antioxidant activity. The antioxidant activity of tuna-shredded fortified banana blossoms was carried out using the DPPH method. Determination of antioxidant activity using the DPPH method shows the ability of antioxidant substances to neutralize free radicals *in vitro*.

The antioxidant activity of tuna-shredded fortified banana blossoms extract shown in Table 5. The antioxidant activity of tuna-shredded fortified banana blossoms extract was 4.38 ppm, while the banana blossoms extract 3.06 ppm, and also ascorbic acid as standard was 0.61 ppm. Based on the results of the IC₅₀ value showed the ability of the tuna-shredded extract to have a very strong antioxidant category. Compounds that have biological activity as antioxidants also have the potential for other biological activities [27]. The difference in antioxidant activity in the three samples is thought to be caused by a decrease in the antioxidant compound content in shredded. The decreasing antioxidant activity after processing tuna-shredded fortified banana blossoms is caused by a deep-fried or heating process. During the processing process, the

ingredients for making tuna-shredded go through two heating processes. The first heating is the process of boiling the banana blossoms-tuna meat, and the second heating is the process of frying the tuna-shredded dough using hot oil until cooked.

Cooking tuna-shredded using hot oil is done using the deep-frying method [13]. During the heating process, the antioxidant compounds in the banana blossoms and herbs as spices, i.e., phenol and flavonoid compounds, will be destroyed. Research shows that the antioxidant activity of raw vegetables decreases when the vegetables are sautéed [28].

Pharmacokinetic Drug-Likeness Lipinski's Rule

Before docking the ligand to the receptor/enzyme XO, each ligand of the active compound of tuna-shredded fortified banana blossom was analyzed according to Lipinski's rule. The Lipinski rule states that a ligand can be continued for the docking process if (1) the mass is less than 500 g/mol, (2) the Log P value is less than 5, (3) the number of hydrogen bond donors is less than 5, and (4) hydrogen bond acceptor is less than 10 [19]. The suitability of the test ligand characteristics with the parameters of Lipinski's rule is a requirement that must be met before molecular docking is carried out. Lipinski's rule can be used in the physicochemical properties of a ligand that can cross cell membranes in the body. The results of the analysis of the suitability of the test ligand characteristics with Lipinski's rule parameters are presented in Table 6.

Ligands with a molecular weight of less than 500 Da more easily penetrate cell membranes than ligands with a molecular weight is more than 500 Da. The log P value is related to the polarity of the ligand in fat, oil, and non-polar solvents. Ligands with a log P value is more than 5 will interact more quickly through

Table 5. Antioxidant activity of extracts banana blossoms and tuna-shredded fortified banana blossoms extracts

No.	Sample	Antioxidant activity (IC ₅₀) (ppm)
1	Extract Banana Blossoms	3.06
2	Extract Tuna-Shredded Fortified Banana Blossoms	4.38
3	Ascorbic Acid (Vitamin C)	0.61

Table 6. Ligand parameters to comply with Lipinski's rules

No.	Ligand	Mass (g/mol)	Log P	H Bond Donor	H Bond Acceptor
1	Flurandrenolide	436.000000	2.498700	2	6
2	DL-Stachydrine	143.000000	1.024900	0	2
3	Quercetin-3 β -D-glucoside	463.000000	1.143710	4	8
4	Sakuranetin	274.000000	0.318340	2	5
5	Curcumin	350.000000	0.439250	2	6
6	Nootkatone	218.000000	3.904199	0	1
7	(+)-ar-Turmerone	196.000000	0.682600	0	1
8	Acetophenone	120.000000	1.889200	0	1
9	Ferulic acid	194.000000	1.498600	2	4
10	trans-Cinnamaldehyde	132.000000	1.898700	0	1
11	Acetylcholine	146.000000	0.255700	0	2
12	2-Amino-4-methyl pyrimidine	109.000000	0.367220	2	3
13	L-Pipecolinic acid	129.000000	0.213100	2	3
14	Hypoxanthine	136.000000	0.187100	2	4
15	4-Aminophenol	109.000000	0.974400	3	2
16	Adenosine	267.000000	1.980000	4	8
17	N-Cyclohexyl-N-methylcyclohexanamine	195.000000	3.583599	0	1
18	Bis-(2-ethylhexyl) phthalate	388.000000	3.698699	0	4
19	Diphenhydramine	255.000000	3.354199	0	2
20	3,5-di-tert-Butyl-4-hydroxybenzoic acid	250.000000	3.685399	2	3
21	Prolylleucine	362.000000	2.403100	2	7
22	Acetyl-L-carnitine	203.000000	1.235701	0	4
23	Valine	117.000000	0.054300	3	3
24	Creatinine	113.000000	1.226900	2	4
25	L-Histidine	155.000000	0.635900	4	4
26	DL-Arginine	174.000000	1.548100	4	6
27	DL-Tryptophan	204.000000	1.122300	4	3
28	Dibenzylamine	197.000000	2.976400	1	1
29	Oleamide	281.000000	3.509200	2	2
30	Hexadecanamide	255.000000	3.952999	2	2
31	Stearamide	283.000000	3.062230	2	1
32	Erucamide	337.000000	4.083392	2	1

the lipid bilayer of cell membranes and are widely distributed in the body. It can affect the sensitivity of the ligand binding to the target molecule will decrease, and the ligand toxicity to increase. The smaller the log P value, the more ligands tend to be water soluble and hydrophobic [29]. The log P value of the ligand must not be a negative value because it cannot pass through the lipid bilayer membrane. Then, the number of hydrogen bonds in the donor and acceptor correlates with the biological activity of the ligand or drug [30].

Molecular Docking Active Compound of Tuna-Shredded Fortified Banana Blossom Extract

Various active compounds from natural ingredients have multifunction for health, one of which is as anti-arthritis gout. The initial method to determine the potential of the active compound as an anti-arthritis gout is by *in silico* molecular docking method, namely the binding of the active compound as a test ligand to the target anti-arthritis gout receptor XO enzyme. Prior to molecular docking, the docking method validation must

first be carried out. The validation of the molecular docking method was carried out with the aim of re-docking the ligand on the active site of the XO enzyme by selecting a conformation similar to the natural ligand conformation that was known through re-docking.

At this stage, grid box measurements are carried out to determine the area where the test and control ligands will attach. The grid box obtained shows that the two types of ligands will attach to the center position X 27.5292, Y 17.1729, and Z 107.1436 and the dimensions (Å) X 89.9546, Y 69.5777, and Z 70.1696. The docking process is carried out in 10 repetitions, and then the docking results are selected by looking at the conformation that is most similar to the native ligand. The overall ligand conformation that has been selected is then calculated as the Root Mean Square Deviation (RMSD) value using the Discovery Studio application. The results of molecular docking that show good performance have an RMSD value of less than 2 Å. The RMSD value resulting from the validation of re-tethering between the receptor and the natural ligand showed the lowest value of 0 Å and the highest value of 1.3521. This molecular docking validation is said to be valid or appropriate since the average RMSD value obtained is less than 2 Å [31].

The results of the molecular docking of the active compound of tuna-shredded fortified with banana blossom extract can be seen in Table 7. Based on the binding affinity score (Table 7), it can be seen that the *in silico* analysis of the activity of the tuna-shredded fortified with banana blossom extract to the XO enzyme showed that the more stable ligand to the XO enzyme is ferulic acid (a phenolic compound) with binding affinity score -9.70 kcal/mol and trans-cinnamaldehyde (an organic compound) with binding affinity score -9.20 kcal/mol. The results of method validation obtained an RMSD score

of less than 2 Å. These results show that the calculation of the docking between protein and ligand gives results that are almost similar to the position of the native ligand since it has an RMSD score of less than 2 Å. In addition, the data presented in Table 7 only test ligands that have binding affinity scores lower than allopurinol as the control ligand (-5.90 kcal/mol). In contrast, test ligands with binding affinity scores greater than control ligands allopurinol are not shown. Since these ligands have a very low affinity for binding to the XO enzyme. Toppo et al. [32] explained that the lower the binding affinity score of the interaction of the ligand-receptor complex, the stronger the potential to bind and the higher the inhibitory ability of the ligand to the target enzyme.

Based on the binding affinity score of allopurinol as ligand control (-5.90 kcal/mol), the compound that can bind strongly to the receptor and have the potential as anti-arthritis gout is a compound that has a lower binding affinity score than allopurinol. The compound that has the lowest binding affinity score to the control and has the potential to bind to the XO enzyme is ferulic acid (-9.70 kcal/mol). This indicates that the ferulic acid compound has the potential to anti-arthritis gout. This is also supported by data that tuna-shredded fortified with banana blossoms has antioxidant capacity by DPPH assay. A compound that has antioxidant capacity also has the potential to have other biological activities [24]. This is confirmed by Nile et al. [33] reported that the ferulic acid compound had an inhibitory activity of more than 50% at 100 µg/mL against the XO enzyme and also against the cyclooxygenase-2 (COX-2) enzyme. Wang et al. [34] also reported that the ferulic acid compound had an IC₅₀ value to the XO enzyme 1.35 × 10⁻⁵ M, and this IC₅₀ value was higher than the IC₅₀

Table 7. Binding affinity score ligands of tuna-shredded fortified with banana blossom active compounds against xanthine oxidase enzyme

No.	Ligand	Enzyme/Receptor	Binding affinity (kcal/mol)
1	Ferulic Acid	Xanthine Oxidase	-9.70
2	Trans-cinnamaldehyde		-9.20
3	Diphenhydramine		-7.00
4	Allopurinol (Positive Control)		-5.90

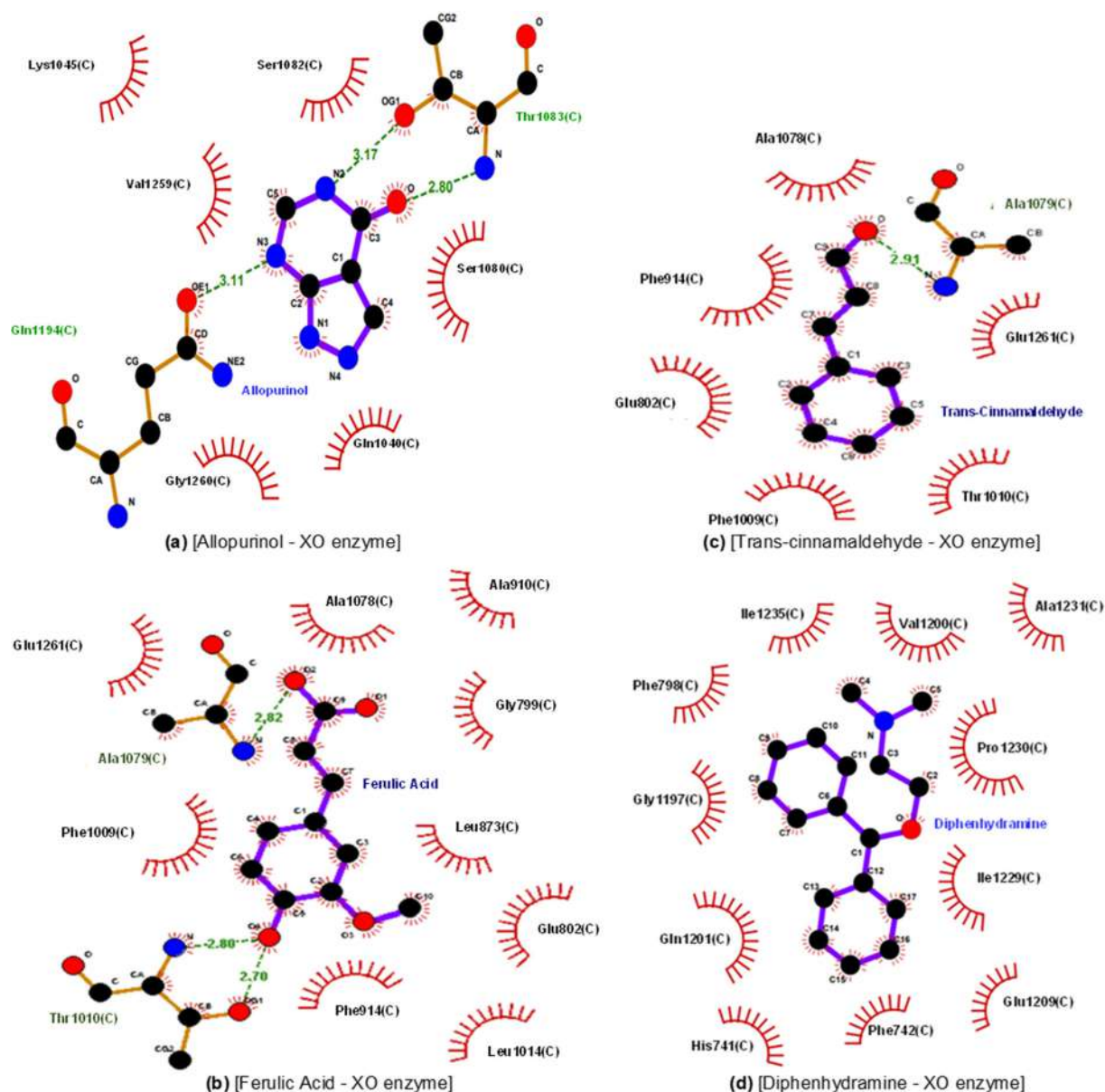


Fig 1. The 2D visualization of the interaction of the ligand allopurinol, ferulic-acid, Trans-cinnamaldehyde, and Diphenhydramine with XO enzyme as receptor

value of allopurinol as a positive control. The more OH group in the ferulic acid compound, the stronger its activity against XO enzyme inhibition.

The 2D Visualization

The lower binding affinity score of the control or higher inhibitory power of the drug to the XO enzyme becomes clearer through a 2D visualization. The visualization of the interaction between each ligand and with XO enzyme is shown in Fig. 1.

It can be seen that there are differences in the types and amino acid residues of the receptor that bind to the ligand, the type of bond formed between the amino acid residue of the receptor and the ligand and the distance between the amino acid residues and the ligand (Fig. 1). The interaction of these things determines the size of the binding affinity score of the ligand-receptor complex. According to Patrick [35], the strength of ionic bonds and hydrogen bonds, and hydrophobic interactions is determined by the difference in electronegativity of a

Table 8. The interaction type of each ligand complex of the active compound of tuna-shredded fortified banana blossom extract against the XO enzyme

[Complex ligand-receptor]	Type of interaction	Amino acids residues
[Ferulic Acid-XO enzyme]	Hydrogen bond Hydrophobic	Ala1079, Thr1010 Gly799, Ala910, Ala1078, Glu1261, Phe1009, Phe914, Leu1014, Glu802, Leu873
[Diphenhydramine-XO enzyme]	Hydrophobic	Phe798, Gly1197, Gln1201, His741, Phe742, Glu1209, Ile1229, Pro1230, Ala1231, Val1200, Ile1235
[Trans-Cinnamaldehyde-XO enzyme]	Hydrogen bond Hydrophobic	Ala1079 Ala1078, Phe914, Glu802, Phe1009, Thr1010, Glu1261
[Allopurinol-XO enzyme]	Hydrogen bond Hydrophobic	Thr1083, Gln1194 Lys1045, Ser1082, Val1259, Gln1040, Ser1080, Gly1260

compound. The greater the difference in electronegativity of a compound, the greater will be ionic bonds or hydrogen bonds or hydrophobic interactions. The shorter the bond distance, the stronger the bond [36].

The differences in the type and number of amino acid residues bound to allopurinol ligand as control positive ligand, as well as ligands from the active compound of tuna-shredded fortified banana blossoms, extract indicated differences in the mechanism of inhibition of each ligand on the XO enzyme as the target protein. The interactive form of each ligand complex of the active compound of tuna-shredded fortified banana blossoms extract against the XO enzyme can be seen in Table 8. *In silico* method used, the amino acid residues are amino acid residues on the active site of the XO enzyme, so the mechanism of inhibition of compounds from tuna shredded fortified banana blossoms extract is a competitive inhibition mechanism [37].

Toxicity and Bioavailability

The results of the pharmacokinetic and toxicity analysis of the potential ligands that have the lowest binding affinity score with the XO enzyme through the http://tox.charite.de/protox_II/ that the test ligand ferulic-acid showed the predicted toxicity class categorized as class 4 of 6 and predicted LD₅₀ 1190 mg/kg. Thus, the ferulic acid as a test ligand compound is predicted not to be toxic to body organs.

After knowing the toxicity of the two potential compounds, the bioavailability analysis of the compound

was then carried out. This analysis was carried out online through access at <http://www.swissadme.ch/>. The results of the analysis showed that ferulic acid had a high category of human gastrointestinal absorption. This analysis was carried out based on the fact that the material consumed orally should ideally be easily absorbed by the digestive system organs, be able to be distributed specifically to target sites, be able to be metabolized by the body and eliminated without causing any harm to the body's organs [38].

CONCLUSION

The results showed that the compound contents of the tuna-shredded fortified banana blossoms extract contained 32 active compounds, which had a total phenolic content was 0.00134 mg GAE/g, total flavonoid content was 0.0006670 mg QE/g, and the IC₅₀ for the antioxidant activity was 4.38 ppm. The results of the *in silico* showed that the most potent compound, ferulic acid, had the potential to inhibit the XO enzyme with a binding affinity score was -9.70 kcal/mol through hydrogen bonds on Ala1079, Thr1010 amino acids residues and hydrophobic interactions on Gly799, Ala910, Ala1078, Glu1261, Phe1009, Phe914, Leu1014, Glu802, and Leu873 amino acids residues. As a potential compound, ferulic acid meets Lipinski's rules, is a high category of human gastrointestinal absorption, and is not potentially toxic to the body. The tuna-shredded fortified banana blossoms have the potency to be developed as a functional food, especially to prevent gout arthritis.

■ ACKNOWLEDGMENTS

The authors would like to thank “Lembaga Penelitian dan Pengabdian kepada Masyarakat (LPPM) Brawijaya University” for the financial support for this research. This research is funded by LPPM - Brawijaya University through “Hibah Penelitian Strategis 2022” (No. 1665.20/UN.01/UB/2022).

■ REFERENCES

- [1] Palani, T., Shobha, K., Thirunavukkarasu, P., and Hari, R., 2018, *In vitro* and *in silico* antigout arthritic activities of ethanolic and aqueous stem extracts of *Cissus quadrangularis* – A TLR2 and TLR4 Receptor approach, *J. Appl. Pharm. Sci.*, 8 (09), 015–022.
- [2] Soltani, Z., Rasheed, K., Kapusta, D.R., and Reisin, E., 2013, Potential role of uric acid in metabolic syndrome, hypertension, kidney injury, and cardiovascular diseases: Is it time for reappraisal, *Curr. Hypertens. Rep.*, 15 (3), 175–181.
- [3] Kostalova, E., Pavelka, K., Vlaskova, H., and Stiburkova, B., 2015, Hyperuricemia and gout due to deficiency of hypoxanthine-guanine phosphoribosyl transferase in female carriers: New insight to differential diagnosis, *Clin. Chim. Acta*, 440, 214–217.
- [4] Raucci, F., Iqbal, A.J., Saviano, A., Minosi, P., Piccolo, M., Irace, C., Caso, F., Scarpa, R., Pieretti, S., Mascolo, N., and Maione, F., 2019, IL-17A neutralizing antibody regulates monosodium urate crystal-induced gouty inflammation, *Pharmacol. Res.*, 147, 104351.
- [5] Billy, C.A., Lim, R.T., Ruospo, M., Palmer, S.C., and Strippoli, G.F.M., 2018, Corticosteroid or nonsteroidal antiinflammatory drugs for the treatment of acute gout: A systematic review of randomized controlled trials, *J. Rheumatol.*, 45 (1), 128–136.
- [6] Hadinoto, S., and Idrus, S., 2018, Proporsi dan kadar proksimat bagian tubuh ikan tuna ekor kuning (*Thunnus albacares*) dari perairan Maluku, *Majalah BIAM*, 14 (2), 51–57.
- [7] Hardoko, H., Suprayitno, E., Sulistiyati, T.D., Sasmito, B.B., Chamidah, A., Panjaitan, M.A.P., Tambunan, J.E., and Djamaludin, H., 2022, Banana blossom addition to increase food fiber in tuna (*Thunnus* sp.) floss product as functional food for degenerative disease’s patient, *IOP Conf. Ser.: Earth Environ. Sci.*, 1036, 012095.
- [8] Gang, M., 2013, *Changes in the quality and yield of fish fillets due to temperature fluctuations during processing*, Final Project, United Nations University Fisheries Training Programme, Iceland.
- [9] Dara, W., and Arlinda, A., 2017, Mutu organoleptik dan kimia abon ikan gabus (*Channa striata*) yang disubstitusi sukun (*Artocarpus altilis*), *Jurnal Katalisator*, 2, 61–66.
- [10] Parvez, G.M.M., and Akanda, M.K.M., 2019, “Foods and Arthritis: An Overview” in *Bioactive Food as Dietary Interventions for Arthritis and Related Inflammatory Diseases*, 2nd Ed., Eds. Watson, R.R., and Preedy, V.R., Academic Press, Cambridge, MA, 3–22.
- [11] Kesuma, C.P., Adi, A.C., and Muniroh, L., 2015, Pengaruh substitusi rumput laut (*Eucheuma cottonii*) dan jamur tiram (*Pleurotus ostreatus*) terhadap daya terima dan kandungan serat pada biskuit, *Media Gizi Indonesia*, 10 (2), 146–150.
- [12] Asare, E.O., Bhujel, N.K., Čížková, H., and Rajchl, A., 2022, Fortification of fruit products – A review, *Czech J. Food Sci.*, 40 (4), 259–272.
- [13] Djamaludin, H., Hardoko, H., Dailami, M., Nurhadianty, V., Ananta, D.R., and Prayoga, D.R., 2022, The peroxide, organoleptic and proximate content of *Thunnus albacares* shredded fortified with banana blossoms, *Jurnal Sumberdaya Akuatik Indopasifik*, 6 (4), 319–330.
- [14] Sulistiyati, T.D., Suprayitno, E., Djamaludin, H., Tambunan, J.E., and Muchayaroh, U., 2022, The effect of fortification *Moringa oleifera* leaves powder on calcium content in otak-otak products of *Clarias* sp., *IOP Conf. Ser.: Earth Environ. Sci.*, 1036, 012071.
- [15] Sharma, V., Shukla, K.V., and Golani, P., 2019, Traditional and medicinal effect of banana blossom, *Int. J. Sci. Dev. Res.*, 4 (5), 377–381.
- [16] Hardoko, H., Sari, P.Y., and Puspitasari, Y.E., 2015, Substitusi jantung pisang dalam pembuatan abon dari pindang ikan tongkol, *JPK*, 20 (1), 1–10.

- [17] Mohammed, E.T., Khalil, R.R., and Mustafa, Y.F., 2022, Phytochemical analysis and antimicrobial evaluation of quince seeds' extracts, *J. Med. Chem. Sci.*, 5 (6), 968–979.
- [18] Khalil, R.R., Mohammed, E.T., and Mustafa, Y.F., 2022, Evaluation of *in vitro* antioxidant and antidiabetic properties of *Cydonia oblonga* seeds' extracts, *J. Med. Chem. Sci.*, 5 (6), 1048–1058.
- [19] Lipinski, C.A., 2004, Lead- and drug-like compounds: The rule-of-five revolution, *Drug Discovery Today: Technol.*, 1 (4), 337–341.
- [20] Jayaram, B., Singh, T., Mukherjee, G., Mathur, A., Shekhar, S., and Shekhar, V., 2012, Sanjeevini: A freely accessible web-server for target directed lead molecule discovery, *BMC Bioinf.*, 13 (Suppl. 17), S7.
- [21] Jasim, S.F., Mustafa, Y.F., 2022, Synthesis, ADME study, and antimicrobial evaluation of novel naphthalene-based derivatives, *J. Med. Chem. Sci.*, 5 (5), 793–807.
- [22] Banerjee, P., Eckert, A.O., Schrey, A.K., and Preissner, R., 2018, ProTox-II: A webserver for the prediction of toxicity of chemicals, *Nucleic Acids Res.*, 46 (W1), W257–W263.
- [23] Daina, A., Michielin, O., and Zoete, V., 2017, SwissADME: A free web tool to evaluate pharmacokinetics, drug- likeness and medicinal chemistry friendliness of small molecules, *Sci. Rep.*, 7 (1), 42717.
- [24] Sukisman, S., Purnomo, H., Rosyidi, D., and Radiati, L.E., 2014, Quality properties, antioxidant capacity and total phenolic content of traditional deep-fried shredded meat (abon) of Palu, Central Sulawesi, *Am. J. Food Technol.*, 9 (2), 80–88.
- [25] Esmaeili, A.K., Mat Taha, R., Mohajer, S., and Banisalam, B., 2015, Antioxidant activity and total phenolic and flavonoid content of various solvent extracts from *in vivo* and *in vitro* grown *Trifolium pratense* L. (red clover), *BioMed Res. Int.*, 2015, 643285.
- [26] Baba, S.A., and Malik, S.A., 2015, Determination of total phenolic and flavonoid content, antimicrobial and antioxidant activity of a root extract of *Arisaema jacquemontii* Blume, *J. Taibah Univ. Sci.*, 9 (4), 449–454.
- [27] Djamaludin, H., Bintang, M., and Priosoeryanto, B.P., 2019, Cytotoxicity and antiproliferative effects of ethyl acetate fraction of *Padina australis* against MCM-B2 and K562 cell lines, *J. Appl. Biol. Biotechnol.*, 7 (2), 25–29.
- [28] Aisyah, Y., Rasdiansyah, R., and Muhaimin, M., 2014, Pengaruh pemanasan terhadap aktivitas antioksidan pada beberapa jenis sayuran, *JTIPI*, 6 (2), 28–32.
- [29] Yadav, D.K., and Khan, F., 2013, QSAR, docking and ADMET studies of camptothecin derivatives as inhibitors of DNA topoisomerase-I, *J. Chemom.*, 27 (1-2), 21–33.
- [30] Giménez, B.G., Santos, M.S., Ferrarini, M., and Fernandes, J.P.S., 2010, Evaluation of blockbuster drugs under the rule-of-five, *Pharmazie*, 65 (2), 148–152.
- [31] Hernández-Santoyo, A., Tenorio-Barajas, A.Y., Altuzar, V., Vivanco-Cid, H., and Mendoza-Barrera, C., 2013, “Protein-Protein and Protein-Ligand Docking” in *Protein Engineering – Technology and Application*, Eds. Ogawa, T., IntechOpen, Rijeka, 63–81.
- [32] Toppo, A.L., Yadav, M., Dhagat, S., Ayothiraman, S., and Eswari, J.S., 2021, Molecular docking and ADMET analysis of synthetic statins for HMG-CoA reductase inhibition activity, *Indian J. Biochem. Biophys.*, 58 (2), 127–134.
- [33] Nile, S.H., Ko, E.Y., Kim, D.H., and Keum, Y.S., 2016, Screening of ferulic acid related compounds as inhibitors of xanthine oxidase and cyclooxygenase-2 with anti-inflammatory activity, *Rev. Bras. Farmacogn.*, 26 (1), 50–55.
- [34] Wang, F., Yang, L., Huang, K., Li, X., Hao, X., Stöckigt, J., and Zhao, Y., 2007, Preparation of ferulic acid derivatives and evaluation of their xanthine oxidase inhibition activity, *Nat. Prod. Res.*, 21 (3), 196–202.
- [35] Patrick, G., 2001, *Instant Notes in Medicinal Chemistry*, BIOS Scientific Publishers, Oxford.

- [36] Wardaniati, I., and Herli, M.A., 2018, Studi molecular docking senyawa golongan flavonol sebagai antibakteri, *JOPS*, 1 (2), 20–27.
- [37] Ouertani, A., Neifar, M., Ouertani, R., Masmoudi, A.S., Mosbah, A., and Cherif, A., 2019, Effectiveness of enzyme inhibitors in biomedicine and pharmacotherapy, *Adv. Tissue Eng. Regener. Med.*, 5 (2), 85–90.
- [38] Drwal, M.N., Banerjee, P., Dunkel, M., Wettig, M.R., and Preissner, R., 2014, ProTox: A web server for the *in silico* prediction of rodent oral toxicity, *Nucleic Acids Res.*, 42 (W1), W53–W58.

Supplementary Data

This supplementary data is a part of a paper entitled “Synthesis of a New DPTYEAP Ligand and Its Complexes with Their Assessments on Physical Properties, Antioxidant, and Biological Potential to Treat Breast Cancer”.

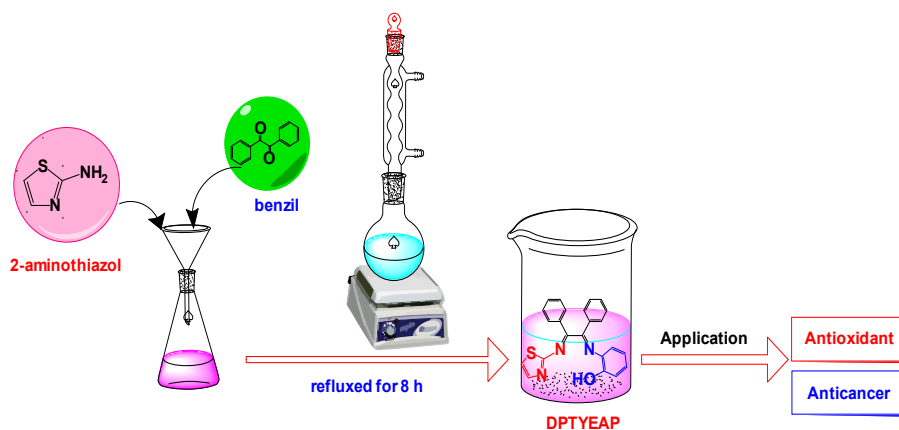


Fig S1. Graphical abstract

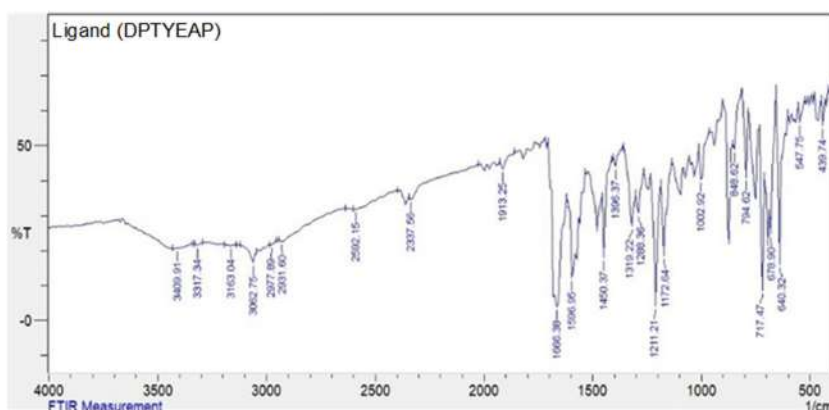


Fig S2. FTIR spectra of the synthesized ligand (DPTYEAP)

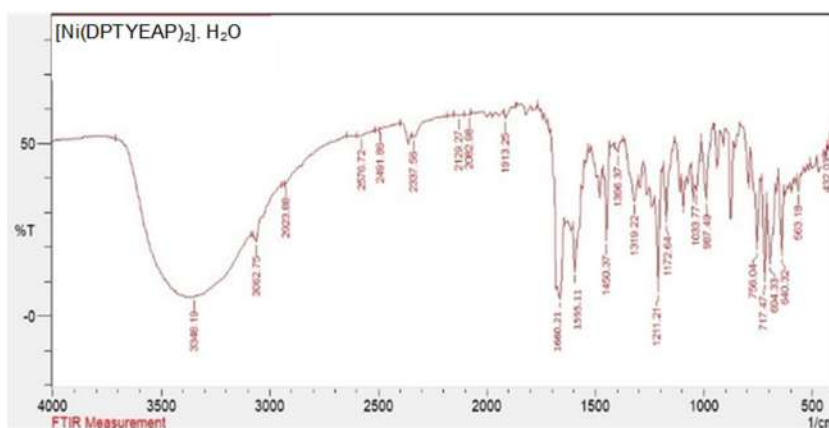


Fig S3. FTIR spectra of the Ni(II) complex

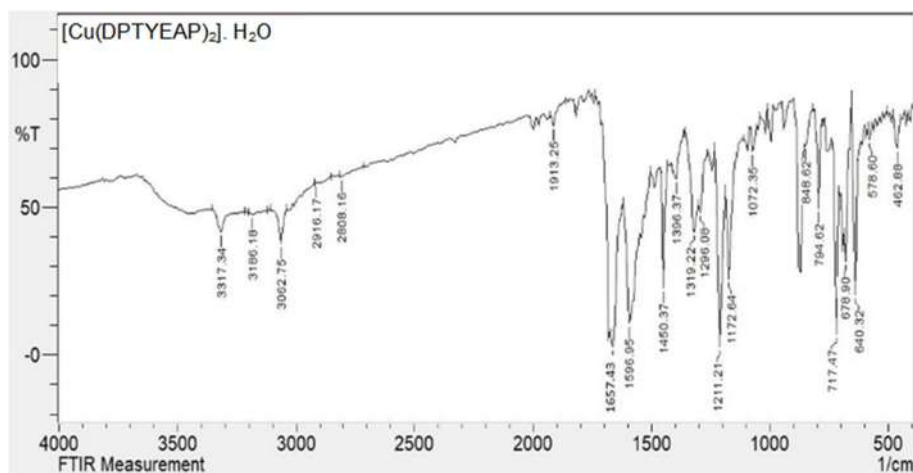


Fig S4. FTIR spectra of the Cu(II) complex

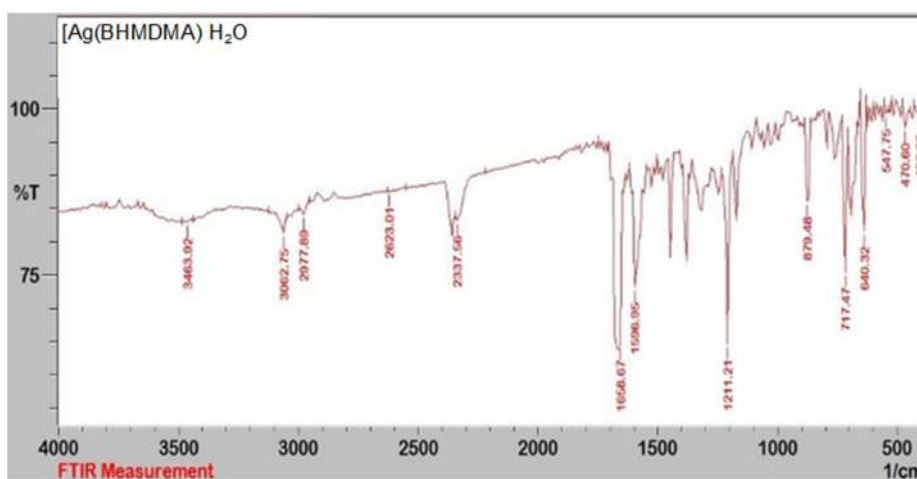


Fig S5. FTIR spectra of the Ag(I) complex

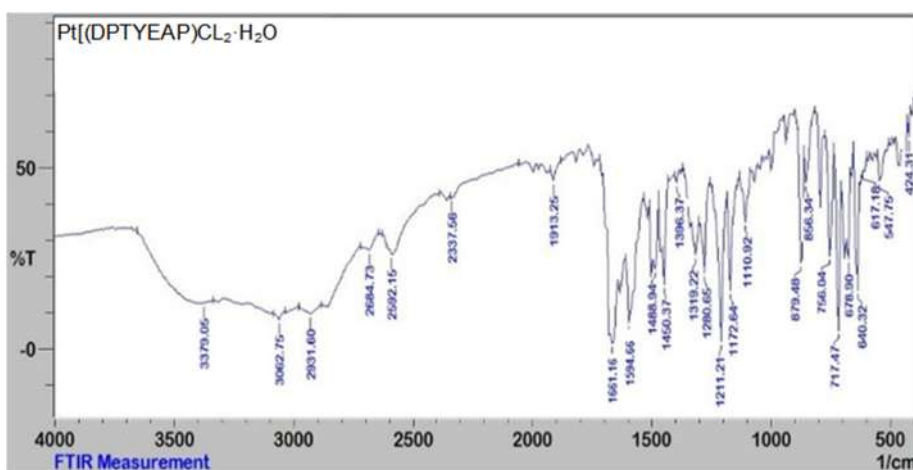


Fig S6. FTIR spectra of the Pt(IV) complex

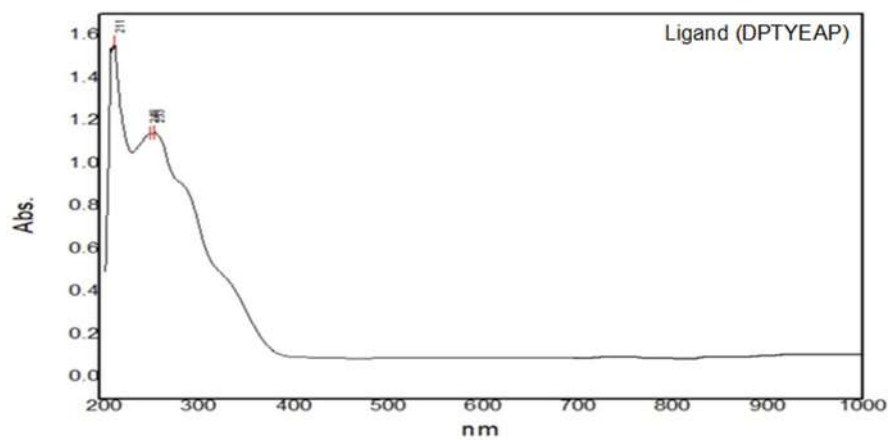


Fig S7. Electronic spectra of the synthesized ligand (DPTYEAP)

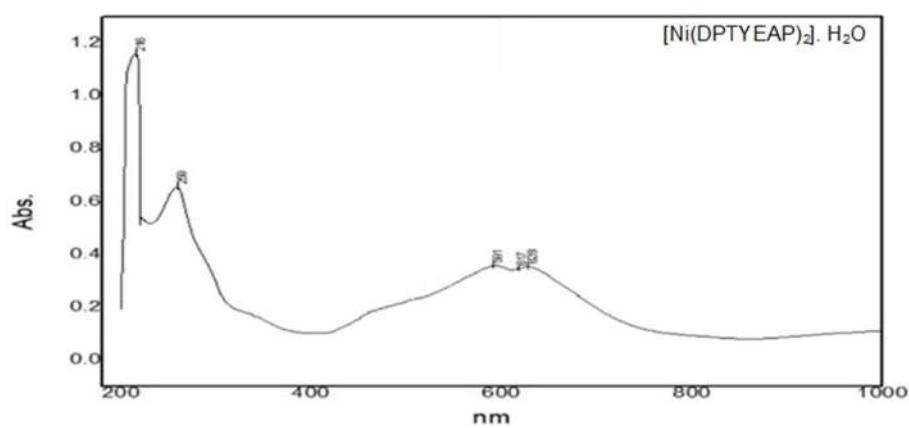


Fig S8. Shows the absorption peaks of each of the Ni(II) complexes

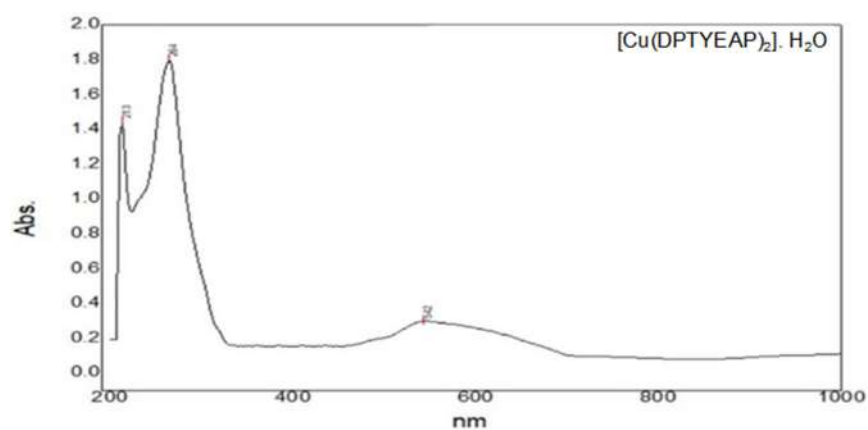


Fig S9. Shows the absorption peaks of each of the Cu(II) complexes

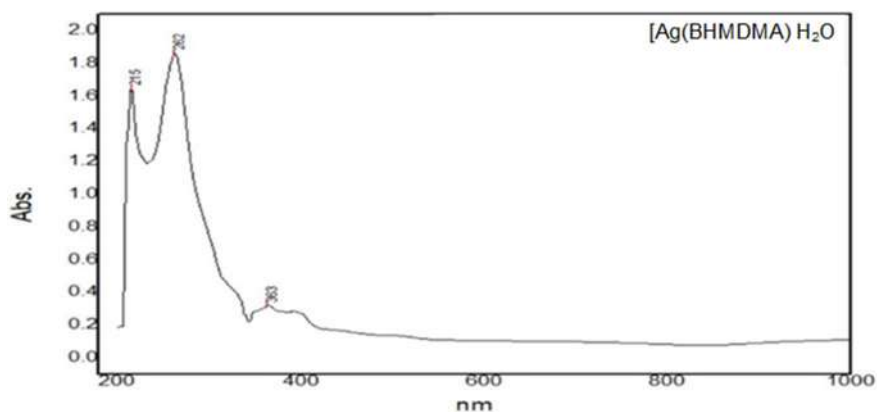


Fig S10. Shows the absorption peaks of each of the Ag(I) complexes

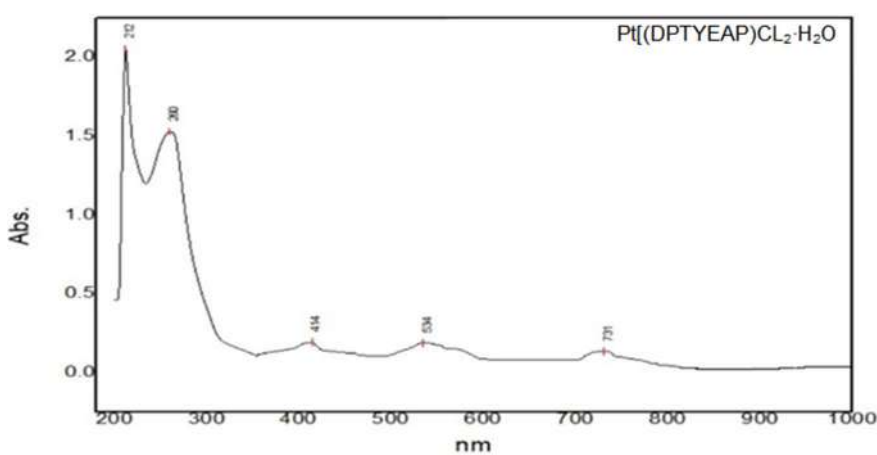


Fig S11. Shows the absorption peaks of each of the Pt(IV) complexes

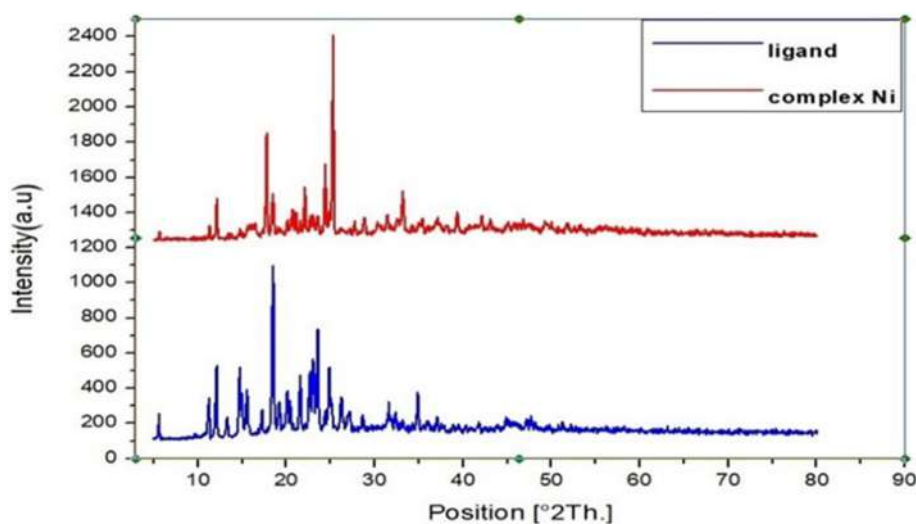


Fig S12. Shows the XRD patterns for ligand (DPTYEAP) and Ni(II) complexes

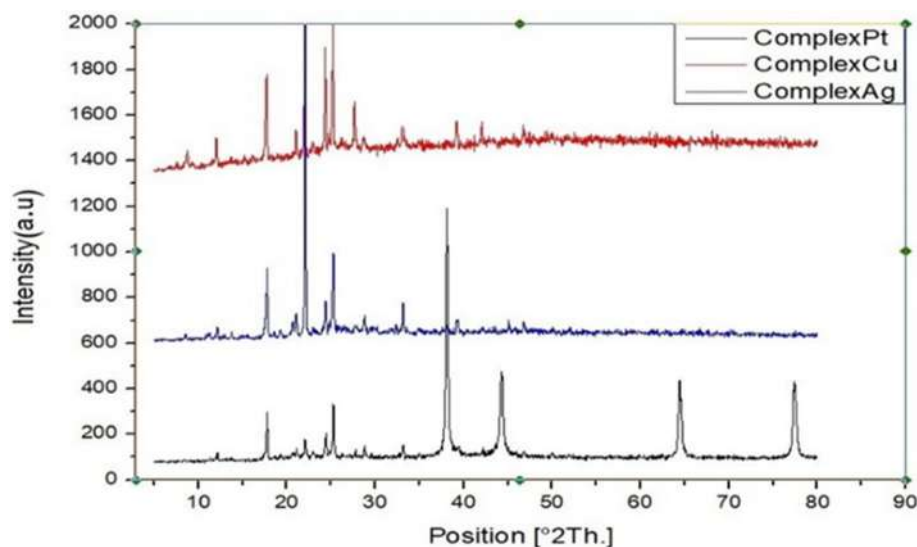


Fig S13. Shows the XRD patterns for the Cu(II), Ag(I) and Pt(IV) complexes

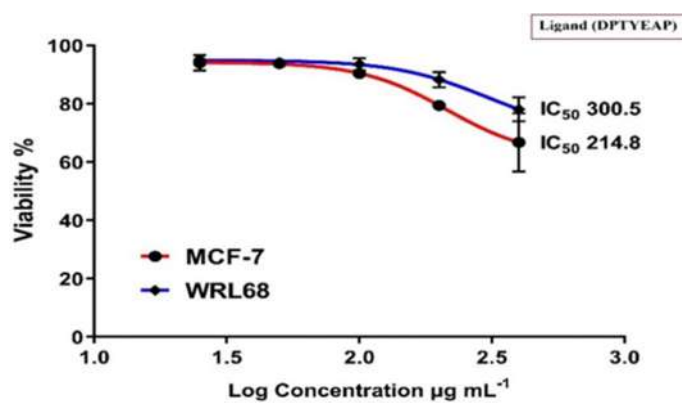


Fig S14. IC₅₀ for (DPTYEAP) ligand of cancer cell line (MCF-7) and natural cell line (WRL68)

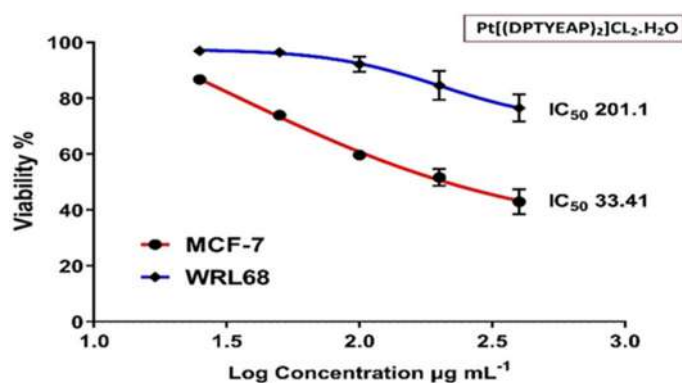


Fig S15. IC₅₀ for the Pt(IV) complex in the cancer cell line (MCF-7) and natural cell line (WRL68)

Synthesis of a New DPTYEAP Ligand and Its Complexes with Their Assessments on Physical Properties, Antioxidant, and Biological Potential to Treat Breast Cancer

Abbas Fadhil Yasir* and Hayder Obaid Jamel

Department of Chemistry, College of Education, University of Al-Qadisiyah, 58001 Al-Diwaniyah, Iraq

* Corresponding author:

email: abbas9025@gmail.com

Received: January 26, 2023

Accepted: February 17, 2023

DOI: 10.22146/ijc.81734

Abstract: A new series of complexes of the 2-((1E,2E)-1,2-diphenyl-2-(thiazol-2-ylimino)ethylidene)amino)phenol (DPTYEAP) has been synthesized by the reaction of the ligand with metal chlorides of Ni(II), Cu(II), Pt(IV), and AgNO₃ in ethanol as a solvent. The ligand was prepared for the two steps. In the first step, compound (A) was synthesized by reacting 2-aminothiazol with benzil in ethanol. Another step is the preparation of the ligand from the reaction of compound (A) with 2-aminophenol. The structures of the ligand and its complexes were confirmed by FTIR, ¹H-¹³C-NMR, UV-Vis spectra, melting points, molar conductivity (C, H, and N), and magnetic susceptibility. The synthesized complexes were prepared in a 1:2 ratio for Ni(II), Cu(II), and Pt(IV) complexes and a 1:1 ratio (M:L) for Ag(I) complexes. The geometric shape of all complexes is octahedral, except for the Ag(I) complex, which is tetrahedral. The antioxidant test for the prepared compounds was carried out. The anticancer test was conducted for each of the ligands and the platinum(IV) complex, and it was found that the platinum complex is more effective against breast cancer cells (MCF-7); thus, it can be used as a potential drug after studying it well.

Keywords: Schiff base; 2-aminothiazoles; anticancer; antioxidant; platinum(IV)

■ INTRODUCTION

Breast cancer occurs when some of the breast cells begin to grow abnormally. These cells divide more rapidly than healthy cells and continue to accumulate, forming a lump or tumor [1]. The cells may spread through the breast to the lymph nodes or other body parts [2]. Breast cancer comes after skin cancer as the most common type of cancer among women [3]. Breast cancer sometimes affects both men and women, but it is more common in women. Substantial support for breast cancer awareness and research funding has helped advance breast cancer diagnosis and treatment [4]. Breast cancer survival rates have increased, and the number of deaths associated with this disease has regularly decreased, largely due to several factors, such as early detection and a better understanding of the nature of this disease.

Among the used treatments, the thiazole compound had an important and effective role in preparing many anti-breast cancer complexes, especially when it is linked to platinum [5]. One of the drugs containing thiazoles,

which has been used as an anti-cancer compound, is Bleomycin [6]. The 2-aminothiazole compound is effective in treating and controlling breast cancer, in addition to its various and wide applications in various fields, especially in the pharmaceutical industry. Amino-thiazole is recently identified as a desirable compound; it has been diagnosed and examined in many medicinal chem drugs because of its thiourea-like properties and its tendency to target multiple biological targets [7]. It has also been used as an anti-bacterial [8], an antioxidant, an anti-viral [9], and a fungicide [10]. 2-Amino-thiazole and its derivatives have a wide range of medical applications as well, such as anti-tuberculosis [11], anti-inflammatory [12], anti-platelet, and are used as anti-tumors [13]. This study observed that the prepared ligand derived from amino thiazoles and its platinum(IV) complex had high antioxidant activity against free radicals. As well as high effectiveness against breast cancer cells (MCF-7), and this has been proven through applications and examinations conducted on them, which

can be used as an anti-cancer treatment. In addition, they are considered nanocomposites after confirming this through the XRD and FESEM tests. This characteristic makes these compounds could be used in many fields, including the medical and industrial fields [14].

■ EXPERIMENTAL SECTION

Materials

In this study, 2-amino thiazoles (98% purity, Merck), benzil (98%, Sigma-Aldrich), acetic acid (99%, BDH), and 2-aminophenol (99%, Sigma-Aldrich) were used. At the same time, all metal chlorides (platinum(IV), nickel(II), copper(II)), and silver nitrate) were brought from Sigma-Aldrich. They were of varying purity 99.9, 98, 97.5, and 99%, respectively. Also, the study used free radical 1,1-diphenyl-2-picrylhydrazyl, supplied by Sigma-Aldrich for an antioxidant check. Breast cancer cell lines (MCF-7) and normal cell lines (WRL-68) were obtained from the Center for Natural Product Research and Drug Discovery, Department of Pharmacology, Faculty of Medicine, University of Malaya, Kuala Lumpur.

Instrumentation

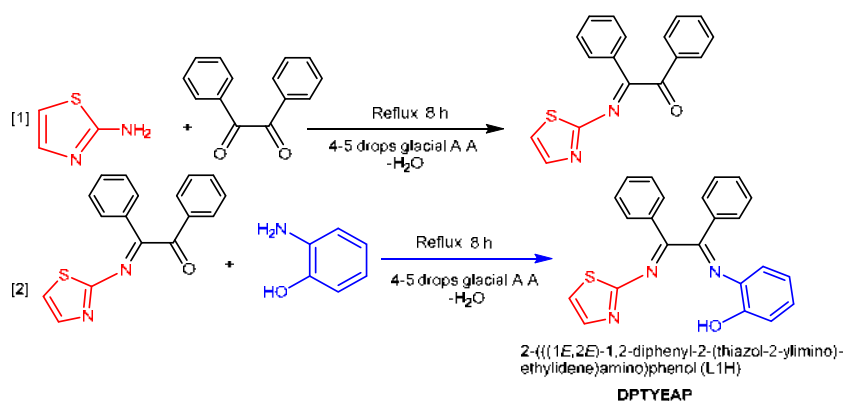
UV-Vis spectra in the region of 200–1000 nm were obtained using Shimadzu UV-165 PCS spectrophotometer. On the Fourier Transform Varian Spectrometer, ^1H , ^{13}C -NMR spectra were acquired at 300 MHz with tetramethyl silane as a standard internal reference in DMSO- d_6 solvent. The FTIR 8400S Shimadzu Spectrophotometer was used to record FTIR Spectra in the 400–4000 cm^{-1} range. The Stuart melting point was used to determine the melting points of all compounds.

At room temperature, magnetic susceptibility measurements were taken using the Balance Magnetic Susceptibility Model MSB-MKI; flame atomic absorption spectrophotometer, Shimadzu AA-6300 was used to determine metal percentage in the complexes; Elemental analysis was recorded on instrument type EA-300.mth.

Procedure

Preparation of the ligand DPTYEAP

The ligand was prepared in two steps. The first step was the preparation of (*E*)-1,2-diphenyl-2-(thiazol-2-ylimino)ethan-1-one (compound-A) from the reaction between 2-aminothiazol (2.002 g, 0.02 mol) in 25 mL of the absolute ethanol with benzil (4.204 g, 0.02 mol) in 25 mL ethanol with a continuous stirring. The mixture was refluxed for 8 h. After that, it was cooled, filtered, and collected. It was recrystallized by removing the residue of the starting material with 99.9% ethanol, allowing the precipitate to dry; then, it will be collected and weighed to be employed in the second stage, yielding an 84% yield percentage. The ligand 2-(((1*E*,2*E*)-1,2-diphenyl-2-(thiazol-2-ylimino)ethylidene)amino) phenol (DPTYEAP) was prepared by dissolving compound-A (4.385 g, 0.015 mol) in 25 mL of ethanol with a solution of 2-aminophenol (1.636 g, 0.015 mmol) in 25 mL of ethanol. Then, 5–6 drops of concentrated hydrochloric acid were added to the mixture with continuous stirring, the mixture was refluxed for 8 h. It was cooled, precipitated, filtered, dried, and recrystallized by using absolute ethanol. The product gave a yield of 79%, and a melting point of 113 °C, as stated in Scheme 1.



Scheme 1. Synthesis of the 2-(((1*E*,2*E*)-1,2-diphenyl-2-(thiazol-2-ylimino)-ethylidene)amino)phenol (DPTYEAP) ligand

Synthesis of the complexes

Two types of the complex are prepared with a ratio of 1:1 and 1:2, which are as follows:

Preparation of Ni(II), Cu(II), Pt(IV) complexes with DPTYEAP ligand. These complexes were prepared in 1:2 using the following general method. A solution of DPTYEAP ligand (1.533 g, 0.004 mol) in 10 mL ethanol was mixed with 0.002 mol of metal chlorides in 10 mL of absolute ethanol. The mixture was refluxed for 2 h while stirring. After that, it was cooled, filtrated, and dried before re-crystallized using absolute ethanol to obtain pure complexes.

Preparation of Ag(I) complexes with DPTYEAP ligand. The above complex was made using the same method but in a different ratio 1:1 M:L. DPTYEAP ligand solution (0.766 g, 0.002 mol) in 10 mL ethanol was added to silver nitrate solution (0.339 g, 0.002 mol) in 10 mL absolute ethanol. The mixture was refluxed for 2 h with stirring before being cooled, filtrated, and dried.

Measuring antioxidant capacity

The concentration of the tested compound which causes 50% of radical scavenging activity (IC_{50}) was determined by the linear regression analysis from the obtained RSA values using GraphPad Prism 8.3.1 software. DPTYEAP ligand and metal complexes were tested for radical scavenging activity against DPPH using a spectrophotometric method. In practice, 1 mL of the ligand and metal complexes in DMSO at various concentrations 3.90–500 g/mL was mixed with 1 mL of 0.1 mM DPPH in methanol. For 30 min, the tested samples were allowed to react with DPPH. After 30 min of incubation in the darkness at room temperature, the absorbance at 517 nm was measured with Shimadzu UV-165PCS spectrophotometer. Then, the RSA% was calculated. The linear regression analysis was performed on the obtained RSA values to determine the IC_{50} value. The lower the value of IC_{50} , the more efficient the antioxidant [15].

Biological activity (Cytotoxic assay MTT)

In this study, two cell lines were used, namely the breast cancer cell line (MCF-7) and the normal human liver cell line (WRL-68). Cell lines were preserved in liquid nitrogen and were maintained and tested at the Biotechnology Research Center - Al-Nahrain University.

After the cells of cancer lines (MCF-7) and the suspension were prepared at a concentration of 1×10^5 cells/well completely, the cell suspension was placed in a plate containing 96 holes with a flat base, and it was incubated in an incubator with 5% carbon dioxide (CO_2) at a temperature of 37 °C, for 24 h. Then, 100 μ L of this suspension was added to each well. After that, the concentrations that had been prepared for each of the ligands and the platinum complex 25, 50, 100, 200, and 400 μ g/mL were added to those wells at the rate of three wells for each concentration. After that, the plate was incubated for a full day at an incubation temperature of 37 °C, and 10 mL of MTT solution at a concentration of 0.45 mg/mL was added to each hole. Then that plate was incubated for 4 h at 37 °C. 100 μ L of DMSO solution was added to each hole and incubated for 5 min [16]. Finally, the absorbance of that sample was read at a wavelength of 570 nm using the ELASIS device, then the statistical analysis was conducted on the optical density readings to calculate the IC_{50} .

RESULTS AND DISCUSSION

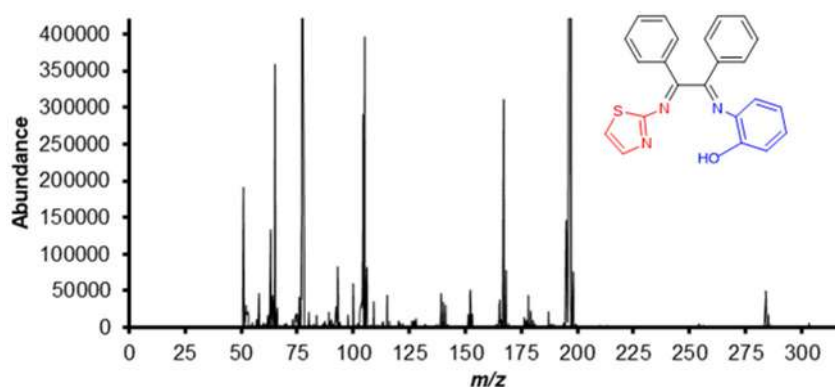
The new ligand (DPTYEAP) was synthesized from the consecutive reaction of 2-aminothiazol with benzil and 2-aminophenol. The complexes have been prepared from the reaction of DPTYEAP with metal chlorides hydrates and $AgNO_3$ dissolved in ethanol. Table 1 shows the physical attributes and elemental analyses for each of the ligands and the complexes. The synthesized complexes were created in a 1:2 ratio for Ni(II), Cu(II) and Pt(IV) complexes, whereas Ag(I) complex was prepared in a 1:1 ratio (M:L).

Mass Spectrum of the DPTYEAP Ligand

It is one of the analytical techniques used in an accurate diagnosis to determine the prepared compound and what elements are present in its composition, as well as its molecular and structural formula. The idea behind its operation is to break the compound into ions, after which the mass-to-charge ratio is measured using a mass spectrometer. Fig. 1 shows the DPTYEAP ligand fragmentation with the appearance of a peak for the parent ion at $m/z^+ = 383.99$, as well as the rest of the divisions.

Table 1. Elemental analysis and some physical properties of the ligand (DPTYEAP) and its metallic complexes

Compound (Chemical Formula)	Color	M P (°C)	Yield (%)	M.W (g/mol)	Calc. (Found)%			
					C	H	N	M
Ligand (DPTYEAP) (C ₂₃ H ₁₇ N ₃ OS)	Brown	113		383.50	71.55 (72.04)	4.12 (4.47)	8.90 (10.96)	----- -----
[Ni (DPTYEAP) ₂].H ₂ O (C ₄₆ H ₃₄ N ₆ NiO ₃ S ₂)	Dark green	120		841.63	64.18 (65.65)	4.43 (4.07)	8.18 (9.99)	5.65 (6.97)
[Cu (DPTYEAP) ₂].H ₂ O (C ₄₆ H ₃₄ CuN ₆ O ₃ S ₂)	Dark brown	118		846.48	63.32 (65.27)	3.80 (4.05)	8.11 (9.93)	6.98 (7.51)
[Ag (DPTYEAP) H ₂ O] (C ₂₃ H ₁₈ AgN ₃ O ₂ S)	Yellowish green	123		508.34	61.09 (54.34)	3.79 (3.57)	7.98 (8.27)	20.17 (21.22)
Pt[(DPTYEAP) ₂].Cl ₂ .H ₂ O (C ₄₆ H ₃₄ Cl ₂ N ₆ O ₃ PtS ₂)	Dark golden	117		1048.92	52.03 (52.67)	3.03 (3.27)	6.67 (8.01)	17.97 (18.60)

**Fig 1.** Mass spectrum of Schiff base DPTYEAP ligand

The ¹H-NMR spectra of the DPTYEAP ligand

The ¹H-NMR Spectrum of the DPTYEAP ligand exhibited a singlet signal at $\delta = 8.655$ ppm (s, 1H) due to hydroxide proton (OH) [17], while the multiple signals were observed at the range $\delta = 6.986$ – 7.438 ppm (m, 4H) due to the 2-aminophenol ring protons [18]. Where the multiple signals at $\delta = 7.456$ – 7.793 ppm (m, 5H) and $\delta = 7.464$ – 7.837 ppm (m, 5H) are attributed to rings protons found in benzil [19]. While the doublet signals at $\delta = 7.166$ – 7.545 ppm (d, 2H) are attributed to ring protons found in thiazole [20]. Fig. 2 shows the ¹H-NMR spectra of the DPTYEAP ligand.

The ¹³C-NMR spectrum of the ligand (DPTYEAP)

The ¹³C-NMR Spectrum of the ligand DPTYEAP exhibited a signal at 40.311 ppm, due to DMSO. The carbon C₂₃ containing the group OH gave a signal at 136.648 ppm [21], while the carbon C₉ gave the signal at 116.476 ppm due to thiazole [22]. Where the following

carbon atoms C₃–C₄–C₁₀–C₂₂ gave values between 129.092–131.752 ppm due to the connection of carbon atoms with nitrogen atoms [23–24]. As for these two signals at 144.818–141.912 ppm, C₁–C₂ is due to the two groups of azomethane (–C=N–) [25]. Several signals at 129.275–129.627, 129.000–129.927, and 115.742–124.927 ppm indicated the carbon atoms C₁₂–C₁₆, C₁₇–C₂₁, and C₂₄–C₂₇ belong to the phenyls of benzil and phenol, respectively [26]. Fig. 3 shows the ¹³C-NMR spectra of the DPTYEAP ligand.

The Infrared Spectra

Diagnosis of free ligand DPTYEAP by infrared spectrometer for the purpose of determining the effective groups. The ligand showed many important bands at the wavenumber 3425, 3062, and 1666 cm⁻¹ belonging to the ν (O–H), ν (C–H) aromatic [27], and ν (C=N) azomethine, respectively [28], as shown in (Fig. S2).

Table 2. The important infrared spectral bands for the synthesized ligand (DPTYEAP) and its metallic complex

Compound	$\nu(\text{O-H})$ of water molecules	$\nu(\text{O-H})$	$\nu(\text{C-H})$ aromatic	$\nu(\text{C=N})$		$\nu(\text{M-N})$	$\nu(\text{M-O})$
				Imine	Thiazole		
Ligand (DPTYEAP)	-----	3425 (bro)	3062 (w)	1666 (s)	1596 (s)	-----	-----
[Ni(DPTYEAP) ₂].H ₂ O	3348 (bro)	-----	3062 (w)	1660 (s)	1595 (s)	563 (w)	432 (m)
[Cu(DPTYEAP) ₂].H ₂ O	3317 (bro)	-----	3062 (w)	1657 (s)	1596 (s)	578 (w)	462 (s)
[Ag (DPTYEAP) H ₂ O]	3464 (bro)	-----	3062 (w)	1658 (w)	1596 (s)	547 (m)	470 (s)
Pt[(DPTYEAP) ₂]Cl ₂ .H ₂ O	3379 (bro)	-----	3062 (w)	1661 (s)	1594 (s)	547 (w)	424 (s)

The electronic spectra of the synthesized metallic complexes

The spectrum of the Ni(II) complex showed five absorption peaks, two of which belong to the ligand field, which are 46296 and 38610 cm^{-1} . While the next three absorption peaks at 16920, 16207, and 15923 cm^{-1} indicate the following transitions ${}^3\text{A}_{2g}(\text{P}) \rightarrow {}^3\text{T}_{1g}(\text{F})$, ${}^3\text{A}_{2g}(\text{F}) \rightarrow {}^3\text{T}_{2g}(\text{F})$, ${}^3\text{A}_{2g}(\text{F}) \rightarrow {}^3\text{T}_{1g}(\text{F})$, respectively, as in Fig. S8 [33]. While the spectrum of the Cu(II) complex showed three absorption peaks, which are 46948, 37878, and 18450 cm^{-1} , two of them belong to the ligand field, and the last one belongs to the ${}^2\text{B}_{1g} \rightarrow {}^2\text{E}_g$ transition, as in Fig. S9 [34]. While the spectrum of Ag(I) complex did not show any transitions (d-d) due to the saturation of the metal with electrons, and at the same time, it showed three absorption peaks, which are 46511, 38167, and 27548 cm^{-1} two of them belong to the ligand field. The last peak belongs to the M-L charge transitions as in Fig. S10 [35]. The Pt(IV) complex showed five absorption peaks, which are 47169, 38461, 24154, 18726, and 13679 cm^{-1} ; two belong to the ligand field and

three belong to the transitions of ${}^1\text{A}_{1g} \rightarrow {}^1\text{T}_{1g}$, ${}^1\text{A}_{1g} \rightarrow {}^1\text{T}_{2g}$ respectively as in Fig. S11 [36]. Table 3 shows the electronic transitions, the geometric shape, as well as the magnetic sensitivity. It turned out that the geometric shape of all complexes is octahedral, except for the Ag(I) complex, which is tetrahedral. Fig. 4 shows the proposed chemical structure formula of the complexes.

Molar Conductivity

In coordination chemistry, the electrical conductivity technique was used for the purpose of knowing the ionic formula of the prepared ligand complexes and that the conductivity depends on the number of ions present in the solution as well as the concentration so that when the crystal molar conductivity is close to zero here, the compound has a non-ionic character, and if it is greater, it is ionic. It was found that most of the prepared complexes are non-ionic while the silver complex is ionic [37], which is clarified in Table 3.

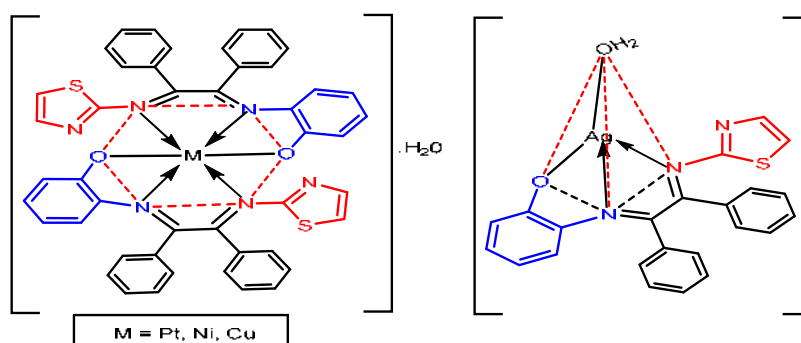
**Fig 4.** The proposed chemical structure formula of the complexes

Table 3. Electronic spectra, magnetic moments and molar conductivity of the DPTYEAP ligand and its metallic

Compounds	λ (nm)	ν^- (cm^{-1})	Transitions	μ_{eff} (B.M)	Hyperdization and Geometry	Λ (ohm^{-1} , $\text{cm}^2, \text{mol}^{-1}$)
DPTYEAP	211	47393	$\pi-\pi^*$			
	248	40322	$\pi-\pi^*$	-----	-----	-----
	253	39525	$n-\pi^*$			
[Ni(DPTYEAP) ₂].H ₂ O	216	46296	Ligand Field			
	259	38610	Ligand Field		sp^3d^2	
	591	16920	$^3\text{A}_{2g}(\text{F}) \rightarrow ^3\text{T}_{1g}(\text{P})$	3.87	Octahedral	15.8
	617	16207	$^3\text{A}_{2g}(\text{F}) \rightarrow ^3\text{T}_{2g}(\text{F})$	(Para.)	Distorted	no ionic
	628	15923	$^3\text{A}_{2g}(\text{F}) \rightarrow ^3\text{T}_{1g}(\text{F})$			
[Cu(DPTYEAP) ₂].H ₂ O	213	46948	Ligand Field			9.9
	264	37878	Ligand Field	1.74	sp^3d^2	no ionic
	542	18450	$^2\text{B}_{1g} \rightarrow ^2\text{E}_g$	(Para.)	Octahedral	
[Ag (DPTYEAP) H ₂ O]	215	46511	Ligand Field	0.00	sp^3	10.5
	262	38167	Ligand Field	(Dia.)	Tetrahedral	no ionic
	363	27548	Charge transfer (MLCT)			
Pt[(DPTYEAP) ₂] Cl ₂ .H ₂ O	212	47169	Ligand Field		d^2sp^3	37.1
	260	38461	Ligand Field		Octahedral	Ionic
	534	18726	$^1\text{A}_{1g} \rightarrow ^1\text{T}_{1g}$		Distorted	1:2
	731	13679	$^1\text{A}_{1g} \rightarrow ^1\text{T}_{2g}$			

X-Ray Diffraction

It was found by measuring the X-ray diffraction spectra that the ligand DPTYEAP and complexes of nickel, platinum, silver, and copper have crystal structures, meaning with a crystalline level and a crystal lattice. This was also shown clearly in Fig. 5(a-e), as well as Table 4 and when comparing the intensity and locations of the peaks of the results obtained with the international standard cards, it was found that these locations belonged to the original basic compounds from which the compounds were prepared and also that the presence of any strange location or peak was not indicated or that it belongs to a substance that is not originally found in the basic compounds, and the reason is that the compounds are new and has not been compared with the various international standard cards [38]. By taking advantage of the data contained in the X-ray diffraction, it was found that the materials that were prepared can be said to be of a nanoscale nature. Fig. S12 and S13 show the XRD patterns for DPTYEAP ligand and chelate complexes.

Scanning Electron Microscopy (FESEM)

The crystal structure of every DPTYEAP ligand and

its complexes was known and studied through the scanning microscopy technique, as well as the surface characteristics morphology, shape, and size of the particles. The ligand was discovered to have a somewhat spherical shape, and the average particle size was 69.19 nm. While the Ni(II) complexes FESEM image revealed that it was entirely spherical and homogeneous and that the average particle size was 71.57 nm. It was discovered that a FESEM image appeared for Ag(I) complexes with a granular and spherical shape and an average particle size of 86.31 nm, as well as for Pt(IV) complexes with a heterogeneous shape and average particle size of 88.67 nm. Lastly, the FESEM image of the Cu(II) complexes revealed that they have square shapes and do not qualify as a nanoscale compound. Through research on FESEM technology, it was discovered that substances with granular crystal structures, or those that fall within the nanoscale, are substances of importance because of the advantages that can be derived from them in the fields of industry, such as thermal or electrical conduction, or in the fields of medicine and pharmacology, such as the treatment of some forms of cancer or some dangerous bacteria, as shown in Fig. 5

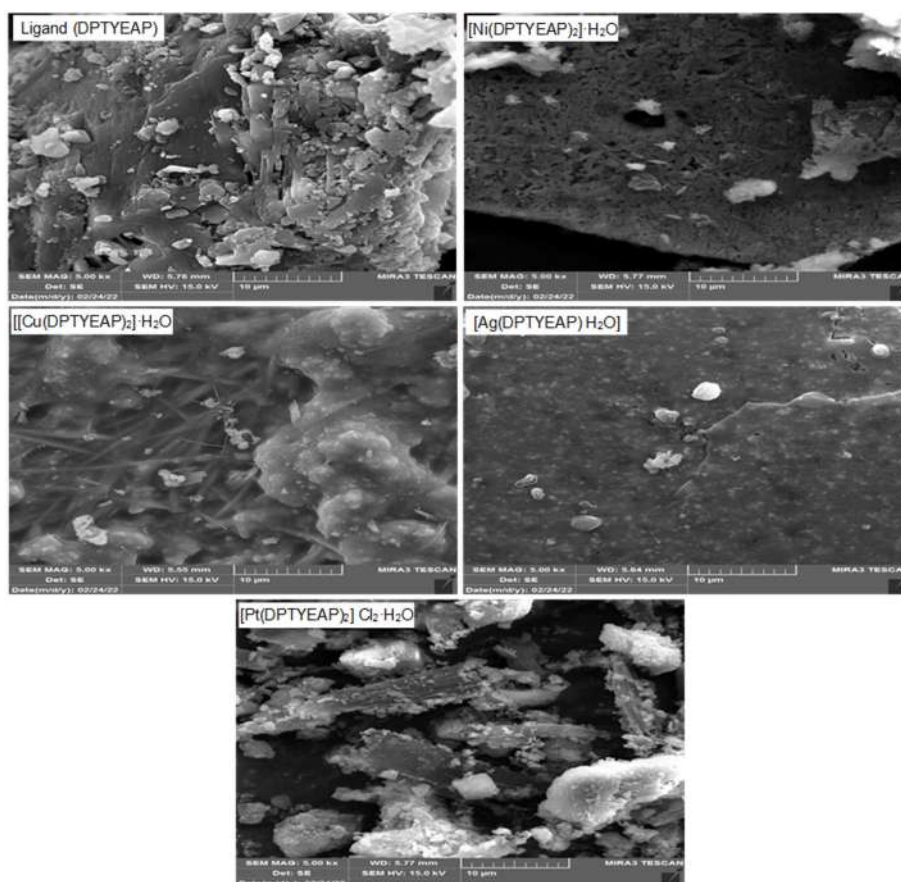


Fig 5. Shows the FESEM image of the (a) synthesized (DPTYEAP) ligand, (b) Ni(II) complex, (c) Cu(II) complex, (d) Ag(I) complex, and (e) Pt(IV) complex

Table 4. Crystallographic data for DPTYEAP ligand and its complexes

Compound	No.	Peak position 2θ ($^{\circ}$)	Height (cts)	Peak width (FWHM)	d -spacing [\AA]	Rel. Int. (%)	D Crystal-lite size (nm)
DPTYEAP	1-	18.5074	969.3600	0.2362	4.7942	100.0000	36.5700
	2-	23.5473	579.5100	0.1968	3.7783	59.7800	43.2600
	3-	12.1177	406.1300	0.1968	7.3040	41.9000	42.4200
	4-	23.0260	385.1600	0.1574	3.8626	39.7300	53.9600
	5-	24.8659	352.8100	0.1574	3.5808	36.4000	54.1400
	6-	14.6978	348.1400	0.1181	6.0271	35.9100	70.9290
[Ni (DPTYEAP) ₂].H ₂ O	1-	25.2984	1095.5000	0.1574	3.5206	100.0000	54.1900
	2-	17.7801	610.1600	0.1574	4.9886	55.7000	53.5200
	3-	24.4030	392.7500	0.1574	3.6477	35.8500	54.1000
[Cu (DPTYEAP) ₂].H ₂ O	1-	25.2370	594.0300	0.1181	3.5290	100.0000	72.0900
	2-	24.3631	457.0400	0.1574	3.6536	76.9400	54.0890
	3-	17.7079	377.3800	0.1574	5.0088	63.5300	53.1000
[Ag (DPTYEAP)H ₂ O]	1-	22.1160	1726.4800	0.1181	4.0194	100.0000	71.6790
	2-	25.2823	351.4500	0.1574	3.5228	20.3600	54.1900
	3-	17.7757	305.9900	0.1181	4.9899	17.7200	71.2000
[Pt (DPTYEAP) ₂]Cl ₂ .H ₂ O	1-	38.1092	1097.3000	0.2362	2.3614	100.0000	37.1800
	2-	44.3202	367.3400	0.2362	2.0439	33.4800	37.9500
	3-	64.4137	345.4300	0.1968	1.4465	31.4800	50.0500

FESEM images of the synthesized DPTYEAP ligand and metal complexes.

Applications

Antioxidant activity

The anti-free radical test was carried out for each of the ligands DPTYEAP and all the prepared metal complexes used in recent years on a large scale to estimate the antioxidant activity. This test depends on the presence of an antioxidant compound that is able to donate an electron or a hydrogen radical to the compound DPPH, which has a violet color, the interaction of the prepared compounds with the compound DPPH and the disappearance of the violet color and its transformation into a more stable compound is an indication that the compounds possess high antioxidants. The measurements for each of the DPTYEAP ligands and the complexes of platinum and nickel showed a high activity of antioxidants towards DPPH. The highest inhibition percentage was reached for the prepared compounds at a concentration of 500 µg/mL, ranging between 71.43–90.83%. While the lowest inhibition percentage which was

at a concentration of 3.9 g/mL, ranged between 16.83–35.00%. The copper complex showed weak antioxidant activity towards DPPH, while the silver complex did not show any antioxidant activity. On the other hand, the value of the half inhibitory concentration IC_{50} for each of the ligand DPTYEAP and all the metal complexes under study ranged between 0.9819–1430.5430, as shown in Table 5 and Fig. 6 shows the antioxidant activity of DPPH scavenger radical for DPTYEAP ligand and its complexes. Based on the values of IC_{50} , that is the lower its value, the greater its antioxidant effectiveness, the compound's effectiveness can be arranged as follows: Ascorbic Acid > Pt[(DPTYEAP)₂] > Ligand > [Ni (DPTYEAP)₂] > [Cu (DPTYEAP)₂] > [Ag (DPTYEAP) H₂O].

Anticancer activity

The MTT cytotoxicity assay was performed on the (MCF-7) breast cancer cell line for both the DPTYEAP ligand and the Pt(IV) complex because it is the most common type of cancer in women. In addition, the normal cell line WRL-68 was used to determine the effect of the DPTYEAP ligand and the Pt(IV) complex on

Table 5. Antioxidant activity from the analysis in vitro for ligand (DPTYEAP) and its metal complexes

Compound	Concentration µg/mL									IC_{50}
	0.00	3.90	7.81	15.62	31.25	62.50	125.00	250.00	500.00	
Ascorbic Acid	0.00	64.50	68.12	72.24	78.66	80.02	85.33	89.66	95.54	0.98
Ligand (DPTYEAP)	0.00	35.00	42.50	47.50	55.83	56.25	62.50	66.66	74.16	17.95
[Ni(DPTYEAP) ₂]. H ₂ O	0.00	25.55	35.60	38.66	45.87	49.81	55.76	59.88	71.43	102.33
[Cu(DPTYEAP) ₂]. H ₂ O	0.00	0.00	4.16	8.30	10.00	12.50	14.16	17.50	22.50	1430.54
[Ag (DPTYEAP) H ₂ O]	0.00	0.00	0.00	0.00	0.00	0.00	0.00	0.00	0.00	-
Pt[(DPTYEAP) ₂]Cl ₂ .H ₂ O	0.00	16.83	25.00	55.00	72.25	75.83	83.33	84.16	90.83	13.33

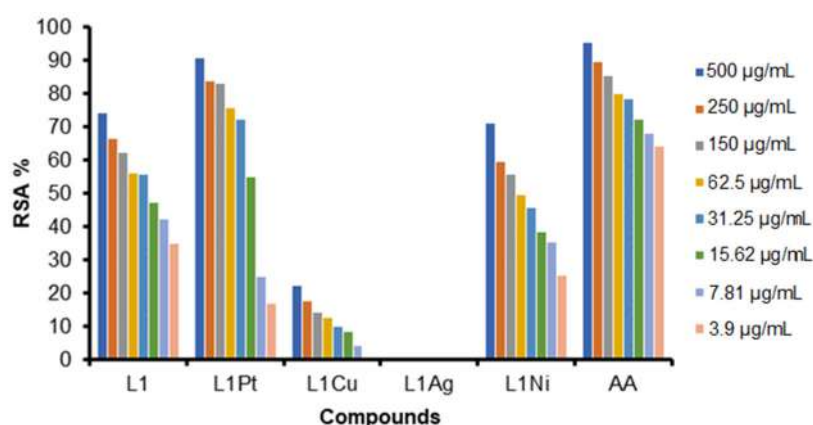


Fig 6. Antioxidant activity of DPPH scavenger radical for DPTYEAP ligand and its complexes

Table 6. Evaluation of the cytotoxicity of both the ligand and the Pt(IV) complex against the MCF-7 cancer cell line after incubation (24 h) at (37 °C)

Conc.	Viability % Mean \pm SD							
	MCF-7 L1	Inhibition of dead cells % MCF-7	WRL-68 L1	Inhibition of dead cells % WRL-68	MCF-7 L1Pt	Inhibition of dead cell % MCF-7	WRL-68 L1Pt	Inhibition of dead cells % WRL-68
400	66.74 \pm 10.04	33.26%	78.13 \pm 4.07	21.87%	42.98 \pm 4.46	57.02%	76.50 \pm 4.58	23.50%
200	79.44 \pm 1.60	20.56%	88.27 \pm 2.61	11.73%	51.66 \pm 2.99	48.34%	84.59 \pm 5.22	15.41%
100	90.39 \pm 1.45	9.61%	93.60 \pm 2.10	6.4%	59.68 \pm 1.54	40.32%	92.21 \pm 2.78	7.79%
50	93.83 \pm 1.29	6.17%	94.17 \pm 1.57	5.83%	73.96 \pm 1.73	26.04%	96.49 \pm 1.29	3.51%
25	94.02 \pm 2.63	5.98%	95.22 \pm 0.82	4.78%	86.73 \pm 1.30	13.27%	96.95 \pm 1.14	3.05%
IC ₅₀	214.8		300.5		33.41		201.1	

healthy cells. By integrating MCF-7 cancer cells and WRL-68 normal cells separately with the prepared compounds at 5% CO₂ atmosphere and 37 °C temperature for 24 h at different concentrations ranging from 400–25 g/mL and using the ELISA device, the absorbance was calculated at the wavelength of 570 nm and using the statistical program and IC₅₀ calculation, the absorbance was calculated at the wavelength of 570 nm and by using the statistical program and IC₅₀ calculation. The ligand's effect on the MCF-7 cancer cell line was found to be less than that of the platinum complex, as it inhibited cells by 33.26, 20.56, 9.61, 6.17, and 5.98% at concentrations of 400, 200, 100, 50 and 25 g/mL, respectively. While at concentrations of 400–25 g/mL, it inhibited the normal cell line WRL-68 by 21.87–4.78%. The platinum complex performed better than the ligand, inhibiting MCF-7 cancer cells with a rate ranging between 57.02–13.27%, while inhibiting normal cells WRL-68 with a rate ranging between 23.5–3.05%. Table 6 and Fig. S14 and S15 show the percentages of inhibition as well as the IC₅₀ for each of the ligands and the platinum complex.

■ CONCLUSION

The measurements were used to determine the geometry of the compound (elementary analysis, electronic and atomic absorption spectroscopy, infrared spectroscopy, molar conductivity, and magnetic susceptibility experiments). These observations were also supported by the octahedral geometry of the Ni(II), Cu(II), and Pt(IV) complexes, as well as the tetrahedral geometry of the Ag(I) complexes. We concluded that the ligand and the Pt(IV) complex have high antioxidants

against free radicals after conducting applications and biological activity tests on the ligand and the prepared complexes. In addition, we discovered through MTT toxicity testing that they are highly effective against breast cancer MCF-7 cells. Through this research, it will be possible to work intensively and precisely on these proposed compounds in the future in order to benefit from them in the medical field and use them as anti-breast cancer drugs. It was also concluded that all compounds exhibit nanotechnology characteristics, indicating the position and direction of the world's view on these compounds, their importance, and their entry into many industrial, medical, and electronic fields.

■ REFERENCES

- [1] Miller, M.M., Vasiliadis, T., Rochman, C.M., Repich, K., Patrie, J.T., Anderson, R.T., and Harvey, J.A., 2023, Factors associated with perceived personal risk for breast cancer among women with dense breasts, *Clin. Imaging*, 93, 34–38.
- [2] Mathelin, C., Domínguez-Gil, B., Özmen, V., and Lodi, M., 2023, European guidelines concerning the transplantation of organs from donors with a history of breast cancer, *Eur. J. Breast Health*, 19 (1), 106–109.
- [3] Karademas, E.C., Roziner, I., Mazzocco, K., Pat-Horenczyk, R., Sousa, B., Oliveira-Maia, A.J., Stamatakis, G., Cardoso, F., Frasilho, D., Kolokotroni, E., Lemos, R., Marzorati, C., Mattson, J., Pettini, G., Spyropoulou, E., Poikonen-Saksela, P., and Simos, P., 2022, The mutual determination of self-efficacy to cope with cancer and cancer-

- related coping over time: A prospective study in women with breast cancer, *Psychol. Health*, 1–14.
- [4] Terrisse, S., Derosa, L., Iebba, V., Ghiringhelli, F., Vaz-Luis, I., Kroemer, G., Fidelle, M., Christodoulidis, S., Segata, N., Thomas, A.M., Martin, A.L., Sirven, A., Everhard, S., Aprahamian, F., Nirmalathasan, N., Aarnoutse, R., Smidt, M., Ziemons, J., Caldas, C., Loibl, S., Denkert, C., Durand, S., Iglesias, C., Pietrantonio, F., Routy, B., André, F., Pasolli, E., Delalogue, S., and Zitvogel, L., 2021, Intestinal microbiota influences clinical outcome and side effects of early breast cancer treatment, *Cell Death Differ.*, 28 (9), 2778–2796.
- [5] Scarim, C.B., and Chin, C.M., 2022, Recent trends in drug development for the treatment of adenocarcinoma breast cancer: Thiazole, triazole, and thiosemicarbazone analogues as efficient scaffolds, *Anti-Cancer Agents Med. Chem.*, 22 (12), 2204–2240.
- [6] Campana, L.G., Galuppo, S., Valpione, S., Brunello, A., Ghiotto, C., Ongaro, A., and Rossi, C.R., 2014, Bleomycin electrochemotherapy in elderly metastatic breast cancer patients: Clinical outcome and management considerations, *J. Cancer Res. Clin. Oncol.*, 140 (9), 1557–1565.
- [7] Özbek, O., and Gürdere, M.B., 2021, Synthesis and anticancer properties of 2-aminothiazole derivatives, *Phosphorus, Sulfur Silicon Relat. Elem.*, 196 (5), 444–454.
- [8] Alizadeh, S.R., and Hashemi, S.M., 2021, Development and therapeutic potential of 2-aminothiazole derivatives in anticancer drug discovery, *Med. Chem. Res.*, 30 (4), 771–806.
- [9] Minickaitė, R., Grybaitė, B., Vaickelionienė, R., Kavaliauskas, P., Petraitis, V., Petraitienė, R., Tumosienė, I., Jonuškienė, I., and Mickevičius, V., 2022, Synthesis of novel aminothiazole derivatives as promising antiviral, antioxidant and antibacterial candidates, *Int. J. Mol. Sci.*, 23 (14), 7688.
- [10] Ding, M., Wu, N., Lin, Q., Yan, Y., Yang, Y., Tian, G., An, L., and Bao, X., 2022, Discovery of novel quinazoline-2-aminothiazole hybrids containing a 4-piperidinylamide linker as potential fungicides against the phytopathogenic fungus *Rhizoctonia solani*, *J. Agric. Food Chem.*, 70 (33), 10100–10110.
- [11] Makam, P., and Kannan, T., 2014, 2-Aminothiazole derivatives as antimycobacterial agents: Synthesis, characterization, *in vitro* and *in silico* studies, *Eur. J. Med. Chem.*, 87, 643–656.
- [12] Farouk Elsadek, M., Mohamed Ahmed, B., and Fawzi Farahat, M., 2021, An overview on synthetic 2-aminothiazole-based compounds associated with four biological activities, *Molecules*, 26 (5), 1449.
- [13] Niu, Z.X., Wang, Y.T., Zhang, S.N., Li, Y., Chen, X.B., Wang, S.Q., and Liu, H.M., 2023, Application and synthesis of thiazole ring in clinically approved drugs, *Eur. J. Med. Chem.*, 250, 115172.
- [14] Ates, B., Koytepe, S., Ulu, A., Gurses, C., and Thakur, V.K., 2020, Chemistry, structures, and advanced applications of nanocomposites from biorenewable resources, *Chem. Rev.*, 120 (17), 9304–9362.
- [15] Razzaq, A.S., and Nahi, R.J., 2021, *In vitro*, evaluation of antioxidant and antibacterial activities of new 1,2,3-triazole derivatives containing 1,2,4-triazole ring, *Syst. Rev. Pharm.*, 12 (1), 196–200.
- [16] Kyhoiesh, H.A.K., and Al-Adilee, K.J., 2021, Synthesis, spectral characterization, antimicrobial evaluation studies and cytotoxic activity of some transition metal complexes with tridentate (N,N,O) donor azo dye ligand, *Results Chem.*, 3, 100245.
- [17] Charisiadis, P., Kontogianni, V.G., Tsiafoulis, C.G., Tzakos, A.G., Siskos, M., and Gerothanassis, I.P., 2014, ¹H-NMR as a structural and analytical tool of intra- and intermolecular hydrogen bonds of phenol-containing natural products and model compounds, *Molecules*, 19 (9), 13643–13682.
- [18] Mohammadi, K., and Zahedi, M., 2012, Tridentate Schiff base compounds of 2-aminophenol: Synthesis, characterization and complexation with IIIA elements, *Global J. Inorg. Chem.*, 3 (2), 1–12.
- [19] Raman, N., 2002, Synthesis, structural characterization, redox and antimicrobial studies of Schiff base copper(II), nickel(II), cobalt(II), manganese(II), zinc(II) and oxovanadium(II) complexes derived from benzil and 2-aminobenzyl

- alcohol, *Pol. J. Chem.*, 76 (8), 1085–1094.
- [20] Abouzied, A.S., Break, M.K.B., Huwaimel, B., Hussein, W., Alafnan, A., and Younes, K.M., 2023, Discovery of a novel synthetic thiazole-benzimidazole conjugate that acts as a potent pancreatic lipase inhibitor using *in silico* and *in vitro* approaches, *Indian J. Pharm. Educ. Res.*, 57 (1), 218–227.
- [21] Emadi, A., 2020, Schiff benzimidazole derivatives: synthesis, properties and antimicrobial activity, *Int. J. Farming Allied Sci.*, 9, 72–82.
- [22] Çakmak, Ş., Koşar Kırca, B., Veyisoğlu, A., Yakan, H., Ersanlı, C.C., and Kütük, H., 2022, Experimental and theoretical investigations on a furan-2-carboxamide-bearing thiazole: Synthesis, molecular characterization by IR/NMR/XRD, electronic characterization by DFT, Hirshfeld surface analysis and biological activity, *Acta Crystallogr., Sect. C: Struct. Chem.*, 78 (3), 201–211.
- [23] More, R.M., Kadam, A.B., Dalvi, S.P., Humne, V.T., and Junne, S.B., 2022, Synthesis, characterization and anti-bacterial activity of Schiff base hybrid from 2-aminothiazole-pyrazolecarboxaldehyde, *J. Adv. Chem. Sci.*, 8 (4), 781–783.
- [24] Rathnayaka, C., George, S., Abeysinghe, J.P., Lynch, V.M., and Gross, D.E., 2022, Synthetic, spectroscopic, and computational investigations of readily accessible 2-phenyl-3-alkylbenzoxazaboroles, *J. Heterocycl. Chem.*, 59 (6), 1036–1044.
- [25] Zelelew, D., Endale, M., Melaku, Y., Kedir, F., Demissie, T.B., Ombito, J.O., and Eswaramoorthy, R., 2022, Synthesis, anti-bacterial, and antioxidant activities of thiazolyl-pyrazoline Schiff base hybrids: A combined experimental and computational study, *J. Chem.*, 2022, 3717826.
- [26] Duc, D.X., and Lanh, H.T., 2022, Microwave-assisted, [Bmim]HSO₄-catalyzed synthesis of tetrasubstituted imidazoles via four-component reaction, *Vietnam J. Sci. Technol.*, 60 (3), 383–390.
- [27] Al-Jibouri, M.N., Hafidh, F.R., and Rasheed, A.M., 2014, Synthesis and characterization of some transition metal complexes with tridentate N₃ donor Schiff base derived from 2-aminothiazole, *Eur. Chem. Bull.*, 3 (6), 559–562.
- [28] Camellia, F.K., Ashrafuzzaman, M., Islam, M.N., Banu, L.A., and Zahan, M.K.E., 2022, Isoniazid derived Schiff base metal complexes: Synthesis, characterization, thermal stability, anti-bacterial and antioxidant activity study, *Asian J. Chem. Sci.*, 11 (4), 23–36.
- [29] Al-Amery, H., Al-Abdaly, B.I., and Albayaty, M.K., 2016, Synthesis, characterization and anti-bacterial activity of new complexes of some lanthanide ions with 15-crown-5 and 18-crown-6, *Orient. J. Chem.*, 32 (2), 1025–1048.
- [30] Abdel-Rahman, L.H., Adam, M.S.S., Al-Zaqri, N., Shehata, M.R., Ahmed, H.E.S., and Mohamed, S.K., 2022, Synthesis, characterization, biological and docking studies of ZrO(II), VO(II) and Zn(II) complexes of a halogenated tetra-dentate Schiff base, *Arabian J. Chem.*, 15 (5), 103737.
- [31] Gul, Z., Din, N.U., Khan, E., Ullah, F., and Nawaz Tahir, M., 2020, Synthesis, molecular structure, anti-microbial, antioxidant and enzyme inhibition activities of 2-amino-6-methylbenzothiazole and its Cu(II) and Ag(I) complexes, *J. Mol. Struct.*, 1199, 126956.
- [32] Barfeie, H., Grivani, G., Eigner, V., Dusek, M., and Khalaji, A.D., 2018, Copper(II), nickel(II), zinc(II) and vanadium(IV) Schiff base complexes: Synthesis, characterization, crystal structure determination, and thermal studies, *Polyhedron*, 146, 19–25.
- [33] Thakar, A., Joshi, K., Pandya, K., and Pancholi, A., 2011, Coordination modes of a Schiff base derived from substituted 2-aminothiazole with chromium(III), manganese(II), iron(II), cobalt(II), nickel(II) and copper(II) metal ions: Synthesis, spectroscopic and antimicrobial studies, *J. Chem.*, 8, 282061.
- [34] Daravath, S., Kumar, M.P., Rambabu, A., Vamsikrishna, N., Ganji, N., and Shivaraj, S., 2017, Design, synthesis, spectral characterization, DNA interaction and biological activity studies of copper(II), cobalt(II) and nickel(II) complexes of 6-amino benzothiazole derivatives, *J. Mol. Struct.*, 1144, 147–158.
- [35] Swami, S., Sharma, N., Agarwala, A., Shrivastava, V.,

- and Shrivastava, R., 2021, Schiff base anchored silver nanomaterial: An efficient and selective nano probe for fluoride detection in an aqueous medium, *Mater. Today: Proc.*, 43, 2926–2932.
- [36] Adnan, S., Al-Adilee, K.J., and Abedalrazaq, K.A., 2020, Synthesis, spectral characterization and anticancer studies of novel azo Schiff base and its complexes with Ag(I), Au(III) and Pt(IV) ions, *Egypt. J. Chem.*, 63 (12), 4749–4756.
- [37] Elkanzi, N.A., Hrichi, H., Salah, H., Albqmi, M., Ali, A.M., and Abdou, A., 2023, Synthesis, physicochemical properties, biological, molecular docking and DFT investigation of Fe(III), Co(II), Ni(II), Cu(II) and Zn(II) complexes of the 4-[(5-oxo-4,5-dihydro-1,3-thiazol-2-yl)hydrazono]methyl} phenyl 4-methylbenzenesulfonate Schiff-base ligand, *Polyhedron*, 230, 116219.
- [38] Rajmane, S., Ubale, V.P., Dama, L.B., Asabe, M.R., and More, P.G., 2013, Synthesis, spectral and biological studies of thiazole Schiff base derived from 4-(2'-fluorophenyl)-2-aminothiazole, *Int. J. Pharm. Sci. Invent.*, 2 (7), 33–36.

Supplementary Data

This supplementary data is a part of a paper entitled “The Dependence of Boron Concentration in Diamond Electrode for Ciprofloxacin Electrochemical Sensor Application”.

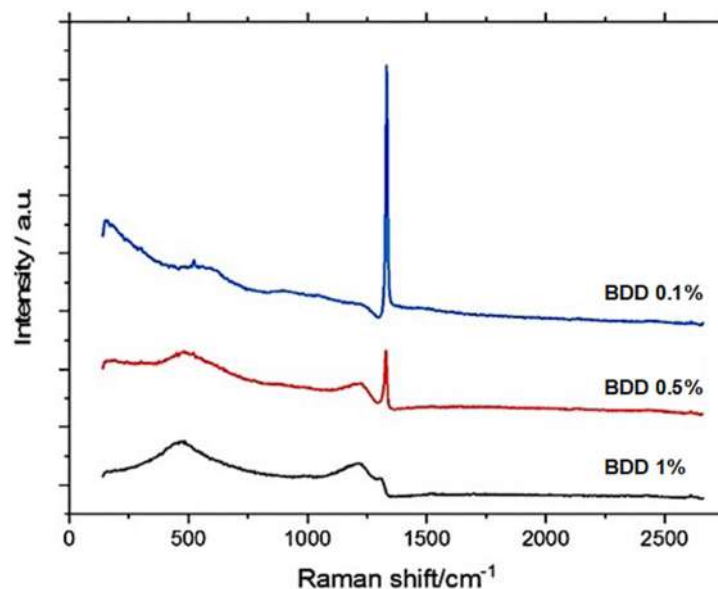


Fig S1. Raman spectra of BDD electrodes with a boron concentration of 0.1, 0.5, and 1%

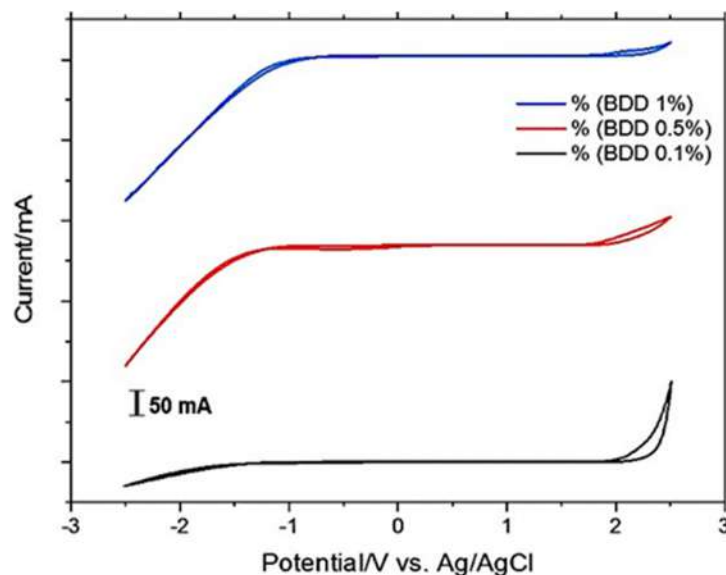


Fig S2. CV curves of the BDD electrodes with a boron concentration of 1% (blue), 0.5% (red), and 0.1% (black), with potentials ranging from -2.5 to 2.5 V in an aqueous solution of 0.1 M H₂SO₄ at a scan rate of 100 mV s⁻¹

The Dependence of Boron Concentration in Diamond Electrode for Ciprofloxacin Electrochemical Sensor Application

Ilmi Nur Indriani Savitri¹, Prastika Krisma Jiwanti^{2*}, Ilmanda Zalzabhila Danistya Putri¹, Irkham Irkham³, Yasuaki Einaga⁴, Ganden Supriyanto¹, Yew Hoong Wong^{5,6}, Sachin Kumar Srivastava⁷, and Che Azurahaman Che Abdullah⁸

¹Department of Chemistry, Faculty of Science and Technology, Universitas Airlangga, Surabaya 60115, Indonesia

²Nanotechnology Engineering, Faculty of Advanced Technology and Multidiscipline, Universitas Airlangga, Surabaya 60115, Indonesia

³Department of Chemistry, Faculty of Mathematics and Natural Sciences, Universitas Padjadjaran, Jl. Raya Bandung-Sumedang Km. 21, Jatinangor, Sumedang 45363, Indonesia

⁴Department of Chemistry, Keio University, 3-14-1 Hiyoshi, Yokohama 223-8522, Japan

⁵Department of Mechanical Engineering, Faculty of Engineering, Universiti Malaya, Kuala Lumpur 50603, Malaysia

⁶Center of Advanced Materials, Faculty of Engineering, Universiti Malaya, Kuala Lumpur 50603, Malaysia

⁷Department of Physics, Indian Institute of Technology Roorkee, Haridwar, Uttarakhand 247667, India

⁸Department of Physics, Faculty of Science, Universiti Putra Malaysia, Serdang 43400, Malaysia

* **Corresponding author:**

email: prastika.krisma@ftmm.unair.ac.id

Received: February 7, 2023

Accepted: April 11, 2023

DOI: 10.22146/ijc.82135

Abstract: This study investigates the effects of boron concentration on boron-doped diamond (BDD) electrodes for electrochemical sensors of ciprofloxacin. The effects of boron concentration, scan rate, and pH of BDD electrodes with boron concentrations of 0.1, 0.5, and 1% were examined to determine the optimal conditions. Furthermore, square wave voltammetry (SWV) in phosphate buffer pH 7 was used to analyze the electrochemical behavior of ciprofloxacin. The results revealed a linear calibration curve in the concentration range of 30–100 μM with a recovery of 85–110%. Meanwhile, BDD electrode with the highest boron concentration in this experiment (1%) showed a very low limit of detection of 0.17 μM , meaning that 1% BDD gave a highly sensitive and significant measurement result for the electrochemical sensor of ciprofloxacin. With the results given, this study provides new insights for controlling boron concentrations in diamond electrodes for the electrochemical sensors of quinolone antibiotics.

Keywords: boron-doped diamond; ciprofloxacin; human and health; voltammetry

■ INTRODUCTION

Ciprofloxacin (1-cyclopropyl-6-fluoro-4-oxo-7-piperazin-1-yl-quinolone-3-carboxylic acid) or CIP is a second-generation fluoroquinolone, the most active quinolone antibiotic derivative in medical treatment which has effective antibacterial activity [1-4]. CIP is commonly used in farm and animal husbandry, as well as in the prevention and etiology of microbial diseases.

However, CIP is poorly metabolized in the human body; in which 70% of this antibiotic will be excreted in feces and urine, and large amounts of the residues can be found in surface water and wastewater [2,5-6]. In addition, the residue of CIP is one of the major chemical contaminants in milk and dairy products, making them unfit for consumption and can pose several risks to public health [5-6]. Due to the presence of these antibiotic compounds in the environment for a long time,

pathogenic microorganisms can become persistent and survive in the environment as they are difficult to decompose on their own. Therefore, European countries, through the European Union law (Eur-Lex), state that CIP in the aquatic environment (threshold $EC_{50} \leq 1$ ppm) is highly toxic to aquatic and soil organisms [7], and set the maximum residue limit for this antibiotic in the milk of 0.1 mg L^{-1} [8].

To produce CIP detection results with high sensitivity and accuracy, several methods can be employed, such as high-performance liquid chromatography (HPLC) [9], UV-VIS spectrophotometry [10], electrochemical analysis [11], and capillary electrophoresis [12]. However, these methods are expensive. They require a lot of chemicals and take a long time. As an alternative, the application of electrodes as electrochemical sensors was analyzed in this study using the electroanalytical voltammetry method. This is possible because CIP has electroactive molecules; the piperazine ring in the structure of CIP can be oxidized electrochemically. This method has numerous advantages, including being effective and efficient and having high sensitivity, low cost, fast analysis speed, and simple instrumentation [13].

Studies to determine the electrochemical properties of CIP by electrochemical methods have been carried out with various electrodes, such as glassy carbon electrode modified with graphene oxide and nickel nanoparticles (NiONPs-GO-CTS: EPH/GCE) [14], reduced-GO/GCE [5], gold nanoparticles (AuNPs), and a chitosan (CHI) nanocomposite film coated on a screen-printed electrode (SPE) [4], GCE modified with activated carbon and AuNPs (AuNPs/AC/GCE) [3], and glassy carbon paste electrode [15] for laboratory analyses of sensing in biological samples and wastewater. In the last 10 years, the uses of boron-doped diamond (BDD) electrodes have grown rapidly and attracted the attention of researchers around the world, especially for their application as electrochemical sensors. For example, the voltammetric behavior of irreversibly oxidized CIP has been investigated using the cyclic voltammetry (CV) technique with BDD electrodes [16]. The effect of doping level on the electrochemical reduction of CO_2 at BDD electrodes has also been studied [17].

Different from conventional metal and carbon sp^2 electrodes, BDD electrodes have good electrochemical properties, i.e., wide potential window (up to 3.5 V), good sensitivity and stability, low background current, high thermal conductivity, and electrochemical corrosion resistance, thus having been widely used for electroanalysis, electrocatalyst, and electrosynthesis applications [18-22]. These properties may depend on several factors, such as boron doping level, surface termination, and impurities of non-diamond sp^2 -bonded carbon [23]. BDD electrode consists of a carbon structure with mostly sp^3 C-C bonds; lattice defects generated by boron atoms can produce electrodes with adjustable conductivity [24]. In other words, the boron concentration of the BDD electrode determines the electrical conductivity of the diamond, which affects its electrochemical properties. The level of doping can control conductivity, and a diamond can be changed from an insulator to a conductor-like metal diamond if doped with boron in a relatively high doping concentration (103–104 ppm) so that it can be used as an electrode material.

This study aims to examine the effects of boron concentration in BDD electrodes on the performance of electrochemical sensors of ciprofloxacin. For experimental purposes, three BDD electrodes with different boron concentrations were prepared by controlling the ratio of boron and carbon sources to be used to study the relationship between boron concentration in BDD electrode and its ability to detect quinolone antibiotics.

■ EXPERIMENTAL SECTION

Materials

CIP ($\geq 98\%$), sulfuric acid (H_2SO_4 , 95–98%), Levofloxacin (LEV, 98–102%), Ofloxacin (OFL, $\geq 98\%$), and D-glucose (D-GLU, $\geq 99\%$) were purchased from Sigma Aldrich. Two samples of pharmaceutical tablets containing 500 mg CIP were purchased at a local pharmacy. In addition, this study used sodium dihydrogen phosphate (NaH_2PO_4 , $\geq 99\%$) and sodium hydrogen phosphate (Na_2HPO_4 , $\geq 99\%$) from Merck, sterilized animal milk, and wastewater from a river in

East Java, Indonesia. Milk and wastewater were filtered before use, whereas all chemicals were used without further purification.

Instrumentation

The preparation of 0.1, 0.5, and 1% (B/C) BDD electrodes refers to a previous report, namely by depositing BDD on the surface of the silicon wafer (111) using a microwave plasma-assisted chemical vapor deposition (MPCVD) machine (Model AX6500X, CORNES Technology Corp) [23]. The deposition time was 6 h. Raman spectra were recorded with Acton SP2500 (Prince Instruments) in ambient air at room temperature. All electrochemical measurements were performed with an Emstat3+ Blue Palmsens potentiostat.

Procedure

BDD electrodes were characterized by Raman spectroscopy with an excited wavelength of 532 nm and CV. Prior to electrochemical measurements, the BDD electrodes with a diameter of 0.5 cm were always rinsed with an aqueous solution by sonication. To remove contaminants from the surface electrodes, electrochemical pretreatment was carried out by CV prepared with a potential range of -2.5 to 2.5 V for 40 cycles in an aqueous solution of 0.1 M H_2SO_4 . The CV measurements also checked the potential window for each BDD electrode.

CIP stock solution of 1 mM was prepared by dissolving CIP in 0.1 M H_2SO_4 , while the phosphate-buffered saline (PBS) was made by mixing 0.1 M NaH_2PO_4 and 0.1 M Na_2HPO_4 and then adjusting it to the required pH ($5-8$). Meanwhile, the standard stock solution of the pharmaceutical tablet sample was produced by crushing a tablet in a mortar and dissolving the powder in 0.1 M H_2SO_4 . A single-compartment three-electrode cell was used for electrochemical measurements with BDD as the working electrode, Ag/AgCl (saturated KCl) as the reference electrode, and Pt mesh as the counter electrode. The measurements of electrochemical sensors for CIP were performed using the square wave voltammetry (SWV) method by dissolving 1 mM CIP in 0.1 M PBS pH 7 and placing it into an electrochemical cell with a total volume of 5 mL. The optimization of parameters in these measurements includes signal per

background, potential scan rate, linearity, selectivity, and optimal pH. Linearity determines the limit of detection (LOD), limit of quantification (LOQ), and the sensitivity of the BDD electrode. LOD was defined as three times the standard deviation of the intercept, while LOQ was defined as ten times the standard deviation of the intercept, both divided by the slope of the calibration curve. In this study, the voltammetry method was applied to detect CIP in pharmaceutical tablets, milk, and wastewater samples. The parameters of the validity of this method are characterizations of %RSD, %reproducibility, and %recovery.

RESULTS AND DISCUSSION

Characteristics of the BDD Electrode

Raman spectroscopy provides information to determine the presence of sp^2 -bonded carbon on the surface electrode [23]. In addition, the structure of the diamond can be identified by the Raman peaks corresponding to the sp^3 -bonded carbon [17]. Fig. S1 shows that the peaks of 0.1 , 0.5 , and 1% BDD electrodes were at around 1331 , 1329 , 1215 cm^{-1} ; none of them was around 1500 cm^{-1} , meaning that all BDD electrodes have no sp^2 carbon impurities. In the BDD electrode, boron atoms whose radius is larger than carbon displace diamond carbon atoms, which can cause expansion of the diamond lattice and tensile stresses. With an increase in the boron concentration of the BDD electrode, the wavenumber gradually becomes lower due to the tensile stress. Meanwhile, the potential window of the BDD electrodes with various boron concentrations of 0.1 , 0.5 , and 1% was measured by CV with a potential window of -2.5 to 2.5 V in an aqueous solution of 0.1 M H_2SO_4 at a scan rate of 100 $mV s^{-1}$. As seen in Fig. S2, the width of the potential window decreases with increasing boron concentration [25]. This may be due to the lower fraction of the exposed grain boundaries. Furthermore, the low boron concentration in the BDD structure causes the electronic state at a negative potential to decrease [17].

The signals per background (S/B) of the three BDD electrodes with various boron concentrations were measured by SWV in 50 μM CIP and 0.1 M PBS at

potentials ranging from 0 to 1.8 V (vs. Ag/AgCl), with and without CIP. The ratio between the background current and the CIP signal was identified from these measurements. The S/B values of 0.1, 0.5, and 1% BDD electrodes were 11.85, 14.97, and 16.90, respectively. These results show that 1% BDD electrode, which has the highest boron concentration, has a greater current response per background than the other two BDD electrodes with lower boron concentrations of 0.1 and 0.5% (Fig. 1). The higher the anodic peak current, the higher the electrochemical reactivity due to the increased density of electronic states formed between the band gaps of the diamond structure [17]. Meanwhile, the background currents of all BDD electrodes in this study are relatively low.

Effects of Scan Rate Variations

Determination of variations in the scan rate of BDD electrodes with various boron concentrations was measured by CV in 0.1 M PBS pH 7 containing 50 μM CIP at scan rates ranging from 20 to 120 mV/s; the peak increases with increasing scan rate (Fig. 2). This proves

that the difference of scan rate affects the anodic peak current response. These results also reveal that the higher the scan rate, the faster the electron transfer occurs to the surface electrode and the higher the peak of each BDD electrode. In addition, the peak potential is shifted to the positive potential only and not to the negative potential, indicating that the electrode process is electrochemically irreversible (Fig. 2) [16].

The scan rate also corresponds to an increase in the rate of diffusion of species to the electrode; the higher the scan rate, the thinner the resulting diffusion layer. This leads to easier electron transfer on the surface of the electrode, resulting in a higher peak current. Conversely, the smaller the scan rate, the larger the diffusion layer. Thus, the electron transfer process on the surface of the electrode can be inhibited, and the peak current is also smaller. Diffusion control can be seen from the linearity between the square root of the scan rate and the peak current. The linearity between the increased square root of the scan rate and the anodic peak at the BDD electrodes with various boron concentrations of 0.1, 0.5, and 1% is shown by the correlation coefficient (R^2) value

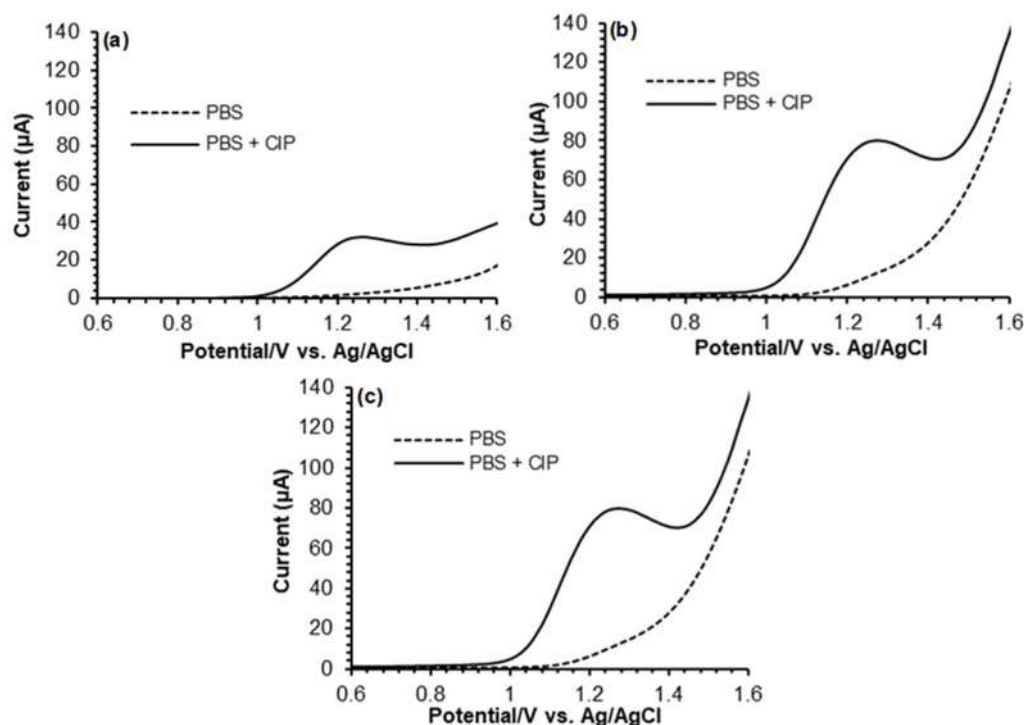


Fig 1. Background current curves by SWV technique of BDD electrodes with a boron concentration of (a) 0.1%, (b) 0.5%, and (c) 1% in 0.1 M PBS pH 7 containing 50 μM CIP

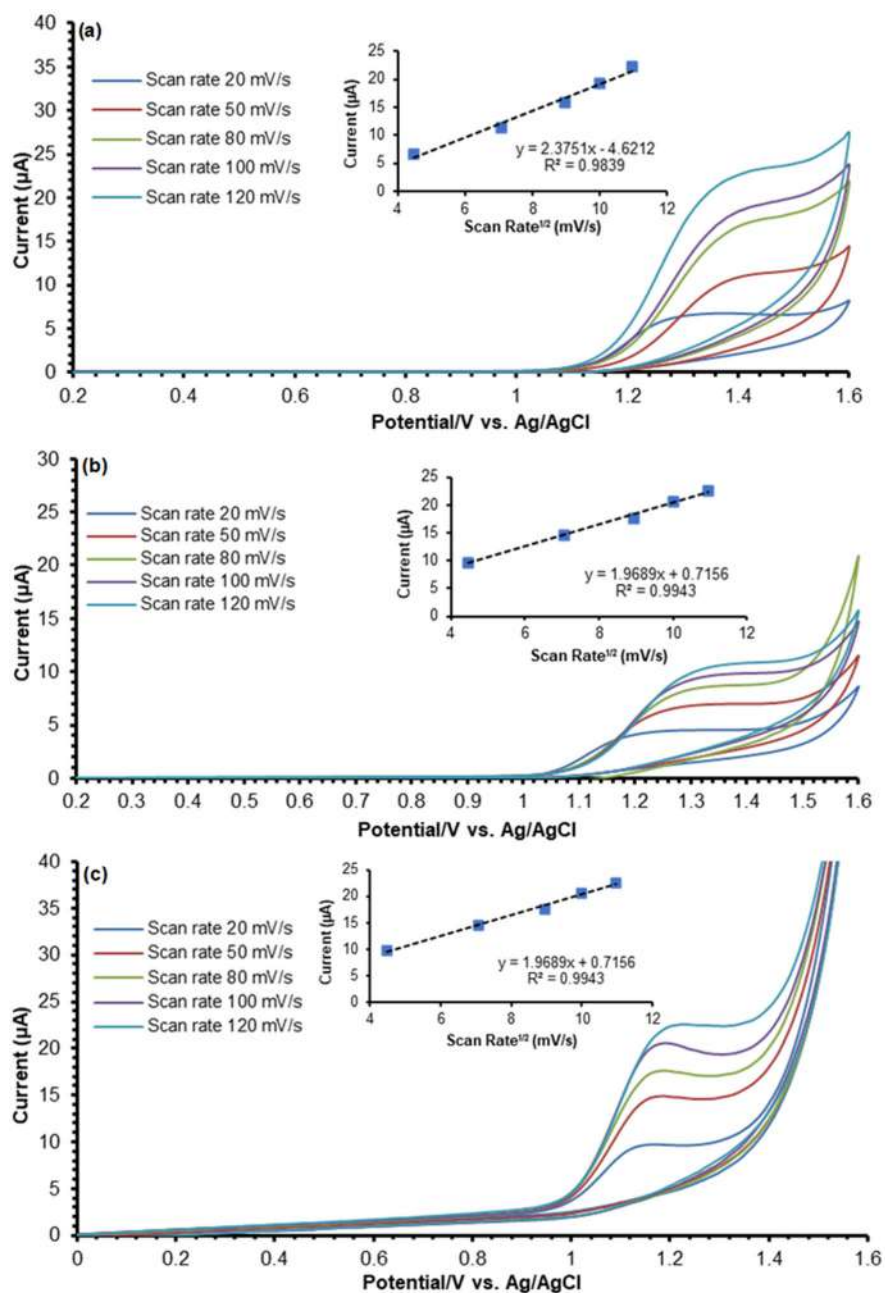


Fig 2. CV with variations in scan rate and the linearity with the square root of the scan rate of BDD electrodes with boron concentration of (a) 0.1%, (b) 0.5%, and (c) 1% in 0.1 M PBS pH 7 containing 50 µM. Inset data is the correlation between square root of scan rate and the current

of 0.99. This suggests that the electrochemical reaction is a diffusion-controlled process [26].

Effects of pH

The investigation of the effects of pH on BDD electrode was carried out to determine the optimal pH conditions indicated by the highest current response. This

is extremely important as the redox reactions of organic compounds mainly depend on the pH of the supporting electrolyte [4]. Measurements were made using SWV, as the method is known to promote high sensitivity measurements and have a high scanning speed, thus allowing for a short analysis time. These measurements were performed in the potential range from 0 to 1.8 V in

0.1 M PBS (with a pH variation of 5 to 8) containing 50 μM CIP. From these measurements, PBS pH 7 was determined for use in further experiments in this study. Phosphate buffer is used to maintain the pH of the solution and reduce the rate of migration. In addition, the use of phosphate buffer also produces better peak intensity, peak resolution, and voltammogram curves [4].

As shown in Fig. 3, the CIP oxidation potential and current are influenced by pH. The different peak current responses can be caused by the large number of measurable molecules of CIP on the surface electrode; the higher the peak current, the more analyte molecules are measured on the surface electrode.

An increase in pH shifts the potential to a negative

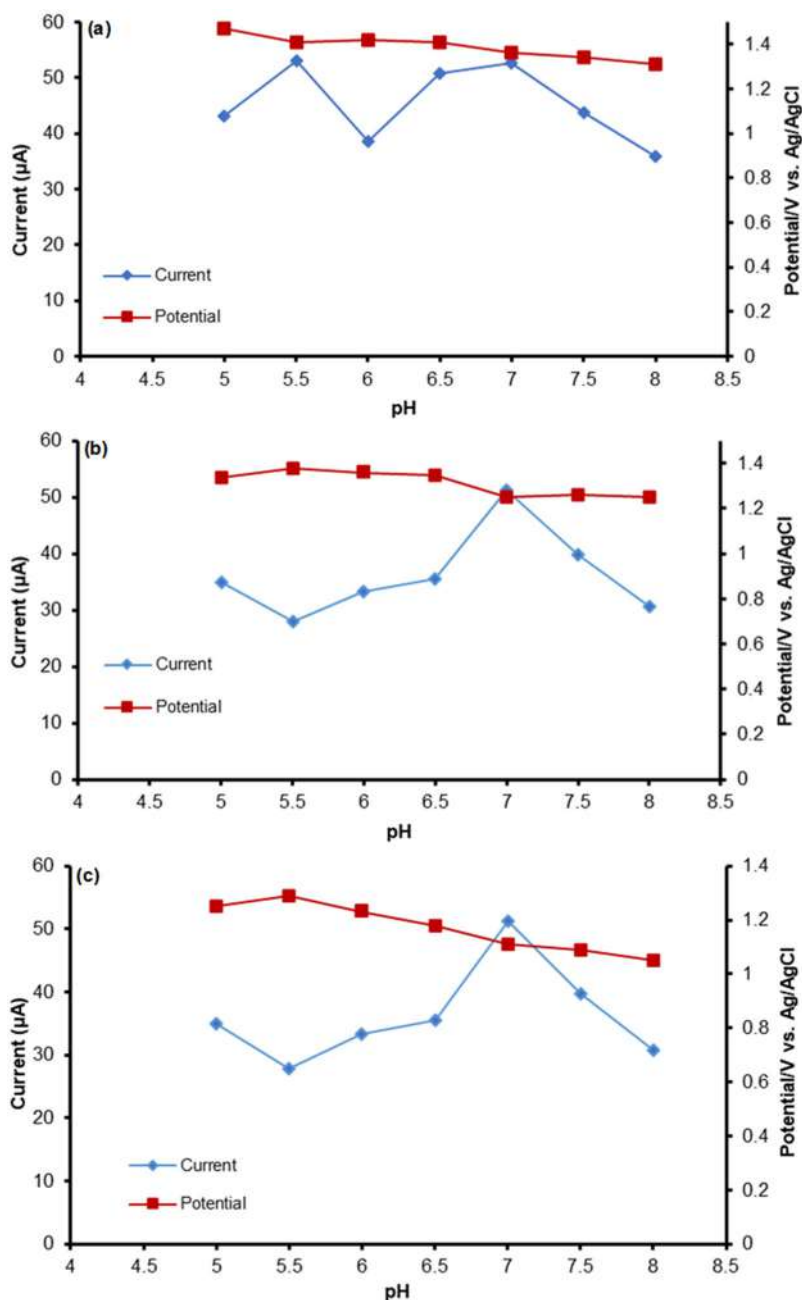


Fig 3. SWV of BDD electrodes with a boron concentration of (a) 0.1%, (b) 0.5%, and (c) 1% in PBS pH 5–8 containing 50 μM CIP; the effects of pH on the anodic peak current and peak potential at the three BDD electrodes are shown in the inset

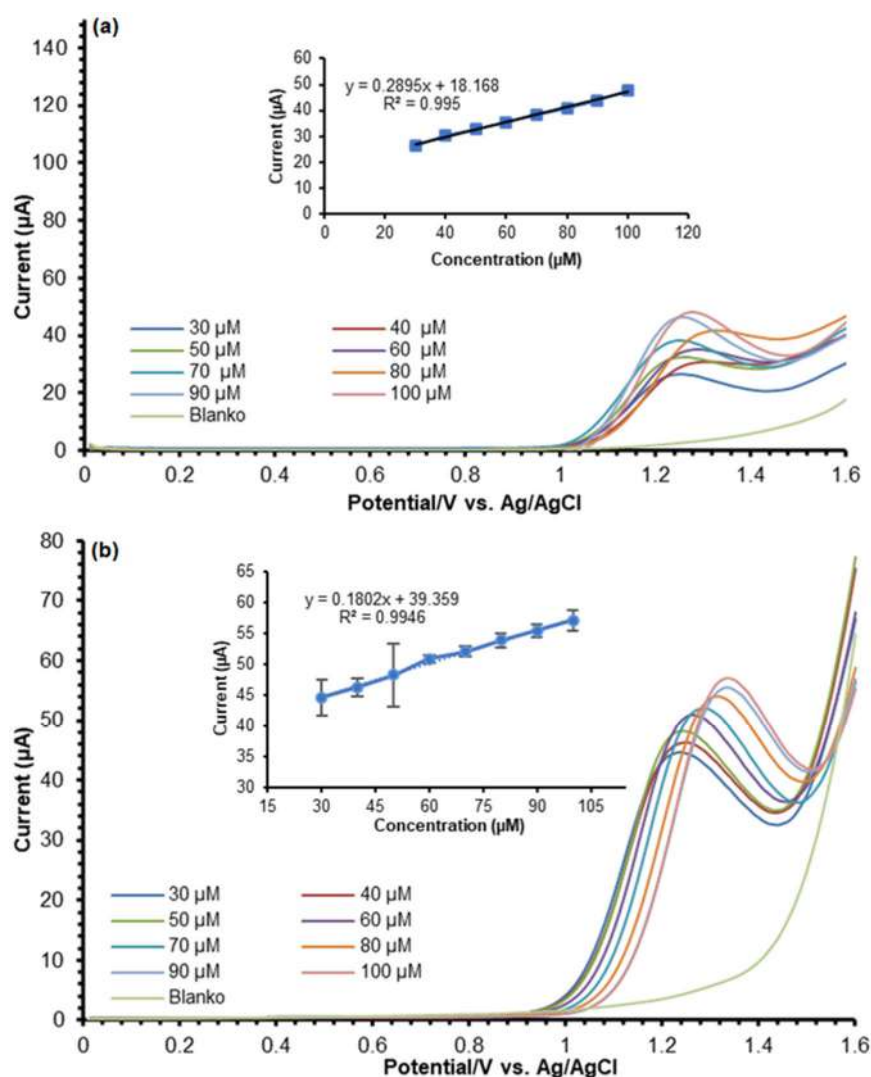
value, suggesting the involvement of protons in the electrooxidation of CIP. Furthermore, the pKa values of CIP, which were reported to be 6.16 and 8.23, can also be negatively and positively charged under various pH values (Fig. 3). CIP is present in the cationic form at $\text{pH} < 6.16$, in zwitterionic form at $\text{pH} 6.16\text{--}8.23$, and in the anionic form at $\text{pH} > 8.23$ [27].

Effects of CIP Concentration

The electrochemical behavior of CIP in the three BDD electrodes was examined using SWV in 0.1 M PBS at potentials ranging from 0 to 1.8 V (vs. Ag/AgCl) and compared. In this analysis, linearity is the ability of the method to provide a balanced response to the analysis of concentrations in a sample. The calibration curves for the

detection of CIP in the BDD electrodes were plotted linearly from the range of 30 to 100 μM . Meanwhile, the correlation coefficient (R^2) values of 0.1, 0.5, and 1% BDD electrodes were 0.995, 0.9946, and 0.997, respectively (Fig. 4).

Limit of detection (LOD) is the smallest quantity of detectable analyte contained in a sample that gives a significant response compared to the blank [28]. The LOD of the three BDD electrodes was measured by the SWV method at various concentrations of CIP from 0 to 1.8 V, with an amplitude of 0.05 V, a frequency of 50 Hz, and a step potential of 0.012 V (Table 1). Measurements were repeated three times for each concentration to obtain the average peak current. To find the LOD, the standard deviation is multiplied by three and divided by



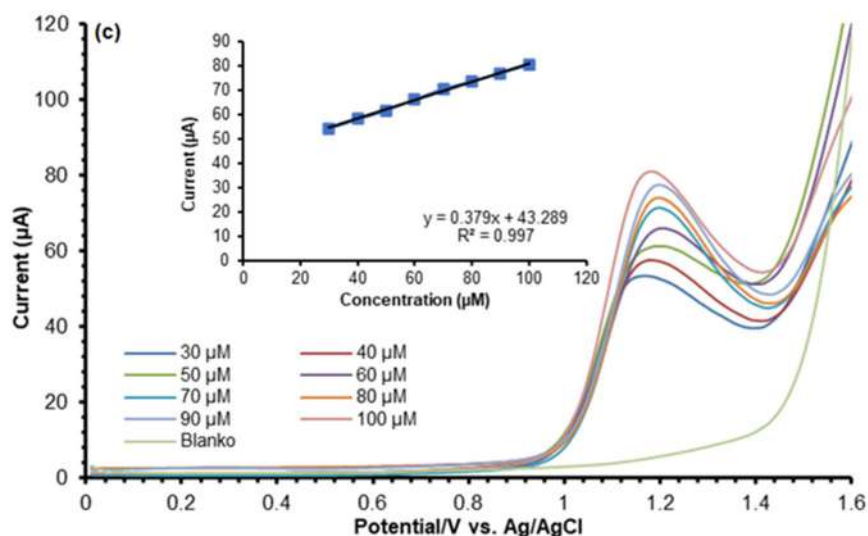


Fig 4. SWV of the BDD electrode with the boron content of (a) 0.1%, (b) 0.5%, (c) 1% in different CIP concentrations range 30–100 μM . The insets show the linear correlation between CIP concentration and CIP oxidation current response

Table 1. Comparison of the performance of CIP electrochemical sensors in the present work with the results of other published studies

Working electrode	Linear range (μM)	LOD (μM)	Ref.
NiONPs-GO-CTS: EPH/GCE	0.04–0.97	6.00	[14]
rGO/GCE	6.00–40.00	0.21	[5]
AuNPs/AC/GCE	0.50–25.00	0.20	[3]
BDDP-printed	1.00–30.00	0.58	[30]
0.1% BDD	30.00–100.00	0.53	This work
0.5% BDD	30.00–100.00	0.43	This work
1% BDD	30.00–100.00	0.17	This work

the slope of the calibration curve. The limits of detection for the measurement of CIP in 0.1, 0.5, and 1% BDD electrodes were 0.53, 0.43, and 0.17 μM , respectively. Meanwhile, the limits of quantitation (LOQ) for CIP of the three BDD electrodes were 1.78, 1.44, and 0.59 μM , respectively. These results show that 1% BDD electrode has the smallest LOD and LOQ among the three BDD electrodes. This can be explained by the relatively higher electrical conductivity of 1% BDD electrode compared to the other BDD electrodes with boron concentrations of 0.5 and 0.1% [17,29], which then can drive higher current response for CIP analysis. On the other hand, as displayed in Fig. 3 and 6, the background current is relatively the same for all BDD electrodes. In addition, from the inset data presented in Fig. 4, it can be seen that the 1% BDD electrode shows the highest sensitivity (0.379 $\mu\text{M}/\mu\text{A}$).

The LOD of 1% BDD electrode is 0.17 μM , while the maximum residue limit for CIP in milk, according to Eur-Lex is 0.1 mg L^{-1} (= 0.30 μM). Thus, the developed method can be considered successful in detecting CIP after simple dilution of real samples, which does not require laborious extraction procedures or other materials to maintain the electroactivity of the sensor. Overall, the wide linear concentration range and good sensitivity of the developed method make it a suitable electrochemical application for sensing CIP in pharmaceuticals and real samples.

Reproducibility and Selectivity

In this study, the %RSD shows the stability and good precision of the BDD electrodes. The lower the concentration of the analyte tested, the greater the %RSD

value and the higher the difficulty of the test to achieve good precision. The developed method was employed with 10 replications on different measurement days using 50 μM CIP to test its reproducibility. The %RSD values of the BDD electrodes with boron concentrations of 0.1, 0.5, and 1% were 1.46, 3.23, and 1.77%, respectively. The acceptable %RSD value can be determined by the Horwitz ratio (HorRat) based on the concentration of the analyte used, where the %RSD of the three BDD electrodes is acceptable as the value is < 7 at 50 μM analyte concentration, meaning that all BDD electrodes have good precision. This also indicates good reproducibility of the developed method. The validation parameters for the determination of CIP electrochemical sensors are shown

in Table 2. Among the three electrodes, 1% BDD electrode shows better sensitivity, lower LOD, and higher S/B compare to 0.1 and 0.5% BDD electrodes.

In the analysis, selectivity is the ability of the method to measure a particular substance, such as an analyte, for an accurate and specific determination of the presence of other compounds in an aquatic environment or other environments that may be present in complex matrices. Apart from CIP, two other antibiotics, namely LEV and OFL are considered as potential interfering agents. These antibiotics, as well as D-GLU which may be contained in milk, are known to oxidize at potentials close to that of CIP. Therefore, these compounds can affect the voltammetry response of CIP.

Table 2. Validation parameters for the determination of CIP electrochemical sensors

Electrode	Parameter				
	S/B	Sensitivity	R ²	LOD (μM)	%RSD
0.1% BDD	11.850	0.280	0.995	0.530	1.460
0.5% BDD	14.970	0.180	0.994	0.430	3.230
1% BDD	16.900	0.370	0.997	0.370	1.770

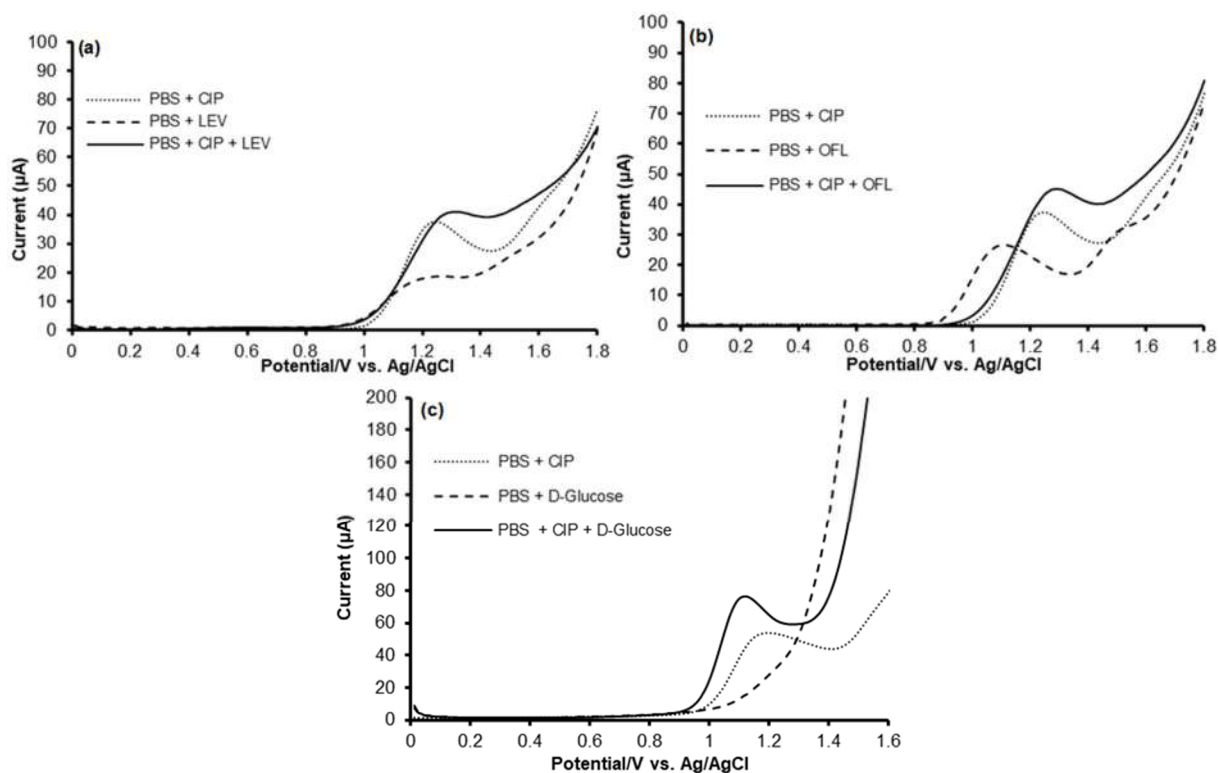


Fig 5. SWV of BDD electrodes with boron concentration of (a) 0.1%, (b) 0.5%, and (c) 1% in 0.1 M PBS pH 7 containing 50 μM CIP and LEV

The ratio of the concentrations of CIP to interfering substances is 1:1. In this study, the oxidation peaks of CIP at 0.1, 0.5, and 1% BDD electrodes were found to increase after the addition of LEV and OFL, with LEV and OFL peaks having different currents and potentials from CIP peak. This suggests that the presence of LEV and OFL in an aqueous solution together with CIP is unobtrusive as they have different current peaks (Fig. 5-7). Furthermore, in the presence of D-GLU, only the peak of CIP gives a

signal response, meaning that the presence of D-GLU does not interfere with the detection of CIP. Overall, LEV and OFL have the greatest impact on CIP as they are quinolone antibiotics, and the structural similarity of the coexisting antibiotics and interfering ions affects the detection of CIP within an acceptable level. The differences between the peak current and peak potential of CIP with the addition of interferences are shown in Table 3.

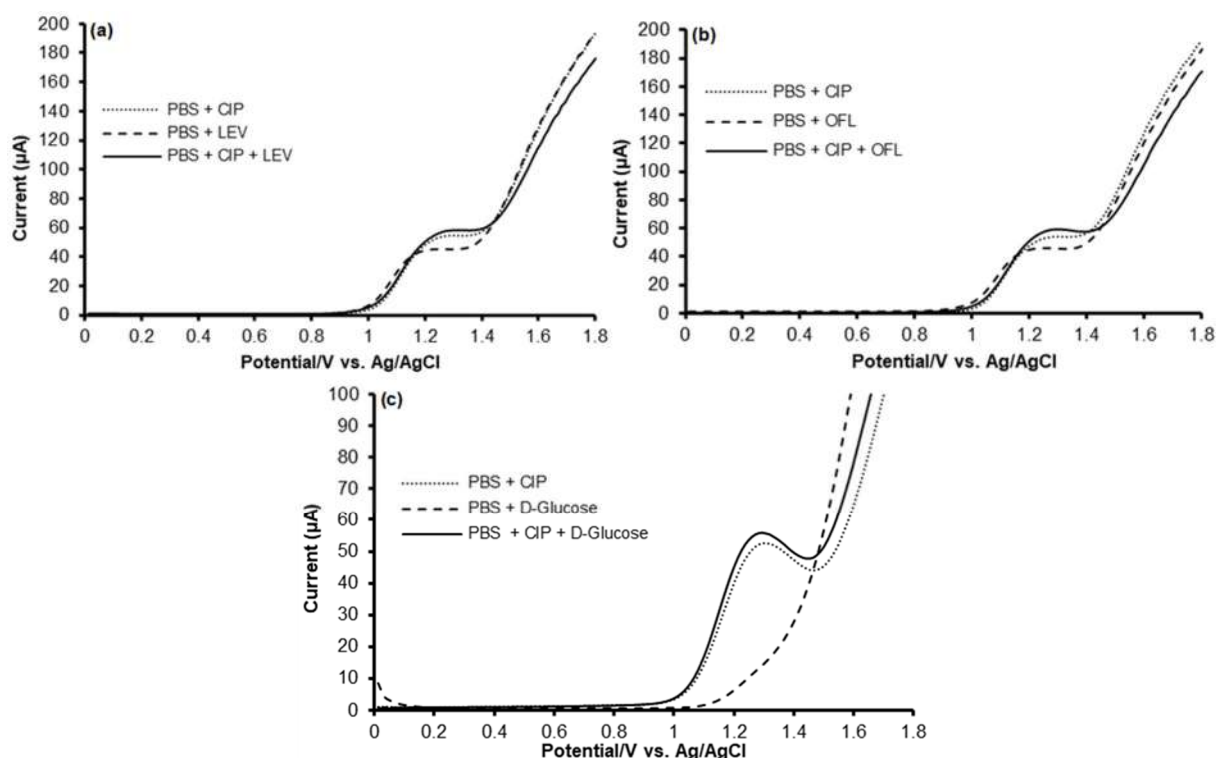
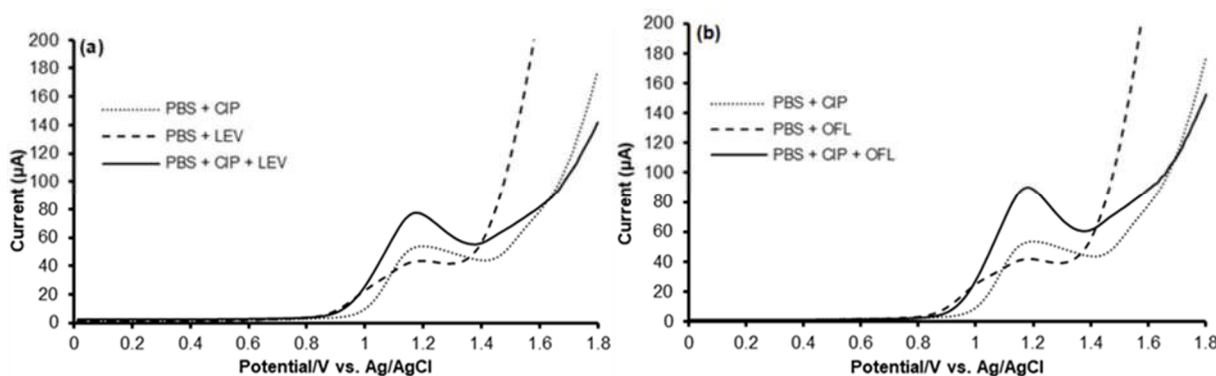


Fig 6. SWV of BDD electrodes with boron concentration of (a) 0.1%, (b) 0.5%, and (c) 1% in 0.1 M PBS pH 7 containing 50 μM CIP and OFL



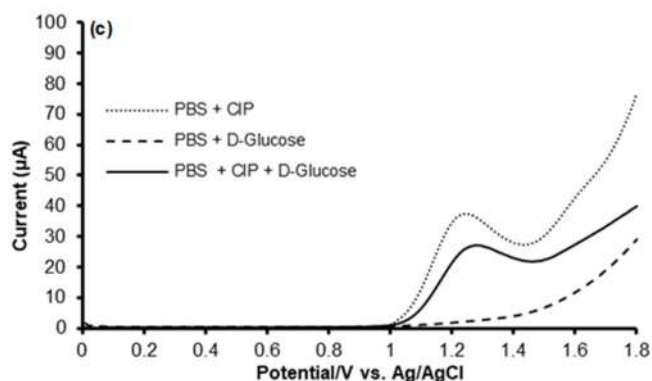


Fig 7. SWV of BDD electrodes with boron concentration of (a) 0.1%, (b) 0.5%, and (c) 1% in 0.1 M PBS pH 7 containing 50 μM CIP and D-GLU

Table 3. The differences between the peak current and peak potential in the selectivity test with the addition of interferences to the BDD electrodes

Electrode	Current				Potential			
	CIP	Interference	Difference	CIP	Interference	Difference		
0.1% BDD	37.48	OFL	45.15	7.66	1.24	OFL	1.30	0.06
	37.48	LEV	41.05	3.56	1.24	LEV	1.30	0.06
	37.48	D-GLU	27.04	10.43	1.24	D-GLU	1.28	0.03
0.5% BDD	54.33	OFL	45.87	8.45	1.29	OFL	1.29	0.00
	54.33	LEV	45.63	8.70	1.29	LEV	1.30	0.01
	54.33	D-GLU	55.92	1.59	1.29	D-GLU	1.29	0.00
1% BDD	53.63	OFL	89.96	36.33	1.18	OFL	1.17	0.01
	53.63	LEV	77.26	23.63	1.18	LEV	1.17	0.01
	53.63	D-GLU	76.48	22.85	1.18	D-GLU	1.11	0.07

Table 4. Results obtained by analysis of CIP in pharmaceutical tablets

Electrode	Pharmaceutical tablets	Concentration (μM)		%Recovery	%RSD
		Expected	Found		
0.1% BDD	Sample 1	50	48.16	96.33	2.13
	Sample 2	50	42.78	85.56	3.39
0.5% BDD	Sample 1	50	51.61	103.23	2.24
	Sample 1	50	48.58	97.17	3.08
1% BDD	Sample 1	50	53.11	106.22	2.93
	Sample 2	50	43.81	87.63	0.22

Table 5. Results obtained by analysis of CIP in wastewater and milk

Electrode	Samples	Concentration (μM)		%Recovery	%RSD
		Expected	Found		
0.1% BDD	Wastewater	50	45.96	91.92	2.36
	Milk	50	46.18	92.37	3.93
0.5% BDD	Wastewater	50	50.32	100.64	3.45
	Milk	50	48.58	97.17	3.08
1% BDD	Wastewater	50	53.40	106.80	1.44
	Milk	50	53.45	106.91	1.93

Detection of CIP in Real Samples

The analyses of two pharmaceutical tablets containing 500 mg of CIP and the sensors used in real samples were carried out in environmental water matrices. To verify the developed method, CIP simultaneously detected in synthetic samples was measured by the standard addition method. Furthermore, all samples were spiked with 50 μM CIP in an electrochemical cell to evaluate the accuracy of the developed method. The wastewater and milk samples were only diluted in phosphate-buffered saline as the supporting electrolyte prior to analysis. Tables 4 and 5 present the %recovery of each BDD electrode with a boron concentration of 0.1, 0.5, and 1%.

These results indicate that the %recovery in all measurement analyses is in the range of 85–110%, signifying good accuracy and good results of the method developed in this study. In addition, the developed sensor is proven to allow the simultaneous determination of analytes with high accuracy. Sensors with BDD electrodes of various boron concentrations are capable of detecting CIP in pharmaceutical, wastewater, and milk samples with simple dilution which does not require laborious extraction procedures or chemical additives to maintain the electroactivity of the sensor.

CONCLUSION

In this study, three BDD electrodes with a boron concentration of 0.1, 0.5, and 1% prepared through the microwave plasma-assisted CVD method were used as sensors for CIP antibiotics. From the Raman spectroscopy, three BDD electrodes do not contain sp^2 carbon impurities. In addition, the CV characterization shows that the potential window of BDD electrode becomes narrower with increasing boron concentration. Although 0.1 and 0.5% BDD electrodes have a wider potential window, they have a slower response to redox systems compared to 1% BDD electrodes. Furthermore, evaluation of the effects of possible interfering compounds such as D-GLU, LEV, and OFL shows significant results on the current response of the observed analyte. Based on the results, the method developed in this study is proven to have higher accuracy and precision

than other methods employed to real samples. Among the three BDD electrodes, 1% BDD electrode is highly recommended for application as electrochemical sensor of CIP in pharmaceutical samples, wastewater, and milk due to its good response and fast redox reaction. This study reveals that boron concentration in BDD electrode affects the determination of its application as the electrochemical sensor of ciprofloxacin; it is successfully applied in the analysis of sensors of antibiotics in complex samples and can be potentially used in future development of real detection devices.

ACKNOWLEDGMENTS

This research was funded by Universitas Airlangga under SATU joint research grant with grant number 1242/UN3.15/PT/2022.

AUTHOR CONTRIBUTIONS

Prastika Krisma Jiwanti conceptualized, writing—review and editing, resources, funding acquisition, supervision. Ilmi Nur Indriani Savitri written original draft preparation, formal analysis, and data curation. Ilmanda Zalzabhila Danistya Putri did the formal analysis, and data curation. Irkham and Yasuaki Einaga provided resources and supervision. Ganden Supriyanto, Yew Hoong Wong, Sachin Kumar Srivastava, Che Azurahaman Che Abdullah supervised the research.

REFERENCES

- [1] Zhang, G.F., Liu, X., Zhang, S., Pan, B., and Liu, M.L., 2018, Ciprofloxacin derivatives and their antibacterial activities, *Eur. J. Med. Chem.*, 146, 599–612.
- [2] Gayen, P., and Chaplin, B.P., 2016, Selective electrochemical detection of ciprofloxacin with a porous nafion/multi-walled carbon nanotube composite film electrode, *ACS Appl. Mater. Interfaces*, 8 (3), 1615–1626.
- [3] Gissawong, N., Srijaranai, S., Boonchiangma, S., Uppachai, P., Seehamart, K., Jantrasee, S., Moore, E., and Mukdasai, S., 2021, An electrochemical sensor for voltammetric detection of ciprofloxacin using a glassy carbon electrode modified with

- activated carbon, gold nanoparticles and supramolecular solvent, *Microchim. Acta*, 188 (6), 208.
- [4] Reddy, K.R., Brahman, P.K., and Suresh, L., 2018, Fabrication of high performance disposable screen printed electrochemical sensor for ciprofloxacin sensing in biological samples, *Measurement*, 127, 175–186.
- [5] Faria, L.V., Pereira, J.F.S., Azevedo, G.C., Matos, M.A.C., Munoz, R.A.A., and Matos, R.C., 2019, Square-wave voltammetry determination of ciprofloxacin in pharmaceutical formulations and milk using a reduced graphene oxide sensor, *J. Braz. Chem. Soc.*, 30, 1947–1954.
- [6] Radičová, M., Behúl, M., Marton, M., Vojs, M., Bodor, R., Redhammer, R., and Vojs Staňová, A., 2017, Heavily boron doped diamond electrodes for ultra sensitive determination of ciprofloxacin in human urine, *Electroanalysis*, 29 (6), 1612–1617.
- [7] Girardi, C., Greve, J., Lamshöft, M., Fetzer, I., Miltner, A., Schäffer, A., and Kästner, M., 2011, Biodegradation of ciprofloxacin in water and soil and its effects on the microbial communities, *J. Hazard. Mater.*, 198, 22–30.
- [8] Hu, X., Goud, K.Y., Kumar, V.S., Catanante, G., Li, H., Zhu, Z., and Marty, J.L., 2018, Disposable electrochemical aptasensor based on carbon nanotubes-V₂O₅-chitosan nanocomposite for detection of ciprofloxacin, *Sens. Actuators, B*, 268, 278–286.
- [9] Vella, J., Busuttill, F., Bartolo, N.S., Sammut, C., Ferrito, V., Serracino-Inglott, A., Azzopardi, L.M., and LaFerla, G., 2015, A simple HPLC-UV method for the determination of ciprofloxacin in human plasma, *J. Chromatogr. B*, 989, 80–85.
- [10] Pascual-Reguera, M.I., Pérez Parras, G., and Molina Díaz, A., 2004, A single spectroscopic flow-through sensing device for determination of ciprofloxacin, *J. Pharm. Biomed. Anal.*, 35 (4), 689–695.
- [11] Fotouhi, L., and Alahyari, M., 2010, Electrochemical behavior and analytical application of ciprofloxacin using a multi-walled nanotube composite film-glassy carbon electrode, *Colloids Surf., B*, 81 (1), 110–114.
- [12] Xu, X., Liu, L., Jia, Z., and Shu, Y., 2015, Determination of enrofloxacin and ciprofloxacin in foods of animal origin by capillary electrophoresis with field amplified sample stacking–sweeping technique, *Food Chem.*, 176, 219–225.
- [13] Forster, R.J., Walsh, D., and Adamson, K., 2019, "Voltammetry | Overview" in *Encyclopedia of Analytical Science*, 3rd Ed., Eds. Spain, E., Worsfold, P., Poole, C., Townshend, A., and Miró, M., Academic Press, Oxford, UK, 209–217.
- [14] Santos, A.M., Wong, A., Almeida, A.A., and Fatibello-Filho, O., 2017, Simultaneous determination of paracetamol and ciprofloxacin in biological fluid samples using a glassy carbon electrode modified with graphene oxide and nickel oxide nanoparticles, *Talanta*, 174, 610–618.
- [15] Kawde, A.N., Aziz, M.A., Odewunmi, N., Hassan, N., and AlSharaa, A., 2014, Electroanalytical determination of antibacterial ciprofloxacin in pure form and in drug formulations, *Arabian J. Sci. Eng.*, 39 (1), 131–138.
- [16] Cinková, K., Andrejčáková, D., and Švorc, L., 2016, Electrochemical method for point-of-care determination of ciprofloxacin using boron-doped diamond electrode, *Acta Chim. Slovaca*, 9 (2), 146–151.
- [17] Xu, J., Natsui, K., Naoi, S., Nakata, K., and Einaga, Y., 2018, Effect of doping level on the electrochemical reduction of CO₂ on boron-doped diamond electrodes, *Diamond Relat. Mater.*, 86, 167–172.
- [18] Jiwanti, P.K., and Einaga, Y., 2020, Further study of CO₂ electrochemical reduction on palladium modified bdd electrode: Influence of electrolyte, *Chem. - Asian J.*, 15 (6), 910–914.
- [19] Diksy, Y., Rahmawati, I., Jiwanti, P.K., and Ivandini, T.A., 2020, Nano-Cu modified Cu and nano-Cu modified graphite electrodes for chemical oxygen demand sensors, *Anal. Sci.*, 36, 1323–1330.
- [20] Putri, Y.M.T.A., Jiwanti, P.K., Irkham, I., Gunlazuardi, J., Einaga, Y., and Ivandini, T.A., 2021, Nickel-cobalt modified boron-doped diamond as an electrode for a urea/H₂O₂ fuel cell, *Bull. Chem. Soc. Jpn.*, 94 (12), 2922–2928.

- [21] Ivandini, T.A., Ariani, J., Jiwanti, P.K., Saepudin, E., and Einaga, Y., 2017, Electrochemical detection of neuraminidase based on zanamivir inhibition reaction at platinum and platinum-modified boron-doped diamond electrodes, *Makara J. Sci.*, 21, 34–42.
- [22] Song, Y., and Swain, G.M., 2007, Total inorganic arsenic detection in real water samples using anodic stripping voltammetry and a gold-coated diamond thin-film electrode, *Anal. Chim. Acta*, 593 (1), 7–12.
- [23] Watanabe, T., Honda, Y., Kanda, K., and Einaga, Y., 2014, Tailored design of boron-doped diamond electrodes for various electrochemical applications with boron-doping level and sp²-bonded carbon impurities, *Phys. Status Solidi A*, 211 (12), 2709–2717.
- [24] dos Santos, A.J., Fortunato, G.V., Kronka, M.S., Vernasqui, L.G., Ferreira, N.G., and Lanza, M.R.V., 2021, Electrochemical oxidation of ciprofloxacin in different aqueous matrices using synthesized boron-doped micro and nano-diamond anodes, *Environ. Res.*, 204, 112027.
- [25] Schwarzová-Pecková, K., Vosáhlová, J., Barek, J., Šloufová, I., Pavlova, E., Petrák, V., and Zavázalová, J., 2017, Influence of boron content on the morphological, spectral, and electroanalytical characteristics of anodically oxidized boron-doped diamond electrodes, *Electrochim. Acta*, 243, 170–182.
- [26] Kingsley, M.P., Kalambate, P., and Srivastava, A.K., 2016, Simultaneous determination of ciprofloxacin and paracetamol by adsorptive stripping voltammetry using copper zinc ferrite nanoparticles modified carbon paste electrode, *RSC Adv.*, 6 (18), 15101–15111.
- [27] Zeng, Y., Chen, D., Chen, T., Cai, M., Zhang, Q., Xie, Z., Li, R., Xiao, Z., Liu, G., and Lv, W., 2019, Study on heterogeneous photocatalytic ozonation degradation of ciprofloxacin by TiO₂/carbon dots: Kinetic, mechanism and pathway investigation, *Chemosphere*, 227, 198–206.
- [28] Voigtman, E., 2017, *Limits of Detection in Chemical Analysis*, John Wiley & Sons, Hoboken, New Jersey, US.
- [29] Švorc, Ľ., Jambrec, D., Vojs, M., Barwe, S., Clausmeyer, J., Michniak, P., Marton, M., and Schuhmann, W., 2015, Doping level of boron-doped diamond electrodes controls the grafting density of functional groups for DNA assays, *ACS Appl. Mater. Interfaces*, 7 (34), 18949–18956.
- [30] Matsunaga, T., Kondo, T., Osasa, T., Kotsugai, A., Shitanda, I., Hoshi, Y., Itagaki, M., Aikawa, T., Tojo, T., and Yuasa, M., 2020, Sensitive electrochemical detection of ciprofloxacin at screen-printed diamond electrodes, *Carbon*, 159, 247–254.

Development of Methylmercury Analysis by Ultra-High Performance Liquid Chromatography Coupled with ICP-MS and Its Application on Sharks' Meat Measurement

Suratno Suratno^{1,2}, Satriyo Krido Wahono², Dwi Siswanta¹, and Nurul Hidayat Aprilita^{1*}

¹Department of Chemistry, Faculty of Mathematics and Natural Sciences, Universitas Gadjah Mada, Sekip Utara, Yogyakarta 55281, Indonesia

²Research Center for Food Technology and Processing (PRTTP), National Research and Innovation Agency (BRIN), Gunungkidul, Yogyakarta 55861, Indonesia

* **Corresponding author:**

email: nurul.hidayat@ugm.ac.id

Received: February 22, 2023

Accepted: March 24, 2023

DOI: 10.22146/ijc.82512

Abstract: This study analyzed MeHg in a fast, simple, low-waste, and accurate by using ultra-high liquid chromatography coupled with inductively coupled plasma mass spectrometry. Simple preparation by liquid extraction with sonication at room temperature was effective extract MeHg from Certified Reference Material (CRM) and shark meat samples. Effective MeHg separation was achieved in less than 300 s using a C18 Hypersil Gold analytical column with a mobile gradient phase of 0.5% (w/v) L-cysteine in 2% (v/v) HNO₃ and 100% methanol. The MeHg was extracted from 100 mg of shark meat using 1 mL of 0.5% (w/v) L-cysteine in 2% (v/v) HNO₃ and sonicated for 30 min. Analysis of certified reference material (DORM-4) showed values between the experimental and certified values. The observed limit of detection and quantification MeHg were 0.86 and 2.85 µg/L, respectively. This method was applied to measure MeHg in shark meat from Binuangeun areas. The MeHg concentration in *Rhizoprionodon acutus* was 0.22–0.63 mg/kg wet weight (w.w.), *Squalus hemipinis* 0.68–1.14 mg/kg w.w., and 0.29–1.22 mg/kg w.w. for *Sphyrna lewini*. This study provides a quick and easy method to evaluate MeHg in shark meat or other seafood products and applies to many samples in a single assay.

Keywords: UHPLC-ICP-MS; methylmercury; sonication-assisted extraction; shark meat

■ INTRODUCTION

In particular, methylmercury (MeHg) is the most toxic food web and bioaccumulating mercury. It is the predominant chemical form, accounting for 80–90% of the total mercury present in fish muscle tissue [1-2]. Mercury concentrations of up to 4,000 mg/kg and MeHg concentrations of up to 95% have been found in large carnivorous fish such as sharks, swordfish, and some tuna [2]. As a result, fish and other organisms at the end of the food chain constitute a significant source of MeHg in the human diet [3]. MeHg causes non-fatal effects, including impaired reproductive function [4], decreased liver function and metabolism [5], and neurological damage [6-7].

The most effective instrumental methods of mercury speciation analysis are based on chromatography, such as gas (GC) [8] or liquid chromatography (LC) [9-11] and combined with specific and sensitive detectors (such as inductively coupled plasma mass spectrometry (ICP-MS)). Compared to GC, mercury speciation does not need to be converted to volatile compounds prior to High Performance Liquid Chromatography (HPLC) separation, so LC is a suitable separation technique for mercury speciation [12]. Several methods have been developed to determine mercury speciation using HPLC-ICPMS on biological samples. However, they all use many solvents in the extraction methods and

produce large amounts of waste products containing MeHg [9,12-13].

Therefore, this article's objective was to evaluate a method for determining the MeHg concentration in shark meat by incorporating a more straightforward and economical extraction process using ultra-high-performance chromatography combined with ICP-MS with a fast procedure and less waste-containing MeHg.

■ EXPERIMENTAL SECTION

Materials

The materials used in this study were MS Grade for water (Thermo Fisher, USA), HNO₃ 65% (Merck), methylmercury chloride (CH₃HgCl) standard (Sigma, USA), methanol for LC grade (Merck, Germany), DORM-4 as CRM for MeHg and L-cysteine (99% purity Sigma, USA). All glassware was washed by soaking in 10% (v/v) HNO₃ for 12 h, rinsed three times with double-distilled deionized water and air drying for 12 h. A 1,000 mg/L standard solution for CH₃HgCl was prepared by weight 1 mg CH₃HgCl diluted in 1 mL with 0.5% L-cysteine 2% HNO₃. A series of standard solutions (1, 5, 10, 25, 50, 75, 100 µg/L) were prepared by dilution of 1,000 mg/L MeHg stock solution with 0.5% L-cysteine 2% HNO₃. The standard curve was prepared in duplicate (Fig. 1).

Instrumentation

The instrumentations used in this study were a

UHPLC-ICPMS (Thermo Scientific) with PFA Cyclonic Spray Chamber, PFA Micro mist Nebuliser and ICAP Q/Qnova Quartz Torch Organics. A Thermo Scientific™ Vanquish™ UHPLC Quaternary Pump with reverse-phase column (C18, Hypersil GOLD™, 250 mm × 4.6 mm ID, 5 µm particle size, 175 Å pore size). The mobile phase used was 0.5% L-cysteine in 2% HNO₃ (A) and methanol 100% (B), and the flow rate of the gradient technique was 1.0 mL/min. The mobile phase B was adjusted to 2% and gradually increased to 90% in 132 s. After that, hold at 90% for 20 s and continue at the initial state until 180 s. The temperature of the column was set at 40 °C, and the volume of injection was 50 µL. The optimal experimental conditions for UHPLC and ICPMS are shown in Table 1.

Procedure

Sample preparation and extraction MeHg

Shark samples were collected by direct purchase on September 11-16, 2019, from Binuangun Fish Auction, Lebak, Banten, Indonesia (Southern Java Sea areas). Sixteen sharks were identified as *Rhizoprionodon acutus* (RA), six as *Squalus hemipinis* (SH), and eight as *Sphyrna lewini*. The total weight (TW) was measured using a digital balance, and the total length (TL) was measured using a rolling meter. Shark muscles for mercury analysis were cut from an area near the dorsal fin, placed in a zip-lock plastic bag, and frozen (-20 °C) until further analysis. In the laboratory, shark meat was

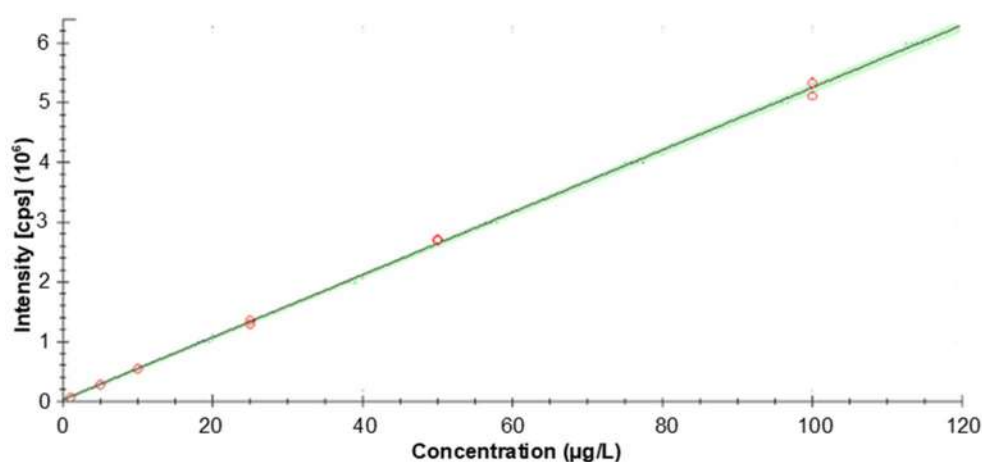


Fig 1. MeHg concentration calibration curve (µg/L) in duplicates with $R^2 = 0.999$, slope = 52.336.311, intercept = 15.501.082 and RSE = 12.34%

Table 1. Liquid chromatography and ICPMS operating condition for mercury speciation (MeHg)

UHPLC condition	
Column	C18, Hypersil GOLD™, 250 mm × 4.6 mm ID, 5 µm particle size, 175 Å pore size
Mobile phase	A: 0.5% L-cysteine in 2% HNO ₃ B: MeOH 100%
Mobile phase flow rate	1.0 mL/min
Elution	Gradient flow with a quaternary pump 0–132 s (2–90%B) 132–144 s (90% B) 145–180 s (2% B)
Volume injection	50 µL
ICP-MS condition	
Plasma power (W)	1550
Auxiliary flow (L/min)	0.8
Nebulizer flow (L/min)	0.6179
Isotopes	²⁰² Hg
¹⁴⁰ Ce. ¹⁶ O/ ¹⁴⁰ Ce ratio	0.0161
Spray chamber	PFA cyclonic spray chamber
Torch	iCAP Q/Qnova torch for organics (FI475-01W)
Quartz injector	Quartz injector (1.0 mm ID) iCAP Q/Qnova

oven-dried for 24 h at 60 °C for MeHg analysis and moisture content to convert the dry weight to wet weight. Dried samples were ground using mortar and pestle to get fine powder for further analysis.

The development method of MeHg extraction was based on de Souza et al. [9] with modifications for the volume of solvent extraction, sonication time, mobile phase, and elution conditions. The use of L-cysteine in acid conditions as the solvent and mobile phase and also the use of gradient elution was the development method compared to de Souza et al. [9]. A 100 mg of the dried sample was placed in 2 mL microtubes containing 1 mL of 0.5% L cysteine in 2% HNO₃ and applied sonication (Elmasonic S60H, f: 50/60 Hz, 550 W) for 30 min at room temperature. The microtube was then centrifuged at 3,000 rpm for 5 min, and the supernatant was filtered through a 0.20 µm nylon syringe filter and placed in a 2 mL HPLC vial.

Method validation

A CRM DORM4 (n = 10) was used as sample preparation to validate the accuracy of the method. The sample was performed in duplicate, and blanks were used

with 0.5% L-cysteine in 2% HNO₃. Two replicates of MeHg standard solutions with concentrations (as mercury) in the range of 1–100 µg/L were used to form linear calibration plots with r² values of 0.999. The limit of detection (LOD) and limit of quantification (LOQ) were measured based on [14] with the equation; LOD = $3.9 \times \frac{S_{Db}}{S_b}$ with SDb was the standard deviation measurement of blank/pseudo blank (n = 10), S_b was the slope of the calibration curve, and the LOQ was 3.33 of LOD.

Data analysis

Graphical from UPLC was analyzed with Qtegra and Chrom Control software (Thermo Scientific, USA), and all graphic plot was based on the open source program platform R (package 4.12 for windows) [15].

RESULTS AND DISCUSSION

Extraction and Validation Method with DORM-4

The development method showed good extraction of MeHg in DORM4 with 1 mL of L-cysteine in acid condition compared to previous studies from Vallant et al. [13] used 5 mL solvent for MeHg extraction, while de

Souza et al. [9] used 10 mL solvent for CRM extraction, and Rodrigues et al. [12] used 4.75 mL solvent. Previous studies commonly use two compounds, such as L-cysteine combined with 2-mercaptoethanol [9-10,16]. Vallant et al. [13] use HCl and NaOH for MeHg extraction while our method shows good results only using L-cysteine in acidic conditions. L-cysteine was used in acid conditions as solvent extraction. We combined L-cysteine with methanol as the mobile phase to increase the sensitivity of Hg on the complex compound of MeHg-L-cysteine [9]. L-cysteine was less toxic than the mercapto compound, and the complexing ability was poor [10]. The development method gives less solvent for extraction, less chemical compound is used in analysis and less waste containing MeHg.

The development method used gradient elution in a UHPLC system and compared it to a previous study [9,11-13] and showed good separation with mobile phase 0.5% L-cysteine and 2% HNO₃ and 100% methanol under gradient conditions of less than 300 s. Inorganic mercury (InHg) was showed a peak at 196.5 s and MeHg around 266 s (Fig. 2). Gradient elution shows low signal noise at a low concentration compared to isocratic elution [9]. The use of gradient elution can reduce 20% of the time of MeHg analysis by comparing isocratic elution [9].

The recovery of MeHg concentration with this method shows good result measurement (Table 2) with values of 96.90%. Our method uses less solvent in this study because solvent extraction is the same as for the mobile phase. The development method shows good

results in reducing the uses of solvent extraction. Our results can reduce 80% on the use of solvent compared with Vallant et al. [13] and reduce by almost 90% compared to de Souza et al. [9]. Compared to previous studies [4,9,12-13,16-17], our method uses a small volume (1 mL) of extraction to reduce organic waste containing MeHg (Table 3). The observed limit of detection and limit of quantification MeHg in this method was 0.86 and 2.85 pg/L, respectively.

Method Application for Methylmercury Measurement on Shark Meat

The total length of milk sharks ranged from 34.5–46.8 cm, 49.5–62.3 cm for Squalus sharks, and 56.4–68 cm for hammerhead sharks. The total weight of milk sharks was 195–450 g, 485–1190 g for Squalus shark, and 825–1335 g for hammerhead shark, respectively (Table 4).

The concentration of MeHg in the meat/muscle tissue ranged between 0.22 and 0.63 mg/kg w.w. (mean concentration of MeHg: 0.41 ± 0.13 mg/kg w.w.) for *R. acutus*, 0.68 to 1.14 mg/kg w.w. (0.81 ± 0.17 mg/kg w.w.)

Table 2. Recovery of MeHg concentration in DORM-4 by UHPLC-ICP-MS (n = 10) extracted with 0.5% (m/v) L-cysteine in 2% (v/v) HNO₃ using gradient elution condition

CRM	Analyte	Certified value (mg/kg)	Measurement value (mg/kg)
DORM-4	MeHg	0.355 ± 0.028	0.344 ± 0.028
Recovery (%)			96.90

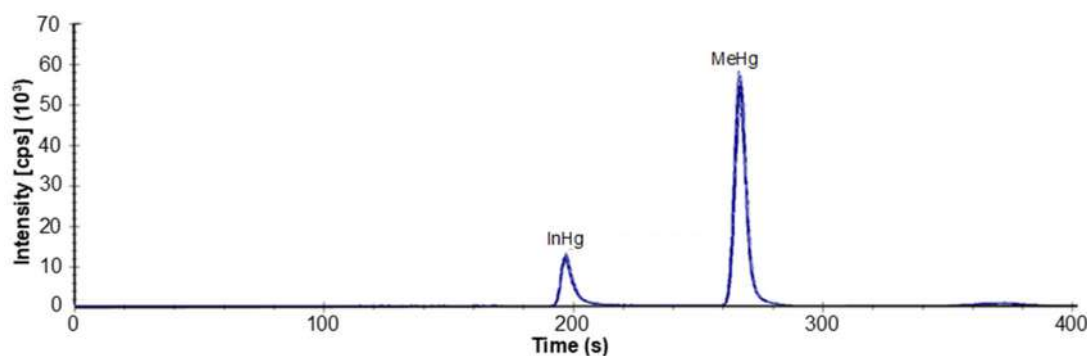


Fig 2. Chromatogram showing the separation of inorganic mercury (InHg) and methyl mercury (MeHg) in DORM-4 (n = 10) with mobile phase 0.5% (m/v) L-cysteine in 2% (v/v) HNO₃, Methanol 100% on gradient condition

Table 3. Comparison MeHg analysis using HPLC-ICPMS on biological samples with previous research

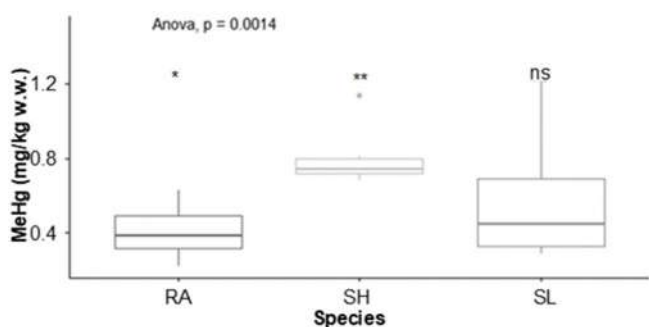
Type of samples	Mobile phase and type of elution	Solvent extraction	Weight of samples	Volume of extraction	Time of extraction	LOD	Ref.	
Human hair	0.05% v/v mercaptoethanol; 0.4% m/v L-cysteine; 5% v/v methanol and 0.06 mol/L ammonium acetate. <i>Isocratic elution</i>	0.10% v/v HCl + 0.05% m/v L-cysteine + 0.10% v/v 2-mercaptoethanol	50 mg	10 mL	10 min sonication	MeHg: 10.0 ng/g InHg: 15.0 ng/g EtHg: 38.0 ng/g	[9]	
DORM-2 DOLT-3	50 mmol/L pyridine, 0.5% w/w L-cysteine, 5% v/w MeOH, at pH 2. <i>Isocratic elution</i>	5 M HCl; 10 M NaOH	250 mg	5 mL	15 min sonication; 20 min centrifugation	InHg: 0.05 µg/L MeHg: 0.08 µg/L	[13]	
Human plasma NIST 966	3% v/v methanol + 97% v/v (0.5% v/v 2-mercaptoethanol + 0.05% v/v formic acid). <i>Isocratic elution</i>	0.10% v/v HCl + 0.05% m/v L-cysteine + 0.10% v/v 2-mercaptoethanol	250 µL	2.75 mL	15 min sonication	InHg: 12 ng/L EtHg: 5 ng/L MeHg: 4 ng/L	[16]	
Blood SRM 966	0.05% v/v mercaptoethanol; 0.4% m/v L-cysteine; 5% v/v methanol and 0.06 mol/L ammonium acetate. <i>Isocratic elution</i>	0.10% (v/v) HCl + 0.05% (m/v) L-cysteine + 0.10% (v/v) 2-mercaptoethanol	250 µL	4.75 mL	15 min sonication	InHg: 0.25 µg/L MeHg: 0.1 µg/L	[12]	
ERM CE-464	<i>Isocratic elution</i>	50 mM pyridine, 0.5% (w/v) L-cysteine, 5% (v/v) MeOH, pH 3.	25% (w/v) KOH in MeOH.	300 mg	9 mL (3 mL × 3)	30 min waterbath, 30 min sonication, 10 min centrifugation	InHg: 0.46 µg/L MeHg: 0.78 µg/L	[17]
			25% (w/v) TMAH in MeOH	300 mg	9 mL (3 mL × 3)	30 min waterbath, 30 min sonication, 10 min centrifugation		
			5% (w/v) TMAH in MeOH	200 mg	10 mL	20 min microwave digestion		
			5 M HCl	300 mg	5 mL	5 min sonication, 10 min centrifugation		
			4 M HNO ₃	500 mg	10 mL	20 min microwave digestion		
			Glacial acetic acid	300mg	9 mL	10 min microwave digestion		
Sea cucumber	8% MeOH; 92% H ₂ O containing 0.12% L-cysteine + 0.01 mol/L ammonium acetate. <i>Isocratic elution</i>	0.10% HCl (v/v), 0.12% L-cysteine (m/v), and 0.10% 2-mercaptoethanol (v/v)	500 mg	10 mL	30 min sonication	InHg: 0.12 µg/L MeHg: 0.08 µg/L EtHg: 0.20 µg/L	[10]	
		1% (w/v) L-cysteine hydrochloride hydrate	200 mg	20 mL	2 h waterbath, 2 h heating			
		20 mg protease type XIV, 0.1 M phosphate buffer pH 7.5 containing 0.05% (w/v) cysteine	200 mg	8 mL	2 h enzyme digestion, 20 min centrifugation			
DORM-4 Shark meat	0.5% (m/v) L-cysteine in 2% (v/v) HNO ₃ + MeOH 100%. <i>Gradient elution</i>	0.5% (m/v) L-cysteine in 2% (v/v) HNO ₃	100 mg	1 mL	30 min sonication	MeHg: 0.86 pg/L	This study	

for *S. hemipinis* and 0.29 to 1.22 mg/kg w.w. (0.56 ± 0.32 mg/kg w.w.), and for *S. lewini* as described in Fig. 3. The mercury concentration on hammerhead sharks in this study is relatively lower compared to previous research by Mohammed and Mohammed [18]. The difference in size

and weight of hammerhead sharks from this study were correlated to the mercury concentration. Based on the size, hammerhead sharks from Binuangun are still in the juvenile phase compared to previous research in Trinidad, the Gulf of California and the Korean coast [18-20]. Based

Table 4. Morphometric of samples *R. acutus*, *S. hemipinis* and *S. lewini*. M: male; F: female

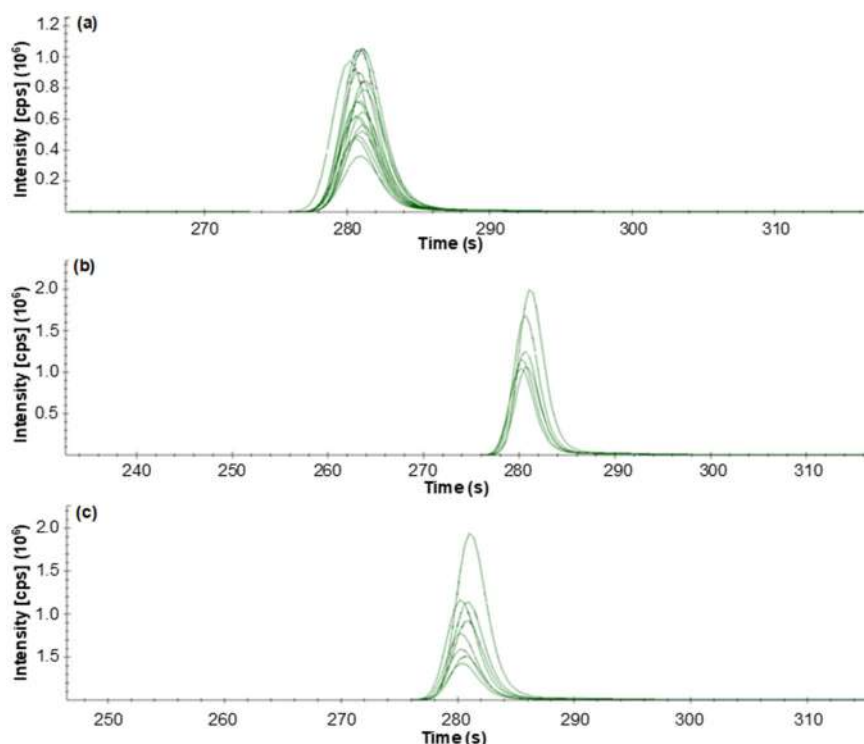
Common name	N	Scientific name	The total weight (g)	Total length (cm)	Sex
Milk shark	16	<i>Rhizoprionodon acutus</i>	195–450	34.5–46.8	M: 11; F: 5
Squalus shark	6	<i>Squalus hemipinis</i>	485–1190	49.5–62.3	M: 1; F:5
Hammerhead shark	8	<i>Sphyrna lewini</i>	825–1335	56.4–68.0	M:4; F:4

**Fig 3.** Methylmercury (MeHg) concentration (mg/kg w.w.) on shark samples. SH: *S. hemipinis*, SL: *S. lewini*, and RA: *R. acutus*

on our results, there are no differences MeHg concentration between sex on *R. acutus* and *S. lewini* (*p*-

value 0.93 and 0.2, respectively). The chromatogram peak of MeHg from each sample of sharks showed in Fig. 4.

MeHg concentrations in milk sharks from the Binuangeun area were higher than in previous research on the Korean coast [20]. MeHg concentration in Squalus sharks from Binuangeun was lower than in Brazil [21] and Southeast Australia [22]. Due to limited studies on *S. hemipinis*, mercury concentrations in these sharks compared to *S. acanthias* and *S. albicaudus* indicate the same habitat on the shelf and upper slopes of the ocean (from 0–600 m) [23]. Some studies have shown that several factors influence mercury accumulation in sharks, such as age, body length, habitat, sex and local pollution [24–25].

**Fig 4.** Chromatogram showing the separation methylmercury (MeHg) with mobile phase 0.5% (m/v) L-cysteine in 2% (v/v) HNO₃, Methanol 100% on gradient condition in (a) *R. acutus* (n = 16), (b) *S. hemipinnis* (n = 6), and (c) *S. lewini* (n = 8)

■ CONCLUSION

A quick and easy method has been developed for analyzing MeHg using UHPLC-ICPMS. Gradient elution applied using a C18 reversed-phase column with 0.5% L cysteine in 2% HNO₃ and methanol as mobile phase can separate inorganic Hg and MeHg on CRM (DORM-4) with an accuracy of fewer than 300 s. The small amount of solvent used for extraction produces small amounts of waste containing MeHg. Finally, this method was successfully applied to analyze MeHg in shark meat samples.

■ ACKNOWLEDGMENTS

This research was fully funded by the Final Recognition Program (RTA) from Universitas Gadjah Mada, Yogyakarta, contract no: 3143/UN1.P.III/DIT-LIT/PT/2021. The authors would like to thank Aristya B.N. Jati for assisting during the analysis. The authors also thank the National Research and Innovation Agency (BRIN), Gunungkidul, Yogyakarta, for promoting the UHPLC-ICPMS.

■ AUTHOR CONTRIBUTIONS

Suratno wrote the original draft, conceptualization, formal analysis, sample analysis, and writing review and editing. Dwi Siswanta performed the statistical analysis, investigation, and data curation. Nurul Hidayat Aprilita supporting for funding acquisition, project administration and writing review and editing. Satriyo Krido Wahono wrote and reviewed the manuscript.

■ REFERENCES

- [1] Nalluri, D., Baumann, Z., Abercrombie, D.L., Chapman, D.D., Hammerschmidt, C.R., and Fisher, N.S., 2014, Methylmercury in dried shark fins and shark fin soup from American restaurants, *Sci. Total Environ.*, 496, 644–648.
- [2] Brombach, C.C., Manorut, P., Kolambage-Dona, P.P.P., Ezzeldin, M.F., Chen, B., Corns, W.T., Feldmann, J., and Krupp, E.M., 2017, Methylmercury varies more than one order of magnitude in commercial European rice, *Food Chem.*, 214, 360–365.
- [3] Karimi, R., Silbernagel, S., Fisher, N.S., and Meliker, J.R., 2014, Elevated blood Hg at recommended seafood consumption rates in adult seafood consumers, *Int. J. Hyg. Environ. Health*, 217 (7), 758–764.
- [4] Huang, X., Liu, Z., Xie, Z., Dupont, S., Huang, W., Wu, F., Kong, H., Liu, L., Sui, Y., Lin, D., Lu, W., Hu, M., and Wang, Y., 2018, Oxidative stress induced by titanium dioxide nanoparticles increases under seawater acidification in the thick shell mussel *Mytilus coruscus*, *Mar. Environ. Res.*, 137, 49–59.
- [5] Nogara, P.A., Madabeni, A., Bortoli, M., Teixeira Rocha, J.B., and Orian, L., 2021, Methylmercury can facilitate the formation of dehydroalanine in selenoenzymes: Insight from DFT molecular modeling, *Chem. Res. Toxicol.*, 34 (6), 1655–1663.
- [6] Man, Y.B., Wu, S.C., and Wong, M.H., 2014, Shark fin, a symbol of wealth and good fortune may pose health risks: the case of mercury, *Environ. Geochem. Health*, 36 (6), 1015–1027.
- [7] Yu, X., Khan, S., Khan, A., Tang, Y., Nunes, L.M., Yan, J., Ye, X., and Li, G., 2020, Methyl mercury concentrations in seafood collected from Zhoushan Islands, Zhejiang, China, and their potential health risk for the fishing community: Capsule: Methyl mercury in seafood causes potential health risk, *Environ. Int.*, 137, 105420.
- [8] Kim, T.H., Cho, M.J., Lee, Y., Kim, J.H., Hwang, J.Y., Lee, H.E., Kim, S.H., Choi, J.D., and Kang, G.J., 2020, Methylmercury determination in fish by direct mercury analyzer, *J. AOAC Int.*, 103 (1), 244–249.
- [9] de Souza, S.S., Rodrigues, J.L., de Oliveira Souza, V.C., and Barbosa, F., 2010, A fast sample preparation procedure for mercury speciation in hair samples by high-performance liquid chromatography coupled to ICP-MS, *J. Anal. At. Spectrom.*, 25 (1), 79–83.
- [10] Liu, H., Luo, J., Ding, T., Gu, S., Yang, S., and Yang, M., 2018, Speciation analysis of trace mercury in sea cucumber species of *Apostichopus japonicus* using high-performance liquid chromatography conjunction with inductively coupled plasma mass

- spectrometry, *Biol. Trace Elem. Res.*, 186 (2), 554–561.
- [11] Anual, Z.F., Maher, W., Krikowa, F., Hakim, L., Ahmad, N.I., and Foster, S., 2018, Mercury and risk assessment from consumption of crustaceans, cephalopods and fish from West Peninsular Malaysia, *Microchem. J.*, 140, 214–221.
- [12] Rodrigues, J.L., de Souza, S.S., de Oliveira Souza, V.C., and Barbosa, F., 2010, Methylmercury and inorganic mercury determination in blood by using liquid chromatography with inductively coupled plasma mass spectrometry and a fast sample preparation procedure, *Talanta*, 80 (3), 1158–1163.
- [13] Vallant, B., Kadnar, R., and Goessler, W., 2007, Development of a new HPLC method for the determination of inorganic and methylmercury in biological samples with ICP-MS detection, *J. Anal. At. Spectrom.*, 22 (3), 322–325.
- [14] Wenzl, T., Haedrich, J., Schaechtele, A., Robouch, P., and Stroka, J., 2016, *Guidance Document on the Estimation of LOD and LOQ for Measurements in the Field of Contaminants in Feed and Food*, EUR 28099, Publications Office of the European Union, Luxembourg.
- [15] R Core Team, 2021, *R: A Language and Environment for Statistical Computing*, R Foundation for Statistical Computing, Vienna, Austria.
- [16] de Souza, S.S., Campiglia, A.D., and Barbosa, F., 2013, A simple method for methylmercury, inorganic mercury and ethylmercury determination in plasma samples by high performance liquid chromatography-cold-vapor-inductively coupled plasma mass spectrometry, *Anal. Chim. Acta*, 761, 11–17.
- [17] Reyes, L.H., Mizanur Rahman, G.M., Fahrenholz, T., and Skip Kingston, H.M., 2008, Comparison of methods with respect to efficiencies, recoveries, and quantitation of mercury species interconversions in food demonstrated using tuna fish, *Anal. Bioanal. Chem.*, 390 (8), 2123–2132.
- [18] Mohammed, A., and Mohammed, T., 2017, Mercury, arsenic, cadmium and lead in two commercial shark species (*Sphyrna lewini* and *Caraharinus porosus*) in Trinidad and Tobago, *Mar. Pollut. Bull.*, 119 (2), 214–218.
- [19] Bergés-Tiznado, M.E., Márquez-Farías, F., Lara-Mendoza, R.E., Torres-Rojas, Y.E., Galván-Magaña, F., Bojórquez-Leyva, H., and Páez-Osuna, F., 2015, Mercury and selenium in muscle and target organs of scalloped hammerhead sharks *Sphyrna lewini* of the se gulf of California: Dietary intake, molar ratios, loads, and human health risks, *Arch. Environ. Contam. Toxicol.*, 69 (4), 440–452.
- [20] Kim, S.J., Lee, H.K., Badejo, A.C., Lee, W.C., and Moon, H.B., 2016, Species-specific accumulation of methyl and total mercury in sharks from offshore and coastal waters of Korea, *Mar. Pollut. Bull.*, 102, 210–215.
- [21] Hauser-Davis, R.A., Pereira, C.F., Pinto, F., Torres, J.P.M., Malm, O., and Vianna, M., 2020, Mercury contamination in the recently described Brazilian white-tail dogfish *Squalus albicaudus* (Squalidae, Chondrichthyes), *Chemosphere*, 250, 126228.
- [22] Elsayed, H., Yigiterhan, O., Al-Ansari, E.M.A.S., Al-Ashwel, A.A., Elezz, A.A., and Al-Maslamani, I.A., 2020, Methylmercury bioaccumulation among different food chain levels in the EEZ of Qatar (Arabian Gulf), *Reg. Stud. Mar. Sci.*, 37, 101334.
- [23] Wosnick, N., Niella, Y., Hammerschlag, N., Chaves, A.P., Hauser-Davis, R.A., da Rocha, R.C.C., Jorge, M.B., de Oliveira, R.W.S., and Nunes, J.L.S., 2021, Negative metal bioaccumulation impacts on systemic shark health and homeostatic balance, *Mar. Pollut. Bull.*, 168, 112398.
- [24] Teffer, A.K., Staudinger, M.D., Taylor, D.L., and Juanes, F., 2014, Trophic influences on mercury accumulation in top pelagic predators from offshore New England waters of the northwest Atlantic Ocean, *Mar. Environ. Res.*, 101, 124–134.
- [25] Lyons, K., and Lowe, C.G., 2013, Mechanisms of maternal transfer of organochlorine contaminants and mercury in the common thresher shark (*Alopias vulpinus*), *Can. J. Fish. Aquat. Sci.*, 70 (12), 1667–1672.

Supplementary Data

This supplementary data is a part of a paper entitled “Synthesis, Characterization, Antimicrobial and Time Killing Activities of New Sulfa-Derived Schiff Bases Coordinated with Cu(II)”.

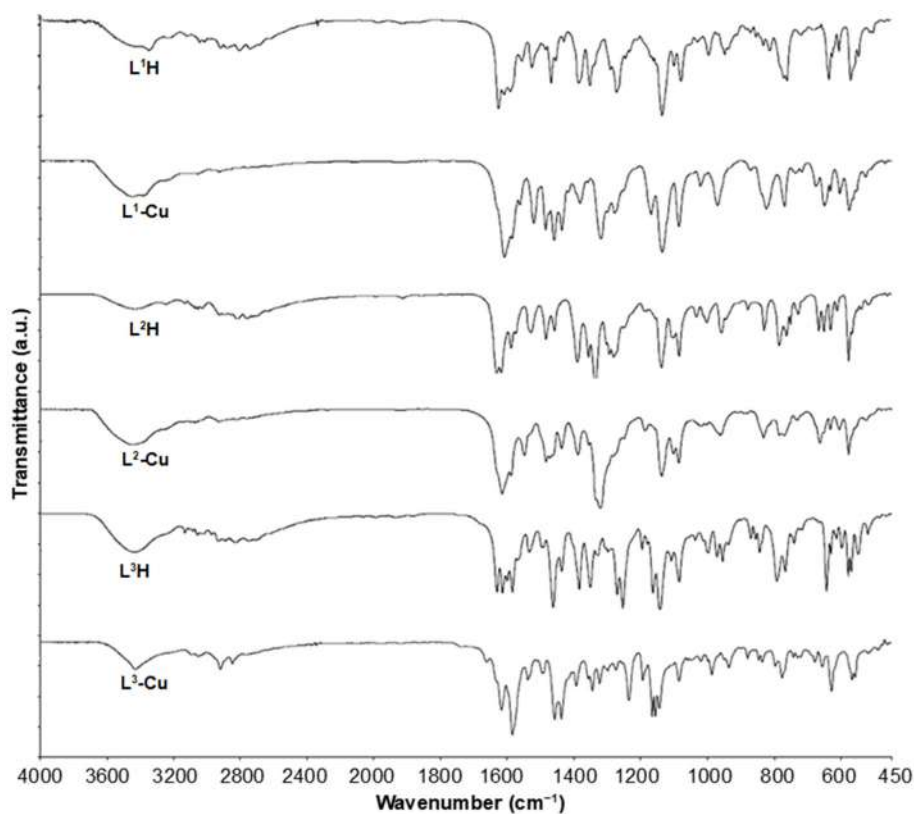


Fig S1. FTIR spectrum of the compounds

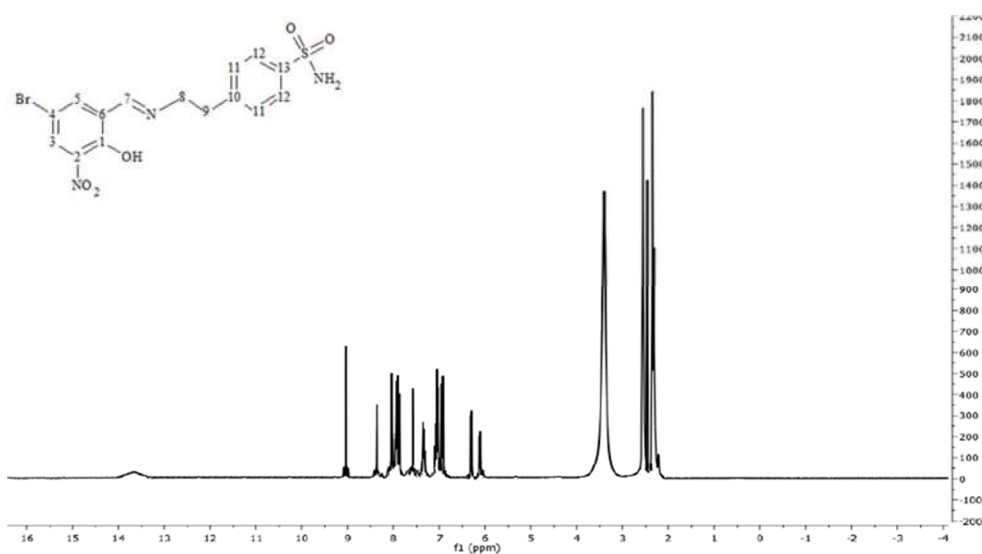
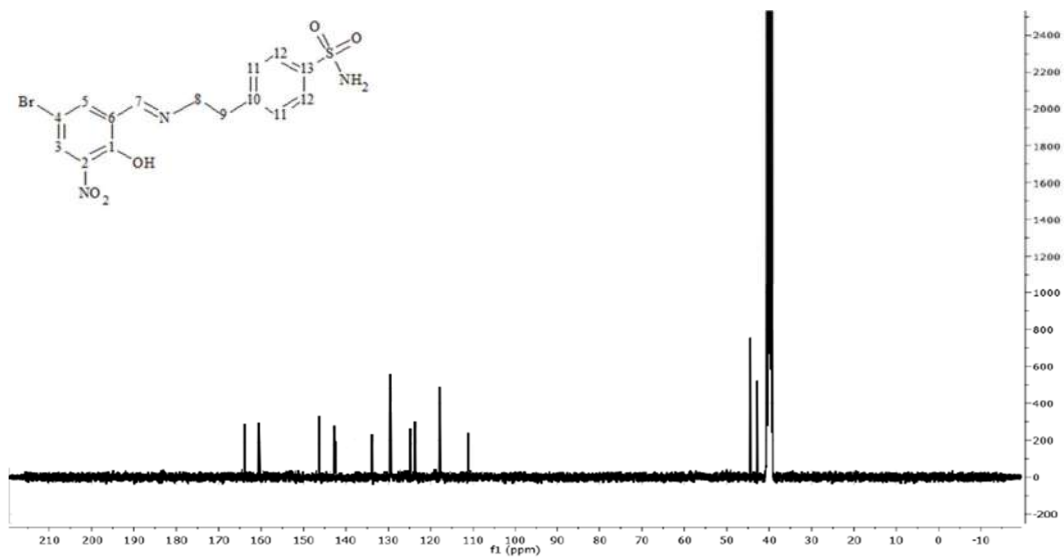
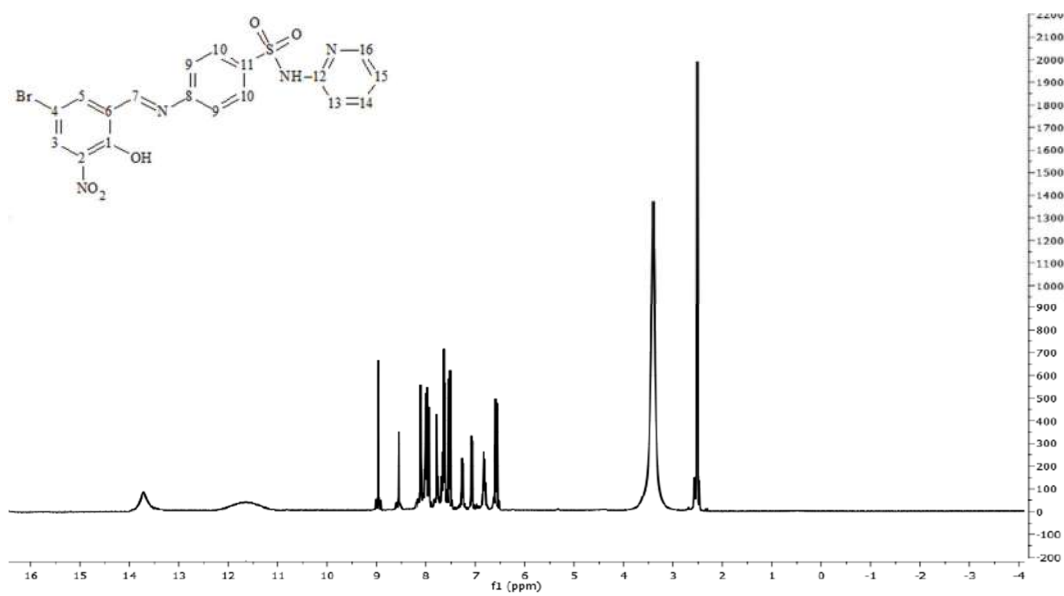


Fig S2. ¹H-NMR spectrum of the L¹H ligand

Fig S3. ¹³C-NMR spectrum of the L¹H ligandFig S4. ¹H-NMR spectrum of the L²H ligand

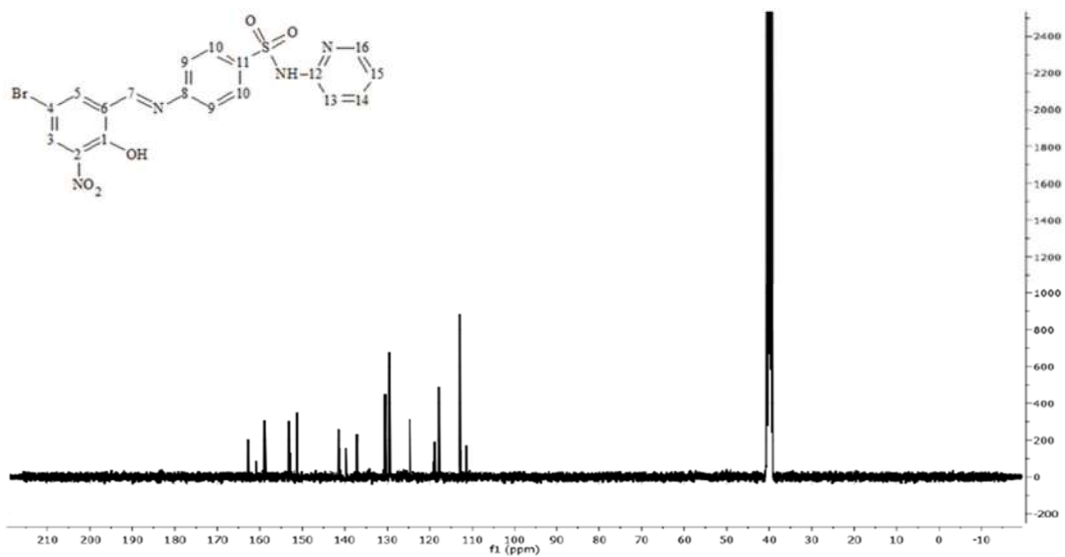


Fig S5. ^{13}C -NMR spectrum of the L^2H ligand

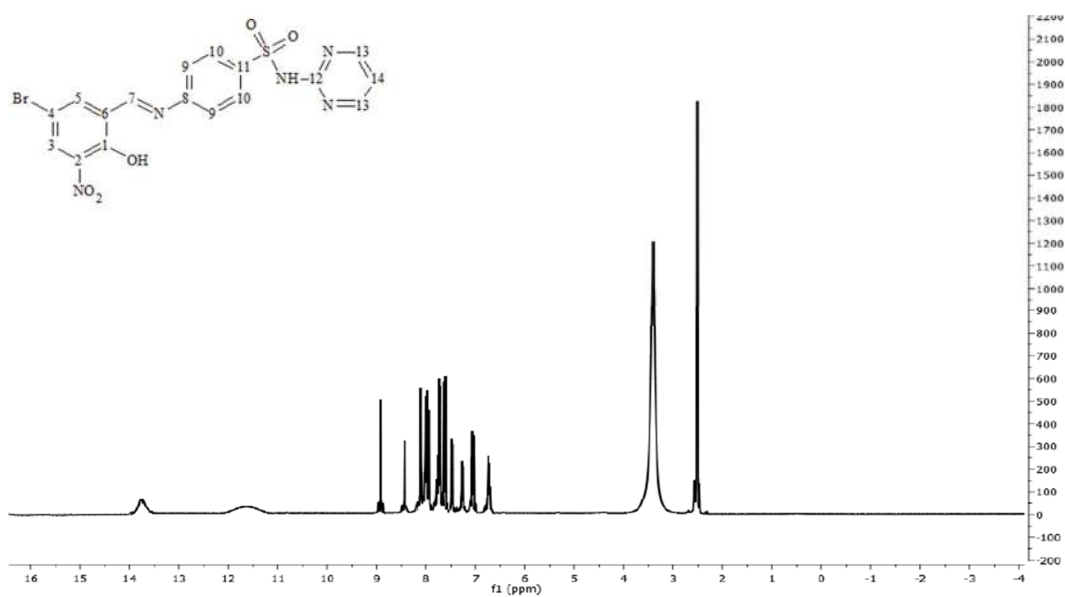
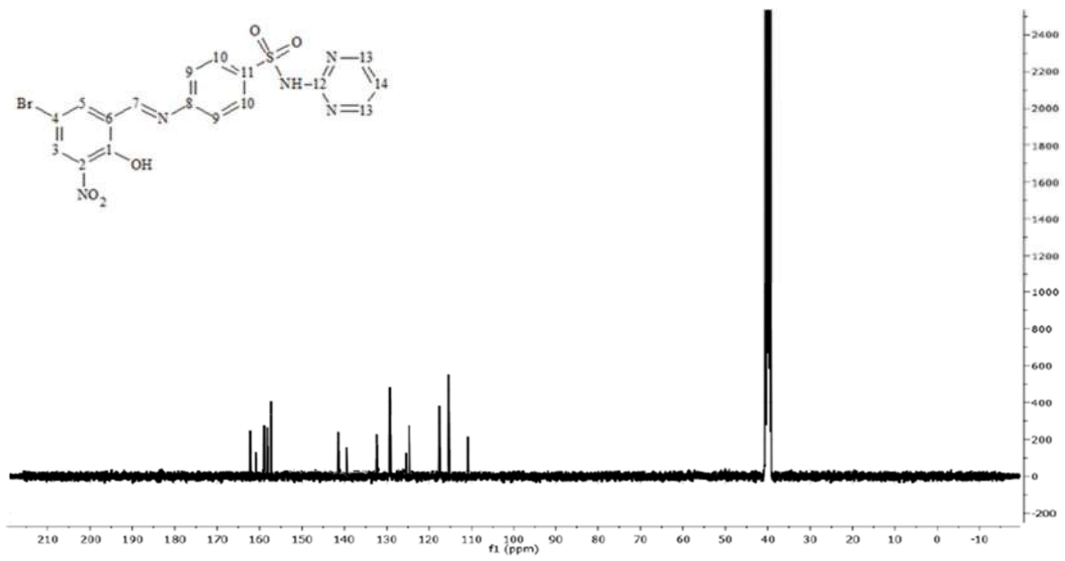


Fig S6. ^1H -NMR spectrum of the L^3H ligand

Fig S7. ¹³C-NMR spectrum of the L³H ligand

Synthesis, Characterization, Antimicrobial and Time Killing Activities of New Sulfa-Derived Schiff Bases Coordinated with Cu(II)

Önder İdil^{1*}, Hakan Şahal², Erdal Canpolat³, and Mustafa Özkan⁴

¹Department of Basic Education, Faculty of Education, Amasya University, Amasya 05100, Turkey

²Vocational School of Tunceli, Department of Food Processing, Munzur University, Tunceli 62000, Turkey

³Department of Elementary Science Education, Faculty of Education, Firat University, Elazig 23200, Turkey

⁴Department of Elementary Science Education, Faculty of Education, Bursa Uludag University, Bursa 16059, Turkey

* Corresponding author:

email: onidil@amasya.edu.tr

Received: April 13, 2023

Accepted: May 1, 2023

DOI: 10.22146/ijc.83873

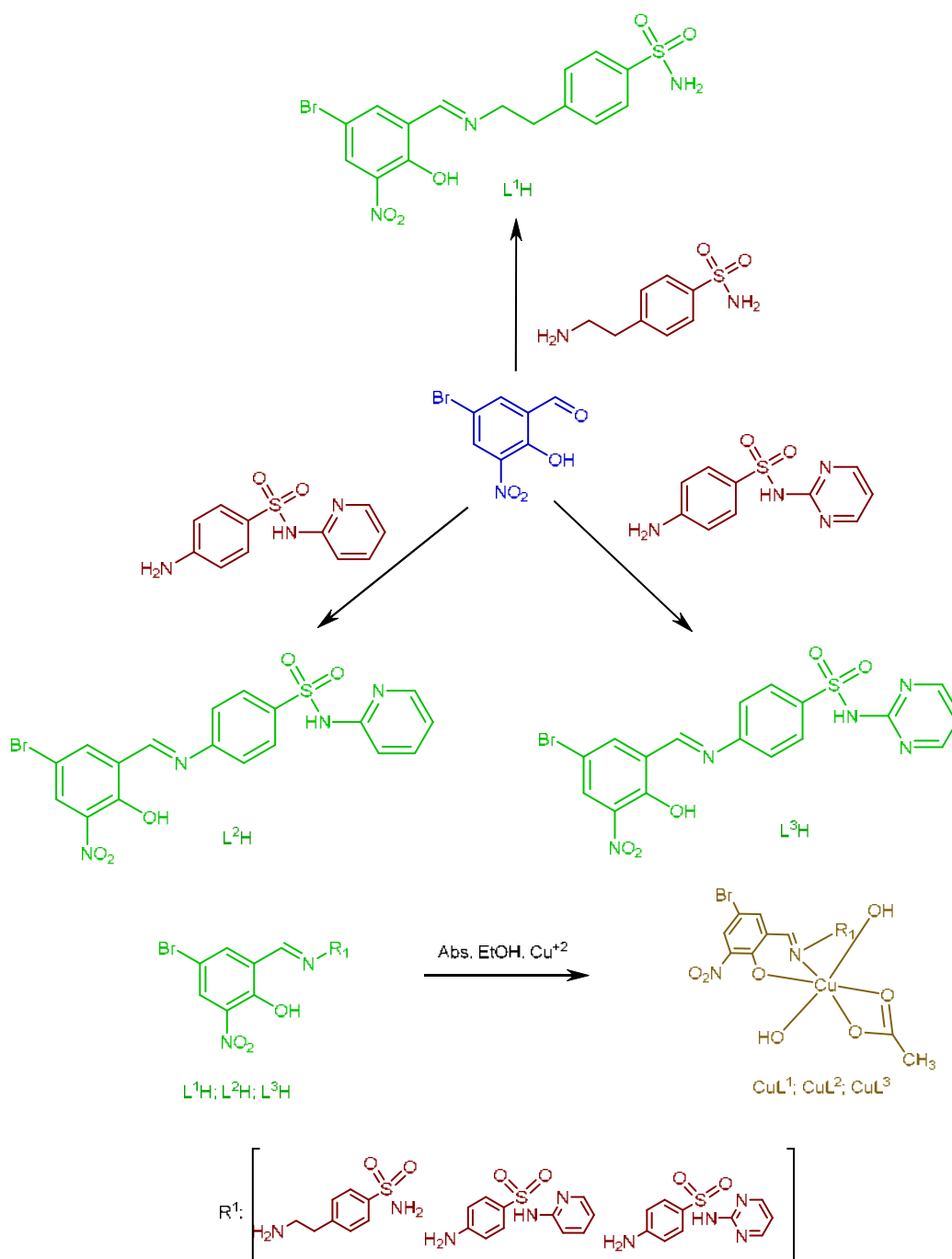
Abstract: Synthesis of three Schiff bases of 5-bromo-3-nitro salicylaldehyde containing different sulfonamide group antibiotic compounds and their Cu(II) complexes was carried out. Structures of all compounds were characterized with spectroscopic methods, including Fourier transform infrared, proton nuclear magnetic resonance, and elemental analysis. The *in vitro* antimicrobial activity of ligands and complexes against Gram-negative and Gram-positive bacteria and the yeast *Candida albicans* was evaluated. It was determined that the ligand and complexes showed outstanding antimicrobial activity against almost all of the microorganisms tested. It has been observed that the newly synthesized complexes have more antimicrobial effects than the corresponding ligands. It has been determined that the newly synthesized complexes have more antimicrobial effects than the others (*E. coli*, *L. monocytogenes*, and *C. albicans*), especially on *Staphylococcus aureus* and *Pseudomonas aeruginosa*.

Keywords: Cu(II) complex; Schiff base; sulfonamide antibiotic; time killing

■ INTRODUCTION

Schiff bases are considered to be one of the versatile classes of biologically active compounds due to their ability to interact well with periodic table transition elements. Schiff bases and complexes used as models for biological systems show antibacterial, anti-inflammatory, antifungal, herbicidal, and anti-cancer activities [1-2]. However, they are also widely used in various chemical and photochemical reactions due to their catalyst properties [3-4]. Schiff bases and their metal complexes affect electronic variations due to substituent effects [5]. In the presence of sulfur atoms in the compounds, biological activity is thought to improve due to its specific interaction with enzymes with sulfhydryl groups [6]. Sulfonamides are a class of therapeutic drugs used against infections caused by microbes. Sulfa drugs are important compounds used in pharmaceutical and agricultural fields due to their low toxicity, affordability, and significant activity profile.

Since sulfonamides are structurally similar to *p*-aminobenzoic acid (PABA), a cofactor in folic acid synthesis by bacteria, they can compete with it efficiently to inhibit the synthesis of proteins and nucleic acids, resulting in the inhibition of various microorganisms. Also, it is a sulfonamide, versatile half for its various pharmacological activities, including antibacterial, antifungal, anti-inflammatory, anti-carbonic anhydrase, diuretic, hypoglycemic, antithyroid and antiproton activities, and enzyme inhibition [7-16]. Sulfonamides, which inhibit the growth of bacterial cells by blocking the synthesis of an important vitamin called folic acid, have also been the subject of many studies due to their significant antitumor activity both *in vitro* and *in vivo* [17-21]. Some of these derivatives are currently being evaluated in clinical trials, and there is much optimism that they could lead to new alternative anti-cancer drugs that are devoid of the side effects of current pharmacological agents [22].



Scheme 1. Synthetic routes of $L^{1-3}H$ and their Cu^{+2} complexes

In this study, the synthesis of three Schiff bases of 5-bromo-3-nitro salicylaldehyde containing different sulfonamide group compounds and their $\text{Cu}(\text{II})$ complexes was carried out. The structures of all compounds were characterized by spectroscopic methods such as Fourier transform infrared, proton nuclear magnetic resonance, and elemental analysis. *In vitro*, the antimicrobial activity

of ligands and synthesized new complexes against Gram-negative and Gram-positive bacteria and yeast *Candida albicans* were evaluated. As a result of the antimicrobial study performed according to the microdilution method, the effects of the most effective complexes on the colony-forming abilities of the bacteria and their time-killing kinetics were determined.

■ EXPERIMENTAL SECTION

Materials

4-(2-Aminoethyl)benzenesulfonamide, sulfapyridine, sulfadiazine, 5-bromo-3-nitro salicylaldehyde, absolute ethanol (EtOH), copper(II) acetate hydrate ($\text{Cu}(\text{CH}_3\text{CO}_2)_2 \cdot \text{H}_2\text{O}$) used for the synthesis and analysis were purchased from Merck and used without purifications. Nutrient and broth nutrient agar from Merck and DMSO (Sigma) were used in antimicrobial experiments.

Instrumentation

The FTIR spectra were carried out by a Shimadzu QATR-S (IR Spirit S1102SC) in the range of 4000–600 cm^{-1} . ^1H (400 MHz) NMR spectra were obtained in $\text{DMSO}-d_6$ solutions by Bruker DRX-400 high-performance digital FT-NMR spectrometer. C, H, N, and S content was determined by using a LECO CHNS-932 analyzer.

Procedure

Preparation and characterization

4-(2- $\{(E)\}$ [(5-bromo-2-hydroxy-3-nitrophenyl)methylidene]amino}ethyl)benzene-1-sulfonamide (L^1H). To a solution of 4-(2-aminoethyl)benzenesulfonamide (0.600 g, 3 mmol) dissolved in 20 mL EtOH, 5-bromo-3-nitro salicylaldehyde (0.738 g, 3 mmol) dissolved in 15 mL EtOH was added dropwise. This mixture interacted at 200 °C for 12 h using the hydrothermal technique. The solid (powder) precipitate was filtered, washed with cold EtOH, and dried at room temperature to give a compound of L^1H as given in Scheme 1. (428.26 g/mol) Yield: 1.15 g (89%). m.p. 204 °C. Anal. Calc. for $\text{C}_{15}\text{H}_{14}\text{BrN}_3\text{O}_5\text{S}$: C, 42.07; H, 3.30; N, 9.81; S, 7.49%. Found: C, 41.58; H, 3.24; N, 9.68; S, 7.41.

FTIR (ATR, $\nu_{\text{max}}/\text{cm}^{-1}$): 685, 762, 928, 973, 1089, 1130 ($-\text{SO}_2$ sym), 1276, 1324, 1361 ($-\text{SO}_2$ asym), 1452 (C–O), 1609 (C=N), 3295 (N–H, sym), 3421 (O–H); ^1H -NMR ($\text{DMSO}-d_6$, δ , ppm): 13.68 (s, 1H, O–H), 9.02 (s, 1H, CH=N), 8.34–6.04 (m, 6H, Ar–H), 7.65 (s, 2H, $-\text{NH}_2$), 2.54 (t, 2H, $-\text{CH}_2$), 2.36 (t, 2H, $-\text{CH}_2$). ^{13}C -NMR ($\text{DMSO}-d_6$, δ , ppm): 162.4 (C1), 160.2 (C7), 146.5 (C10), 142.6

(C13), 142.1 (C2), 134.2 (C11), 129.5 (C5), 124.6 (C3), 123.6 (C12), 117.9 (C6), 110.9 (C4), 44.5 (C9), 41.7 (C8).

Preparation of the Cu(II)L1 complex

To a solution of L^1H ligand (0.428 g, 1 mmol) dissolved in 20 mL EtOH, $\text{Cu}(\text{CH}_3\text{CO}_2)_2 \cdot \text{H}_2\text{O}$ (0.199 g, 1 mmol) dissolved in 15 mL absolute EtOH was added dropwise. This reaction mixture interacted at 200 °C for 12 h using the hydrothermal technique. The solid (powder) precipitate was filtered, washed with cold EtOH, and dried in an oven at 80 °C for 24 h to give a compound of CuL^1 (585.87 g/mol) as given in Scheme 1. Yield: 0.43 g (74%). Anal. Calc. for $\text{C}_{17}\text{H}_{20}\text{BrN}_3\text{O}_9\text{SCu}$: C, 34.85; H, 3.44; N, 7.17; S, 5.47%. Found: C, 34.52; H, 3.39; N, 7.06; S, 5.38.

FTIR (ATR, $\nu_{\text{max}}/\text{cm}^{-1}$): 1126 ($-\text{SO}_2$ sym), 1355 ($-\text{SO}_2$ asym), 1441 (C–O), 1584 (C=O, Acetate), 1604 (C=N), 3291 (N–H, sym), 3415 (H_2O).

4- $\{(E)\}$ [(5-bromo-2-hydroxy-3-nitrophenyl)methylidene]amino}-N-(pyridin-2-yl)benzene-1-sulfonamide (L^2H).

To a solution of sulfapyridine (0.747 g, 3 mmol) dissolved in 20 mL EtOH, 5-bromo-3-nitro salicylaldehyde (0.738 g, 3 mmol) dissolved in 15 mL EtOH was added dropwise. This mixture was reacted at 200 °C for 12 h using the hydrothermal technique. The solid (powder) precipitate was filtered, washed with cold EtOH, and dried at room temperature to give a compound of L^2H (477.29 g/mol) as given in Scheme 1. Yield: 1.26 g (88%). m.p. 218 °C. Anal. Calc. for $\text{C}_{18}\text{H}_{13}\text{BrN}_4\text{O}_5\text{S}$: C, 45.30; H, 2.75; N, 11.74; S, 6.72%. Found: C, 44.86; H, 2.71; N, 11.65; S, 6.64.

FTIR (ATR, $\nu_{\text{max}}/\text{cm}^{-1}$): 692, 759, 926, 979, 1078, 1135 ($-\text{SO}_2$ sym), 1249, 1318, 1339 ($-\text{SO}_2$ asym), 1454 (C–O), 1613 (C=N), 3236 (N–H, sym), 3434 (O–H); ^1H -NMR ($\text{DMSO}-d_6$, δ , ppm): 13.74 (s, 1H, O–H), 11.68 (s, 1H, N–H), 8.96 (s, 1H, CH=N), 8.58–6.63 (m, 10H, Ar–H). ^{13}C -NMR ($\text{DMSO}-d_6$, δ , ppm): 162.6 (C1), 160.7 (C7), 159.3 (C8), 153.2 (C12), 151.1 (C16), 141.3 (C2), 139.9 (C11), 137.2 (C14), 130.5 (C10), 129.8 (C5), 124.8 (C9), 124.4 (C3), 119.3 (C15), 118.2 (C6), 112.8 (C13), 111.7 (C4).

Preparation of the Cu(II)L2 complex

To a solution of L^2H ligand (0.477 g, 1 mmol)

dissolved in 20 mL EtOH, $\text{Cu}(\text{CH}_3\text{CO}_2)_2 \cdot \text{H}_2\text{O}$ (0.199 g, 1 mmol) dissolved in 15 mL EtOH was added dropwise. This mixture was reacted at 200 °C for 12 h using the hydrothermal technique. The solid (powder) precipitate was filtered, washed with cold EtOH, and dried in an oven at 80 °C for 24 h to give a compound of CuL^2 (634.90 g/mol) as given in Scheme 1. Yield: 0.45 g (71%). Anal. Calc. for $\text{C}_{20}\text{H}_{19}\text{BrN}_4\text{O}_9\text{SCu}$: C, 37.83; H, 3.02; N, 8.82; S, 5.05%. Found: C, 37.41; H, 2.97; N, 8.74; S, 4.99.

FTIR (ATR, $\nu_{\text{max}}/\text{cm}^{-1}$): 1130 ($-\text{SO}_2$ sym), 1334 ($-\text{SO}_2$ asym), 1441 (C–O), 1585 ($-\text{C}=\text{O}$, Acetate) 1609 (C=N), 3231 (N–H, sym), 3414 (H_2O).

4- $\{(E)\text{-}[(5\text{-bromo-}(2\text{-hydroxy-3-nitrophenyl)methylidene]amino\}-N\text{-}(pyrimidin-2\text{-yl)benzene-1-sulfonamide (L}^3\text{H)}$. To a solution of sulfadiazine (0.750 g, 3 mmol) dissolved in 20 mL EtOH, 5-bromo-3-nitro salicylaldehyde (0.738 g, 3 mmol) dissolved in 15 mL EtOH was added dropwise. This mixture was reacted at 200 °C for 12 h using the hydrothermal technique. The solid (powder) precipitate was filtered, washed with cold EtOH, and dried at room temperature to give a compound of L^3H (478.28 g/mol) as given in Scheme 1. Yield: 1.30 g (90%). m.p. 194 °C. Anal. Calc. for $\text{C}_{17}\text{H}_{12}\text{N}_5\text{O}_5\text{S}$: C, 42.69; H, 2.53; N, 14.64; S, 6.70%. Found: C, 42.30; H, 2.49; N, 14.52; S, 6.63.

FTIR (ATR, $\nu_{\text{max}}/\text{cm}^{-1}$): 688, 762, 976, 1081, 1128 ($-\text{SO}_2$ sym), 1245, 1314, 1330 ($-\text{SO}_2$ asym), 1452 (C–O), 1614 (C=N), 3230 (N–H, sym), 3432 (O–H); $^1\text{H-NMR}$ (DMSO- d_6 , δ , ppm): 13.76 (s, 1H, O–H), 11.65 (s, 1H, N–H), 8.93 (s, 1H, CH=N), 8.45–6.71 (m, 9H, Ar–H). $^{13}\text{C-NMR}$ (DMSO- d_6 , δ , ppm): 162.3 (C1), 161.2 (C7), 159.1 (C8), 158.3 (C12), 157.5 (C13), 141.7 (C2), 139.4 (C11), 132.3 (C10), 129.3 (C5), 125.2 (C3), 124.6 (C9), 117.8 (C6), 115.6 (C14), 110.9 (C4).

Preparation of the Cu(II)L3 complex

To a solution of L^3H ligand (0.478 g, 1 mmol) dissolved in 20 mL EtOH, $\text{Cu}(\text{CH}_3\text{CO}_2)_2 \cdot \text{H}_2\text{O}$ (0.199 g, 1 mmol) dissolved in 15 mL EtOH was added dropwise. This mixture was reacted at 200 °C for 12 h using the hydrothermal technique. The solid (powder) precipitate was filtered, washed with cold EtOH, and dried in an oven at 80 °C for 24 h to give a compound of CuL^3 (635.89 g/mol) as given in Scheme 1. Yield: 0.43 g (68%).

Anal. Calc. for $\text{C}_{19}\text{H}_{18}\text{BrN}_5\text{O}_9\text{SCu}$: C, 35.89; H, 2.85; N, 11.01; S, 5.04%. Found: C, 35.56; H, 2.80; N, 10.89; S, 5.00.

FTIR (ATR, $\nu_{\text{max}}/\text{cm}^{-1}$): 1124 ($-\text{SO}_2$ sym), 1328 ($-\text{SO}_2$ asym), 1438 (C–O), 1587 ($-\text{C}=\text{O}$, Acetate) 1608 (C=N), 3228 (N–H, sym), 3416 (H_2O).

Antimicrobial activity

In this study, 4 different standard bacterial strains and 1 yeast cell were used. These are Gram-positive *S. aureus* ATCC 25923 and *L. monocytogenes* ATCC 19111, Gram-negative *E. coli* ATCC 25922 and *P. aeruginosa* ATCC 27853, and yeast *C. albicans* ATCC 10231. The solutions of newly synthesized complexes and ligands were prepared by dissolving them in DMSO at appropriate concentrations. The antimicrobial effects of the prepared complexes on microorganisms were determined by calculating the minimal inhibition concentration (MIC) values according to the broth dilution method. For the broth dilution method, cultures were grown in 5 mL nutrient broth (Merck) at 37 °C for 18 h in shaking at 175 rpm. Bacterial and yeast cells were suspended in 50 mL nutrient broth at a concentration of approximately 10^6 cells/mL by matching with 0.5 McFarland turbidity standards. The nutrient broth is added into 10 different tubes. Then, the complexes are added to the first tubes at appropriate concentrations, and serial dilution is made. In this way, the appropriate MIC values are determined by making half the dilution each time. Then all test tubes are left to grow overnight in an incubator at 37 °C. MIC values were determined after bacterial strains and yeast strains were kept in the incubator for 24 h. The last tube without growth was taken as the MIC ($\mu\text{g/mL}$), representing the mean of at least three determinations.

Viability experiments in microorganisms

Microorganisms to be used in this study were incubated for 1 night at 37 °C in a sterile nutrient broth medium. An amount of the microorganism that was left to grow for 1 night was taken and added to another nutrient broth medium. Thus, the number of bacteria was adjusted to 10^5 per mL. At the same time, considering the MIC value determined in the antimicrobial study, the complexes were added to the

medium in amounts determined as MIC, 2×MIC, and 4×MIC. Colony counts were made by taking microorganism samples at 37 °C for 24 h at appropriate times. The obtained colony numbers were converted to logarithmic (log) values, and T_{99} values were calculated. The T_{99} value is expressed as the value corresponding to a 2-log decrease in the number of bacteria over 24 h [23].

■ RESULTS AND DISCUSSION

Synthesis and Characterization of the Ligands and Their Cu(II) Complexes

In this study, sulfa-derived Schiff bases (L^1H-L^3H) were synthesized by reacting equimolar amounts of 4-(2-aminoethyl)benzene sulphonamide, sulfapyridine, and sulfadiazine with 5-bromo-3-nitro salicylaldehyde in EtOH, and followed by Cu(II) complexes of these ligands. All products were purified, and their structures were elucidated with general spectroscopic methods and elemental analysis, and the findings supported each proposed structure. The characteristic IR peaks of the ligands are the peaks of C=N, C-O, O-H, and S=O stretching vibrations. Others are C=C and C=O stretch vibration peaks, aliphatic C-H and N-H, and aromatic C-H stretch vibration peaks. When the IR spectrums of compounds are examined, the O-H stretching vibrations of the phenolic -OH group is broad at the range of 3434–3421 cm^{-1} , and the C=N stretching vibrations of the azomethine group are seen as sharply in the range of 1614–1609 cm^{-1} . These bands support the completion of the formation reaction of compounds L^1H-L^3H . These values agree with those found for similar compounds [14–16].

The most significant changes in the spectra of the Cu^{2+} complexes of L^1H-L^3H ligands were observed in the C=N stretching vibrations of the Schiff base group, the bending vibrations of the phenolic O-H group, the C=N vibrations, and the S=O symmetrical and asymmetrical stretching vibrations. The characteristic C=N (aliphatic) stretching vibration observed in the ligands in the 1614–1609 cm^{-1} range shifted to 1609–1604 cm^{-1} with the formation of metal chelates. This shift indicated that the azomethine group's nitrogen atom was involved in forming the metal-nitrogen (M-N) bond.

In other words, the nitrogen atom gave its unshared electrons to the metal ion and entered into coordination with the metal [24]. In addition, the band observed in the ligands in the range of 1454–1452 cm^{-1} and characteristic of C-O (phenolic) stretching vibration shifted up to 11–14 cm^{-1} in complex structures. This shift supports that deprotonated phenolic oxygen enters coordination with metal ions during complex formation [25]. In addition, the new peak in the range of 1587–1584 cm^{-1} indicates the presence of acetate coordinated with the metal and the presence of metal-coordinated water in the complexes at the peak in the range of 3416–3414 cm^{-1} [26–27]. The most useful infrared spectral bands of the compounds are listed in the experimental section (Fig. S1).

In addition to the IR spectrum data of the complexes, the percentages of C, H, S, and N in the elemental analysis results support the presence of acetate and water molecules that are bound to the structure and support that the predicted structure is in octahedral order [28] (Fig. S1).

The 1H -NMR of the compounds L^1H-L^3H was recorded in $DMSO-d_6$ at room temperature. It belongs to a singlet -OH proton of one proton observed in the 13.76–13.68 ppm range in the 1H -NMR spectrums taken in $DMSO-d_6$ solvent of compounds L^1H-L^3H . In addition, the peak was observed as a singlet at a proton intensity range of 9.02–8.93 ppm and also belonged to the azomethine proton in the structure. In addition, the chemical shift observed in the spectrum in the range of 11.68–7.65 ppm belongs to the (-NH) proton(s) attached to the -SO₂ group in the structure. The -NH proton(s) of the L1H ligand is lower field than the other ligands because the structure is connected to the linear chain structure instead of the aromatic ring directly. In addition, chemical shifts in the 2.54–2.36 ppm range belong to the methyl groups present in the L^1H ligand. The specified chemical shifts confirm the formation of structures (Fig. S2, S4, S6).

The most useful 1H -NMR spectrums bands of the compounds are listed in the experimental section. The observed peaks agree with the structure and literature [29–30]. The chemical shifts of all carbons in the ^{13}C -

NMR spectra of the ligands are given in the experimental part. The resonance observed in the range of 161.2–160.2 ppm belongs to the carbon of the azomethine group (C7). Peaks of other aromatic ring carbons were observed in the range of 162.6–110.9 ppm. In addition, the resonances observed in the range of 44.5–41.7 ppm in the spectrum of the L¹H ligand belong to the carbons (C9 and C8) (Fig. S3, S5, S7). The observed peaks are consistent with the structure and literature [29–30].

Antimicrobial Activity

In this study, the antimicrobial properties of newly synthesized complexes using the microdilution method were investigated. *S. aureus* and *L. monocytogenes* as Gram-positive, *E. coli* and *P. aeruginosa* as Gram-negative, and *C. albicans* as yeast were used as standard strains. In these experiments based on the determination of MIC values, stock solutions of newly synthesized complexes were prepared by dissolving them in DMSO. Therefore, firstly, the MIC value of DMSO for control purposes was calculated and compared with the newly synthesized complexes. According to the results obtained, it was observed that the MIC value of DMSO was > 4000 µg/mL. In other words, it was determined that DMSO did not have a significant antimicrobial effect. When the antimicrobial effects of ligands (L¹H, L²H, and L³H) were examined, it was determined that the MIC values ranged between 93.75 and 3000 µg/mL. As a matter of fact, the antimicrobial value of the ligand coded L¹H was found to be 1500, 375, 375, 3000, and 93.75 µg/mL for *E. coli*, *P. aeruginosa*, *S. aureus*, *L. monocytogenes*, and *C. albicans*, respectively. MIC values for another ligand, L²H,

were found to be 1500 µg/mL for *E. coli*, 750 µg/mL for *P. aeruginosa* and *C. albicans*, 93.75 µg/mL for *S. aureus* and 3000 µg/mL for *L. monocytogenes*. When the antimicrobial results of the L³H ligand are examined, it can be stated that these values are 375 µg/mL in *E. coli*, 187.5 µg/mL in *P. aeruginosa*, 93.75 µg/mL in *S. aureus*, 375 µg/mL in *L. monocytogenes* and 93.75 µg/mL in *C. albicans* (Table 1). In addition, antimicrobial activities of new complexes obtained from ligands were investigated, and MIC values were observed to vary between 11.7 and 3000 µg/mL. As a matter of fact, the MIC values that the newly synthesized L¹-Cu complex is effective on microorganisms were determined as 750 µg/mL for *E. coli*, 93.75 µg/mL for *P. aeruginosa*, 23.4 µg/mL for *S. aureus* and 46.8 µg/mL for *C. albicans*. In addition, these values for L²-Cu were found to be 750, 93.75, 23.4, 750, and 187.5 µg/mL in *E. coli*, *P. aeruginosa*, *S. aureus*, *L. monocytogenes*, and *C. albicans*, respectively. In the continuation of the study, the MIC values of the new complex coded as L³-Cu were determined to be 187.5 and 23.4 µg/mL for *E. coli* and *P. aeruginosa* and 11.7 and 375 µg/mL for Gram-positive *S. aureus* and *L. monocytogenes*. Another result is that the MIC value for *C. albicans*, which is yeast, is 187.5 µg/mL.

Effects of Complexes on the Life of Bacteria and Time-Killing Activities

The effects of L¹-Cu and L²-Cu, which have the most antimicrobial effects, on the survival of Gram-positive *S. aureus* and Gram-negative *P. aeruginosa* was investigated in this study, which was carried out considering the data obtained from the MIC study. In the

Table 1. Antimicrobial effects of complexes on microorganisms (µg/mL)

	Gram-negative (-) bacteria		Gram-positive (+) bacteria		Yeast
	<i>E. coli</i> ATCC 25922	<i>P. aeruginosa</i> ATCC 27853	<i>S. aureus</i> ATCC 25923	<i>L. monocytogenes</i> ATCC 19111	<i>C. albicans</i> ATCC 10231
L ¹ H	1500.00	375.00	375.00	3000.00	93.75
L ² H	1500.00	750.00	187.50	3000.00	750.00
L ³ H	375.00	187.50	93.75	375.00	93.75
L ¹ -Cu	750.00	93.75	23.40	3000.00	46.80
L ² -Cu	750.00	93.75	23.40	750.00	187.50
L ³ -Cu	187.50	23.40	11.70	375.00	1500.00
DMSO	> 4000.00	> 4000.00	> 4000.00	> 4000.00	> 4000.00

study conducted for 24 h, the complexes were added to the medium containing the bacteria in MIC, 2×MIC, and 4×MIC concentrations, and the results were evaluated according to the colony count. Table 2 shows the effects of the complexes added to the nutrient broth medium on the colony-forming abilities of the microorganisms. Bacteria samples taken from the liquid medium at 0, 12, and 24 h were inoculated into the solid medium, kept in the incubator for 24 h, and the former colonies were counted and recorded.

The results obtained in the second stage of the study were converted to logarithmic values and recorded by calculating T_{99} values (Table 3). Therefore, as a result of this study, how long the newly synthesized complexes kill the microorganism *in vitro* will be determined precisely. Both *P. aeruginosa* and *S. aureus* control samples showed a very high increase in colony numbers after 24 h. As a matter of fact, while the number of colonies at the 0 h was

45×10^4 in the *P. aeruginosa* control sample, it was determined that this number was 550×10^{10} at the end of 24 h. In addition, at the end of 24 h (L^1 -Cu addition) in the samples to which MIC, 2×MIC, and 4×MIC were added, the number of bacteria was found to be 6300, 240, and 39, respectively. In the samples with L^2 -Cu added, it was determined that the bacterial numbers were 5800 with the addition of MIC, 180 with the addition of 2×MIC and 105 with the addition of 4×MIC. Adding L^3 -Cu (MIC, 2×MIC, 4×MIC) to the broth containing *P. aeruginosa* also revealed that the bacterial counts were 4570, 15, and 0.

When the survival test results of Gram-positive *S. aureus* were examined, it was seen that the colony numbers in the control samples were 26×10^4 at 0 h and 1524×10^{11} at the end of 24 h. Although the number of bacteria in the samples added to the medium at MIC concentration was 26×10^4 at 0 h, this number was found

Table 2. Bacterial cell count (colony forming unit-cfu/mL)

Complexes	Microorganisms		0 h ($\times 10^4$ cfu/mL)	12 h (cfu/mL)	24 h (cfu/mL)
L^1 -Cu	<i>P. aeruginosa</i> ATCC 27853	Control	45	67×10^5	550×10^{10}
		MIC	45	88×10^3	63×10^2
		2×MIC	45	47×10^2	24×10^1
		4×MIC	45	250×10^1	39
	<i>S. aureus</i> ATCC 25923	Control	26	224×10^5	1524×10^{11}
		MIC	26	158×10^3	282×10^1
		2×MIC	26	104×10^2	198
		4×MIC	26	458×10^1	8
L^2 -Cu	<i>P. aeruginosa</i> ATCC 27853	Control	45	67×10^5	550×10^{10}
		MIC	45	350×10^3	58×10^2
		2×MIC	45	145×10^2	180
		4×MIC	45	452×10^1	105
	<i>S. aureus</i> ATCC 25923	Control	26	224×10^5	1524×10^{11}
		MIC	26	205×10^3	76×10^2
		2×MIC	26	276×10^2	64
		4×MIC	26	327×10^1	2
L^3 -Cu	<i>P. aeruginosa</i> ATCC 27853	Control	45	67×10^5	550×10^{10}
		MIC	45	557×10^3	296×10^1
		2×MIC	45	653×10^1	45
		4×MIC	45	250×10^1	5
	<i>S. aureus</i> ATCC 25923	Control	26	224×10^5	1524×10^{11}
		MIC	26	463×10^2	457×10^1
		2×MIC	26	48×10^2	15
		4×MIC	26	59×10^1	0

Table 3. Survival times of bacteria under the influence of complexes (time-killing activities) (T_{99} values)

Strain	Complexes	0 h (log)	24 h (log)	T_{99} (h)		
Gram(-) <i>P. Aeruginosa</i> ATCC 27853	Control	6.65	13.74	>24.00		
	L ¹ -Cu	MIC	6.65	4.79	>24.00	
		2×MIC	6.65	3.38	15.38	
		4×MIC	6.65	2.59	12.50	
	L ² -Cu	MIC	6.65	4.94	>24.00	
		2×MIC	6.65	3.25	14.20	
		4×MIC	6.65	3.02	13.30	
		MIC	6.65	4.47	22.20	
		L ³ -Cu	2×MIC	6.65	2.65	12.50
			4×MIC	6.65	2.39	11.76
	Gram(+) <i>S. Aureus</i> ATCC 25923	Control	6.41	15.18	>24.00	
		L ¹ -Cu	MIC	6.41	4.26	22.47
2×MIC			6.41	2.99	14.28	
4×MIC			6.41	1.90	11.10	
L ² -Cu		MIC	6.41	5.24	>24.00	
		2×MIC	6.41	2.80	13.30	
		4×MIC	6.41	1.30	9.50	
		MIC	6.41	3.65	17.39	
		L ³ -Cu	2×MIC	6.41	2.17	11.30
			4×MIC	6.41	1.00	8.80

to be 2820 for L¹-Cu, 7600 for L²-Cu, and 4570 for L³-Cu after 24 h (Table 2). Again, with the addition of L¹-Cu, L²-Cu, and L³-Cu in 2×MIC concentration to the medium, the bacterial counts were determined to be 198, 64, and 15, respectively, after 24 h. Finally, the addition of L¹-Cu, L²-Cu, and L³-Cu at 4×MIC concentration to the medium caused a decrease in bacterial numbers. The number of bacteria was 8 when L¹-Cu was added to the medium, 2 when L²-Cu was added, and 0 when L³-Cu was added to the medium.

Colony numbers obtained in the second part of this study were converted to logarithmic values, and T_{99} values were calculated. It is known that the T_{99} value is considered as the time corresponding to 2 logarithmic drops. The T_{99} value is considered important data in terms of showing us how long the bacteria live in any environment. Table 3 presents logarithmic values and T_{99} calculations of the effects of newly synthesized complexes on *P. aeruginosa* and *S. aureus*. The medium in which no complex was added was considered the control. And it was determined that the control samples continued to live more than 24 h according to the T_{99} value. When L¹-Cu is added to the medium at MIC

concentration, it can be stated that *P. aeruginosa* continues to live for more than 24 h. As a result of the addition of the same complex to the medium in 2×MIC concentration, it was observed that the life of the bacteria decreased, and this period was 15.38 h.

On the other hand, it was determined that the bacteria continued to live for 12.5 h by adding complex at 4×MIC concentration to the medium. In addition, with the addition of L²-Cu and L³-Cu with MIC value to the medium, it was observed that *P. aeruginosa* lived for more than 24 and 22.2 h. On the other hand, the addition of L²-Cu to the medium at 2×MIC concentration caused the survival of the bacteria to decrease to 14.2 h, and the addition of L³-Cu to 12.5 h. In addition, it was determined that the bacteria continued to live for 13.3 h with the addition of L²-Cu at 4×MIC concentration to the medium in which the bacteria were present and 11.76 h with the addition of L³-Cu.

Table 3 shows the results of the studies that determined how long the Gram-positive *S. aureus* could survive with the addition of complexes at different concentrations. According to this, it was observed that

the bacteria continued to live for 22.47, > 24, 17.39 h in media with the addition of L¹-Cu, L²-Cu, and L³-Cu, respectively, at MIC concentrations. When the complex was added to the medium at 2×MIC concentration, T₉₉ values were found to be 14.28, 13.3, and 11.3 h. On the other hand, the addition of the complexes (L¹-Cu, L²-Cu, and L³-Cu; 11.1, 9.5, and 8.8 h, respectively) to the medium at 4×MIC concentration resulted in significant reductions in the survival of *S. aureus*.

The development of resistance of microorganisms to antibiotics adversely affects the fight against diseases. This necessitated the discovery of new chemicals. Therefore, studies on the synthesis of new complexes to be used for chemotherapeutic purposes have become very important in recent years. Investigations, primarily to obtain new antimicrobials from plants, are continuing rapidly [31-32]. However, the increasing resistance of microorganisms to chemotherapeutics has made it necessary to synthesize new chemicals. Studies on the synthesis of new complexes and the acquisition of new antimicrobials in the laboratory environment have gained importance in recent years, and quite a lot of new studies are being done on this subject [33-39]. It is known that sulfonamides are the oldest and most well-known antimicrobial agents widely used against bacterial and fungal infections. Like sulfonamides, Schiff bases are commonly used in drug discovery.

Even now, sulfonamides are used to treat infections caused by bacteria and other microorganisms. It is thought that the study conducted here is very important in terms of supporting this. As a matter of fact, according to the results obtained, it was determined that ligands and complexes synthesized from ligands had high antimicrobial effects. Moreover, it was determined that the newly synthesized copper complexes showed higher activity than the ligands. It is stated that this effect is due to the atomic structure of copper and the possibility of easy electron transfer. It is known that the increased copper level in the cell creates an oxidative stress effect. Therefore, oxidative stress causes oxidative damage in cells. It is known that increased copper level weakens membrane integrity and causes deterioration of protein functions [40]. It is considered one of the most important

factors that cause the disappearance of microorganisms from the environment. This study is important for being a precursor for using the newly synthesized complexes as a new chemotherapeutic for the future. As a result of bacterial survival experiments, it was revealed that the number of both bacteria (*P. aeruginosa*, *S. aureus*) increased during 24 h in control samples. However, the addition of the complex to the medium caused significant reductions in the number of bacteria. In addition, no bacteria were found at the end of 24 h in environments where high concentrations of complexes were added. Moreover, it was determined that the higher the amount of complex added to the medium, the corresponding decrease in the number of bacteria. In this study, it was also determined that Gram-positive bacteria were affected more than Gram-negative bacteria. It is known that this is due to the Gram-positive bacterial wall structure. Therefore, it can be stated that the new chemicals synthesized here are important in terms of shedding light on future studies.

■ CONCLUSION

In this study, syntheses of 4-(2-((E)-[(5-bromo-2-hydroxy-3-nitrophenyl)methylidene]amino)ethyl)benzene-1-sulfonamide L¹H, Cu(II)L¹, 4-((E)-[(5-bromo-2-hydroxy-3-nitrophenyl)methylidene]amino)-N-(pyridin-2-yl)benzene-1-sulfonamide L²H, Cu(II)L², 4-((E)-[(5-bromo-(2-hydroxy-3-nitrophenyl)methylidene]amino)-N-(pyrimidin-2-yl)benzene-1-sulfonamide L³H, Cu(II)L³ were described.

Ligand and copper complexes were found to have significant antimicrobial activities on all microorganisms. However, it was also determined that the newly synthesized complexes had higher antimicrobial activity than the ligands. Moreover, it has been determined that all newly synthesized complexes have more antimicrobial effects than others, especially on *S. aureus* and *P. aeruginosa*. And it has been determined that L³-Cu has a very high antimicrobial effect on both *S. aureus* and *P. aeruginosa*. It is thought that this study is important in terms of giving us the idea of using newly synthesized complexes in the pharmacological field in the future.

■ ACKNOWLEDGMENTS

The authors did not receive support from any organization for the submitted work.

■ AUTHOR CONTRIBUTIONS

Önder İdil wrote the experimental part on biological activity studies (Antimicrobial and Time killing) and prepared the draft of the article. Hakan Şahal and Erdal Canpolat completed the synthesis and characterization and wrote this part. Mustafa Özkan revised the manuscript. All authors agreed to the final version of this manuscript.

■ REFERENCES

- [1] Garai, M., Das, A., Joshi, M., Paul, S., Shit, M., Choudhury, A.R., and Biswas, B., 2018, Synthesis and spectroscopic characterization of a photo-stable tetrazinc(II)–Schiff base cluster: A rare case of ligand centric phenoxazinone synthase activity, *Polyhedron*, 156, 223–230.
- [2] Pal, C.K., Mahato, S., Joshi, M., Paul, S., Choudhury, A.R., and Biswas, B., 2020, Transesterification activity by a zinc(II)-Schiff base complex with theoretical interpretation, *Inorg. Chim. Acta.*, 506, 119541.
- [3] Yousif, E., Hasan, A., and El-Hiti, G.A., 2016, Spectroscopic, physical and topography of photochemical process of PVC films in the presence of Schiff base metal complexes, *Polymers*, 8, 204.
- [4] Ibrahim, F.M., and Abdalhadi, S.M., 2021, Performance of Schiff bases metal complexes and their ligand in biological activity: A review, *Al-Nahrain J. Sci.*, 24 (1), 1–10.
- [5] Tigineh, G.T., and Liu, L.K., 2017, Solvatochromic photoluminescence investigation of functional Schiff-bases: A systematic study of substituent effects, *J. Photochem. Photobiol., A*, 338, 161–170.
- [6] Chouhan, S., Sharma, K., and Guleria, S., 2017, Antimicrobial activity of some essential oils—Present status and future perspectives, *Medicines*, 4 (3), 58.
- [7] Ahmed, M., Qadir, M.A., Ahmad, S., Ul-Haq, I., Hussain, R., Habib, T., Ikram, R., and Muddassar, M., 2020, Studies on the synthesis of benzene sulfonamides, evaluation of their antimicrobial activities, and molecular docking, *Lat. Am. J. Pharm.*, 39, 38–46.
- [8] Apaydin, S., and Török, M., 2019, Sulfonamide derivatives as multi-target agents for complex diseases, *Bioorg. Med. Chem. Lett.*, 29, 16, 2042–2050.
- [9] Krátký, M., Vinšová, J., Volková, M., Buchta, V., Trejtnar, F., and Stolaříková, J., 2012, Antimicrobial activity of sulfonamides containing 5-chloro-2-hydroxybenzaldehyde and 5-chloro-2-hydroxybenzoic acid scaffold, *Eur. J. Med. Chem.*, 50, 433–440.
- [10] Gaffer, H.E., 2019, Antimicrobial sulphonamide azo dyes, *Color. Technol.*, 135 (6), 484–500.
- [11] Pervaiz, M., Riaz, A., Munir, A., Saeed, Z., Hussain, S., Rashid, A., Younas, U., and Adnan, A., 2020, Synthesis and characterization of sulfonamide metal complexes as antimicrobial agents, *J. Mol. Struct.*, 1202, 127284.
- [12] El-Ghamry, H.A., Alharbi, B.K., Takroni, K.M., and Khedr, A.M., 2023, A series of nanosized Cu(II) complexes based on sulfonamide azo dye ligands: An insight into complexes molecular structures, antimicrobial, antitumor and catalytic performance for oxidative dimerization of 2-aminophenol, *Appl. Organomet. Chem.*, 37 (2), e6978.
- [13] Althagafi, I., Elghalban, M.G., and El-Metwaly, N.M., 2019, Novel synthesized benzenesulfonamide nanosized complexes; Spectral characterization, molecular docking, molecular modeling and analytical application, *J. Inorg. Organomet. Polym. Mater.*, 29 (3), 876–892.
- [14] Ghomashi, R., Ghomashi, S., Aghaei, H., and Massah, A.R., 2023, Recent advances in biological active sulfonamide based hybrid compounds Part A: Two-component sulfonamide hybrids, *Curr. Med. Chem.*, 30 (4), 407–480.
- [15] Ogden, R.C., and Flexner, C.W., 2001, *Protease Inhibitors in AIDS Therapy*, Marcel Dekker, Inc., New York, US.
- [16] Mahapatra, M., Mohapatra, P., Sahoo, S.K., Bishoyi, S.K., Padhy, R.N., and Paidesetty, S.K., 2023, Design, synthesis, and *in-silico* study of chromen-

- sulfonamide congeners as potent anti-cancer and antimicrobial agents, *J. Mol. Struct.*, 1283, 135190.
- [17] Abdul Qadir, M., Ahmed, M., Aslam, H., Waseem, S., and Shafiq, M.I., 2015, Amidine sulfonamides and benzene sulfonamides: Synthesis and their biological evaluation, *J. Chem.*, 2015, 524056.
- [18] Alghuwainem, Y.A.A., Abd El-Lateef, H.M., Khalaf, M.M., Abdelhamid, A.A., Alfarsi, A., Gouda, M., Abdelbaset, M., and Abdou, A., 2023, Synthesis, structural, DFT, antibacterial, antifungal, anti-inflammatory, and molecular docking analysis of new VO(II), Fe(III), Mn(II), Zn(II), and Ag(I) complexes based on 4-((2-hydroxy-1-naphthyl)azo) benzenesulfonamide, *J. Mol. Liq.*, 369, 120936.
- [19] Feng, G., Zou, W., Zhong, Y., 2022, Sulfonamides repress cell division in the root apical meristem by inhibiting folates synthesis, *J. Hazard. Mater. Adv.*, 5, 100045.
- [20] Cheong, M.S., Seo, K.H., Chohra, H., Yoon, Y.E., Choe, H., Kantharaj, V., and Lee, Y.B., 2020, Influence of sulfonamide contamination derived from veterinary antibiotics on plant growth and development, *Antibiotics*, 9 (8), 456.
- [21] Al-Dosari, M.S., Ghorab, M.M., Al-Said, M.S., and Nissan, Y.M., 2013, Discovering some novel 7-chloroquinolines carrying a biologically active benzenesulfonamide moiety as a new class of anti-cancer agents, *Chem. Pharm. Bull.*, 61 (1), 50–58.
- [22] Jawad, W.A., Balakit, A.A., and Al-Jibouri, M.N.A., 2021, Synthesis, characterization and antibacterial activity study of cobalt(II), nickel(II), copper(II), palladium(II), cadmium(II) and platinum(IV) complexes with 4-amino-5-(3,4,5-trimethoxyphenyl)-4H-1,2,4-triazole-3-thione, *Indones. J. Chem.*, 21 (6), 1514–1525.
- [23] Lewis, A., and Keevil, C.W., 2004, *Antibacterial Properties of Alloys and Its Alloys in HVAC&R Systems*, International Copper Association, New York, US.
- [24] Dayan, S., Ozpozan, N.K., Özdemir, N., and Dayan, O., 2014, Synthesis of some ruthenium(II)–Schiff base complexes bearing sulfonamide fragment: New catalysts for transfer hydrogenation of ketones, *J. Organomet. Chem.*, 770, 21–28.
- [25] Maurya, M.R., Chaudhary, N., Avecilla, F., and Correia, I., 2015, Mimicking peroxidase activity by a polymer-supported oxidovanadium(IV) Schiff base complex derived from salicylaldehyde and 1,3-diamino-2-hydroxypropane, *J. Inorg. Biochem.*, 147, 181–192.
- [26] Canpolat, E., Şahal, H., Kaya, M., and Gür, S., 2014, Synthesis, characterization, antibacterial and antifungal activities studies of copper(II), cobalt(II) and zinc(II) complexes of the Schiff base ligand derived from 4,4-diaminodiphenylether, *J. Chem. Soc. Pak.*, 36 (1), 106–112.
- [27] Fellah, M.F., Bakirdere, E.G., Canpolat, E., and Kaya, M., 2014, A density functional theory study of [(4-aminophenyl)imino]methyl-6-methoxy4-nitrophenol complexes with Co, Ni, Cu and Zn metals, *J. Indian Chem. Soc.*, 91, 1321–1326.
- [28] Şahal, H., Fellah, M.F., Gur, S., Kaya, M., Turkoglu, S., and Canpolat, E., 2017, Studies of novel sulfapyridine derivatives containing Schiff bases and Co(II), Ni(II) and Zn(II) complexes: Synthesis, experimental and theoretical (DFT) approach for characterization and biological efficacy, *J. Chem. Soc. Pak.*, 39 (4), 650–660.
- [29] Şahal, H., Pişkin, M., Organ, G.A., Öztürk, Ö.F., Kaya, M., and Canpolat, E., 2018, Zinc(II) phthalocyanine containing Schiff base containing sulfonamide: synthesis, characterization, photophysical, and photochemical properties, *J. Coord. Chem.*, 71 (22), 3763–3775.
- [30] Pişkin, M., Canpolat, E., and Öztürk, Ö.F., 2020, The new zinc phthalocyanine having high singlet oxygen quantum yield substituted with new benzenesulfonamide derivative groups containing Schiff base, *J. Mol. Struct.*, 1202, 127181.
- [31] Hundur, Ö.D., İdil, Ö., Kandemir, N., Gül, M., and Konar, V., 2018, Phytochemical screening and in-vitro antioxidant, antimicrobial activity and DNA interaction of *Leucojum aestivum*, *Fresenius Environ. Bull.*, 27 (10), 6704–6710.

- [32] Gul, M., Ozturk, C.I., Cansaran, A., Idil, O., Kulu, I., and Celikoglu, U., 2017, Evaluation of phytochemical content, antioxidant, antimicrobial activity and DNA cleavage effect of endemic *Linaria corifolia* Desf. (Plantaginaceae), *Cogent Chem.*, 3 (1), 1337293.
- [33] Vural, H., and Idil, O., 2019, Synthesis, spectroscopic investigation and biological activities of copper(II) complex of 2-(2,4-difluorophenyl)pyridine: A combined theoretical and experimental study, *J. Mol. Struct.*, 1177, 242–248.
- [34] Evecen, M., Kara, M., Idil, O., and Tanak, H., 2017, Investigation of antimicrobial activities, DNA interaction, structural and spectroscopic properties of 2-chloro-6-(trifluoromethyl)pyridine, *J. Mol. Struct.*, 1137, 206–215.
- [35] Gul, M., Turk Celikoglu, E., Idil, O., Tas, G., and Pelit, E., 2023, Synthesis, antimicrobial activity and molecular docking studies of spiroquinoline-indoline-dione and spiropyrazolo-indoline-dione derivatives, *Sci. Rep.*, 13 (1), 1676.
- [36] Zülfikaroğlu, A., Taş, M., Vural, H., Çelikoğlu, E., and İdil, Ö., 2021, Synthesis, structural characterization, DNA cleavage studies, antimicrobial activities, and time-killing kinetics of tetranuclear Cu(II) with partial cubane Cu₄O₄ cores and mononuclear Co(II) and Ni(II) complexes of a new acylhydrazone ligand, *Appl. Organomet. Chem.*, 35 (6), e6218.
- [37] Isik, K., and Özdemir-Kocak, F., 2009, Antimicrobial activity screening of some sulfonamide derivatives on some *Nocardia* species and isolates, *Microbiol. Res.*, 164, (1), 49–58.
- [38] Heiran, R., Jarrahpour, A., Riazimontazer, E., Gholami, A., Troudi, A., Digiorgio, C., Brunel, J.M., and Turos, E., 2021, Sulfonamide-β-lactam hybrids incorporating the piperazine moiety as potential anti-inflammatory agent with promising antibacterial activity, *ChemistrySelect*, 6 (21), 5313–5319.
- [39] Verma, S.K., Verma, R., Xue, F., Thakur, P.K., Girish, Y.R., and Rakesh, K.P., 2020, Antibacterial activities of sulfonyl or sulfonamide containing heterocyclic derivatives and its structure-activity relationships (SAR) studies: A critical review, *Bioorg. Chem.*, 105, 104400.
- [40] Konieczny, J., and Rdzawski, Z., 2012, Antibacterial properties of copper and its alloys, *Arch. Mater. Sci. Eng.*, 56 (2), 53–60.

Structural, Electronic, Elastic, and Optical Properties of Cubic BaLiX₃ (X = F, Cl, Br, or I) Perovskites: An *Ab-initio* DFT Study

Redi Kristian Pingak^{1*}, Soukaina Bouhmaidi², Larbi Setti², Bartholomeus Pasangka¹, Bernandus Bernandus¹, Hadi Imam Sutaji¹, Fidelis Nitti³, and Meksianis Zadrak Ndi⁴

¹Department of Physics, Faculty of Science and Engineering, Universitas Nusa Cendana, Jl. Adisucipto Penfui, Kupang 85001, Nusa Tenggara Timur, Indonesia

²Laboratory of Advanced Science and Technologies, FPL, Abdelmalek Essaadi University, Tetouan 93030, Morocco

³Department of Chemistry, Faculty of Science and Engineering, Universitas Nusa Cendana, Jl. Adisucipto Penfui, Kupang 85001, Nusa Tenggara Timur, Indonesia

⁴Department of Mathematics, Faculty of Science and Engineering, Universitas Nusa Cendana, Jl. Adisucipto Penfui, Kupang 85001, Nusa Tenggara Timur, Indonesia

* Corresponding author:

email: rpingak@staf.undana.ac.id

Received: March 19, 2023

Accepted: May 8, 2023

DOI: 10.22146/ijc.83261

Abstract: This study reports for the first time the theoretical prediction of structural, electronic, elastic and optical properties of cubic BaLiCl₃, BaLiBr₃, and BaLiI₃ perovskites. The corresponding properties of the well-known BaLiF₃ are also theoretically investigated. Density Functional Theory (DFT) using the Generalized Gradient Approximation (GGA) was implemented within the Quantum Espresso package to investigate the properties of the perovskites. The results revealed that BaLiX₃ (X = F, Cl, Br, and I) are in ionic crystal forms with optimized lattice parameters of 4.04, 4.90, 5.21, and 5.66 Å, respectively. The minor band gaps were found to be 6.62 eV ($\Gamma \rightarrow \Gamma$), 4.29 eV ($R \rightarrow \Gamma$), 3.50 eV ($R \rightarrow \Gamma$), and 2.58 eV ($R \rightarrow \Gamma$) for the respective compounds. The investigation of their elastic properties indicated that these perovskites are all mechanically stable, while only BaLiBr₃ and BaLiI₃ are malleable. Finally, the studied perovskites exhibit excellent optical properties, including low reflectivity and high absorption in the ultraviolet region. Hence, it is predicted that these perovskites are suitable for various optoelectronic applications involving absorption in the UV region. However, BaLiBr₃ and BaLiI₃ are more favorable than BaLiF₃ and BaLiCl₃ to be deposited as thin films due to their flexibility.

Keywords: Density Functional Theory; Quantum Espresso; BaLiX₃ perovskites; elastic properties; optoelectronic properties

■ INTRODUCTION

Perovskites ABX₃, where A and B are two cations, and X is an anion, can be formed by an arrangement of many possible atoms. This is because most of the elements in the periodic table can replace elements in the A and B sites. In a unit cell, the B-site cation occupies the center of the octahedron and is coordinated by six X anions, whereas the top corner of the cube is occupied by A cations [1].

Due to its enormous number of structural families with specific properties, the ABX₃ perovskites have found

substantial roles in various potential applications. This fact has therefore garnered significant attention and thus attracted a considerable amount of research conducted on the ABX₃ perovskites by the scientific community. For example, hybrid organic-inorganic perovskites have been widely applied in optoelectronic devices, including solar cells, due to their tunable electronic properties [2-7]. Because of their low cost and easily-tailored structure, the perovskites can be specifically designed and applied in catalysts and thermoelectric devices [8-9].

BaLiF₃, in particular, has been intensively investigated in some recent studies due to its potential application in various fields, including dosimetry and computed radiography. The first theoretical study on the physical properties of cubic BaLiF₃ (space group $\text{pm}\bar{3}\text{m}$) was presented by Korba et al. [10], which was in good agreement with previously reported experimental results by Boumriche et al. [11]. In addition, Düvel and co-workers [12] successfully synthesized a highly pure BaLiF₃ nanocrystal with this cubic perovskite structure, further verifying the theoretical prediction presented in [10]. Since then, there have been several studies conducted to investigate further these perovskites, which covered not only the theoretical and computational aspects [13-17] but also the experimental point of view [18].

A literature study indicated that the above-mentioned computational studies revealed that BaLiF₃ perovskite possesses quite a flat band diagram. This is crucial as materials with flat band energy diagrams are highly likely to have strong anharmonicity and excellent thermoelectric properties [19-20]. Indeed, Song and co-workers [19] confirmed the flat band diagrams of some Thallium-based fluoro perovskites reported in our previous work [21]. They further confirmed that these types of perovskites have strong anharmonicity and high thermoelectric performance. This finding strongly suggests that BaLiF₃ and its isoelectronic compounds might have other applications as thermoelectric materials due to the overall flat band diagram of BaLiF₃.

Although the properties of BaLiF₃ have been intensively investigated, those of their isoelectronic, including BaLiCl₃, BaLiBr₃, and BaLiI₃, have not been fully addressed. Due to its accuracy, Density Functional Theory (DFT) has long been used to accurately predict the properties of a wide range of materials, some of which can be found in several recent studies reported in Refs [22-30]. Therefore, the present work aims to conduct a DFT study to investigate the structural, electronic, elastic and optical properties of cubic BaLiX₃ (X = F, Cl, Br, or I) perovskites. The results of this study are expected to pave the way to the understanding of their physical properties and potential applications in various devices.

■ COMPUTATIONAL DETAILS

Using the Quantum Espresso (QE) code [31], the DFT calculation with Generalized Gradient Approximation Perdew-Burke-Ernzerhof (GGA-PBE) functional [32] was conducted to investigate the structural, electronic, optical and elastic properties of cubic BaLiX₃ (X = F, Cl, Br, or I) perovskites. The ultrasoft pseudopotential was used to consider the interaction between electrons and nuclei of the constituent atoms in the materials. The structure was optimized using Broyden Fletcher-Goldfarb-Shanno (BFGS) minimization procedure. Furthermore, the thermo_pw program, which uses Quantum Espresso as the underlying engine, was used to calculate the optical and elastic properties of the perovskites. The Quantum Espresso code has recently been applied to accurately predict the properties of a wide range of materials [33-35].

The wave function and the charge density energy cut-offs were 40 Ry and 400 Ry, respectively. K-points of $5 \times 5 \times 5$ and $12 \times 12 \times 12$ were used for Self-Consistent Field (SCF) and Non-Self-Consistent Field (NSCF) calculation, respectively. The convergence threshold for the total energy was 10^{-8} Ry.

■ RESULTS AND DISCUSSION

Structural Properties

The cubic structure of BaLiX₃ (X = F, Cl, Br, or I) perovskites has space group #221 ($\text{pm}\bar{3}\text{m}$). Fig. 1 shows the unit cell structure of the perovskites, where Ba cations are located at Wyckoff coordinates of (0, 0, 0), and Li is at (0.5, 0.5, 0.5). Meanwhile, the three X anions are located at (0.5, 0, 0.5), (0.5, 0.5, 0) and (0, 0.5, 0.5).

The total energy of the compounds was calculated as a function of the lattice constants, as illustrated in Fig. 2. Cell relaxation was then performed to optimize the cubic structure of BaLiX₃ (X = F, Cl, Br, or I) perovskites, using the Birch-Murnaghan equation of states [36-38], as shown in Eq. (1).

$$E(V) = E_0 + \frac{B}{B'(B'-1)} \left[V \left(\frac{V_0}{V} \right)^{B'} - V_0 \right] + \frac{B}{B'(V - V_0)} \quad (1)$$

Computed optimized lattice parameters of the materials are depicted in Table 1, whereas other computed structural parameters are shown in Table 2.

Table 1 shows that the optimized lattice constant of BaLiF_3 obtained in this study strongly agrees with the corresponding value obtained by Refs [10,12,15-16,39] using the GGA functional and is only slightly larger than the experimental value [11]. This step illustrates the reliability of our calculation, which should apply to other compounds studied in this work. Meanwhile, the optimized lattice parameters of BaLiCl_3 , BaLiBr_3 , and BaLiI_3 are reported for the first time in the present study and, therefore, can be used as a reference for further studies on these compounds.

It can also be seen from Table 1 that there is an increase in the optimized lattice constants of the compounds as Cl, Br, and I substitute F. This is due to the increase in the ionic radii when tuning the halide ions. This fact was also actual for other ABX_3 ($X = \text{F, Cl, Br, or I}$)

perovskites ranging from lead-based halide perovskites [41-44] to lead-free perovskites including Ge-based compounds [45-49], Sn-based compounds [50-53], and other lead-free perovskite materials [54-59]. Indeed, this is also verified by experimental studies.

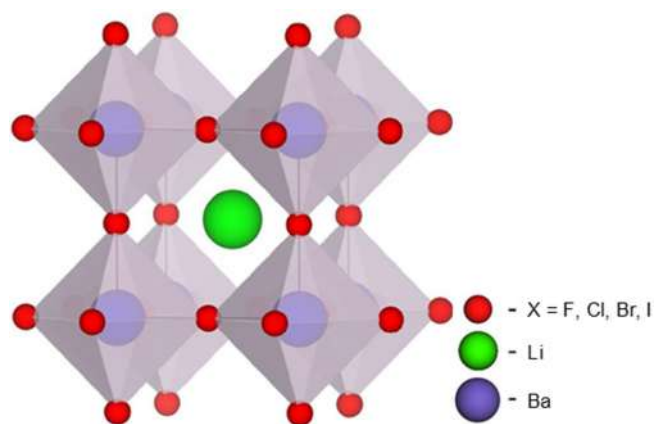


Fig 1. The unit cell structure of the cubic BaLiX_3 ($X = \text{F, Cl, Br, or I}$) perovskites

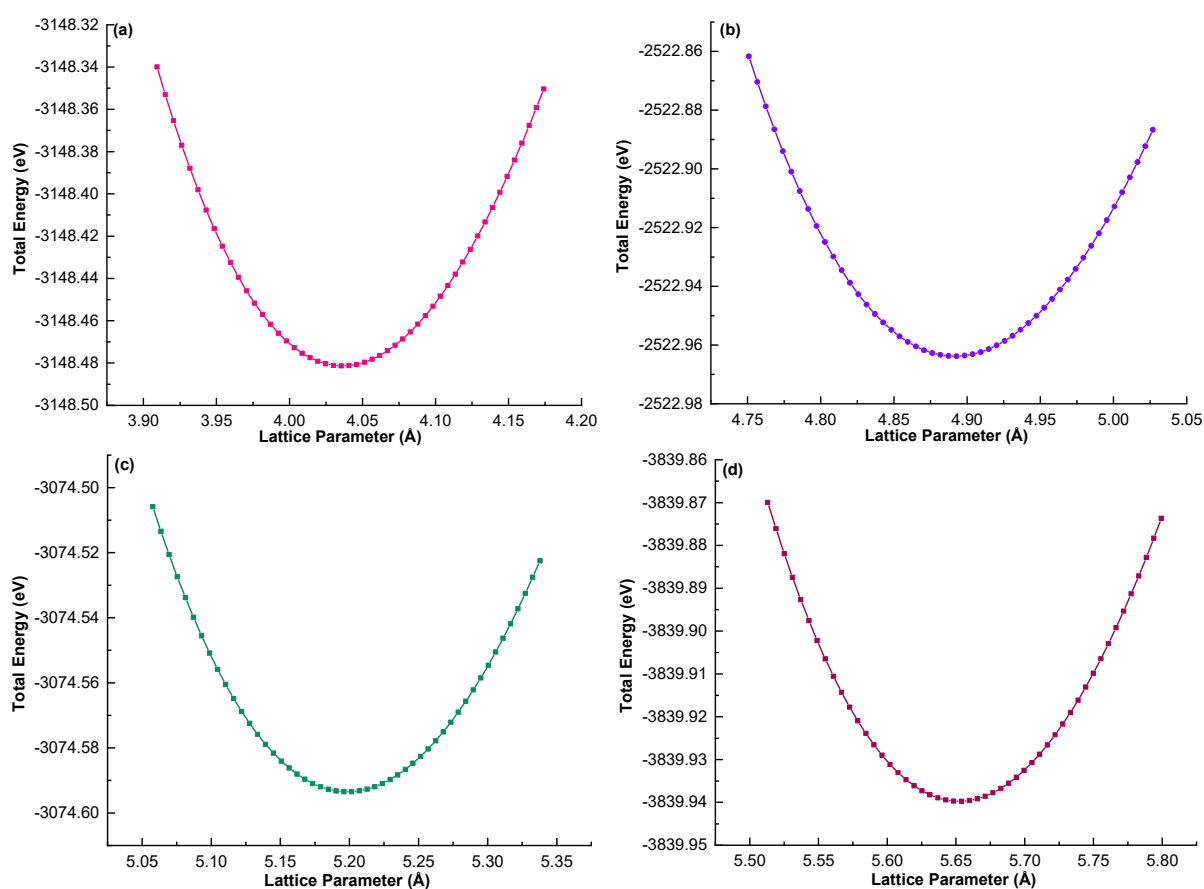


Fig 2. Total energy vs. lattice parameters of BaLiF_3 (a), BaLiCl_3 (b), BaLiBr_3 (c), and BaLiI_3 (d) perovskites

Table 1. Optimized lattice parameters and energy gaps of cubic BaLiX₃ (X = F, Cl, Br, or I) perovskites using the GGA functional

Compounds	Optimized lattice parameters (Å)		Energy gap (eV)	
	This work	Literature	This work	Literature
BaLiF ₃	4.04	GGA: 4.05 [10]; 4.04 [12]; 4.04 [15]; 4.04 [16]; 4.03 [39] Exp.: 3.996 [11]	6.62 (Γ→Γ) 6.73 (R→Γ) 6.77 (M→Γ) 7.03 (X→Γ)	GGA (Γ→Γ): 6.66 [10]; 6.8 [15]; 6.72 [16] Exp. (Γ→Γ): 9.8 [40]
BaLiCl ₃	4.90	-	4.37 (Γ→Γ) 4.29 (R→Γ) 4.36 (M→Γ) 4.74 (X→Γ)	-
BaLiBr ₃	5.21	-	3.62 (Γ→Γ) 3.50 (R→Γ) 3.57 (M→Γ) 4.00 (X→Γ)	-
BaLiI ₃	5.66	-	2.77 (Γ→Γ) 2.58 (R→Γ) 2.67 (M→Γ) 3.15 (X→Γ)	-

Table 2. Structural parameters of cubic BaLiX₃ (X = F, Cl, Br, or I) using the GGA functional

Compound	V (a.u.) ³	B (GPa)	B'	E ₀ (Ry)	Total mass (a.m.u.)	Density (g/cm ³)
BaLiF ₃	466.52021	67.90	4.69	-231.409	201.2632	5.049
BaLiCl ₃	795.00231	33.86	4.54	-185.434	250.6180	3.530
BaLiBr ₃	954.66886	27.14	4.53	-225.978	383.9680	4.505
BaLiI ₃	1227.40669	20.67	4.25	-282.230	524.9800	4.791

For instance, the experimental value of the lattice parameter of CsPbCl₃ is 5.61 Å [60], slightly lower than that of CsPbBr₃ (5.87 Å) [43] and CsPbI₃ (6.29 Å) [61]. This verification by the experimental studies implies the accuracy of the DFT calculation.

Other computed structural parameters of the BaLiX₃ (X = F, Cl, Br, or I) perovskites, including their volume (V), bulk modulus (B), pressure derivative (B'), total energy (E₀), total mass and density are depicted in Table 2.

The computed value of the bulk modulus (B) of BaLiF₃ in this study (67.90 GPa) as a result of fitting Eq. (1), as shown in Table 2, is in excellent agreement with a value of 64.45 GPa [10], 66.46 GPa [14], and 65.7 GPa [15]. Likewise, the derivative of the bulk modulus concerning pressure (B') obtained in this study (4.69) is

approximately the same as that reported by Korba et al. [10] (4.60), Mubarak and Mousa [14] (5.17), and Mousa et al. [15] (5.20). The other structural properties in Table 2, especially those of BaLiCl₃, BaLiBr₃, and BaLiI₃ perovskites, are presented for the first time in this study.

The formation energy ΔE_f of the compounds has been calculated using Eq. (2) to investigate the chemical and thermodynamic stability of the perovskites.

$$\Delta E_f = \frac{E_{\text{tot}}(\text{BaLiX}_3) - E(\text{Ba}) - E(\text{Li}) - 3E(\text{X})}{N} \quad (2)$$

where E_{tot} (BaLiX₃) is the unit cell total energy of the BaLiX₃ perovskites, E(Ba), E(Li), and E(X) are the energy of Ba, Li, and X (X = F, Cl, Br, or I) atoms, respectively, and N is the number of atoms in the unit cell. The calculated values of the formation energy are -3.96, -3.21, -2.27, and -1.60 eV/atom for BaLiF₃, BaLiCl₃,

BaLiBr₃, and BaLiI₃, respectively. The negative values of the formation energy of all the studied perovskites indicate that they are thermodynamically and chemically stable and, therefore, can be experimentally synthesized. BaLiF₃ has been experimentally observed [11,40]. By assessing the formation energy of the compounds, we observe that the substitution of F with Cl, Br, or I increases the formation energy. This finding indicates a slight reduction in the chemical stability of the compounds following the halogen replacement. This decrease can be partly attributed to the decrease in the ionic character of the compounds, as the order of the halogen replacement was from F to I, as discussed in the following section.

Electronic Properties

The optimized lattice parameters obtained were then used to calculate other properties of the compounds, including the electronic properties. In this section, the

electronic properties: Density of States (DOS), band diagram and charge density are presented and discussed.

The energy band diagrams and the total density of states of the compounds are plotted in Fig. 3, whereas the values of their band gap energies are summarized in Table 1. From columns 4 and 5 of Table 1, it is evident that the band gap of BaLiF₃ obtained in the present work agrees with that obtained using the GGA functional reported in [10,15-16]. It is also worth noting that the experimental band gap is underestimated in the present study and those using the GGA, as expected.

Table 1 also reveals that the band gap of the materials is tuned to lower values as Cl, Br, and I replace F. This is generally true for ABX₃ perovskites. Moreover, some recent studies also reported the same phenomenon for double perovskites of the form of A₂B'B''X₆ (X = Cl, Br, or I), such as Rb₂SnX₆ [62], Cs₂InBiX₆ [63-64], Cs₂AgCrX₆ [65], Rb₂AlInX₆ [66], Cs₂KTlX₆ [67],

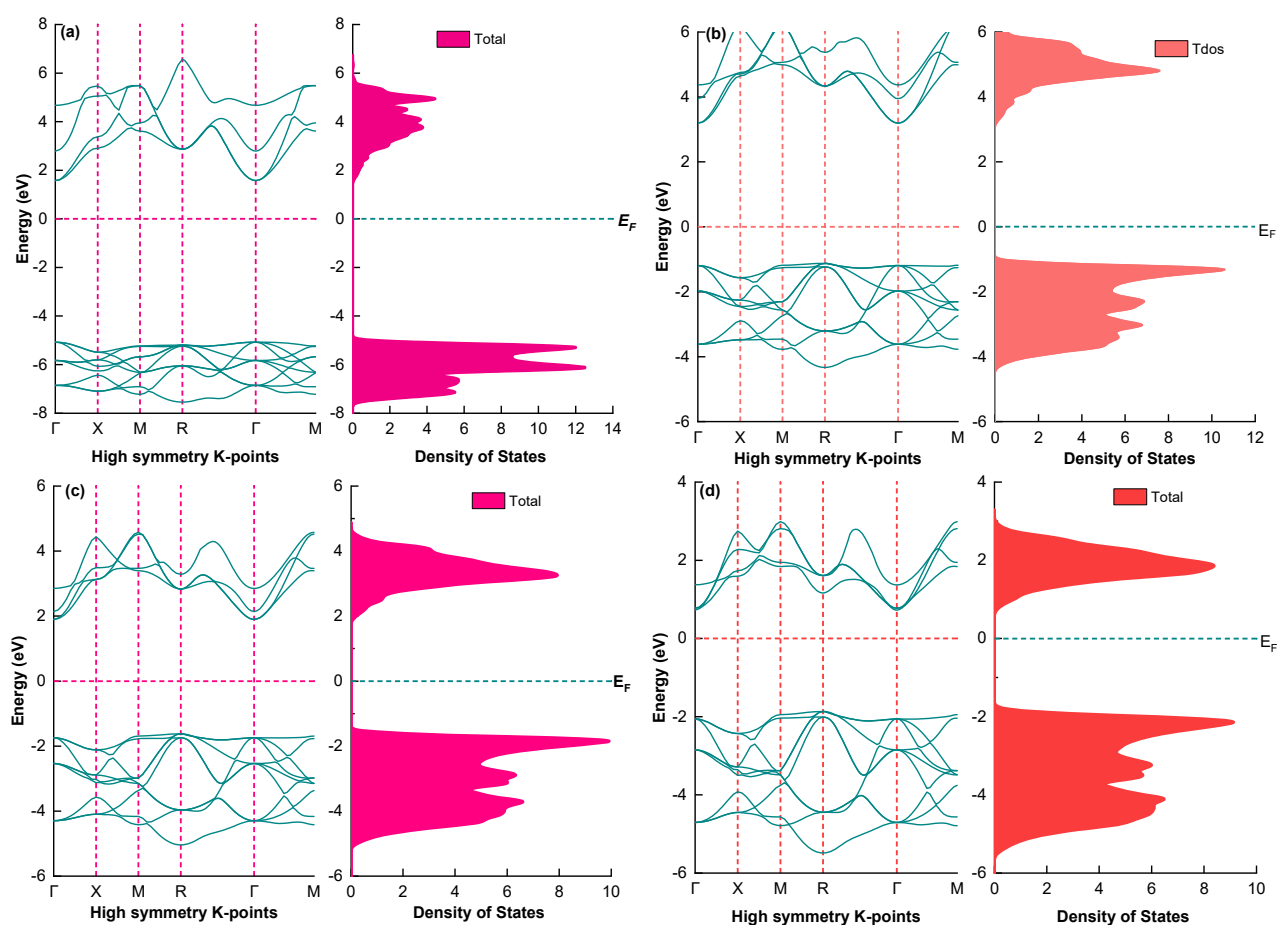


Fig 3. Energy band diagram and DOS of the cubic BaLiF₃ (a), BaLiCl₃ (b), BaLiBr₃ (c), and BaLiI₃ (d) perovskites

Cs₂AgBiX₆ [68], K₂ScAgX₆ [69], (CsMA)NaSbX₆ [70], Cs₂ScAgX₆ [71], Cs₂NaBiX₆ [72], Rb₂InBiX₆ [73], and Rb₂AgInX₆ [74]. Some new double perovskites of the form A₂BX₆ (X = Cl, Br, or I) also possess the corresponding tunable energy gap due to changing halogens. These include Cs₂PtX₆ [75], Ga₂TiX₆ [76], Cs₂PdX₆ [77], Tl₂PtX₆ [78], Cs₂TeX₆ [79], and Tl₂TiX₆ [80].

It is important to note that when F is replaced by Cl, Br, or I in BaLiX₃, the lattice parameters of the compounds are inversely proportional to their band gap energies (Table 1). As seen from Table 1, the lattice constants of the compounds increase while their energy gaps decrease with the ion replacement. This fact is due to the increase in the bond length of the compound following the increase in its lattice parameter, which causes the valence electrons within the compounds to be less bound to their parent atoms. Therefore, less energy is required to move them freely as conduction electrons, decreasing the compounds' energy gap. This phenomenon has also been observed in many other perovskites and double perovskites, in which the halide ion is substituted by its counterparts [41-59,62-80].

In ionic solids, electrons are firmly bound to their parents' atoms, and therefore relatively large energy is required to excite them to the conduction bands of the compounds. Consequently, ionic compounds tend to have significant band gap energy. In the case of the present study, the corresponding compounds have significant band gap energy, more significant than 2.5 eV, when using the GGA functional. Moreover, as the ionic character of the compounds decreases when F is replaced by Cl, Br, or I (Fig. 4), the band energy of the compounds is expected to decrease, as confirmed by our results. This finding demonstrates that the decrease in the ionic characters causes the valence electrons to be less bound to the nuclei, requiring less energy to be excited to the conduction band.

The general feature of the band diagram and the density of states of BaLiF₃ (as shown in Fig. 3(a)) is in excellent agreement with that reported in Refs [10,13-17]. The band diagrams and the density of states of BaLiCl₃, BaLiBr₃, and BaLiI₃ perovskites, on the other hand, are

studied for the first time in the present work, where the smallest band gap energies of the compounds are found to be indirect: 4.29 eV (R→Γ), 3.5 eV (R→Γ), and 2.58 eV (R→Γ), for the respective compounds. The smallest band gap energies of the compounds are in bold in Table 1, where band gap energies of (Γ→Γ), (M→Γ), and (X→Γ) are also presented for comparison.

Furthermore, Fig. 3 clearly illustrates that the materials have relatively flat band gaps, especially valence bands. This is a unique and interesting property that might lead to potential applications in other devices, including thermoelectric devices [19-20]. More importantly, the coexistence of the flat band gaps and the high dispersion in the band structure contributes to the immense power factor (PF), as the former provides a larger thermopower (S). In contrast, the latter provides a higher electrical conductivity (σ) [19]. As seen in Fig. 3, the flat bands are observed in the valence bands of the compounds along M, R, and Γ high symmetry points. Further investigation on the thermoelectric properties of these materials is therefore highly recommended, with BaLiI₃ predicted to have better thermoelectric properties due to its smaller band gap than the other 3 materials. The material will be more suitable for thermoelectric materials by tuning further its band gap to a lower value, such as by applying external pressure.

To investigate chemical bonds present within the perovskites, their electron density in the (110) and (100) planes is illustrated in Fig. 4. Fig. 4(a) and 4(b) clearly show that the Ba-F and Li-F bonds within BaLiF₃ are primarily ionic, as seen from nearly spherical electronic distribution around the corresponding atoms. This finding can be further verified using Eq. (3) [81].

$$\%IC = \left[1 - e^{-0.25(X_1 - X_2)^2} \right] \times 100 \quad (3)$$

where IC stands for Ionic Character while X₁ and X₂ are the electronegativities of atom 1 and atom 2, respectively. Using Eq. (3), % ionic character values for Ba-F and Li-F bonds are 90.81 and 89.46%, respectively. This finding is consistent with the analysis reported by Lv et al. [17].

Furthermore, the present study reveals that the strength of the Li-X ionic bonds decreases as F is

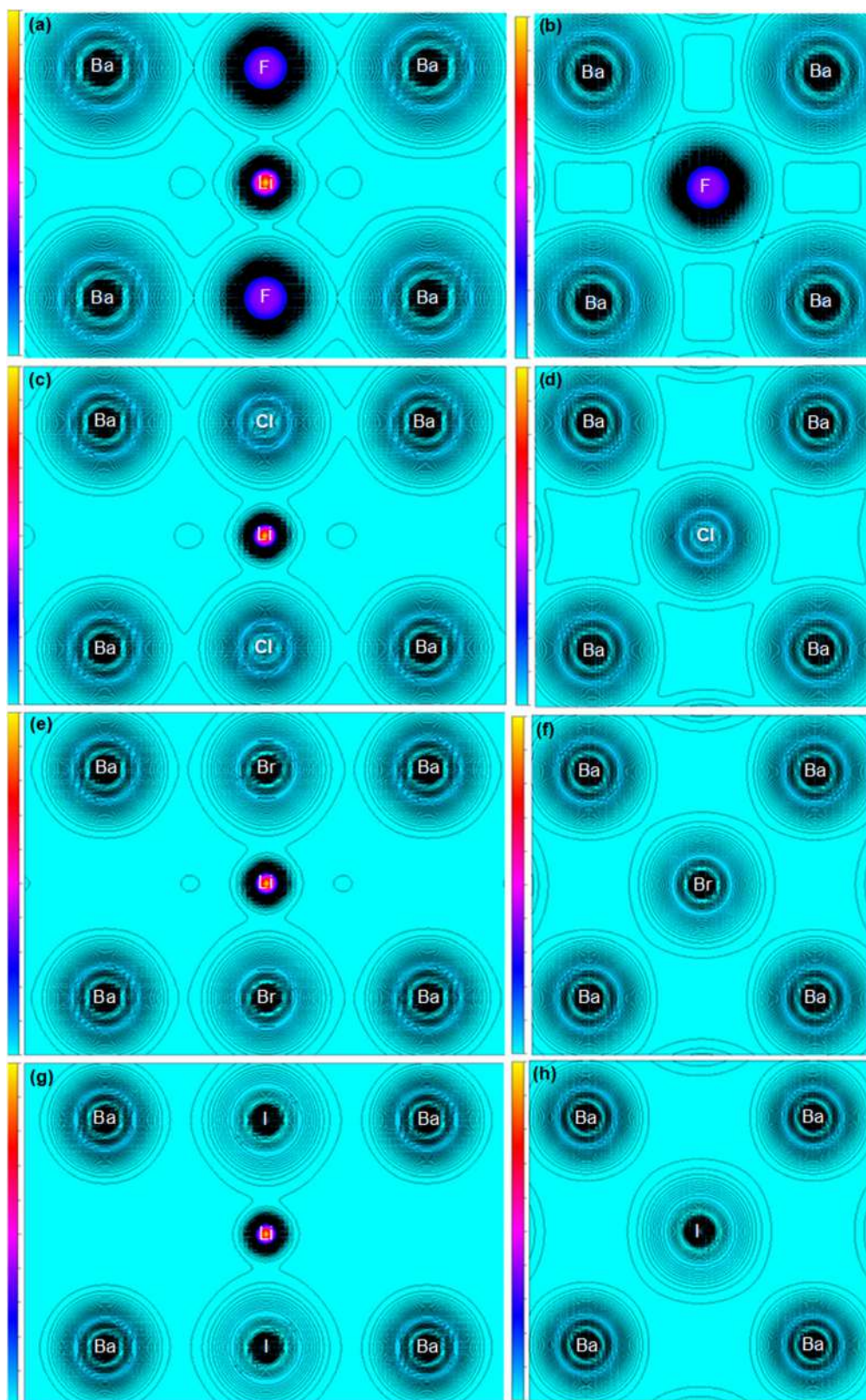


Fig 4. (110) Electron density of BaLiF_3 (a), BaLiCl_3 (c), BaLiBr_3 (e) and BaLiI_3 (g) and (100) electron density of BaLiF_3 (b), BaLiCl_3 (d), BaLiBr_3 (f) and BaLiI_3 (h)

substituted by Cl, Br, or I. This can be clearly seen from their electron charge density in the (110) plane as presented in Fig. 4(a, c, e and g), where electron distribution around X anions becomes more distorted as F is substituted by Cl, Br, or I, respectively. The distortion results in the charge density being less spherical, which implies a decrease in the ionic character of Li-X bonds for the ion replacement. This finding is attributed to the fact that the ions are of different sizes, with I^- the largest anion, followed by Br^- , Cl^- , and F^- . Larger X^- anions will be more electrically polarized in the presence of the Li^+ ion, and therefore their charge distribution will be less spherical, resulting in more electrons being more localized in the regions between Li-X. This is an indication that the covalent character of the Li-X bonds increases as X becomes more prominent in size. In other words, the ionic character of Li-X decreases due to the substitution of X with larger anions. Despite the decrease in the ionic character, the Li-X (X = F, Cl, Br, and I) bonds are still mainly ionic and partly covalent. This character can be verified using Eq. (3), from which the ionic character percentages of Li-F, Li-Cl, Li-Br, and Li-I bonds are 89.46, 69.52, 62.47, and 50.62%, respectively.

To see the character of Ba-X bonds more clearly, the electron density of the cubic BaLiF_3 , BaLiCl_3 , BaLiBr_3 , and BaLiI_3 perovskites in the (100) plane is plotted and shown in Fig. 4(b, d, f, and h), respectively. It is evident from the figures that the electron distribution around the Ba^{2+} and X^- ions (X = F, Cl, Br, or I) are almost perfectly spherical. This finding indicates that the Ba-X bonds within the cubic BaLiF_3 , BaLiCl_3 , BaLiBr_3 , and BaLiI_3 perovskites are mostly ionic. Hence, the materials can be categorized as ionic crystals.

Elastic Properties

The elastic properties of the compounds are summarized in Table 3, while the equations used in calculating the elastic properties are presented in our previous study [82].

The mechanical stability of materials is a significant property for applying materials in devices. In general, the mechanical stability of a compound is evaluated using the Born-Huang mechanical stability criteria [83]. Materials are mechanically stable if their elastic constants satisfy $C_{11} > 0$, $C_{44} > 0$, $(C_{11}-C_{12}) > 0$, $(C_{11} + 2C_{12}) > 0$, and $C_{12} < B < C_{11}$. Evaluation of the elastic

Table 3. Elastic properties of the cubic BaLiX_3 (X = F, Cl, Br, or I) perovskites calculated using the GGA functional

Parameters	Compounds			
	BaLiF_3	BaLiCl_3	BaLiBr_3	BaLiI_3
Elastic Const. C_{11} (GPa)	118.88	61.02	49.30	37.05
Elastic Const. C_{12} (GPa)	42.76	19.68	16.11	12.56
Elastic Const. C_{44} (GPa)	43.19	18.66	14.31	10.34
Bulk modulus B (GPa)	68.14	33.46	27.17	20.72
Shear modulus G (GPa)	41.06	19.44	15.19	11.06
Pugh Ratio B/G	1.66	1.72	1.79	1.87
Anisotropy Factor A	1.14	0.90	0.86	0.84
Young modulus E (GPa)	102.57	48.85	38.41	28.17
Poisson Ratio ν	0.25	0.26	0.27	0.27
Kleinman Parameter ζ	0.50	0.47	0.47	0.48
Cauchy Pressure ($C_{11}-C_{12}$)	76.12	41.34	33.19	24.49
Debye Temperature θ_D (K)	398.25	270.62	199.37	151.88
Melting Temperature T_m (K)	1255.7 ± 300	913.69 ± 300	844.41 ± 300	772.0 ± 300
Average sound velocity V_m (m/s)	3164.09	2606.31	2040.65	1690.43
Longitudinal Sound Velocity V_l (m/s)	3673.34	3078.78	2455.68	2079.83
Transverse Sound Velocity V_t (m/s)	2851.51	2346.50	1835.98	1519.42
Lame Const. λ	41.03	21.00	17.75	13.02
Lame Const. μ	41.03	19.38	15.12	11.09

constants and the bulk moduli in Table 3 based on this criterion shows that all studied perovskites in the present work are mechanically stable. In addition, C_{11} of the four compounds is considerably larger than C_{12} and C_{14} . This large value of C_{11} is due to the directional Li-X ionic bond within the $BaLiX_3$ ($X = F, Cl, Br, \text{ or } I$) compounds, as discussed in the previous section.

Another important property related to the elastic constants is the bulk modulus (B), representing the resistance of a material to applied external pressure. It is apparent from Table 3 that the elastic constants and the bulk modulus of $BaLiF_3$ are significantly larger than those of $BaLiCl_3$, $BaLiBr_3$, and $BaLiI_3$. This finding implies that $BaLiF_3$ has the most substantial resistance of all. Similarly, $BaLiF_3$ is predicted to have the largest shear modulus (41.06 GPa), substantially more significant than the shear modulus of $BaLiCl_3$ (19.44 GPa), $BaLiBr_3$ (15.19 GPa), and $BaLiI_3$ (11.06 GPa). This fact demonstrates that $BaLiF_3$ has stronger shear resistance compared to the other three isoelectronic perovskites, although all of them still have relatively high shear resistance. In addition, since the Young modulus (E) represents the stiffness of materials, $BaLiF_3$ is expected to be significantly stiffer than the other three compounds due to its highest Young modulus. It is also found that for all studied perovskites, the Young modulus is larger than the bulk modulus, indicating that $BaLiX_3$ perovskites are more resistant to tension than the effect of compression.

Reddy et al. [84] have found a systematic relationship between the bulk modulus and the energy gap of some materials. The authors reported that the bulk modulus is linearly proportional to the band energy of the materials, which is consistent with the result in the present study. However, it should be noted that this relationship does not apply to all materials. For example, Li et al. [85] claimed that the trend is not generally true for alloys, as the band gap energy in alloy systems varies due to the combination of size and chemical effects [86].

The Poisson ratio and Pugh's ratio can be used to evaluate the ductility or brittleness of materials. A material is ductile if its Poisson ratio is larger than 0.26 and brittle if it is lower than 0.26 [41]. From Table 3, the Poisson ratio of $BaLiF_3$ is 0.25, strongly indicating its

brittle behavior. This is in excellent accordance with the previous studies [16-17]. The ductility and brittleness of the compound can be further verified by its Pugh's ratio [87]: materials are ductile if their Pugh's ratio is larger than 1.75. As its Pugh's ratio is 1.66 (Table 3), it is anticipated that $BaLiF_3$ is brittle.

Interestingly, the Poisson ratio and the Pugh ratio of the perovskites are found to increase following the replacement of F by Cl, Br, or I, which implies a decrease in their brittleness. With the Poisson and Pugh ratios of 0.26 and 1.72, respectively, $BaLiCl_3$ still possesses brittle behavior despite being less brittle than $BaLiF_3$. More importantly, it was found that $BaLiBr_3$ and $BaLiI_3$ are malleable. The change of behavior from brittle to ductile by changing halogens is an essential finding since ductile materials can be quickly deposited as high-quality thin films for various applications [3,88]. This phenomenon is also an alternative way to change the brittle behavior of compounds in addition to increasing applied pressure [17].

Furthermore, the Poisson ratio can be used to study the bonding character within solids. A value of Poisson ratio close to 0.25 implies that the material is an ionic crystal due to the central force within the material [17,89]. The computed Poisson ratio values for all perovskites in this study range between 0.25 and 0.27, indicating that these materials are ionic crystals, consistent with our previous discussions regarding the electronic density plots.

The first Lamé's constant λ measures the compressibility of materials, while the second constant μ is related to the shear stiffness of materials [90-91]. As seen from Table 3, the two constants λ and μ of $BaLiF_3$ are significantly larger than those of $BaLiCl_3$, $BaLiBr_3$, and $BaLiI_3$. This fact has been anticipated since it is well-known that the two constants are directly proportional to the Young modulus. Also, the values of the second constant μ resemble those of the shear modulus, which was true for many other isoelectronic compounds presented in Refs [92-95].

The Kleinman parameter ζ represents the internal strain of materials [90]. The value of ζ is between 0 and 1 for solids. $\zeta = 0$ corresponds to minimizing bond

bending, while $\zeta = 1$ is related to minimizing bond stretching [96]. The computed Kleinman parameter ζ for BaLiF₃, BaLiCl₃, BaLiBr₃, and BaLiI₃ are 0.50, 0.47, 0.47, and 0.48 for the respective perovskites. This fact suggests that the bond bending and the bond stretching are equal for BaLiF₃, while the bond bending within BaLiCl₃, BaLiBr₃, and BaLiI₃ compounds are slightly more dominant than the bond stretching.

Table 3 also shows that BaLiF₃ has the highest Debye temperature θ_D (398.25 K), significantly higher than BaLiCl₃ (270.62 K), BaLiBr₃ (199.37), and BaLiI₃ (151.88 K). This finding follows that the Debye temperature of materials is closely related to their specific heat, melting temperature, and elastic constants [91].

Some elastic properties of BaLiF₃ have been investigated both experimentally and theoretically. Therefore, a comparison with these previous values is necessary. Table 4 depicts the elastic properties of BaLiF₃ along with previously reported values. Overall, the three elastic constants, the bulk modulus, and the shear modulus of BaLiF₃ calculated using GGA functional in the present study and other GGA-based theoretical results in Table 4 are closer to the corresponding experimental

values compared with Local Density Approximation (LDA)-based theoretical calculation. This does not necessarily mean that the GGA function is always more accurate than the LDA function in the study of the elastic properties of materials, as Råsander and Moram [97] showed that the performance of functionals is system-dependent. The authors evaluated the performance of various functionals in predicting the elastic properties of some insulators and semiconductors and found that the LDA is more accurate for some particular compounds.

It is important to note that some elastic properties of BaLiF₃ do not currently have experimental values. Therefore, our theoretical results and those in the literature are of great importance for further studies on this perovskite. Also, as previously mentioned, the elastic properties for BaLiCl₃, BaLiBr₃, and BaLiI₃ are presented for the first time in this work. The excellent agreement between the current theoretical results for BaLiF₃ and its corresponding experimental values and other theoretical results strongly indicates that our results for BaLiCl₃, BaLiBr₃, and BaLiI₃ can be considered a reliable prediction of the materials' properties.

Table 4. Comparison of elastic properties of the cubic BaLiF₃ from the present study using the GGA with other theoretical calculations and experiments

Parameters	This work	Other theoretical results	Experiment
Elastic Const. C_{11} (GPa)	118.88	GGA: 149.2 [39], 134.0 [17] LDA: 232.3 [39], 163.84 [10]	130 ± 1 [11]
Elastic Const. C_{12} (GPa)	42.76	GGA: 33.1 [39], 45.4 [17] LDA: 31.2 [39], 50.81 [10]	46.5 ± 0.5 [11]
Elastic Const. C_{44} (GPa)	43.19	GGA: 58.0 [39], 46.5 [17] LDA: 42.2 [39], 60.02 [10]	48.7 ± 0.5 [11]
Bulk modulus B (GPa)	68.14	GGA: 74.9 [17], 64.45 [10], 66.46 [14] LDA: 88.84 [10]	79 [11]
Shear modulus G (GPa)	41.06	GGA: 58.0 [39], 45.6 [17] LDA: 65.5 [39]	45.9 [11]
Poisson Ratio ν	0.25	GGA: 0.25 [17]	-
Pugh Ratio B/G	1.66	GGA: 1.64 [17]	-
Anisotropy Factor A	1.14	GGA: 1.12 [16]	-
Transverse Sound Velocity V_t (m/s)	2851.51	GGA: 2822.93 [16]	-
Longitudinal Sound Velocity V_l (m/s)	3673.34	GGA: 4873.80 [16]	-
Average sound velocity V_m (m/s)	3164.09	GGA: 3133.10 [16]	-
Debye Temperature θ_D (K)	398.25	GGA: 290.72 [16]	-

Table 4 indicates that there is a discrepancy between the C_{11} value (118.88 GPa) obtained in this study compared to that reported in references [17] (134.0 GPa) and [39] (149.2 GPa). The reason for this discrepancy is the use of different methods in the calculation despite using the GGA functional. In the present study, we used the thermo_pw code under Quantum Espresso. At the same time, Ref [17] implemented the CASTEP code, and Ref [39] used the all-electron linear muffin-tin orbital method in the full-potential implementation. Different packages imply different computational approaches, and therefore different results are expected. However, the accuracy of the methods can be evaluated in this case since the experimental value of C_{11} of BaLiF₃ is known, i.e., 130 GPa [11]. The % errors of C_{11} from the CASTEP code (3.07%) are smaller than those from our results using the thermo_pw package (8.55%) and the linear muffin-tin orbital method used in [39] (14.77%). This trend is also observed when evaluating the accuracy of the three methods in obtaining some other elastic properties, including C_{12} , C_{44} , and the shear modulus (G). These findings strongly suggest the CASTEP code used in [17] is expected to be more accurate than the thermo_pw code, which is also more accurate than the all-electron linear muffin-tin orbital method used in Ref [39] when calculating elastic properties.

Optical Properties

Optical properties of the BaLiX₃ (X = F, Cl, Br, or I) perovskites were successfully calculated, and the results within the photon energy interval 0–20 eV are presented and discussed in this section.

The imaginary part of the dielectric function $\epsilon_2(\omega)$ and the real part of the dielectric function $\epsilon_1(\omega)$ can be calculated using Eq. (4) and Eq. (5), respectively [98-100].

$$\epsilon_2(\omega) = \frac{2e^2\pi}{\Omega\epsilon_0} \sum_{K,V,C} \left| \langle \Psi_K^C | \hat{U} \cdot \vec{r} | \Psi_K^V \rangle \right|^2 \delta(E_K^C - E_K^V - E) \quad (4)$$

$$\epsilon_1(\omega) = 1 + \frac{2}{\pi} P \int_0^\infty \frac{\omega' \epsilon_2(\omega')}{\omega'^2 - \omega^2} d\omega' \quad (5)$$

where e and Ω are the electronic charges and the unit cell volume, respectively; Ψ_K^V and Ψ_K^C are wave functions at a particular k in the valence band and the conduction band, respectively; E_K^C and E_K^V represent the energy of electrons

at a special k in the conduction and the valence bands, respectively; \hat{U} is the unit vector in the direction of the polarization of the incident electric field of the light; δ is the delta function to account for the energy and momentum conservation during a transition.

After $\epsilon_2(\omega)$ and $\epsilon_1(\omega)$ are obtained, the refractive index as a function of photon energy $\eta(\omega)$ and the extinction coefficient $k(\omega)$ of the perovskites are calculated using Eq. (6) and (7), respectively [99].

$$\eta(\omega) = \frac{1}{\sqrt{2}} \left[\left(\epsilon_1(\omega)^2 + \epsilon_2(\omega)^2 \right)^{1/2} + \epsilon_1(\omega) \right]^{1/2} \quad (6)$$

$$k(\omega) = \frac{1}{\sqrt{2}} \left[\left(\epsilon_1(\omega)^2 + \epsilon_2(\omega)^2 \right)^{1/2} - \epsilon_1(\omega) \right]^{1/2} \quad (7)$$

The computed values of the real part of the dielectric function $\epsilon_1(\omega)$, the imaginary part of the dielectric function $\epsilon_2(\omega)$, the refractive index $\eta(\omega)$, and the extinction coefficient $k(\omega)$ of the BaLiX₃ (X = F, Cl, Br, or I) perovskites compounds within 0–20 eV are plotted in Fig. 5.

Fig. 5(a) shows the appearance of the highest peak of $\epsilon_1(\omega)$ for BaLiF₃ (5.04) at 8.58 eV, which corresponds well with previous studies where the highest peak was observed at 8.6 eV [14-15]. Although the numerical value of the prominent peak was not explicitly stated in [10,16], it can be seen from their curve that the central peak was located at about 9 eV. Meanwhile, the static dielectric function $\epsilon_1(0)$ of BaLiF₃ is found to be 2.57 in this study, which is also consistent with the previous reports, i.e., 2.5 [14], 2.6 [15], and about 1.96 [10,16]. In addition, the main feature of $\epsilon_1(\omega)$ for BaLiF₃ obtained in this study is in excellent agreement with previous studies.

Fig. 5(a) also presents the real part of the dielectric function $\epsilon_1(\omega)$ of BaLiCl₃, BaLiBr₃, and BaLiI₃, where a clear shift of the main peak to lower photon energy and an increase in static dielectric function are observed. The main peaks for the respective perovskites are observed at 5.72, 4.84, and 3.74 eV, whereas the static dielectric function values $\epsilon_1(0)$ were found at 3.35, 3.83, and 4.56. It is important to note that the real part of the dielectric function $\epsilon_1(\omega)$ is shifted toward lower photon energies as we move from F to Cl, Br, or I, which is also true for

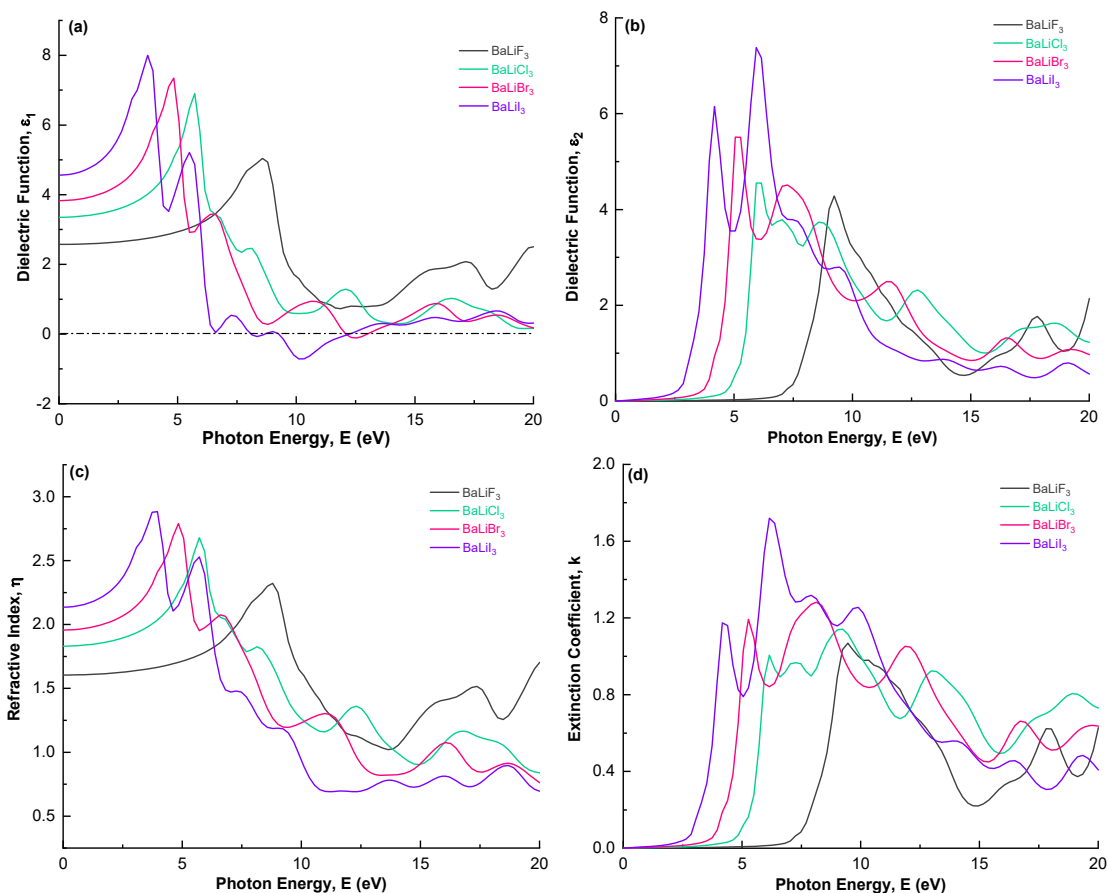


Fig 5. $\epsilon_1(\omega)$ (a), $\epsilon_2(\omega)$ (b), $\eta(\omega)$ (c), and $k(\omega)$ (d) of the cubic BaLiX₃ (X = F, Cl, Br, or I)

other optical properties presented in Fig. 5(b-d), Fig. 6(a-c). This trend is in close agreement with the electronic band structure of the compounds, as previously discussed, where the electronic band gaps of the materials decrease when Cl, Br, or I replace F. Additionally, the static dielectric function values $\epsilon_1(0)$ are inversely proportional to the band gap energy of the compounds, which is also consistent with the Penn model [101]. Moreover, since a material with a larger static dielectric constant generally has better optoelectronic properties due to a lower rate of charge recombination [100,102-103], BaLiI₃ is predicted to possess better optoelectronic properties compared to BaLiBr₃, BaLiCl₃, and BaLiF₃ perovskites. A similar trend was also reported recently [104], where FrGeF₃ which has a larger static dielectric constant than KGeF₃ and RbGeF₃, was found to demonstrate better optoelectronic performance than KGeF₃ and RbGeF₃.

Fig. 5(b) presents the imaginary part of the dielectric function $\epsilon_2(\omega)$, which represents the absorption behavior

of the perovskites and, therefore, should be directly related to the band structure. It is evident from Fig. 5(b) that the threshold energy for the dielectric function $\epsilon_2(\omega)$, i.e., the energy at which materials start absorbing light, shifts towards lower energy as F is replaced by Cl, Br, or I. This finding is consistent with the band structure and DOS of the materials, as depicted in Fig. 3, where the forbidden gap between valence and conduction bands of the compounds decreases due to the halogen replacement. The prominent absorption peaks for the BaLiF₃, BaLiCl₃, BaLiBr₃, and BaLiI₃ are at 9.24, 5.94, 5.06, and 5.94 eV, respectively. More importantly, Fig. 5(b) strongly reveals that BaLiCl₃, BaLiBr₃, and BaLiI₃ perovskites have a much more comprehensive absorption range compared to BaLiF₃ and that BaLiI₃ has the widest absorption range within 0–20 eV, followed by BaLiBr₃, BaLiCl₃, and BaLiF₃. As before, the overall feature of the $\epsilon_2(\omega)$ curve in this study agrees very well with previous studies [10,14-16].

As expected, the refractive index of BaLiX_3 as a function of energy $\eta(\omega)$ (Fig. 5(c)) is very similar in shape to $\epsilon_1(\omega)$ (Fig. 5(a)). The computed static refractive index $\eta(0)$ of BaLiF_3 is 1.60, which is in excellent agreement with the corresponding predicted value of 1.59 by [14-15], and is slightly larger than a value of 1.40 reported by Yalcin et al. [16] and Korba et al. [10]. Meanwhile, the computed static refractive index $\eta(0)$ for BaLiCl_3 , BaLiBr_3 , and BaLiI_3 are 1.83, 1.96, and 2.14, respectively. Additionally, the most significant values of the refractive index of BaLiX_3 ($X = \text{F, Cl, Br, or I}$) are 2.32 (at 8.80 eV), 2.68 (at 5.72 eV), 2.79 (at 4.84 eV), and 2.88 (at 3.96 eV), respectively.

As for the extinction coefficient $k(\omega)$ (Fig. 5(d)), it is well known that the feature of extinction coefficient $k(\omega)$ should resemble that of $\epsilon_2(\omega)$, which is also the case in the present study. In addition, Eq. (6) clearly indicates that a local maximum of $k(\omega)$ should correspond to a local minimum of $\epsilon_1(\omega)$. The comparison of Fig. 5(a) and 5(d) confirms this. Finally, the most significant values of the

$k(\omega)$ of BaLiX_3 ($X = \text{F, Cl, Br, and I}$) within 0–20 eV are 1.07 (at 9.46 eV), 1.14 (at 9.24 eV), 1.28 (at 8.14 eV), and 1.69 (at 6.38 eV), respectively.

The reflectivity $R(\omega)$, the absorption coefficient $\alpha(\omega)$, and the loss function $L(\omega)$ of the BaLiX_3 compounds are also essential properties that can be used to evaluate the potential of the materials for applications in devices. $R(\omega)$, $L(\omega)$, and $\alpha(\omega)$ were calculated using Eq. (8-10) [99]. Fig. 6 depicts computed values of $R(\omega)$, $\alpha(\omega)$ and $L(\omega)$ of the perovskites.

$$R(\omega) = \frac{(\eta - 1)^2 + k^2}{(\eta + 1)^2 + k^2} \quad (8)$$

$$\alpha(\omega) = \frac{2\omega}{c} k(\omega) \quad (9)$$

$$L(\omega) = \frac{\epsilon^2}{\epsilon_1^2 + \epsilon_2^2} \quad (10)$$

Fig. 6(a) shows that all studied compounds have low reflectivity, which is suitable for device applications.

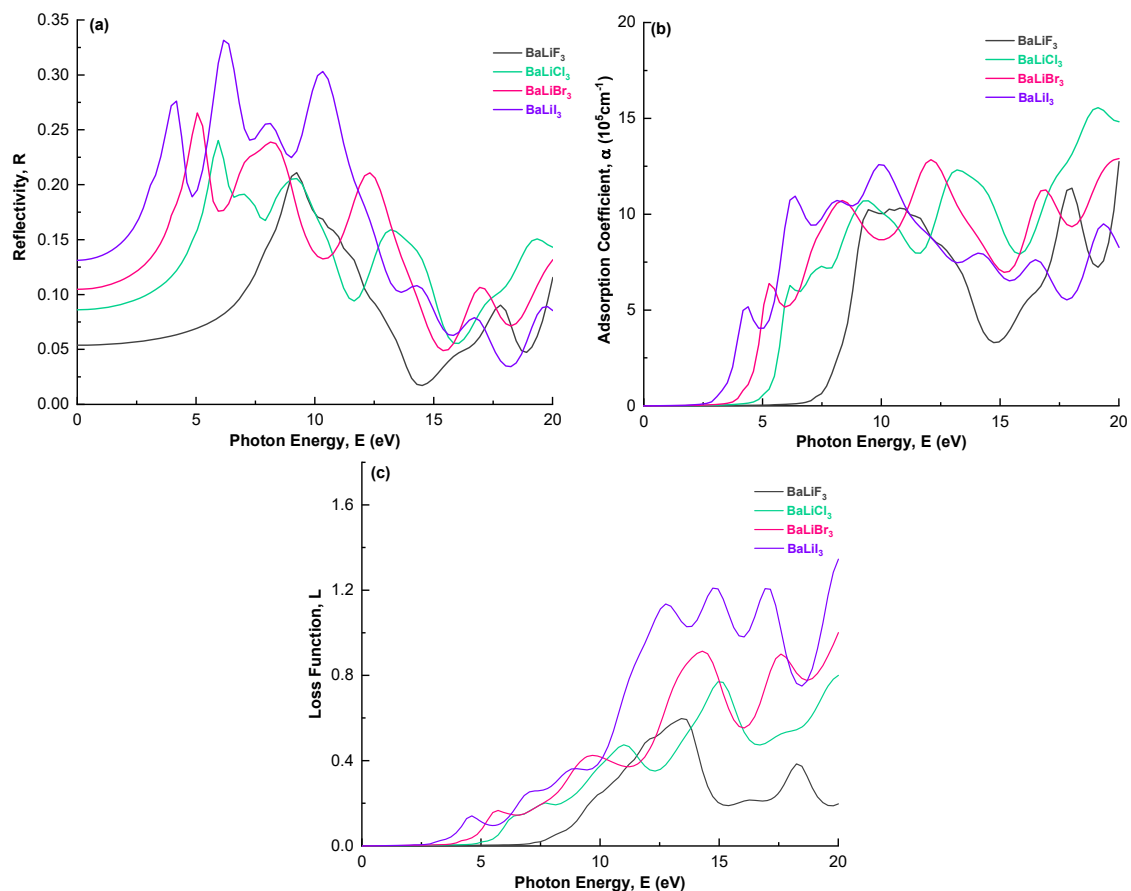


Fig 6. $R(\omega)$ (a), $\alpha(\omega)$ (b), and $L(\omega)$ (c) of cubic BaLiX_3 ($X = \text{F, Cl, Br, and I}$)

Overall, BaLiI₃ has the highest reflectivity, respectively followed by BaLiBr₃, BaLiCl₃, and BaLiF₃ within 0–15 eV. Between 15 and 20 eV, BaLiCl₃ is predicted to have slightly higher reflectivity than the others. The highest reflectivity of BaLiI₃ is about 33.14% (at 6.16 eV), followed by BaLiBr₃: 26.53% (at 5.06 eV), BaLiCl₃: 24.02% (at 5.94 eV), and BaLiF₃: 21.10% (at 9.24 eV). The general feature of reflectivity in this study matches very well with that reported by Mousa et al. [15] and Mubarak and Mousa [14].

The considerable absorption of BaLiF₃ was previously predicted by Mousa et al. [15]. This prediction is confirmed here, where the absorption coefficient $\alpha(\omega)$ of BaLiF₃ is in the order of 10^5 cm^{-1} (Fig. 6(b)). Similar absorption behavior is also predicted for BaLiCl₃, BaLiBr₃, and BaLiI₃. Another important finding from Fig. 6(b) is that BaLiCl₃, BaLiBr₃, and BaLiI₃ perovskites have a much broader absorption range compared to BaLiF₃, implying that they can be applied in a wider range of applications.

As $L(\omega)$ represents an inelastic scattering process, Fig. 6(c) shows that inelastic scattering is negligible for low photon energy. A comparison of Fig. 6(c) and 6(b) suggests that the threshold values of the absorption coefficients and the loss function are in good agreement, as expected. This finding implies that the scattering process becomes more apparent when the materials absorb incident light. Above the threshold values, the loss function of the BaLiCl₃, BaLiBr₃, and BaLiI₃ materials increases up to 20 eV while that of BaLiF₃ increases to peak at about 13 eV and then decreases. Overall, across the whole energy range 0–20 eV, the highest loss function is experienced by BaLiI₃, followed by BaLiBr₃, BaLiCl₃, and BaLiF₃ compounds.

■ CONCLUSION

Theoretical DFT predictions of the structural, electronic, elastic and optical properties of the BaLiX₃ (X = F, Cl, Br, or I) perovskites are reported for the first time in the present study. The properties of BaLiF₃ agreed very well with experimental and other theoretical results in the literature. The optimized lattice constants of the BaLiX₃ (X = F, Cl, Br, or I) compounds increased when Cl, Br replace F or I, while the reverse was true for their

electronic band gaps. The exceptional optical properties of these materials and their mechanical stability suggest that they are suitable for various applications.

■ ACKNOWLEDGMENTS

This research is supported by a 2023 DIPA grant provided by the Faculty of Science and Engineering, the University of Nusa Cendana, with contract's number: 10/UN15.15.3.PPK/SPP/FST/IV/2023.

■ AUTHOR CONTRIBUTIONS

Redi Kristian Pingak wrote the original draft of the manuscript; Redi Kristian Pingak, Soukaina Bouhmaidi, and Larbi Setti conducted the DFT calculations; Redi Kristian Pingak, Soukaina Bouhmaidi, Larbi Setti, Bartholomeus Pasangka, Bernandus, Hadi Imam Sutaji, Fidelis Nitti, and Meksianis Zadrak Ndi wrote and revised the manuscript as well as interpreting the results. All authors agreed to the final version of this manuscript.

■ REFERENCES

- [1] Zhang, L., Zhuang, Z., Fang, Q., and Wang, X., 2022, Study on the automatic identification of ABX₃ perovskite crystal structure based on the bond-valence vector sum, *Materials*, 16 (1), 334.
- [2] Wang, Y., Tang, Y., Jiang, J., Zhang, Q., Sun, J., Hu, Y., Cui, Q., Teng, F., Lou, Z., and Hou, Y., 2020, Mixed-dimensional self-assembly organic–inorganic perovskite microcrystals for stable and efficient photodetectors, *J. Mater. Chem. C*, 8 (16), 5399–5408.
- [3] Roknuzzaman, M., Alarco, J.A., Wang, H., Du, A., Tesfamichael, T., and Ostrikov, K., 2019, *Ab initio* atomistic insights into lead-free formamidinium based hybrid perovskites for photovoltaics and optoelectronics, *Comput. Mater. Sci.*, 169, 109118.
- [4] Roknuzzaman, M., Ostrikov, K., Wang, H., Du, A., and Tesfamichael, T., 2017, Towards lead-free perovskite photovoltaics and optoelectronics by *ab-initio* simulations, *Sci. Rep.*, 7, 14025.
- [5] Tao, Q., Xu, P., Li, M., and Lu, W., 2021, Machine learning for perovskite materials design and discovery, *npj Comput Mater.*, 7, 23.
- [6] Veldhuis, S.A., Boix, P.P., Yantara, N., Li, M., Sum,

- T.C., Mathews, N., and Mhaisalkar, S.G., 2016, Perovskite materials for light-emitting diodes and lasers, *Adv. Mater.*, 28 (32), 6804–6834.
- [7] Li, L., Tian, G., Chang, W., Yan, Y., Ling, F., Jiang, S., Xiang, G., and Zhou, X., 2020, A novel double-perovskite LiLaMgTeO₆:Mn⁴⁺ far-red phosphor for indoor plant cultivation white LEDs: Crystal and electronic structure, and photoluminescence properties, *J. Alloys Compd.*, 832, 154905.
- [8] Ekström, E., le Febvrier, A., Bourgeois, F., Lundqvist, B., Palisaitis, J., Persson, P.O.A., Caballero-Calero, O., Martín-González, M.S., Klarbring, J., Simak, S.I., Eriksson, F., Paul, B., and Eklund, P., 2020, The effects of microstructure, Nb content and secondary Ruddlesden–Popper phase on thermoelectric properties in perovskite CaMn_{1-x}Nb_xO₃ (x = 0-0.10) thin films, *RSC Adv.*, 10 (13), 7918–7926.
- [9] Sydoruk, V., Lutsyuk, I., Shved, V., Hreb, V., Kondyr, A., Zakutevskyy, O., and Vasylychko, L., 2020, PrCo_{1-x}Fe_xO₃ perovskite powders for possible photocatalytic applications, *Res. Chem. Intermed.*, 46 (3), 1909–1930.
- [10] Korba, S.A., Meradji, H., Ghemid, S., and Bouhaf, B., 2009, First principles calculations of structural, electronic and optical properties of BaLiF₃, *Comput. Mater. Sci.*, 44 (4), 1265–1271.
- [11] Boumriche, A., Gesland, J.Y., Bulou, A., Rousseau, M., Fourquet, J.L., and Hennion, B., 1994, Structure and dynamics of the inverted perovskite BaLiF₃, *Solid State Commun.*, 91 (2), 125–128.
- [12] Düvel, A., Wilkening, M., Uecker, R., Wegner, S., Šepelák, V., and Heitjans, P., 2010, Mechanothesized nanocrystalline BaLiF₃: The impact of grain boundaries and structural disorder on ionic transport, *Phys. Chem. Chem. Phys.*, 12 (37), 11251–11262.
- [13] Mishra, A.K., Garg, N., Shanavas, K.V., Achary, S.N., Tyagi, A.K., and Sharma, S.M., 2011, High pressure structural stability of BaLiF₃, *J. Appl. Phys.*, 110 (12), 123505.
- [14] Mubarak, A.A., and Mousa, A.A., 2012, The electronic and optical properties of the fluoroperovskite BaXF₃ (X = Li, Na, K, and Rb) compounds, *Comput. Mater. Sci.*, 59, 6–13.
- [15] Mousa, A.A., Mahmoud, N.T., and Khalifeh, J.M., 2013, The electronic and optical properties of the fluoroperovskite XLiF₃ (X = Ca, Sr, and Ba) compounds, *Comput. Mater. Sci.*, 79, 201–205.
- [16] Yalcin, B.G., Salmankurt, B., and Duman, S., 2016, Investigation of structural, mechanical, electronic, optical, and dynamical properties of cubic BaLiF₃, BaLiH₃ and SrLiH₃, *Mater. Res. Express*, 3, 036301.
- [17] Lv, Z.L., Cui, H.L., Wang, H., Li, X.H., and Ji, G.F., 2016, Electronic and elastic properties of BaLiF₃ with pressure effects: First principles study, *Phys. Status Solidi B*, 253 (9), 1788–1794.
- [18] Chowdhury, N., Riesen, N., and Riesen, H., 2019, Efficient generation of stable Sm²⁺ in nanocrystalline BaLiF₃:Sm³⁺ by UV- and X-irradiation, *J. Phys. Chem. C*, 123 (41), 25477–25481.
- [19] Song, X., Zhao, Y., Wang, X., Ni, J., Meng, S., and Dai, Z., 2023, Strong anharmonicity and high thermoelectric performance of cubic thallium-based fluoride perovskites TlXF₃ (X = Hg, Sn, Pb), *Phys. Chem. Chem. Phys.*, 25 (7), 5776–5784.
- [20] Huang, Y.T., Kavanagh, S.R., Scanlon, D.O., Walsh, A., and Hoyer, R.L.Z., 2021, Perovskite-inspired materials for photovoltaics and beyond-from design to devices, *Nanotechnology*, 32 (13), 132004.
- [21] Pingak, R.K., 2022, A DFT study of structural and electronic properties of cubic thallium based fluoroperovskites TlBF₃ (B = Ge, Sn, Pb, Zn, Cd, Hg, Mg, Ca, Sr, Ba), *Comput. Condens. Matter*, 33, e00747.
- [22] Lynn, M.O., Ologunagba, D., Dangi, B.B., and Kattel, S., 2023, Density functional theory study of bulk properties of transition metal nitrides, *Phys. Chem. Chem. Phys.*, 25 (6), 5156–5163.
- [23] Sholihun, S., Kadarisman, H.P., and Nurwantoro, P., 2018, Density-functional-theory calculations of formation energy of the nitrogen-doped diamond, *Indones. J. Chem.*, 18 (4), 749–754.
- [24] Hutama, A.S., Marlina, L.A., Chou, C.P., Irle, S., and Hofer, T.S., 2021, Development of density-functional tight-binding parameters for the molecular dynamics simulation of zirconia, yttria,

- and yttria-stabilized zirconia, *ACS Omega*, 6 (31), 20530–20548.
- [25] Hauwali, N.U.J., Syuhada, I., Rosikhin, A., and Winata, T., 2021, Fundamental properties of parallelogram graphene nanoflakes: A first principle study, *Mater. Today: Proc.*, 44, 3305–3308.
- [26] Prasetyo, N., and Pambudi, F.I., 2021, Toward hydrogen storage material in fluorinated zirconium metal-organic framework (MOF-801): A periodic density functional theory (DFT) study of fluorination and adsorption, *Int. J. Hydrogen Energy*, 46 (5), 4222–4228.
- [27] Utama, A.S., Huang, H., and Kurniawan, Y.S., 2019, Investigation of the chemical and optical properties of halogen-substituted *N*-methyl-4-piperidone curcumin analogs by density functional theory calculations, *Spectrochim. Acta, Part A*, 221, 117152.
- [28] Pradipta, M.F., Pranowo, H.D., Alfiyah, V., and Utama, A.S., 2021, Theoretical study of oxygen atom adsorption on a polycyclic aromatic hydrocarbon using density-functional theory, *Indones. J. Chem.*, 21 (5), 1072–1085.
- [29] Utama, A.S., Hijikata, Y., and Irle, S., 2017, Coupled cluster and density functional studies of atomic fluorine chemisorption on coronene as model systems for graphene fluorination, *J. Phys. Chem. C*, 121 (27), 14888–14898.
- [30] Amalia, W., Nurwantoro, P., and Sholihun, S., 2018, Density-functional-theory calculations of structural and electronic properties of vacancies in monolayer hexagonal boron nitride (h-BN), *Comput. Condens. Matter*, 18, e00354.
- [31] Giannozzi, P., Baroni, S., Bonini, N., Calandra, M., Car, R., Cavazzoni, C., Ceresoli, D., Chiarotti, G.L., Cococcioni, M., Dabo, I., Dal Corso, A., Stefano, de Gironcoli, S., Fabris, S., Fratesi, G., Gebauer, R., Gerstmann, U., Gougoussis, C., Kokalj, A., Lazzeri, M., Martin-Samos, L., Marzari, N., Mauri, F., Mazzarello, R., Paolini, S., Pasquarello, A., Paulatto, L., Sbraccia, C., Scandolo, S., Sclauzero, G., Seitsonen, A.P., Smogunov, A., Umari, P., and Wentzcovitch, R.M., 2009, QUANTUM ESPRESSO: A modular and open-source software project for quantum simulations of materials, *J. Phys.: Condens. Matter*, 21 (39), 395502.
- [32] Perdew, J.P., Burke, K., and Ernzerhof, M., 1996, Generalized gradient approximation made simple, *Phys. Rev. Lett.*, 77 (18), 3865–3868.
- [33] Pitriana, P., Wungu, T.D.K., Herman, H., and Hidayat, R., 2019, The characteristics of band structures and crystal binding in all-inorganic perovskite APbBr₃ studied by the principle calculations using the density functional theory (DFT) method, *Results Phys.*, 15, 102592.
- [34] Behzadi, P., Ketabi, S.A., and Amiri, P., 2021, First-principles investigation of the electronic and optical properties of As₂GeTe nanotubes, *Solid State Commun.*, 336, 114421.
- [35] Johannes, A.Z., 2018, Simulasi perubahan densitas muatan adsorpsi atom hydrogen-grafena dengan teori fungsi kerapatan, *JFiSA*, 3 (2), 179–184.
- [36] Birch, F., 1947, Finite elastic strain of cubic crystals, *Phys. Rev.*, 71 (11), 809–824.
- [37] Zhuravlev, K.K., 2007, PbSe vs. CdSe: Thermodynamic properties and pressure dependence of the band gap, *Phys. B*, 394 (1), 1–7.
- [38] Hastuti, D.P., Nurwantoro, P., and Sholihun, S., 2019, Stability study of germanene vacancies: The first-principles calculations, *Mater. Today Commun.*, 19, 459–463.
- [39] Vaitheeswaran, G., Kanchana, V., Zhang, X., Ma, Y., Svane, A., and Christensen, N.E., 2016, Calculated high-pressure structural properties, lattice dynamics and quasi particle band structures of perovskite fluorides KZnF₃, CsCaF₃ and BaLiF₃, *J. Phys.: Condens. Matter*, 28 (31), 315403.
- [40] Sarukura, N., Murakami, H., Estacio, E., Ono, S., El Ouenzerfi, R., Cadatal, M., Nishimatsu, T., Terakubo, N., Mizuseki, H., Kawazoe, Y., Yoshikawa, A., and Fukuda, T., 2007, Proposed design principle of fluoride-based materials for deep ultraviolet light emitting devices, *Opt. Mater.*, 30 (1), 15–17.
- [41] Ghaithan, H.M., Alahmed, Z.A., Qaid, S.M.H., and Aldwayyan, A.S., 2021, Density functional theory analysis of structural, electronic, and optical

- properties of mixed-halide orthorhombic inorganic perovskites, *ACS Omega*, 6 (45), 30752–30761.
- [42] Chen, K., Schünemann, S., Song, S., and Tüysüz, H., 2018, Structural effects on optoelectronic properties of halide perovskites, *Chem. Soc. Rev.*, 47 (18), 7045–7077.
- [43] Ahmad, M., Rehman, G., Ali, L., Shafiq, M., Iqbal, R., Ahmad, R., Khan, T., Jalali-Asadabadi, S., Maqbool, M., and Ahmad, I., 2017, Structural, electronic and optical properties of CsPbX₃ (X = Cl, Br, I) for energy storage and hybrid solar cell applications, *J. Alloys Compd.*, 705, 828–839.
- [44] Chen, Y., Feng, Z., Pal, A., and Zhang, J., 2022, Recent progress on the performance of lead-based halide perovskite APbX₃ detectors, *Phys. Status Solidi A*, 219 (9), 2200018.
- [45] Thi Han, N., Khuong Dien, V., and Lin, M.F., 2022, Electronic and optical properties of CsGeX₃ (X = Cl, Br and I) compounds, *ACS Omega*, 7 (29), 25210–25218.
- [46] Bouhmaidi, S., Marjaoui, A., Talbi, A., Zanouni, M., Nouneh, K., and Setti, L., 2022, A DFT study of electronic, optical and thermoelectric properties of Ge-halide perovskites CsGeX₃ (X = F, Cl and Br), *Comput. Condens. Matter*, 31, e00663.
- [47] Hasan, N., Arifuzzaman, M., and Kabir, A., 2022, Structural, elastic, and optoelectronic properties of inorganic cubic FrBX₃ (B = Ge, Sn; X = Cl, Br, I) perovskite: The density functional theory approach, *RSC Adv.*, 12 (13), 7961–7972.
- [48] Hamideddine, I., Tahiri, N., El Bounagui, O., and Ez-Zahraouy, H., 2022, Ab initio study of structural and optical properties of the halide perovskite KBX₃ compound, *J. Korean Ceram. Soc.*, 59, 350–358.
- [49] Abdulkareem, N.A., Ilyas, B.M., and Sami, S.A., 2021, A first principle investigation of the non-synthesized cubic perovskite LiGeX₃ (X = I, Br, and Cl), *Mater. Sci. Semicond. Process.*, 131, 105858.
- [50] Rahman, M.H., Jubair, M., Rahaman, M.Z., Ahasan, M.S., Ostrikov, K., and Roknuzzaman, M., 2022, RbSnX₃ (X = Cl, Br, I): Promising lead-free metal halide perovskites for photovoltaics and optoelectronics, *RSC Adv.*, 12 (12), 7497–7505.
- [51] Ur Rehman, J., Usman, M., Amjid, S., Sagir, M., Bilal Tahir, M., Hussain, A., Alam, I., Nazir, R., Alrobei, H., Ullah, S., and Assiri, M.A., 2022, First-principles calculations to investigate structural, electronics, optical and elastic properties of Sn-based inorganic Halide-perovskites CsSnX₃ (X = I, Br, Cl) for solar cell applications, *Comput. Theor. Chem.*, 1209, 113624.
- [52] Hayatullah, H., Murtaza, G., Muhammad, S., Naeem, S., Khalid, M.N., and Manzar, A., 2013, Physical properties of CsSnM₃ (M = Cl, Br, I): A first principle study, *Acta Phys. Pol. A*, 124 (1), 102–107.
- [53] Rashid, M.A., Saiduzzaman, M., Biswas, A., and Hossain, K.M., 2022, First-principles calculations to explore the metallic behavior of semiconducting lead-free halide perovskites RbSnX₃ (X = Cl, Br) under pressure, *Eur. Phys. J. Plus*, 137, 649.
- [54] Saiduzzaman, M., Ahmed, T., Hossain, K.M., Biswas, A., Mitro, S.K., Sultana, A., Alam, M.S., and Ahmad S., 2023, Band gap tuning of non-toxic Sr-based perovskites CsSrX₃ (X = Cl, Br) under pressure for improved optoelectronic applications, *Mater. Today Commun.*, 34, 105188.
- [55] Harbi, A., and Moutaabbid, M., 2022, Thermoelectric and optoelectronic properties of novel lead-free halide perovskites CsRbTiX₆ (X= I, Br and Cl) for photovoltaic applications, *Comput. Condens. Matter*, 32, e00733.
- [56] Zelai, T., Rouf, S.A., Mahmood, Q., Bouzgarrou, S., Amin, M.A., Aljameel, A.I., Ghrib, T., Hegazy, H.H., and Mera, A., 2022, First-principles study of lead-free double perovskites Ga₂PdX₆ (X = Cl, Br, and I) for solar cells and renewable energy, *J. Mater. Res. Technol.*, 16, 631–639.
- [57] Sharma, R., Dey, A., Ahmed Dar, S., and Srivastava, V., 2021, A DFT investigation of CsMgX₃ (X = Cl, Br) halide perovskites: Electronic, thermoelectric and optical properties, *Comput. Theor. Chem.*, 1204, 113415.
- [58] Mousa, A.A., Abu-Jafar, M.S., Dahliah, D., Shaltaf, R.M., and Khalifeh, J.M., 2018, Investigation of the perovskite KSrX₃ (X = Cl and F) compounds, examining the optical, elastic, electronic and

- structural properties: FP-LAPW study, *J. Electron. Mater.*, 47 (1), 641–650.
- [59] Mahmood, Q., Hedhili, F., Al-Shomar, S., Chebaaneef, S., Al-Muhimeed, T.I., AlObaid, A., Mera, A., and Alamri, O.A., 2021, Electronic, optical, and transport properties of RbYbX_3 ($X = \text{Cl, Br}$) for solar cells and renewable energy: A quantum DFT study, *Phys Scr.*, 96, 095806.
- [60] Moreira, R.L., and Dias, A., 2007, Comment on “Prediction of lattice constant in cubic perovskites”, *J. Phys. Chem. Solids*, 68 (8), 1617–1622.
- [61] Trots, D.M., and Myagkota, S.V., 2008, High-temperature structural evolution of caesium and rubidium triiodoplumbates, *J. Phys. Chem. Solids*, 69 (10), 2520–2526.
- [62] Tang, Y., Zhang, J., Zhong, X., Wang, Q., Zhang, H., Ren, C., and Wang, J., 2019, Revealing the structural, electronic and optical properties of lead-free perovskite derivatives of Rb_2SnX_6 ($X = \text{Cl, Br}$ and I): A theory calculation, *Sol. Energy*, 190, 272–277.
- [63] Aslam, F., Ullah, H., and Hassan, M., 2021, Theoretical investigation of $\text{Cs}_2\text{InBiX}_6$ ($X = \text{Cl, Br, I}$) double perovskite halides using first-principle calculations, *Mater. Sci. Eng., B*, 274, 115456.
- [64] Saeed, M., Ul Haq, I., Ur Rehman, S., Ali, A., Shah, W.A., Ali, Z., Khan, Q., and Khan, I., 2021, Optoelectronic and elastic properties of metal halides double perovskites $\text{Cs}_2\text{InBiX}_6$ ($X = \text{F, Cl, Br, I}$), *Chin. Opt. Lett.*, 19 (3), 030004.
- [65] Saeed, M., Ul Haq, I., Saleemi, A.S., Ur Rehman, S., Ul Haq, B., Chaudhry, A.R., and Khan, I., 2022, First-principles prediction of the ground-state crystal structure of double-perovskite halides $\text{Cs}_2\text{AgCrX}_6$ ($X = \text{Cl, Br, and I}$), *J. Phys. Chem. Solids*, 160, 110302.
- [66] Iqbal, S., Mustafa, G.M., Asghar, M., Noor, N.A., Iqbal, M.W., Mahmood, A., and Shin, Y.H., 2022, Tuning the optoelectronic and thermoelectric characteristics of narrow bandgap $\text{Rb}_2\text{AlInX}_6$ ($X = \text{Cl, Br, I}$) double perovskites: A DFT study, *Mater. Sci. Semicond. Process.*, 143, 106551.
- [67] Albalawi, H., Mustafa, G.M., Saba, S., Kattan, N.A., Mahmood, Q., Somaily, H.H., Morsi, M., Alharthi, S., and Amin, M.A., 2022, Study of optical and thermoelectric properties of double perovskites Cs_2KTlX_6 ($X = \text{Cl, Br, I}$) for solar cell and energy harvesting, *Mater. Today Commun.*, 32, 104083.
- [68] Alotaibi, N.H., Mustafa, G.M., Kattan, N.A., Mahmood, Q., Albalawi, H., Morsi, M., Somaily, H.H., Hafez, M.A., Mahmoud, H.I., and Amin, M.A., 2022, DFT study of double perovskites $\text{Cs}_2\text{AgBiX}_6$ ($X = \text{Cl, Br}$): An alternative of hybrid perovskites, *J. Solid State Chem.*, 313, 123353.
- [69] Niaz, S., Khan, M.A., Noor, N.A., Ullah, H., and Neffati, R., 2022, Bandgap tuning and thermoelectric characteristics of Sc-based double halide perovskites K_2ScAgZ_6 ($Z = \text{Cl, Br, I}$) for solar cells applications, *J. Phys. Chem. Solids*, 174, 111115.
- [70] Johnson, A., Gbaorun, F., and Ikkyo, B.A., 2022, First-principles study of $(\text{CsMA})\text{NaSbX}_6$ ($\text{MA} = \text{methylammonium; } X = \text{Cl, Br, I}$) organic-inorganic hybrid double perovskites for optoelectronic applications, *J. Comput. Electron.*, 21 (1), 34–39.
- [71] Khan, M.A., Alburaih, H.A., Noor, N.A., and Dahshan, A., 2021, Comprehensive investigation of opto-electronic and transport properties of $\text{Cs}_2\text{ScAgX}_6$ ($X = \text{Cl, Br, I}$) for solar cells and thermoelectric applications, *Sol. Energy*, 225, 122–128.
- [72] Choudhary, S., Tomar, S., Kumar, D., Kumar, S., and Verma, A.S., 2021, Investigations of lead free halides in sodium based double perovskites $\text{Cs}_2\text{NaBiX}_6$ ($X = \text{Cl, Br, I}$): An *ab initio* study, *East Eur. J. Phys.*, 3, 74–80.
- [73] Behera, D., and Mukherjee, S.K., 2022, Optoelectronics and transport phenomena in $\text{Rb}_2\text{InBiX}_6$ ($X = \text{Cl, Br}$) compounds for renewable energy applications: A DFT insight, *Chemistry*, 4 (3), 1044–1059.
- [74] Kattan, N.A., Mahmood, Q., Nazir, G., Rehman, A., Sfina, N., Al-anazy, M.M., Sofi, S.A., Morsi, M., and Amin, M.A., 2023, Modifying electronic bandgap by halide ions substitution to investigate double perovskites $\text{Rb}_2\text{AgInX}_6$ ($X = \text{Cl, Br, I}$) for solar cells applications and thermoelectric characteristics, *Mater. Today Commun.*, 34, 105166.

- [75] Ye, X., Liu, A., Zhao, Y., Han, Q., Kitamura, T., and Ma, T., 2022, DFT study of X-site ion substitution doping of Cs_2PtX_6 on its structural and electronic properties, *Int. J. Energy Res.*, 46 (6), 8471–8479.
- [76] Al-Muhimeed, T.I., Alzahrani, J., Rouf, S.A., Al-Qaisi, S., Anbarasan, R., Mahmood, Q., Albalawi, H., Alharthi, S., Amin, M.A., and Somaily, H.H., 2022, Tuning of band gap by anion variation of Ga_2TiX_6 (X = Cl, Br, I) for solar cells and renewable energy, *Phys. Scr.*, 97 (8), 085815.
- [77] Bhamu, K.C., Soni, A., and Sahariya, J., 2018, Revealing optoelectronic and transport properties of potential perovskites Cs_2PdX_6 (X = Cl, Br): A probe from density functional theory (DFT), *Sol. Energy*, 162, 336–343.
- [78] Younas, M., Mahmood, Q., Kattan, N., Alshahrani, T., Mera, A., Mersal, G.A.M., Amin, M., and Somaily, H.H., 2022, Study of new double perovskites Tl_2PtX_6 (X = Cl, Br, I) for solar cells and thermoelectric applications, *Phys. Scr.*, 97 (12), 125803.
- [79] Albalawi, H., Nazir, G., Younas, M., Al-Qaisi, S., Ashiq, M.G.B., Alzahrani, J., Somaily, H.H., Morsi, M., and Ghrib, T., 2022, Study of lead-free vacancy ordered double perovskites Cs_2TeX_6 (X = Cl, Br, I) for solar cells, and renewable energy, *Phys. Scr.*, 97, 095801.
- [80] Mahmood, Q., Nazir, G., Bouzgarrou, S., Aljameel, A.I., Rehman, A., Albalawi, H., Ul Haq, B., Ghrib, T., and Mera, A., 2022, Study of new lead-free double perovskites halides Tl_2TiX_6 (X = Cl, Br, I) for solar cells and renewable energy devices, *J. Solid State Chem.*, 308, 122887.
- [81] Callister, W.D., and Rethwisch, D.G., 2018, *Fundamentals of Materials Science and Engineering*, 5th Ed., John Wiley and Sons Inc., Hoboken, NJ, USA.
- [82] Bouhmaidi, S., Azouaoui, A., Benzakour, N., Hourmatallah, A., and Setti, L., 2022, First principles calculations on structural, electronic, elastic, optical, and thermoelectric properties of thallium based chloroperovskites TlMCl_3 (M = Zn and Cd), *Comput. Condens. Matter*, 33, e00756.
- [83] Born, M., 1940, On the stability of crystal lattices, *Math. Proc. Cambridge Philos. Soc.*, 36 (2), 160–172.
- [84] Reddy, R.R., Gopal, K.R., Narasimhulu, K., Reddy, L.S.S., Kumar, K.R., Balakrishnaiah, G., and Kumar, M.R., 2009, Interrelationship between structural, optical, electronic and elastic properties of materials, *J. Alloys Compd.*, 473 (1-2), 28–35.
- [85] Li, K., Kang, C., and Xue, D., 2012, Electronegativity calculation of bulk modulus and band gap of ternary ZnO-based alloys, *Mater. Res. Bull.*, 47 (10), 2902–2905.
- [86] Song, Z., Fan, W., Tan, C.S., Wang, Q., Nam, D., Zhang, D.H., and Sun, G., 2019, Band structure of $\text{Ge}_{1-x}\text{Sn}_x$ alloy: A full-zone 30-band k-p model, *New J. Phys.*, 21 (7), 073037.
- [87] Pugh, S.F., 1954, Relations between the elastic moduli and the plastic properties of polycrystalline pure metals, *Lond. Edinb. Dubl. Phil. Mag.*, 45 (367), 823–843.
- [88] Krishnamoorthy, T., Ding, H., Yan, C., Leong, W.L., Baikie, T., Zhang, Z., Sherburne, M., Li, S., Asta, M., Mathews, N., and Mhaisalkar, S.G., 2015, Lead-free germanium iodide perovskite materials for photovoltaic applications, *J. Mater. Chem. A*, 3 (47), 23829–23832.
- [89] Mattesini, M., Magnuson, M., Tasnádi, F., Höglund, C., Abrikosov, I.A., and Hultman, L., 2009, Elastic properties and electrostructural correlations in ternary scandium-based cubic inverse perovskites: A first-principles study, *Phys. Rev. B*, 79 (12), 125122.
- [90] Shah, M.A.H., Nuruzzaman, M., Hossain, A., Jubair, M., and Zilani, M.A.K., 2023, A DFT insight into structural, mechanical, elasto-acoustic, and anisotropic properties of AePdH_3 (Ae = Ca, Sr, Ba) perovskites under pressure, *Comput. Condens. Matter*, 34, e00774.
- [91] Ghebouli, B., Ghebouli, M.A., Bouhemadou, A., Fatmi, M., Khenata, R., Rached, D., Ouahrani, T., and Bin-Omran, S., 2012, Theoretical prediction of the structural, elastic, electronic, optical and thermal properties of the cubic perovskites CsXF_3 (X = Ca, Sr and Hg) under pressure effect, *Solid State Sci.*, 14 (7), 903–913.
- [92] Bakar, A., Alrashdi, A.O., Fadhali, M.M., Afaq, A., Yakout H.A., and Asif, M., 2022, Effect of pressure

- on structural, elastic and mechanical properties of cubic perovskites $X\text{CoO}_3$ ($X = \text{Nd}, \text{Pr}$) from first-principles investigations, *J. Mater. Res. Technol.*, 19, 4233–4241.
- [93] Erum, N., and Iqbal, M.A., 2020, Elastomechanical and magneto-optoelectronic investigation of RbCoF_3 : An *ab initio* DFT study, *Acta Phys. Pol., A*, 138 (3), 509–517.
- [94] Mubarak, A.A., and Al-Omari, S., 2015, First-principles calculations of two cubic fluoroperovskite compounds: RbFeF_3 and RbNiF_3 , *J. Magn. Magn. Mater.*, 382, 211–218.
- [95] El Amine Monir, M., and Dahou, F.Z., 2020, Structural, thermal, elastic, electronic and magnetic properties of cubic lanthanide based perovskites type oxides PrXO_3 ($X = \text{V}, \text{Cr}, \text{Mn}, \text{Fe}$): Insights from *ab initio* study, *SN Appl. Sci.*, 2 (3), 465.
- [96] Cherif, Y.B., Rouaighia, M., Zaoui, A., and Boukourt, A., 2017, Optoelectronic, elastic and thermal properties of cubic perovskite-type SrThO_3 , *Acta Phys. Pol., A*, 131 (3), 406–413.
- [97] Råsander, M., and Moram, M.A., 2015, On the accuracy of commonly used density functional approximations in determining the elastic constants of insulators and semiconductors, *J. Chem. Phys.*, 143 (14), 144104.
- [98] Green, M.A., Jiang, Y., Soufiani, A.M., and Ho-Baillie, A., 2015, Optical properties of photovoltaic organic-inorganic lead halide perovskites, *J. Phys. Chem. Lett.*, 6 (23), 4774–4785.
- [99] Ambrosch-Draxl, C., and Sofo, J.O., 2006, Linear optical properties of solids within the full-potential linearized augmented plane wave method, *Comput. Phys. Commun.*, 175 (1), 1–14.
- [100] Alam, M.S., Saiduzzaman, M., Biswas, A., Ahmed, T., Sultana, A., and Hossain, K.M., 2022, Tuning band gap and enhancing optical functions of AGeF_3 ($A = \text{K}, \text{Rb}$) under pressure for improved optoelectronic applications, *Sci. Rep.*, 12 (1), 8663.
- [101] Penn, D.R., 1962, Wave-number-dependent dielectric function of semiconductors, *Phys. Rev.*, 128 (5), 2093–2097.
- [102] Rahaman, M.Z., and Hossain, A.K.M.A., 2018, Effect of metal doping on the visible light absorption, electronic structure and mechanical properties of non-toxic metal halide CsGeCl_3 , *RSC Adv.*, 8 (58), 33010–33018.
- [103] Biswas, A., Alam, M.S., Sultana, A., Ahmed, T., Saiduzzaman, M., and Hossain, K.M., 2021, Effects of Bi and Mn codoping on the physical properties of barium titanate: investigation via DFT method, *Appl. Phys. A: Mater. Sci. Process.*, 127 (12), 939.
- [104] Bouhmaid, S., Pingak, R.K., Azouaoui, A., Harbi, A., Moutaabbid, M., and Setti, L., 2023, *Ab initio* study of structural, elastic, electronic, optical and thermoelectric properties of cubic Ge-based fluoroperovskites AGeF_3 ($A = \text{K}, \text{Rb}$ and Fr), *Solid State Commun.*, 369, 115206.

Mini-Review:**Removal of Heavy Metal Ions Using Pristine and Functionalized Natural Zeolites****Khairul Ihsan Solihin¹, St Mardiana², Handajaya Rusli¹, and Grandprix Thomryes Marth Kadja^{2,3,4*}**¹Division of Analytical Chemistry, Faculty of Mathematics and Natural Sciences, Institut Teknologi Bandung, Jl. Ganesha No. 10, Bandung 40132, Indonesia²Division of Inorganic and Physical Chemistry, Faculty of Mathematics and Natural Sciences, Institut Teknologi Bandung, Jl. Ganesha No. 10, Bandung 40132, Indonesia³Center for Catalysis and Reaction Engineering, Institut Teknologi Bandung, Jl. Ganesha No. 10, Bandung 40132, Indonesia⁴Research Center for Nanosciences and Nanotechnology, Institut Teknologi Bandung, Jl. Ganesha No. 10, Bandung 40132, Indonesia*** Corresponding author:**

email: grandprix.thomryes@itb.ac.id

Received: January 8, 2023

Accepted: March 1, 2023

DOI: 10.22146/ijc.81098

Abstract: Heavy metal ions have attracted significant concern regarding their toxicity in living organisms. Concurrently, the removal of heavy metals by the adsorption method is also under the spotlight because it is effective, less cost-demanding, and easy to operate. To date, natural zeolites become one of the most used adsorbents for it is low cost, abundant in reserve, and has high selectivity towards heavy metal. Zeolites possess negatively charged three-dimensional frameworks built by SiO₄ and AlO₄ tetrahedra, which are balanced by counter-cations. The cations within zeolite frameworks can be exchanged with the heavy metal cations in an aqueous environment. This review comprehensively reports the adsorption capacity of heavy metal ions using pristine and modified natural zeolite. The important aspects, including the physicochemical properties of pristine and modified natural zeolites, heavy metal ion adsorption isotherms, kinetics, and thermodynamics, are discussed in detail. It is imperative to note that the physicochemical properties of natural zeolites greatly determine the adsorption capability. Furthermore, natural zeolites could be modified with various molecules such as surfactants and polymers to improve the adsorption capacity and adsorb heavy metal anions. Ultimately, this review is concluded with prospects for future improvement.

Keywords: adsorption capacity; adsorption isotherm; adsorption kinetics; heavy metal; zeolite

■ INTRODUCTION

Environmental pollution is a problem that always appears, even common, in the last decade. This type of pollution can come from anywhere, but the most frequent and dangerous sources of pollution are organic materials and heavy metals from industrial wastewater [1-4]. Heavy metals refer to dense metallic elements with high atomic weights or atomic numbers, such as Cd, Hg, Pb, As, Cu, Cr, Mn, Fe, and Zn, which are toxic at relatively low concentrations [5]. The effect of heavy metal intake on the

human body through water is fatal since it will accumulate and may lead to organ failure [1,6]. According to WHO, there are limits to those metals in the drinking water, i.e., Cd(II): 3 µg L⁻¹, As(V): 10 µg L⁻¹, Pb(II): 10 µg L⁻¹, Cr(VI): 50 µg L⁻¹, Mn: 0.4 mg L⁻¹, Cu(II): 2 mg L⁻¹, Fe(III): 2 mg L⁻¹, and Zn(II): 3 mg L⁻¹.

Cd(II), As(V), and Cr(VI) are classified as carcinogenic heavy metal ions. Cr is divided into two stable species in nature, Cr(III) and Cr(VI), in which the latter is a far more dangerous species than the former. Even so, the limit of Cr(VI) is higher than Cd(II) and

As(V) because it could still be reduced to Cr(III) as long as its dose is under the limit [5]. Pb(II) can cause loss of intelligence quotient in children, whereas Mn(II) has a quite high dose since it is somewhat elusive whether Mn has an adverse effect on humans, albeit it has harmful effects in rodents and other animals [5]. Unlike other heavy metals, Fe and Zn are essential to our bodies. Nevertheless, several studies show that Zn and Fe are poisonous to animals such as fish, sheep, and even humans when it exceeds the limited dose intake [5,7-10].

Several strategies have been devoted to removing heavy metal ions from the aqueous environment, such as ion exchange, neutralization, chelating agent, reverse osmosis, and adsorption [2,11-14]. All these methods have succeeded in removing heavy metal ions from aqueous solutions through the years and have offered some advantages and disadvantages. Those advantages and disadvantages are the keys for researchers and industries to select the preferred method. Neutralization, chelating agent, and reverse osmosis are better in terms of effectiveness for removing heavy metal ions. Yet, the operational cost is very costly, rendering these methods unlikely to be applied in many industries. Ion exchange and adsorption exhibit a high selectivity to the heavy metal ion and a relatively low operational cost. However,

ion-exchange limits metal concentration in a solution, making adsorption generally preferred [2,15].

In the adsorption method, there are many types of adsorbent, including biosorbent [16], activated carbon [17], fly ash [2], clay minerals [18], and zeolite [19-20]. As seen in Fig. 1, these materials are used and proven successful in removing metal ions from an aqueous solution. Biosorbent is a material that utilizes microorganisms, such as algae, bacteria, and fungi, dead or alive, to adsorb pollutants on their cell wall or to detoxify the heavy metal by changing its oxidation number, e.g., Cr(VI) to Cr(III) [16,21-23]. However, biosorbent has a significant drawback since it needs to be in a well-controlled environment, such as pH, temperature, and solution matrix, to perform the adsorption of heavy metal ions [16,21]. Furthermore, the effectiveness of adsorption is limited to low heavy metal concentrations [23]. Activated carbon is a carbon material with a large surface area, great active sites, and a porous structure [17]. Nonetheless, even with great active sites, activated carbon has a little too low adsorption capacity and selectivity toward metal ions [17]. Fly ash is an aluminosilicate-based solid waste from a thermal power plant [2,24]. It is cheap but needs chemical activation to improve its adsorption performance [2].

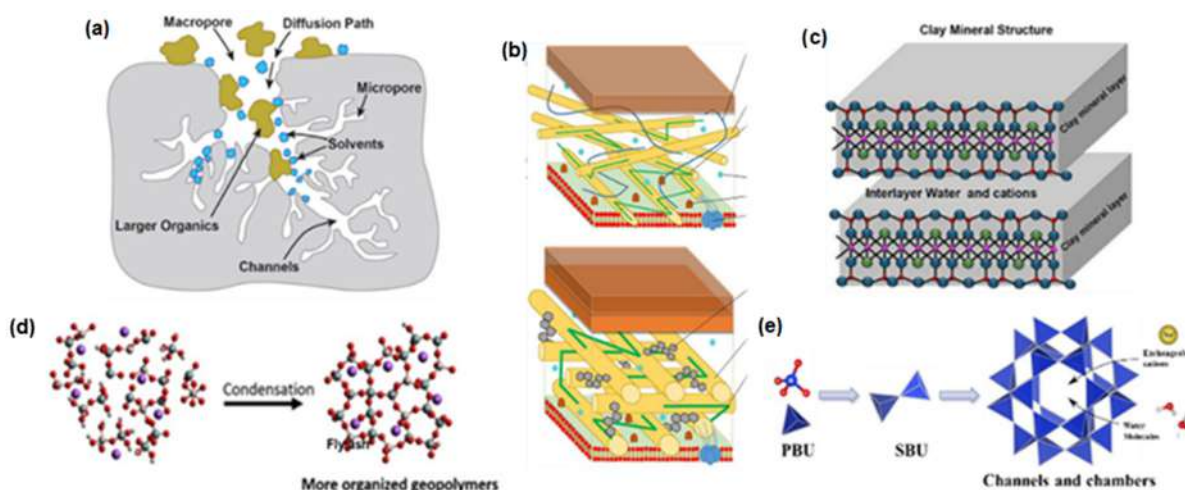


Fig 1. Adsorbent materials structure: (a) Activated carbon. Adapted with permission from Ref [25], Copyright 2017 Sage; (b) Clay. Adapted with permission from Ref [26], Copyright 2018 SCIRP; (c) Biosorbent. Adapted with permission from Ref [27], Copyright 2017 Frontiers; (d) Fly ash. Adapted with permission from Ref [2], Copyright 2019 Elsevier; (e). Zeolite. Adapted with permission from Ref [28], Copyright 2020 MDPI

Clay mineral is an aluminosilicate-based layered material with an ion exchange capacity and large surface area [14,18]. However, due to its swelling properties, it has limited adsorption capacity and low selectivity to heavy metal ions [14]. Zeolite is a crystalline, aluminosilicate material with uniform distribution of micropores (<2 nm) and a large surface area [29-31]. The microporous and negatively-charged structures render the natural zeolite highly effective and efficient for removing heavy metal ions. Zeolite can be naturally-occurred via a hydrothermal-like reaction in the volcanic area. Natural zeolite is cheap yet still possesses high adsorption capacity. Indonesia has more than 400 million tons of natural zeolite reserves [32-33]. Currently, more than 250 different zeolite frameworks to date, and each of them has been assigned a three-letter code by International Zeolite Association (IZA).

This review comprehensively discussed the characteristics of pristine natural zeolite and its application as an adsorbent for removing heavy metal ions from the aqueous environment. Moreover, several routes for modifying the natural zeolites to improve the adsorption performance and enable the removal of heavy metal anions, e.g., Cr(VI), are also elaborated in detail. The heavy metal ions adsorption discussion covers the isotherm, kinetics, and thermodynamic studies.

■ CHARACTERISTICS OF NATURAL AND MODIFIED ZEOLITE

Pristine Natural Zeolite

Over 50 types of pristine zeolite have been identified worldwide, commonly found in volcanic rocks. The zeolite structure has a three-dimensional framework consisting of SiO_4 and AlO_4 tetrahedra. The isomorphous substitution of SiO_4 with AlO_4 renders a negative charge on the zeolite framework. Hence, counter-cations are needed, such as alkaline and alkaline earth metals and ammonium, which could be exchanged with the other heavy metal ion solution because those cations are weakly held [34]. These pristine zeolites have a unique framework and structure that are relevant to their adsorption and ion exchange capacities. Moreover, pristine zeolites also can be used for separation [35] and catalysis [36-41] due to their

structural cavities, porous acid sites, and input channels that can establish molecules like water and other organic molecules. According to IZA, there are over 200 types of zeolite frameworks, and each type is divided by a three-letter code [42].

The physicochemical properties of pristine zeolite determine its structural properties, such as Si/Al ratio, mineral composition, exchangeable cation, and surface area. Si/Al ratio is essential because it causes zeolites to have a negative charge that can attract cations. The lower Si/Al ratio is, the higher its negative charge density, making it better in selectivity and attracting the metal cations [37,43-44].

Mineral composition and exchangeable cations are the factors that are often not considered. Different minerals have distinct properties, making some of the zeolites have higher adsorption capacity than others while having the same solution matrix [45]. Exchangeable cations did play significant roles in the adsorption capacity. For example, the more the exchangeable cation, the more heavy metal ions can be exchanged from the polluted solution [46]. Heavy metal ions are regularly in a divalent state, so a divalent ion exchanger, such as Mg(II) and Ca(II), is commonly better than a monovalent ion exchanger, such as NH_4 (I), H(I), and K(I). In other cases, the surface area also played a significant role in the adsorption capabilities of the zeolite. The larger the surface area, the more heavy metal ion can be adsorbed, giving the zeolite more immense sorption capabilities [47]. Therefore, the factors governing the adsorption course are complex, and the adsorption results between different reports should be comprehensively considered before comparison.

Clinoptilolite is one of the most abundant natural zeolites and is commonly utilized by researchers [48-51]. The presence of clinoptilolite is distributed worldwide, including south-east Asia, South America, Europe, Australia, and Africa. Aside from clinoptilolite, other natural zeolites are also explored, such as mordenite, chabazite, stilbite, and phillipsite. The type and composition of pristine natural zeolites are summarized in Table 1. As seen, the Si/Al ratio is relatively low, ranging from around 1 to 6, which generates a highly

Table 1. Type and the composition of pristine zeolite

Zeolite	Zeolite type	Si/Al Ratio	Major cation	CEC (meq g ⁻¹)	SSA (m ² g ⁻¹)	Ref.
Brazilian zeolite	Clinoptilolite	4.82	-	1.57	59.63	[48]
Philippine zeolite	Mix of mordenite, clinoptilolite, and chabazite	4.29	Ca; Fe; Mg	-	222.63	[44]
Indonesian zeolite	Mix of mordenite and clinoptilolite	4.72	K; Ca	43.20	-	[46]
	Mix of mordenite and clinoptilolite	5.40	K; Na; Ca; Fe	102.80	-	
	Mordenite	3.51	Na; Ca; Mg	-	-	
Indian zeolite	Stilbite	2.08	Ca; Na	-	-	[49]
	Heulandite	2.36	Ca; Na	-	-	
Russian zeolite	Clinoptilolite	5.00–6.00	K; Na	-	-	[50]
Iranian zeolite	Clinoptilolite	4.87	K	-	60.43	[51]
Kazakhstan zeolite	-	4.59	Ca; Fe; Mg; K	-	-	[52]
Jordanian zeolite	Phillipsite	2.96	Fe; Mg; Ca	0.70	41.20	[53]
Serbian zeolite	Clinoptilolite	-	Ca; Mg	1.38	18.00	[54]
Slovakian zeolite	-	4.95	Ca; Fe	-	-	[55]

negative charge. Thus, natural zeolites are balanced by monovalent cations and divalent cations. The cation-exchange capacity (CEC) and the specific surface area are greatly varied due to the difference in crystallinity, impurities, and other variables. It should be noted many natural zeolites are found in low crystallinity.

Modified Natural Zeolite

Pristine natural zeolite's advantages, including abundant reserve, good adsorption, decent cation exchange capacity, and low cost, are still deemed insufficient since the said advantageous properties could be further enhanced. Therefore, researchers have begun modifying pristine zeolites by incorporating acid or base, polymer, and functional groups for the adsorption of heavy metal ions. The modified natural zeolites are also applied in other fields, such as catalysis [56] and the removal of other inorganic pollutants [57-58]. The vast application of the modified pristine natural zeolite does not rule out the possibility that a new or already found modifier for another field is applicable in heavy metal adsorption.

Yousefi et al. [59] analyzed the clinoptilolite modified with Cobalt Hexacyanoferrate nanoparticles to remove Cd(III) ions from an aqueous solution. The result indicated the Cd(III) ions sorption capacity was improved up to two times higher than non-modified clinoptilolite (51 mg g⁻¹).

Meanwhile, Mirbaloochzehi et al. [60] modified the clinoptilolite using a surfactant (Triton X-100) to remove heavy metal cations (i.e., Cu(II), Pb(II), Ni(II), Cd(II), Fe(II), and Zn(II)) from aqueous solution with cation sorption capacity for Pb(II), Cu(II), Cd(II), Ni(II), Zn(II) and Fe(II) was 91.34, 85.71, 78.27, 76.18, 67.41 and 63.45 mg g⁻¹, respectively. Chitosan nanoparticles were also investigated as a modifier to the natural zeolite to improve the sorption capacity of Pb(II) ions [61]. As a result, the adsorption capacity was increased compared to the non-modified zeolite from 43.83 to 49.91%.

Pristine natural zeolite has impurities within its inner architecture, often impeding micropores. Hence, acid or base is added to eliminate other minerals or substances obstructing the pore so that zeolite can adsorb more heavy metal ions. Another challenge is that pristine zeolite carries a negative charge that cannot adsorb heavy metal anions, such as chromate or bichromate. Consequently, surface modification is necessary to equip the natural zeolite with anion adsorption ability. It includes the addition of polymer or functional groups to the surface of zeolites. Table 2 summarizes several modifiers used by the researchers.

■ ADSORPTION CAPACITY

Adsorption methods are commonly used by mixing solid adsorbent materials into a heavy metal solution. The

Table 2. Modifier, textural properties, and cation exchange capacity (CEC)

Zeolite type	Modifier	Textural properties		CEC (meq g ⁻¹)	Ref.
		SSA before modification (m ² m ⁻¹)	SSA after modification (m ² g ⁻¹)		
Iranian zeolite	Cobalt hexacyanoferrate	-	-	-	[59]
Iranian zeolite	Triton x-100 (surfactant)	-	-	-	[60]
Indonesian zeolite	Chitosan	-	-	-	[61]
Iranian zeolite	HDTMA	14.85	9.55	-	[62]
Mexican zeolite	(Hexadecyltrimethylammonium)	7.73	5.41	-	[63]
Taiwan zeolite		746.00	22.90	1.50	[64]
Serbian zeolite	Alginate Composite	-	-	1.49	[65]
Iranian zeolite	HDTMA and dithizone	23.19	HDTMA: 29.72 HDTMA+ dithizone: 34.33	-	[66]
Mexican clinoptilolite		-	-	1.60 ± 0.09	
Mexican mordenite	Metals ion (Fe; Zr; FeZr)	-	-	1.80 ± 0.06	[68]
Mexican chabazite		-	-	2.10 ± 0.05	
Slovakian clinoptilolite	NaCl sonication	31.14	37.25	1.58	[69]
Iranian clinoptilolite	Glycine	97.00	41.14	-	[70]

mixture is then stirred to maximize the adsorption by using a shaker. Then the mixture is separated using centrifugation and screening to free the supernatant from the adsorbent. Afterward, the supernatant is measured, usually by using atomic absorption spectroscopy (AAS) or atomic emission spectroscopy (AES), to determine the number of heavy metal ions that have been absorbed. From these steps, adsorption performance, such as adsorption capacity, isotherm, kinetics, and thermodynamics, can be determined for modeling the adsorption course of adsorption.

Adsorption Capacity of Pristine Zeolite

Budianta et al. [46] used two Indonesian natural zeolites from Bantengwareng and Tegalrejo, named B and T, respectively, with mordenite types of zeolite and other mineral impurities, for Pb(II) and Cd(II) ion removal. The adsorption capacities of zeolite in B and T for Pb(II) adsorption are 416.67 and 384.61 mg g⁻¹, respectively. Besides, the adsorption capacity is 277.77 and 243.91 mg g⁻¹ for Cd(II) removal of B and T samples. It was shown that the adsorption capacity of B is higher than T regarding the more abundant smectite presence. Hence, B has a higher CEC and SSA compared to T.

Previously, Zanin et al. [48] reported Brazilian zeolite,

clinoptilolite type, to adsorb Cu(II), Fe(III), and Cr(III), rendering the adsorption capacity of 1.845, 1.750, and 1.661 mg g⁻¹. The results showed that iron is preferentially to adsorb at the process, which exhibited the selectivity of zeolite to metals. Another natural zeolite, i.e., Slovakian zeolite, is reported by Kovacova and Pla [55], that used successfully to adsorb Ni(II) ion without pre-treatment and achieved an adsorption capacity of 17.62 mg g⁻¹. The sorption process was on the heterogeneous surface with a concentration of nickel solution 50 mg L⁻¹. The Philippine natural zeolite (PNZ), a mixture of mordenite, clinoptilolite, and chabazite, was used for Zn(II) ion removal in an aqueous solution by Gili et al. [44]. The PNZ has rough and corrugated surfaces, high surface area, and contains natural cations, i.e., Fe, which already filled in the zeolite active sites. Hence, it increases the ability to exchange cations, rendering the adsorption capacity of 3.8 mg g⁻¹.

Abd El-Azim and El-Adzim [71] have investigated the clinoptilolite zeolite for Cd(II), Fe(III), and Ni(II) ion removal without pretreating the zeolite. The result exhibited the effectiveness of clinoptilolite, which rendered the adsorption capacity 10.000, 9.971, and 9.901 mg g⁻¹ for Cd(II), Fe(III), and Ni(II), respectively. From these results, it is shown that each metal has

unique properties which affect the adsorption capacity of zeolite. Moreover, clinoptilolite has higher selectivity to Cd compared to other heavy metals. Liu et al. [72] also used clinoptilolite type zeolite for heavy metals removal, i.e., Pb(II), Zn(II), Cd(II), and Cu(II), as depicted in Fig. 2(a). The desorption capacity of Na(I) does not show the distinct difference between Zn-, Cd-, and Cu-Na exchange. In contrast, the Pb-Na exchange exhibits a much larger desorption capacity (Fig. 2(b)). It is because the quantum fluctuation of Pb(II) renders the strong polarization occurs. Therefore, Pb(II) can exchange more Na(I).

Belova [50] reported a mix of mordenite and clinoptilolite-type Russian zeolite to adsorb Cu(II), Ni(II), Co(II), and Fe(II). The adsorption capacity of Russian zeolite is increasing as follows Cu(II) > Fe(II) > Ni(II) > Co(II). Jorfi et al. [51] used clinoptilolite type Iranian zeolite for the adsorption of Cr(VI) and rendering the adsorption capacity of 2.69 mg g⁻¹. Mihajlović et al. [54] used clinoptilolite to determine its adsorption capacity for Pb(II), Cd(II), and Zn(II) ions. The adsorption capacity is increasing as follows Pb(II) > Zn(II) > Cd(II). Obaid et al. [49] investigated three types of Indian zeolite, which are Mordenite, Stilbite, and Heulandite, to determine the adsorption capacity for Co(II), Zn(II), and Mn(II). The adsorption capacity achieved is Co(II) > Zn(II) > Mn(II). Moreover, mordenite exhibited higher extraction efficiency than Stilbite and Heulandite. It is noted that the extraction of heavy metal is affected by the ion exchange and adsorption processes [49].

Adsorption Capacity of Modified Natural Zeolite

Kragović et al. [65] reported the alginate composite to modify clinoptilolite type zeolite for the adsorption of Pb(II). The adsorption capacity increased from 66 to 102 mg g⁻¹. Hence it can conclude that the increase in sorption intake because of the encapsulation is proven to change the CEC of each cation while did not significantly impact the total CEC of the zeolite. The CEC decreased from 0.23 to 0.15 for Na(I), 0.15 to 0.11 for K(I), and 0.22 to 0.1 for Mg(II). Meanwhile, CEC for Ca(II) is increased from 0.85 to 1.12, making the ion exchange of the zeolite more preferable because of the same oxidation number of the heavy metals and the exchangeable cation. Shirzadi and Nezamzadeh-Ejhih [66] investigated an Iranian clinoptilolite zeolite modified by two times using HDTMABr (hexadecyltrimethylammonium bromide) and dithizone (DT) to improve its removal ability of the metal ions by adding a complexation process on top of exchanging cation process. The modified zeolite shows higher removal efficiencies for Hg(II) and Pb(II) due to another phenomenon process besides ion exchange, i.e., the process of removing the cations, regarding the complexation process of the cations with free electron pairs of sulfur or nitrogen atoms in DT. Yulizar et al. [61] have modified natural zeolite with chitosan to improve its adsorption capacity by adding a functionalized group. The modified zeolite shows a material in nano-size scale rendering better adsorption ability with an adsorption percentage of 99.68%. Retnaningrum and Wilopo [67]

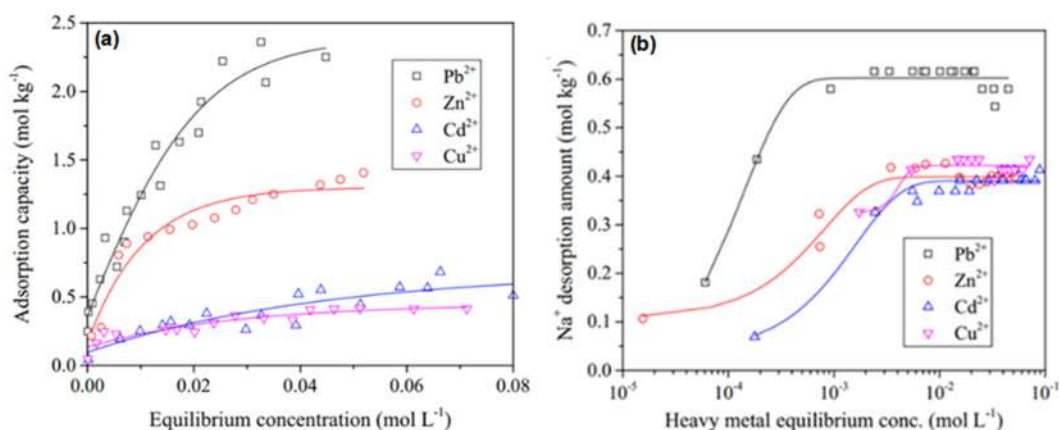


Fig 2. (a) The adsorption isotherms of heavy metals on clinoptilolite at 298 K. (b) The desorption amount of Na⁺ from clinoptilolite. Adapted with permission from Ref [72], Copyright 2019 Springer

used natural zeolite modified as bacterial support materials to reduce sulfate and manganese from synthetic wastewater. The study reported the efficiency of manganese and sulfate removal was up to 23% and 15.4%, respectively.

Triton X-100 modified clinoptilolite type zeolite was investigated by Mirbaloochzahi et al. [60] for the adsorption of several ions, such as Pb(II), Cu(II), Cd(II), Ni(II), Zn(II), and Fe(II) and rendering the adsorption capacity of 91.34; 85.71; 78.2; 76.18; 67.41 and 63.45 mg g⁻¹, respectively. It showed that the adsorption capacity using Triton X-100 to modify clinoptilolite increased approximately 60–90% more than the unmodified clinoptilolite. Nasiri-Ardali and Nezamzadeh-Ejhih [70] pointed out the glycine-modified zeolite to adsorption of Pb(II). The zeolite is divided into two powders of nano-sized particles and micro-sized particles named NCP and MCP and then modified by glycine. The glycine is attached to the surface of the zeolite through an ion exchange process with cation from zeolite. Then when the modified NCP and MCP are mixed with heavy metal, ion exchange occurs. The glycine located on the surface of the zeolite is making a complexation process for the heavy metal ion. The complexation process can be done because there is an amino and carboxylic group in the glycine. Hence, the adsorption capacity of MCP and NCP increased from 87.10 to 123.20 mg g⁻¹ and 96.71 to 183.15 mg g⁻¹.

Nguyen et al. [69] described the sonication and NaCl solution to modify Slovakian clinoptilolite type zeolite to improve its adsorption capacity for Cd(II) ion removal, and this process is called a sonochemical modification. The processes are proven to enhance the natural zeolite's CEC and SSA. Additionally, the sonochemical process significantly reduces the zeolite's particle size and size distribution. Hence, the adsorption capacity of modified zeolite increases from 17.63 to 21.47 mg g⁻¹. Velazquez-Peña et al. [68] used metal ions, Zr(II), Fe(II), and a combination of both, resulting in a new species of zirconium-iron (FeZr) to modify three types of Mexican zeolite for As(V) adsorption. Those metals ion is used for performing complex with arsenic species. The zirconium-modified zeolite is more efficient

than iron-modified zeolite due to the higher affinity of arsenic for zirconium than iron. The adsorption capacity of modified zeolite of Fe(II), Zr(II), and Zr-Fe for clinoptilolite is 0.025, 0.069, and 0.069, respectively. For mordenite, the adsorption capacities are 0.029, 0.079, and 0.072. And for chabazite, the adsorption capacities are 0.05, 0.089, and 0.121 mg g⁻¹.

Yousefi et al. [59] have modified clinoptilolite type zeolite with cobalt Hexacyanoferrate (CoHCF) to find a cheaper adsorbent than activated carbon for the adsorption of Cd(II) ion. CoHCF is a complexing agent, allowing the zeolite to remove metal ions from the solution aside from ion exchange. The modification turned out victorious with an adsorption capacity of 51 mg g⁻¹, twice the amount of adsorption capacity from the unmodified zeolite. Puspitasari et al. [20] used amidoxime to functionalize Indonesian clinoptilolite type zeolite to increase adsorption capacity toward Pb(II) ion. The adsorption capacity of the zeolite is increased from 52 to 72 mg g⁻¹ compared to the initial zeolite. It is due to the chelating functionality of amidoxime groups that adds another prowess to the zeolite, other than ion exchange, to remove the Pb(II) ion. The kinetic study showed that the adsorption rate onto the amidoxime-functionalized zeolite was faster than the initial zeolite. Notably, the adsorption process followed the Langmuir method, and the adsorption kinetics is based on a pseudo-second-order model. Its added prowess proved successful because the zeolite's adsorption capacity was increased.

HDTMA is one of the most used and effective surfactants to modify zeolite to improve its adsorption capacities toward anion metal ions [62-64]. Several studies show that the HDTMA is attached to the surface of zeolite, therefore decreasing the SSA of zeolite. Despite having a decrease in SSA, it appears that HDTMA brings a positive charge into the surface of zeolite, hence making it can adsorb anion metal [62-64]. Dimas Rivera et al. [63] used clinoptilolite type zeolite to be modified by the HDTMA to adsorb Cr(VI) anion (Fig. 3). Clinoptilolite and clinoptilolite modified exhibited an isotherm type IV and flake-shape particles morphology (Fig. 3(a) and 3(b)). The adsorption

isotherms reveal multilayer adsorption regarding a better adjustment to the Freundlich model for clinoptilolite modified ($R^2 = 0.993$) (Fig 3(c)). The kinetic studies show a better fitting to pseudo-second-order and increased adsorption capacity up to 9.83 mg g^{-1} (Fig. 3(d)). HDTMA created the positive exchange sites to the zeolite surface, and chromate anions occur mainly by interacting with the HDTMA.

Zekavat et al. [62] used clinoptilolite type zeolite to be modified by the HDTMA to adsorb Cu(II) cation and Cr(VI) anion. The studies reveal that the zeta potential of zeolite surface changes from negative to positive charge, making adsorption on anionic metal easily occur. However, the modified zeolite is still deemed capable of adsorption Cu(II) cation with an adsorption capacity of

16.98 mg g^{-1} . Thus the sorption of Cu(II) cation on the zeolite improves the intake of Cr(VI) anion because it increases the positive sites on the zeolite. The adsorption capacity for Cr(VI) anion is 27.36 mg g^{-1} . Tran et al. [64] reported HDTMA to improve zeolite capability for adsorbing both anion and cation from solution by making a bilayer on the outside surface area, charge in its inner pore. The modified zeolite was then thus making it have a positive charge while having a negative test for adsorption of Pb(II), Cu(II), and Ni(II) cation, as well as Cr(VI) anion. Adsorption capacities of cationic metal are decreased when comparing the HDTMA-modified zeolite to non-modified zeolite. The adsorption capacities for Pb(II) cation are reduced from 159 to 69, 60.1 to 25.6 mg g^{-1} for Cu(II) cation, and 44 to

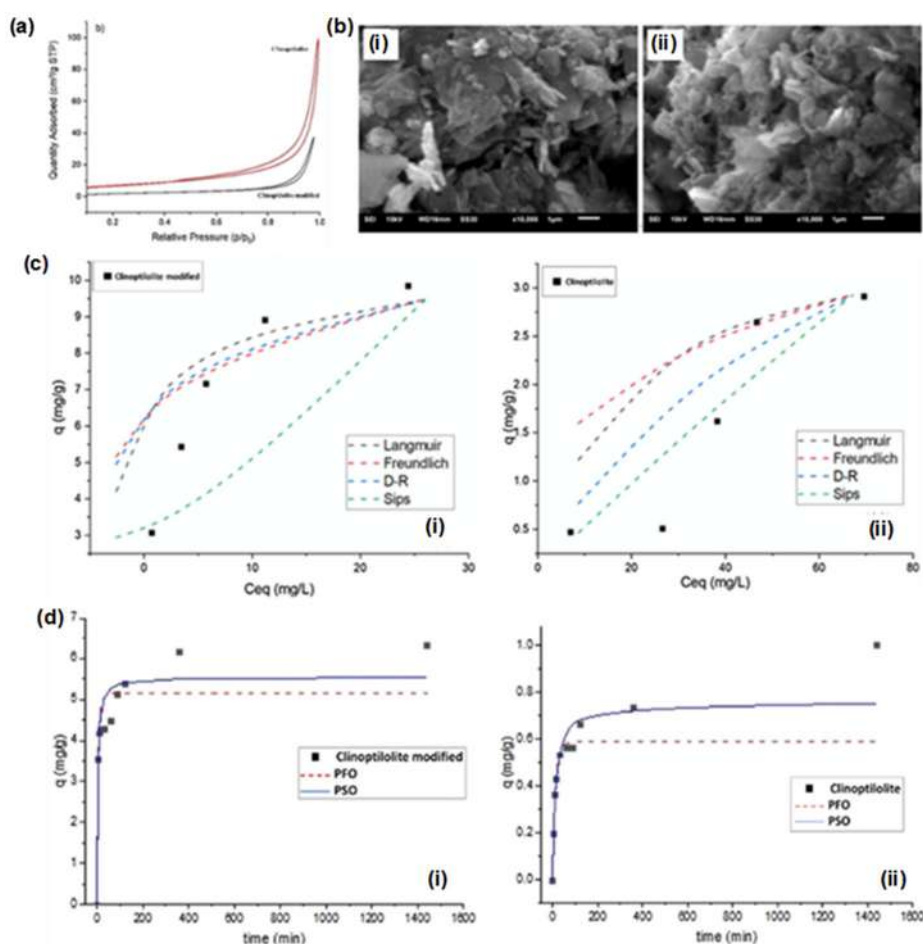


Fig 3. (a). Nitrogen adsorption-desorption isotherms of clinoptilolite and HDTMA-modified clinoptilolite. (b). SEM images of (i) clinoptilolite and (ii) clinoptilolite modified. (c). Adsorption model for (i) clinoptilolite modified and (ii) clinoptilolite. (d). Pseudo-first order and pseudo-second order for (i) clinoptilolite modified and (ii) clinoptilolite. Adapted with permission from ref [63], Copyright 2021 Elsevier

22.6 mg g⁻¹ for Ni(II) cation. However, the adsorption capacity of the Cr(VI) anion is increased from 22.9 to 40.5 mg g⁻¹. This result agrees with Zekavat et al. [62], in which the surface of the zeolite changes from a negative charge to a positive charge. It makes the zeolite have a repulsion force for the cation and an attraction force for the anion, resulting in better anion adsorption capacity than cation adsorption capacity.

■ ADSORPTION KINETIC, THERMODYNAMIC, AND ISOTHERM

As stated before, the determination of adsorption kinetic, thermodynamic, and isotherm is used for modeling the adsorption processes of the zeolite. Adsorption isotherm is used to determine the interactions between adsorbate and adsorbent, as well as adsorbent characteristics [73]. Some mathematical models can determine the adsorption isotherms, viz Langmuir and Freundlich and also Temkin and Dubin. The derivation of the Langmuir isotherms can be seen in several equations below. Suppose the adsorption process takes place according to Eq. (1) below,



where [A] is the adsorbate, [S] is a nonbonding surface (1-θ), while [AS] is a bonding surface (θ),

$$V_a = K_a [A] (1 - \theta) \quad (2)$$

$$V_d = kd\theta \quad (3)$$

V_a is the rate of adsorption, and V_d is the desorption rate. Therefore during equilibrium, we can write Eqs. (4-11) as follow:

$$V_a = V_d \quad (4)$$

$$K_a [A] (1 - \theta) = kd\theta \quad (5)$$

$$\frac{\theta}{(1 - \theta)} = \frac{K_a}{K_d} [A] \quad (6)$$

$$\theta = K [A] (1 - \theta) \quad (7)$$

$$\theta = K [A] - K [A] \theta \quad (8)$$

$$\theta + K [A] \theta = K [A] \quad (9)$$

$$\theta (1 + K [A]) = K [A] \quad (10)$$

$$\theta = \frac{K [A]}{1 + K [A]} \quad (11)$$

Finally, Eq. (11) could be rewritten into Eq. (12) for the adsorption within aqueous solution as follows.

$$Q_e = \frac{Q_{\max} K_L C_e}{1 + K_L C_e} \quad (12)$$

whereas C_e is the concentration of adsorbate at equilibrium, Q_e is the amount of adsorbate per unit of adsorbent mass in equilibrium, Q_{max} is the maximum saturated monolayer adsorption capacity of the adsorbent, and K_L is the Langmuir constant for the affinity between adsorbent and adsorbate. The equation for Freundlich is given in Eq. (13) as follows.

$$\log Q_e = \log K_f + \frac{1}{n} C_e \quad (13)$$

K_f is the Freundlich isotherm constant, and n values vary from zero to one to show the adsorption's surface heterogeneity or intensity. Nevertheless, if the n values are unlimited, the Freundlich equation is the same as the Langmuir equation. The Langmuir model is to determine the adsorption characteristic of the sorbent surface as a monolayer. Therefore, the adsorption processes are happening on the surface at each zeolite pore through ion exchange. While the Freundlich model is used to determine the adsorption characteristic of the sorbent surface is heterogeneous. Therefore, the adsorption processes were more than ion exchange, like complexation and sorption at the bilayer of the surface of the zeolite [53,55,64,73-74].

Thermodynamic studies are used to predict the adsorption mechanisms from physical and chemical aspects [75]. The Gibbs energy change (ΔG°) can be calculated by using Eq. (14):

$$\Delta G^\circ = -RT \ln K_C \quad (14)$$

Meanwhile, the thermodynamic parameters can be checked by using the equation that describes the relationship of ΔG°, the enthalpy change (ΔH°), and the entropy change (ΔS°) can be written in Eq. (15) as follows:

$$\Delta G^\circ = \Delta H^\circ - T \Delta S \quad (15)$$

From the equation above, it can be substituted by Van't Hoff equation, and we can calculate the ΔH° and ΔS° from the slope and intercept in the plot of ln K_C versus 1/T using Eq. (16) as follows:

$$\ln K_C = \frac{-\Delta H^\circ}{R} \times \frac{1}{T} + \frac{\Delta S^\circ}{R} \quad (16)$$

R is the universal gas constant (8.3144 J mol⁻¹.K⁻¹), and T is the temperature (K).

Adsorption kinetics is used to determine the diffusion of adsorbate in the adsorbent pores and to determine the adsorption uptake at a particular concentration or pressure within a specific time [73]. The two most used for adsorption to determine the adsorption kinetic are pseudo-first-order and pseudo-second-order. The equations for pseudo-first-order and pseudo-second-order are expressed in Eqs. (17) and (18) as follows:

$$\frac{dq_t}{dt} = k_{ad} (Q_e - Q_t) \quad (17)$$

$$\frac{dq_t}{dt} = k_{ad} (Q_e - Q_t)^2 \quad (18)$$

whereas K_{ad} is the adsorption kinetics constant, Q_e and Q_t are adsorption capacities at equilibrium and at a particular time. The pseudo-first-order indicates that the rate change of adsorbate adsorption over time is directly proportional to the difference in the saturation concentration and the amount of solid adsorption with time or is called physisorption, while the pseudo-second-order indicates the rate of amount adsorbate that has been adsorbed by the adsorbent or commonly called as chemisorption [19,48].

Adsorption Kinetic, Thermodynamic, and Isotherm of Pristine Zeolite

For the adsorption kinetics, Gili et al. [44] used intraparticle diffusion, pseudo-first-order, and pseudo-second-order to describe the adsorption kinetics of Ni(II) ion adsorption using mixed zeolite from the Philippines. As seen in Fig. 4, all three models had linear regression (R^2) of the curve < 0.90 . However, the pseudo-second-order has the biggest R^2 at 0.89; thus, the adsorption kinetics followed the pseudo-second-order equation. This work describes the linear function of the kinetic rule to determine the adsorption kinetics.

Zanin et al. [48] pointed out the non-linear pseudo-first-order and pseudo-second-order rules to determine the adsorption kinetics of the three metal ions. The non-linear form for the adsorption kinetics was chosen because it is fitted better than the linear form. For the pseudo-second-order, all metal ions adsorption shows $R^2 > 0.90$, while for the pseudo-first-order, the R^2 for Fe(III) ion is 0.85 while both Cu(II) and Cr(III) ion $R^2 > 0.95$. Therefore, for Fe(III) ion adsorption,

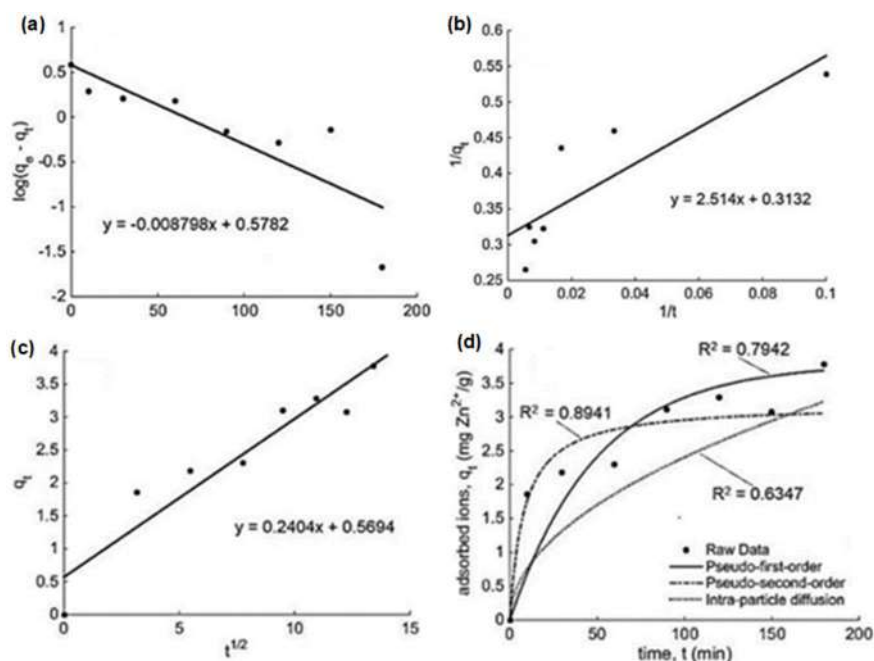


Fig 4. Best fit lines for the linearized kinetic data according to (a) pseudo-first-order, (b) pseudo-second-order and (c) intra-particle diffusion kinetic models; and (d) the resulting plots of each model in comparison to the kinetic data. Adapted with permission from Ref [44], Copyright 2017 IOP Publishing

the adsorption kinetics was best described in pseudo-second-order, while for Cu(II) and Cr(III) ion adsorption, the adsorption kinetics was best described in pseudo-first-order. Hence, it can be concluded that pseudo-second-order dominates the kinetic rules for pseudo-second-order, and chemisorption is more dominant in the pristine zeolite. It shows that the interaction between sorbent and sorbate in pristine zeolite indicates ion exchange between metal ions and substitute metal in the sorbent.

Zanin et al. [48] used Freundlich and Langmuir model for all three metals' adsorption. For Cu(II) ion adsorption for the determination of the adsorption isotherm. It is worth noting that the Langmuir model was not possible because the error is significant. Hence it makes the Freundlich model the best fitted for copper ion adsorption. The two models provide similar R^2 for chromium adsorption, 0.96 for Langmuir and 0.93 for Freundlich.

Nevertheless, because Langmuir R^2 is higher than Freundlich, the Cr(III) ion adsorption isotherm, best followed the Langmuir model. Lastly, for Fe(III) ion, the R^2 was also similar between the two models, 0.98 for Freundlich and 0.95 for Langmuir. For the same reason as Cr(III) ion adsorption, the Freundlich model was chosen for adsorption isotherm of iron(III) ion adsorption because R^2 is higher than the Langmuir. In agreement with Zanin et al. [48], Gili et al. [44] used both Langmuir and Freundlich models. The R^2 value from the Langmuir model was higher (0.99) than the R^2 value of Freundlich (0.97). Therefore, using Philippine zeolites, the Langmuir model was chosen to represent the adsorption isotherm of nickel(II) ion adsorption.

The adsorption of Pb(II) ion using Kazakhstani zeolite shows that the Freundlich model gives an $R^2 < 0.900$ while the Langmuir model gives an R^2 value of 0.999 [52]. Therefore, the Langmuir model was the most fitted for its adsorption isotherm. The adsorption isotherm of Cd(II) ion adsorption using phillipsite type zeolite shows that using the Freundlich model, the R^2 achieved was 0.80, while for the Langmuir model, the R^2 achieved was 0.94 [53]. The data shows that the Langmuir model was best fitted for the zeolite adsorption isotherm.

Abd El-Azim and Mourad [71] used both Langmuir and Freundlich models to describe the adsorption isotherm for its three metal ion adsorption. It is shown that the Langmuir model has $R^2 > 0.99$ for all of its metal ion adsorptions. Freundlich model also give $R^2 > 0.99$ for Fe(II) and Ni(II) ion. For Cd(II) ion, the R^2 value is 0.69, which indicates that for Cd(II) ion adsorption, only the Langmuir model was best fitted for its adsorption isotherm, whereas for Fe(II) and Ni(II) ion, both Langmuir and Freundlich model was best described the adsorption isotherm.

Kovacova and Pla [55] reported both Freundlich and Langmuir models to find its adsorption isotherm for its Ni(II) ion adsorption. Langmuir and Freundlich's model gives $R^2 < 0.90$, which is relatively low. But, R^2 for Freundlich is higher (0.83) than the Langmuir (0.73). Therefore, in this work, the Freundlich model is better to describe the adsorption isotherm than the Langmuir model. The determination of the adsorption isotherm of Cu(II), Co(II), Ni(II), and Fe(II) ion adsorption was conducted using Langmuir and Freundlich model [50]. All four metal ions had $R^2 > 0.95$ using the Langmuir model, while the Freundlich model only gives Fe(II) and Ni(II) ions that had $R^2 > 0.95$ and $R^2 < 0.90$ for Cu(II) and Co(II). Thus, the Langmuir model was chosen for all four metal adsorption isotherms. Mihajlović et al. [54] used three modelings, Freundlich, Langmuir, and Dubinin-Radushkevich, to determine the adsorption isotherm for Pb(II), Zn(II), and Cd(II) ion adsorption. The result exhibited the Langmuir model as an adsorption isotherm for all three metal ion adsorption because, between the three models, Langmuir had the highest R^2 or closest to 1.

While using two or more models to determine the adsorption isotherm is common, Budianta et al. [46] and Liu et al. [72] only used the Langmuir model to determine the adsorption isotherm. Budianta et al. [46] use the Langmuir model to determine the adsorption isotherm of the two zeolite samples from B and T for Pb(II) and Cd(II) metal ions. The result shows that using the Langmuir model, the R^2 for all adsorption batches is > 0.800 . Therefore, the Langmuir model is fitted for explaining the adsorption isotherm. The difference in

the Q_{\max} of both zeolites for two cations can be explained because B samples have higher CEC than T samples. Hence making the B samples have higher Q_{\max} than the T samples. Liu et al. [72] used the Langmuir model to describe the adsorption isotherm of Pb(II), Zn(II), Cd(II), and Cu(II). All data show $R^2 > 0.90$. Hence the Langmuir model effectively depicts the adsorption isotherm.

Adsorption Kinetic, Thermodynamic, and Isotherm of Modified Natural Zeolite

The pseudo-second-order and the Langmuir model are dominant for pristine zeolite because the ion exchange situation in the pristine zeolite is mostly occurring. However, in modified natural zeolite, the kinetic and isotherm will vary with the addition of a modifier. Kragović et al. [65] used Freundlich and Langmuir model to describe the adsorption isotherm of zeolite-modified alginate for Pb(II) ion adsorption. From the model, Freundlich has a higher R^2 (0.96) than the R^2 (0.85) of the Langmuir model. Therefore, the adsorption isotherm was determined by Freundlich. It shows that the modifier successfully modifies the zeolite, making the adsorption processes not limited to monolayer, which is correlated with the Langmuir model and has a complex mechanism and heterogeneous surface, which is correlated with the Freundlich model.

Mirbaloochzahi et al. [60] reported the Langmuir and Freundlich model to find the best fit for the adsorption isotherm of surfactant-modified zeolite for the adsorption of Pb(II), Cu(II), Cd(II), Ni(II), and Zn(II).

The R^2 value of both models was more than 0.98, thus making the adsorption isotherm fit both Langmuir and Freundlich models. It explained that some of the metal ions that got adsorbed by the surfactant and complexation method, not only in the surface of the zeolite, thus making the modification successful.

Nasiri-Ardali and Nezamzadeh-Ejhieh [70] investigated six different models to determine the adsorption isotherm, which are Dubinin-Radushkevich, Langmuir, Freundlich, Temkin, Redlich-Peterson and Toth model. Among these six models, Langmuir is the best fit for the adsorption isotherm of Pb(II) ion adsorption, with an R^2 value of 0.99, as seen in Fig. 5. Adsorption kinetics were studied using both the pseudo-first order and pseudo-second order. With an R^2 value of 0.99, the adsorption kinetics follows pseudo-second-order rules. In the adsorption thermodynamics, ΔG of the adsorption is negative, which means the reaction is performed spontaneously. ΔH of the adsorption is also negative, meaning the adsorption process is exothermic.

Nguyen et al. [69] reported three adsorption kinetics models to determine the adsorption's fittest: pseudo-first-order, pseudo-second-order, and Elovich. According to the R^2 value, the adsorption kinetics is best fitted for the pseudo-second-order rule. For adsorption isotherm, Langmuir, Freundlich, and Temkin models were used. The three models had an R^2 value higher than 0.9, making the three models can be fit to the adsorption isotherm. However, the Langmuir model was identical to the experimental. Therefore, the adsorption isotherm

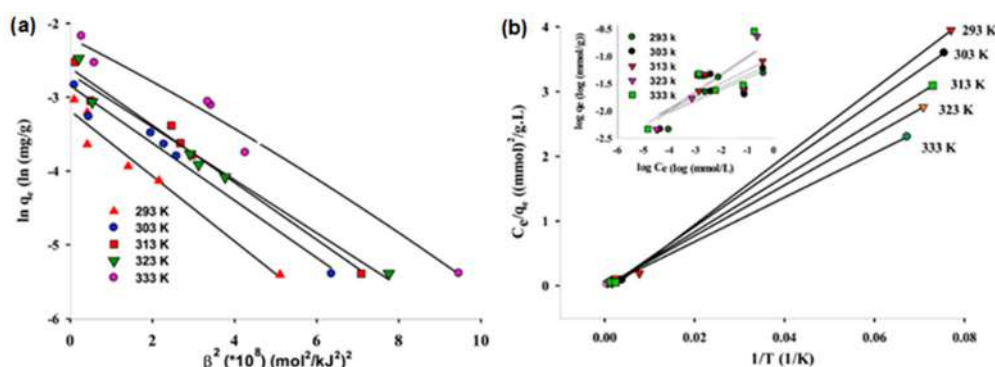


Fig 5. (a) Dubinin-Radushkevich and (b) Langmuir (Freundlich, inset) isotherms for Pb (II) removal by NCP-Gly, (CPb (II): 80, 100, 500, 800, 1000, 2000, 8000, g L⁻¹, sorbent dosage: 0.15 g L⁻¹, agitation time: 4 h, pH 4). Adapted with permission from Ref [70], Copyright 2020 Elsevier

is followed the Langmuir model. The adsorption thermodynamics show that ΔG is negative while ΔH and ΔS are positive. It showed that the adsorption is spontaneous (from ΔG), endothermic (from ΔH), and increased randomness at the solid/solution interface.

Velazquez-Peña et al. [68] employed Langmuir, Freundlich, and Dubinin-Radushkevich to determine the adsorption isotherm. Based on the R^2 value from the three models, Freundlich had the highest R^2 value for each type of modified zeolite. The adsorption kinetics was studied using pseudo-first order, pseudo-second order, Elovich, and intraparticle diffusion. Both pseudo-second-order and intraparticle diffusion are best fitted for the adsorption kinetics. The pseudo-second-order explained the chemisorption mechanism of ion exchange between As(V) ion and FeZr⁻ modified zeolite. Meanwhile, intraparticle diffusion has explained the adsorption of As(V) ions through the modified zeolite's pores, channels, and cages. Yousefi et al. [59] also used Langmuir, Freundlich, Temkin, and Dubinin-Radushkevich to determine the adsorption isotherm. From the R^2 value, Langmuir is the highest, making it the most fitted for cadmium ion adsorption using modified zeolite. The pseudo-second-order and pseudo-first-order were conducted to find the adsorption kinetics. With an R^2 value of 0.91, the adsorption kinetics follows the pseudo-second-order rule.

Puspitasari et al. [20] reported Langmuir, Freundlich, and Temkin to determine the adsorption isotherm. Interestingly, all three of the model give $R^2 > 0.90$, with Langmuir having the highest R^2 with a value of 0.99. Therefore, the Langmuir model was chosen to represent the adsorption isotherm of the modified zeolite. The pseudo-first-order, pseudo-second-order, and intra-particle diffusion are used for adsorption kinetics. Among the three rules, the pseudo-second-order has the highest R^2 with a value of 0.99. Hence, making the modified zeolite follow the pseudo-second-order rule.

Dimas Rivera et al. [63] used pseudo-first-order and pseudo-second-order to determine the adsorption kinetics for the Cr(VI) anion with the HDTMA modifier. R^2 value suggests that the adsorption kinetics followed the pseudo-second-order rule. Langmuir, Freundlich, Sips, and

Dubinin-Radushkevich model was used for adsorption isotherm. Between these four models, the R^2 value determined that the Freundlich model was best fitted for the adsorption kinetics of modified clinoptilolite. Zekavat et al. [62] determined the adsorption kinetics of the adsorption of Cu(II) and Cr(VI) ions using pseudo-first order and pseudo-second order rules. R^2 value tells that the adsorption kinetics follow pseudo-second-order for both metal adsorptions. The adsorption isotherm was determined using Langmuir, Freundlich, and Dubinin-Radushkevich. According to the R^2 value, the highest was the Freundlich model for both metal adsorptions. Tran et al. [64] determined the adsorption isotherm using Langmuir and Freundlich model for each metal ion adsorption. The Langmuir model was best fitted for Pb(II) and Cr(VI) ion adsorption. In comparison, the Freundlich models were best fitted for the adsorption of Cu(II) and Ni(II) ions.

■ SUMMARY AND PERSPECTIVES

Due to their physicochemical properties and abundance reserve, the pristine and modified natural zeolites have been widely used as an adsorbent for heavy metals. Clinoptilolite is the most used pristine zeolite by the researcher because it is abundant in nature, easy to find, and has good adsorption capabilities. Furthermore, the structure of clinoptilolite makes it easier to adsorb metal ions than any other type. The three prominent factors that determine the adsorption capabilities of the pristine and modified natural zeolite are the specific surface area (SSA), cation exchange capacity (CEC), and the pre-treatment before use. If one of the factors has been improved, then prosperity will increase. Hence, if all factors are taken into account, then the capabilities of the zeolite will improve multiple times better than if only one factor has been done or improved.

Moreover, for modified natural zeolite, the modifier that is generally used often reduces the SSA of the pristine zeolite. Nevertheless, the adsorption capacity increases because the modifier added another chemical reaction to the zeolite adsorption process. The adsorption kinetics for most of the zeolite adsorption

Table 4. Summary of adsorption condition

Metal Ion	Pb(II)	Zn(II)	Cd(II)	Ni(II)	Cu(II)	Fe(II)	Cr(VI)*
Concentration range (mg L ⁻¹)	331.20–33120.00	189.40–18940.00	100.00–400.00	50.00–200.00	50.00–200.00	1.00–100.00	100.00–1000.00
Adsorption capacity (mg g ⁻¹)	781.87	232.96	384.61	76.18	85.71	9.97	40.50
Mass of zeolite used (g)	1.00	1.00	10.00	1.00	1.00	0.25–4.00	0.20
pH	6	6	-	2–8	2–8	2–8	5
Contact time (h)	48.00	48.00	5.50	0.30–2.00	0.30–2.00	0.08–3.00	48.00
Zeolite type	Clinoptilolite	Clinoptilolite	Mix Clinoptilolite and mordenite	Clinoptilolite	Clinoptilolite	Clinoptilolite	Clinoptilolite
Modifier	-	-	-	Triton x-100	Triton x-100	-	HDTMA
References	[14]	[14]	[46]	[60]	[60]	[71]	[64]

*in Cr₂O₇²⁻

processes, pristine and modified alike, follow the pseudo-second-order rule. The Langmuir model dominates isotherm for pristine zeolite. For modified natural zeolite, both Langmuir and Freundlich models are frequently used. The Langmuir model explains that the adsorption happens on the surface of the zeolite pore or monolayer. The Freundlich model explained that the adsorption happens not only on the surface of the zeolite but also on the surface of the modifier attached to the zeolite or bilayer. The adsorption processes of pristine and modified natural zeolite are spontaneous. Some are endothermic, while others are exothermic. Table 4 lists the adsorption capacity of metal ions and their tested condition.

Adsorption using zeolite proved to be successful and effective. Nevertheless, the proficiency of adsorbing metal anions is relatively low. The drawback of structure zeolite makes it hard to attract and adsorb the anionic metal phase. The cationic polymer, other than HDTMA with a high affinity toward negative ions, can be a solution to increase the proficiency of the zeolite to adsorb anionic metal. Encapsulating the zeolite surface using inert metal can improve the zeolite catalyst proficiency. It also has made it possible to increase zeolite selectivity between metal ions using the encapsulating method. The metal needed for encapsulating the zeolite does not have to be inert. The more its affinity toward electrons, the more it can attract the anionic metal in an aqueous solution.

Ultimately, several steps should be noted to obtain the optimal zeolite for adsorption processes. First, zeolite must have been through some pre-treatment before use, e.g., grinding, sieving, and washing using deionized or demineralized water. Second, increase the CEC and SSA by dealumination processes using an acid solution, exposure to excess heat using calcination, or washing using alkaline or alkaline earth metal solution. Third, the use of a modifier that added another chemical reaction that can bind metal ions to the zeolite structure other than ion exchange. In addition, it is imperative to acquire the equipose from economic and environmental points of view to bring a majestic impact not only for the human being but also for all living organisms.

■ ACKNOWLEDGMENTS

This work is supported by Hibah Riset Unggulan Institut Teknologi Bandung (ITB) 2023.

■ AUTHOR CONTRIBUTIONS

Khairul Ihsan Solihin and St Mardiana wrote and revised the manuscript, Handajaya Rusli supervised and revised the manuscript, and Grandprix Thomryes Marth Kadja conceived the idea, supervised, and revised the manuscript. All authors agreed to the final version of this manuscript.

■ REFERENCES

- [1] Gao, Y., Feng, J., Wang, C., and Zhu, L., 2017, Modeling interactions and toxicity of Cu-Zn mixtures to zebrafish larvae, *Ecotoxicol. Environ. Saf.*, 138, 146–153.
- [2] Darmayanti, L., Kadja, G.T.M., Notodarmojo, S., Damanhuri, E., and Mukti, R.R., 2019, Structural alteration within fly ash-based geopolymers governing the adsorption of Cu²⁺ from aqueous environment: Effect of alkali activation, *J. Hazard. Mater.*, 377, 305–314.
- [3] Sundari, D., Hananto, M., and Suharjo, S., 2016, Kandungan logam berat dalam bahan pangan di kawasan industri kilang minyak, Dumai, *Buletin Penelitian Sistem Kesehatan*, 19 (1), 55–61.
- [4] Erika, D., Nurdini, N., Mulyani, I., and Kadja, G.T.M., 2023, Amine-functionalized ZSM-5-supported gold nanoparticles as a highly efficient catalyst for the reduction of *p*-nitrophenol, *Inorg. Chem. Commun.*, 147, 110253.
- [5] WHO, 2017, *Guidelines for Drinking-water Quality, Fourth Edition Incorporating the First Addendum*, World Health Organization, Geneva.
- [6] Wan Ngah, W.S., Teong, L.C., Toh, R.H., and Hanafiah, M.A.K.M., 2012, Utilization of chitosan-zeolite composite in the removal of Cu(II) from aqueous solution: Adsorption, desorption and fixed bed column studies, *Chem. Eng. J.*, 209, 46–53.
- [7] Gupta, R.K., 2018, A review of copper poisoning in animals: Sheep, goat and cattle, *Int. J. Vet. Sci. Anim. Husb.*, 3 (5), 1–4.
- [8] Hoseinifard, S.M., Omidzahir, S., Hoseini, S.M., and Beikae, H., 2018, Protective effect of garlic (*Allium sativum*) against zinc poisoning in the testicular tissue of goldfish (*Carassius auratus*), *Comp. Clin. Pathol.*, 27 (2), 357–361.
- [9] Sane, M.R., Malukani, K., Kulkarni, R., and Varun, A., 2018, Fatal iron toxicity in an adult: Clinical profile and review, *Indian J. Crit. Care Med.*, 22 (11), 801–803.
- [10] Shen, X., Chi, Y., and Xiong, K., 2019, The effect of heavy metal contamination on humans and animals in the vicinity of a zinc smelting facility, *PLoS One*, 14 (10), e0207423.
- [11] Li, Y., Xu, Z., Liu, S., Zhang, J., and Yang, X., 2017, Molecular simulation of reverse osmosis for heavy metal ions using functionalized nanoporous graphenes, *Comput. Mater. Sci.*, 139, 65–74.
- [12] Bashir, A., Malik, L.A., Ahad, S., Manzoor, T., Bhat, M.A., Dar, G.N., and Pandith, A.H., 2019, Removal of heavy metal ions from aqueous system by ion-exchange and biosorption methods, *Environ. Chem. Lett.*, 17 (2), 729–754.
- [13] Forsido, T., McCrindle, R., Maree, J., and Mpenyana-Monyatsi, L., 2019, Neutralisation of acid effluent from steel manufacturing industry and removal of metals using an integrated electric arc furnace dust slag/lime process, *SN Appl. Sci.*, 1 (12), 1605.
- [14] Xu, S., Liu, Y., Yu, Y., Zhang, X., Zhang, J., and Li, Y., 2020, PAN/PVDF chelating membrane for simultaneous removal of heavy metal and organic pollutants from mimic industrial wastewater, *Sep. Purif. Technol.*, 235, 116185.
- [15] Masindi, V., and Muedi, K.L., 2018, “Environmental Contamination by Heavy Metals” in *Heavy Metals*, Eds. Saleh, H.M., and Aglan, R.F., IntechOpen, Rijeka, Croatia, 137–144.
- [16] Igiri, B.E., Okoduwa, S.I.R., Idoko, G.O., Akabuogu, E.P., Adeyi, A.O., and Ejiogu, IK, 2018, Toxicity and bioremediation of heavy metals contaminated ecosystem from tannery wastewater: A review, *J. Toxicol.*, 2018, 2568038.
- [17] Naushad, M., Ahamad, T., Al-Maswari, B.M., Abdullah Alqadami, A., and Alshehri, S.M., 2017, Nickel ferrite bearing nitrogen-doped mesoporous carbon as efficient adsorbent for the removal of highly toxic metal ion from aqueous medium, *Chem. Eng. J.*, 330, 1351–1360.
- [18] Otunola, B.O., and Ololade, O.O., 2020, A review on the application of clay minerals as heavy metal adsorbents for remediation purposes, *Environ. Technol. Innovation*, 18, 100692.
- [19] Yuna, Z., 2016, Review of the natural, modified, and

- synthetic zeolites for heavy metals removal from wastewater, *Environ. Eng. Sci.*, 33 (7), 443–454.
- [20] Puspitasari, T., Kadja, G.T.M., Radiman, C.L., Darwis, D., and Mukti, R.R., 2018, Two-step preparation of amidoxime-functionalized natural zeolites hybrids for the removal of Pb²⁺ ions in aqueous environment, *Mater. Chem. Phys.*, 216, 197–205.
- [21] Ayangbenro, A.S., and Babalola, O.O., 2017, A new strategy for heavy metal polluted environments: A review of microbial biosorbents, *Int. J. Environ. Res. Public Health*, 14 (1), 94.
- [22] Negm., N.A., Hefni, H.H.H., and Abd-Elaal, A.A., 2017, “Assessment of Agricultural Wastes as Biosorbents for Heavy Metal Ions Removal from Wastewater” in *Surfactants in Tribology*, Eds. Biresaw, G., and Mittal, K.L., CRC Press, Boca Raton, 465–491.
- [23] Qin, H., Hu, T., Zhai, Y., Lu, N., and Aliyeva, J., 2020, The improved methods of heavy metals removal by biosorbents: A review, *Environ. Pollut.*, 258, 113777.
- [24] Hela, R., and Orsáková, D., 2013, The mechanical activation of fly ash, *Procedia Eng.*, 65, 87–93.
- [25] Kemp, T.J., 2017, A brief 100 year history of carbon, *Sci. Prog.*, 100 (3), 293–298.
- [26] Kennedy, K.K., Maseka, K.J., and Mbulo, M., 2018, Selected adsorbents for removal of contaminants from wastewater: Towards engineering clay minerals, *Open J. Appl. Sci.*, 8 (8), 355–369.
- [27] Loix, C., Huybrechts, M., Vangronsveld, J., Gielen, M., Keunen, E., and Cuypers, A., 2017, Reciprocal interactions between cadmium-induced cell wall responses and oxidative stress in plants, *Front. Plant Sci.*, 8, 1867.
- [28] Król, M., 2020, Natural vs. Synthetic zeolites, *Crystals*, 10 (7), 622.
- [29] Mukaromah, A.H., Kadja, G.T.M., Mukti, R.R., Pratama, I.R., Zulfikar, M.A., and Buchari, B., 2016, Surface-to-volume ratio of synthesis reactor vessel governing low temperature crystallization of ZSM-5, *J. Math. Fundam. Sci.*, 48 (3), 241–251.
- [30] Makertihartha, I.G.B.N., Kadja, G.T.M., and Gunawan, M.L., 2020, Exceptional aromatic distribution in the conversion of palm-oil to biohydrocarbon using zeolite-based catalyst, *J. Eng. Technol. Sci.*, 52, 584–597.
- [31] Kadja, G.T.M., Rukmana, M.D., Mukti, R.R., Mahyuddin, M.H., Saputro, A.G., and Wungu, T.D.K., 2021, Solvent-free, small organic lactam-assisted synthesis of ZSM-5 zeolites, *Mater. Lett.*, 290, 129501.
- [32] Lestari, W.W., Irwinsyah, I., Saraswati, T.E., Krisnandi, Y.K., Arrozi, U.S.F., Heraldly, E., and Kadja, G.T.M., 2020, Composite material consisting of HKUST-1 and Indonesian activated natural zeolite and its application in CO₂ capture, *Open Chem.*, 17 (1), 1279–1287.
- [33] Lestari, W.W., Yunita, L., Saraswati, T.E., Heraldly, E., Khafidhin, M.A., Krisnandi, Y.K., Arrozi, U.S.F., and Kadja, G.T.M., 2021, Fabrication of composite materials MIL-100(Fe)/Indonesian activated natural zeolite as enhanced CO₂ capture material, *Chem. Pap.*, 75 (7), 3253–3263.
- [34] Dionisiou, N.S., and Matsi, T., 2016, “Natural and Surfactant-Modified Zeolite for the Removal of Pollutants (Mainly Inorganic) from Natural Waters and Wastewaters” in *Environmental Materials and Waste: Resource Recovery and Pollution Prevention*, Eds. Prasad, M.N.V., and Shih, K., Academic Press, Cambridge, Massachusetts, US, 591–606.
- [35] Rahmah, W., Kadja, G.T.M., Mahyuddin, M.H., Saputro, A.G., Dipojono, H.K., and Wenten, I.G., 2022, Small-pore zeolite and zeotype membranes for CO₂ capture and sequestration – A review, *J. Environ. Chem. Eng.*, 10 (6), 108707.
- [36] Fajar, A.T.N., Nurdin, F.A., Mukti, R.R., Subagio, S., Rasrendra, C.B., and Kadja, G.T.M., 2020, Synergistic effect of dealumination and ceria impregnation to the catalytic properties of MOR zeolite, *Mater. Today Chem.*, 17, 100313.
- [37] Maghfirah, A., Susanti, Y., Fajar, A.T.N., Mukti, R.R., and Kadja, G.T.M., 2019, The role of tetraalkylammonium for controlling dealumination of zeolite Y in acid media, *Mater. Res. Express*, 6, 094002.
- [38] Kadja, G.T.M., Suprianti, T.R., Ilimi, M.M., Khalil, M., Mukti, R.R., and Subagio, S., 2020, Sequential

- mechanochemical and recrystallization methods for synthesizing hierarchically porous ZSM-5 zeolites, *Microporous Mesoporous Mater.*, 308, 110550.
- [39] Kadja, G.T.M., Azhari, N.J., Mukti, R.R., and Khalil, M., 2021, A mechanistic investigation of sustainable solvent-free, seed-directed synthesis of ZSM-5 zeolites in the absence of an organic structure-directing agent, *ACS Omega*, 6 (1), 925–933.
- [40] Putra, R., Lestari, W.W., Susanto, B.H., and Kadja, G.T.M., 2022, Green diesel rich product (C-15) from the hydro-deoxygenation of refined palm oil over activated NH_4^+ -Indonesian natural zeolite, *Energy Sources, Part A*, 44 (3), 7483–7498.
- [41] Azhari, N.J., Nurdini, N., Mardiana, S., Ilmi, T., Fajar, A.T.N., Makertihartha, N., and Kadja, G.T.M., 2022, Zeolite-based catalyst for direct conversion of CO_2 to C_2^+ hydrocarbon: A review, *J. CO₂ Util.*, 59, 101969.
- [42] Baerlocher, C., and McCusker, L., 2021, *Database of Zeolite Structures*, <http://www.iza-structure.org/databases/>, accessed on April 18, 2021.
- [43] Munthali, M.W., Elsheikh, M.A., Johan, E., and Matsue, N., 2014, Proton adsorption selectivity of zeolites in aqueous media: Effect of Si/Al ratio of zeolites, *Molecules*, 19 (12), 20468–20481.
- [44] Gili, M.B., Olegario-Sanchez, L., and Conato, M., 2019, Adsorption uptake of Philippine natural zeolite for Zn^{2+} ions in aqueous solution, *J. Phys.: Conf. Ser.*, 1191, 012042.
- [45] Ören, A.H., and Kaya, A., 2006, Factors affecting adsorption characteristics of Zn^{2+} on two natural zeolites, *J. Hazard. Mater.*, 131 (1-3), 59–65.
- [46] Budianta, W., Andriyani, N.D., Ardiana, A., and Warmada, I.W., 2020, adsorption of lead and cadmium from aqueous solution by Gunungkidul zeolitic tuff, Indonesia, *Environ. Earth Sci.*, 79 (8), 172.
- [47] Prajitno, M.Y., Harbottle, D., Hondow, N., Zhang, H., and Hunter, T.N., 2020, The effect of pre-activation and milling on improving natural clinoptilolite for ion exchange of cesium and strontium, *J. Environ. Chem. Eng.*, 8 (1), 102991.
- [48] Zanin, E., Scapinello, J., de Oliveira, M., Rambo, C.L., Franscescon, F., Freitas, L., de Mello, J.M.M., Fiori, M.A., Oliveira, J.V., and Dal Magro, J., 2017, adsorption of heavy metals from wastewater graphic industry using clinoptilolite zeolite as adsorbent, *Process Saf. Environ. Prot.*, 105, 194–200.
- [49] Obaid, S.S., Gaikwad, D.K., Sayyed, M.I., Al-Rashdi, K., and Pawar, P.P., 2018, Heavy metal ions removal from waste water by the natural zeolites, *Mater. Today: Proc.*, 5 (9 Part 3), 17930–17934.
- [50] Belova, T.P., 2019, Adsorption of heavy metal ions (Cu^{2+} , Ni^{2+} , Co^{2+} and Fe^{2+}) from aqueous solutions by natural zeolite, *Heliyon*, 5 (9), e02320.
- [51] Jorfi, S., Ahmadi, M.J., Pourfadakari, S., Jaafarzadeh, N., Soltani, R.D.C., and Akbari, H., 2017, Adsorption of Cr(VI) by natural clinoptilolite zeolite from aqueous solutions: Isotherms and kinetics, *Pol. J. Chem. Technol.*, 19 (3), 106–114.
- [52] Rakhym, A.B., Seilkhanova, G.A., and Kurmanbayeva, T.S., 2020, Adsorption of lead(II) ions from water solutions with natural zeolite and chamotte clay, *Mater. Today: Proc.*, 31 (Part 3), 482–485.
- [53] Almjadleh, M., Alasheh, S., and Raheb, I., 2014, Use of natural and modified Jordanian zeolitic tuff for removal of cadmium(II) from aqueous solutions, *Jordan J. Civ. Eng.*, 8 (3), 332–343.
- [54] Mihajlović, M.T., Lazarević, S.S., Janković-Častvan, I.M., Jokić, B.M., Janačković, D.T., and Petrović, R.D., 2014, A comparative study of the removal of lead, cadmium and zinc ions from aqueous solutions by natural and Fe(III)-modified zeolite, *Chem. Ind. Chem. Eng. Q.*, 20 (2), 283–293.
- [55] Kovacova, Z., and Pla, C., 2020, A batch study of Ni(II) sorption on natural Slovak zeolite, *IOP Conf. Ser.: Mater. Sci. Eng.*, 867, 012023.
- [56] Tedesco, S., Hurst, G., Imtiaz, A., Ratova, M., Tosheva, L., and Kelly, P., 2020, TiO_2 supported natural zeolites as biogas enhancers through photocatalytic pre-treatment of *Miscanthus x giganteus* crops, *Energy*, 205, 117954.
- [57] Fu, H., Li, Y., Yu, Z., Shen, J., Li, J., Zhang, M., Ding, T., Xu, L., and Lee, S.S., 2020, Ammonium removal using a calcined natural zeolite modified with sodium nitrate, *J. Hazard. Mater.*, 393, 122481.
- [58] Wahono, S.K., Stalin, J., Addai-Mensah, J., Skinner,

- W., Vinu, A., and Vasilev, K., 2020, Physico-chemical modification of natural mordenite-clinoptilolite zeolites and their enhanced CO₂ adsorption capacity, *Microporous Mesoporous Mater.*, 294, 109871.
- [59] Yousefi, T., Moazami, H.R., Mahmudian, H.R., Torab-Mostaedi, M., and Moosavian, M.A., 2018, Modification of natural zeolite for effective removal of Cd(II) from wastewater, *J. Water Environ. Nanotechnol.*, 3 (2), 150–156.
- [60] Mirbaloochzahi, M.R., Rezvani, A., Samimi, A., and Shayesteh, M., 2020, Application of a novel surfactant-modified natural nano-zeolite for removal of heavy metals from drinking water, *Adv. J. Chem., Sect. A*, 3, 612–620.
- [61] Yulizar, Y., Utari, T., Apriandanu, D.O.B., and Utami, R., 2020, Adsorption enhancement of heavy metal ions using chitosan-modified natural zeolite nanocomposite, *AIP Conf. Proc.*, 2242, 040057.
- [62] Zekavat, S.R., Raouf, F., and Talesh, S.S.A., 2020, Simultaneous adsorption of Cu²⁺ and Cr (VI) using HDTMA-modified zeolite: Isotherm, kinetic, mechanism, and thermodynamic studies, *Water Sci. Technol.*, 82 (9), 1808–1824.
- [63] Dimas Rivera, G.L., Martínez Hernández, A., Pérez Cabello, A.F., Rivas Barragán, E.L., Liñán Montes, A., Flores Escamilla, G.A., Sandoval Rangel, L., Suarez Vazquez, S.I., and De Haro Del Río, DA, 2021, Removal of chromate anions and immobilization using surfactant-modified zeolites, *J. Water Process Eng.*, 39, 101717.
- [64] Tran, H.N., Viet, PV, and Chao, H.P., 2018, Surfactant modified zeolite as amphiphilic and dual-electronic adsorbent for removal of cationic and oxyanionic metal ions and organic compounds, *Ecotoxicol. Environ. Saf.*, 147, 55–63.
- [65] Kragović, M., Pašalić, S., Marković, M., Petrović, M., Nedeljković, B., Momčilović, M., and Stojmenović, M., 2018, Natural and modified zeolite—alginate composites. Application for removal of heavy metal cations from contaminated water solutions, *Minerals*, 8 (1), 11.
- [66] Shirzadi, H., and Nezamzadeh-Ejhieh, A., 2017, An efficient modified zeolite for simultaneous removal of Pb(II) and Hg(II) from aqueous solution, *J. Mol. Liq.*, 230, 221–229.
- [67] Retnaningrum, E., and Wilopo, W., 2017, removal of sulphate and manganese on synthetic wastewater in sulphate reducing bioreactor using Indonesian natural zeolite, *Indones. J. Chem.*, 17 (2), 203–210.
- [68] Velazquez-Peña, G.C., Solache-Ríos, M., Olguin, M.T., and Fall, C., 2019, As(V) sorption by different natural zeolite frameworks modified with Fe, Zr and FeZr, *Microporous Mesoporous Mater.*, 273, 133–141.
- [69] Nguyen, V.D., Pham, T.T., Vranova, V., Nguyen, H.T.H., Nguyen, L.T.N., Vuong, X.T., and Bui, Q.M., 2020, removal of cadmium from aqueous solution using sonochemically modified clinoptilolite: Optimization and modeling, *Environ. Technol. Innovation*, 20, 101166.
- [70] Nasiri-Ardali, M., and Nezamzadeh-Ejhieh, A., 2020, A comprehensive study on the kinetics and thermodynamic aspects of batch and column removal of Pb(II) by the clinoptilolite–glycine adsorbent, *Mater. Chem. Phys.*, 240, 122142.
- [71] Abd El-Azim, H., and Mourad, F., 2018, Removal of heavy metals Cd(II), Fe(III) and Ni(II), from aqueous solutions by natural (clinoptilolite) zeolites and application to industrial wastewater, *Asian J. Environ. Ecol.*, 7 (1), 1–13.
- [72] Liu, X., Tian, R., Ding, W., He, Y., and Li, H., 2019, Adsorption selectivity of heavy metals by Na-clinoptilolite in aqueous solutions, *Adsorption*, 25 (4), 747–755.
- [73] Saha, D., and Grappe, HA, 2017, “Adsorption Properties of Activated Carbon Fibers” in *Activated Carbon Fiber and Textiles*, Eds. Chen, J.Y., Woodhead Publishing, Oxford, UK, 143–165.
- [74] Sims, R.A., Harmer, S.L., and Quinton, J.S., 2019, The role of physisorption and chemisorption in the oscillatory adsorption of organosilanes on aluminium oxide, *Polymers*, 11 (3), 410.
- [75] Tran, H.N., You, S.J., Hosseini-Bandegharai, A., and Chao, H.P., 2017, Mistakes and inconsistencies regarding adsorption of contaminants from aqueous solutions: A critical review, *Water Res.*, 120, 88–116.

Review:**Synthesis and Application of Zinc Layered Hydroxide: A Short Review**

Norhayati Hashim^{1,2*}, Zuhailimuna Muda³, Illyas Md Isa^{1,2}, Norlaili Abu Bakar¹,
Wan Rusmawati Wan Mahamod¹, Noorshida Mohd Ali^{1,2}, Sharifah Norain Mohd Sharif^{1,2},
Maizatul Najwa Jajuli^{1,2}, Syazwan Afif Mohd Zobir⁴, and Suyanta Suyanta⁵

¹Department of Chemistry, Faculty of Science and Mathematics, Universiti Pendidikan Sultan Idris,
35900 Tanjong Malim, Perak, Malaysia

²Nanotechnology Research Centre, Faculty of Science and Mathematics, Universiti Pendidikan Sultan Idris,
35900 Tanjong Malim, Perak, Malaysia

³Sekolah Menengah Kebangsaan Dato' Dol Said, 78000 Alor Gajah, Melaka, Malaysia

⁴Faculty of Agriculture, Universiti Putra Malaysia, 43400 Serdang, Selangor, Malaysia

⁵Department of Chemistry Education, Universitas Negeri Yogyakarta, Jl. Colombo No. 1, Yogyakarta 55281, Indonesia

*** Corresponding author:**

tel: +6015-48797314

email: norhayati.hashim@fsm.ups.edu.my

Received: February 13, 2023

Accepted: May 18, 2023

DOI: 10.22146/ijc.82281

Abstract: Zinc Layered hydroxide (ZLH) is a layered material easily synthesized with a structure identical to brucite-like material. Due to the exchangeable anions in the interlayer compensating for the positive charge of a brucite-type layer, ZLH provides a wide application in many fields. This review focuses on the properties and method of synthesis of ZLH by giving an overview of intercalated guest anion in the interlayer of ZLH. The further discussion involved the application of intercalated guest anion in zinc layered hydroxide layer and its properties as a sensitizer, controlled release biomedical, and agriculture to provide the scientific community for research and development by giving current findings. This brief review also presents the success of anion intercalation for controlled release along with the kinetic model involved, which increases the bioavailability and effectiveness of the nanocomposite on its target. It shows the development of research on ZLH nanocomposites toward the sustainability of human life and the environment. This study implies that it is a source of knowledge for researchers about zinc-layered hydroxide materials involving synthesis methods and their application to produce more beneficial nanomaterials.

Keywords: zinc layered hydroxide; synthesis; intercalation; nanocomposite

■ INTRODUCTION

Layered metal hydroxides (LMHs) are layered materials, including layered hydroxide salts (LHSs, $M_x^{II}(\text{OH})_{2x-my}A_y^{m-} \cdot n\text{H}_2\text{O}$) and layered double hydroxides (LDHs, $M_{1-x}^{II}M_x^{III}(\text{OH})_2(A^{m-})_{x/m} \cdot n\text{H}_2\text{O}$), where typically $M^{II} = \text{Mg, Fe, Co, Ni, and Zn}$, $M^{III} = \text{Al, Cr, Fe, Co, and In}$, $A^{m-} = \text{Cl}^-, \text{NO}_3^-, \text{SO}_4^{2-}, \text{and CO}_3^{2-}$ [1]. LMH consists of two parts: an inorganic layer, such as positively charged brucite, and exchangeable anions and water molecules in

the interlayer, which has attracted attention due to its potential applications. Layered hydroxide salts, also known as layered single metal hydroxides (LSHs), which only consist of one metal on an inorganic layer, have shown a huge opportunity in industrial and environmental research nowadays [2]. Therefore, this article will briefly discuss the properties, method of synthesis, and application of one of the compounds of LSHs, namely zinc layered hydroxide (ZLH). This review aims to give a general overview of ZLH properties

due to the variety of intercalated guest anion species between the interlayers of the nanocomposite. The synthesis method used in the intercalation process via guest anions is also listed in this article. This review also compiles and updates the application of the ZLH nanocomposite, focusing on ZLH as a sensitizer and controlled release formulation, along with the kinetic model in biomedical and agricultural applications. To our knowledge, no review articles have been published on the synthesis of ZLH using direct reaction, ion exchange, co-precipitation, and hydrothermal precipitation methods. Therefore, it is hoped that this review will update the current discovery of intercalated guest anion in zinc-layered hydroxide. The positive development of research in this field allows for various applications in the future, which increases progress in related fields.

■ PROPERTIES OF ZINC LAYERED HYDROXIDE

Zinc-layered hydroxide is one of the inorganic layered materials that has a layer structure similar to that of brucite ($\text{Mg}(\text{OH})_2$) and correlates to anionic clay [3]. In brucite, Mg is octahedrally coordinated into six hydroxyl groups that share an edge to build infinitely large layers arranged along the basal direction [4]. Modifying the brucite structure may occur through isomorphic substitution of intra-layer cations or anions or interlayer water molecules for part of the hydroxide groups. In the latter case, the charge of the layer was balanced by the additional anion present in the second sphere. The slightly altered formula for these types of compounds called hydroxide salts (LHS) is generally the formula of $\text{M}^{2+}(\text{OH})_{2-x}(\text{A}^{m-})_{x/m} \cdot n\text{H}_2\text{O}$ where M^{2+} is the metal cation (e. g. Mg^{2+} , Ni^{2+} , Zn^{2+} , Ca^{2+} , Cd^{2+} , Co^{2+} , Cu^{2+}) while A^{m-} is the counterions in the interlayer space. Zinc-layered hydroxide (ZLH) is a layered hydroxide salt with the formula of $\text{Zn}_5(\text{OH})_8(\text{NO}_3)_2 \cdot 2\text{H}_2\text{O}$ [5].

The basic structure of ZLH consists of a brucite type where one-quarter of the octahedrally coordinated zinc ion sites is empty. The Zn atoms tetrahedral bonded to the layer through OH groups, forming the base of a tetrahedron. Besides, the coordinated water molecules were located at the apex of the tetrahedrons, and the nitrate groups occupied the interlayer space of ZLH [5].

The nitrate anions are surrounded by water molecules, which are not directly bonded to zinc atoms [6]. Nitrate, sulfate, phosphate, and chloride anions are also used to synthesize ZLH [7]. The lamellar structure is positively charged; therefore, the counter anions and water molecules were intercalated in the lamellar space to neutralize the layer charge [8-9].

In contrast to LDH, hydroxide ions are removed from the structure instead of metal replacement and replaced by water molecules or other types of oxoanions, generating materials with anionic exchange capacity [10]. Besides that, the water molecules may also be incorporated into the interlayer region, culminating in enhanced stability [11]. The oxoanions are positioned in the second coordination sphere of the metal to stabilize the electrostatic charge or by the direct substitution by another single-charged anion [4,12-14]. Some active agents are occasionally charged with neutral and poorly soluble pesticides that are difficult to intercalate in the ZLH interlayer. Most literature focuses exclusively on anionic pesticides. For charge-neutral and poorly water-soluble pesticides, their intercalation usually depends on anionic surfactants in the gallery, which form a hydrophobic region [15-19]. The interlayer space of ZLH can adsorb targets such as pesticide molecules due to its hydrophobicity and accessibility.

Liu et al. [20] developed a new method for solubilizing chlorpyrifos (CPF) into the interlayer of zinc hydroxide nitrate (ZHN) intercalated with dodecyl benzene sulfonate (DBS). ZHN is modified with DBS to form a hydrophobic region in the ZHN-DBS gallery [20-21]. Liu et al. [20] also suggest that DBS is a tilt monolayer in the gallery when three oxygen atoms in the SO_3 group approach the ZHN layer. According to Demel et al. [22], the mechanism of synthesis of layered zinc hydroxide-dodecyl sulfate (LZH-DS) was described by an extra- and intra- lamellar space template model. The sodium dodecyl sulfate (SDS) bilayer is an extra-lamellar template in which electrostatic interactions occur between zinc atoms and sulfate groups. The insertion of alcohols that act as active agents into the layered sulfate arrangement was assisted by two possible interactions, and one of them is a hydrophobic interaction between

the dodecyl chain of SDS and the alkyl chain of the alcohol. The other interaction is an ion-dipole interaction between the hydroxyl group of the alcohol and the sulfate group of SDS. Both interactions contribute to the stability and packed layered dodecyl sulfate arrangement. Therefore, it can conclude that long alkyl chain alcohols have enlarged the extra-lamellar templates. Meanwhile, short alkyl chain alcohols, such as ethanol and 1-propanol, are not successfully intercalated into the layered dodecyl sulfate arrangement. The small size and low stability of ethanol or 1-propanol with an extra-lamellar template will result in ethanol or 1-propanol being outside the extra-lamellar template resulting in encroachment of the adjoining extra-lamellar template.

The interaction of cationic and anionic surfactants will form neutral micelles that permit the anion to be intercalated in the interlayer of ZLH. Since there is an increased distance between the interlayers of the starting material, this method offers particular promise for incorporating large anions [23-25].

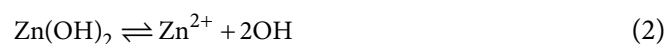
■ SYNTHESIS METHODS OF ZINC LAYERED HYDROXIDE

There are various synthesis methods have been used to synthesize ZLH nanocomposite, which an ion-exchange method [26-28], co-precipitation method [4,18-20], hydrothermal precipitation methods [12,29-30], and direct reaction method [31-33]. Above all, the direct reaction method is often chosen in preparing ZLH nanocomposites because various anions can be directly intercalated alternately between the hydroxylated sheets and increase the quantity of the synthesized material [26,31-34]. The ion exchange process is not involved in this method. The intercalation process of anions into ZLH only involves the direct incorporation of ZnO, which is used as a starting material [35-37]. The advantage of this method is that it is simpler, more environmentally friendly, and more economical because it involves fewer steps and fewer chemicals compared to other synthesis methods of ZLH [3]. The dissociation-deposition mechanism was used in the direct reaction method [35], which is composed of three stages, as shown in Eq. (1-3) [3,35,38-39]:

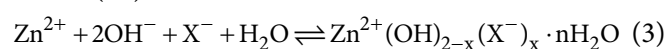
Stage 1: The process on the surface of solid particles: hydrolysis of ZnO in water to form Zn(OH)₂.



Stage 2: Dissociation of Zn(OH)₂ layer to form Zn²⁺ ions and OH ions. Zn(OH)₂ layer dissolves more easily than ZnO in acid.



Stage 3: Formation of nanocomposites resulting from the reaction of Zn²⁺ ions with hydroxyl, H₂O, and guest anions (X⁻).



The co-precipitation method involves slowly adding a cationic salt solution in a known molar ratio to an aqueous solution, followed by the simultaneous acquisition of an alkaline solution. The pH value is controlled to produce a mixed hydroxide precipitate. In contrast, ion exchange is a method that is applied for the intercalation of ZLHs with anions of different natures. Diffusion of anions into the interlayer is the rate-determining step in the reaction; therefore, the exchange reaction is performed by alternating stirring the ZLH precursor in an excess solution. Ultrasound methods are encouraged to speed up the exchange reaction [28,38,40-42]. Based on Hashim et al. [33], ZLH nanocomposite prepared by the co-precipitation method showed less thermal stability and crystallinity than ZLH nanocomposite synthesis using the ion exchange method.

Meanwhile, the BET analysis found that the co-precipitation method produced a higher surface area nanocomposite than the ion exchange method. The ion exchange method is useful when the co-precipitation method is inapplicable due to unstable metal cations or anions in an alkaline solution or when intercalated with a bigger size anion [43]. Hydrothermal and microwave treatments are another method used to synthesize ZLH nanocomposite. This method has been used to improve the crystallinity and other properties of ZLHs [12,29,44-46]. Compared to other methods, the advantage of the hydrothermal synthesis method for ZLH nanocomposite is that it can produce unstable nanomaterials at high temperatures. In this method,

ZLH nanocomposites can form in a wide temperature range, from room to very high temperatures. Apart from that, the morphology of the nanocomposite can be controlled by controlling the vapor pressure of the main composition in the reaction [30]. Fig. 1 shows the schematic structure of ZLH nanocomposite synthesis using the four methods discussed above. The list of methods and intercalated anions has been summarized in Table 1.

■ APPLICATION OF ZINC-LAYERED HYDROXIDE

The potential for ZLH inorganic hybridization has been extensively explored and studied recently. The ability to tune a material's performance involves tailoring the material's physicochemical properties to lead to the application, elaboration, and relating of novel concepts; therefore, it will open the door to new ideas for a new

world in materials science. For example, the rapid development of industry has led to increased waste disposal, such as solid waste or wastewater containing heavy metals [66-68]. The ZLH-based material nanocomposites have been reported to contribute to wastewater treatment, especially in removing heavy metals, through their ability to absorb them [66]. It has the advantages of good selectivity, high efficiency, high adsorption capacity, and no secondary pollution, as well as being a low-cost material [69,72]. ZLH nanocomposite material is one of the ultrafine and tiny powders with a diameter below 100 nm. The nanometer scale particle size of the ZLH material will cause changes in the surface characteristics and crystal structure due to quantum effects, surface effects, and interface effects [71,73-75]. This condition causes the particles to become smaller while the particle surface area, surface energy, surface binding energy, and the number of surface atoms

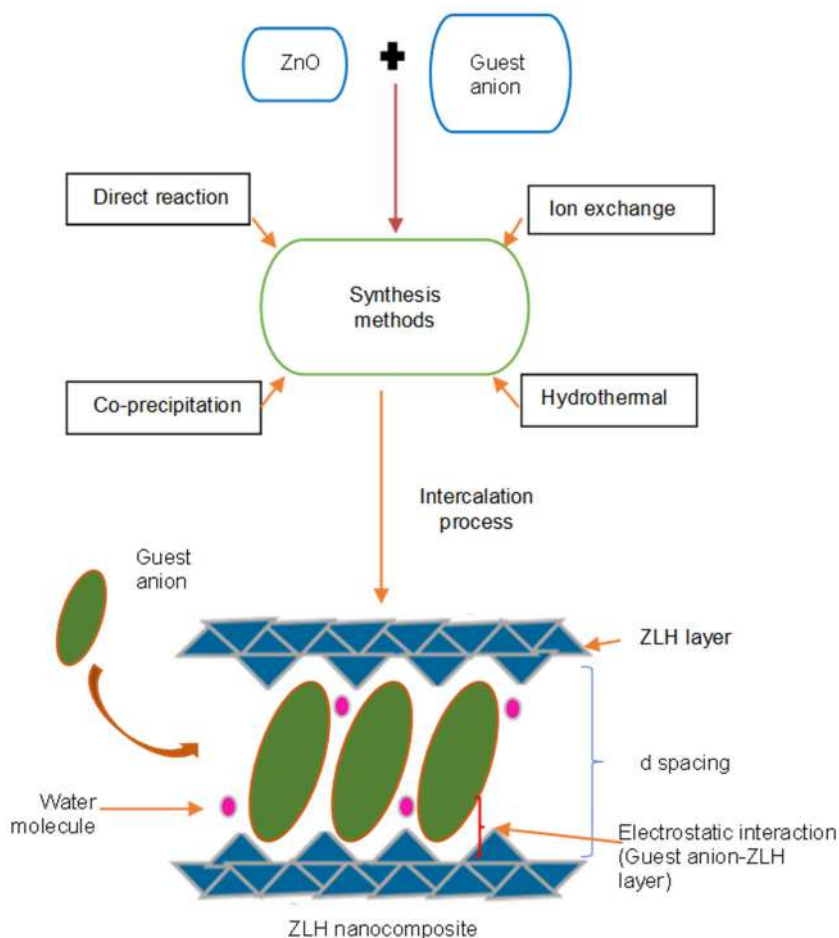


Fig 1. Schematic view ZLH nanocomposite general structure with anions intercalated in the interlayer structure

Table 1. List of methods and intercalated anions that have been intercalated into the interlayer of ZLH

Methods	Guest anions	Ref.
Co-precipitation	Valeric acid	[47]
	Oxalatooxoniobate complex ion	[4]
	3-(4-methoxyphenyl) propionic acid	[42]
	Indigo carmine ion	[48]
	Sodium salicylate ion	[20]
	Sodium heptanoate ion	[49]
	Porphyrin ion	[50]
	Methyl orange, orange II ion	[51]
	Aspartic acid	[52]
	Nitrate, phosphate anions	[53]
	Triarylmethane dyes	[18]
	4-aminobenzoic acid	[54]
Direct reaction	Chloroacetic acid	[33]
	3-(4-methoxyphenyl) propionic acid	[32]
	2-(2,4-dichlorophenoxy) butyric acid	[55]
	4-chloro-2-methylphenoxy acetic acid	[56]
	Hippuric acid	[36]
	Cinnamic acid	[3]
	Para-aminosalicylic acid	[57]
	Protocatechuate ion	[38]
	Salicylic acid	[39]
	Cinnamic acid	[58]
Ferulic acid	[59]	
Ion exchange	3-(4-methoxyphenyl)propionic acid	[42]
	Hippuric acid	[36]
	Caffeic acid	[27]
	Ciprofloxacin ion	[60]
	2-(2,4-dichlorophenoxy)butyric acid	[55]
	2-aminobenzoate	[61]
	2-Methyl-4-chlorophenoxyacetic acid	[34]
	Curcumin anion	[62]
	Diclofenac ion	[5]
	Molybdate anion	[63]
	β -glucan ion	[64]
Amoxicillin trihydrate	[65]	
Hydrothermal precipitation	Hexamethylenetetramine	[12]
	2-Methyl-4-chlorophenoxyacetic acid	[34]

increase rapidly, surface atoms lack contiguousness, leading to unsaturated properties. Indirectly, it will stabilize and combine with other atoms [76-77]. It is also supported by the strong adsorption capacity of this material due to the basic structure of nanomaterials that can reach equilibrium quickly. Therefore, ZLH

nanocomposites have been used to isolate and enrich ideal materials used to analyze trace elements [70]. Some researchers have conducted studies to evaluate the performance of ZLH in removing heavy metals from wastewater, such as de Oliveira and Wypych [66]. They used zinc hydroxide nitrate layered (ZnHN) to

determine the effectiveness of ZnHN on the removal of chromate ions from the solution. The results show that the retention capacity of ZnHN is higher compared to the theoretical value because the presence of CrO_4^{2-} acts to destroy the structure of the material. The chromate removal capacity in the experiment showed a value of 210.1 mg CrO_4^{2-} /g material.

XRD analysis before and after chromate removal of ZnHN shows that the layered material has changed into a new compound, mainly amorphous. The removal of heavy metals from wastewater using ZLH was also done by Jia et al. [70]. Mine wastewater containing Pb^{2+} was treated using nanometer-layered zinc hydroxide, involving several parameters such as pH, temperature, coexisting ions, initial concentration, and time on the performance of the layered material. The results show that the metal ion removal efficiency is higher than 85%, while the concentration of Pb^{2+} in the permeation liquid shows permeation lower than 0.5 mg/L. The pH results show that the pH value influences the adsorption rate, and the temperature has the maximum impact on the adsorption of Pb^{2+} ions. Studies show that the adsorption of nanoparticles is due to nanoparticles that have surface hydroxyl groups. Hydroxyl groups on the surface of nanoparticles allow bonds to be formed with various cations and fulfill the characteristics of ion or organic substance adsorbents. In addition, the large surface area of the nanoparticles also produces unsaturated bonds, which in turn cause the formation of charges on the surface of the nanoparticles. Therefore, ions of different charges are attracted to the surface of the substrate to balance its surface charge [78]. Rhodamine B is one of the water-tracer fluorescent substances widely used as a dye in the textile industry and a substance in the food industry. Studies show that rhodamine B is a carcinogenic substance for humans and animals. Prolonged exposure to this substance can irritate the eyes, skin, and respiratory tract [79-82].

Thao et al. [83] have developed the reaction of zinc hydroxide-layered Ti-doped nanomaterials as a catalyst for decomposing rhodamine B in water under visible light irradiation. The synthesis involves the substitution of Zn^{2+} ions for Ti^{4+} on the ZLH layer to form a heterogeneous

catalyst material containing Ti, which gives variation to the solid composition and creates a lot of OH on the hydroxide layer. Zn-based modification as a catalyst material with photocatalytic properties broadens the potential of ZLH to accommodate the difference in cation size and valence for guest anion intercalation in the interlayer domain.

■ SENSITIZERS

Organic sensitizers with strong UV absorption properties have frequently been intercalated into the interlayer of ZLH to convert light energy into excited states [3,23,84]. It is reasonable that the final properties of inorganic-organic functional hybrids depend on the interaction between the host layer, which is an inorganic matrix, and the guest anions that cause interaction and influence the distribution, orientation, the electronic properties of the guest anions [50,85] and control the chemical composition, mesomorphology, and micromorphology of layered material [86]. Much research has been done to study these hybrid materials' spectral, photochemical, and photophysical properties due to the stability and interlayer protection of the inorganic host structure [87-90]. At the same time, the chromophore species has an optical function such as color [91], thermochromicity [92], luminescence [93-94], formation of singlet oxygen [95], nonlinear optical properties, photo-oxidation [96], or UV absorption [97]. This study is important for developing layered materials for energy storage and conversion, photocatalysis, sunscreens, and even devices for sensing or photochemistry. Demel et al. [50] have reported that a solid-state $\text{O}_2(1 \Delta_g)$ sensor was developed based on an anionic porphyrin-intercalated layered zinc hydroxide (LZH) hybrid. The newly discovered layered material has an inorganic host layer that provides stability and protection to photo-functional guest species. From the results, both new layered materials, LZH-PdTPPS and LZH-PdTPPC, show strong signals of photo-produced $\text{O}_2(1 \Delta_g)$. The obtained $\text{O}_2(1 \Delta_g)$ luminescence intensity decays monoexponentially, which gives an effective $\text{O}_2(1 \Delta_g)$ lifetime of 30 and 41 μs , respectively, in an oxygen atmosphere for LZH-PdTPPS and LZH-

PdTPPC. The hybrid material shows good potential as an $O_2(1 \Delta g)$ producer and extends the life of $O_2(1 \Delta g)$. It shows that the host LZH is a potential material that can be used as an ion porphyrin carrier.

■ CONTROLLED RELEASE FORMULATION IN BIOMEDICAL

A slow-release drug delivery system is one example of applying ZLH materials in biomedicine. Most drugs are difficult to dissolve in water, making delivering the dose to the target area challenging to achieve and less effective. In addition to that, there are unwanted side effects [98-101]. Therefore, the drug delivery system using ZLH material is one of the alternative methods as a drug delivery vector that effectively controls the release rate of drug molecules to maintain drug molecules *in vivo* proportional to time. [57,102-105]. Table 2 shows the biomolecules that have been intercalated into the interlayer of ZLH and the kinetic model of the respective controlled release system.

A kinetic model has been used to explain the process that occurs to study the release behavior of substances in a specific medium. It involves mathematical formulas to determine the quantitative analysis value obtained for the release rate and to explain the process involved easily. The chosen mathematical model will help optimize therapeutic device design by informing the effectiveness of different release models [2,106-109]. Furthermore, the kinetic model output data can be used for several

approaches in sustained release or stimulus-responsive systems [109]. Engineers, pharmacists, and researchers are pouring out ideas together to produce new and potentially efficient products in various fields by using controlled-release formulations. Mathematical modeling is helpful in proving the prediction of the kinetic release model before the product is used or implemented on the actual target, which involves the measurement of certain physical parameters, such as drug diffusion coefficients, as well as the use of models that will be selected based on experimental output data [110-111]. Therefore, the mathematical modeling developed needs to be understood by focusing on all the factors that affect the kinetics and has a very important value in optimizing the mathematical formulation used [2,113-114]. The model can be simply a mathematical metaphor for many aspects of reality involved in identifying the set of phenomena governing release kinetics [111,114-116]. UV radiation consists of UV A, B, and C in the electromagnetic spectrum's wavelength range between 200–400 nm. The ozone layer absorbs UV B and UV C radiation, while UV A radiation that reaches the ground will affect human health. Recently, sunscreen formulations made from organic and inorganic compounds have been widely produced to prevent or minimize the effects of being exposed to UV rays [25,117]. Mohsin et al. [3] have intercalated cinnamate acid (CA), which is an efficient UV A and UV B absorber anion, into the interlayer of ZLH. The result shows that

Table 2. List of active agents in the interlayer of ZLH nanocomposite and kinetic model in biomedical applications

Active agent	Kinetic model	Researcher
Cinnamate ion	Pseudo-second order	[3]
Indole-3-acetic acid	Modified Freundlich model	[102]
Hippuric acid	First-order: pH 7.4 Pseudo-second-order: Na_2CO_3 Bhaskar equation: pH 4.8	[36]
Ciprofloxacin ion	Modified Freundlich model	[60]
Ellagic acid	Pseudo-second-order	[35]
4-amino salicylic acid	Pseudo-second-order	[57]
Protocatechuic acid	Pseudo-second-order	[38]
Cetirizine ion	Pseudo-second-order	[103]
Gallic acid	Elovich and Freundlich models	[2]
Ferulic ion	Pseudo-second-order	[59]

the UV-Vis spectrum of the intercalated material has excellent UV A and UV B absorption abilities. The retention of the cinnamate ion in the interlayer of ZLH in selected media shows slow release over an extended period for sunscreen usage. The MTT assay on human dermal 47 fibroblasts (HDF) cells for intercalated compounds shows the cytotoxicity of ZLH-CA to be concentration-dependent overall and less toxic than its precursor, ZnO. Biswick et al. [27] also intercalate an active agent, caffeic acid, into ZLH nanocomposite as sunscreen material. Caffeic acid was chosen due to its high potential as a material for cosmetic applications and its low stability against UV and oxygen irradiation [117-119]. The finding of slow release for caffeic acid-zinc basic salt (CA-ZBS) shows a fast release in the first 20 min, which is due to small amounts of anions adsorbed on the surface of the inorganic matrix and to anions intercalated close to the edges of the crystals, followed by slow release with time. The slow release of the caffeic ion from the inorganic matrix is due to the strong covalent bonding interaction between the carboxylate group of the anions and the matrix cation. This observation is supported by the FTIR spectrum of the CA-ZBS nanocomposite, where the $\Delta\nu$ value for the caffeate anion in sodium caffeate is higher than that of CA-ZBS. A novel nanocomposite with the guest molecule protocatechuic acid that acts as an anticancer agent has been synthesized by Barahuie et al. [38]. The cytotoxicity test of the nanocomposite for all cancer cells showed an increase compared to the free form of the guest anion. *In vitro* tests of this nanocomposite show that it is an effective anticancer agent, suitable for use as a controlled-release formulation of protocatechuic acid, and has good potential as a chemotherapeutic drug for human cancer [120-122]. A pseudo-second-order kinetic model governed the release study of protocatechuic acid from the interlayer of ZLH nanocomposite into the phosphate-buffered saline solution. Similar research was done by Saifullah et al. [123], who found that anti-tuberculosis drugs in zinc hydroxide-4-aminosalicylate (4-ASA-ZLH) nanocomposite gave minimal drug side effects and protected the drug from enzymatic degradation. It also increases the therapeutic efficacy by delivering the drug at the target site. The release rate of 4-

amino salicylic acid from nanocomposite depends on pH, and the release mechanism of 4-amino salicylic acid occurs through both the dissolution of ZLH layers and diffusion [124]. Abdul Latip et al. [60] have also used PBS at pH 7.4 as a medium for the controlled release of the ciprofloxacin (CFX) ion. The release study of CFX release data was fitted with the Freundlich model, followed by the parabolic diffusion model. Sustained release of CFX from the interlayer of ZLH increases the antiproliferative effect. It is due to the strong interaction that occurs between ZLH and CFX, which will facilitate cell uptake and protect guest ions from degradation, causing a slow release of CFX and “killing” A549 cells. The unique properties of ZLH have revolutionized it as a nano vehicle in medical science, especially in drug delivery. ZLH, with drug intercalation between the spaces in its layer, has improved chemical and thermal stability, cell targeting, drug solubility, reduced side effects, and increased drug resistance to disease, further increasing the drug's plasma half-life [38]. Overall, layered zinc hydroxide shows effective potential as a nanocarrier for drugs with efficient delivery and improving the therapeutic efficiency of drugs in treating different diseases.

■ CONTROLLED RELEASE FORMULATION IN AGRICULTURE

Special attention has also been focused on controlled-release formulations of pesticides using layered materials in agriculture. There are many new nanocomposites involving pesticides that have been intercalated into interlayer of ZLH such as cetyltrimethylammonium bromide [125], chloroacetic acid [33], valeric acid [47], propoxur [41], isoprocarb [126], thiacloprid [28], 2-methyl-4-chlorophenoxyacetic acid [34], 2-(2,4-dichlorophenoxy) butyric acid [55], and 4-chlorophenoxyacetic acid [127]. The successful intercalation process of pesticides into the interlayer of ZLH was due to positively charged ZLH layers that promote the attraction force between the guest anion pesticides and the host. Most researchers only use one type of guest anion in the intercalation process into the ZLH interlayer. However, Hussein et al. [128] have

successfully intercalated two different guest anions simultaneously into the ZLH interlayer, namely 4-(2,4-dichlorophenoxy) butyrate (DPBA) and 2-(3-chlorophenoxy) propionate (CPPA), using direct reaction method. The release study for both anions showed that the release rate depended on the guest anion size and the interaction between the hydroxide layer and CPPA, DPBA anions. This finding indicates that zinc-layered hydroxide is a versatile use material that can simultaneously intercalate more than one guest anion. ZLH, as a controlled release agent, acts as a host and delivery system that protects the active agent from degradation and increases the stability of the chemical while also preventing loss through leaching or evaporation, thereby increasing the duration of activity of the active agent.

Furthermore, ZLH also prevents active agents from being directly exposed to humans or the environment, which will reduce application and promote a safer environment [47]. To this end, controlled-release formulations encourage the effective use of agrochemical herbicides and produce new products that can be used in the agricultural sector [2,129]. Therefore, it can limit the amount available for unwanted processes and reduce the presence of agricultural chemicals in soil and surface water [32]. The use of mathematical modeling is beneficial in cases where the prediction of release kinetics is controlled before it is realized in a real system [130-131]. It directly collects measurements of important physical parameters, such as diffusion coefficients, and model matching to experimental output data. Therefore, the

Table 3. List of pesticide anions that intercalated into the interlayer of ZLH and its kinetic model

Pesticides	Kinetic models	Researcher
2,4-dichlorophenoxy acetic acid	Pseudo-second-order	[31]
Valeric acid	Pseudo-second-order	[47]
Hexenoic acid	Pseudo-second-order	[135]
Cloprop	Parabolic diffusion	[32]
4-chlorophenoxyacetic acid	Pseudo-second-order	[127]
Chlorpyrifos	pseudo-second-order (ZHN-DBS-CPF) parabolic diffusion (ZHN-TX-10-CPF)	[20]
Cetyltrimethylammonium bromide		[125]
Chloroacetic acid		[33]
3-(4-methoxyphenyl) propionic acid	Pseudo-second-order (phosphate medium) The first order (sulfate and chloride medium)	[32]
(2-(2,4-dichlorophenoxy)butyric acid		[55]
4-(2,4-dichlorophenoxy) butyric acid and 2-(3-chlorophenoxy) propionic acid	Pseudo-second-order	[128]
4-chlorophenoxy acetic acid	Pseudo-second-order	[127]
Nitrate anion	Pseudo-second-order	[53]
Phosphate anion		
Isoprocab	The first order (phosphate solution) Pseudo-second order (sulfate and chloride solutions) First-order kinetics (phosphate solution)	[126]
Thiacloprid	Parabolic diffusion kinetics (sodium sulfate and sodium chloride solutions)	[28]
Imidacloprid	Pseudo-second-order	[136]
Bispyribac	Pseudo-second-order (phosphate and sulfate solutions) Parabolic diffusion (chloride solutions)	[137]
Fluazinam	Pseudo-second-order	[138]

mathematical modeling developed needs to be understood to see the factors that influence the kinetics of pesticide release [132-134]. It has important value in optimizing the formulation process. The list of pesticides intercalated into ZLH and its kinetic model are presented in Table 3.

■ CONCLUSION

The zinc layered hydroxide intercalated with anion can be synthesized using four methods such as co-precipitation, direct reaction, ion exchange, and hydrothermal. Each method is chosen due to the difficulty of the intercalation process. Among them, the co-precipitation method was found to be the most popular choice to be used due to the simple and lower cost of synthesizing ZLH nanocomposite. This intercalated nanocomposite has shown great potential as a sensitizer due to the stabilization and protection layer, which gives effective life to the guest anion. While the controlled release formulation of ZLH nanocomposite for biomedical and agriculture enables it to produce material that has better efficacy and is safe for humans and the environment. It can also reduce overall costs by eliminating the time and cost of repeated and redundant applications. Therefore, knowledge and awareness about the application of nanocomposites in agriculture and biomedicine need to be expanded to fully utilize this technology fully, thereby increasing the income of related sectors. This knowledge will indirectly also help researchers diversify ZLH nanocomposite applications in the future.

■ ACKNOWLEDGMENTS

The author would like to extend their gratitude to Universiti Pendidikan Sultan Idris for University Research Grants, Project Code No: 2016-0183-102-01, that helped fund the research.

■ AUTHOR CONTRIBUTIONS

Norhayati Hashim, Zuhailimuna Muda, Illyas Md Isa, Norlaili Abu Bakar, Wan Rusmawati Wan Mahamod, Noorshida Mohd Ali, Sharifah Norain Mohd Sharif, Maizatul Najwa Jajuli, and Suyanta, have written and reviewed this article, while Syazwan Afif Mohd Zobir provides diagram 1.

■ REFERENCES

- [1] Shinagawa, T., Chigane, M., and Izaki, M., 2021, Electrochemical growth of $Mg(OH)_x$ layered films stacked parallel to the substrates and their thermal conversion to (111)-oriented nanoporous MgO films, *ACS Omega*, 6 (3), 2312–2317.
- [2] Ruiz, C.V., Rodríguez-Castellón, E., and Giraldo, O., 2019, Hybrid materials based on a layered zinc hydroxide solid and gallic acid: Structural characterization and evaluation of the controlled release behavior as a function of the gallic acid content, *Appl. Clay Sci.*, 181, 105228.
- [3] Mohsin, S.M.N., Hussein, M.Z., Sarijo, S.H., Fakurazi, S., Arulselvan, P., and Yun Hin, T.T., 2013, Synthesis of (cinnamate-zinc layered hydroxide) intercalation compound for sunscreen application, *Chem. Cent. J.*, 7, 26–38.
- [4] Arizaga, G.G.C., Gardolinski, J.E.F.C., Schreiner, W.H., and Wypych, F., 2009, Intercalation of an oxalatoxonobate complex into layered double hydroxide and layered zinc hydroxide nitrate, *J. Colloid Interface Sci.*, 330 (2), 352–358.
- [5] Nabipour, H., and Sadr, M.H., 2015, Controlled release of diclofenac, an anti-inflammatory drug by nanocompositing with layered zinc hydroxide, *J. Porous Mater.*, 22 (2), 447–454.
- [6] Mohd Zobir, S.A., Ali, A., Adzmi, F., Sulaiman, M.R., and Ahmad, K., 2021, A review on nanopesticides for plant protection synthesized using the supramolecular chemistry of layered hydroxide hosts, *Biology*, 10 (11), 1077.
- [7] Shinagawa, S., Watanabe, M., Mori, T., Tani, J., Chigane, M., and Izaki, M., 2018, Oriented transformation from layered zinc hydroxides to nanoporous ZnO: A comparative study of different anion types, *Inorg. Chem.*, 57 (21), 13137–13149.
- [8] Zhang, H., Xu, H., and Lu, S., 2021, Preparation and application of layered double hydroxide nanosheets, *RSC Adv.*, 11 (39), 24254–24281.
- [9] Brini, E., Fennell, C.J., Fernandez-Serra, M., Hribar-Lee, B., Lukšič, M., and Dill, K.A., 2017, How water's properties are encoded in its molecular

- structure and energies, *Chem. Rev.*, 117 (19), 12385–12414.
- [10] da Gama, B.M.V., Selvasembian, R., Giannakoudakis, D.A., Triantafyllidis, K.S., McKay, G., and Meili, L., 2022, Layered double hydroxides as rising-star adsorbents for water purification: A brief discussion, *Molecules*, 27 (15), 4900.
- [11] Theiss, F.L., Couperthwaite, S.J., Ayoko, G.A., and Frost, R.L., 2014, A review of the removal of anions and oxyanions of the halogen elements from aqueous solution by layered double hydroxides, *J. Colloid Interface Sci.*, 417, 356–368.
- [12] Machovsky, M., Kuritka, I., Sedlak, J., and Pastorek, M., 2013, Hexagonal ZnO porous plates prepared from microwave synthesized layered zinc hydroxide sulphate via thermal decomposition, *Mater. Res. Bull.*, 48 (10), 4002–4007.
- [13] Tang, L., Xie, X., Li, C., Xu, Y., Zhu, W., and Wang, L., 2022, Regulation of structure and anion-exchange performance of layered double hydroxide: Function of the metal cation composition of a brucite-like layer, *Materials*, 15 (22), 7983.
- [14] Hebert, A., and McCalla, E., 2021, The role of metal substitutions in the development of Li batteries, part I: Cathodes, *Mater. Adv.*, 2 (11), 3474–3518.
- [15] Sanati, S., and Rezvani, Z., 2018, Co-intercalation of acid red-27/sodium dodecyl sulfate in a Ce-containing Ni-Al-layered double hydroxide matrix and characterization of its luminescent properties, *J. Mol. Liq.*, 249, 318–325.
- [16] Yadav, D.K., Uma, S., and Nagarajan, R., 2023, Surfactant intercalation in Li-Al-based binary and ternary layered double hydroxides by the microwave-assisted rapid ion-exchange process and its application in iodine adsorption, *Minerals*, 13 (3), 303.
- [17] Shimamura, A., Jones, M.I., and Metson, J.B., 2013, Anionic surfactant enhanced phosphate desorption from Mg/Al-layered double hydroxides by micelle formation, *J. Colloid Interface Sci.*, 411, 1–7.
- [18] da Rocha, M.G., Nakagaki, S., Ucoski, G.M., Wypych, F., and Sippel Machado, G., 2019, Comparison between catalytic activities of two zinc layered hydroxide salts in brilliant green organic dye bleaching, *J. Colloid Interface Sci.*, 541, 425–433.
- [19] Zhang, X., Liu, J., and Ren, J., 2022, Structure and release properties of pyrethroid/sulfobutyl ether β -cyclodextrin intercalated into layered double hydroxide and layered hydroxide salt, *Front. Chem.*, 10, 894386.
- [20] Liu, J., Zhang, X., and Zhang, Y., 2015, Preparation and release behavior of chlorpyrifos adsorbed into layered zinc hydroxide nitrate intercalated with dodecylbenzenesulfonate, *ACS Appl. Mater. Interfaces*, 7 (21), 11180–11188.
- [21] Quispe-Dominguez, R., Naseem, S., Leuteritz, A., and Kuehnert, I., 2019, Synthesis and characterization of MgAl-DBS LDH/PLA composite by sonication-assisted masterbatch (SAM) melt mixing method, *RSC Adv.*, 9 (2), 658–667.
- [22] Demel, J., Hynek, J., Kovář, P., Dai, Y., Taviot-Guého, C., Demel, O., Pospíšil, M., and Lang, K., 2014, Insight into the structure of layered zinc hydroxide salts intercalated with dodecyl sulfate anions, *J. Phys. Chem. C*, 118 (46), 27131–27141.
- [23] Khan, N., and Brettmann, B., 2019, Intermolecular interactions in polyelectrolyte and surfactant complexes in solution, *Polymers*, 11 (1), 51.
- [24] Sachin, K.M., Karpe, S.A., Singh, M., and Bhattarai, A., 2018, An interaction of anionic- and cationic-rich mixed surfactants in aqueous medium through physicochemical properties at three different temperatures, *J. Chem.*, 2018, 4594062.
- [25] Sato, R., Machida, S., Sohmiya, M., Sugahara, Y., and Guégan, R., 2021, Intercalation of a cationic cyanine dye assisted by anionic surfactants within Mg–Al layered double hydroxide, *ACS Omega*, 6, 23837–23845.
- [26] He, Y., Wu, Z., Tu, L., Han, Y., Zhang, G., and Li, C., 2015, Encapsulation and characterization of slow-release microbial fertilizer from the composites of bentonite and alginate, *Appl. Clay Sci.*, 109–110, 68–75.
- [27] Biswick, T., Park, D.H., and Choy, J.H., 2012, Enhancing the UV A1 screening ability of caffeic acid by encapsulation in layered basic zinc

- hydroxide matrix, *J. Phys. Chem. Solids*, 73 (12), 1510–1513.
- [28] Muda, Z., Hashim, N., Md Isa, I., Abu Bakar, S., Mohd Ali, N., Hussein, M.Z., Mamat, M., and Sidik, S.M., 2019, Synthesis and characterization of mesoporous zinc layered hydroxide-isopropyl carb nanocomposite, *J. Saudi Chem. Soc.*, 23 (4), 486–493.
- [29] Yang, G., and Park, S.J., 2019, Conventional and microwave hydrothermal synthesis and application of functional materials: A review, *Materials*, 12 (7), 1177.
- [30] Gan, Y.X., Jayatissa, A.H., Yu, Z., Chen, X., and Li, M., 2020, Hydrothermal synthesis of nanomaterials, *J. Nanomater.*, 2020, 8917013.
- [31] Bashi, A.M., Hussein, M.Z., Zainal, Z., and Tichit, D., 2013, Synthesis and controlled release properties of 2,4-dichlorophenoxy acetate-zinc layered hydroxide nanohybrid, *J. Solid State Chem.*, 203, 19–24.
- [32] Hashim, N., Hussein, M.Z., Md Isa, I., Kamari, A., Mohamed, A., Jaafar, A.M., and Taha, H., 2014, Synthesis and controlled release of cloprop herbicides from cloprop-layered double hydroxide and cloprop-zinc-layered hydroxide nanocomposites, *Open J. Inorg. Chem.*, 4 (1), 1–9.
- [33] Hashim, N., Muda, Z., Mohd Sharif, S.N., Md Isa, I., Modh Ali, N., Ghazuli, M.R., and Hussein, M.Z., 2017, Preparation of zinc layered hydroxide–chloroacetate nanohybrid using direct reaction method, *Mater. Res. Innovations*, 21 (6), 396–400.
- [34] Mohd Foad, N.S.I., Dzulkifli, N.N., Abdullah, A., Jadam, M.L., and Sheikh Mohd Ghazali, S.A.I., 2021, Synthesis and characterisation of zinc layered hydroxide intercalated with 2-methyl-4-chlorophenoxyacetic acid and its controlled release application, *ASM Sci. J.*, 15, 580.
- [35] Hussein, M.Z., Al Ali, S.H., Zainal, Z., and Hakim, M.N., 2011, Development of antiproliferative nanohybrid compound with controlled release property using ellagic acid as the active agent, *Int. J. Nanomed.*, 6, 1373–1383.
- [36] Al Ali, S.H., Al-Qubaisi, M., Hussein, M.Z., Zainal, Z., and Hakim, M.N., 2011, Preparation of hippurate-zinc layered hydroxide nanohybrid and its synergistic effect with tamoxifen on HepG2 cell lines, *Int. J. Nanomed.*, 6 (1), 3099–3111.
- [37] Khudheyer, F.Y., Kzar, K.O., Bashi, A.M., Ali, S., Jawad, E., Faisal, A., and Al-Barry, Z.A., 2016, Ciprofloxacin intercalated with ZnO to produce a nanohybrid used as a delivery machine, *Chem. Mater. Res.*, 8 (3), 61–69.
- [38] Barahuie, F., Hussein, M.Z., Gani, S.A., Fakurazi, S., and Zainal, Z., 2014, Anticancer nanodelivery system with controlled release property based on protocatechuate–zinc layered hydroxide nanohybrid, *Int. J. Nanomed.*, 9, 3137–3149.
- [39] Adam, N., Sheikh Mohd Ghazali, S.A.I., Dzulkifli, N.N., and Hak, C.R.C., 2021, Characterization, physicochemical, controlled release studies of zinc–aluminium layered double hydroxide and zinc layered hydroxide intercalated with salicylic acid, *Bull. Mater. Sci.*, 44 (2), 155.
- [40] Sokol, D., Vieira, D.E.L., Zarkov, A., Ferreira, M.G.S., Beganskiene, A., Rubanik, V.V., Shilin, A.D., Kareiva, A., and Salak, A.N., 2019, Sonication accelerated formation of Mg–Al–phosphate layered double hydroxide via sol-gel prepared mixed metal oxides, *Sci. Rep.*, 9 (1), 10419.
- [41] Muda, Z., Hashim, N., Isa, I.M., Ali, N.M., Bakar, S.A., Mama, M., Hussein, M.Z., Bakar, N.A., and Mahamod, W.R.W., 2018, Synthesis and characterization of carbamate insecticide intercalated zinc layered hydroxide modified with sodium dodecyl sulphate, *IOP Conf. Ser.: Mater. Sci. Eng.*, 440, 012003.
- [42] Hashim, N., Muda, Z., Md Isa, I., Mohd Ali, N., Abu Bakar, S., and Hussein, M.Z., 2018, The effect of ion exchange and co-precipitation methods on the intercalation of 3-(4-methoxyphenyl)propionic acid into layered zinc hydroxide nitrate, *J. Porous Mater.*, 25 (1), 249–258.
- [43] Mishra, G., Dash, B., and Pandey, S., 2018, Layered double hydroxides: A brief review from fundamentals to application as evolving biomaterials, *J. Appl. Clay Sci.*, 153, 172–186.
- [44] Caramazana, P., Dunne, P., Gimeno-Fabra, M., McKechnie, J., and Lester, E., 2018, A review of the environmental impact of nanomaterial synthesis

- using continuous flow hydrothermal synthesis, *Curr. Opin. Green Sustainable Chem.*, 12, 57–62.
- [45] Moezzi, A., Michael, C., and Andrew, M., 2016, Transformation of zinc hydroxide chloride monohydrate to crystalline zinc oxide, *Dalton Trans.*, 45 (17), 7385–7390.
- [46] Gordeeva, A., Hsu, Y.J., Jenei, I.Z., Brant Carvalho, P.H.B., Simak, S.I., Andersson, O., and Häussermann, U., 2020, Layered zinc hydroxide dihydrate, $Zn_5(OH)_{10} \cdot 2H_2O$, from hydrothermal conversion of ϵ - $Zn(OH)_2$ at giga pascal pressures and its transformation to nanocrystalline ZnO, *ACS Omega*, 5 (28), 17617–17627.
- [47] Ahmad, R., Hussein, M.Z., Sarijo, S.H., Wan Abdul Kadir, W.R., and Yun Hin, T.Y., 2016, Synthesis and characteristics of valeric acid-zinc layered hydroxide intercalation material for insect pheromone controlled release formulation, *J. Mater.*, 2016, 1285721.
- [48] Maruyama, S.A., Tavares, S.R., Leitão, A.A., and Wypych, F., 2016, Intercalation of indigo carmine anions into zinc hydroxide salt: A novel alternative blue pigment, *Dyes Pigm.*, 128, 158–164.
- [49] Rocca, E., Caillet, C., Mesbah, A., Francois, M., and Steinmetz, J., 2006, Intercalation in zinc-layered hydroxide: Zinc hydroxyheptanoate used as protective material on zinc, *Chem. Mater.*, 18 (26), 6186–6193.
- [50] Demel, J., Kubát, P., Jirka, I., Kovář, P., Pospíšil, M., and Lang, K., 2010, Inorganic-organic hybrid materials: Layered zinc hydroxide salts with intercalated porphyrin sensitizers, *J. Phys. Chem. C*, 114 (39), 16321–16328.
- [51] Da Silva, M.L.N., Marangoni, R., Cursino, A.C.T., Schreiner, W.H., and Wypych, F., 2012, Colorful and transparent poly(vinyl alcohol) composite films filled with layered zinc hydroxide salts, intercalated with anionic orange azo dyes (methyl orange and orange II), *Mater. Chem. Phys.*, 134 (1), 392–398.
- [52] Arizaga, G.G.C., 2012, Intercalation studies of zinc hydroxide chloride: Ammonia and amino acids, *J. Solid State Chem.*, 185, 150–155.
- [53] Khadiran, N.F., Hussein, M.Z., Ahmad, R., Khadiran, T., Zainal, Z., Wan Abdul Kadir, W.R., and Hashim, S.S., 2021, Preparation and properties of zinc layered hydroxide with nitrate and phosphate as the counter anion, a novel control release fertilizer formulation, *J. Porous Mater.*, 28 (6), 1797–1811.
- [54] Abdul Aziz, I.N.F., Sarijo, S.H., Mohd Rajidi, F.S., Yahaya, R., and Musa, M., 2019, Synthesis and characterization of novel 4-aminobenzoate interleaved with zinc layered hydroxide for potential sunscreen application, *J. Porous Mater.*, 26 (3), 717–722.
- [55] Hussein, M.Z., Hashim, N., Yahaya, A.H., and Zainal, Z., 2010, Synthesis and characterization of [4-(2,4-dichlorophenoxybutyrate)-zinc layered hydroxide] nanohybrid, *Solid State Sci.*, 12 (5), 770–775.
- [56] Salleh, N.M., Mohsin, S.M.N., Sarijo, S.H., and Ghazali, S.A.I.S.M., 2017, Synthesis and physico-chemical properties of zinc layered hydroxide-4-chloro-2-methylphenoxy acetic acid (ZMCPA) nanocomposite, *IOP Conf. Ser.: Mater. Sci. Eng.*, 204, 012012.
- [57] Saifullah, B., El Zowalaty, M.E., Arulselvan, P., Fakurazi, S., Webster, T.J., Geilich, B.M., and Hussein, M.Z., 2014, Antimycobacterial, antimicrobial, and biocompatibility properties of para-aminosalicylic acid with zinc layered hydroxide and Zn/Al layered double hydroxide nanocomposite, *Drug Des., Dev. Ther.*, 8, 1029–1036.
- [58] Adam, N., Sheikh Mohd Ghazali, S.A.I., Dzulkifli, N.N., Jamion, N.A., and Jiwal, K., 2018, Synthesis and physicochemical properties of zinc layered hydroxide-cinnamate, *Int. J. Eng. Technol.*, 7 (4.47), 49–51.
- [59] Hashim, N., Mohd Sharif, S.N., Muda, Z., Md Isa, I., Mohd Ali, N., Abu Bakar, S., Sidik, S.M., and Hussein, M.Z., 2019, Preparation of zinc layered hydroxide-ferulate and coated zinc layered hydroxide ferulate nanocomposites for controlled

- release of ferulic acid, *Mater. Res. Innovations*, 23 (4), 233–245.
- [60] Abdul Latip, A.F., Hussein, M.Z., Stanslas, J., Wong, C.C., and Adnan, R., 2013, Release behavior and toxicity profiles towards A549 cell lines of ciprofloxacin from its layered zinc hydroxide intercalation compound, *Chem. Cent. J.*, 7 (1), 119–130.
- [61] Cursino, A.C.T., Rives, V., Arizaga, G.G.C., Trujillano, R., and Wypych, F., 2015, Rare earth and zinc layered hydroxide salts intercalated with the 2-aminobenzoate anion as organic luminescent sensitizer, *Mater. Res. Bull.*, 70, 336–342.
- [62] Jaafar, A.M., Anuar, A.N., Hashim, N., and Ayob, F.H., 2016, Intercalation study of curcumin into zinc layered hydroxide, *Malays. J. Anal. Sci.*, 20 (6), 1359–1364.
- [63] Abrantes Leal, D., Wypych, F., and Bruno Marino, C.E., 2020, Zinc-layered hydroxide salt intercalated with molybdate anions as a new smart nanocontainer for active corrosion protection of carbon steel, *ACS Appl. Mater. Interfaces*, 12 (17), 19823–19833.
- [64] Velazquez-Carriles, C., Macias-Rodríguez, M.E., Carbajal-Arizaga, G.G., Silva-Jara, J., Angulo, C., and Reyes-Becerril, M., 2018, Immobilizing yeast β -glucan on zinc-layered hydroxide nanoparticle improves innate immune response in fish leukocytes, *Fish Shellfish Immunol.*, 82, 504–513.
- [65] Nabipour, H., Sadr, M.H., and Thomas, N., 2015, Synthesis, characterisation and sustained release properties of layered zinc hydroxide intercalated with amoxicillin trihydrate, *J. Exp. Nanosci.*, 10 (16), 1269–1284.
- [66] de Oliveira, H.B., and Wypych, F., 2016, Evaluation of layered zinc hydroxide nitrate and zinc/nickel double hydroxide salts in the removal of chromate ions from solutions, *J. Solid State Chem.*, 243, 136–145.
- [67] Liu, P., Li, Y., Xu, Y., Qing, Y., and Han, C., 2018, Chitosan assisted synthesis of multi-layered zinc carbonate hydroxides for massive removal of Cu^{2+} from water, *J. Chil. Chem. Soc.*, 63 (1), 3819–3824.
- [68] Almasri, D.A., Essehli, R., Tong, Y., and Lawler, J., 2021, Layered zinc hydroxide as an adsorbent for phosphate removal and recovery from wastewater, *RSC Adv.*, 11 (48), 30172–30188.
- [69] Younas, F., Mustafa, A., Farooqi, Z.U.R., Wang, X., Younas, S., Mohy-Ud-Din, W., Hameed, M.A., Abrar, M.M., Maitlo, A.A., Noreen, S., and Hussain, M.M., 2021, Current and emerging adsorbent technologies for wastewater treatment: Trends, limitations, and environmental implications, *Water*, 13 (2), 215.
- [70] Jia, H.H., Xu, G.X., and Zhou, H.Y., 2012, Treatment of Pb^{2+} -containing mine wastewater with layered nanometer zinc hydroxide, *Adv. Mater. Res.*, 550-553, 2081–2084.
- [71] Yu, G., Cheng, Y., and Duan, Z., 2022, Research progress of polymers/inorganic nanocomposite electrical insulating materials, *Molecules*, 27 (22), 7867.
- [72] Ikhsani, I.U., Santosa, S.J., and Rusdiarso, B., 2016, Comparative study of Ni-Zn LHS and Mg-Al LDH adsorbents of navy blue and yellow F3G dye, *Indones. J. Chem.*, 16 (1), 36–44.
- [73] Jeevanandam, J., Barhoum, A., Chan, Y.S., Dufresne, A., and Danquah, M.K., 2018, Review on nanoparticles and nanostructured materials: history, sources, toxicity and regulations, *Beilstein J. Nanotechnol.*, 9, 1050–1074.
- [74] Ou, C., and Wang, D.W., 2021, Structural performance characteristics of nanomaterials and its application in traditional architectural cultural design and landscape planning, *Adv. Civ. Eng.*, 2021, 5531679.
- [75] Khan, Y., Sadia, H., Ali Shah, S.Z., Khan, M.N., Shah, A.A., Ullah, N., Ullah, M.F., Bibi, H., Bafakeeh, O.T., Ben Khedher, N., Eldin, S.M., Fadhil, B.M., and Khan, M.I., 2022, Classification, synthetic, and characterization approaches to nanoparticles, and their applications in various fields of nanotechnology: A review, *Catalysts*, 12 (11), 1386.
- [76] Vollath, D., Fischer, F.D., and Holec, D., 2018, Surface energy of nanoparticles - influence of particle size and structure, *Beilstein J. Nanotechnol.*, 9, 2265–2276.

- [77] Heinz, H., Pramanik, C., Heinz, O., Ding, Y., Mishra, R.K., Marchon, D., Flatt, R.J., Estrela-Lopis, I., Llop, J., Moya, S., and Ziolo, R.F., 2017, Nanoparticle decoration with surfactants: Molecular interactions, assembly, and applications, *Surf. Sci. Rep.*, 72 (1), 1–58.
- [78] Pandey, R.K., Ao, C.K., Lim, W., Sun, Y., Di, X., Nakanishi, H., and Soh, S., 2020, The relationship between static charge and shape, *ACS Cent. Sci.*, 6 (5), 704–714.
- [79] Jain, R., Mathur, M., Sikarwar, S., and Mittal, A., 2007, Removal of the hazardous dye rhodamine B through photocatalytic and adsorption treatments, *J. Environ. Manage.*, 85 (4), 956–964.
- [80] Cao, J.L., Gaojie, L., Yan, W., Guang, S., Hari, B., Xiaodong, W., and Zhanying, Z., 2014, Synthesis and characterization of hierarchical porous α -FeOOH for the adsorption and photodegradation of rhodamine B, *Int. J. Photoenergy*, 2014, 468921.
- [81] Kadam, R.L., Kim, Y., Gaikwad, S., Chang, M., Tarte N.H., and Han, S., 2020, Catalytic decolorization of rhodamine B, Congo red, and crystal violet dyes, with a novel niobium oxide anchored molybdenum (Nb–O–Mo), *Catalysts*, 10 (5), 491.
- [82] Al-Gheethi, A.A., Azhar, Q.M., Senthil Kumar, P., Yusuf, A.A., Al-Buriah, A.K., Radin Mohamed, R.M.S., and Al-shaibani, M.M., 2022, Sustainable approaches for removing rhodamine B dye using agricultural waste adsorbents: A review, *Chemosphere*, 287 (2), 132080.
- [83] Thao, N.T., Ly, D.T.H., Nga, H.T.P., and Hoan, D.M., 2016, Oxidative removal of rhodamine B over Ti-doped layered zinc hydroxide catalysts, *J. Environ. Chem. Eng.*, 4 (4, Part A), 4012–4020.
- [84] Wang, P., Guo, S., Wang, H.J., Chen, K.K., Zhang, N., Zhang, Z.M., and Lu, T.B., 2019, A broadband and strong visible-light-absorbing photosensitizer boosts hydrogen evolution, *Nat. Commun.*, 10 (1), 3155.
- [85] Taviot-Guého, C., Prévot, V., Forano, C., Renaudin, G., Mousty, C., and Leroux, F., 2017, Tailoring hybrid layered double hydroxides for the development of innovative applications, *Adv. Funct. Mater.*, 28 (27), 1703868.
- [86] Xu, R., and Xu, Y., 2017, “Functional Host–Guest Materials” in *Modern Inorganic Synthetic Chemistry*, Elsevier, Amsterdam, Netherland, 493–543.
- [87] Takagi, S., Eguchi, M., Tryk, D.A., and Inoue, H., 2006, Porphyrin photochemistry in inorganic/organic hybrid materials: Clays, layered semiconductors, nanotubes, and mesoporous materials, *J. Photochem. Photobiol., C*, 7 (2), 104–126.
- [88] Tarhini, A., Aguirre-Araque, J., Guyot, M., Costentin, C., Rogez, G., Chardon-Noblat, S., Prevot, V., and Mousty, C., 2023, Behavior of iron tetraphenylsulfonato porphyrin intercalated into LDH and LSH as materials for electrocatalytic applications, *Electrocatalysis*, 14, 111–120.
- [89] Demel, J., and Lang, K., 2012, Layered hydroxide–porphyrin hybrid materials: Synthesis, structure, and properties, *Eur. J. Inorg. Chem.*, 2012 (32), 5154–5164.
- [90] Tang, P., Feng, Y., and Li, D., 2014, Facile synthesis of multicolor organic–inorganic hybrid pigments based on layered double hydroxides, *Dyes Pigm.*, 104, 131–136.
- [91] Marzec, A., Szadkowski, B., Rogowski, J., Maniukiewicz, W., Moszyński, D., Rybiński, P., and Zaborski, M., 2019, Carminic acid stabilized with aluminum-magnesium hydroxycarbonate as new colorant reducing flammability of polymer composites, *Molecules*, 24 (3), 560.
- [92] Wang, X., Lu, J., Shi, W., Li, F., Wei, M., Evans, D.G., and Duan, X., 2010, A thermochromic thin film based on host-guest interactions in a layered double hydroxide, *Langmuir*, 26 (2), 1247–1253.
- [93] Zhang, F.D., Chang, G.L., Shu, J.D., Haralampos, N.M., and Yu, F.S., 2021, Direct molecular confinement in layered double hydroxides: From fundamental to advanced photo-luminescent hybrid materials, *Inorg. Chem. Front.*, 8, 1324–1333.
- [94] Gao, R., Yan, D., and Duan, X., 2021, Layered double hydroxides-based smart luminescent materials and the tuning of their excited states, *Cell Rep. Phys. Sci.*, 2 (8), 100536.
- [95] Mosinger, J., Lang, K., and Kubát, P., 2016, Photoactivatable nanostructured surfaces for

- biomedical applications, *Top. Curr. Chem.*, 370, 135–168.
- [96] Xu, J., Cai, E., Zhang, S., Fan, X., Wang, M., Lou, F., Wang, M., Wang, X., and Xu, L., 2021, Nickel-vanadium layered double hydroxide nanosheets as the saturable absorber for a passively Q-switched 2 μm solid-state laser, *Appl. Opt.*, 60 (7), 1851–1855.
- [97] Chakraborty, P., Singh, P., Singh, J., and Tripathi, A., 2019, Novel layered Zn-Y hydroxide and study of their UV properties by intercalation of organic aliphatic and aromatic UV-absorbent molecules, *AIP Conf. Proc.*, 2142 (1), 180001.
- [98] Lerner, D.A., Bégu, S., Aubert-Pouëssel, A., Polexe, R., Devoisselle, J.M., Azais, T., and Tichit, D., 2020, Synthesis and properties of new multilayer chitosan@layered double hydroxide/drug loaded phospholipid bilayer nanocomposite bio-hybrids, *Materials*, 13 (16), 3565.
- [99] Kalepu, S., and Nekkanti, V., 2015, Insoluble drug delivery strategies: Review of recent advances and business prospects, *Acta Pharm. Sin. B*, 5 (5), 442–453.
- [100] Göke, K., Lorenz, T., Repanas, A., Schneider, F., Steiner, D., Baumann, K., Bunjes, H., Dietzel, A., Finke, J.H., Glasmacher, B., and Kwade, A., 2018, Novel strategies for the formulation and processing of poorly water-soluble drugs, *Eur. J. Pharm. Biopharm.*, 126, 40–56.
- [101] Boyd, B.J., Bergström, C.A.S., Vinarov, Z., Kuentz, M., Brouwers, J., Augustijns, P., Brandl, M., Bernkop-Schnürch, A., Shrestha, N., Prétat, V., Müllertz, A., Bauer-Brandl, A., and Jannin, V., 2019, Successful oral delivery of poorly water-soluble drugs both depends on the intraluminal behavior of drugs and of appropriate advanced drug delivery systems, *Eur. J. Pharm. Sci.*, 137, 104967.
- [102] Yang, J.H., Han, Y.S., Park, M., Park, T., Hwang, S.J., and Choy, J.H., 2007, New inorganic-based drug delivery system of indole-3-acetic acid-layered metal hydroxide nanohybrids with controlled release rate, *Chem. Mater.*, 19 (10), 2679–2685.
- [103] Hasan, S., Al Ali, H., Al-Qubaisi, M., Hussein, M.Z., Ismail, M., Zainal, Z., and Hakim, M.N., 2012, Controlled-release formulation of antihistamine based on cetirizine zinc-layered hydroxide nanocomposites and its effect on histamine release from basophilic leukemia (RBL-2H3) cells, *Int. J. Nanomed.*, 7, 3351–3363.
- [104] Ramli, M., Hussein, M.Z., and Yusof, K., 2013, Preparation and characterization of an anti-inflammatory agent based on a zinc-layered hydroxide-salicylate nanohybrid and its effect on viability of Vero-3 cells, *Int. J. Nanomed.*, 8, 297–306.
- [105] Saifullah, B., Arulselvan, P., Fakurazi, S., Webster, T.J., Bullo, N., Hussein, M.Z., and El Zowalaty, M.E., 2022, Development of a novel anti-tuberculosis nanodelivery formulation using magnesium layered hydroxide as the nanocarrier and pyrazinamide as a model drug, *Sci. Rep.*, 12 (1), 14086.
- [106] Akter, F., Muhury, R., Sultana, A., and Deb, U.K., 2022, A comprehensive review of mathematical modeling for drying processes of fruits and vegetables, *Int. J. Food Sci.*, 2022, 6195257.
- [107] Ramteke, K.H., Dighe, P.A., Kharat, A.R., and Patil, S.V., 2014, Mathematical models of drug dissolution: A review, *Scholars Acad. J. Pharm.*, 3 (5), 388–396.
- [108] Raza, S.N., and Khan, N.A., 2017, Role of mathematical modelling in controlled release drug delivery, *Int. J. Med. Res. Pharm. Sci.*, 4 (5), 84–95.
- [109] Trucillo, P., 2022, Drug carriers: A review on the most used mathematical models for drug release, *Processes*, 10 (6), 1094.
- [110] Mansfeld, F.M., Davis, T.P., and Kavallaris, M., 2017, “Nanotechnology in Medical Research” in *Micro- and Nanotechnology in Vaccine Development*, Eds. Skwarczynski, M., and Toth, I., William Andrew Publishing, Norwich, New York, US, 21–45.
- [111] Bruschi, M.L., 2015, *Strategies to Modify the Drug Release from Pharmaceutical Systems*, Woodhead Publishing, Kidlington, UK.
- [112] Abbasnezhad, N., Kebdani, M., Shirinbayan, M., Champmartin, S., Tcharkhtchi, A., Kouidri, S., and Bakir, F., 2021, Development of a model based on physical mechanisms for the explanation of drug

- release: Application to diclofenac release from polyurethane films, *Polymers*, 13 (8), 1230.
- [113] Mircioiu, C., Voicu, V., Anuta, V., Tudose, A., Celia, C., Paolino, D., Fresta, M., Sandulovici, R., and Mircioiu, I., 2019, Mathematical modeling of release kinetics from supramolecular drug delivery systems, *Pharmaceutics*, 11 (3), 140.
- [114] Malekjani, N., and Jafari, S.M., 2020, Modeling the release of food bioactive ingredients from carriers/nanocarriers by the empirical, semiempirical, and mechanistic models, *Compr. Rev. Food Sci. Food Saf.*, 20 (1), 3–47.
- [115] Chiarappa, G., Abrami, M., Dapas, B., Farra, R., Trebez, F., Musiani, F., Grassi, G., and Grassi, M., 2017, Mathematical modeling of drug release from natural polysaccharides based matrices, *Nat. Prod. Commun.*, 12 (6), 873–880.
- [116] Öztürk, Y., Gülsu, A., and Gülsu, M., 2013, A numerical approach for solving modified epidemiological model for drug release systems, *Nevşehir Bilim. Teknol. Derg.*, 2 (2), 56–64.
- [117] Magnani, C., Isaac, V.L.B., Correa, M.A., and Salgado, H.R.N., 2014, Caffeic acid: A review of its potential use in medications and cosmetics, *Anal. Methods*, 6 (10), 3203–3210.
- [118] Fernandes, I.A.A., Maciel, G.M., Ribeiro, V.R., Rossetto, R., Pedro, A.C., and Haminiuk, C.W.I., 2021, The role of bacterial cellulose loaded with plant phenolics in prevention of UV-induced skin damage, *Carbohydr. Polym. Technol. Appl.*, 2, 100122.
- [119] Kumar, N., and Pruthi, V., 2014, Potential applications of ferulic acid from natural sources, *Biotechnol. Rep.*, 4, 86–93.
- [120] Usman, M.S., Hussein, M.Z., Kura, A.U., Fakurazi, S., Masarudin, M.J., and Ahmad Saad, F.F., 2018, Synthesis and characterization of protocatechuic acid-loaded gadolinium-layered double hydroxide and gold nanocomposite for theranostic application, *Appl. Nanosci.*, 8 (5), 973–986.
- [121] AbouAitah, K., Piotrowska, U., Wojnarowicz, J., Swiderska-Sroda, A., El-Desoky, A.H.H., and Lojkowski, W., 2021, Enhanced activity and sustained release of protocatechuic acid, a natural antibacterial agent, from hybrid nanoformulations with zinc oxide nanoparticles, *Int. J. Mol. Sci.*, 22 (10), 5287.
- [122] Kuen, C.Y., Tiew, G., Fakurazi, S., Othman, S.S., and Masarudin, M.J., 2020, Increased cytotoxic efficacy of protocatechuic acid in A549 human lung cancer delivered via hydrophobically modified-chitosan nanoparticles as an anticancer modality, *Polymers*, 12 (9), 1951.
- [123] Saifullah, B., Hussein, M.Z., Hussein-Al-Ali, S.H., Arulselvan, P., and Fakurazi, S., 2013, Sustained release formulation of an anti-tuberculosis drug based on paraamino salicylic acid-zinc layered hydroxide nanocomposite, *Chem. Cent. J.*, 7 (1), 72–83.
- [124] Najem Abed, N.A.R., Abudoleh, S.M., Alshawabkeh, I.D., Najem Abed, A.R., Abuthawabeh, R.K.A., and Hussein-Al-Ali, S.H., 2017, Aspirin drug intercalated into zinc-layered hydroxides as nanolayers: Structure and *in vitro* release, *Nano Hybrids Compos.*, 18, 42–52.
- [125] Ramimoghadam, D., Hussein, M.Z., and Taufiq-Yap, Y.H., 2012, The effect of sodium dodecyl sulfate (SDS) and cetyltrimethylammonium bromide (CTAB) on the properties of ZnO synthesized by hydrothermal method, *Int. J. Mol. Sci.*, 13 (10), 13275–13293.
- [126] Muda, Z., Hashim, N., Isa, I.M., Bakar, S.A., Saidin, M.I., Ahmad, M.S., Mamat, M., and Hussein, M.Z., 2020, Carbamate insecticide release kinetics for controlled release formulation of isoprocarb insecticide from modified zinc layered hydroxide nanocomposite, *J. Mater. Environ. Sci.*, 11 (3), 378–388.
- [127] Hussein, M.Z., Nazarudin, N.F., Sarijo, S.H., and Yarmo, M.A., 2012, Synthesis of a layered organic-inorganic nanohybrid of 4-chlorophenoxyacetate-zinc layered hydroxide with sustained release properties, *J. Nanomater.*, 2012, 860352.
- [128] Hussein, M.Z., Abdul Rahman, N.S.S., Sarijo, S.H., and Zainal, Z., 2012, Herbicide intercalated zinc layered hydroxide nanohybrid for a dual-guest controlled release formulation, *Int. J. Mol. Sci.*, 13 (6), 7328–7342.

- [129] Navath, S., 2021, Design and synthesis of capecitabine-tris(nonofluorotert-butyl) a highly symmetrical fluorinated hydrocarbons as multifunctional image-guided drug delivery vehicles using CuAAC reaction, *J. Drug Delivery Controlled Release*, 1, 1–7.
- [130] Grassi, M., and Grassi, G., 2014, Application of mathematical modeling in sustained release delivery systems, *Expert Opin. Drug Delivery*, 11 (8), 1299–1321.
- [131] Wang, S., Liu, R., Fu, Y., and Kao, W.J., 2020, Release mechanisms and applications of drug delivery systems for extended-release, *Expert Opin. Drug Delivery*, 17 (9), 1289–1304.
- [132] Heng, P.W.S., 2018, Controlled release drug delivery systems, *Pharm. Dev. Technol.*, 23 (9), 833.
- [133] Irfan, S.A., Razali, R., KuShaari, K., Mansor, N., Azeem, B., and Versypt, A.N.F., 2018, A review of mathematical modeling and simulation of controlled-release fertilizers, *J. Controlled Release*, 271, 45–54.
- [134] Banerjee, S., Mazumder, S., Chatterjee, D., Bose, S., and Majee, S.B., 2022, “Nanotechnology for cargo delivery with a special emphasis on pesticide, herbicide, and fertilizer” in *Nano-enabled Agrochemicals in Agriculture*, Eds. Ghorbanpour, M., and Shahid, M.A., Elsevier Academic Press, Oxford, 105–136.
- [135] Ahmad, R., Hussein, M.Z., Wan Abdul Kadir, W.R., Sarijo, S.H., and Yun Hin, T.Y., 2015, Evaluation of controlled-release property and phytotoxicity effect of insect pheromone zinc-layered hydroxide nanohybrid intercalated with hexenoic acid, *J. Agric. Food Chem.*, 63 (51), 10893–10902.
- [136] Mohd Sharif, S.N., Hashim, N., Md Isa, I., Abu Bakar, S., Saidin, M.I., Ahmad, M.S., Mamat, M., Hussein, M.Z., Zainul, R., and Kamari, A., 2021, The effect of swellable carboxymethyl cellulose coating on the physicochemical stability and release profile of a zinc hydroxide nitrate–sodium dodecylsulphate–imidacloprid, *Chem. Phys. Impact*, 2, 100017.
- [137] Mohd Sharif, S.N., Hashim, N., Md Isa, I., Abu Bakar, S., Saidin, M.I., Ahmad, M.S., Mamat, M., Hussein, M.Z., and Zainul, R., 2021, Carboxymethyl cellulose hydrogel based formulations of zinc hydroxide nitrate-sodium dodecylsulphate-bispyribac nanocomposite: Advancements in controlled release formulation of herbicide, *J. Nanosci. Nanotechnol.*, 21 (21), 5867–5880.
- [138] MadJin, H.M., Hashim, N., Md Isa, I., Hussein, M.Z., Abu Bakar, S., Mamat, M., Ahmad, R., and Zainul, R., 2020, Synthesis and characterisation of zinc hydroxides nitrates–sodium dodecyl sulphate fluazinam nano hosts for release properties, *J. Porous Mater.*, 27 (5), 1467–1479.